Investigation of iodine plasmas for space propulsion applications

Benjamin Esteves

INSTITUT POLYTECHNIQUE DE PARIS

NNT : 2022IPPAX134

Thèse de doctorat

Investigation of iodine plasmas for space propulsion applications

Thèse de doctorat de l'Institut Polytechnique de Paris
préparée à l'École polytechnique

École doctorale n°626 École doctorale de l'Institut Polytechnique de Paris (EDIPP)
Spécialité de doctorat : Laser et Plasma

Thèse présentée et soutenue à Palaiseau, le 13 Décembre 2022, par

BENJAMIN ESTEVES

Composition du Jury :

Jérôme Perez Professeur, ENSTA Paris	Président
Stéphane Mazouffre Directeur de recherche, CNRS-ICARE	Rapporteur
Daniel Comparat Directeur de recherche, CNRS-LAC	Rapporteur
Trevor Lafleur Senior scientist, ThrustMe	Examinateur
Emilie Despiau-Pujo Maître de conférence, Université Grenoble-Alpes	Examinateur
Olivier Duchemin Ingénieur, Safran	Examinateur
Pascal Chabert Directeur de recherche, CNRS-LPP	Directeur de thèse
Cyril Drag Directeur de recherche, CNRS-LPP	Co-directeur de thèse

Investigation of iodine plasmas for space propulsion applications

Benjamin Esteves

Dissertation submitted in partial satisfaction of
the requirements for the degree of
Philosophiae Doctor

in

Plasma Physics

of the

Institut Polytechnique de Paris at **École polytechnique**.

Supervisor: Pascal Chabert

Co-supervisors: Cyril Drag & Anne Bourdon

This work was funded by École polytechnique and
Agence Innovation Défense de la Délégation Générale de L'Armement.

Successfully defended on December 13, 2022.

No amount of experimentation can ever prove me right; a single experiment can prove me wrong.

Albert Einstein

La vraie science est une ignorance qui se sait.

Michel de Montaigne

La racine du travail est parfois amère, mais la saveur de ses fruits est toujours exquise.

Victor Hugo

RÉSUMÉ

Depuis les années 1960, le gaz privilégié dans le domaine de la propulsion spatiale électrique est le xénon, un atome lourd et facile à ioniser. Néanmoins, bien que produit de la distillation de l'air, a priori inépuisable, la très faible concentration de xénon dans l'atmosphère limite sa production annuelle et la demande grandissante obligent à trouver une alternative pérenne, aux performances comparables.

L'iode, élément voisin du xénon dans le tableau périodique, est un candidat viable pour lui succéder malgré sa nature moléculaire et électronégative. Dans ce travail, nous tâchons de comprendre comment et pourquoi l'iode, à l'état plasma, peut envisager sereinement la bataille avec ses concurrents, et notamment le krypton, dans la course à l'espace. L'étude des plasmas d'iode, à basse pression, a été menée dans deux directions complémentaires.

D'une part, ont été mis en place et développés, deux montages expérimentaux de plasmas d'iode (un propulseur à grille et une cellule en quartz) au sein desquels de nombreux diagnostiques électriques et optiques (sonde de Langmuir, photodétachement des ions négatifs I^-, absorption sur des états atomiques excités, TALIF sur le niveau atomique fondamental) ont été développés et appliqués avec succès, dont certains pour la première fois. Ces travaux expérimentaux ont permis de mesurer les valeurs absolues de différentes espèces du plasmas (électrons, ions négatifs I^-, ions positifs, molécules, différence de population entre les deux premiers états atomiques), de mettre en évidence la présence non négligeable d'un état atomique excité à 0.94 eV, de décaler tous les niveaux excités atomiques de 0.167 cm^{-1} vers le bas par rapport à la table spectroscopique de référence ou encore de mesurer le degré de dissociation moléculaire, avoisinant pour une puissance suffisante, plus de 95 %. Également, la température des atomes a été mesurée et des mécanismes de chauffage bien plus prégnants que dans des plasmas de gaz nobles ont été mis en lumière et discutés.

D'autre part, un travail rigoureux de bibliographie sur les données collisionnelles (recensement et questionnement des sections efficaces et taux de réaction mesurés ou calculés) de l'iode atomique et moléculaire, a permis de développer des outils de simulation numérique visant à reproduire le fonctionnement des plasmas d'iode. Premièrement, un modèle global, moyenné en volume et permettant de décrire les caractéristiques essentielles du plasma, a été largement mis à jour avec le nouveau jeu de sections efficaces et enrichi pour prendre en compte le chauffage des espèces neutres. Deuxièmement, un modèle multi-fluide unidimensionnel des trois

espèces neutres majoritaires dans un plasma d'iode (atome dans son niveau fondamental $I(^2P^\circ_{3/2})$, premier état atomique excité $I(^2P^\circ_{1/2})$ et molécule I_2) a été développé afin de simuler leurs densités, vitesses et températures le long de l'axe de poussée du propulseur. Les termes d'inertie et les flux de chaleur de chaque espèce ont été pris en compte.

Les comparaisons entre les expériences et les modèles se sont révélées pertinentes et ont permis de dresser plusieurs conclusions. A faible flux d'injection ou faible pression (autour de 1 mTorr pour notre propulseur), le plasma est complètement dissocié et se comporte comme un plasma de gaz noble, composé quasi uniquement d'atomes, d'ions atomiques positifs I^+ et d'électrons. C'est dans ce régime de fonctionnement, où la dissociation est peu coûteuse énergétiquement, que l'iode peut révolutionner le domaine de la propulsion électrique en étant plus efficace que ses concurrents nobles (argon, krypton et xénon) pour produire des ions, et donc engendrer une meilleure poussée. A plus haut débit, en revanche, les molécules I_2 ne sont plus négligeables et produisent facilement des ions négatifs I^- et moléculaires I_2^+. Dans ces conditions là, l'iode n'est plus du tout compétitif pour la propulsion, le krypton offrant même de meilleures performances.

ABSTRACT

Since the 1960s, the most used gas for electric space propulsion has been xenon, a heavy atom that is easy to ionise. However, although it is a product of air distillation, which is a priori inexhaustible, the very low concentration of xenon in the atmosphere limits its annual production and the growing demand makes it necessary to find a sustainable alternative with comparable performance.

Iodine, an element next to xenon in the periodic table, is a viable candidate to succeed it despite its molecular and electronegative nature. In this work, we try to understand how and why iodine, in its plasma state, can serenely consider the battle with its competitors, and in particular krypton, in the space race. The study of low-pressure iodine plasmas was conducted in two complementary directions.

On the one hand, two experimental iodine plasma set-ups (a gridded-ion-thruster and a quartz cell) were set up and developed, within which numerous electrical and optical diagnostics (Langmuir probe, photodetachment of negative I^- ions, absorption on excited atomic states, TALIF on the fundamental atomic level) were developed and successfully applied, some of them for the first time. These experimental works allowed to measure the absolute values of different species of the plasma (electrons, I^- negative ions, positive ions, molecules, population difference between the first two atomic states), to highlight the non-negligible presence of an excited atomic state at 0.94 eV, to shift all the excited atomic levels downwards by 0.167 cm^{-1} with respect to the reference spectroscopic table, or to measure the degree of molecular dissociation, approaching, for a sufficient power, more than 95 %. Also, the temperature of the atoms was measured and heating mechanisms much more prevalent than in noble gas plasmas were brought to light and discussed.

On the other hand, a rigorous bibliography on collisional data (census and questioning of the effective sections and reaction rates measured or calculated) of atomic and molecular iodine, allowed the development of numerical simulation tools aiming at reproducing the functioning of iodine plasmas. Firstly, a global model, averaged in volume and allowing the description of the essential characteristics of the plasma, was largely updated with the new set of cross-sections and enriched to take into account the heating of neutral species. Secondly, a one-dimensional multi-fluid model of the three major neutral species in an iodine plasma (atom in its ground state $I(^2P^\circ_{3/2})$, first excited atomic state $I(^2P^\circ_{1/2})$ and molecule I_2) has been developed to simulate their densities, velocities and temperatures along the thrust axis of the thruster. The inertia terms and heat fluxes of each species were taken into account.

Comparisons between experiments and models proved to be relevant and led to several conclusions. At low injection flux or pressure (around 1 mTorr for our thruster), the plasma is completely dissociated and behaves like a noble gas plasma, composed almost entirely of atoms, I^+ atomic positive ions and electrons. It is in this operating regime, where dissociation is energetically inexpensive, that iodine can revolutionise the field of electric propulsion by being more efficient than its noble competitors (argon, krypton and xenon) in producing ions, and thus generating better thrust. At higher rates, however, the I_2 molecules are no longer negligible and easily produce negative I^- and molecular I_2^+ ions. Under these conditions, iodine is no longer competitive for propulsion, with krypton offering even better performance.

ACKNOWLEDGEMENTS

Since most of the people I wish to thank are French-speaking, the following will be written in the language of Molière.

Pour entamer cette section, je tenais à remercier Jérôme Pérez d'avoir accepté la présidence du jury de soutenance de mon doctorat. J'en profite pour souligner sa bienveillance et son soutien sans faille dès notre première rencontre à l'ENSTA Paris en 2016. Son goût pour la physique, sa rigueur ainsi que le soin avec lequel il transmet sa passion ont été déterminants dans mon envie de conclure mes études par une thèse en physique.

Je tiens à remercier sincèrement Stéphane Mazouffre et Daniel Comparat pour avoir examiné avec précision le manuscrit. Leurs consciencieux rapports et leur retours positifs m'ont permis d'aborder plus sereinement la soutenance. Je remercie également Emilie Despiau-Pujo, Olivier Duchemin (mon nouveau collègue chez Safran Spacecraft Propulsion) et Trevor Lafleur (dont la rencontre au Japon a décuplé ma motivation pour les années à venir, nos collaborations futures me réjouissent d'avance) d'avoir accepté de faire partie du jury pour la soutenance.

C'est maintenant l'occasion de remercier les deux derniers membres du jury, à savoir Pascal Chabert et Cyril Drag, respectivement mon directeur et co-directeur de thèse.

Pascal m'a permis de réaliser une thèse sur un sujet passionnant. Il est celui qui, avec générosité, n'a pas hésité à me laisser m'épanouir dans son domaine de prédilection. Sans lui, pas de propulsion spatiale électrique à l'Ecole polytechnique, encore moins d'utilisation de l'iode dans un propulseur. Ses conseils se sont toujours avérés justes, il est celui qui a dessiné les grandes orientations et les axes de mon sujet de recherche. Malgré toutes les sollicitations qu'il reçoit, il a toujours répondu présent quand j'en exprimais le besoin, m'a permis d'explorer des directions qui n'étaient pas forcément les plus simples ou les plus directes mais qui *in fine* me permirent d'étoffer ma compréhension globale du sujet : Pascal m'a offert une immense liberté de recherche. Durant plus de trois ans, notre relation amicale ne s'est jamais dégradée voire distendue. Je mesure à quel point il est difficile d'obtenir pleine satisfaction de son doctorat (à la fois humainement et scientifique-

ment) mais je peux aujourd'hui l'affirmer avec fierté, si je devais changer quelque chose, je ne changerais rien : merci Pascal pour cette aventure !

Cyril fut, de son côté, mon guide expérimental, présent au quotidien, toujours de bonne humeur, celui qui transforme le travail en passion et plaisir. Il fut toujours là pour me remonter le moral les jours où rien ne semblait fonctionner. Il est celui dont la rigueur ne laisse aucune place au hasard : tout doit être vérifié, compris et maîtrisé plutôt deux fois qu'une. Il fut plus qu'un collègue, un compagnon de salle d'expérience, un passionné de physique, un curieux de tout. Nous avons passé tellement d'heures côte-à-côte à faire et refaire des calculs, analyses de données et signaux optiques, sans jamais se démotiver ni perdre le sourire. Notre relation s'est renforcée au fil des mois pour devenir un véritable point de repère, indispensable pour mener à bien mon doctorat comme je l'avais imaginé initialement. Merci du fond du coeur Cyril, je suis ravi que nos carrières ne se séparent pas tout de suite.

Pour poursuivre cette section de remerciements, comment ne pas remercier celle avec qui tout a commencé, Anne Bourdon. C'est Anne, qui à l'automne 2018, a répondu favorablement à ma sollicitation pour faire un projet de recherche hebdomadaire au LPP. Ce projet s'est vite transformé en stage de fin d'études avant d'aboutir à la présente thèse. Anne est dotée de qualités humaines et scientifiques extrêmement rares de nos jours. Toujours souriante et à l'écoute, elle m'a immédiatement donné confiance et mis à l'aise. Si venir au laboratoire n'a jamais été contraignant c'est en grande partie grâce à sa joie de vivre communicative, Anne, merci.

Je souhaite également remercier Alejandro Alvarez Laguna, un futur très grand Monsieur du domaine de la physique des plasmas. Alex m'a accompagné dès mes premiers pas au LPP. Depuis, il est devenu plus qu'un collègue, un véritable ami. Cette thèse serait bien plus courte et moins solide sans son aide et ses conseils d'expert pour développer un modèle fluide inédit et pourtant crucial pour la compréhension du sujet. Il est adorable, abordable et tellement compétent...

Evidemment, dans l'équipe des plasmas froids du LPP, je n'étais pas le seul étudiant embarqué dans un périple dont les conclusions ne se dessinent qu'après des milliers d'heures de labeur. Je souhaite d'abord remercier mes prédécesseurs Florian Marmuse et Romain Lucken qui ont assuré une merveilleuse passation de leurs connaissance, outils et méthodes de travail. Grâce à eux, je me suis retrouvé dans des conditions idéales pour débuter sereinement un doctorat. Je remercie également Antoine Tavant et Thomas Charoy avec qui je n'ai jamais directement travaillé mais qui ont fait régner une ambiance de travail à la fois agréable et studieuse. J'adresse un merci tout particulier à ceux que j'ai cotoyés au quotidien et avec qui j'ai eu l'honneur de partager le PhDrium : Federico Petronio, Tarek Ben Slimane, Nicolas Lequette et Edmond Baratte. Plus que des collègues de travail, ce sont devenus des amis avec qui j'ai adoré rire, voyager et échanger sur n'importe quel sujet.

Je remercie également les différents collègues du LPP avec qui j'ai toujours pris plaisir à échanger ou travailler : Olivier Guaitella, Christophe Blondel, Jean-Luc Raimbault, David Pai ou encore Jean-Paul Booth. Les équipes techniques (Bruno Dufour, Pascal Pariset, Nadjirou Ba et Garrett Curley) ont été d'un soutien précieux

tout au long de la thèse et leur savoir-faire m'a permis d'appréhender bien plus facilement la salle d'expériences. Je remercie également les équipes informatiques et admnistratives du laboratoire avec une pensée particulière pour Catherine Jégu.

Je tiens à remercier ici tous ceux qui ont fait l'effort d'assister à ma soutenance de thèse. Mes amis depuis toujours et pour la vie : Charlotte et Clément ; mes copains des années rugby à Clermont, compagnons de *la Meute* : Rubi, Charnouille, Lantu et Hanz ; mes copains de l'ENSTA : Rouzoul et Valentin ; des connaissances plus récentes comme Maëva, Vergnes et Camille ou encore ma future belle-mère Catherine. Je remercie également ceux qui n'ont pas pu être là mais dont j'avais l'entier soutien : Brubru, Josselin, Poison, Xavi, Lulu et les autres qui m'ont suivi à distance. Aussi, j'ai une pensée pour tout ceux que j'oublierais de mentionner.

Pour clôre cette section, je souhaiterais prendre le temps de remercier les êtres les plus chers à mon coeur. Je remercie donc mes frères Adrien et Josselin qui, je le sais, seront toujours là pour m'épauler ou me détruire les épaules… Je pense à mes parents, Florence et Antonio, sans qui je ne serais pas devenu le même homme. Qu'ils soient assurés de la fierté que cela représente d'être leur fils. Ils m'ont toujours soutenu et accompagné sans jamais me juger ni se désunir, merci pour tout. J'espère les avoir rendu aussi fiers qu'ils me rendent heureux. Je remercie enfin Constance, mon ange, ma fiancée, qui a fait preuve d'une patience incroyable afin que je concrétise le présent manuscrit. Notre rencontre a changé ma vie et fait de moi un homme comblé. Sa joie de vivre, son humour et son amour m'ont permis de tenir : je lui dédie cet ouvrage.

J'ai finalement une pensée émue pour mes proches disparus que j'espère rendre fiers où qu'ils se trouvent.

RELATED PUBLICATIONS AND PRESENTATIONS

Publications in peer-reviewed journals

- B. Esteves, F. Marmuse, C. Drag, A. Bourdon, A. Alvarez Laguna and P. Chabert. ***Experimental and numerical investigation of iodine plasmas for space propulsion applications.*** Plasma Sources Science and Technology **31**, 085007 (2022) [1].
  Work related to Chapter 3 and Chapter 5.

- B. Esteves, C. Blondel, P. Chabert and C. Drag. ***Two-photon absorption laser induced fluorescence (TALIF) detection of atomic iodine in low-temperature plasmas and a revision of the energy levels of I I.*** Journal of Physics B: Atomic, Molecular and Optical Physics (Accepted on Jan., 2023) [2].
  Work related to Chapter 4 and Appendix D.

- A. Alvarez Laguna, B. Esteves, A. Bourdon and P. Chabert. ***A regularized high-order moment model to capture non-Maxwellian electron energy distribution function.*** Physics of Plasmas **29**, 083507 (2022) [3].
  Work related to Chapter 6 and Appendix C.

- A. Alvarez Laguna, B. Esteves, J.-L. Raimbault, A. Bourdon and P. Chabert. ***Discussion on the transport processes in electrons with non-Maxwellian energy distribution function in partially-ionized plasmas.*** Plasma Physics and Controlled Fusion (Submitted in Nov., 2022) [4]
  Work related to Chapter 3.

Proceedings

- B. Esteves, C. Drag, A. Bourdon, A. Alvarez Laguna, P. Chabert. ***Experimental and numerical investigation of a gridded ion thruster running with different propellants (I_2, Xe, Kr, Ar).*** 37th International Electric Propulsion Conference, IEPC-2022-416 [5].
  Work related to Chapter 2, Chapter 3 and Chapter 5.

Oral contributions

- B. Esteves, C. Drag, A. Bourdon, A. Alvarez Laguna and P. Chabert. ***Experimental and numerical investigation of low-pressure iodine plasmas.*** 75th Gaseous Electronics Conference, 2022, Sendai, Japan.
  One of the five **Student Award for Excellence** finalists.
  Work related to Chapter 3, Chapter 4 and Chapter 6.

- A. Bourdon, B. Esteves, N. Lequette, A. Alvarez Laguna, C. Drag and P. Chabert. ***Chemistry of low-pressure iodine plasmas.*** 75th Gaseous Electronics Conference, 2022, Sendai, Japan.
  Work related to Chapter 1.

- B. Esteves, C. Drag, A. Bourdon, A. Alvarez Laguna, P. Chabert. ***Experimental and numerical investigation of a gridded ion thruster running with different propellants (I_2, Xe, Kr, Ar).*** 37th International Electric Propulsion Conference, 2022, Boston, USA.
  Work related to Chapter 2, Chapter 3 and Chapter 5.

- B. Esteves, A. Alvarez Laguna, A. Bourdon, C. Drag and P. Chabert. ***Diagnostics expérimentaux des espèces négatives dans le propulseur PEGASES fonctionnant à l'iode.*** GDR EMILI, 2021, Palaiseau, France.
  Work related to Chapter 3.

- B. Esteves, A. Alvarez Laguna, A. Bourdon, C. Drag and P. Chabert. ***Experimental diagnostics of negative species in low pressure non-magnetized iodine plasmas.*** PLAS@PAR Scientific day, 2021, Paris, France.
  Work related to Chapter 3.

- B. Esteves, A. Alvarez Laguna, A. Bourdon, C. Drag and P. Chabert. ***Experimental diagnostics for electrons and atoms in low pressure iodine plasmas.*** 74th Gaseous Electronics Conference, 2021, remote participation.
  Work related to Chapter 3.

- B. Esteves, A. Alvarez Laguna, A. Bourdon, C. Drag and P. Chabert. ***Spatially resolved Langmuir probe measurements in a non magnetized iodine ICP thruster.*** 36th International Electric Propulsion Conference, 2021, remote participation.
  Work related to Chapter 3.

Posters

- B. Esteves , P. Chabert, C. Blondel and C. Drag. ***Optical diagnostics of neutral species in iodine plasmas.*** ESCAMPIG, 2022, Paris, France.
  Work related to Chapter 4.

LIST OF ACRONYMS

0D	Zero Dimension
1D	One Dimension
2D	Two Dimensions
3D	Three Dimensions
BPBSR	Breit-Pauli B-Spline R-matrix
CFL	Courant-Friedrichs-Lewy
CI-MBPT	Configuration-Interaction Many-Body Perturbation Theory
CRC	Chemical Rubber Company
CRM	Collisional Radiative Model
CW	Continuous Wave
DC	Direct Current
DEA	Dissociative Electron Attachment
DESIREE	Double ElectroStatic Ion Ring ExpEriment
EEDF	Electron Energy Distribution Function
EEPF	Electron Energy Probability Function
EP	Electric Propulsion
FWHM	Full Width at Half Maximum
ICP	Inductively Coupled Plasma
IR	Infrared
LCPMR	Laboratoire de Chimie Physique - Matière et Rayonnement
LIF	Laser Induced Fluorescence
LP	Langmuir Probe
LPP	Laboratoire de Physique des Plasmas
MFPA	Multifunction Plasma Probe Analyser
MP	Measuring Probe (Langmuir probe measurements)
MUSCL	Monotonic Upwind Scheme for Conservation Laws
NIST	National Institute of Standards and Technology

ODE	Ordinary Differential Equation
PD	Photodetachment
PEGASES	Propulsion with Electronegative GASES
PIC	Particle-In-Cell
PMT	Photomultiplier Tube
PTE	Power Transfer Efficiency
RF	Radio Frequency
RP	Reference Probe (Langmuir probe measurements)
TALIF	Two-photon Absorption Laser Induced Fluorescence
TVD	Total Variation Diminishing
UV	Ultraviolet
VT	Vibrational Translational

CONTENTS

LIST OF FIGURES

LIST OF TABLES

INTRODUCTION

Plasma propulsion engines are based on obtaining force through an accelerated quasi-neutral plasma. The idea is one century old [6], with implementations beginning in the 1960s and ongoing investigations [7]. Standard plasma thrusters have in common that they accelerate positive xenon ions (Xe^+) to produce thrust and are now routinely used on both space missions and commercial satellites. Xenon has been the most used propellant mainly because of its high mass and low ionisation energy, two key parameters for a good thrust-to-power ratio. Nowadays, however, xenon hegemony is mainly questioned for its cost, its scarcity, and its need for a compressed gas handling: an alternative propellant is saught.

A viable alternative already exists in the form of krypton, which is very similar in use to xenon but has a lower performance (krypton is the noble gas preceding xenon in the periodic table and therefore lighter and more difficult to ionise). For example, the StarLink satellite constellation programme, which aims to provide internet access in the most remote parts of the world, has been attracted by the lower cost of krypton to power hundreds of satellites in recent years. If krypton were also to run out, the use of a lighter noble gas such as argon, whose abundance in the Earth's atmosphere prevents any shortage, could be envisaged. However, the performance of argon propulsion is much poorer than that of xenon or even krypton.

One may wonder whether molecular propellants would not be more advantageous alternatives [8]. Several molecular alternative propellants are therefore being studied, such as water, adamantine or ammonium [8]. However, iodine has emerged as the most promising alternative to xenon and is being studied by several groups around the world [1, 8–17]. The work of this thesis is part of the same general problematic:

To what extent can the iodine molecule be considered as a viable alternative to xenon as a propellant for electric space propulsion ?

With a $Z = 53$ charge number next lower to the one of xenon and naturally present in molecular form, iodine can advantageously replace xenon because of the low dissociation energy of I_2 and low ionization energies of both I and I_2. Contrary to xenon, iodine is solid at standard temperature and pressure, so the storage tank of iodine electric propulsion systems can be lighter and does not need to be pressur-

ized. This could be a great advantage for small satellites where the pressurized tanks have higher mass to volume ratios. Also, iodine is abundant on earth and thus, inexpensive. While massively contained in seawater (approximatively 35 million tons) but with a very low concentration, iodine is mostly extracted from underground brines in Japan, USA, Turkmenistan, Azerbaijan, Indonesia or from caliche ore (a nitrate found in the Atacama desert) in Chile [18, 19]. It is estimated that the iodine reserves of Japan and Chile represent 90% of the world reserves (65% for Japan and 25% for Chile). Iodine is, for instance, mostly needed in the production of X-ray contrast media or in polarizing film in liquid-crystal display (LCD) screens. It is estimated that the existing global reserves of iodine will support iodine production for at least the next two centuries [18, 19].

In the plasma (electric) propulsion community, iodine has been considered for almost two decades. At LPP (Laboratoire de Physique des Plasmas), the first work on iodine dates back to 2005 and a patent filed by P. Chabert for the original concept of the PEGASES thruster [20], where an electronegative gas (such as iodine) was used to alternatively generate positive and negative ion beams. Since then, three theses dedicated to the study of iodine plasmas for space propulsion [13, 21, 22] and the *ThrustMe*® start-up have emerged from the laboratory. However, iodine has not yet convinced the major industrial manufacturers. The main reluctance to use iodine stems from its corrosive nature as well as the costs generated by the adaptation of industrial ground testing facilities operating exclusively with noble gases. Nevertheless, *Busek*® is already marketing Hall effect thrusters fueled by iodine, and *ThrustMe*® recently reported promising in-orbit performances of their iodine electric propulsion system [12].

Even if xenon and iodine thrusters performances are found to be very similar [1, 12, 23], iodine and xenon plasmas should exhibit very different properties, in particular as the mass flow rate (and the resulting gas pressure in the plasma chamber) and the electric power used to generate the plasma are varied. Iodine is a molecular and electronegative gas, which is expected to have a higher energy cost per electron-ion pair created, because of the the energy cost of dissociation and dissipated in electronic, vibrational and rotational heating of the molecules. A significant fraction of negative ions is also expected given the very high cross section for dissociative attachement. Furthermore, transport phenomena are also different in molecular gases, and the electron energy relaxation length is expected to be shorter in iodine than in noble gases [1]. All the above effects remain to be quantified. Accurate diagnostic techniques, both optical and electrical, are therefore necessary to quantify the plasma properties and guide the development of reliable models [13, 16, 17]. This will be the first step towards the optimization of propulsion devices, both for gridded-ion-thrusters [11, 24] and/or Hall thrusters [9, 23].

Even though many investigations have been carried out on iodine plasmas, they have been made mainly outside the context of propulsion [25–27]. To guide the theoretical calculations concerning the operation of thrusters [13, 16], especially at low-pressure, the literature lacks basic data describing the chemical reactions of various species, although there is a renewed interest in new calculations, such as electron impact collisions cross sections on I and I_2 [28, 29] or line strengths and atomic probabilities for some transitions of neutral iodine [30]. Electrical or optical diagnostics are also rare. A LIF scheme has been studied on I^+ [31] and measurements of the ratio between I^+ and I_2^+ were performed using a mass spectrometer, at

the output of a radio frequency ion thruster [8].

In order to address the general issue outlined above, two experimental devices were used: an ICP discharge replicating the ionization chamber of a gridded-ion-thruster and a quartz iodine cell, as well as the experimental and theoretical legacy left by my predecessors: P. Grondein [32], R. Lucken [21] and F. Marmuse [22]. The ion extraction, the ion acceleration, and the plume recombination are not investigated here (the reader may refer to the thesis work of L. Habl for such considerations [33]), the focus is rather on low-pressure iodine plasmas composition and physical properties. At the beginning of this thesis, many questions were still open, which we address in this Ph.D. report:

- Which experimental diagnostics are best suited to study low-pressure iodine plasmas?
- Are there sufficient theoretical data to model low-pressure iodine plasmas?
- How to accurately model low-pressure iodine plasmas?
- To what extent are low-pressure iodine plasmas spatially homogeneous?
- What is the behavior of neutral species (atoms and molecules) in an iodine plasma?
- What are the main transport and heating mechanisms in iodine plasmas?
- How do iodine plasmas behave compared to noble gases plasmas ?
- Are negative ions an obstacle to the use of iodine as an alternative propellant?

The thesis is divided into six chapters, each with a dedicated introduction. At the end of each of the Chapters 3, 4, 5 and 6, which represent the body of this work, there is a summary with the main findings. A general conclusion with perspectives and four appendices complete the manuscript.

Chapter 1 details the physical chemistry of iodine with a focus on the atomic and molecular properties that will be useful for developing experimental diagnostics. It also provides a rigorous description of the cross sections data available in the literature that we have used to develop models. This chapter can be seen as a toolbox to be used when reading the manuscript.

Chapter 2 presents the two experimental devices used during this thesis to generate low-pressure iodine plasmas: the PEGASES thruster and the iodine cell. Their specific operating conditions are highlighted.

Chapter 3 presents the experimental diagnostics developed to measure the densities and temperatures of charged species (electrons and ions) in iodine plasmas along the main axis of the PEGASES thruster. In particular, Langmuir probes and laser-induced detachment on I^- are studied.

Chapter 4 describes the optical diagnostics developed to probe neutral species

(atoms and molecules) in low-pressure iodine plasmas. In particular, absorption, LIF (Laser Induced Fluorescence) and TALIF (Two photon Absorption Laser Induced Fluorescence) techniques are presented and applied on both experimental setups.

Chapter 5 presents an updated iodine 0D global model using the reaction set detailed in Chapter 1. The model is applied to the two different experimental setups and validated using the experimental results presented in Chapters 3 and 4.

Finally, Chapter 6 presents a one-dimensional multi-fluid code used to study the neutral dynamics along the axis of the thruster, at the center of the discharge. The model is compared to experimental measurements presented in Chapters 3 and 4.

CHAPTER 1

IODINE PHYSICAL CHEMISTRY

Contents

1.1 Introduction

Noble gases have been extensively studied over the last decades so that optical lines, Einstein coefficients, transition probabilities, or oscillator strengths are well documented (see NIST database [34] and references therein). Cross section datasets are numerous and easily available [35]. Even if some questions remain about their accuracy or completeness, numerous collisional radiative, fluid, and PIC models have been developed using the existing data [36–39]. Today, the EP community massively relies on those collisional data. In this thesis, noble gas plasmas will be studied in order to put their behavior into perspective with that of iodine plasmas. The reader can refer to Appendix A to find the properties of the noble gases used during this thesis (argon, krypton and xenon) as well as the effective cross section data used in various simulations.

Inversely, iodine physical chemistry is more complex because iodine is molecular at standard temperature and pressure. While the molecule has been extensively studied by spectroscopy [40–42] and hundreds of levels were identified, the atomic state has been barely studied over the years because dissociation needs to happen first. There are three main ways of dissociating the molecule: (i) by heating the cell containing iodine, (ii) by igniting a plasma, (iii) by photodissociation [43–45]. This explains why only a few Einstein coefficients have been experimentally determined [46–50] or calculated [30] and the experimental collisional data are scarce (see Section 1.4).

Emission spectroscopy in the near-UV, visible and near-infrared ranges is a convenient tool to give first qualitative insights about the complexity of iodine plasmas. Figure 1.1 shows an iodine plasma ignited at 20 mTorr within a transparent thruster prototype (described in Chapter 2) and the emission spectra obtained at $z = 2$ cm and $z = 9$ cm away from the exciting RF antenna. Two coupled spectrometers were used: the AvaSpec-4096CL-UB-10 in the range 200 – 715 nm and AvaSpec-4096CL-NB-10 in the range 555 – 1050 nm, for a resolution of 0.3 nm. The plasma appears inhomogeneous with drastic color changes along the $\hat{z}$-axis: turquoise near the antenna (on the left) then yellow-orange in the center and blue-violet on the right of Figure 1.1a. The inhomogeneities are confirmed in the UV-Visible spectra. Near the antenna, atomic and ionic emission lines are dominating the broad I_2 emission bands. However, near the exit plane of the thruster ($z = 9$ cm), the lines are much less numerous and molecular bands dominate. In the infrared, both spectra are similar with 5 strong atomic emission lines whose relative intensities slightly differ. The emission spectra are not corrected for the wavelength sensitivity of the detectors, but in each figure, the maximum has been set to 1.

In this first chapter, the focus is on the physical chemistry properties of iodine. The aim is not to describe with precision the spectroscopic characteristics of iodine (molecular and atomic) but rather to give a general overview of the available knowledge to develop experimental diagnostics and numerical models for studying iodine plasmas. The chapter can be seen as a toolbox to be used in the course of the manuscript. The first section will describe the iodine molecule properties while the atom will be the concern of the following section. Both the molecular and atomic levels and transitions used in our diagnostics will be highlighted. In the last section, the iodine set of cross sections used to develop numerical models of iodine plasmas will be extensively presented.

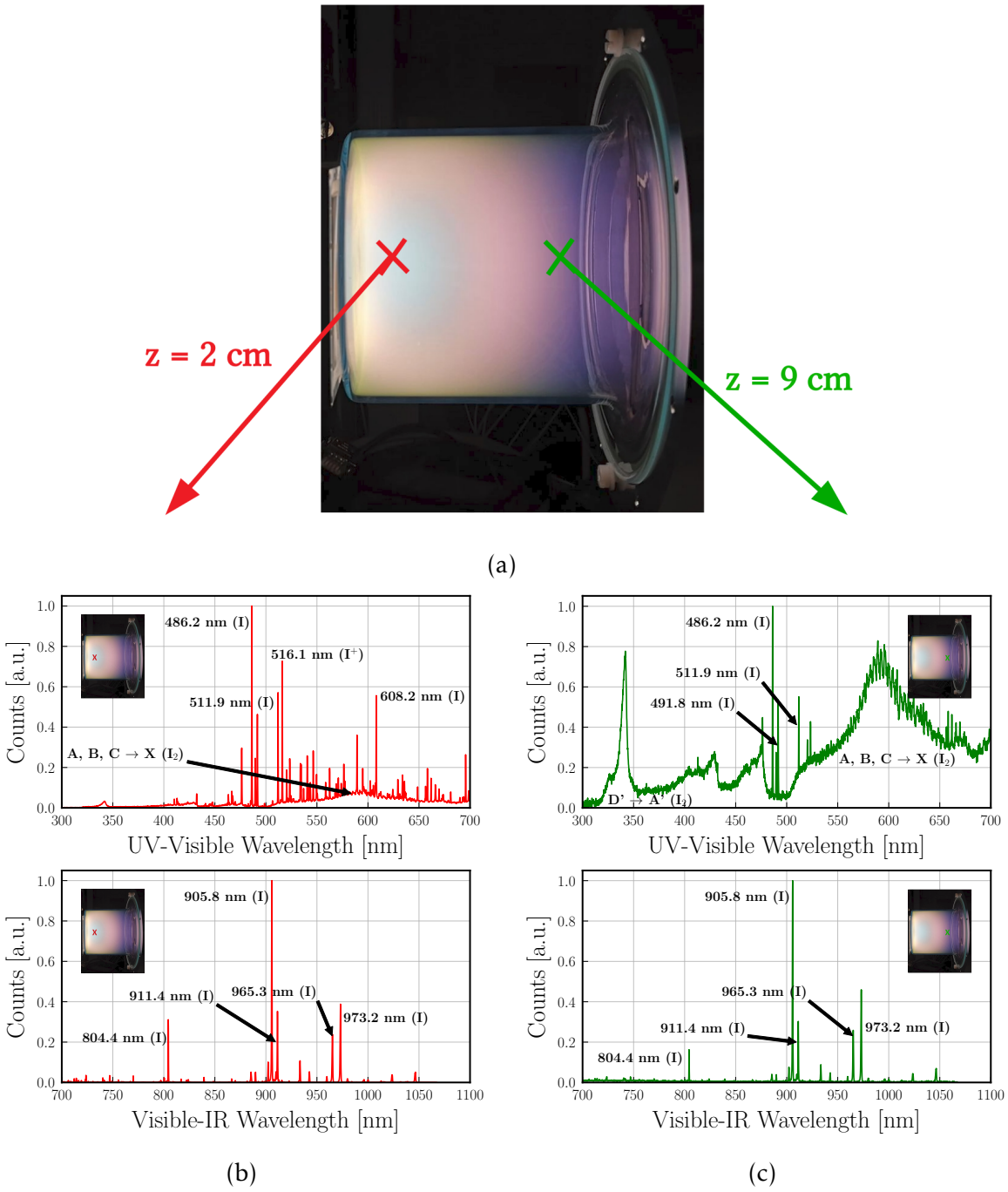

Figure 1.1: (a) Photography of an iodine plasma running in a transparent prototype of the PEGASES thruster at 20 mTorr and 200 W. Locations of the spectroscopy measurements are highlighted. (b) Spectra obtained at $z = 2$ cm. (c) Spectra obtained at $z = 9$ cm. The wavelengths (recorded in air) of some transitions are indicated.

1.2 The iodine molecule

In this section, the physical chemistry properties of the iodine molecule are presented. The various characteristics of the ground state but also of the first excited levels will be detailed. The electronic spectroscopy and some dissociation processes relevant to the experimental diagnostics developed in the course of the thesis (see Chapter 4), will be presented.

1.2.1 Generalities

In nature, elemental iodine forms diatomic molecules with chemical formula I_2, where two iodine atoms share a pair of electrons in order to each achieve a stable octet for themselves; at high temperatures, these diatomic molecules reversibly dissociate in a pair of iodine atoms. The heaviest of the stable halogens was discovered in 1811 by French chemist Bernard Courtois. At standard conditions, I_2 forms dark crystals. The halogens darken in colour as the group is descended: fluorine is a very pale yellow, chlorine is greenish-yellow, bromine is reddish-brown, and iodine is violet (the French name *iode* comes from the Ancient Greek word meaning "violet-coloured").

Molecular iodine sublimates when heated; the vapor-pressure can be calculated as a function of the temperature using either:

$$\log_{10}\left(\frac{p}{133.32}\right) = 12.1891 - 0.001301T - 0.3523\log_{10}(T) - \frac{3410.71}{T}, \tag{1.1}$$

or,

$$\log_{10}\left(\frac{p}{133.32}\right) = 18.8 + 0.00044T - 2.98\log_{10}(T) - \frac{3594}{T}. \tag{1.2}$$

Equation (1.1) is taken from Tellinghuisen's work [51] while equation (1.2) comes from Kono *at al.* [50]. The pressure p is in Pascal and the temperature T in Kelvin. Each formula is plotted in Figure 1.2. They give very similar results with a difference not exceeding 0.1 to 0.8 Pa between 260 K and 280 K.

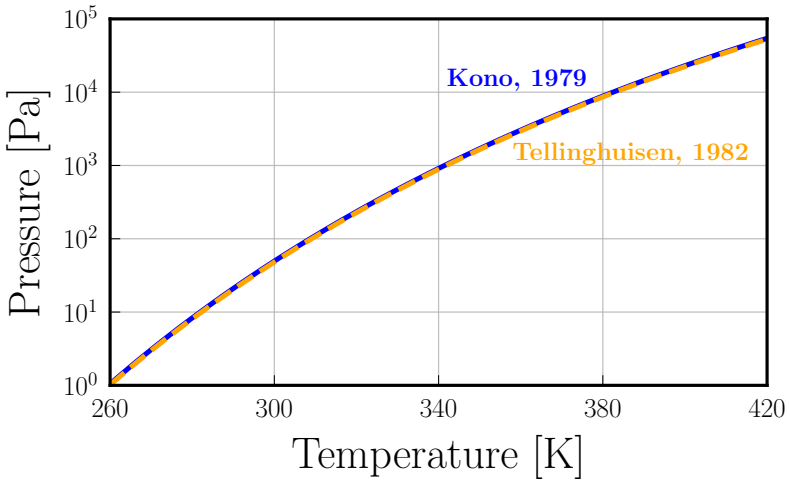

Figure 1.2: Iodine vapor pressure [Pa] as a function of Temperature [K]. Kono [50] and Tellinghuisen [51] formulae very slightly differ around 270 K.

1.2.2 Molecular ground state

For a diatomic molecule, an electronic state is represented by its potential curve (energy as a function of the internuclear distance). The curve can be either attractive (also called a bound state with an equilibrium internuclear distance at r_e = 2.666 Å [52], in the case of the iodine ground state) or diffusive (strictly decreasing and leading to dissociation). At high internuclear distance, the potential curve reaches an asymptotic value synonymous with dissociation. It has been found that the iodine ground state ($X\ ^1\Sigma_g^+$) can be well approximated by a Morse potential for low internuclear distances [41, 53]. Such a potential is plotted in Figure 1.3.

Unlike an atom, a diatomic molecule has two additional degrees of freedom which, until now, have been largely ignored in the study of iodine plasmas: vibration and rotation. Any attractive electronic state of a molecule is composed of several vibrational levels. In the case of the iodine ground state, over 60 vibrational levels are present. The first vibrational level $v = 0$ has an energy of 107.1 $cm^{-1} \approx 0.0133$ eV and the energy gap between the two first levels (E_1-E_0) is 213.3 $cm^{-1} \approx 0.0264$ eV, in the Morse potential approximation. The energy gap between higher consecutive levels (E_{v+1}-E_v, $v > 0$) diminishes with increasing v because the potential is anharmonic. Each vibrational level can be represented by a vibrational wave function, whose radial profiles are schematically drawn for a few v-levels in Figure 1.3. Note, that except for $v = 0$, the two extrema of the wave functions are located near the potential curve and the transition probability between two vibrational levels (within the same electronic state or located in two different electronic states) is higher when the overlap of the wave functions is maximum.

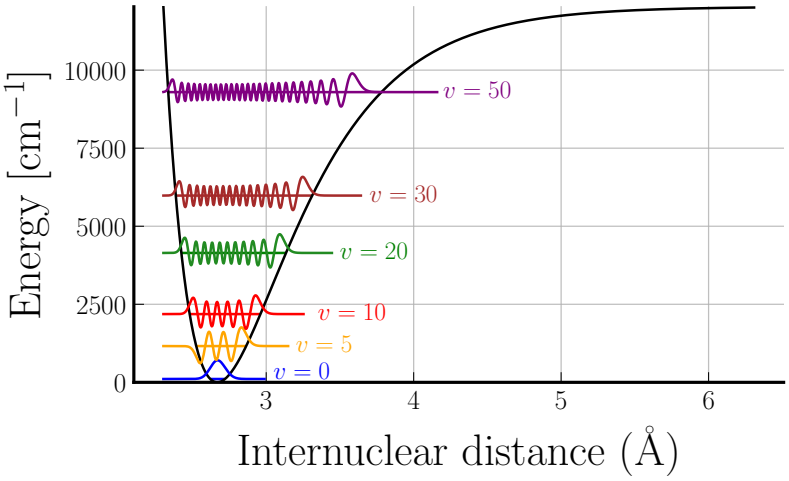

Figure 1.3: Iodine ground state ($X\ ^1\Sigma_g^+$) Morse potential curve. Some vibrational wave functions (with a maximum set to the same arbitrary value) are represented.

The distribution of iodine vibrational levels is plotted in Figure 1.4 for three different temperatures (300 K, 900 K and 1500 K) assuming a Boltzmann distribution and using spectroscopic data for the energy of vibrational levels from [54]. At room temperature, the $v = 0$ level is by far the most populated (> 60 %) and the first three v-levels are enough to account for more than 90 % of the total population. At 1500 K, however, the distribution is much more homogeneous and 11 v-levels are necessary to reach 90 %. In iodine plasmas, where gas temperature above 1000 K

have been measured (see Chapter 4), the first ten v-levels are expected to be populated to a significant extent.

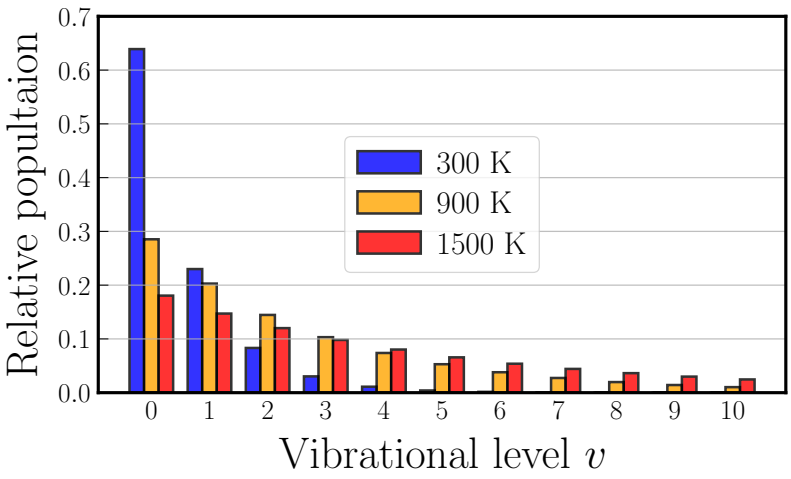

Figure 1.4: Distribution of the I_2 population in the first 15 vibrational levels for 3 temperatures: 300 K, 900 K and 1500 K, assuming a Boltzmann distribution.

The iodine molecule can be also excited rotationally. Its rotational constant B_e is 3.766794×10^{-2} cm^{-1} [52]. At 300 K, the mean number of rotational levels for each v-levels is 67. In the following, the effect of the rotational excitation of I_2 will be neglected as the developed diagnostic techniques do not allow to study it. From a modeling point of view, it is assumed that the rotational excitation of I_2 has a negligible influence in the plasma conditions studied as observed in low-pressure capacitively coupled oxygen plasmas [55]. Furthermore, currently no cross sections for electron impact rotational excitation of I_2 are available. It is unfortunate as the rotational excitation could very well be a source of electron energy losses in the plasma conditions studied in this thesis.

1.2.3 Electronic spectroscopy

In the second part of the XX$^{\text{th}}$ century, the electronic spectroscopy of the iodine molecule has been extensively studied. In 1978, an Atlas of the absorption spectrum of the iodine molecule in the range 14800-20000 cm^{-1} was written [40]. The study of the visible absorption spectrum of I_2 vapors even became a classic molecular spectroscopy experiment for undergraduate students in physical chemistry, to determine some spectroscopic constants of iodine [56]. Indeed, the vibrational-electronic spectrum of I_2 in the region 640-500 nm displays a large number of well-defined bands (visible in Figure 1.1c). Near-UV transitions (such as the D'→A' visible in Figure 1.1c where A' and D' denote I_2 excited states that will not be studied in this manuscript) and UV transitions were also well studied [41, 57].

1.2.3.1 Franck-Condon principle

The Franck–Condon principle is a spectroscopic rule explaining the intensity of vibronic transitions (the simultaneous changes in electronic and vibrational energy levels of a molecule due to the absorption or emission of a photon of the appropriate

energy). The principle states that during an electronic transition, a change from one vibrational energy level to another will be more likely to happen if the two vibrational wave functions overlap significantly.

In a plasma, the interaction time for the collision of a typical electron (1-10 eV) with a molecule ($\sim 10^{-16} - 10^{-15}$ s) is short compared to the typical time for a molecule to vibrate or rotate ($\sim 10^{-14} - 10^{-13}$ s) [58]. Hence for electron collisional excitation of a molecule to an excited electronic state, the new vibrational (and rotational) state can be determined by freezing the nuclear motions during the collision: this is known as the Franck–Condon principle [59–61], discovered almost a century ago using, amongst other molecules, the absorption spectra of iodine. In a potential diagram, it simply means that the excitation between an initial and a final states can be represented by a vertical line at fixed internuclear distance r. The greater the overlap between the wave functions of the initial and final states, the greater the transition probability.

Besides, the typical transition time for electric dipole radiation ($\sim 10^{-9} - 10^{-8}$ s) is long compared to the dissociation time ($\sim 10^{-14} - 10^{-13}$ s), so excitation to an excited state will generally lead to dissociation when it is energetically permitted (*i.e.* when $\mathcal{E}_{ex} < \mathcal{E}_{diss}$) [58].

1.2.3.2 Iodine absorption in the visible

While known and studied for a century [59, 62], the visible spectrum of I_2 has been carefully investigated by Tellinghuisen ([42, 51, 63, 64]). Three electronic transitions contribute to the absorption in the visible region between 400 and 650 nm, which is continuous below 500 nm (~ 20000 cm^{-1}) but shows pronounced rovibrational structure between 500 and 630 nm ($\sim 12500 - 20000\,\text{cm}^{-1}$) as seen in Figure 1.1c. These transitions are from the ground state X $^1\Sigma_g^+$ to the bound state B $^3\Pi(0_u^+)$, correlated to the $^2P^\circ_{1/2}$ + $^2P^\circ_{3/2}$ dissociation limit and the two 1_u states, A $^3\Pi(1_u)$ and C $^1\Pi(1_u)$, correlated to the $^2P^\circ_{3/2}$ + $^2P^\circ_{3/2}$ dissociation limit. In Figure 1.5, the excited states potential curves are plotted: A $^3\Pi(1_u)$ is taken from [65], B $^3\Pi(0_u^+)$ from [66] and C $^1\Pi(1_u)$ from [67]. The ground state potential curve is the same than plotted in Figure 1.3.

Recently, hyperfine spectroscopy studies have been carried out in this spectral range to develop an iodine atomic clock around 532 nm [69]. Beyond $20000\,\text{cm}^{-1}$, the diffuse part of the absorption spectrum leads exclusively to molecular photodissociation, via the $B^3\Pi(0_u^+)$ and $C^1\Pi(1_u)$ states. This region is very interesting, in different ways, for absorption-based density measurements between a bound state and the continuum, especially in a plasma where pressures and temperatures are different from what they are in the normal gas phase. Contrary to an optical transition between bound states, the resonance condition is independent of the gas velocity and there is no saturation related to the stimulated emission at high laser intensity. It is also possible to detect the population of different rotational and vibrational levels of the molecule without changing the laser wavelength. In Chapter 4, we will take advantage of this particularity to directly measure the dissociation rate in iodine plasmas.

The effective absorption cross section is well known experimentally at room temperature (see (b) in Figure 1.5), thanks to the growing interest in the role that iodine chemistry plays in a number of atmospheric processes. The latest measurements

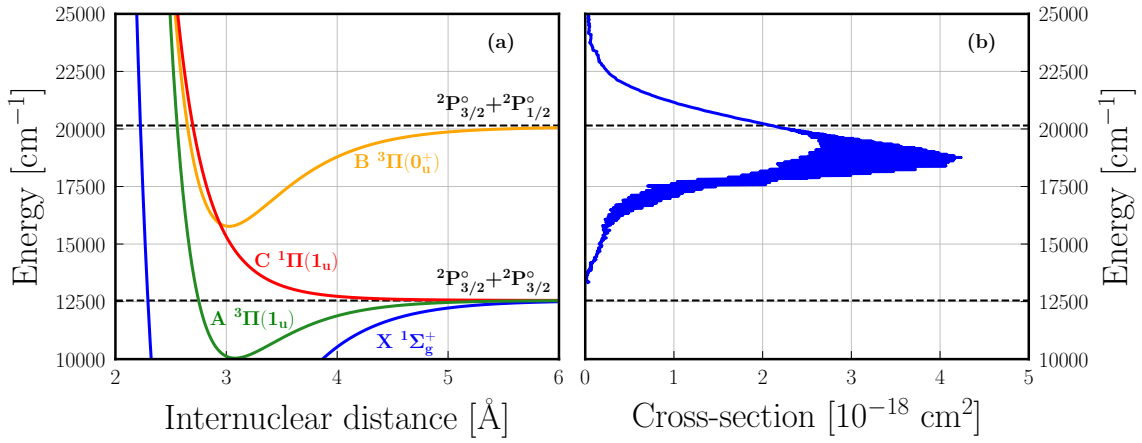

Figure 1.5: Visible absorption spectrum of I_2. (a) Relevant potential curves. (b) Absorption cross section as a function of the wavenumber, taken from [68]. $^2P^\circ_{3/2}$ + $^2P^\circ_{3/2}$ and $^2P^\circ_{3/2}$ + $^2P^\circ_{1/2}$ dissociation limits are indicated by horizontal dashed lines.

of the absorption cross sections of I_2 have been reviewed in a technical report [70] from the Jet Propulsion Laboratory-Caltech committee about standards for atmospheric cross sections (see section 4H of the report). The recommended data are those computed by Saiz-Lopez *et al.* [68].

1.2.4 Dissociation processes

The iodine molecule can be ionized into I_2^+ when colliding with an energetic electron, the ionization threshold for the molecular ground state being $\mathcal{E}_{iz,I_2}$ = 9.31 eV [71]. At lower collision energy, ionization is impossible but several dissociation processes may occur.

1.2.4.1 Dissociation into a pair of atoms

The electronic impact dissociation process is conveniently represented by:

$$I_2 + e^- \longrightarrow I + I + e^-, \tag{1.3}$$

where the two produced atoms can be either in the ground state or excited. This notation is simple and concise but omits the intermediate step in which the molecule is first excited before dissociating.

In Figure 1.5, two dissociation limits are visible: I($^2P^\circ_{3/2}$) + I($^2P^\circ_{3/2}$) and I($^2P^\circ_{3/2}$) + I($^2P^\circ_{1/2}$). The five first dissociation limits are listed in Table 1.1, the energy levels with respect to I_2 (X $^1\Sigma^+_g$, v = 0) are also given. The notations used for the excited atomic levels are described in Section 1.3.

1.2.4.2 The formation of negative ions

Since the first experimental works on I_2 discharge, iodine has been known to be a very electronegative gas [72–77]. Woolsey *et al.* used a Langmuir probe and orbital-limited theory and found electronegativity values (ratio of the negative ions density over the electron density) above two thousands in a nearly ion-ion plasma (I_2^+-I_3^-),

Table 1.1: First dissociation limits of the iodine molecule. The energy origin is set to the first vibrational level ($v = 0$) of the molecular ground state.

Dissociation limit	Energy [eV]
$^2P^\circ_{3/2} + {}^2P^\circ_{3/2}$	1.542
$^2P^\circ_{3/2} + {}^2P^\circ_{1/2}$	2.485
$^2P^\circ_{1/2} + {}^2P^\circ_{1/2}$	3.428
$^2P^\circ_{3/2} + (^3P_2)6s\ ^2[2]_{5/2}$	8.316
$^2P^\circ_{3/2} + (^3P_2)6s\ ^2[2]_{3/2}$	8.497

produced by allowing the plasma produced in the Faraday dark space of a DC iodine glow discharge to diffuse into a side-arm for pressures between 0.2 and 1 Torr [26].

More recently, the electron affinity of the iodine atom has been measured with great precision at $\mathcal{E}_{A,I} = 3.0590463$ eV by Pelaez *et al.* [78]. It is more than twice the dissociation energy of the iodine molecule (from the molecular ground state) $\mathcal{E}_{diss,I_2} = 1.542$ eV[52]. In such a configuration, the threshold energy for production of negative ion fragments is lower than for pure dissociation processes (see Figure 8.7.c in [58]).

The potential curves of the molecular ground state I_2 ($X\ ^1\Sigma_g^+$), the anionic molecular ground state I_2^- and an anionic excited state I_2^{-*} are schematically represented in Figure 1.6, using [28, 29]. The dissociation limits of each molecular potential, the electron affinity of the iodine molecule $\mathcal{E}_{A,I_2} = 2.52$ eV [79] and the first atomic excitation energy $\mathcal{E}_{ex_1,I_{3/2}} = 0.9426$ eV [34] are also indicated.

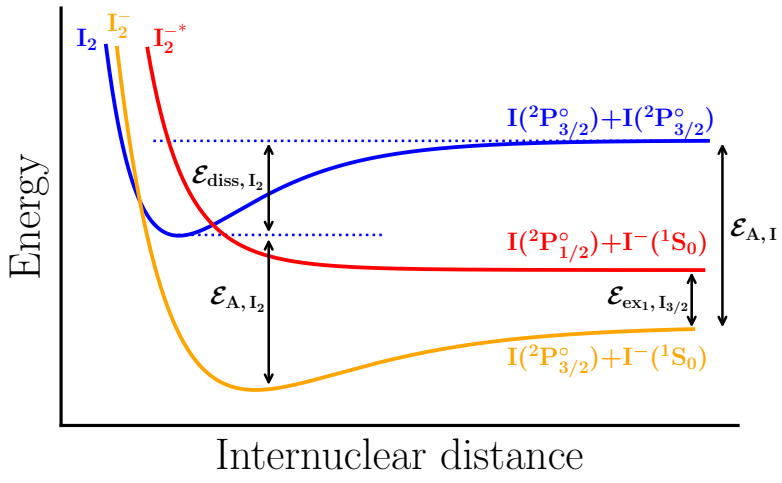

Figure 1.6: Schematical representation of some iodine potential curves and their respective dissociation limits: I_2 is the molecular ground state, I_2^- the anionic molecular ground state and I_2^{-*} an excited state of I_2^-. $\mathcal{E}_{diss,I_2} = 1.542$ eV [52] is the dissociation energy of I_2, $\mathcal{E}_{A,I} = 3.059$ eV [78] the electron affinity of the iodine atom, $\mathcal{E}_{A,I_2} = 2.52$ eV [79] the electron affinity of the iodine molecule and $\mathcal{E}_{ex_1,I_{3/2}} = 0.9426$ eV [34] the first atomic excitation energy.

According to the Franck-Condon principle and the configuration of the iodine potential curves, the production of negative ions following the collision between an electron and the molecule I_2 (also called the "Dissociative Attachment by electronic

impact" and abreviated DEA):

$$I_2 + e^- \longrightarrow I + I^-, \tag{1.4}$$

will more probably occur via the intermediary excitation towards the I_2^{-*} level which is repulsive and dissociates into $I^-(^1S_0)$ + $I(^2P^\circ_{1/2})$, where $I(^2P^\circ_{1/2})$ is the first atomic excited state (see subsection 1.3.2.1 for more details on this level). So far, in iodine plasma models [13, 16, 22], this had always been ignored and the atom produced was assumed to be in the ground state $I(^2P^\circ_{3/2})$.

1.3 The iodine atom

In this section, some physical chemistry properties of the iodine atom are presented. The various characteristics of the ground state but also of the excited levels will be detailed. Transitions between some key levels will be highlighted as they have been experimentally investigated during the thesis (see Chapter 4).

1.3.1 Generalities

1.3.1.1 Atomic properties

Iodine is the fourth halogen, being a member of group 17 in the periodic table, below fluorine, chlorine, and bromine; it is the heaviest stable member of its group. Figure 1.7 presents the atomic notation of iodine. The mass is indicated in atomic unit. Amongst thirty-seven known isotopes of iodine, only one occurs in nature, iodine-127. The others are radioactive and have half-lives too short to be primordial but known to be dangerous. [1]

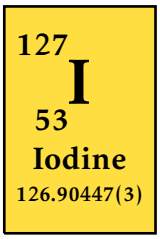

Figure 1.7: Iodine atomic notation. The atomic mass is given in atomic unit.

Iodine ground state has an electron configuration of $[Kr]4d^{10}5s^25p^5$, with the seven electrons in the fifth and outermost shell being its valence electrons. Like the other halogens, it is one electron short of a full octet and is hence an oxidising agent, reacting with many elements in order to complete its outer shell.

1.3.1.2 Atomic excited states classification

The excited levels of the $5s^25p^4nl$ type configurations of I, are divided into several groups, each of which corresponds to a level of the $5s^25p^4$ ion: $^3P_{2,1,0}$, $^1D_0$ or $^1S_0$ (with $nl \in \{6s, 7s, 6p, 7p, 5d, 6d, 4f\}$). Let's mention that the excited state $5s5p^6$ also exists.

Minnhagen [80], in 1962, has interpreted the set of known levels through the pairwise coupling scheme $< (\{p^4(S_C, L_C)J_C\ l\}K\ s)\ J >$ which is the most appropriate to describe the level distribution in some configurations of the iodine spectrum [81]. Luc-Koenig [80] kept this coupling and so do we. Except for the degenerated upper level of the ground state (see subsection 1.3.2.1), an atomic iodine excited level will

[1] In some radiation emergencies, usually nuclear power plant accidents, radioactive iodine may be released into the environment and enter the body by inhaling or eating it. Potassium iodide (KI) is a type of iodine that is not radioactive and can be used to help block one type of radioactive material, radioactive iodine (I-131), from being absorbed by the thyroid.

be written:

$$5s^2 5p^4 \left(^{2S_C+1}L_{C J_C}\right) nl\ ^{2s+1}[K]_J \qquad \text{if even,} \tag{1.5}$$

$$5s^2 5p^4 \left(^{2S_C+1}L_{C J_C}\right) nl\ ^{2s+1}[K]^\circ_J \qquad \text{if odd.} \tag{1.6}$$

In the former expressions, S_C, J_C and L_C are respectively the total spin, total angular momentum and total orbital quantum numbers of the core electrons. $\vec{K} = \vec{J_C} + \vec{l}$, and $\vec{J} = \vec{K} + \vec{s}$, are quantum numbers built by using the orbital momentum $\vec{l}$ and the spin $\vec{s}$ of the external electron.

The iodine atomic levels used in this thesis are schematically represented in Figure 1.8. The ionization energy is indicated by a dashed line at 84295.1 $cm^{-1} \approx$ 10.45 eV [80], I I being the notation for the I atom while I II is the notation for I^+.

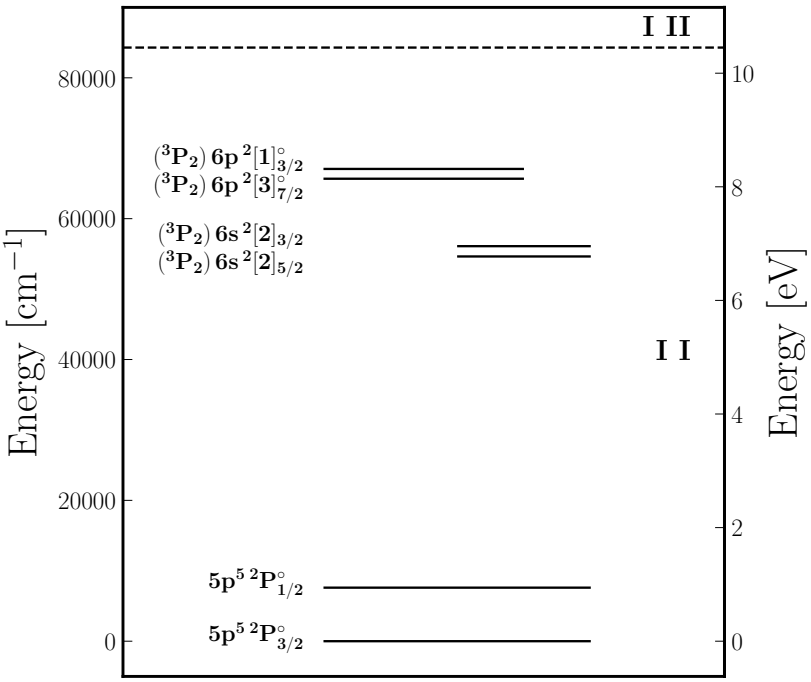

Figure 1.8: Energy diagram of the levels of atomic iodine used in this thesis. The ionization energy is indicated by a dashed line at 84295.1 cm^{-1}.

The nuclear spin number of iodine is $I = 5/2$, meaning that any of the iodine excited levels of quantum number J is divided into several hyperfine sublevels from $F = |I - J|$ to $F = I + J$. In 1975, by using the Fourier transform spectrometry in the infrared, Luc-Koenig *et al.* [81] observed 440 structures and analysed 130 hyperfine structures, giving the magnetic dipole and the electric quadrupole hyperfine structure constants for 37 even levels and 42 odd levels. Since then, only a few experimental works have provided measurements of Einstein coefficients, oscillator strengths or levels lifetime [46–50] which mostly concerned transitions between the three lowest excited states of the iodine atom to the ground state. Recently, Filin [30], calculated numerous line strengths and atomic probabilities for the transitions between different types of excited atomic iodine, using configuration-interaction many-body perturbation theory (CI-MBPT).

For completeness, the positions of the hyperfine components, with respect to the fine structure energy level, are calculated as a function of the hyperfine structure

constants A and B of the 2 levels, according to the Casimir formula [81]:

$$\Delta E = \frac{1}{2}A \times C + B\frac{3C(C+1) - 4I(I+1)J(J+1)}{8I(2I-1)J(2J-1)}, \tag{1.7}$$

where $C = F(F+1) - I(I+1) - J(J+1)$.

1.3.2 Levels and transitions involved in our diagnostics

Chapter 4 will be devoted to the various optical diagnostics developed during this thesis to study iodine plasmas and measure temperatures and densities: absorption, LIF and TALIF. In this subsection, we present the atomic levels and transitions investigated or relevant to our work.

1.3.2.1 Fine-structure transition at 7602.9762(2) cm^{-1} (1314.9 nm)

The iodine atom has a transition from the fundamental state $5s^2 5p^5\ ^2P^\circ_{3/2}$ towards the first excited state $5s^2 5p^5\ ^2P^\circ_{1/2}$ at 7602.9762(2) cm^{-1} [82], or around 1.3149 μm, as shown in Figure 1.9. The splitting between both states that share the same electronic configuration and spectral terms is due to spin-orbit coupling. The transition between this state and the fundamental, which is forbidden with respect to electric dipole radiation, is in the near-infrared and has been studied by Luc-Koenig *et al.* by using Fourier transform spectrometry [83] and by Ha *et al.* in measuring absorption spectra of the transition with a tunable near-IR diode laser [49]. At least 10 other authors have studied this transition (see Table 1 in [49]). The upper level has a quantum number $J = 1/2$ and the fundamental state has a quantum number $J = 3/2$. Such an inverted fine structure is common when the electronic layer is more than half-full, in any atoms. The nuclear spin number of iodine ($I = 5/2$) leads to six possible dipolar magnetic transitions within the hyperfine structure (electrons can only desexcite from one level to another following the strict selection rule $\Delta F = 0, \pm 1$) and two quadrupolar electric transitions ($\Delta F = \pm 2$). However, it has been calculated [47] and measured experimentally [83] that the quadrupolar electric transitions are much weaker than the dipolar magnetic ones and could be neglected (a ratio of 3.5/1000 has been measured between the transition $F' = 2 \leftarrow F = 4$ and strongest transition $F' = 3 \leftarrow F = 4$, the value of 2.7×10^{-3} is also given by Engleman *et al.* [48]).

Analysis of the absorption spectrum around 7602.9762 cm^{-1} gives access to the atomic temperature from any of the six absorption peaks via Doppler broadening and provides an absolute measure of the population difference between the two states, defined as:

$$\Delta n = n_{I_{3/2}} - 2n_{I_{1/2}}, \tag{1.8}$$

by using the total area of the peaks, or from the area of a single peak, as the line ratios are available in the literature [49, 83] and the absorption cross section has been measured [49]. $n_{I_{3/2}}$ and $n_{I_{1/2}}$ are the densities [m^{-3}] respectively in the lower and upper state and the factor 2 comes from the ratio of the statistical weight of each electronic state:

$$\frac{g_{I_{3/2}}}{g_{I_{1/2}}} = \frac{2 \times 3/2 + 1}{2 \times 1/2 + 1} = 2. \tag{1.9}$$

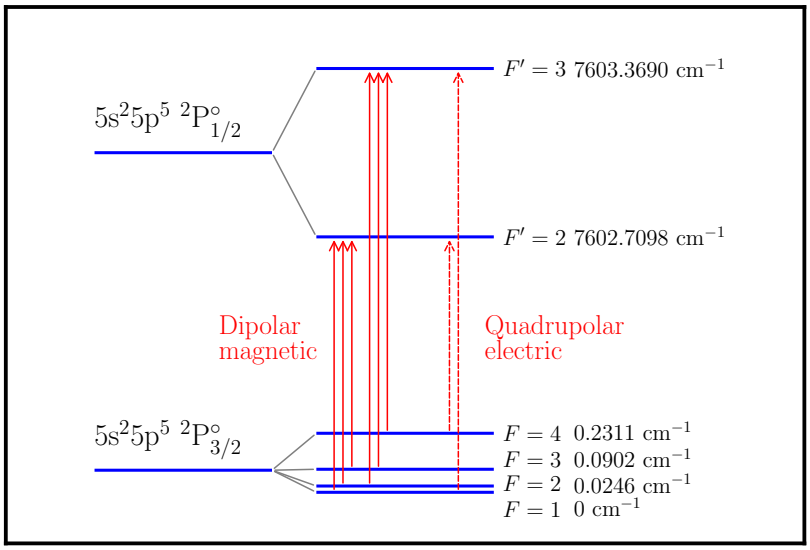

Figure 1.9: Diagram of the levels of the transition $5s^25p^5\ ^2P^\circ_{3/2} \rightarrow 5s^25p^5\ ^2P^\circ_{1/2}$. Dipolar magnetic and purely electric quadrupolar transitions are indicated. Hyperfine levels values are taken from [83] where the uncertainty of 0.0003 cm^{-1} has been omitted. More precise values were even obtained by using the atomic-beam magnetic resonance method by Jaccarino *et al.* [84].

The abusive notation $X_{I_{1/2}}$ or $X_{I_{3/2}}$ designates the quantity X of the upper or lower levels of the atomic ground state and will be extensively used in this manuscript.

Such an absorption experiment had already been conducted, within the PEGASES thruster, by Marmuse [22]. The absorption signal was shown to be very weak (below 1% of absorption after 7 passes through the plasma) because the transition is forbidden and the gas pressure is very low. Temperatures above 1000 K were obtained but it was assumed that the upper state population was negligible. In this thesis, we will go beyond this simplistic approximation adding spatial resolution along the thruster axis and taking into account the upper state population (see Chapter 4).

1.3.2.2 Absorption in the near infrared

The emission spectroscopy of iodine plasma shows three strong I lines at 10 969 cm^{-1}, 11 036 cm^{-1}, and 12 429 cm^{-1} (respectively 911.4 nm, 905.8 nm and 804.4 nm for wavelegths in air), clearly visible in Figures 1.1b and 1.1c. These emission lines highlight the presence of electronic transitions that can be probed by absorption with a laser in the relevant wavelength range, and where the absorption should be strong. Electrons can only be excited from one level to another if parity changes and $\Delta J = 0, \pm 1$. In Figure 1.10, a graphical representation of the four excited levels generating the three lines in the near-infrared is given.

Such transitions show degeneracy due to the hyperfine structure of the atomic levels (see subsection 1.3.1.2), with many peaks separated by a spectral distance smaller than the Doppler width. In Chapter 4, an hyperfine transition of the 11036.528 cm^{-1} transition has been investigated by laser absorption to measure the temperature of the $5s^25p^4(^3P_2)6s\ ^2[2]_{5/2}$ excited level from Doppler broadening.

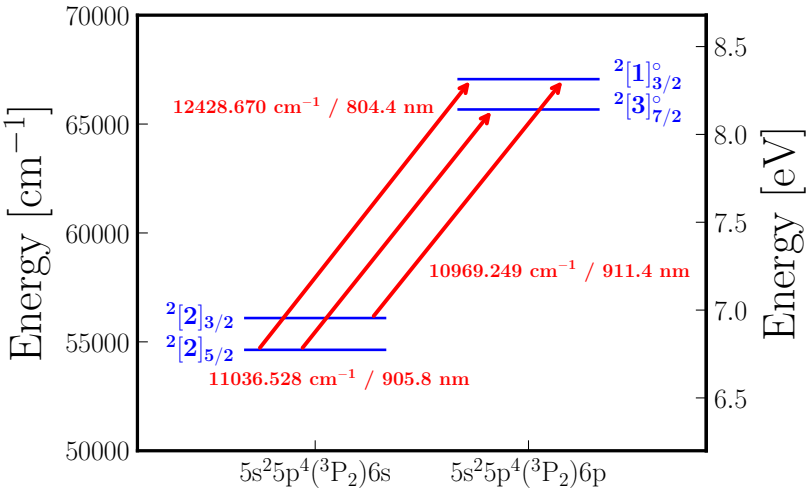

Figure 1.10: Energy diagram of four excited atomic iodine states responsible for the strong emission lines at 911.4 nm, 905.8 nm and 804.4 nm that can be probed by laser absorption (wavelengths in air). The levels notation comes from [80] and is described in subsection 1.3.1.2. The transition values comes from [34, 81]. In this thesis, only the transition at 11036.528 cm^{-1} has been investigated by laser absorption.

1.3.2.3 TALIF

The TALIF method consists in recording the fluorescence signal that follows the resonant absorption of two photons of UV light. The first levels accessible by a two-photon odd-parity preserving transition, starting from the 5s^{2}5p^5 ^{2}P$^\circ_{3/2}$ ground level of I, are those of the 5s^{2}5p^4(^{3}P$_2$)6p° electron configuration, located around 65000 cm^{-1}. Among these, we mainly applied excitation towards the (^{3}P$_2$)6p $^2[1]^\circ_{3/2}$ level, with detection of the fluorescence at 804.4 nm. Occasionally, we also excited the (^{3}P$_2$)6p $^2[3]^\circ_{7/2}$ level, which fluoresces only at 905.8 nm (see Figure 1.11).

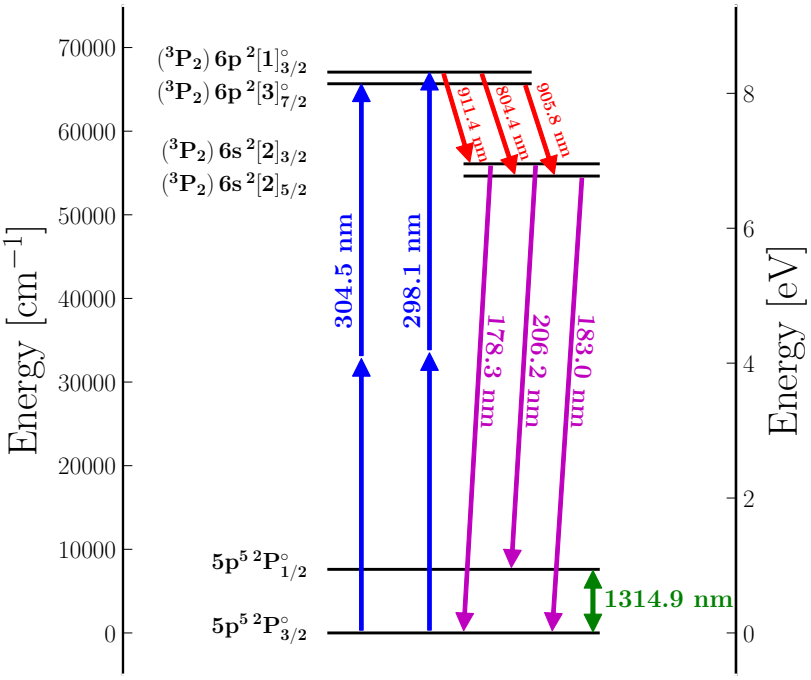

Figure 1.11: Energy diagram of the levels of atomic iodine, with the two-photon absorption and infrared fluorescence transitions used in the TALIF experiment presented in Chapter 4. For the upper excited $(^3P_2)6p\,^2[1]^\circ_{3/2}$ level, a very weak de-excitation transition to the $(^3P_1)6s^2[1]_{3/2}$ level, in the infrared (≈ 1.907 μm), has not been represented.

1.4 Set of cross sections for iodine

Modeling of iodine plasmas is not straightforward because iodine can form a variety of species and reliable collision cross sections are scarce (the basics of plasma collisions are provided in Appendix B). The first model was proposed in 2016 by Grondein *et al.* [13], based mostly on the calculations from Quantemol Ltd [85], where six species were considered:

$$I, I_2, I^+, I_2^+, I^-, e^-$$

The particle balance equations of the 0D (volume-average) model were then slightly modified by Lucken [21, 86] and Marmuse [22] by adding some new calculated cross sections (electron detachment from I^-, electron impact dissociation of I_2^+ and I_2-I^+ charge exchange) [87] and extrapolating some others at low and/or high energy [22]. In 2021, Levko *et al.* [16], used the same set of cross sections than [13] to build a 2D plasma-fluid model.

The first comparisons between experimental measurements and 0D models were done by Marmuse [22] during his thesis. Grondein's model was then acceptably validated by measurements of electron density, electron temperature and electronegativity at very low pressure only (below 3 mTorr) presented in Chapter 3 of this manuscript, where the isothermal assumption still holds for the electrons (see Esteves *et al.* [1]). Still, these first experiment-modeling comparisons alone argued in favor of expanding and consolidating the existing set of iodine cross sections.

In 2020, Yadav *et al.* [29] and, in 2021, Ambalampitiya *et al.* [28] calculated new sets of iodine cross sections. Some calculations concern the same reactions as those calculated originally [85] (dissociative attachment, molecular ionization, molecular dissociative ionization, etc...) and allow for the comparison but some others are totally new and give first cross sections for atomic electronic excitation (with level-by-level details), molecular electronic and vibrational excitation.

Experimental measurements of cross sections for collisional processes occurring within an iodine plasma are few. One can cite the work of Poline *et al.* for the ion recombination of I^- and I^+ [88], the work of Greaves [89] for the ion recombination of I^- and I_2^+ or the works of the last century on dissociative attachment cross section measurements [73, 74]. The charge exchange reaction between the I_2 molecule and the I^+ ion was recently studied by Hause *et al.* [90]. Concerning elastic collisions between an electron and a neutral species, a few measurements have been performed at high electron energies by Zatsarinny *et al.* [91] but none have been made for electron energies below 10 eV. In addition, no swarm parameters have been measured.

A lot of cross sections are still missing if we compare with models developed by the low-temperature plasma community to study other molecules such as O_2 [92] or the halogen Cl_2 [93–95]. However, we intend to present an updated set of iodine cross sections to model low-pressure iodine plasmas.

Just days before the submission of this thesis, a paper from Lafleur, presenting an iodine plasma model for gridded thrusters using an updated set of cross sections as compared to Grondein's model [13], taking into account the cross sections of Ambalampitiya *et al.* [28] in particular, was published [17]. The following was written before the publication of that paper, so we will not necessarily refer to it, but the reader will find similarities between the two independent works.

1.4.1 Electron impact on I

1.4.1.1 Ionization and elastic collisions

For electrons colliding with atoms, the main processes are elastic scattering in which primarily the electron momentum is changed, and inelastic processes such as excitation and ionization. The reactions occurring when an electron collides with an iodine atom, and which are considered in this manuscript, are listed in Table 1.4. In this subsection, the focus is on elastic collisions and ionization only, excitation and de-excitation by electron impact, also listed in Table 1.4, will be presented in the next subsection. Corresponding cross sections as a function of the electron energy are plotted in the top subfigure of Figure 1.12 while the corresponding reaction rates assuming a Maxwellian electron distribution function are plotted as a function of the electron temperature in the bottom subfigure (see Appendix B for the computation of the reaction rates).

Table 1.2: List of reactions occurring when an electron collides with an iodine atom. $I_{3/2}$ and $I_{1/2}$ respectively refers to $^2P^\circ_{3/2}$ and $^2P^\circ_{1/2}$ atomic states. $I^*_{b_2}$, $I^*_{b_3}$ and $I^*_{b_4}$ respectively refers to excited iodine atoms of bins b_2, b_3 and b_4 of the coarse-grain model described in subsection 1.4.1.2.

Reaction	Process	Rate	Threshold [eV]	Ref
$I_{3/2} + e^- \longrightarrow I^+ + 2e^-$	Ionization	$K_{iz,I_{3/2}}$	10.45	[28]
$I_{3/2} + e^- \longrightarrow I_{3/2} + e^-$	Elastic scattering	$K_{el,I_{3/2}}$	0.	[28]
$I_{1/2} + e^- \longrightarrow I_{1/2} + e^-$	Elastic scattering	$K_{el,I_{1/2}}$	0.	[28]
$I_{3/2} + e^- \longrightarrow I_{1/2} + e^-$	Excitation (0→1)	$K_{ex_1,I_{3/2}}$	0.9426	[28]
$I_{3/2} + e^- \longrightarrow I^*_{b_2} + e^-$	Excitation (0→2)	$K_{ex_2,I_{3/2}}$	6.7736	[28]
$I_{3/2} + e^- \longrightarrow I^*_{b_3} + e^-$	Excitation (0→3)	$K_{ex_3,I_{3/2}}$	8.0473	[28]
$I_{3/2} + e^- \longrightarrow I^*_{b_4} + e^-$	Excitation (0→4)	$K_{ex_4,I_{3/2}}$	8.1848	[28]
$I_{1/2} + e^- \longrightarrow I^*_{b_2} + e^-$	Excitation (1→2)	$K_{ex_2,I_{1/2}}$	5.831	[28]
$I_{1/2} + e^- \longrightarrow I^*_{b_3} + e^-$	Excitation (1→3)	$K_{ex_3,I_{1/2}}$	7.1047	[28]
$I_{1/2} + e^- \longrightarrow I^*_{b_4} + e^-$	Excitation (1→4)	$K_{ex_4,I_{1/2}}$	7.2422	[28]
$I_{1/2} + e^- \longrightarrow I_{3/2} + e^-$	De-excitation (1→0)	$K_{de-ex,I_{1/2}}$	0.	This work

The ionization cross section for electron energies up to 1000 eV is taken from [28] and has not been extrapolated for electron energies higher than 100 eV. The threshold is fixed to 10.45 eV, a value measured more than fifty years ago [80] and indicated in the ionization energies table of any CRC Handbook of Chemistry and Physics.

The elastic scattering cross sections for electron energies up to 100 eV, for $I_{3/2}$ and $I_{1/2}$ are taken from Ambalampitiya *et al.* [28]. The cross section for $I_{1/2}$ is totally new and had never been calculated before. However, the cross section for $I_{3/2}$ can be compared to the elastic cross section previously calculated [85] and used in Grondein *et al.* [13] or by Marmuse [22] (see Figure 1.13). While the behavior at high energy is similar, the behavior at low energy with a Ramsauer minimum (below 2 eV), largely differs. This will have a major impact on the simulations as it will be highlighted in Chapter 5 and such a behavior at low electron energy must be experimentally confirmed. As of now, no data are available for elastic momentum transfer cross sections (see equation B.15 in Appendix B for the definition), so in the following, the elastic cross section (see equation B.14 in Appendix B) is used as momentum transfer cross section of I. In Figure 1.13, we have also plotted the elas-

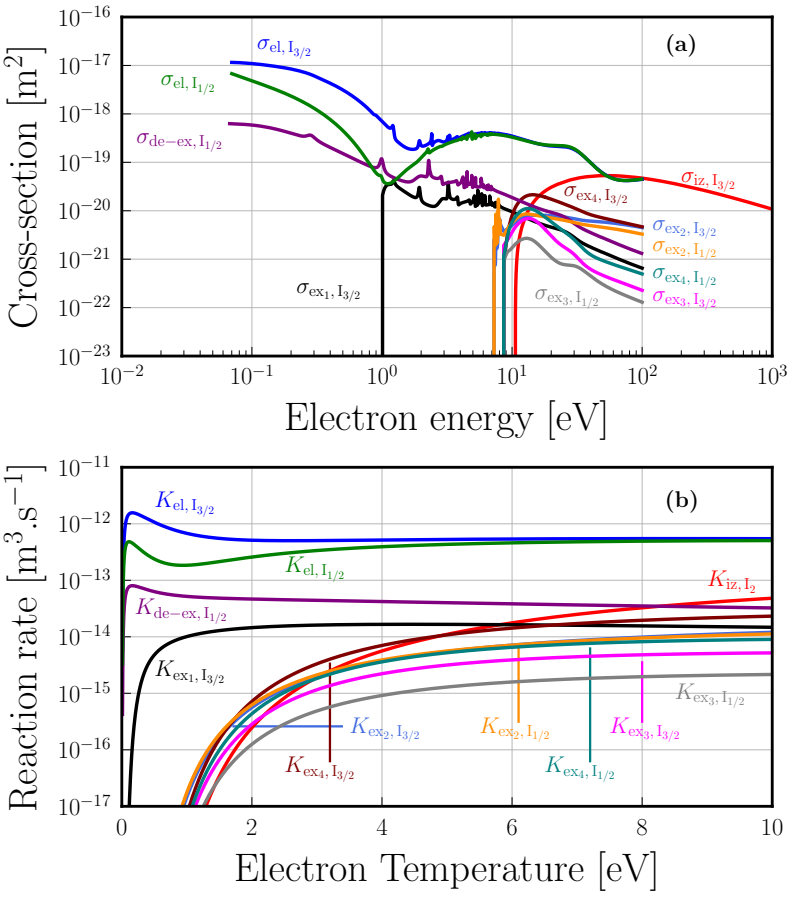

Figure 1.12: (a) Electron-I collision cross sections. (b) Electron-I collision reaction rates for Maxwellian electrons. The different collision processes are listed in Table 1.2.

tic momentum transfer cross section for xenon. As I and Xe atoms have almost the same mass, one could expect similar values of the elastic momentum transfer cross sections. We note that at low energy (0.1-2 eV), the Ramsauer mimimum is much more pronounced in xenon than iodine, resulting in a cross section for iodine which is 2-3 orders of magnitude higher. The impact of the current uncertainties on the elastic and elastic momentum transfer cross sections on the plasma characteristics will be discussed in Chapter 5. There is clearly a need of additional calculations or measurements of these cross sections at low energy (< 2 eV).

Note that none of the electron-I collision cross sections were extrapolated at high energy since the calculations provided data for electron energies up to 100 eV (1000 eV for ionization). It has been checked that extrapolations at very low energy (below 0.1 eV for cross sections without threshold) did not have a significant impact on the reaction rates calculated.

1.4.1.2 Electronic excitation and de-excitation by electron impact

The spin-orbit coupling degeneracy of the atomic ground state (presented in subsection 1.3.2.1) results in the presence of an atomic excited state ($I(^2P^\circ_{1/2})$ hereafter designated $I_{1/2}$) only 0.9426 eV [34] above the ground state ($I(^2P^\circ_{3/2})$ hereafter desig-

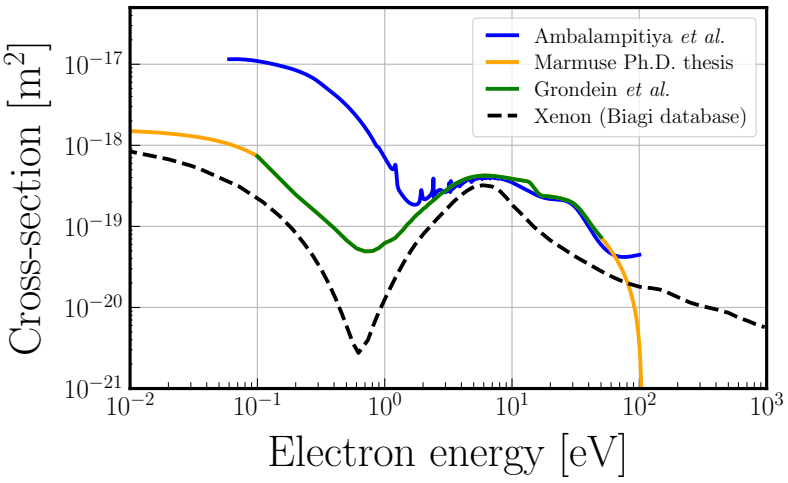

Figure 1.13: $I_{3/2}$ elastic cross sections found from several works. The elastic momentum transfer cross section for xenon (dashed line) has been added to extend the comparison.

nated $I_{3/2}$). When dissociation is produced by heating (around 1000 K for instance), the upper state is always much less populated than the lower state (assuming a Boltzmann distribution at 1000 K $\approx$ 0.086 eV, the ratio of population of the upper level over the lower level is $0.5\exp(-0.9426/0.086) \approx 8.7\times10^{-6}$). In a plasma, though, dissociation occurs mainly via electron impact and the electron temperature is around a few electron-volts (between 1 and 5 eV in this thesis and so larger than 0.9426 eV). Thus it is impossible to neglect the upper population. In this thesis, the $I_{1/2}$ state will be treated not only as an excited species but as a second and genuine atomic species.

As of 2021, the atomic excitation cross section calculated by Quantemol in 2015 [85] and used both by Grondein *et al.* [13] and Marmuse [22] was the only one available in the literature. It consisted of a global cross section for the process:

$$e^- + I \rightarrow e^- + I^*, \tag{1.10}$$

where I* was a "super" excited state accounting for all the atomic excited species. The threshold was fixed to 0.9426 eV, the energy gap between $I_{3/2}$ and $I_{1/2}$. Nevertheless, in a recent paper from Ambalampitiya *et al.* [28], new electron impact excitation cross sections were calculated by using two models with either 10, or 29 iodine electronic states. We chose to use the model with 29 levels (denoted BPBSR-29) as recommended by K. Bartschat in a private communication. This new set of cross sections allows for building more sophisticated models than the previously published ones. The now available cross sections model the excitation from the ground state ($^2P^\circ_{3/2}$ or $I_{3/2}$) towards the 28 upper levels and from the first excited state ($^2P^\circ_{1/2}$ or $I_{1/2}$) towards the 27 upper levels.

Instead of directly using the 55 excitation cross sections, we built up a coarse-grain, or reduced-order state-to-state model by lumping the 29 electronic levels of the BPBSR-29 model into 5 electronic bins. The levels were identified by using the NIST database [34]. Note that the notations, the ordering and the energy of the levels differ slightly between the BPBSR-29 model and the NIST website (where notations are similar to the one presented in subsection 1.3.1.2). Table 1.3 summarizes

the characteristics of the 5 bins of the coarse-grain model with corresponding levels in the BPBSR-29 model and on the NIST website. The first two bins (b_0 and b_1) are "true" electronic levels and composed of only one level: the ground state $^2P^\circ_{3/2}$ and the first electronic state $^2P^\circ_{1/2}$. For upper bins $2 \leq i \leq 4$, we chose to group the electronic levels of the BPBSR-29 model based on their internal structure. We also chose to give as energy of each bin ($\mathcal{E}_i$), the NIST energy of the first electronic level in that bin. A different choice for the energy of the bin could have been used [96] but the small differences between energy levels should not give very different results. The cardinality (or number of levels) of b_i (denoted $\#_i$) is different for each bin and indicated in Table 1.3.

As in [96], the statistical weight of the bin b_i (g_i), is the sum of the statistical weights of all electronic levels j in that bin.

$$g_i = \sum_{j \in b_i} g_j \,. \tag{1.11}$$

Table 1.3: Coarse-grain electronic model with the corresponding levels in the BPBSR-29 model [28] and on the NIST website [34]. i is the bin number, $\mathcal{E}_i$, g_i and $\#_i$ are respectively the energy, the statistical weight and the cardinality of the bin i.

i	$\mathcal{E}_i$ [eV]	g_i	BPBSR-29 level [28]	NIST level [34]	$\#_i$
0	0.	4	001	$^2P^\circ_{3/2}$	1
1	0.9426	2	002	$^2P^\circ_{1/2}$	1
2	6.7736	18	(003-006, 008)	$(^3P_2)6s\,^2[2]_{3/2,5/2}$, $(^3P_1)6s\,^2[1]_{1/2,3/2}$, $(^3P_0)6s\,^2[0]_{1/2}$	5
3	8.0473	26	(007, 009-012)	$(^3P_2)6p\,^2[2]^\circ_{3/2,5/2}$, $(^3P_2)6p\,^2[3]^\circ_{5/2,7/2}$, $(^3P_2)6p\,^2[1]^\circ_{1/2}$	5
4	8.1848	82	(013-029)	$(^3P_2)6p\,^2[1]^\circ_{3/2}$, 5d levels and above	17

To calculate σ_{ki} ($k \in \{0, 1\}$, $k < i \leq 4$) the excitation cross section from the bin b_k towards an upper bin of the coarse-grain model b_i, we simply sum the excitation cross sections (σ_{kj}) from b_k to all the j levels of BPBSR-29 model constituting b_i as explained in [97]:

$$\sigma_{ki} = \sum_{j \in b_i} \sigma_{kj},\ k \in \{0, 1\},\ k < i \leq 4. \tag{1.12}$$

As the energy threshold and the energy step are different in each file, an interpolation was realized to calculate σ_{ki} with the energy step of the file for the excitation cross section σ_{kj} to the first level j of the bin b_i. Finally, when considering excitation from b_1 towards b_i ($i > 1$), the threshold energy $\tilde{\mathcal{E}}_i$ is given by:

$$\tilde{\mathcal{E}}_i = \mathcal{E}_i - \mathcal{E}_1, \tag{1.13}$$

where the energy of the first excited state ($\mathcal{E}_1 = 0.9426$ eV) is substracted.

The cross sections of the coarse-grain model and corresponding reactions rates calculated assuming a Maxwellian distribution for electrons are gathered in Figure 1.12.

Ambalampitiya *et al.* [28] did not calculate any cross sections for electron impact de-excitation such as:

$$e^- + I^* \rightarrow e^- + I_{3/2}, \tag{1.14}$$

nor,

$$e^- + I^* \rightarrow e^- + I_{1/2}, \tag{1.15}$$

where I^* is an excited above $I_{3/2}$ or $I_{1/2}$, included in the BPBSR-29 model. Because the first electronic $I_{1/2}$ is only 0.9426 eV above the ground state $I_{3/2}$ (whereas other electronic levels are at more than 6.77 eV above), we only consider the de-excitation reaction between the $I_{1/2}$ and the $I_{3/2}$ state:

$$e^- + I_{1/2} \longrightarrow e^- + I_{3/2}. \tag{1.16}$$

The principle of detailed balance connects the cross sections for a process and its inverse. For electron impact de-excitation reactions between two electronic levels i and $j > i$ of a given atom, according to [98] we have:

$$(\mathcal{E} + \mathcal{E}_{ij}) g_i \sigma_{ij}(\mathcal{E} + \mathcal{E}_{ij}) = \mathcal{E} g_j \sigma_{ji}(\mathcal{E}), \tag{1.17}$$

where σ_{ij} and σ_{ji} are the cross sections for the electron impact excitation from i to j and de-excitation from j to i, respectively; g_i and g_j are the statistical weights of each electronic state of the atom; $\mathcal{E} \geq 0$ is the electron energy and $\mathcal{E}_{ij} = \mathcal{E}_j - \mathcal{E}_i > 0$ is the excitation energy (the difference of energy between the electronic levels j and i). From the detailed balance relation, we see that the de-excitation cross section has no energy threshold. We assume that the energy gained by the electron is 0.9426 eV.

Figure 1.12 shows the cross sections for the electron impact excitation $e^- + I(^2P_{3/2}) \rightarrow e^- + I(^2P_{1/2})$ and, using the detailed balance relation of equation (1.17), the cross section for the de-excitation process $e^- + I(^2P_{1/2}) \rightarrow e^- + I(^2P_{3/2})$.

If a Maxwellian distribution is assumed for electrons at the temperature T_e [eV], then the detailed balance can be written between the electron impact rate coefficient K_{ji} for the de-excitation from j to i and K_{ij} for the excitation from i to j as:

$$K_{ji}(T_e) = \frac{g_i}{g_j} \exp\left(\frac{\mathcal{E}_j - \mathcal{E}_i}{T_e}\right) K_{ij}(T_e). \tag{1.18}$$

In Figure 1.12, K_{01} and K_{10} are plotted as a function of the electron temperature. The notations $K_{\mathrm{ex}_1,I_{3/2}}$ and $K_{\mathrm{de-ex},I_{1/2}}$ have been preferred to respectively K_{01} and K_{10}, to be consistent with the other collision processes notations.

1.4.2 Electron impact on I_2

In 2020, Yadav *et al.* [29] calculated most of the cross sections for the reactions presented in this subsection. However, for consistency with the previous subsection, most of the cross sections used come from Ambalampitiya *et al.* [28]. Still, references to Yadav's work will be made to broaden the discussion.

1.4.2.1 Elastic collisions and ionization

The collisions involving an electron and an iodine molecule are listed in Table 1.4. I_2 refers to the molecular ground state I_2 ($X\,^1\Sigma_g^+$). Corresponding cross sections as a function of the electron energy are plotted in the top subfigure of Figure 1.14 while

the corresponding reaction rates assuming a Maxwellian electron distribution function are plotted as a function of the electron temperature in the bottom subfigure. Some cross sections have been extrapolated at low and/or high energy, this is indicated by dotted lines in subfigure (a). The extrapolation at high energy is mandatory when calculations give data for electron energies up to 10 eV only but has an effect on the reaction rates above a few eVs of electron temperature. The extrapolation at low electron energies has a very limited effect the calculated reaction rates and could be ignored (less than 1% of difference).

Table 1.4: List of reactions occurring when an electron collides with an iodine molecule. I_2 refers to I_2 ($X\ ^1\Sigma_g^+$). The electronic excitation reaction towards a global excited state I_2^* gathers 4 different reactions as described in subsection 1.4.2.3. Only the ten first vibrational excitations are considered and gathered into one process.

Reaction	Process	Rate	Threshold [eV]	Ref
$I_2 + e^- \longrightarrow I_2 + e^-$	Elastic scattering	K_{el,I_2}	0	[28]
$I_2 + e^- \longrightarrow I_2 + e^-$	Elastic momentum transfer	K_{elm,I_2}	0	[28]
$I_2 + e^- \longrightarrow I_2^+ + 2\,e^-$	Ionization	K_{iz,I_2}	9.31	[22]
$I_2 + e^- \longrightarrow I^+ + I_{3/2} + 2e^-$	Dissociative ionization	$K_{diss.iz,I_2}$	11.94	[28]
$I_2 + e^- \longrightarrow I^- + I_{1/2}$	Dissociative attachement	$K_{diss.att,I_2}$	0	[28]
$I_2 + e^- \longrightarrow 2\,I_{3/2} + e^-$	Dissociation	K_{diss,I_2}	1.542	[22]
$I_2 + e^- \longrightarrow I_2^* + e^-$	Total electronic excitation	K_{ex,I_2}	2.18	[28]
$I_2\ (v=0) + e^- \longrightarrow I_2(v=1,...,10) + e^-$	Total vibrational excitation	K_{vibr,I_2}	0.02575	[28]

Elastic scattering and elastic momentum transfer cross sections cross sections are taken from [28]. They were extrapolated at low energy (on the interval [0.01 eV; 0.1 eV] assuming a constant value and above 10 eV assuming a $1/\mathcal{E}$ law as done by Marmuse [22] in Appendix C of his thesis and suggested by [99]. The extrapolation does affect the rate reaction for electron temperature above 5 eV. Yadav [29] also calculated these cross sections up to 20 eV. The elastic scattering cross section appears similar but the momentum cross section appears 4 times higher than the cross section we use.

The molecular ionization cross section is the same that was used by Grondein *et al.* [13] and [22]. It comes from [85] and has not been extrapolated. Ambalampitiya *et al.* [28] calculated a new cross section for this reaction using the same method than [85], the discrepancies are small. However, the reaction threshold in [28] was set at 10.19 eV and their calculation was limited to 1000 eV against 5000 eV with a threshold of 9.31 eV for [85] (as determined experimentally by Cockett *et al.* [71]). Yadav *et al.* [29], also calculated this cross section using several methods, the agreement between each method is acceptable with a maximum value around $1.1{\times}10^{-19}$ m^2 between 40 and 80 eV, close to the cross section we use.

1.4.2.2 Dissociative processes

Dissociation

The dissociation cross section is taken from [85]. No other data are available nor is any information about the atoms produced: we assumed that they are both in the ground state ($^2P^\circ_{3/2}$). The threshold was fixed to 1.542 eV because the dissociation limit value has been measured with great precision by spectroscopists at 12440.23 cm^{-1} [52]. Contrary to Grondein *et al.*, the cross section has been extrapolated at high energy (above 10 eV) assuming a $\log(\mathcal{E})/\mathcal{E}$ law as done by Marmuse [22]

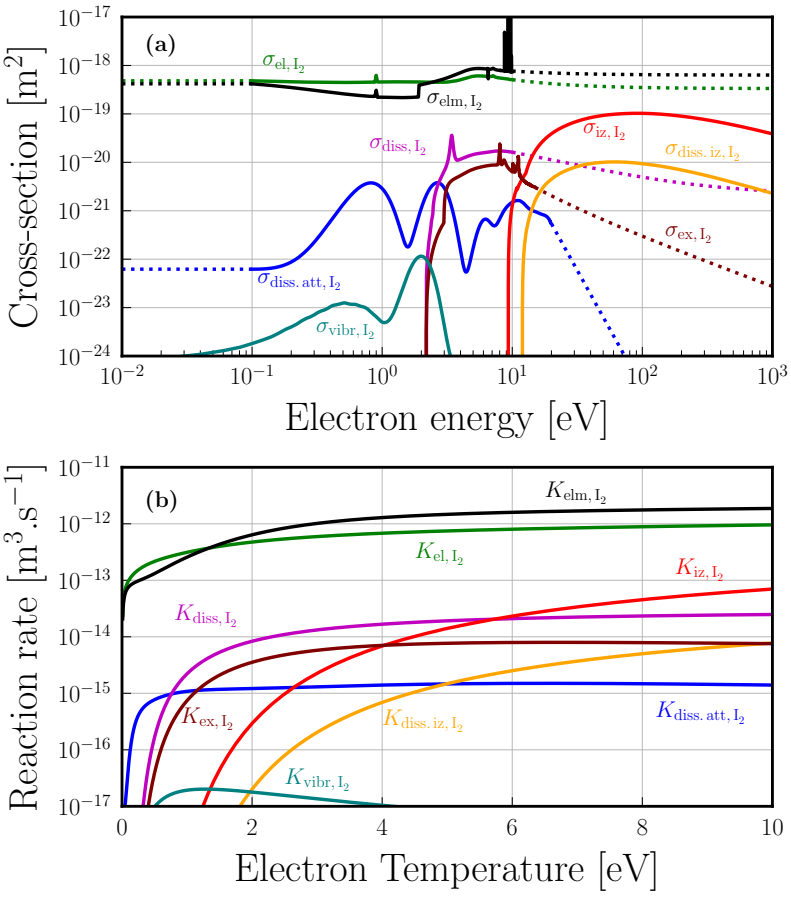

Figure 1.14: (a) Electron-I_2 collision cross sections. (b) Electron-I_2 collision reaction rates for Maxwellian electrons. The different collision processes are listed in Table 1.4.

and suggested by [99]. Lucken [21] also used this cross section but extrapolated it by using a power law; the discrepancies between Marmuse and Lucken extrapolations are very small [22]. The extrapolations do affect the reaction rate above an electron temperature of 4 eV only. In our opinion, this cross section is the one that should be recalculated in priority as it directly impacts the dissociation value inside the plasma and thus the density of all species. Besides, cross sections about dissociation into $^2P^\circ_{3/2} + ^2P^\circ_{1/2}$ or $^2P^\circ_{1/2} + ^2P^\circ_{1/2}$ are not available yet but are of great importance given the low energy difference between the $^2P^\circ_{3/2}$ and $^2P^\circ_{1/2}$ states. Experimentally, the photodissociation process

$$I_2 + h\nu \rightarrow \alpha\ I\left(^2P^\circ_{3/2}\right) + \beta\ I\left(^2P^\circ_{1/2}\right), \text{ with } \alpha + \beta = 2, \tag{1.19}$$

has been studied in the visible to quantify the proportion of atoms produced in each state [45]. Is was shown that more than 25 % of the produced atoms could be in the $^2P^\circ_{1/2}$ excited state.

Dissociative attachment

The dissociative attachment cross section is also taken from [28]. Note that the atom produced by the reaction is in the $^2P^\circ_{1/2}$ state which was ignored by previous

works. The cross section is higher than the one used by Grondein *et al.* which was calculated by Hamilton [85] (see Figure 1.15) and not so far from the experimental value measured in the middle of the XX$^{\text{th}}$ century [73, 74]. The cross section has been extrapolated at low energy (on the interval [0.01 eV; 0.1 eV]) assuming a constant value according to Hamilton's calculation on this interval [85] and above 20 eV assuming a power law. The extrapolations do affect the reaction rate but for electron temperatures above 10 eV only. Note, however, that at low energy, a $1/\mathcal{E}$ law has been determined by Biondi [75] and a similar behavior has been found by Yadav [29]. The cross section we use is more than two orders of magnitude smaller than the cross section calculated by Yadav for electron energies below 0.5 eV and more than three orders of magnitude smaller than Biondi's cross section at 0.01 eV. In conclusion, there is clearly a need for more accurate data on the dissociative attachment reaction cross section, especially at very low electron energy.

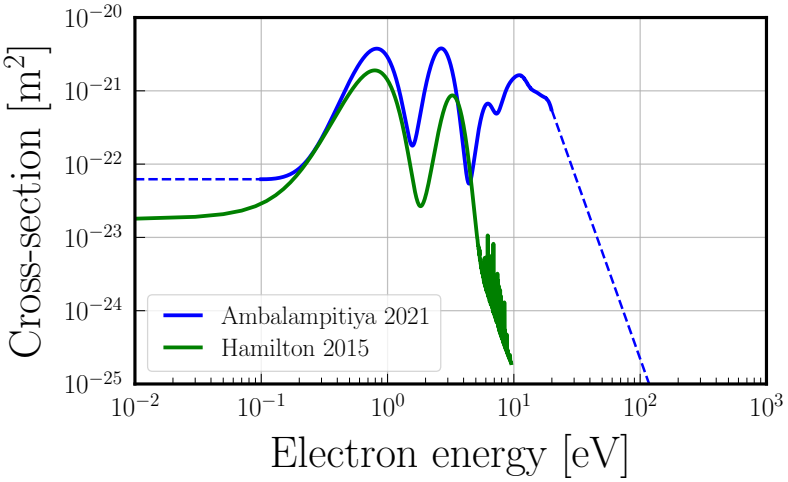

Figure 1.15: Electron impact dissociative attachment cross sections from Ambalampitiya *et al.* [28] and from [85]. The green curve was used in Grondein *et al.* [13].

Dissociative ionization

The dissociative ionization cross section is taken from [28] and has not been extrapolated above 1000 eV. The atom is assumed to be produced in its ground state. The threshold of 11.94 eV is close to the sum of the photoionization energy ($\approx$ 8.9 eV [100]) and the electron affinity of iodine ($\approx$ 3.06 eV [78]) or to the experimentally measured value of 11.63 $\pm$0.05 eV [101]. The discrepancies with the cross section originally calculated by Hamilton [85] are very minor.

1.4.2.3 Electronic excitation of I_2

The first collisional data about the electronic excitation of the I_2 molecule by electron impact were calculated in 2020 by Yadav *et al.* [29], considering six excited states ($^3\Pi_u$, $^1\Pi_u$, $^3\Sigma_g^-$, $^1\Sigma_g^+(\times 2)$ and $^1\Sigma_g^-$). In 2021, Ambalampitiya *et al.* [28] did the same with four excited states ($^3\Pi_u$, $^1\Pi_u$, $^3\Sigma_g^-$ and $^1\Sigma_g^+$), the reactions are listed in Table 1.5. Before that, iodine plasma models did not take into account any molecular electronic excited state because no cross section was available in the literature

and also because the dissociation energy is below any excited energy threshold and it was assumed that any excited state would end up being dissociated [21].

The levels and notations of the molecular excited states used by Ambalampitiya *et al.* [28] or Yadav *et al.* [29] differ from the notations used by other authors [88]. This is due to whether or not relativistic effects are taken into account in the calculations of molecular potentials. The notation used by the spectroscopists [52, 102] is much closer to that used by Poline *et al.* [88]. It is not easy to match exactly the states obtained by relativistic calculations with the states obtained by non-relativistic calculations. Moreover, the threshold values depend on the method of calculation used, which differs from one author to another and is different from the very precise spectroscopic measurements: this explains the discrepancies observed in Table 1.5.

Table 1.5: List of reactions of the molecular iodine electronic excitation. I_2 alone refers to the ground state I_2 ($X\ ^1\Sigma_g^+$, $v = 0$). Threshold values found in the literature are also given.

Reaction	Rate	Calculation thr. [ev]	Theory thr. [eV] [102]	Experimental thr. [eV]
$I_2 + e^- \longrightarrow I_2(^3\Pi_u) + e^-$	K_{ex_1,I_2}	2.18 [28, 29]	2.37	1.25 [103], 1.95 [104]
$I_2 + e^- \longrightarrow I_2(^1\Pi_u) + e^-$	K_{ex_2,I_2}	3.00 [28], 2.99 [29]	2.38	–
$I_2 + e^- \longrightarrow I_2(^3\Sigma_g^-) + e^-$	K_{ex_3,I_2}	5.18 [28], 5.44 [29]	3.90	5.04 [104]
$I_2 + e^- \longrightarrow I_2(^1\Sigma_g^+) + e^-$	K_{ex_4,I_2}	5.70[28], 6.80 [29]	–	–

The molecular excitation cross sections are plotted in Figure 1.16. They were calculated on the electron energy interval [0.1 eV; 15 eV]. The sum of the four cross sections is plotted in black and has been extrapolated at high energy (up to 1000 eV) assuming a $1/\mathcal{E}^2$ law as suggested by Shemansky for N_2 [105] ($1/\mathcal{E}$ or $1/\mathcal{E}^3$ were also found in the literature [94, 106]). The total cross section, and the corresponding reaction rate calculated assuming Maxwellian electrons are plotted in Figure 1.14 with all the other electron-I_2 processes. As expected, the electronic excitation reaction rate is below the reaction rate for dissociation.

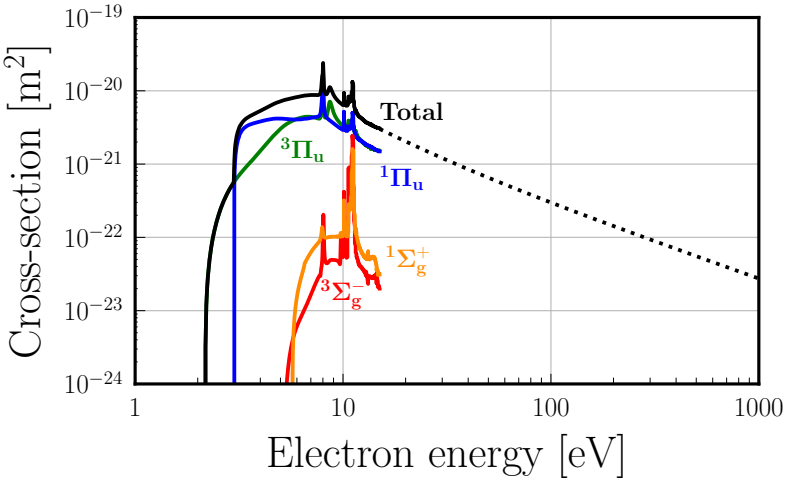

Figure 1.16: Cross sections for electronic excitation to the $^3\Pi_u$, $^1\Pi_u$, $^3\Sigma_g^-$, and $^1\Sigma_g^+$ states from the ground state (taken from [28]). "Total" is the sum of the four cross sections, it has been extrapolated above 15 eV (dotted line).

A qualitative comparison with Yadav *et al.* [29] show that the trends are the same

for the four cross sections but the peaks seen in Ambalampitiya *et al.* are not resolved by Yadav *et al.* calculations. Cross sections for $^3\Pi_u$ and $^1\Pi_u$ appear around 1.5 times higher in Yadav *et al.*

1.4.2.4 Vibrational excitation of I_2

The first electron impact vibrational excitation cross sections were calculated by Ambalampitiya *et al.* [28]. They consist in the excitation from the ground state $I_2(X\ ^1\Sigma_g^+, v = 0)$ towards the ten first vibrationally excited levels (from $v = 1$ to $v = 10$) of the ground state. In Figure 1.17, we plotted the cross section for the first transition (from $v = 0$ to $v = 1$) and the sum of the ten contributions. Two peaks are observed in the cross sections, one around 0.5 eV (due to the $^2\Pi_g$ resonance) and one around 2 eV (due to the $^2\Pi_u$ resonance).

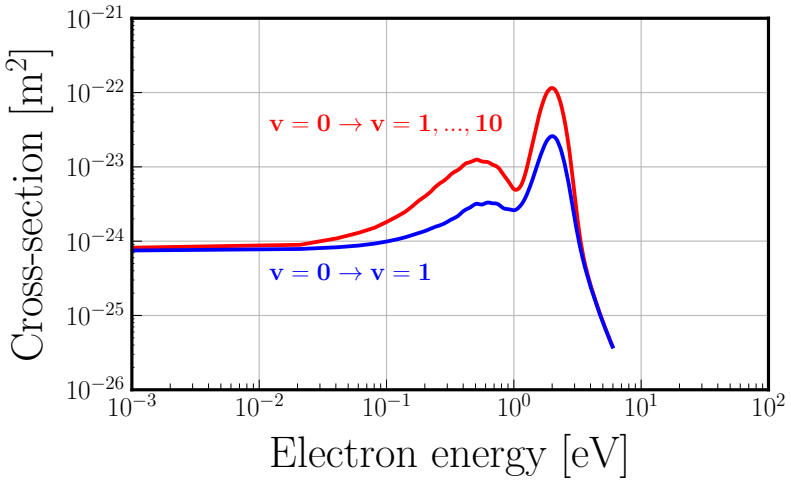

Figure 1.17: Iodine ground state vibrational excitation cross sections from $v = 0$ to $v = 1$ (blue curve) and for the sum from $v = 0$ to $v = k$ for $k \in \{1, ..., 10\}$ (red curve).

The total vibrational cross section is also plotted in Figure 1.14 with all the other electron-I_2 collision cross sections. The reaction rate has also been calculated assuming Maxwellian electrons. The contribution of the electron impact vibrational excitation appears negligible when compared with all the other electron impact processes for an electron temperature above 2 eV. Still, it will be taken into account in the global modeling approach to correctly account for the electron losses (see Chapter 5). However, its impact is expected to be minor. It is interesting to note that Thompson *et al.* [107] calculated the relaxation of $I_2(v)$ by collisions with I at about 1000 K. The order of magnitude is the same as for the relaxation of $Cl_2(v)$+Cl. In chlorine ICP plasmas, in conditions close to those studied in this PhD work, it has been observed that the population of the first vibrational levels of Cl_2 are populated following a local equilibrium at the gas temperature [108] due to the efficient vibrational-translational (VT) relaxation between Cl_2 and Cl atoms. In a first approximation, we will assume it is the same in iodine.

1.4.3 Collisions between charged species

Ion loss mechanisms are of two kinds in a plasma: in volume via collisions with other species or via neutralization at the walls. In this subsection, the focus is on the first mechanism only.

1.4.3.1 Ion-ion mutual neutralization

Grondein *et al.* [13] only considered that negative ions I^- were lost via mutual neutralization with I^+ (to produce two I atoms) or I_2^+ ions (to produce an atom and a molecule). The reaction rates were assumed to be constant:

- $K_{\text{rec},I^- - I^+} = 9.311 \times 10^{-15}$ m^3.s^{-1}, citing Yeung [109],
- $K_{\text{rec},I^- - I_2^+} = 1.22 \times 10^{-13}$ m^3.s^{-1}, citing Greaves [89].

Lucken [21] and Marmuse [22] also used these values. However, they are not correct for several reasons and must be modified. First, in 1957, Yeung [109], never explicitly mentioned which mutual neutralization process was being investigated, he only assumed that all ions are molecular, as suggested by Spencer-Smith's early work on iodine discharges in 1935 [72], who found that I_2^+ was, by far, the most dominant ion. Then in 1964, Greaves [89], took up exactly the same experiment as Yeung and drew two major conclusions: (1) Yeung was wrong by a factor of 10 in his experiments because of "a fault in one of the amplifiers". (2) Mass spectrometry assessed that mutual neutralization occurs exclusively between I^- and I_2^+ species. His two conclusions prove that Yeung's work can not be cited to consider recombination between I^+ and I^-. Furthermore, Greaves measured reaction rates for pressures between 30 mTorr and 1 Torr and gas temperatures around 300 K. He measures that above 230 mTorr, and at room temperature, $K_{\text{rec},I^- - I_2^+} = 1.22 \times 10^{-13}$ m^3.s^{-1}. Nevertheless, between 30 mTorr and 230 mTorr, the effect of diffusion turns out to be non-negligible and the reaction rate decreases with pressure; the value measured at 30 mTorr is $K_{\text{rec},I^- - I_2^+} = 5.8 \times 10^{-14}$ m^3.s^{-1}: the value retained by Grondein appears to be at least twice as large (we are mainly working between 0.3 and 30 mTorr). Based on the above, a reasonable choice would be to use:

$$K_{\text{rec},I^- - I^+} = K_{\text{rec},I^- - I_2^+} = 5 \times 10^{-14} \sqrt{\frac{300}{T_{\text{gas}}[\text{K}]}} \text{ m}^3.\text{s}^{-1}, \tag{1.20}$$

as it is done in chlorine plasma models [95] and close to Greaves' measurements at 30 mTorr [89].The dependency on the gas temperature is an assumption here: it comes from the integration of a cross section proportional to $1/\mathcal{E}$ over a Maxwellian [98]. It was not proven by Greaves because he only did experiments for gas temperatures between 296 K and 338 K. Finally, we will consider that the products of the I^--I_2^+ mutual neutralization are three atoms in the ground state and not a molecule and an atom as was assumed by Grondein *et al.* [13] and the following works. This is chosen by analogy with chlorine [95] and confirmed in private discussions with N. Sisourat and his team (LCPMR lab) when they carried out preliminary experiments at the double electrostatic ion-beam storage-ring facility Double ElectroStatic Ion Ring ExpEriment (DESIREE) (Stockholm University, Sweden).

Very recently, Poline *et al.* [88] studied the mutual neutralization reaction of atomic iodine ions (i.e., $I^+ + I^- \rightarrow I + I$) at the DESIREE facility. They showed that the reaction forms iodine atoms either in the ground-state configuration ($I(5p5\ ^2P^\circ)$, ~40%) or with one atom in an electronically excited state ($I(6s\ ^2[2])$, ~60%), with no significant variation over the branching ratios in the studied collision-energy range (0.1-0.8 eV). They estimate the total cross section to be of the order of 10^{-17} m^2 (more or less one order of magnitude) at 0.1 eV collision energy. In the group of N. Sisourat, at LCPMR, calculations of these cross sections have been undertaken (private discussions). The obtained cross sections are presented in Figure 1.18. They depend on the species produced by the process and the products $I(5p5\ ^2P^\circ_{3/2}) + I(6s)$ are by far the most probable, where I(6s) designates the highly excited 6s Rydberg states. The corresponding Maxwellian rates calculated by assuming that I^- and I^+ are at the same temperature are plotted in the bottom subfigure. The sum of the four products-differenciated rates is represented by a dashed line while equation (1.20) is also plotted. In the interval 0.1-1 eV, the agreement between the simple formula of equation (1.20) and the sum of the rates is very good.

Therefore, and because our simulation will not include excited states above the $I(5p5\ ^2P^\circ_{1/2})$ level (particularly not the I(6s) levels), the mutual neutralization processes considered in this manuscript are listed in Table 1.6, with $I(5p5\ ^2P^\circ_{3/2})$ the only atoms produced.

Table 1.6: List of mutual neutralization reactions.

Reaction	Rate	Threshold [eV]
$I^- + I_2^+ \longrightarrow I_{3/2} + I_{3/2} + I_{3/2}$	$K_{\mathrm{rec},I^- - I_2^+} = 5\times10^{-14}\sqrt{300/T_{\mathrm{gas}}}$	0.
$I^- + I^+ \longrightarrow I_{3/2} + I_{3/2}$	$K_{\mathrm{rec},I^- - I^+} = 5\times10^{-14}\sqrt{300/T_{\mathrm{gas}}}$	0.

1.4.3.2 Electron impact on ions

Here, we consider two additional processes: negative ion detachment by electron impact and I_2^+ dissociation, listed in Table 1.7. The corresponding cross sections and reaction rates are plotted in Figure 1.19.

Table 1.7: List of reactions between charged species.

Reaction	Process	Rate	Threshold [eV]	Ref
$I^- + e^- \longrightarrow I_{3/2} + e^- + e^-$	Detachment	K_{el,I_2}	3.059	[87]
$I_2^+ + e^- \longrightarrow I^+ + I + e^-$	Dissociation	K_{diss,I_2^+}	2.18	[87]

The detachment cross section was calculated by Hamilton [87], no other data are available in the literature. It has been used by Marmuse [22] and Lucken [21]. The energy resolution of the calculation is of 1 eV only, the first non-zero value being found at 4 eV while it has been precisely measured that the iodine electron affinity is 3.0590463 eV [78], a threshold value we retain. Negative ion detachment by electron impact was found to be not negligible in chlorine at low pressure [95] and could very well be even more important in iodine. Nonetheless, some doubts persist on the magnitude of this cross section as it appears one order of magnitude higher than the cross section for electron impact detachment from Cl^- [110].

Finally, the I_2^+ dissociation by electronic impact cross section was also calculated by Hamilton [87]. The threshold is fixed to 2.18 eV and no other data are available.

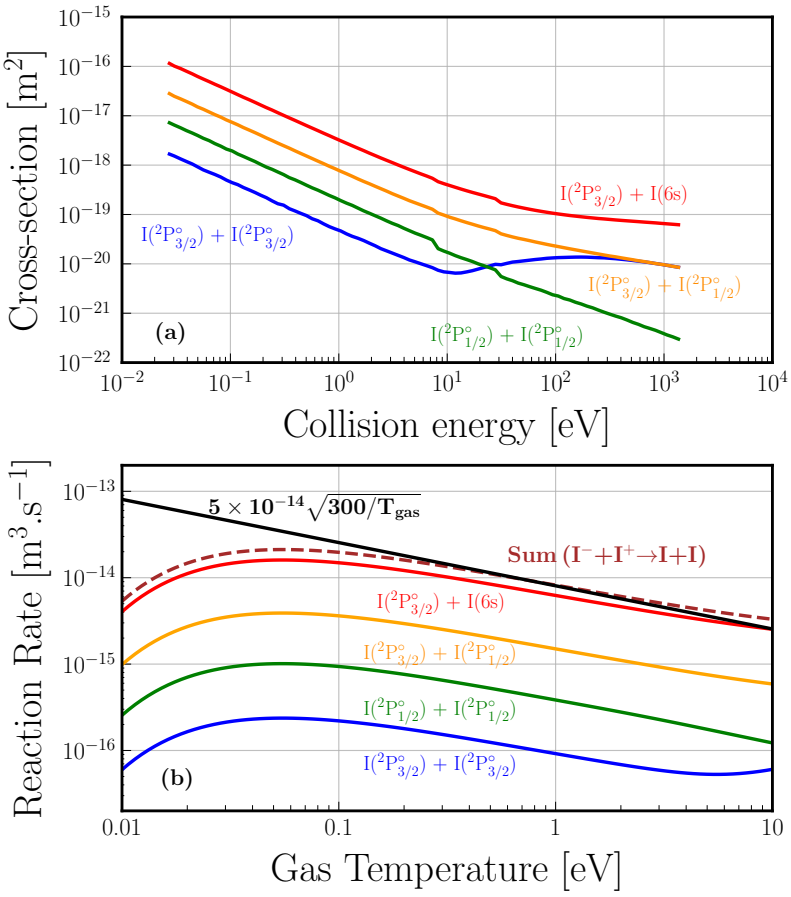

Figure 1.18: (a) Cross sections of the mutual neutralization reaction of atomic iodine ions ($I^+ + I^- \rightarrow I + I$) depending on the produced species. I(6s) designates the highly excited 6s Rydberg states (from Nicolas Sisourat ad his group, LCPMR, private communication). (b) Corresponding reaction rates calculated by assuming a Maxwellian distribution function with the reduced mass $\mu_R = m_I/2$. The sum of the four products-differenciated rates is represented by a dashed line and equation (1.20) is also plotted to extend the comparison.

1.4.4 Neutral-Neutral collisions

1.4.4.1 Elastic collisions

The exact way to treat elastic collisions between neutral particles is by introducing collision integrals where the relative velocity of the two colliding species is taken into account. The formalism, derived from Benilov's work [111, 112], is presented in detail in Appendix C. In this thesis, collisions between neutral species are of importance in Chapter 5, to correctly model gas heating in the global model and in Chapter 6, where the multi-fluid approach is used to model neutral species in PEGASES. The collisions between neutrals are assumed to be hard-sphere collisions.

As an example, let's consider the elastic collision between an iodine atom ($I_{3/2}$ or $I_{1/2}$) and an iodine molecule:

$$I + I_2 \rightarrow I + I_2. \tag{1.21}$$

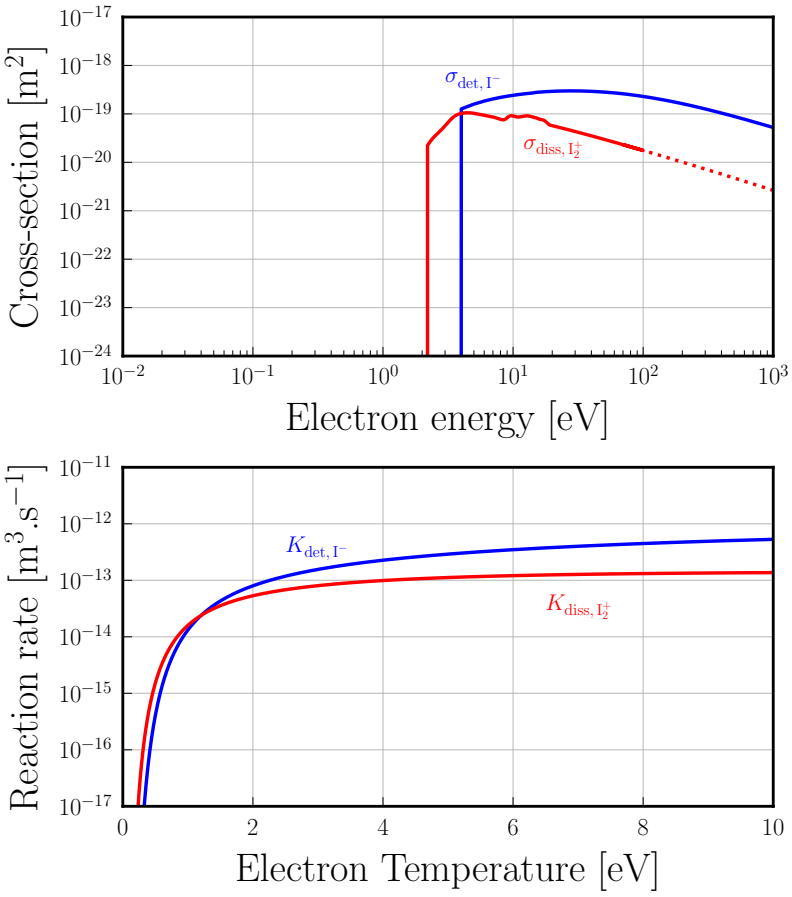

Figure 1.19: (a) Electron-ion collision cross sections. (b) Electron-ion collision reaction rates for Maxwellian electrons and ions at rest.

The hard-sphere momentum transfer cross section reads:

$$Q^{(1)}_{\mathrm{II_2}} = \pi\left(\frac{d_{\mathrm{I}} + d_{\mathrm{I_2}}}{2}\right)^2, \tag{1.22}$$

with d_{I} the iodine atom diameter and $d_{\mathrm{I_2}}$ the iodine molecule diameter. We used

$$d_{\mathrm{I}} = \frac{1}{2}d_{\mathrm{I_2}} = 280\ \mathrm{pm}, \tag{1.23}$$

so that $Q^{(1)}_{\mathrm{II_2}} = 5.81\times10^{-19}\mathrm{m}^2$. The corresponding collision integral (same dimension as a reaction rate) is:

$$\Omega^{(1,1)}_{\mathrm{II_2}} = Q^{(1)}_{\mathrm{II_2}}\sqrt{\frac{k_{\mathrm{B}}T_{\mathrm{II_2}}}{2\pi m_{\mathrm{II_2}}}}, \tag{1.24}$$

where

$$T_{\mathrm{II_2}} = \frac{m_{\mathrm{I_2}}T_{\mathrm{I}} + m_{\mathrm{I}}T_{\mathrm{I_2}}}{m_{\mathrm{I}} + m_{\mathrm{I_2}}}, \tag{1.25}$$

$$m_{\mathrm{II_2}} = \frac{m_{\mathrm{I}}m_{\mathrm{I_2}}}{m_{\mathrm{I}} + m_{\mathrm{I_2}}}, \tag{1.26}$$

are the reduced temperature and reduced mass of the colliding species. When $T_{\mathrm{I}} = T_{\mathrm{I}_2} = 300$ K, $\Omega^{(1,1)}_{\mathrm{II}_2} = 1.33 \times 10^{-17} \mathrm{m}^3.\mathrm{s}^{-1}$. Finally, the diffusion coefficient reads

$$D_{\mathrm{II}_2} = \frac{1}{n_{\mathrm{gas}}} \frac{3\pi}{16} \sqrt{\frac{2k_{\mathrm{B}} T_{\mathrm{II}_2}}{\pi m_{\mathrm{II}_2}}} \frac{1}{Q^{(1)}_{\mathrm{II}_2}}. \tag{1.27}$$

with $n_{\mathrm{gas}} = n_{\mathrm{I}_{1/2}} + n_{\mathrm{I}_{3/2}} + n_{\mathrm{I}_2}$.

The former reasoning applies for the elastic collisions between $\mathrm{I}_{1/2}$ and $\mathrm{I}_{3/2}$. Assuming the same temperature for both atomic species, the iodine atoms diffusion coefficient is:

$$D_{\mathrm{I}} = D_{\mathrm{II}} = \frac{3}{8} \sqrt{\frac{k_{\mathrm{B}} T_{\mathrm{I}}}{\pi m_{\mathrm{I}}}} \frac{1}{n_{\mathrm{gas}} d_{\mathrm{I}}^2}. \tag{1.28}$$

1.4.4.2 Quenching processes

A quenching process is a collision that induces a de-excitation (electronic or vibrational). In this thesis, only one quenching process will be considered:

$$\mathrm{I}_2 + \mathrm{I}_{1/2} \rightarrow \mathrm{I}_2 + \mathrm{I}_{3/2}. \tag{1.29}$$

The reaction rates for this reaction have been gathered in a thorough work by Chichinin [113] and are plotted in Figure 1.20. At 300 K, almost all of the authors found

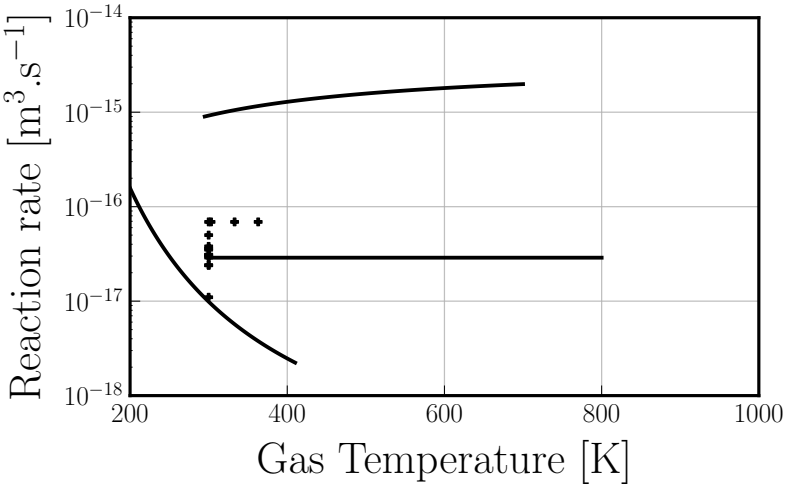

Figure 1.20: Quenching of $\mathrm{I}_{1/2}$ by I_2 reaction rates found in the work of Chichinin [113], as a function of the gas temperature.

a quenching rate between 10^{-17} and 10^{-16} $\mathrm{m}^3.\mathrm{s}^{-1}$. The quenching rate behavior with the gas temperature is not very clear and we will assume the rate to be constant. A statistical analysis on the value measured at 300 K has been performed (including only measurements where the incertitude was mentioned) and we found:

$$K_{\mathrm{quench},\mathrm{I}_2-\mathrm{I}_{1/2}} = \sum_i \frac{K_{\mathrm{quench},\mathrm{I}_2-\mathrm{I}_{1/2},\mathrm{i}}}{\sigma_i^2} \Bigg/ \sum_i \frac{1}{\sigma_i^2} = 3.23 \times 10^{-17}\ \mathrm{m}^3.\mathrm{s}^{-1}, \tag{1.30}$$

where the sum is taken over all the measured rates $K_{\text{quench},I_2-I_{1/2},i}$ of incertitude σ_i. The standard deviation of the analysis is 0.09×10^{-17} m^3.s^{-1} and will be ignored.

In the reference [113], the quenching process of $I_{1/2}$ by $I_{3/2}$ is also mentioned but found to be three orders of magnitude smaller than the quenching with molecular iodine: it will not be considered.

1.4.5 Ion-Neutral collisions

In PIC simulations of molecular gases such as chlorine [94] or oxygen [55], it is necessary to go into the details of all the possible processes between the different ions and neutrals and usually, collisions are splitted in scattering cross sections, charge exchange cross sections and fragmentation reactions. However, even in well studied gases, many of these cross sections are not well known. In Lucken's thesis [21], a first model has been proposed for the relevant ion-neutral cross sections in iodine for PIC simulations. In the present work, as we use 0D global models and fluid models, we do not need all these cross sections and we only focus on two cross sections that will be used in following chapters.

1.4.5.1 Backscattering of ions - Charge Transfer Process

The term backscattering of ions designates a collision in which an ion collides with a neutral species and the charge is transferred from one collider to the other one. It is also called charge transfer process and can be resonant when the neutral (atom or molecule) and ion are parent and child. For global models, as the one presented in Chapter 5, the particle balance equations are only affected by reactions where a species is lost or produced. Amongst all the backscattering processes occuring within an iodine plasma, only one will be taken into account:

$$I_2 + I^+ \longrightarrow I_2^+ + I_{3/2}. \tag{1.31}$$

The reverse process will be neglected as it requires a collision energy threshold of $\mathcal{E}_{iz,I} - \mathcal{E}_{iz,I_2} \approx 1.14$ eV, very unlikely to occur in our plasma conditions.

In Marmuse and Lucken theses [21, 22], the reaction (1.31) was taken into account with a simple model. In the present work, we use the cross section measured in 2015 by Hause *et al.* [90] for energies between 0.67 eV and 100 eV (energy in the collision center of mass). The cross section was fitted using the measured values and extrapolated, at low energy using a Langevin cross section ($\propto \mathcal{E}_R^{-1/2}$) and at high energy using an $-\log_{10}(\mathcal{E}_R)$ law to take into account a slow decay of the cross section:

$$\sigma_{\text{ch. ex},I_2-I^+}(\mathcal{E}_R) = \begin{cases} \sqrt{\alpha_{I_2} e^2/(2\pi\mathcal{E}_0\mathcal{E}_R)} & \text{for } \mathcal{E}_R \leq 10\,\text{eV}, \\ A - B\log_{10}(\mathcal{E}_R) & \text{for } \mathcal{E}_R > 10\,\text{eV}, \end{cases} \tag{1.32}$$

with $\alpha_{I_2} = 10.42\times10^{-30}$ m^3 the I_2 polarizability [90], $A = 21.7\times10^{-20}$ m^2 and $B = 4.7\times10^{-20}$ m^2.

Figure 1.21 shows the charge exchange cross section as a function of the relative energy in the center of mass (top subfigure) and the rate coefficient calculated using a Maxwellian distribution function calculated by using the reduced mass $m_{II_2} = m_I m_{I_2}/(m_I + m_{I_2}) = 2/3\ m_I$ (bottom subfigure).

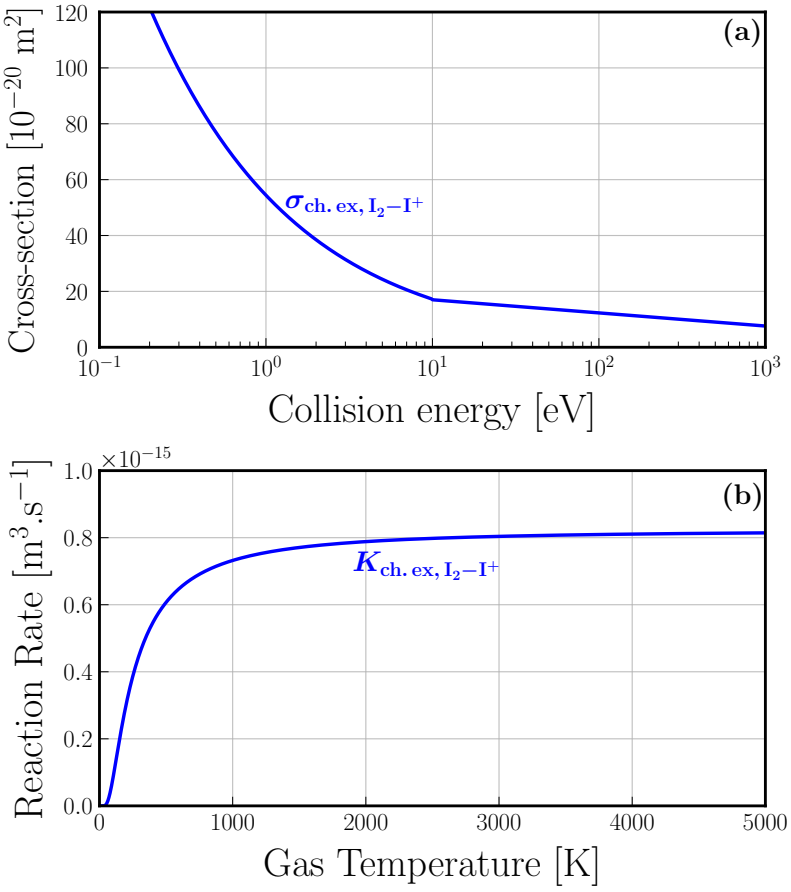

Figure 1.21: (a) Cross section for the charge exchange process: $I_2 + I^+ \longrightarrow I_2^+ + I_{3/2}$ as a function of the relative energy in the center of mass. Fitted from experimental measurements [90]. (b) Corresponding reaction rates calculated by assuming a Maxwellian distribution function with the reduced mass $\mu_R = 2/3 m_I$.

1.4.5.2 Global ion-neutral cross section for the global model

In the calculation of the ion mean free path, a global cross section including charge exchange and elastic scattering collisions is used [13, 114]. In a paper about global modeling of chlorine discharges [95], table 5 gives values of the global cross section for any reaction between two heavy species: they are all about $\sigma_{in} = 10^{-18}$ m^2. In iodine, there are also several different ions and neutrals. Based on the only existing measurements performed by [90] on $I^+ + I_2$ and $I_2^+ + I_2$, we assume that the average value of 10^{-18} m^2 is also a good approximation for iodine.

1.4.6 Surface recombination

At the walls, iodine atoms are known to recombine into molecules:

$$I + I \longrightarrow I_2. \tag{1.33}$$

Brewer and Tellinghuisen [115] gives the expression for the flux of iodine atoms stuck at the walls, in the low-pressure limit:

$$\Gamma_{\text{wall,I}} = \frac{1}{4} n_{\text{I}} \overline{v_{\text{I}}} \left(\frac{2\gamma_{\text{wall}}}{2 - \gamma_{\text{wall}}} \right), \tag{1.34}$$

where γ_{wall} is the wall sticking probability ($0 < \gamma_{\text{wall}} < 1$), n_{I} the atomic density and $\overline{v_{\text{I}}}$ the thermal speed of iodine atoms. This formula has more recently been obtained by Lucken [21] using collision physics basics. A value of $\gamma_{\text{wall}} = 0.1$ means that an iodine atom undergoes ten collisions with the walls before recombining into I_2.

γ_{wall} is a key-parameter to correctly model plasmas because it directly affects the atom/molecule gas balance. It depends on the nature of the surface and can vary over a very large range. In chlorine plasmas, γ_{wall} has been measured from 0.01 (silicon at room temperature) to 0.85 (stainless steel) [116]. It also depends on the temperature of the walls.

The wall sticking probability γ_{wall} has already been measured with iodine in several works but rarely when an iodine plasma is running. In Table 1.8, we gathered all the values encountered in the literature and their determination technique (values that were only assumed and used in simulations are also listed).

Table 1.8: Wall sticking probability γ_{wall} values found in the literature and their determination technique.

γ_{wall}	Comments	Reference
Measurements with plasma		
0.001 - 0.01	Acid-coated surface	[117]
0.04 - 0.065	Quartz surface	[115]
Measurements without plasma		
0.14	BK7 surface	[118]
0.014	DMDCS surface	[118]
0.05	Quartz surface	C. Drag (priv. com.)
Best fit to experimental data		
0.07	Ion beam measurements, *ThrustMe*	[17]
0.001 - 0.01	Quartz surface, iodine cell	This work
0.05 - 0.2	Anodized alum., PEGASES	This work
Assumed values		
0.04	$\Gamma_{\text{I,wall}}$ corrected formula	[1, 13]
0.04		[21]

In Chapter 5, the diffusional losses of the neutral iodine atoms to the reactor walls will be estimated by an effective loss-rate coefficient:

$$K_{\text{wall,I}} = \left[\frac{\Lambda_0^2}{D_{\text{I}}} + \frac{V}{S} \frac{4}{\overline{v}_{\text{I}}} \left(\frac{2 - \gamma_{\text{wall}}}{2\gamma_{\text{wall}}} \right) \right]^{-1} \ [\text{s}^{-1}], \tag{1.35}$$

where D_{I} is the diffusion coefficient for neutral iodine atoms (given by equation (1.28)), $\overline{v}_{\text{I}}$ is the mean I velocity, V and S are the volume and the wall surface area of the reactor chamber, respectively, and Λ_0 is the effective diffusion length of

neutral iodine atoms, given by:

$$\Lambda_0 = \left[\left(\frac{\pi}{L}\right)^2 + \left(\frac{2.405}{R}\right)^2\right]^{-1/2}, \tag{1.36}$$

in the case of a cylindrical chamber of length L and radius R [95].

When the diffusion term Λ_0^2/D_I can be neglected, equation (1.35) simply reads:

$$n_\mathrm{I} K_{\mathrm{wall,I}} = \frac{S}{V}\Gamma_{\mathrm{wall,I}}. \tag{1.37}$$

1.4.7 Synthesis on electron impact collisions and related plasma physics quantities

Electron impact collisions and electron-neutral momentum transfer collision frequency

In Table 1.9 are listed all the reactions where an electron collides with an heavy iodine species. In those processes, electrons lose a part of their energy. For inelastic collisions, the thresholds values are indicated. For the elastic collisions between an electron and an heavy species h, the term $3m_e/m_\mathrm{h}(T_e - T_\mathrm{h})$ is the mean energy lost per electron during the collision [58, 119].

Table 1.9: List of the electron impact collisions considered in this thesis. Temperatures are expressed in eV.

Reaction	Rate [$\mathrm{m^3.s^{-1}}$]	Energy loss	More details
Electron impact on $\mathrm{I}_{3/2}$			Subsection 1.4.1
$\mathrm{I}_{3/2} + \mathrm{e}^- \longrightarrow \mathrm{I}_{3/2} + \mathrm{e}^-$	$K_{\mathrm{el,I}_{3/2}}$	$3m_e/m_\mathrm{I}(T_e - T_\mathrm{I})$	
$\mathrm{I}_{3/2} + \mathrm{e}^- \longrightarrow \mathrm{I}^+ + 2\,\mathrm{e}^-$	$K_{\mathrm{iz,I}_{3/2}}$	$\mathcal{E}_{\mathrm{iz,I}_{3/2}} = 10.45$ eV	
$\mathrm{I}_{3/2} + \mathrm{e}^- \longrightarrow \mathrm{I}_{1/2} + \mathrm{e}^-$	$K_{\mathrm{ex_1,I}_{3/2}}$	$\mathcal{E}_{\mathrm{ex_1,I}_{3/2}} = 0.9426$ eV	
$\mathrm{I}_{3/2} + \mathrm{e}^- \longrightarrow \mathrm{I}^*_{\mathrm{b}_2} + \mathrm{e}^-$	$K_{\mathrm{ex_2,I}_{3/2}}$	$\mathcal{E}_{\mathrm{ex_2,I}_{3/2}} = 6.7736$ eV	
$\mathrm{I}_{3/2} + \mathrm{e}^- \longrightarrow \mathrm{I}^*_{\mathrm{b}_3} + \mathrm{e}^-$	$K_{\mathrm{ex_3,I}_{3/2}}$	$\mathcal{E}_{\mathrm{ex_3,I}_{3/2}} = 8.0473$ eV	
$\mathrm{I}_{3/2} + \mathrm{e}^- \longrightarrow \mathrm{I}^*_{\mathrm{b}_4} + \mathrm{e}^-$	$K_{\mathrm{ex_4,I}_{3/2}}$	$\mathcal{E}_{\mathrm{ex_4,I}_{3/2}} = 8.1848$ eV	
Electron impact on $\mathrm{I}_{1/2}$			Subsection 1.4.1
$\mathrm{I}_{1/2} + \mathrm{e}^- \longrightarrow \mathrm{I}_{1/2} + \mathrm{e}^-$	$K_{\mathrm{el,I}_{1/2}}$	$3m_e/m_\mathrm{I}(T_e - T_I)$	
$\mathrm{I}_{1/2} + \mathrm{e}^- \longrightarrow \mathrm{I}^*_{\mathrm{b}_2} + \mathrm{e}^-$	$K_{\mathrm{ex_2,I}_{1/2}}$	$\mathcal{E}_{\mathrm{ex_2,I}_{1/2}} = 5.8310$ eV	
$\mathrm{I}_{1/2} + \mathrm{e}^- \longrightarrow \mathrm{I}^*_{\mathrm{b}_3} + \mathrm{e}^-$	$K_{\mathrm{ex_3,I}_{1/2}}$	$\mathcal{E}_{\mathrm{ex_3,I}_{1/2}} = 7.1047$ eV	
$\mathrm{I}_{1/2} + \mathrm{e}^- \longrightarrow \mathrm{I}^*_{\mathrm{b}_4} + \mathrm{e}^-$	$K_{\mathrm{ex_4,I}_{1/2}}$	$\mathcal{E}_{\mathrm{ex_4,I}_{1/2}} = 7.2422$ eV	
$\mathrm{I}_{1/2} + \mathrm{e}^- \longrightarrow \mathrm{I}_{3/2} + \mathrm{e}^-$	$K_{\mathrm{de-ex,I}_{1/2}}$	$-\mathcal{E}_{\mathrm{ex_1,I}_{3/2}} = -0.9426$ eV	
Electron impact on I_2			Subsection 1.4.2
$\mathrm{I}_2 + \mathrm{e}^- \longrightarrow \mathrm{I}_2 + \mathrm{e}^-$	$K_{\mathrm{el,I}_2}$, $K_{\mathrm{elm,I}_2}$	$3m_e/m_{\mathrm{I}_2}(T_e - T_{\mathrm{I}_2})$	
$\mathrm{I}_2 + \mathrm{e}^- \longrightarrow \mathrm{I}_2^+ + 2\,\mathrm{e}^-$	$K_{\mathrm{iz,I}_2}$	$\mathcal{E}_{\mathrm{iz,I}_{3/2}} = 9.31$ eV	
$\mathrm{I}_2 + \mathrm{e}^- \longrightarrow 2\,\mathrm{I}_{3/2} + \mathrm{e}^-$	$K_{\mathrm{diss,I}_2}$	$\mathcal{E}_{\mathrm{diss,I}_2} = 1.542$ eV	
$\mathrm{I}_2 + \mathrm{e}^- \longrightarrow \mathrm{I}^+ + \mathrm{I}_{3/2} + 2\,\mathrm{e}^-$	$K_{\mathrm{diss.iz,I}_2}$	$\mathcal{E}_{\mathrm{diss.iz,I}_2} = 11.94$ eV	
$\mathrm{I}_2 + \mathrm{e}^- \longrightarrow \mathrm{I}^- + \mathrm{I}_{1/2}$	$K_{\mathrm{diss.att,I}_2}$	0. eV	
$\mathrm{I}_2 + \mathrm{e}^- \longrightarrow \mathrm{I}_2{}^* + \mathrm{e}^-$	$K_{\mathrm{ex,I}_2}$	$\mathcal{E}_{\mathrm{ex,I}_2} = 2.18$ eV	
$\mathrm{I}_2(v=0) + \mathrm{e}^- \longrightarrow \mathrm{I}_2(v=1,...,10) + \mathrm{e}^-$	$K_{\mathrm{vibr,I}_2}$	$\mathcal{E}_{\mathrm{vibr,I}_2} = 0.02575$ eV	
Electron impact on ions			Subsection 1.4.3
$\mathrm{I}_2^+ + \mathrm{e}^- \longrightarrow \mathrm{I}^+ + \mathrm{I}_{3/2} + \mathrm{e}^-$	$K_{\mathrm{diss,I}_2^+}$	$\mathcal{E}_{\mathrm{diss,I}_2^+} = 2.18$ eV	
$\mathrm{I}^- + \mathrm{e}^- \longrightarrow \mathrm{I}_{3/2} + 2\,\mathrm{e}^-$	$K_{\mathrm{det,I}^-}$	$\mathcal{E}_{\mathrm{det,I}^-} = 3.059$ eV	

An useful frequency often in low-temperature plasmas is the electron-neutral momentum transfer collision frequency defined, in the case of iodine and with the set

of reactions considered, as follow:

$$\nu_m = n_{I_{3/2}} K_{elm,I_{3/2}} + n_{I_{1/2}} K_{elm,I_{1/2}} + n_{I_2} K_{elm,I_2}. \tag{1.38}$$

However, we do not have any data for $K_{elm,I_{3/2}}$ and $K_{elm,I_{1/2}}$, we will use $K_{el,I_{3/2}}$ and $K_{el,I_{1/2}}$ instead:

$$\nu_m = n_{I_{3/2}} K_{el,I_{3/2}} + n_{I_{1/2}} K_{el,I_{1/2}} + n_{I_2} K_{elm,I_2}. \tag{1.39}$$

Note that Lafleur *et al.* [17] used a different definition for ν_m but given the orders of magnitude of the different reaction rates, the value used is very similar to the one used in this thesis.

Energy loss per electron–ion pair created

A very important quantity used for plasma discharges is the collisional energy loss $\mathcal{E}_C$ which represents the average energy expended to produce an electron-ion pair when considering all electron collisional processes. For atomic and molecular ground state iodine, the expressions are:

$$\mathcal{E}_{C,I_{3/2}} = \mathcal{E}_{iz,I_{3/2}} + \frac{1}{K_{iz,I_{3/2}}} \left(\sum_{j=1}^{4} K_{ex_j,I_{3/2}} \mathcal{E}_{ex_j,I_{3/2}} + 3\frac{m_e}{m_I}(T_e - T_I) K_{el,I_{3/2}} \right) \tag{1.40}$$

$$\mathcal{E}_{C,I_2} = \frac{1}{K_{iz,I_2} + K_{diss.iz,I_2}} \Big(K_{iz,I_2} \mathcal{E}_{iz,I_2} + K_{diss.iz,I_2} \mathcal{E}_{diss.iz,I_2} + K_{ex,I_2} \mathcal{E}_{ex,I_2} + K_{diss,I_2} \mathcal{E}_{diss,I_2} + 3\frac{m_e}{m_{I_2}}(T_e - T_{I_2}) K_{el,I_2} \Big) \tag{1.41}$$

In Figure 1.22, are plotted the effective collisional energy loss per electron-ion pair as a function of electron temperature for the various species investigated in this thesis: argon, krypton, xenon, atomic and molecular iodine. The data used to generate the noble gases curves are presented in Appendix A. The best propellant is the easier to ionize which means the one with the smallest energy loss per electron-ion pair created.

Depending on the composition of the plasma (or on the rate of molecular dissociation), the creation cost for an electron-ion pair lies somewhere between the molecule curve and the atom curve. As will be presented in Chapter 3, the electron temperature within a xenon or an iodine plasma are very similar, so the curve can be compared for a fixed electron temperature. At low electron temperatures (<1.5 eV), the energy loss in xenon is below the energy loss of both the iodine molecule and atom. When the electron temperature increases, the trend reverses (because different collision cross sections, reaction process, and inelastic energy thresholds) quickly for the molecule but in the case of a pure atomic iodine plasma (dissociation rate of 100%), the electron temperature must exceed 4 eV for iodine to become advantageous. Such a high temperature is only reached at low pressure (at low mass flow rate). Energy losses with krypton and argon are higher than for xenon but exhibit the same behavior with T_e: there exists an electron temperature (roughly between 1.5 and 4 eV) where iodine can become less advantageous than those two alternative propellants.

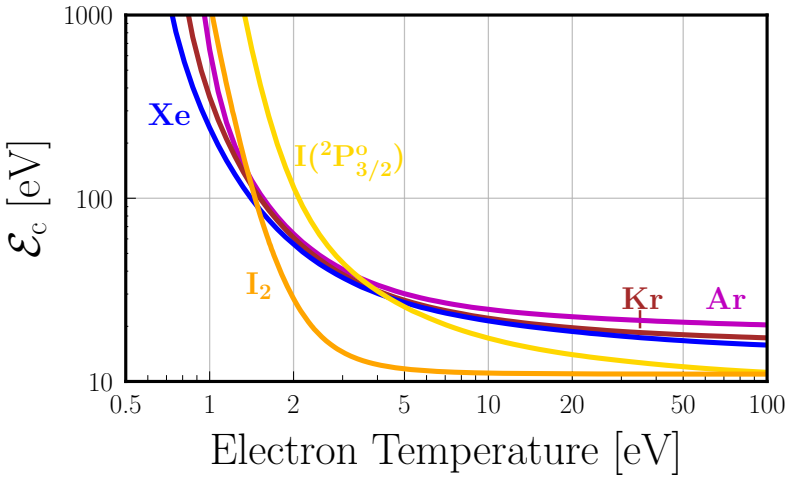

Figure 1.22: Effective collisional energy loss per electron-ion pair as a function of electron temperature for the various species investigated in this thesis: argon, krypton, xenon, atomic and molecular iodine.

Energy relaxation length, adapted from [119]

As will be shown in Chapter 3, the electron temperature is not always independent of the space coordinate. It is particularly important to understand what may lead to non-uniform electron temperature, since inelastic processes are extremely sensitive to this parameter. The first condition for non-uniform electron temperature is that the electric (electromagnetic) energy is deposited non-uniformly in the electron population (which is the case with our discharge described in Chapter 2). Nevertheless, non-uniform energy deposition does not automatically lead to non-uniform temperature, because the electron energy relaxation length may be large compared to the system dimensions. Under these circumstances, electrons may gain their energy in one location and subsequently share this energy with other electrons far away from this location. The rigorous calculation of the electron energy relaxation length requires kinetic theory that is beyond the scope of this work but Godyak [120] proposed a relatively simple expression that accounts for all electron energy loss mechanisms in a discharge. Here, the formula is adapted to our iodine set of reaction:

$$\begin{aligned}\lambda_{\mathcal{E}} \;=\; \lambda_{\mathrm{el}}\Bigg[& 2\frac{m_e}{m_{\mathrm{I}}} + \frac{2}{3}\sum_{j=1}^{4}\frac{n_{\mathrm{I}_{3/2}}K_{\mathrm{ex_j},\mathrm{I}_{3/2}}}{\nu_{\mathrm{m}}}\frac{\mathcal{E}_{\mathrm{ex_j},\mathrm{I}_{3/2}}}{T_e} + \frac{2}{3}\sum_{j=2}^{4}\frac{n_{\mathrm{I}_{1/2}}K_{\mathrm{ex_j},\mathrm{I}_{1/2}}}{\nu_{\mathrm{m}}}\frac{\mathcal{E}_{\mathrm{ex_j},\mathrm{I}_{1/2}}}{T_e} \\ & + \frac{2}{3}\frac{n_{\mathrm{I}_2}K_{\mathrm{ex},\mathrm{I}_2}}{\nu_{\mathrm{m}}}\frac{\mathcal{E}_{\mathrm{ex},\mathrm{I}_2}}{T_e} + \frac{2}{3}\frac{n_{\mathrm{I}_2}K_{\mathrm{iz},\mathrm{I}_2}}{\nu_{\mathrm{m}}}\frac{\mathcal{E}_{\mathrm{iz},\mathrm{I}_2}}{T_e} + \frac{2}{3}\frac{n_{\mathrm{I}_{3/2}}K_{\mathrm{iz},\mathrm{I}_{3/2}}}{\nu_{\mathrm{m}}}\frac{\mathcal{E}_{\mathrm{iz},\mathrm{I}_{3/2}}}{T_e} \\ & + \frac{2}{3}\frac{n_{\mathrm{I}_2}K_{\mathrm{diss.iz},\mathrm{I}_2}}{\nu_{\mathrm{m}}}\frac{\mathcal{E}_{\mathrm{diss.iz},\mathrm{I}_2}}{T_e} + \frac{2}{3}\frac{n_{\mathrm{I}_2}K_{\mathrm{diss},\mathrm{I}_2}}{\nu_{\mathrm{m}}}\frac{\mathcal{E}_{\mathrm{diss},\mathrm{I}_2}}{T_e} \\ & + 3\frac{n_{\mathrm{I}_2}\left(K_{\mathrm{diss.iz},\mathrm{I}_2}+K_{\mathrm{iz},\mathrm{I}_2}\right)+n_{\mathrm{I}_{3/2}}K_{\mathrm{iz},\mathrm{I}_{3/2}}}{\nu_{\mathrm{m}}}\Bigg]^{-1/2},\end{aligned} \tag{1.42}$$

where λ_{el} is the electron-neutral mean free path written as:

$$\lambda_{\mathrm{el}} \;=\; \left[n_{\mathrm{I}_{3/2}} < \sigma_{\mathrm{el},\mathrm{I}_{3/2}} >_{1-10} + n_{\mathrm{I}_{1/2}} < \sigma_{\mathrm{el},\mathrm{I}_{1/2}} >_{1-10} + n_{\mathrm{I}_2} < \sigma_{\mathrm{el},\mathrm{I}_2} >_{1-10}\right]^{-1}, \tag{1.43}$$

with $< \sigma_{el} >_{1-10}$ the mean values of the elastic cross section taken on the interval [1 eV ; 10 eV], listed in Table 1.10. The electrons within this energy interval are the ones contributing the most in our discharge. The contribution of the electron-electron collisions has been considered negligible. In the case of a noble gas, the formula for the energy relaxation length does not contain any molecular terms, which suggests a naturally shorter length in the case of a molecular gas.

Table 1.10: Averaged value of the electron-neutral elastic collisions on the interval [1 eV ; 10 eV] for different species.

Species X	Xe	$I_{3/2}$	$I_{1/2}$	I_2
$< \sigma_{el,X} >_{1-10}$ [m^2]	1.8×10^{-19}	3.4×10^{-19}	2.8×10^{-19}	5.3×10^{-19}

To conclude the discussion on the energy relaxation length we can do the numerical application for xenon and iodine. Let us take the idealized case where the iodine plasma is completely dissociated ($n_{I_2} = 0$) and contains only atoms in their fundamental level ($n_{I_{1/2}} = 0$, not very realistic). The atomic densities $n_{I_{3/2}}$ and n_{Xe} are taken to be equal to 3×10^{-19} m^{-3} in order to reach a condition suitable for electric propulsion (about 1 mTorr at 300 K). For electron temperatures between 2 and 6 eV, the energy relaxation length in iodine is always shorter than in xenon, even in this idealized case without taking into account molecular processes. We understand that when the pressure is higher and the molecules are not negligible, the energy relaxation length of iodine will be much shorter than that of xenon and should become much shorter than the characteristic length of our discharge (presented in Chapter 2).

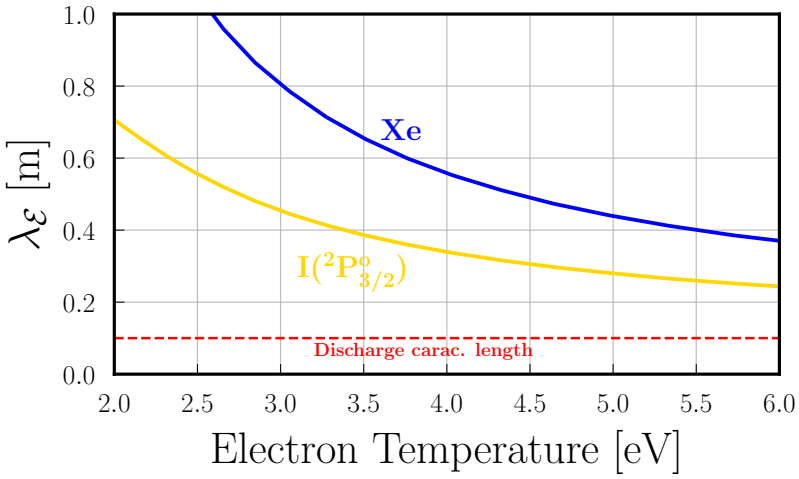

Figure 1.23: Energy relaxation length [m] as a function of the electron temperature [eV] in the idealized case where $n_{I_{3/2}} = n_{Xe} = 3 \times 10^{-19}$ m^{-3} (around 1 mTorr at 300 K) and $n_{I_{1/2}} = n_{I_2} = 0$ m^{-3}.

1.4.8 Neglected species, reactions and lacking data

Neglected species

We are aware that other ionic species than those considered may be present in iodine plasma. Indeed, many works have highlighted the presence of I_2^- and I_3^- ions in non-negligible proportions [26, 121]. Nevertheless, these various works were all carried out for pressures much higher than those used here and, to the first order, it seems legitimate to ignore these species. Besides, one can expect doubly-charged ions I^{2+} to form for high electron energies, as it is observed in Hall thrusters operated with xenon. The energy needed to form I^{2+} from the atomic ground state is 19.13 eV, which is slightly below the energy required to form Xe^{2+} from Xe (20.98 eV). In our experiments, however, the electron temperature will not exceed 5 eV (see Chapter 3) and we do not expect to observe any doubly-charged ions.

Missing or improvable cross sections and neglected reactions

In Table 1.11 are gathered all the cross sections needed to improve the consistency of our current kinetic model for iodine plasmas.

Table 1.11: List of missing or improvable iodine cross sections.

Reaction	Process	Comment
$I_2 + e^- \rightarrow I_{3/2} + I_{1/2} + e^-$	Dissociation	No data available
$I_2 + e^- \rightarrow I_{1/2} + I_{1/2} + e^-$	Dissociation	No data available
$I_2 + e^- \rightarrow I_{3/2} + I_{3/2} + e^-$	Dissociation	No data above 10 eV
$I_2 + e^- \rightarrow I^- + I_{1/2}$	Dissociative attachement	Unclear behavior at very low $\mathcal{E}$
$I_{1/2} + e^- \rightarrow I^+ + 2\,e^-$	Ionization from $I_{1/2}$	No data available
$I^- + e^- \rightarrow I_{3/2} + 2\,e^-$	Detachment by e^-impact	One calculation, very high CS
$I_{3/2} + e^- \rightarrow I_{3/2} + e^-$	Elastic	Need for el. mom. transfer CS
$I_{1/2} + e^- \rightarrow I_{1/2} + e^-$	Elastic	Need for el. mom. transfer CS
$I_2(J) + e^- \rightarrow I_2(J' > J) + e^-$	Rotational excitation	No available data
$I + I \rightarrow I_2$	Wall recombination	Need for experimental laws (similar to [95] for Cl_2)

Some reactions were purposefully neglected, they are listed in Table 1.12 with the explanation for the neglect.

Table 1.12: Neglected reactions in the frame of this work. Adapted from Lucken [21].

Reaction	Process	Reason for neglect
Electron impact on heavy species		
$I_2 + e^- \rightarrow I^+ + I^- + e^-$	Polar dissociation	8.911 eV threshold and low CS
$I^- + e^- \rightarrow I^+ + 3\,e^-$	Ionization from I^-	13.509 eV threshold
$I_2^+ + e^- \rightarrow 2\,I_{3/2}$	Dissociative recombination	Weakly ionized plasma
$I_2 + e^- \rightarrow 2\,I^+ + 3\,e^-$	Dissociative double ionization	High threshold (22.4 eV)
Ion impact on neutrals		
$I_2^+ + I \rightarrow I^+ + I_2$	Charge exchange	Threshold of 1.14 eV > 1 eV
$I_2 + I^+ \rightarrow 2\,I + I^+$	Fragmentation by I^+	Threshold of 1.542 eV > 1 eV
$I_2 + I_2^+ \rightarrow I_2 + I + I^+$	Fragmentation by I_2^+	Threshold of 2.682 eV > 1 eV
$I^- + I_2 \rightarrow I_2 + I + e^-$	Detachment by I_2	Threshold of 3.069 eV > 1 eV
$I^- + I_{3/2} \rightarrow I_2 + e^-$	Detachment by $I_{3/2}$	Threshold of 1.517 eV > 1 eV
$I^- + I_{1/2} \rightarrow I_2 + e^-$	Detachment by $I_{1/2}$	Threshold of 0.5744 eV (neglected but may be non negligible)
$I^- + I_2 \rightarrow I_2^- + I_{3/2}$	Charge exchange	Threshold of 0.539 eV (also neglected in Cl_2 [94] and O_2 [55])

CHAPTER 2

EXPERIMENTAL APPARATUSES

Contents

2.1 The main experimental setup

This section presents the general characteristics of an inductively coupled plasma discharge at low pressure (0.04 - 4 Pa), similar to the environment of a satellite thruster. The vacuum setup and the gas injection are first described before focusing on the ICP discharge configuration. In the third part, the specificities of working with iodine are presented. Finally, an additional experimental apparatus used to develop optical diagnostics for iodine plasmas at higher pressures (2 - 30 Pa), is described.

2.1.1 Vacuum setup and gas injection

2.1.1.1 The vacuum setup

The main vacuum chamber used in this work is a stainless steel spherical chamber from the Kurt J. Lesker company, named BUBBLE, with an internal volume of around 50 L, shown in Figure 2.1. It is pumped with a TPH 521 PC turbopump from Pfeiffer Vacuum designed to pump 440 L.s^{-1} of N_2, and an XDS 35i oil-free scroll pump from Edwards. The vacuum lower limit, when no gas is injected, is around 5×10^{-5} mbar $\sim 3.75 \times 10^{-2}$ mTorr (0.005 Pa).

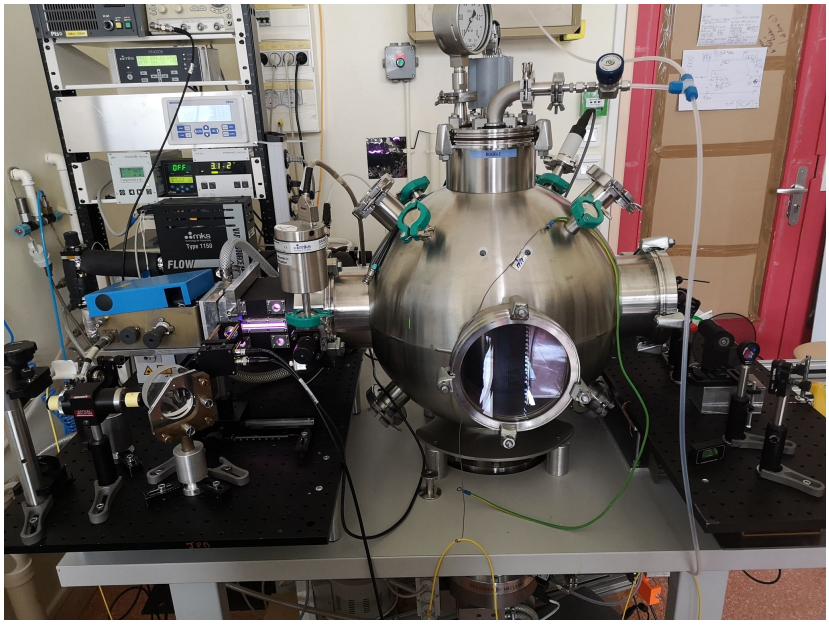

Figure 2.1: Photography of the BUBBLE vacuum setup with PEGASES running on argon during a LIF experiment.

For most of the results presented, the pressure is monitored by three independent probes: a PIRANI IKR050 from Pfeiffer Vacuum placed on top of the main chamber, indicating pressures from atmospheric pressure down to 1 Pa; an MKS hot cathode transducer on top of the main chamber for pressures from 0.5 Pa down to the backpressure; and a capacitance manometer 627D Baratron from MKS measuring pressure within the ionization chamber PEGASES through the intermediate flange whose complete description is presented in the next subsection.

The vacuum setup is shown in Figure 2.2. The PEGASES ion source is connected to the main chamber via an intermediate flange, designed and built at LPP, where

the gas is injected (see next subsection for more details). Iodine is injected through an MKS 1150C-4805M mass flow controller calibrated for 50 sccm of I_2. All pipes in the injection line are heated before and during operation to avoid deposition and clogging. Exhausted iodine is captured by a liquid nitrogen cold trap from Kurt J. Lesker, located between the turbo-molecular pump and the scroll pump. Argon, krypton, and xenon discharges may also be generated with the same setup but using independent mass flow controllers and injection lines (not represented in Figure 2.2 but evidenced in Figure 2.3 and Figure 2.5). The argon mass flow controller is a BROOKS GF40-SA42 calibrated for 50 sccm of Ar while the xenon mass flow controller is a BROOKS GF040-SA40 calibrated for 6.4 sccm of Xe. The xenon and argon mass flow controllers were independently used to inject krypton.

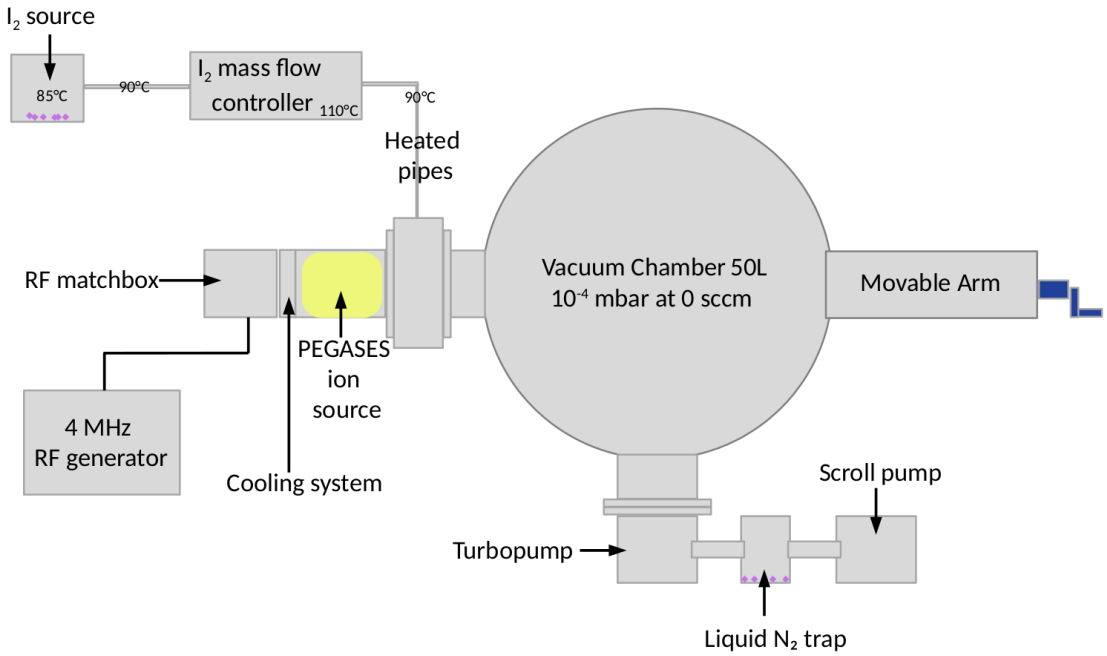

Figure 2.2: Experimental setup schematics. A liquid N_2 trap captures iodine through condensation before it reaches and damages the scroll pump. The movable arm is used to probe for spatial scans along the thrust axis. Slightly adapted from [22].

A movable arm, holding the electrical probes (detailed in Chapter 3), allows to scan 10 cm-long spatial variations inside the discharge with the probes going through the exhaust grid thanks to a centered 1 cm diameter hole. During other experiments, the arm was removed and replaced by a window.

2.1.1.2 The intermediate flange

At the beginning of the thesis (see Marmuse thesis [22] for instance), there was no intermediate flange between the ionization chamber and the vacuum chamber: the gas was directly injected inside the ionization chamber through a 1 cm diameter window, located near the antenna, the grid was not grounded and only fixed to the vacuum chamber with kapton tape. This was not optimal for several reasons:

- The grid was hardly accessible, one needed to go through a window of the vacuum chamber to reach it.
- The grid could move if not correctly taped.
- The discharge chamber was very difficult to separate from the vacuum chamber because the gas injection lines had to be removed first.
- The cleaning of the complete setup took up to a day.

Since then, and because it has been shown in previous theses [122, 123] that the injection location had only minor effects on the plasma behavior, P. Pariset, engineer at LPP, designed and manufactured an intermediate flange shown in Figure 2.3. This new element, always fixed to the vacuum chamber, ensures the gas injection for several gases and eases the replacement of the exhaust grid, the replacement of the thruster prototype, the cleaning of the ionization chamber and laser alignment processes.

As seen in Figure 2.3b, the flange has an octogon shape and offers at most eight independent, vacuum-compatible, direct access to the ionization chamber. The exhaust grid has been drilled to communicate with the internal pipes of the flange. In the presented work, only four pipes were used for:

- I_2 injection.
- Noble gases injection.
- Pressure monitoring assuming an isobar pipe.
- Biasing the exhaust grid.

2.1.1.3 The exhaust grid

Unless otherwise stated, the exhaust grid is a single grounded aluminum grid (74 mm x 114 mm) at the exhaust plane shown in Figure 2.4. It is inserted in a 3D-printed PLA insert (80 mm x 120 mm x 3 mm) and fixed to the intermediate flange using four aluminum screws located in each corner of the grid. The grid is composed of thousands of 1 mm diameter holes and has been drilled at six different locations with 10 mm diameter holes. Five of those holes communicate with the internal pipes of the intermediate flange, for various functions as previously described. The last hole, located in the center of the grid has been used during charged particles and laser-induced fluorescence measurements.

To properly estimate the geometrical grid transparency, one has to take into account that the gas is solely pumped through the 70 mm inner diameter of the intermediate flange located right behind the grid (highlighted by a red circle in Figure 2.4 and Figure 2.3b). The grid transparency, $\beta_{\text{grid,neutrals}}$, is :

$$\beta_{\text{grid,neutrals}} = \frac{\pi r^2_{\text{big hole}} + N_{\text{overlapping}} \pi r^2_{\text{small hole}}}{S_{xy}[\text{mm}^2]}, \tag{2.1}$$

with $r_{\text{small hole}} = 0.5$ mm the radius of small holes, $r_{\text{big hole}} = 5$ mm the radius of the centered hole, $N_{\text{overlaping}} = 2000 \pm 10\%$, the number of 1 mm diameter holes overlapping the flange inner diameter and $S_{xy} = 80 \times 120$ mm^2, the surface in the xy plane. The grid transparency, calculated with equation (2.1) is around 16%.

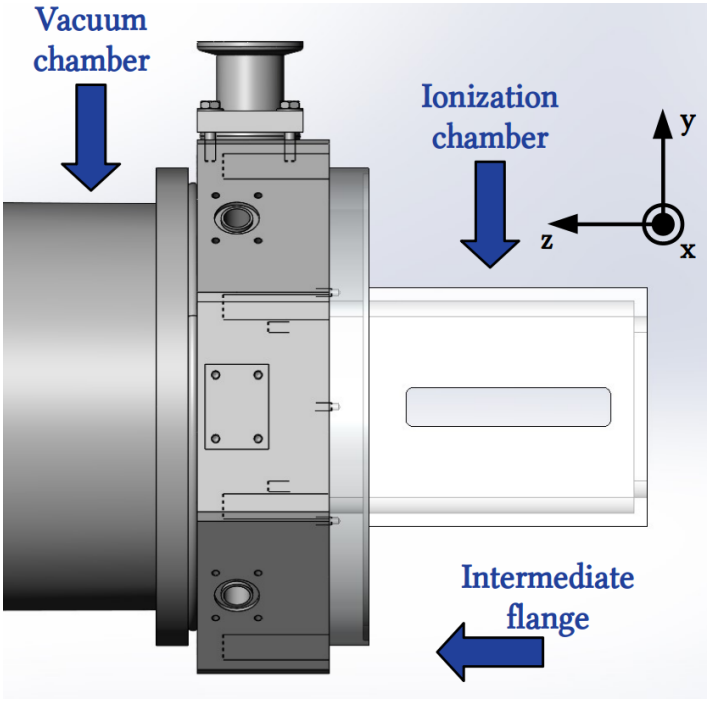

(a)

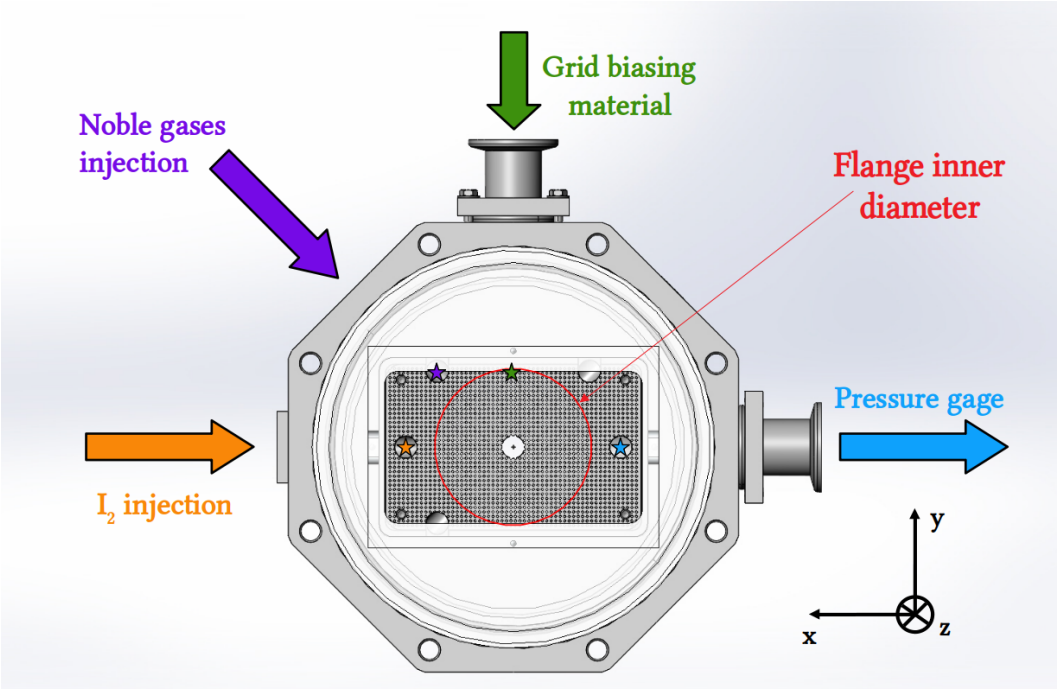

(b)

Figure 2.3: 2D schematics of the intermediate flange. (a) The intermediate flange is located between the vacuum chamber and the ionization chamber. (b) Four direct access to the ionization chamber were used (see stars location). One for the iodine injection (orange), one for the noble gases injection (purple), one for biasing the grid (green) and one for measuring the pressure (blue). The flange has an inner diameter of 70 mm (red circle) were the gas can actually escape.

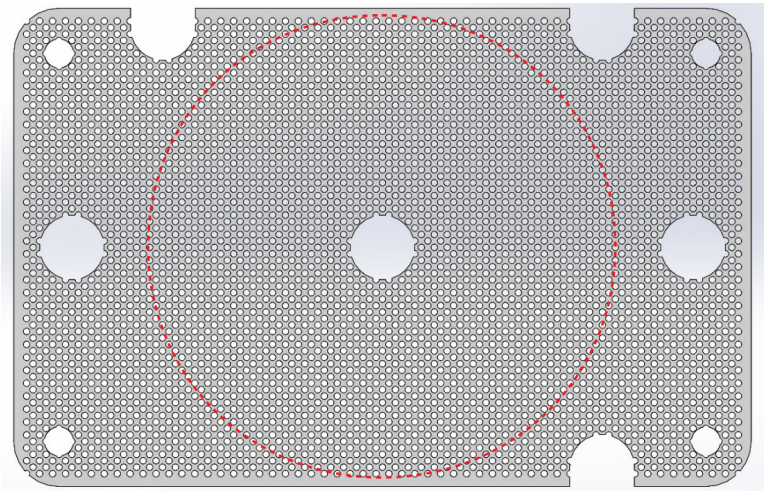

Figure 2.4: 2D view of the exhaust grid mainly used during experiments. The red circle indicates the intermediate flange inner diameter through which the gas is actually pumped.

2.1.2 Discharge configuration

2.1.2.1 ICP discharge configuration

Most of the measurements were performed in the so-called PEGASES thruster setup (described with great details in [32, 123]), where the magnetic barrier and acceleration stages have been removed. A sketch and photography of the system are shown in Figure 2.5. The ionization chamber is a rectangular cuboid of $V = 1.25$ L ($l_x = 12$ cm $\times$ $l_y = 8$ cm $\times$ $l_z = 13$ cm inner dimensions, l_z being the thrust axis length). The RF antenna is a flat coil encapsulated in ferrite at the back of the ionization chamber behind a 3 mm thick alumina plate ensuring vacuum sealing. The ferrite and the antenna are cooled down by circulating cold water. When the plasma is turned on, the reactor wall temperature varied between 300 and 400 K depending on both the plasma conditions and the thruster prototype used (see Section 2.2 for the prototypes characteristics and subsection 2.3.4 for the walls temperature characterization). In the middle of the water-cooling stage is a hole to let two wires connect the matching circuitry (detailed below) to the flat RF antenna. The radio-frequency inductively coupled plasmas are generated using a 4 MHz RF generator (RFPP RF25M). Experiments were mostly performed at fixed pressure and discharge power adjusting respectively the mass flow rate and the power delivered by the generator.

2.1.2.2 Impedance Matching

The theory of impedance matching will not be presented here but the reader can refer to the works of Bowick [124] on RF circuit design or the Appendix D in Marmuse thesis [22] for a more complete understanding.

In short, the role of a matchbox, located between the ionization chamber and the RF generator is to maximize the power transfer from the generator to the plasma. In our case, the 4 MHz generator is purely resistive with a resistance of 50 Ω while the plasma impedance is unknown with both a resistive part and an inductive part. The matchbox (whose design is presented in Figure 2.6), built with variable capacitors,

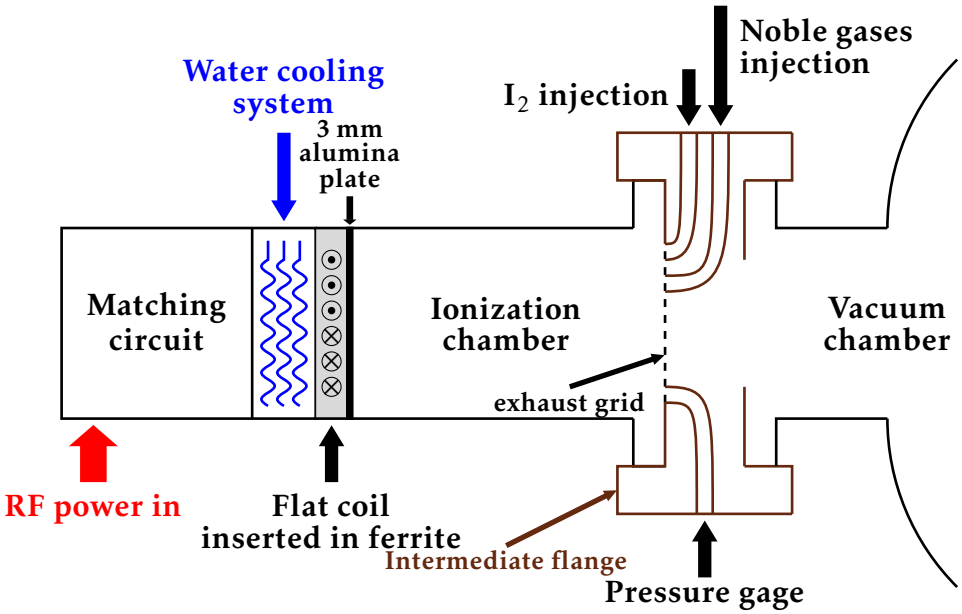

(a)

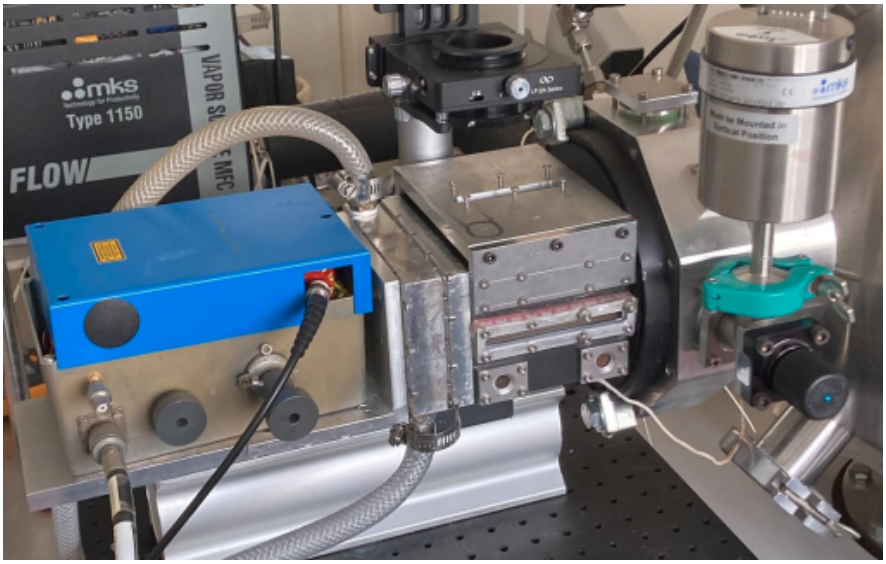

(b)

Figure 2.5: ICP discharge configuration. (a) Schematics View. (b) Photography of the corresponding experimental setup.

aims at reconciling both impedance when the plasma is ON.

2.1.3 Experimentation with iodine

This section is largely based on Marmuse thesis [22].

Using iodine in a plasma source is not as straightforward as plugging an argon or xenon bottle into a mass flow controller. Iodine gas is obtained from iodine crystals heated to around 360 K, hot enough to ensure a relatively high pressure but cold enough to stay colder than the mass flow controller heated to 383 K. This temperature difference avoids deposition in the controller.

The iodine reservoir is a small glass tube, 7 cm long, of 25 mm internal width

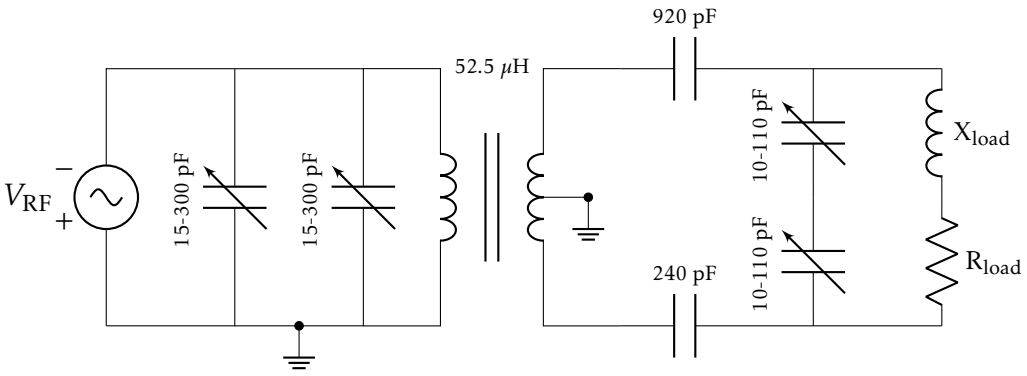

Figure 2.6: Electrical circuit of the matchbox used. The plasma and coil impedance are gathered in a resistance R_{load} and a reactance X_{load}.

manufactured at École polytechnique and directly connected to the metal pipes via a KF40 glass-metal connection, wrapped with aluminum tape and heating wires connected to a 60 V voltage source. Mounting and unmounting are fast and only a small amount of iodine is needed in the experimental room. The heating and cooling times of the reservoir are around 15 min, with no strong temperature gradient or overshoot, preserving the glass reservoir.

Iodine will solidify in the injection pipes at any point colder than its surroundings. Hence, all the pipes along the injection lines must be heated to avoid solidification and clogging: two major issues which can interrupt the flow, and lead to corrosion. In the present work, pipes are heated at 360 K with heating cables wrapped around the stainless steel pipes previously wrapped in aluminum tape. They are then placed in an insulating material used to isolate classic pipes. The heating cables are used with a 220 V voltage source, leading to very short heating times, and large temperature overshoots. The temperature is monitored with PT100 probes connected to a commercial circuit that automatically turns the input voltage ON and OFF. Temperature overshoots are considered smoothed by the stainless steel pipes so that the inner temperature must be rather constant. The pipes' temperature was checked and verified with a thermal camera. Any pipe left uncleaned and in the open air after being used in the injection line will be rapidly corroded. To avoid any issue, heating on the injection line is kept ON between experiments, and the entire line is kept under vacuum, as well as the main chamber. Despite the precautions taken, some material was corroded and changed during the thesis (see Figures 2.7a and 2.7b).

During experiments, the iodine accumulates in the liquid N_2 trap that is filled with N_2 before and during each experiment. At the end of any iodine experiment, a cleaning protocol is strictly applied to avoid any corrosion: the trap is cleaned, under a fume hood, from the resulting I_2 layer shown in Figure 2.7c. Ethanol is used to remove iodine, and the trash is sent to the lab chemical trash.

Between two experimental sessions, if the setup is to be left unused for some time, a purge of the injection line is operated by connecting the argon injection line where the iodine source is usually installed. An argon plasma is run in PEGASES, hence "cleaning" the reactor. The argon flows into the iodine injection line, purging it for the remaining iodine. It is not unusual that the argon plasma takes some hours before the yellow color completely disappears.

(a)

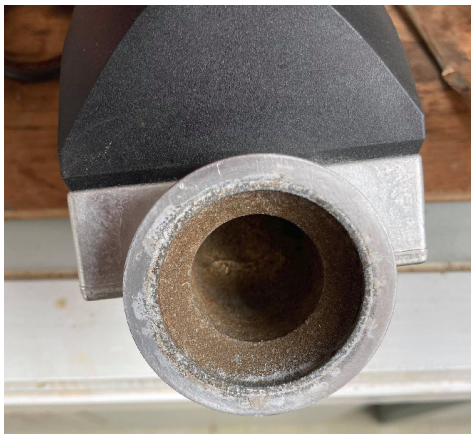

(b)

(c)

Figure 2.7: Handling iodine experimentally. (a) Corroded seals and pipe. (b) Corroded Valve. (c) Iodine trapped inside the nitrogen trap.

2.2 PEGASES thruster prototypes

Three different ionization chambers were used for the experiments. They have the same inner dimensions (l_z = 130 mm × l_x = 120 mm × l_y = 80 mm) but different characteristics presented in this section.

2.2.1 Aluminum prototypes

Two prototypes, made of aluminum, were used during the thesis. A 3D view is given in Figure 2.8a. They were also used by Marmuse [22] and Grondein [32] during their respective thesis. On each side, a 93 mm × 8 mm aperture has been drilled to convey optical access. Quartz windows ensure vacuum sealing. During my thesis, a new aperture (73.4 mm × 12.4 mm) has been drilled on the top of the ionization chamber to perform TALIF measurements. Vacuum sealing is also ensured by a quartz window.

Among those two geometrically identical prototypes, one has been anodised and is insulating: it looks black painted and shown in Figure 2.8b while an iodine plasma at very high pressure is running (150 mTorr with the turbo-pump OFF). Most of the optical measurements, presented in Chapter 4, were conducted with this prototype. The other prototype, perfectly conductor, is shown in Figure 2.8c. It has been mostly used for charged particles measurements, presented in Chapter 3.

At the back of the prototype, vacuum sealing is ensured by an alumina plate, visible in Figure 2.8d. The interior of the thruster, visible in the same figure, has been regularly cleaned with ethanol but iodine has progressively contaminated the walls and partially deteriorated the conductive properties.

2.2.2 Quartz prototype

The optical access allowed by the alumina prototypes are very limited although very useful. Hence, we decided to design a third prototype, fully transparent. The *Quartz Alliance*® company manufactured an ionization chamber made of quartz, shown in Figure 2.9 with iodine and argon plasmas running. Quartz has been chosen to let the UV range usable for further optical diagnostics. The discharge configuration had to be slightly modified when this prototype was used because the alumina plate no longer needed to ensure vacuum sealing. The antenna comes directly in contact with the back surface of the thruster to generate the plasma. In this configuration, the water cooling system, mainly relying on the conduction principle is not very efficient and the walls temperature can reach more than 400 K (see subsection 2.3.4). Before placing the order for the quartz prototype, the glassmaker at the Ecole Polytechnique made a cylindrical glass thruster of equivalent volume (shown during operation with iodine in Figure 1.1a) to ensure that the plasma would work well with this modified excitation configuration.

With noble gases, this prototype allows a great number of optical diagnostics to be performed in three dimensions. In the coming years, at LPP, it will become a very efficient tool to validate CRM codes, perform Abel inversion, or study instabilities in a magnetized configuration.

With iodine, the same diagnostics could be used. However, this fully transparent prototype has the main drawback of producing ozone (O_3) when iodine plasmas

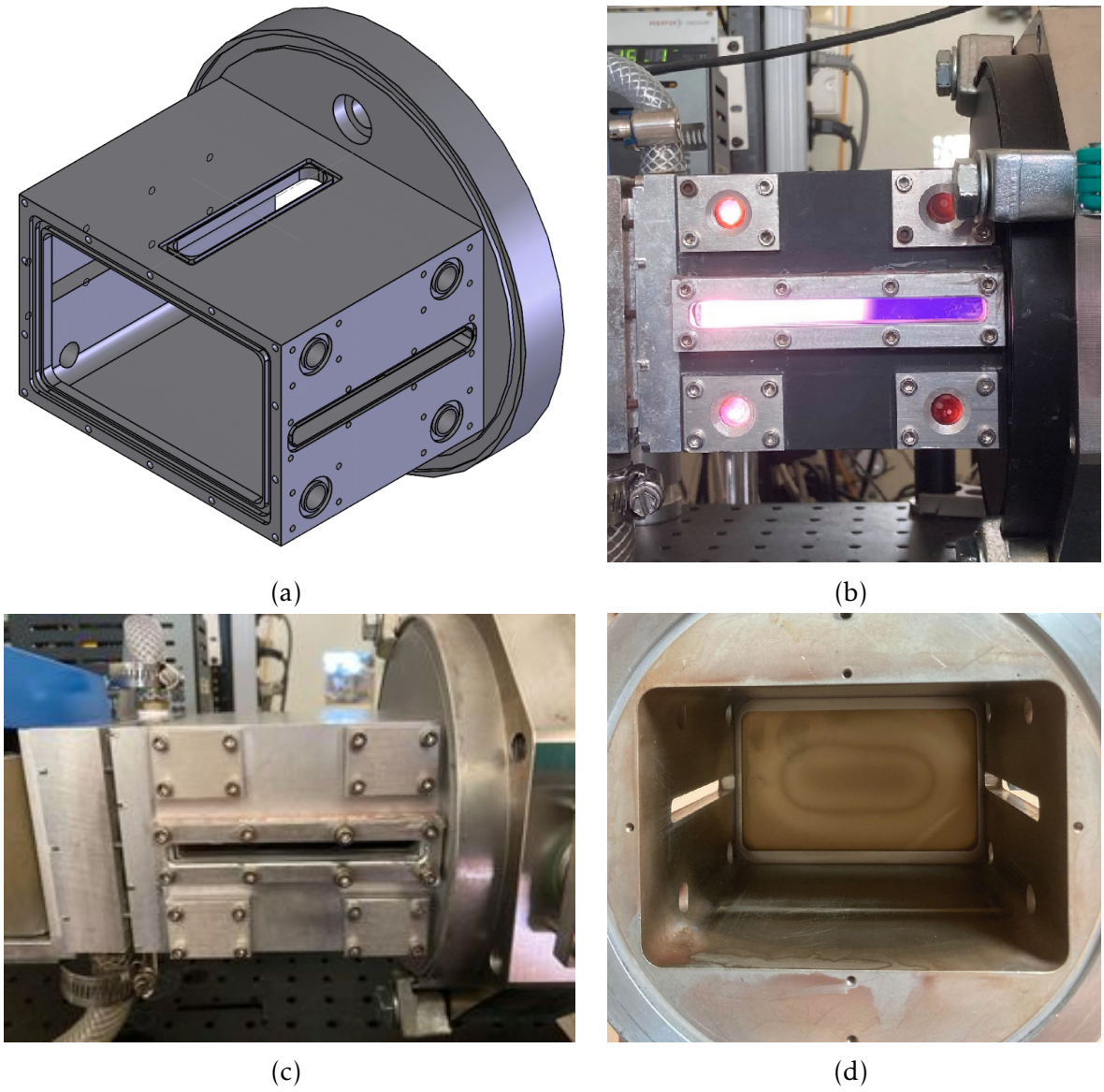

(a) (b)

(c) (d)

Figure 2.8: Metallic thruster prototypes. (a) 3D schematics. (b) Insulating prototype running with iodine at 150 mTorr. (c) Conductor prototype without plasma. (d) Inside view of the thruster with the alumina plate at the back.

are run in it. Indeed, the optical emission spectrum of iodine exhibits strong lines below 240 nm (see Marmuse's thesis [22]). For such wavelengths and shorter ones, oxygen molecules of the surrounding air easily dissociate into two oxygen atoms via photolysis and those atoms then recombine with oxygen molecules to form ozone. Ozone has a recognizable smell and is well-known to be a powerful oxidant that can damage mucous and respiratory tissues. After just a few seconds of running an iodine plasma inside the quartz prototype, the smell was not bearable and the plasma had to be turned off. Therefore, no real experiments have yet been conducted within this transparent prototype. A fan could be used in the future to avoid such an issue.

Nevertheless, the quick use of the quartz prototype was not devoid of interest because one immediately sees that iodine plasmas shown in Figures 2.8b, 2.9b and 2.9c, for three different pressures, exhibit completely different colors which indicates that the plasma composition is different. A spatial non-uniformity along

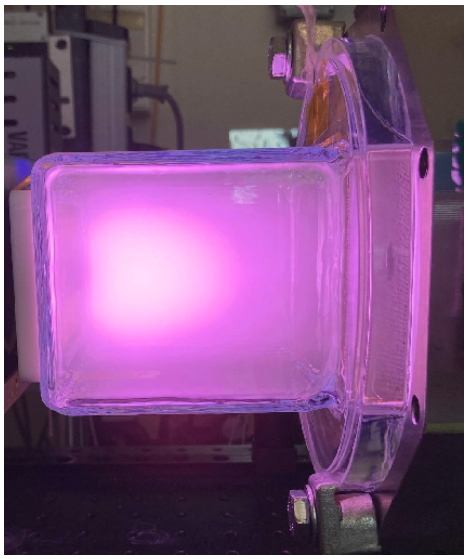

(a)

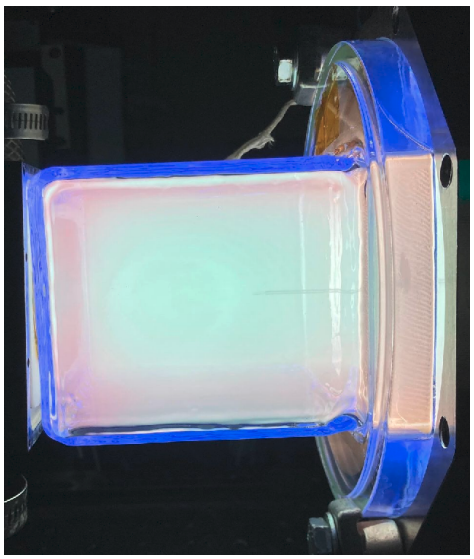

(b)

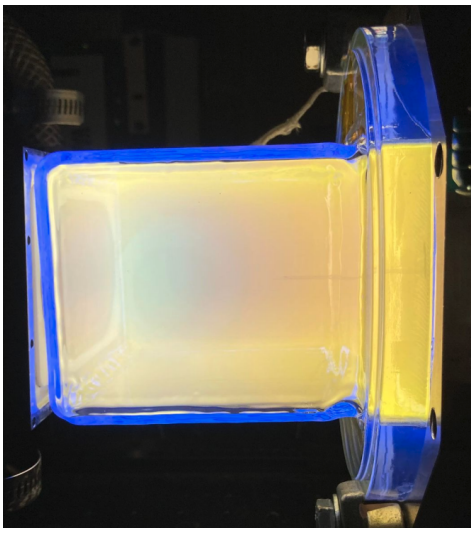

(c)

Figure 2.9: Quartz thruster prototype. (a) Running with argon for a pressure of 15 mTorr and a discharge power of 200 W. (b) Running with iodine for a pressure of 1 mTorr and a discharge power of 200 W. (c) Running with iodine for a pressure of 5 mTorr and a discharge power of 200 W. The blue colour on the edges of the reactor, observed in figures (b) and (c), is probably due to UV-induced fluorescence and impurities in the quartz.

the thrust axis is also evidenced and will be extensively studied throughout this manuscript.

2.3 Physics of the ICP discharge

2.3.1 Electrical characteristics

2.3.1.1 Determination of the discharge power

The absorbed power P_{abs} [W] (also called the discharge power) is the power dissipated in the plasma. It is lower than the RF power, P_{RF}, because of several loss phenomena in the matching circuit and the coil. The power dissipated in the coil is noted P_{coil}. The RF power is equal to the RF power going out of the generator minus any power reflected due to impedance mismatches. One can write:

$$P_{abs} = P_{RF} - P_{coil} = P_{RF,forward} - P_{RF,reflected} - P_{coil}. \tag{2.2}$$

The RF sinusoidal current running through the coil reads:

$$I_{RF}(t) = I_{coil}\cos(\omega_{RF}t), \tag{2.3}$$

where I_{coil} [A] is the signal amplitude and $\omega_{RF} = 2\pi f_{RF}$ the proper frequency, with $f_{RF} = 4$ MHz. The power dissipated in the coil, P_{coil}, is related to the coil current using:

$$P_{coil} = \left\langle R_{coil} I_{RF}^2(t) \right\rangle_{T_{RF}}, \tag{2.4}$$

with R_{coil}, the coil resistance and $T_{RF} = 2\pi/\omega_{RF}$, the period of the signal. Classically, R_{coil} is taken constant and the former equation becomes:

$$P_{coil} = \frac{1}{2} R_{coil} I_{coil}^2. \tag{2.5}$$

However, it is experimentally possible to measure P_{coil} and R_{coil} using the method detailed by Godyak *et al.* [125]. Knowing both the RF power and the coil current in PEGASES running without any gas injection gives a complete characterization of the circuit losses $P_{coil}(I_{coil})$. Indeed, when no gas is injected, $P_{abs} = 0$ W and using equation (2.2), one gets $P_{coil}(I_{coil}) = P_{RF}$. Figure 2.10 shows on the y-axis the coil resistance and on the x-axis the corresponding current amplitude measured in the coil with a Pearson current monitor while maintaining a zero mass flow rate.

A remarkable phenomenon is a strong break at around 6 A, and the presence of a hysteresis near this breaking point. That is a characteristic of the ferrite material in which the antenna is encapsulated. Clearly, the assumption of a constant R_{coil} breaks down and the resistance is a function of I_{coil}. When power is turned off, the coil resistance is not zero but $R_{coil}^0 = 2\ \Omega$. A fitting law for R_{coil} is necessary. The breaking point (or threshold) is reached at $I_{coil}^{thr.} = 6$ A. Two very different behaviors are observed for $I_{coil} \leq I_{coil}^{thr.}$ and $I_{coil} > I_{coil}^{thr.}$. Therefore, both regions are fitted with different functions as follows :

$$R_{coil}(I_{coil}) = \begin{cases} R_{coil}^0 + \alpha I_{coil}^{\beta} & \text{for } 0 \leq I_{coil} \leq I_{coil}^{thr.}, \\ R_{coil}^0 + \frac{R_{coil}^{thr.} - R_{coil}^0}{1+\alpha'(I_{coil} - I_{coil}^{thr.})^{\beta'}} & \text{for } I_{coil} > I_{coil}^{thr.}. \end{cases} \tag{2.6}$$

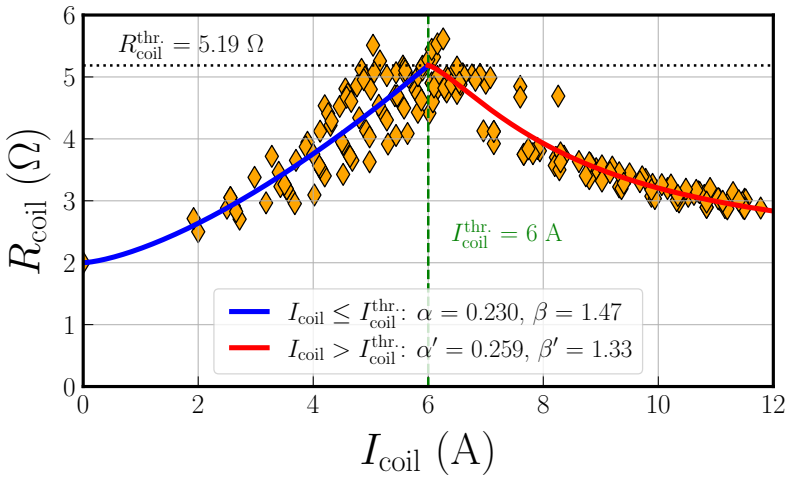

Figure 2.10: Measured coil resitance R_{coil} as a function of the coil current amplitude I_{coil}. Fitting laws are retrieved below and above the threshold value of 6 A.

The fitting values for α, α', β, β' and $R_{coil}^{thr.}$ are given in Figure 2.10.

To conclude, equations (2.2) and (2.6) give the formula to evaluate P_{abs} when a plasma is ON:

$$P_{abs} = P_{RF,forward} - P_{RF,reflected} - \frac{1}{2} R_{coil}(I_{coil}) I_{coil}^2. \tag{2.7}$$

2.3.1.2 Resistance of a purely inductive discharge

The absorbed power can be conveniently linked to the coil current amplitude by introducing the inductive resistance of the plasma R_{ind} [Ω]:

$$P_{abs} = \frac{1}{2} R_{ind} I_{coil}^2. \tag{2.8}$$

Such that one gets:

$$P_{RF} = \frac{1}{2} [R_{ind} + R_{coil}(I_{coil})] I_{coil}^2. \tag{2.9}$$

2.3.1.3 Power transfer efficiency

To evaluate the electrical efficiency of the discharge, it is convenient to evaluate the power transfer efficiency (designated PTE in the following) which is the ratio of the absorbed power over the RF power:

$$PTE = \frac{P_{abs}}{P_{RF}} = \frac{R_{ind}}{R_{ind} + R_{coil}}. \tag{2.10}$$

In Figure 2.11, the ICP discharge PTE is plotted against the RF current amplitude I_{coil} [A]. In the top subfigure, the effect of pressure is studied using iodine plasmas running at 0.35, 0.6, 2.5 and 15 mTorr. Iodine plasmas are generated for I_{coil} between 4 and 8 amps. The PTE increases with both increasing pressure and

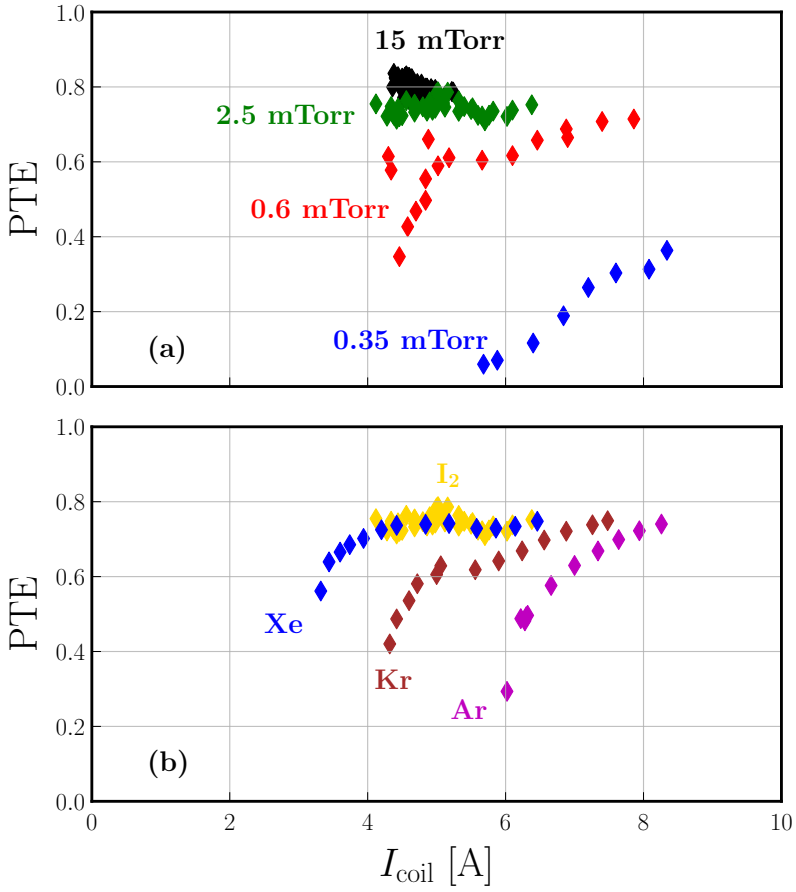

Figure 2.11: ICP discharge Power Transfer Efficiency (PTE) as a function of the RF current amplitude I_{coil} [A]. (a) PTE measurements in iodine plasmas for neutral pressures of 0.35, 0.6, 2.5 and 15 mTorr. (b) PTE measurements in iodine, xenon, krypton and argon plasmas at 2.5 mTorr.

RF current. It reaches more than 80% at the highest pressures and is below 10% at very low pressure and RF current.

In the bottom subfigure, the PTE is plotted for every propergol studied in this work: iodine, xenon, krypton, and argon at a pressure fixed to 2.5 mTorr. Iodine appears to produce the best PTE with xenon behaving very similarly. For a sufficient input current, whatever the gas used, the PTE saturates around 75%.

2.3.2 Requirements for sustaining a plasma

The pressure-absorbed power windows of operation are presented in Figure 2.12 for argon and iodine. It is not possible to ignite a plasma at low power and the breakdown power region is indicated in red: the width of the region is only indicative and subject to hysteresis. The ignited plasmas during the thesis are indicated in blue. The vertical error bars account for ± 0.1 mTorr while horizontal error bars represents ± 5% of the discharge power. The maximum achievable power is not indicated but the experimental setup could be damaged if operated at higher power: we decided not to run a plasma for I_{coil} bigger than 8.5 A and/or an RF reflected power above 50 W. Furthermore, given the mass flow controller ranges, xenon plas-

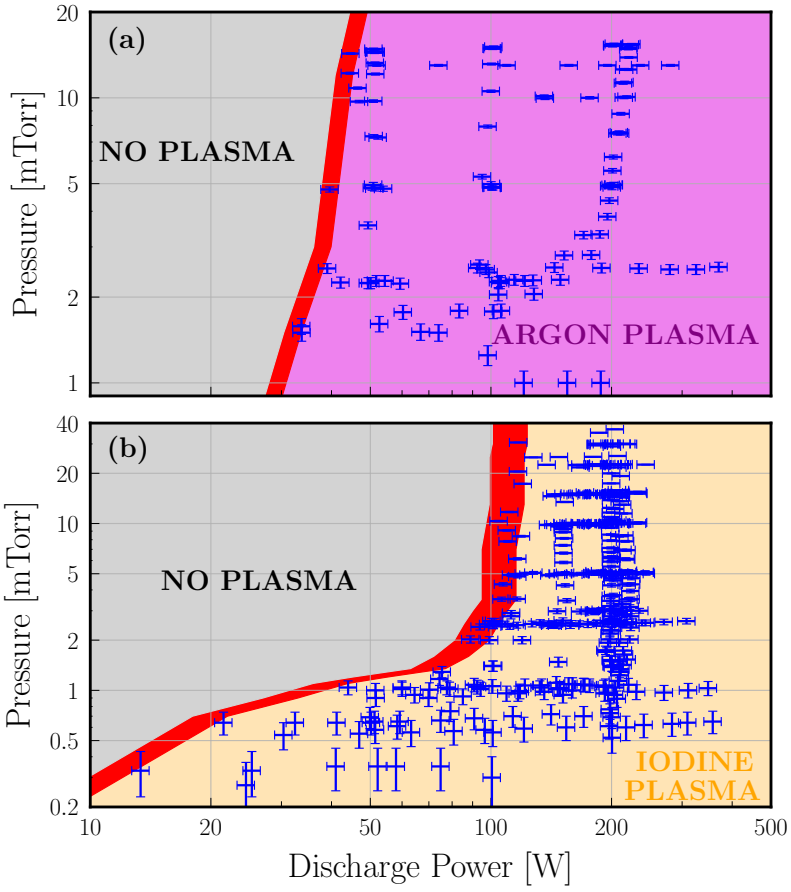

Figure 2.12: Pressure [mTorr] versus Discharge Power [W] characteristics of the experimental setup. The breakdown power region is indicated in red and each blue marker represent a plasma actually ignited during the thesis. (a) Argon map. (b) Iodine map.

mas could be obtained between 0.3 and 3.5 mTorr and krypton plasmas between 0.3 and 2.5 mTorr. The absorbed power range that can be explored with those noble gases is between 40 W and 350 W.

2.3.3 Pressure measurements

2.3.3.1 Gas flow basics

Most of the following concepts and notations are presented with great details in [126]. The flow rate Q of a gas flowing through a duct is defined as transported gas per time. Several approaches of describing the amount of gas yield several different types of flow rates:

$$\text{Volume flow rate :} \quad Q_V = \frac{\Delta V}{\Delta t}, \qquad [Q_V] = \text{m}^3.\text{s}^{-1}. \tag{2.11}$$

$$\text{Mass flow rate :} \quad Q_m = \frac{\Delta m}{\Delta t}, \qquad [Q_m] = \text{kg.s}^{-1}. \tag{2.12}$$

$$\text{Particle flow rate :} \quad Q_N = \frac{\Delta N}{\Delta t}, \qquad [Q_N] = \text{atoms.s}^{-1}. \tag{2.13}$$

Using the equation of state of an ideal gas:

$$pV = Nk_{\mathrm{B}}T = m_{\mathrm{P}}\frac{R}{M_{\mathrm{P}}}T, \tag{2.14}$$

with $R = 8.314\,\mathrm{J.K^{-1}.mol^{-1}}$ and M_{P} [kg.mol^{-1}] the molar mass, the different type of flows can be converted:

$$Q_V = \frac{V}{N}Q_N, \tag{2.15}$$

$$Q_m = \frac{M_{\mathrm{P}}}{N_{\mathrm{A}}}Q_N. \tag{2.16}$$

In the low-temperature plasma community, the volume flow rate is mostly expressed in sccm (standard cm^3.min^{-1}) using the conversion formula:

$$1\,\mathrm{sccm} = 1.6667\times10^{-8}\,\mathrm{m^3.s^{-1}}, \tag{2.17}$$

$$= 4.4779\times10^{17}\,\mathrm{atoms.s^{-1}}. \tag{2.18}$$

In the following, the definition of the mean particle speed will be useful:

$$\overline{v_{\mathrm{P}}} = \sqrt{\frac{8k_{\mathrm{B}}T}{\pi m_{\mathrm{P}}}}. \tag{2.19}$$

Finally, the flow conductance of a component is defined by:

$$C = \frac{Q_N k_{\mathrm{B}}T}{\Delta p}, \qquad [C] = \mathrm{m^3.s^{-1}}. \tag{2.20}$$

$\Delta p = p_{\mathrm{upstream}} - p_{\mathrm{downstream}}$, is the pressure difference between both ends of the component. In the following, we will study the exhaust grid flow conductance with and without plasma, using the measured Δp and Q_N delivered by the mass flow controllers.

2.3.3.2 Pressure measurements within the ionization chamber

In Figure 2.13, the pressure measured within the ionization chamber is plotted as a function of the volume flow rate for several gases. When the plasma is off (top subfigure), argon and iodine measurements are presented. Above 2 sccm, slopes are almost parallel and the ratio between both pressures is close to 2.5. Below 2 sccm, however, the iodine slope changes which may be due to (i) uncertainty about the flow delivered by the iodine mass flow controller and (ii) an outgassing of iodine which is no longer negligible at these low pressures. When the plasma is on (bottom subfigure), we added xenon and krypton to extend the discussion. Xenon and argon curves seems to be parallel. For argon, there are almost no difference between the pressure measured with or without plasma. While the gas temperature increases when the plasma is on, the exhaust velocity through the grid also increases with the temperature which prevents the pressure inside the ionization chamber from increasing significantly. The gap between argon and iodine measurements appears bigger when the plasma is on. This comes from the molecular nature of iodine. Inside an iodine plasma, molecules are partially dissociated which has two effects: (i) it automatically increases the pressure because the number of particles is increased; (ii) the dissociation processes are known to produce energetic fragments which induces an increase in the gas temperature.

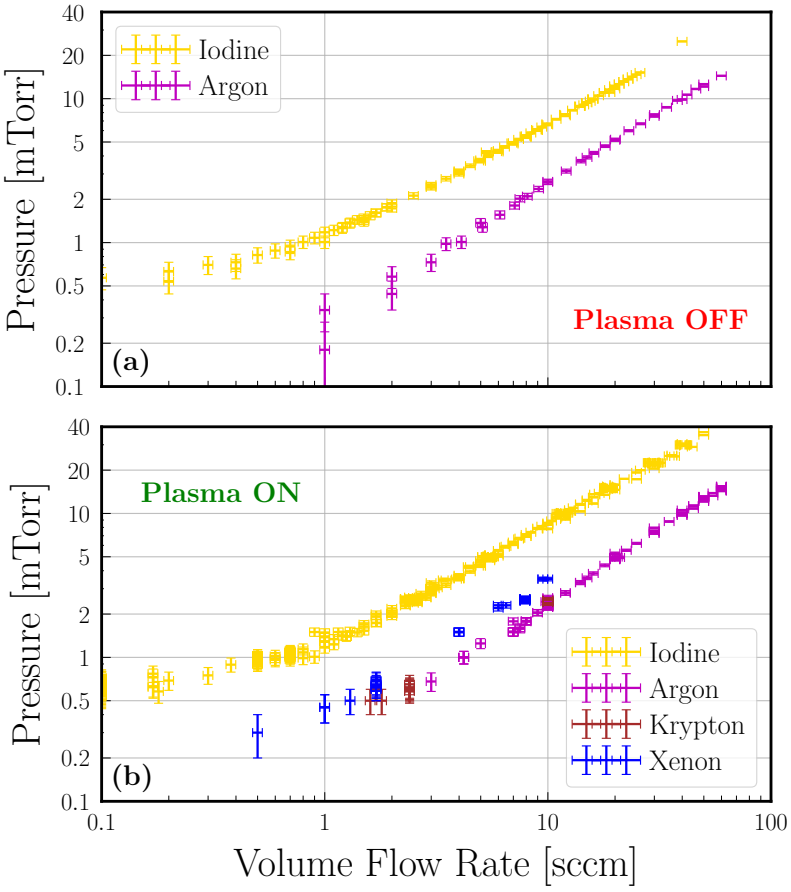

Figure 2.13: Pressure [mTorr] as a function of the Volume Flow Rate [sccm] measured within PEGASES ionization chamber with different gases. (a) Plasma OFF. (b) Plasma ON.

2.3.3.3 Plasma OFF: Conductance and transmission probability

In this section, the plasma is OFF and the problem can be considered isothermal at temperature T. Let's consider a particle flow moving from the ionization chamber (Ch1) to the vacuum chamber (Ch2) (see Figure 2.14). The upstream pressure p_1 has been measured by using a baratron (independent of the gas) and the downstream pressure p_2 has been measured by using a hot cathode transducer from MKS which is gas dependent. Thus, a correction factor f_{corr} was experimentally determined and applied to the measurements ($p_2 = p_{2,\text{measured}}/f_{\text{corr}}$). We used $f_{\text{corr}} = 1.29 \pm 0.05$ for argon and $f_{\text{corr}} = 4.54 \pm 0.25$ for I_2.

At steady state, the net particle flow is

$$Q_N = \frac{1}{4} n_1 \overline{v_1} S_{\text{open,neutrals}} W_{12} - \frac{1}{4} n_2 \overline{v_2} S_{\text{open,neutrals}} W_{21}, \tag{2.21}$$

with $S_{\text{open,neutrals}} = \beta_{\text{grid,neutrals}} S_{xy}$ the open area (the grid transparency $\beta_{\text{grid,neutrals}}$ is fixed to 16.3 %, as determined by equation (2.1), with an estimated error of ± 10 %) and W_{12} the transmission probability to go from Ch1 to Ch2 (also called the Clausing factor). By symmetry of the problem, we set $W_{12} = W_{21} = W$ and by

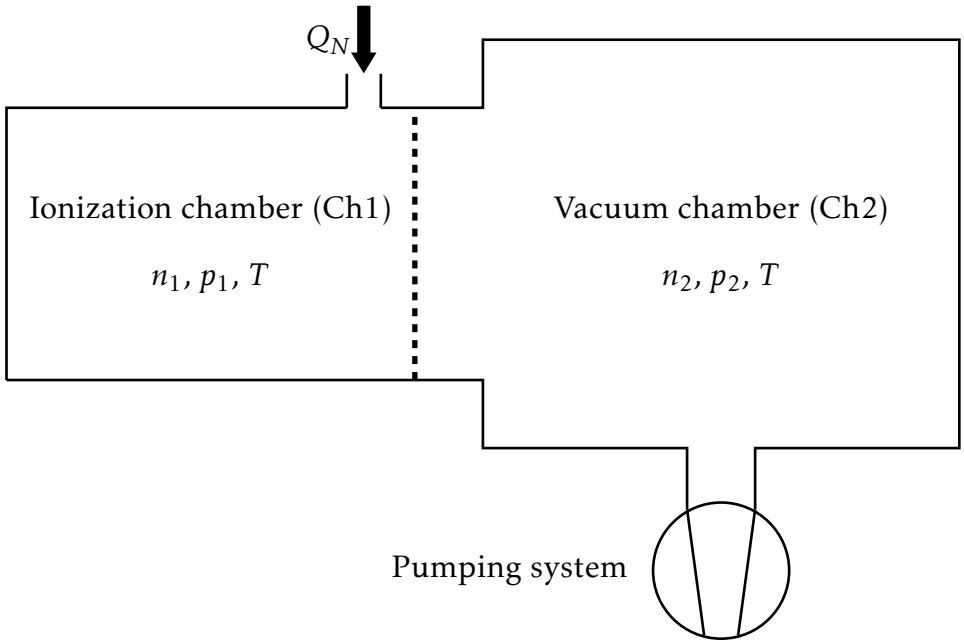

Figure 2.14: Schematics of the ionization and vacuum chambers separated by a grid when the plasma is OFF. The particle flow rate of injection is Q_N. Both chambers are at the same temperature.

multiplying both sides of the previous equation by $k_B T$, one gets:

$$Q_N k_B T = \frac{W}{4} \overline{v} S_{\text{open, neutrals}} \Delta p, \tag{2.22}$$

with $\overline{v} = \overline{v_1} = \overline{v_2}$ because of the constant temperature. Hence, the conductance reads:

$$C_{\text{plasma OFF}} = \frac{Q_N k_B T}{\Delta p} = \frac{W}{4} \overline{v} S_{\text{open, neutrals}}. \tag{2.23}$$

In the top of Figure 2.15, experimental upstream and downstream pressures are plotted as a function of the argon volume flow rate. In the bottom subfigure, the theoretical formula given by equation (2.23), with $T_{\text{room}} = 293$ K, is set equal to the experimentally measured mean conductance of 70 l.s^{-1} to find the transmission probability:

$$W_{\text{plasma OFF, Ar}} \approx 0.45 \tag{2.24}$$

This value of 0.45 is expected, in the molecular flow regime, for a cylindrical aperture whose length equals the diameter (see Figure 4.37 in [126]), and in our configuration, the grid is composed of thousands of holes with length and diameter of 1 mm (aspect ratio of 1).

The same analysis has been done with iodine and is presented in Figure 2.16, with a temperature of injection set to $T_{\text{injection}} = 315$ K. We still assume the problem to be isothermal. The upstream and downstream pressures are presented in the top subfigure. The pressure difference between both chambers is slightly bigger with iodine than with argon meaning that the transmission probability of the grid W is expected to be slightly smaller with iodine than with argon. This is confirmed by the bottom subfigure where the experimental conductance is compared

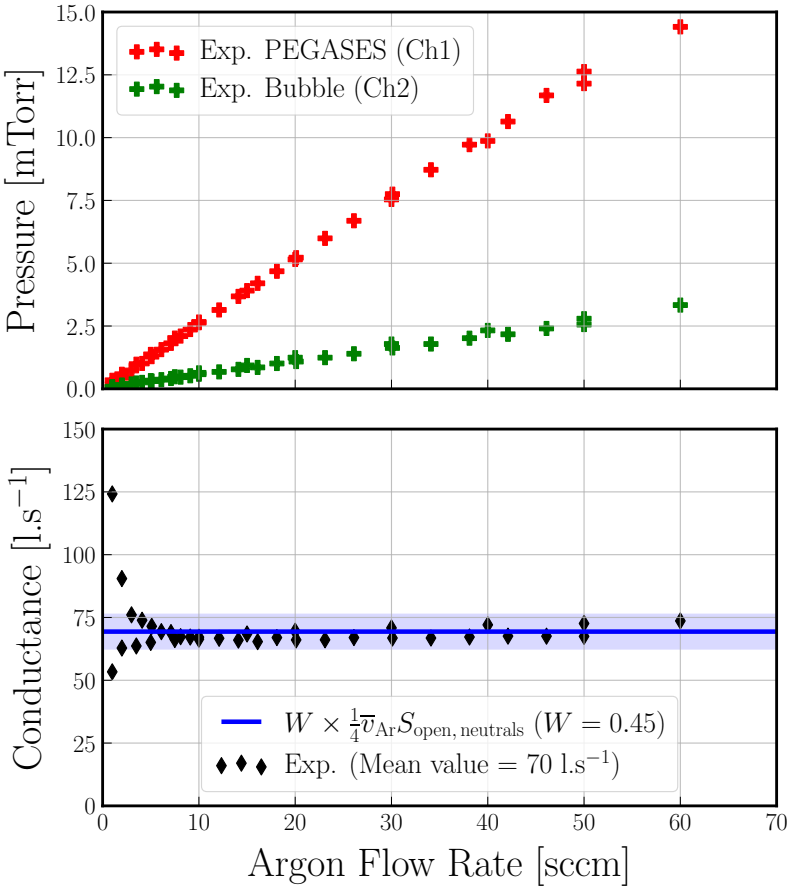

Figure 2.15: Pressure measurements in argon when the plasma is OFF. (a) Upstream and downstream pressures as a function of the argon flow rate [sccm]. (b) Conductance as a function of the argon flow rate. The experimental measurements are indicated by black diamonds. An experimental mean value of 70 l.s^{-1} is found. The theoretical formula of equation (2.23) is plotted in blue with $W = 0.45$, with an errorbar of ± 10 %.

to equation (2.23) with

$$W_{\text{plasma OFF, I}_2} = 0.4. \tag{2.25}$$

Several comments needs to be made here. First, the experimental values below 5 sccm need to be excluded from the discussion. In this low flux domain, the relationship between the flux delivered by the controller and the pressure is no longer linear as already highlighted in Figure 2.13. Then, for $Q_V \geq 5$ sccm, the agreement between experiments and theory is not as good as observed with argon but still acceptable. The discrepancy (non constant behavior) might be explained by the isothermal assumption that might break down when the injected gas is hotter than the room temperature, resulting in a temperature difference between both chambers. Finally, the smaller transmission probability might be explained by the contamination of the grid when iodine is injected.

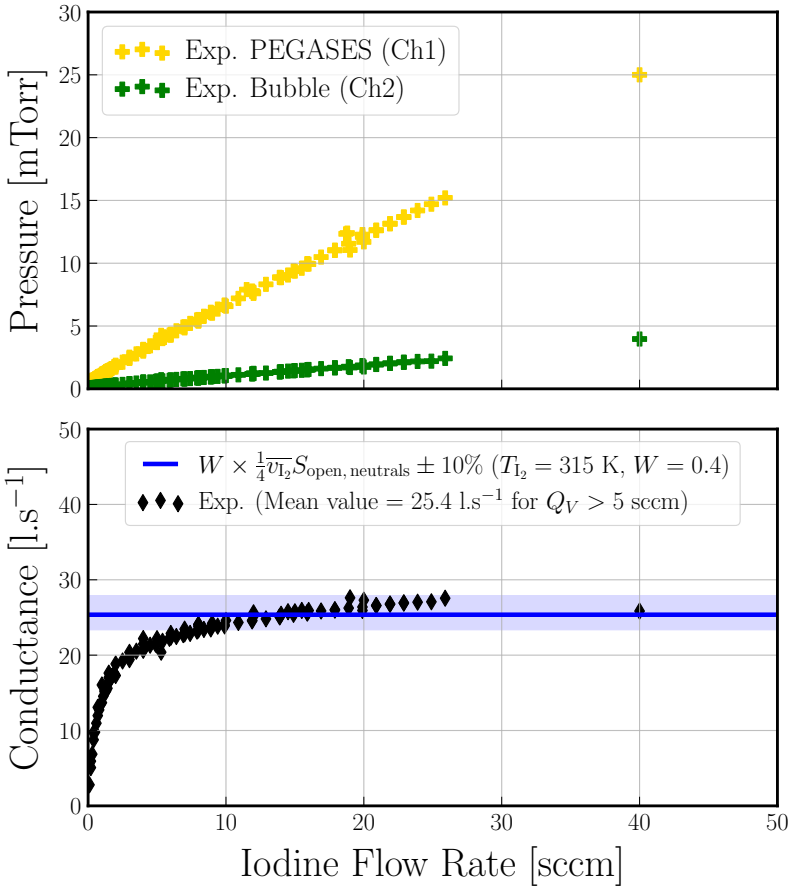

Figure 2.16: Pressure measurements in iodine when the plasma is off. (a) Upstream and downstream pressures as a function of the iodine flow rate [sccm]. (b) Conductance as a function of the iodine flow rate. The experimental measurements are indicated by black diamonds. The theoretical formula of equation (2.23) is plotted in blue with $W = 0.4$, with an errorbar of ± 10 %.

2.3.3.4 Plasma ON: Estimation of the plasma temperature

When the plasma is ON, the former reasoning still holds but the isothermal assumption breaks down. Each chamber has it own temperature T_1 or T_2 (see Figure 2.17). Moreover, the nature of the gas (atomic or molecular) needs to be taken into account because of dissociation.

Atomic gases

In the case of an atomic gas, equation (2.21) holds but three different temperatures need to be taken into account: T_1, T_2 and $T_{\text{injection}}$ the temperature of injection. The transmission probalities are once again assumed equals: $W_{12} = W_{21} = W$. One can write:

$$Q_N k_B T_{\text{injection}} = \frac{W}{4} S_{\text{open, neutrals}} \left(p_1 \overline{v_1} \frac{T_{\text{injection}}}{T_1} - p_2 \overline{v_2} \frac{T_{\text{injection}}}{T_2} \right), \tag{2.26}$$

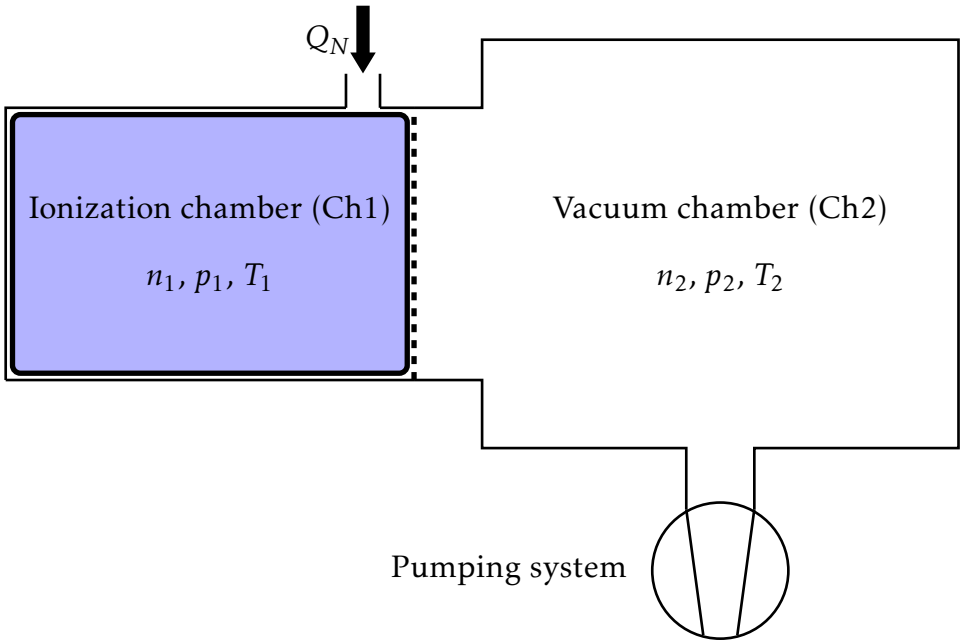

Figure 2.17: Schematics of the ionization and vacuum chambers separated by a grid when a plasma is ON. The particle flow rate of injection is Q_N. Temperatures in each in each chamber are different.

Then, assuming $T_2 = T_{\text{injection}} = T_{\text{room}} = 293$ K, one gets access to T_1:

$$T_1 = \left(\frac{p_1}{p_2}\right)^2 \frac{T_2}{\left(1 + \frac{4Q_N k_B T_2}{W S_{\text{open, neutrals}} p_2 \overline{v_2}}\right)^2} \tag{2.27}$$

In Figure 2.18, T_1 is computed, by using the measured upstream and downstream pressures when an argon plasma was running, and plotted against the volume flow rate. The transmission probability being unknown, we computed T_1 for several values of W (0.45, 0.6 and 0.75). The value of 0.45, found when the plasma was off, is ruled out because it conveys T_1 values lower than the room temperature, which is not physical. In comparison with the absorption measurements performed within PEGASES thruster running on argon and presented in Chapter 4, all the values between 0.6 and 0.8 are acceptable depending on the discharge power used. It seems that the plasma increases the transmission probability of the grid, certainly by heating it up.

Molecular gases

With molecular gases, such as iodine, the situation is more complex and we will not be able to go further using pressure measurements only. Indeed, as soon as a plasma is on, a portion of the injected molecules are dissociated and the pressure inside the thruster can be written as:

$$p_1 = p_{\text{neutrals}} = n_{\text{I}_2} k_B T_{\text{I}_2} + n_{\text{I}} k_B T_{\text{I}}, \tag{2.28}$$

where T_{I_2} and T_{I} are not necessarily equal. Even if they were equal, the dissociation fraction being unknown, it is impossible to relate n_{I} and n_{I_2} without making strong assumptions or performing an additional diagnostic.

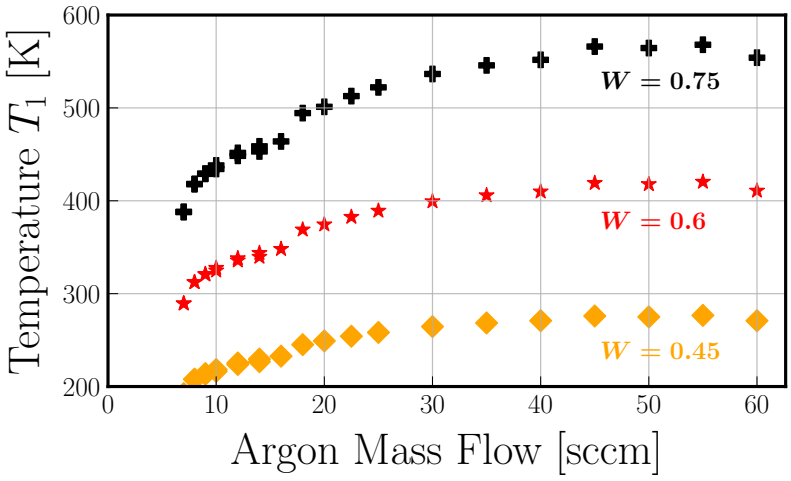

Figure 2.18: Estimated temperature inside the thruster when an argon plasma is running, according to equation (2.27), for 3 different values of the grid transmission probability.

2.3.4 Wall temperature

Collision and dissociation processes inside a plasma directly induce an increase in the neutral species temperature. In some operating conditions, the plasma becomes much hotter than the room temperature. Moreover, when ions cross the sheath, they acquire a lot of energy that will be transferred to the walls after the collision and induce an increase in the temperature of the walls. In this section, we characterize the temperature of the walls when argon and iodine plasmas are run. Several thermocouples were taped on the bottom wall of the ionization chamber, along the thrust axis, to measure the wall temperature.

We start our investigation by recording the temporal evolution of the wall temperature when argon plasmas are run in the quartz prototype (shown in Figure 2.9a) for several operating conditions. Only one thermocouple was used here and located at $z = 6.5$ cm away from the antenna. Results are presented in Figure 2.19. A steady state is always reached 30 minutes after plasma ignition. The heating characteristic time (obtained by fitting the profiles by an exponential law) is shown to be mostly controlled by the absorbed power and independent of the neutral pressure (approximately 6 minutes at 100 W and 9 minutes at 40 W). With this prototype, the water-cooling system is not efficient enough and the wall temperature can become very hot because of the poor thermal conductivity of quartz. When the discharge power is increased, more ions are produced and cross the sheaths, increasing the wall temperature. The effect of pressure is more subtle. For the same absorbed power, a lower mass flow rate induces a higher wall temperature because decreasing the pressure makes the electron temperature increase and thus increases the energy gained by the ions crossing the sheath (the sheath potential drop is proportional to the electron temperature at the first order). Because of the ozone production issue already mentioned within the quartz prototype, no temporal evolution measurements were conducted with iodine plasmas running. Still, by approaching the hand to the quartz prototype when an iodine plasma is run for a few minutes only, the wall temperature appears much higher with iodine than with argon (for the same

operating conditions).

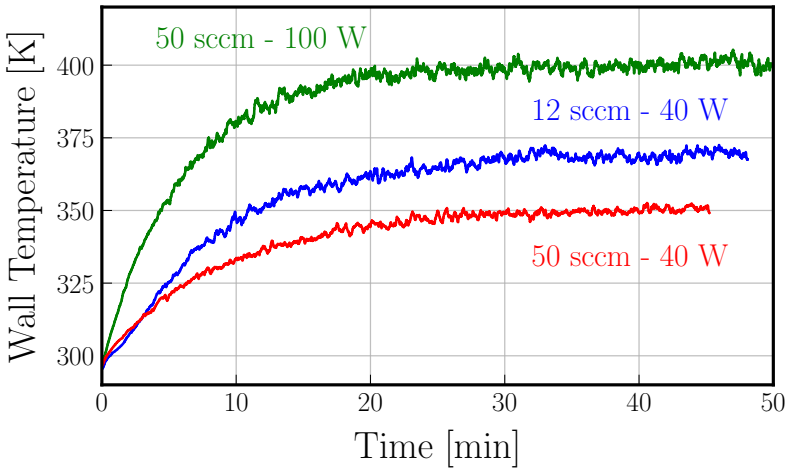

Figure 2.19: Temporal evolution of the wall temperature when argon plasmas are run in the PEGASES quartz prototype.

In what follows, wall temperature measurements were only conducted when plasmas were running within the aluminum prototypes (anodized or not), in which most of the experiments of the thesis were conducted. As previously observed, increasing the discharge power heats the walls (see Figure 2.20). Once again, only one thermocouple was used here and located at $z = 6.5$ cm away from the antenna. Above 200 W of discharge power, with argon and iodine, the wall temperature exceeds 320K, which is clearly above the room temperature (around 293 K) but well below the temperature reached with the quartz prototype, confirming the efficiency of the water-cooling system with aluminum prototypes, which have a much better thermal conductivity. No net difference is observed between argon and iodine. A fitting power law is indicated in the figure. However, the effect of pressure on the wall temperature appeared to be very limited, probably diminished by the cooling system.

Finally, the influence of the water cooling system location is investigated. In Figure 2.21, spatial profiles of the wall temperature were recorded over time when an iodine plasma was ON at 200 W of discharge power with a gas injection flow rate fixed to 18.8 sccm. Five thermocouples were located along the thruster axis. Temporal characteristics already observed in Figure 2.19 are retrieved with a steady state reached after 30 minutes. The sensor located at $z = -0.5$ cm was measuring the temperature of the water cooling system which was more than 20 K colder than the hottest location. Apart from the region near the water cooling system ($z < 0.5$ cm), at steady state, the wall temperature is quite homogeneous along the thrust axis and can be considered constant.

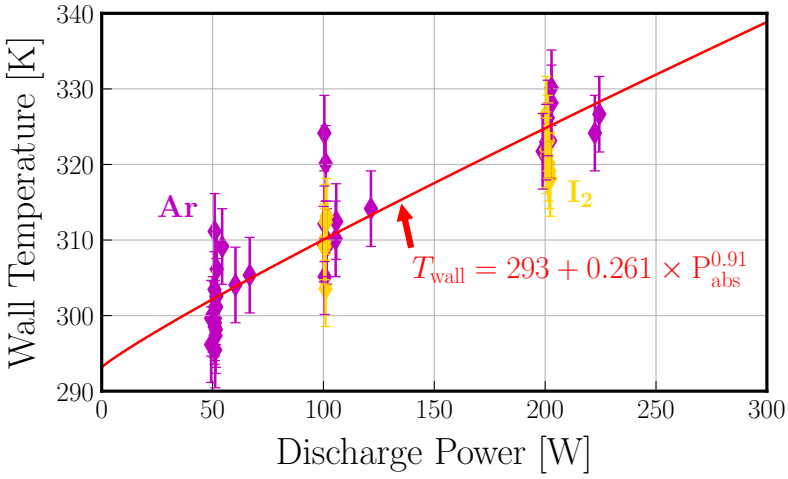

Figure 2.20: Influence of the discharge power on the walls temperature. Measurements were performed in argon and iodine using a thermocouple located on the bottom wall of the ionization chamber (made of anodised aluminum) at $z = 6.5$ cm from the antenna. A fitting power law is indicated in red.

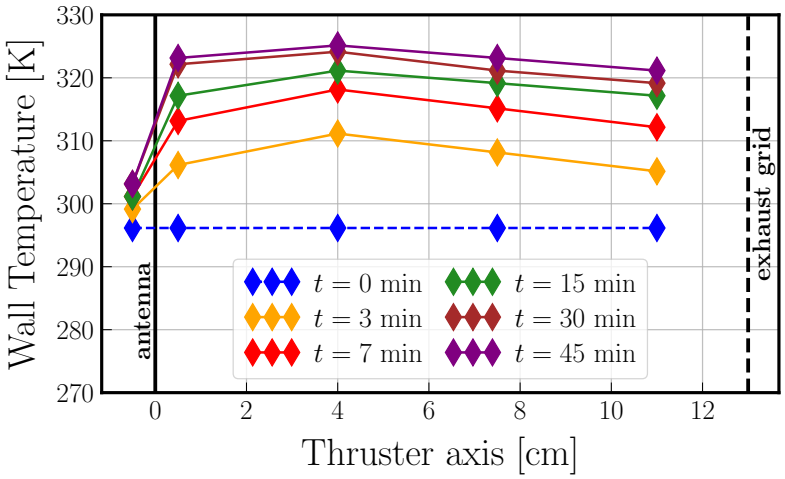

Figure 2.21: Spatial profiles of the walls temperature over time. Measurements were performed when an iodine plasma was run with a fixed mass flow rate of 18.8 sccm and a discharge power of 200 W inside the anodised aluminum prototype.

2.4 The iodine cell

In addition to the thruster setup described so far, an other experimental setup has been used to study iodine plasmas: the iodine cell. The main purpose of this additional experimental setup was to develop optical diagnostics for iodine plasmas in a more favorable environment (higher pressure and better optical access) before applying them within the thruster. It will be used in Chapter 4 and Chapter 5.

Iodine plasmas are generated using an iodine cell coupled to an RF generator. The quartz cell, without optical coatings, is sealed under vacuum and contains some iodine crystals (shown in operation in Figure 2.22). It is a 25 cm long cylinder (l_{cell} = 0.25 m) with an internal diameter of 3 cm (r_{cell} = 0.015 m). A 12 cm long and around 1 cm of external diameter "cold finger" is attached to the main cylinder as a reservoir of solid iodine. Temperature regulation of the finger, as long as it remains below room temperature, makes it possible to set the pressure inside the main cylinder. For that purpose, the finger is immersed in a 200 ml beaker, which is temperature-regulated by a ministat 230 controller from Huber, with heat transfer improved by a copper coil. The cooling liquid is a mixture of alcohol and water, which makes it possible to regulate the temperature of the cold point from -10°C to 20°C.

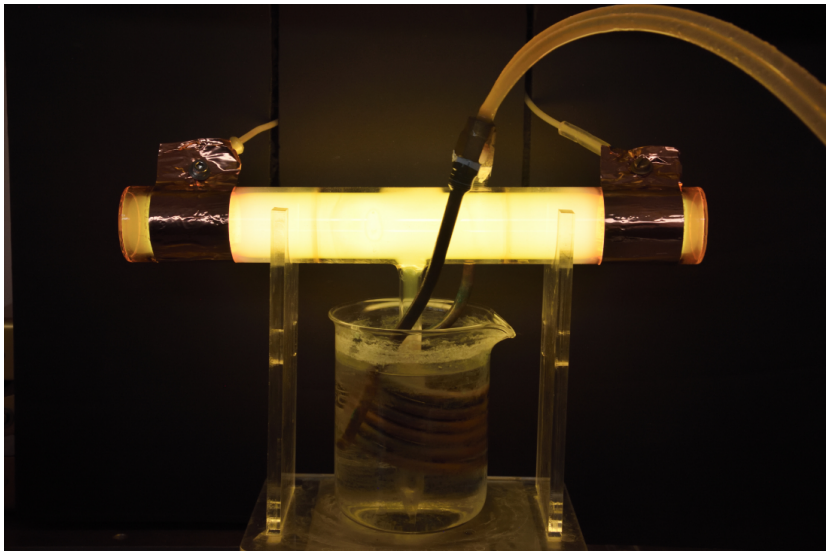

Figure 2.22: The 25 cm long and 3 cm in-internal-diameter iodine cell. In this example, the “cold finger” temperature is set at 2°C and the cell is excited with an input power of 20 W.

When no plasma is on, the pressure p_0 as a function of temperature T_{cold} is described in the literature by two empirical formulas that lead to similar values (see equations (1.2) and (1.1)), with a difference that does not exceed 0.1 to 0.8 Pa over the studied temperature range (see Figure 1.2). In this work, we decided to use the average value provided by the two vapor-pressure laws. A thermometer is used to monitor the temperature within the cold beaker and the initial pressure was varied from 1.5 to 30 Pa (11.25 to 225 mTorr). The initial molecular density $n_{I_2,0}$ is deduced from the ideal gas law at room temperature:

$$n_{I_2,0} = \frac{p_0}{kT_{\text{room}}} \tag{2.29}$$

The room used for the iodine cell experiments was air-conditioned with $T_{\text{room}} = 293$ K leading to $n_{I_2,0}$ values between 3.7×10^{20} m^{-3} and 7.4×10^{21} m^{-3}.

When the plasma is on, the pressure is not monitored but is expected to largely increase because of dissociation and an increase in the gas temperature. If we introduce the dissociation fraction $\eta = 1 - n_{I_2}/n_{I_2,0}$, the only valid relation when the plasma is on is:

$$2 \times \eta \times n_{I_2,0} = n_{I_{3/2}} + n_{I_{1/2}}, \tag{2.30}$$

with $n_{I_{3/2}}$ and $n_{I_{1/2}}$ the atomic densities introduced in Chapter 1 and where charged species densities were assumed to be negligible.

Two 35 mm wide copper tape electrodes are placed on the outer surface of the cell and spaced 15 cm apart. These electrodes are connected through an impedance matching circuit to a 13.56 MHz RF generator from Sairem. The input and reflected powers are measured by a Vigilant Monitor probe from Solayl. Once again, the RF power is the difference between the incident and the reflected powers. Two problems can appear with this cell used to produce a plasma:

- The power must be limited not to generate a plasma in the "cold finger". In such conditions, the temperature increases and it is no longer possible to consider the discharge perfectly cylindrical.
- A high plasma power could make the cell opaque, certainly due to etching on the internal walls. The optical transmission can be partially restored by heating the cell with a heat gun. However, the initial optical quality, which deteriorates with the operating time when a plasma is on, has never been fully recovered.

Note that ozone production was also induced by the cell but it remained tolerable because the emission lines below 240 nm were weaker than within the quartz thruster (higher pressure and lower power with the cell).

CHAPTER 3
CHARGED-PARTICLES MEASUREMENTS

Contents

3.1 Introduction

This chapter presents the experimental diagnostics developed to measure the densities and temperatures of charged species (electrons and ions) in iodine plasmas along the main axis of the PEGASES thruster (z-axis).

The Langmuir probe technique is first presented (Section 3.2) and applied to noble gas plasmas, used for electric propulsion (xenon, krypton and argon), in order to validate the method.

In a second step (Section 3.3), the photodetachment technique is described in view of its use to probe negative I^- ions.

Section 3.4 compares the Langmuir probe results obtained with iodine and noble gases, in the regime of interest for electric propulsion (low mass-flow rates and high power density, 0.5-2.5 mTorr with our experimental setup).

The final section of results (Section 3.5) combines Langmuir probe and laser-induced detachment measurements obtained in iodine plasmas for operating conditions beyond the interest of space propulsion application alone (large range of mass-flow rates and high power density, 0.5-15 mTorr with our experimental setup). The quasi-neutrality assumption (satisfied within the discharge) gives access to the density of positive species.

The main findings of the chapter are gathered in a summary at the end.

3.2 Langmuir probe

In this section, the Langmuir probe diagnostics used to measure the electrons properties is presented. The Druyvesteyn method [127] has been preferred to the commonly used Langmuir method [128, 129] because recent works from Godyak [130, 131] evidenced some limits of the later procedure. Accuracy and repeatability of the measurements are studied to estimate error bars. Finally, an application to noble gases plasmas is presented to validate the method and collect experimental data to further compare with numerical models.

3.2.1 Probe characteristics and data acquisition

The Langmuir probe design is presented in Figure 3.1a. It consists of two tungsten wires of 100 μm diameter inserted in a bi-holed 15 cm long ceramic (or quartz) tube with an external diameter of 1.5 mm. The first wire is used as the Measuring Probe (MP) and the other wire is used as a Reference Probe (RP). The probes are 3.5 mm long. The probe is mounted on a movable arm (see Figure 2.2) in order to scan the axial position in a 10 cm range, from $z = 1.5$ cm to $z = 11.5$ cm. The alumina window located in front of the inductive coil (antenna) is at $z = 0$ cm (see Figure 3.1b) while the exhaust grid is located at $z = 13$ cm.

Data are acquired using the Multifunction Plasma Probe Analyser (MFPA) from *Plasma Sensors*®. An example of the software user interface, taken during an argon measurement, is shown in Figure 3.2. The MFPA takes advantage of the RP to compensate for plasma potential drifts or fluctuations. The probe is cleaned by ion bombardment between each scan (a negative bias is imposed to the probe). The Druyvesteyn method [127] is used to measure $f(\mathcal{E})$, the Electron Energy Probability Function (thereafter designated EEPF in [$\mathrm{eV}^{-3/2}\mathrm{m}^{-3}$]), by double differentiation of the collected electronic current $I_e(V)$:

$$\frac{\mathrm{d}^2 I_e}{\mathrm{d}V^2} = \frac{e^2 S_\mathrm{p}}{4}\sqrt{\frac{2e}{mV}}F(\mathcal{E}) = \frac{e^3 S_\mathrm{p}}{2\sqrt{2m}}f(\mathcal{E})\,, \tag{3.1}$$

where $F(\mathcal{E}) = \mathcal{E}^{1/2} f(\mathcal{E})$ is the Electron Energy Distribution Function (EEDF in [$\mathrm{eV}^{-1}\mathrm{m}^{-3}$]) and S_p the probe surface. The electron density n_e [m^{-3}] and the effective electron temperature $T_e = \frac{2}{3}\langle\mathcal{E}\rangle$ [eV] are then obtained by integration of the distribution over energy:

$$n_e = \int_0^{+\infty} \mathcal{E}^{1/2} f(\mathcal{E})\mathrm{d}\mathcal{E}\,, \tag{3.2}$$

$$T_e = \frac{2}{3} n_e^{-1} \int_0^{+\infty} \mathcal{E}^{3/2} f(\mathcal{E})\mathrm{d}\mathcal{E}\,. \tag{3.3}$$

Note that the ion current has not been subtracted to the probe current because of the issues underlined in [131, 132].

Probe signals were corrected using the procedure described by Godyak in [131] and detailed in subsection 3.2.2.2. The correction modified the results up to +20% for n_e and -15% for T_e in the highest pressures in iodine, where very strong spatial gradients have been observed and contamination of the probe is expected to be the greatest. Contamination of the discharge walls may also lower the conductive

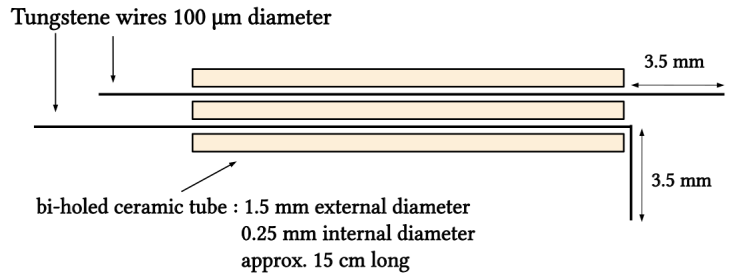

(a)

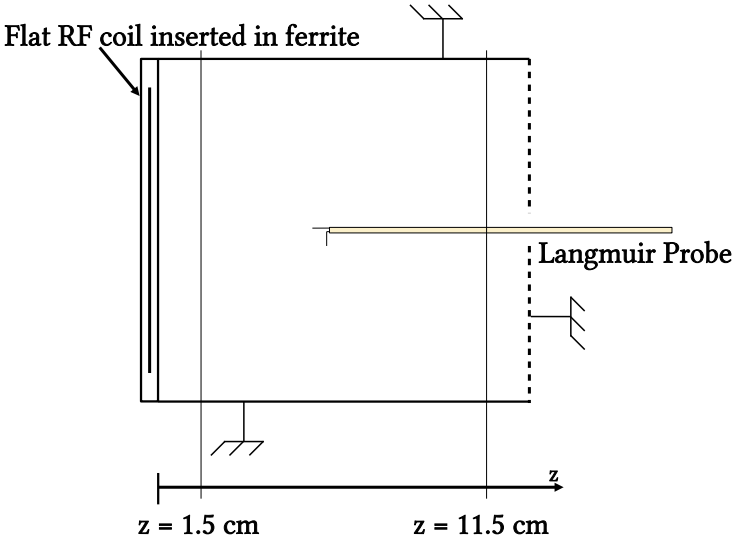

(b)

Figure 3.1: (a) Langmuir probe design and characteristics. (b) Insertion of the Langmuir probe inside the ICP chamber. The probe goes through the exhaust grid and can scan the plasma from $z = 1.5$ cm to $z = 11.5$ cm, the axis origin being the alumina plate location. Internal walls and the exhaust grid are grounded.

properties of the surfaces and affects the return current. Finally, the repeatability of the Langmuir probe measurements has been checked by reproducing the same plasma conditions with several probes on several experimental campaigns (over several months), and the error in the measured electron density and temperature was less than 15% (see subsection 3.2.2.3 for more details). Unless otherwise stated, error bars will not be plotted in this section.

3.2.2 Accuracy and correction of the LP measurements

3.2.2.1 Electrical issues

Langmuir probe measurements were taken within two different thruster protoypes: a conductor one and a dielectric one where walls are covered with anodized aluminium (see Section 2.2 for the description of different thruster prototypes). In both cases, the exhaust grid was grounded.
Below 5 mTorr, both with noble gases and iodine, no difference was observed be-

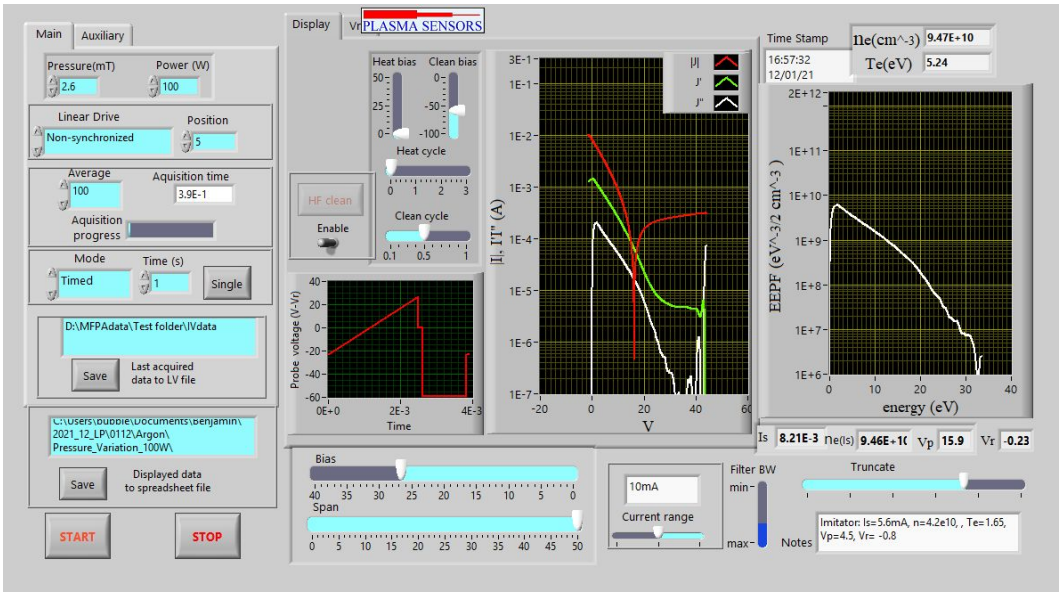

Figure 3.2: MFPA software user interface during an argon measurement at 2.5 mTorr for a discharge power of 100 W. The current (red curve) and its derivatives (first order in green and second order in white) are plotted in absolute against the absolute voltage. The EEPF is plotted on the right, with estimated n_e and T_e in the top-right corner.

tween measurements in the conductor or dielectric configuration, the discrepancies lying within the systematic error bars discussed in subsection 3.2.2.3.

However, when pressure was increased, the discrepancies became obvious. In Figure 3.3, for a pressure of 15 mTorr in an iodine plasma, the electron density profile clearly saturates for $z \leq 5$ cm in the dielectric configuration but no saturation is observed in the conductor case. An analog phenomenon is observed with the electron temperature. The measurements cannot be considered accurate in this case. The antenna and the exhaust grid are materialized by vertical black lines (respectively solid and dashed).

Physically, with the dielectric configuration, the only conductive surface of the thruster is the exhaust grid. When the probe goes away from the grid and comes closer to the antenna, the plasma resistance that ions undergo to escape the discharge becomes bigger because the electron density decays towards the grid and the plasma resistance is inversely proportional to n_e [119]. In this case, the current collected by the probe is limited and so does the reachable electron density. The phenomenon is very important in iodine where the corrosive nature of the molecule quickly deteriorates the conductive properties of the walls. Note that even with the conductor configuration, accurate Langmuir probe measurements were impossible to achieve near the antenna for pressures above 20 mTorr.

3.2.2.2 Correction of the measurements

Theoretically, the EEPF should increase all the way to $\mathcal{E} = 0$. However, the experimental EEPF is always depleted at very low energies and exhibits a maximum at $\mathcal{E} > 0$. The position of this maximum depends on the plasma noise suppression and the acquisition rate of the full EEDF. The best measurements should minimize

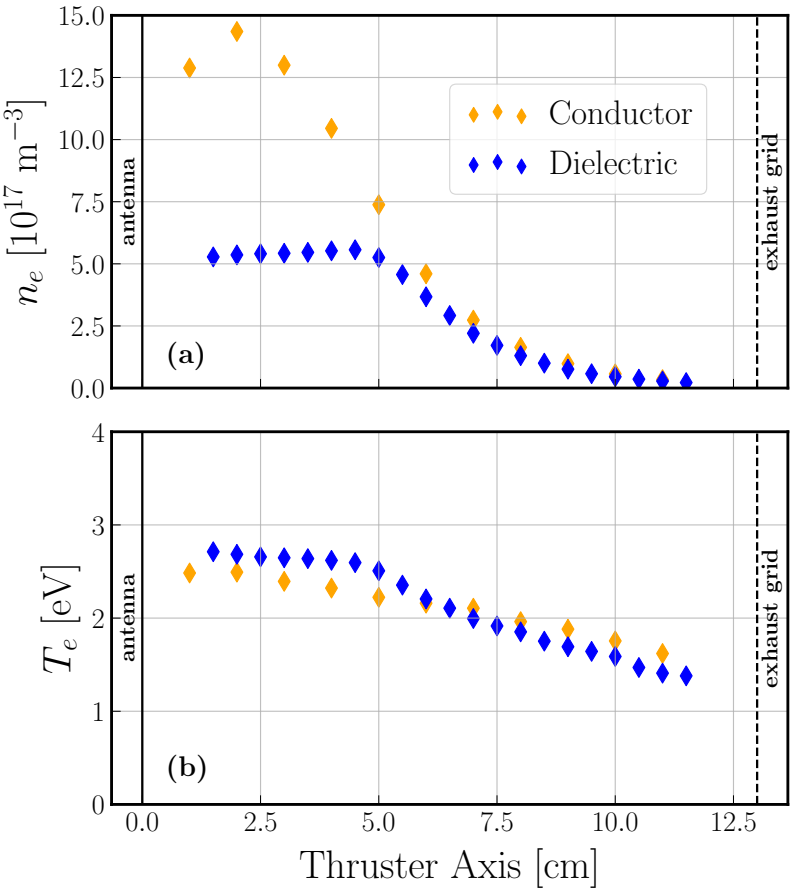

Figure 3.3: Langmuir probe measurements in a purely iodine plasma for a discharge power of 200 W and a pressure of 15 mTorr. The measurements were conducted within a conductor and a dielectric prototype of PEGASES thruster. A clear saturation is observed with the dielectric configuration. (a) Spatial profiles of the electron density n_e [m^{-3}] along the thrust axis. (b) Spatial profiles of the electron temperature T_e [eV] along the thrust axis.

the energy at which the maximum occurs. The shift towards higher energies can be greatly increased by the size of the probe and its holder, the circuit resistance, the probe contamination and plasma potential fluctuations [130]. We will use the same notation as used by Godyak [131] and note $\delta_\mathcal{E}$, the energy at which the EEPF maximum is reached.

The first criterion to accurately measure the EEPF is therefore to correctly collect the low energy electrons (electrons with energies below the mean energy $\langle\mathcal{E}\rangle$). These electrons are the major contributors to the electron density. Distortion in this part of the EEPF significantly affects the accuracy of n_e and T_e deduced from the EEPF. In reference [130] it is stated that the EEPF measurement is acceptable when $\delta_\mathcal{E} < T_e$ and of high accuracy when $\delta_\mathcal{E} \leq (0.3 - 0.5)\ T_e$. In this work, all the iodine measurements where such that $0.3 \leq \delta_\mathcal{E}/T_e \leq 0.65$, the worst case being for iodine at the highest pressures (see Figure 3.4 where spatial effects on $\delta_\mathcal{E}/T_e$ appear above 5 mTorr). At the lowest pressures (where the electron temperature is the highest) and with noble gases, the ratio $\delta_\mathcal{E}/T_e$ was around 0.2. In order to reach lower values for this ratio (below 0.1 for instance), it would have been mandatory to design a tele-

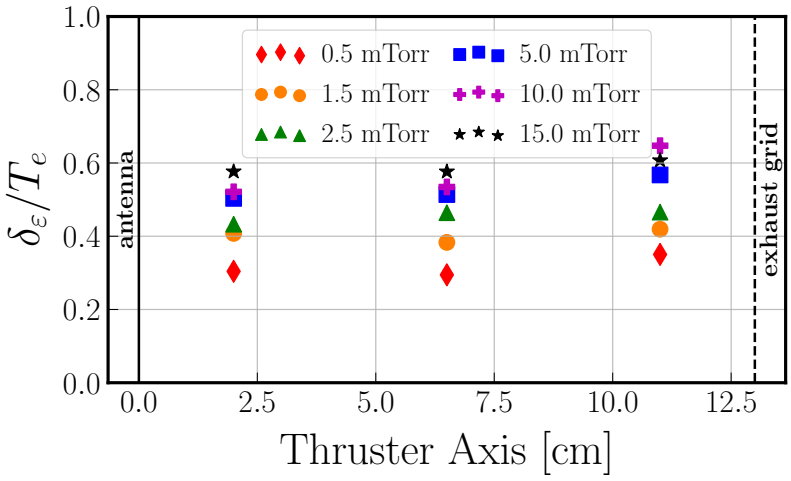

Figure 3.4: $\delta_\mathcal{E}/T_e$ ratio along the thruster axis in iodine plasmas for pressures from 0.5 mTorr to 15 mTorr and a discharge power of 200 W. The plotted values were computed before applying the correction process detailed in the present subsection.

scopic Langmuir probe where the probe holder radius is progressively diminished and much smaller than the one used in this work, as proposed by Godyak [132, 133] or used by Bredin [123]. Nevertheless, the accuracy of the measurements has been considered good enough to avoid such a care.

The second criterion for a correct EEPF measurement is to have a large enough dynamic range (which is the ratio between the EEPF maximum and its minimal values undistorted by noise [130]). This criterion is mandatory to correctly capture electrons of high energy responsible for inelastic processes (such as excitation and ionization). The fastest electrons are also those which escape to the walls because they overcome the sheath potential. Measurements are considered of high accuracy when the dynamic range exceeds 10^3 [130]. In what will be presented next, the dynamic range has always been found between 2×10^2 and 10^4.

To illustrate the above discussion, two experimental EEPFs are presented (blue curves) in Figure 3.5. They were both measured in an iodine plasma but for different plasma conditions and at a different location inside the chamber. For the best quality EEPF of Figure 3.5a, $\delta_\mathcal{E}/T_e \approx 0.3$ while for the worst quality EEPF of Figure 3.5b, $\delta_\mathcal{E}/T_e \approx 0.65$. The resulting electron density and temperature using equations (3.2) and (3.3) are given in the legend. By comparison to an extrapolation explained below, it can be seen that the bad collection of low energy electrons leads to an underestimation of the electron density and an overestimation of the effective electron temperature. Obviously, the error is larger in the worst case.

We decided to correct our measurements using the procedure detailed by Godyak in [131]. However, instead of defining $\mathcal{E}^*$ as the first excitation energy, we set $\mathcal{E}^* = 3\,T_e$. This is because it is difficult to evaluate the exact composition of iodine plasmas which varies both spatially and with the input power and the gas pressure; the plasma can be either highly dissociated everywhere or partially dissociated near the antenna and entirely molecular near the exhaust grid. As stated by Godyak [131], when $\delta_\mathcal{E}$ is not too large the measured EEPF may be extrapolated from its Maxwellian part to the zero electron energy. This extrapolated EEPF should be used to obtain the effective electron temperature $T_e = 2/3\langle\mathcal{E}\rangle$ and the

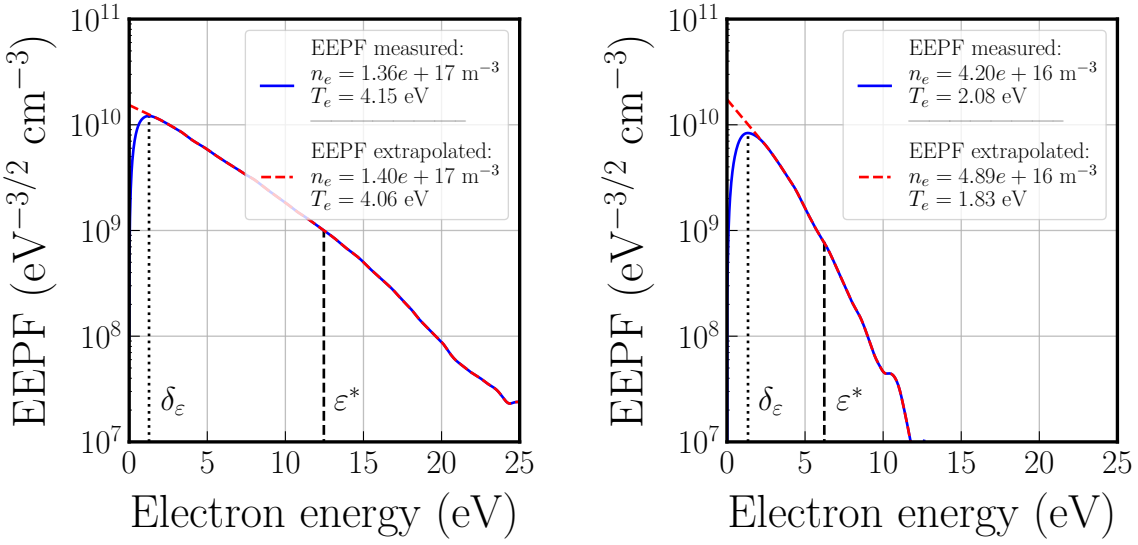

(a) (b)

Figure 3.5: Electron Energy Probability Function (EEPF) in iodine plasmas (blue curves). The EEPF, extrapolated at lower energies using the method detailed before, is drawn in red. $\delta_\mathcal{E}$ corresponds to the energy of the measured EEPF maximum and $\mathcal{E}^*$ is set to $3T_e$. Two very different EEPFs are presented to highlight the effect of extrapolation. (a) 0.6 mTorr - 100 W - z = 6.5 cm: Almost no difference between the measured and the extrapolated EEPF. (b) 10 mTorr - 200 W - z = 11.5 cm: The extrapolation does affect n_e and T_e.

electron density. Practically, the linear extrapolation (in log-scale) was done using experimental data whose energy lies within the interval [1.5 $\delta_\mathcal{E}$; $\mathcal{E}^*$]. With this procedure, as seen above, the corrected electron temperature is lower while the plasma density is larger. In our experiments, distributions are not far from Maxwellian in the energy range $\mathcal{E} < \mathcal{E}^*$ because the electron density is high, which favors electron thermalisation [130–132].

Unless otherwise stated, the EEPFs obtained in this work have all been corrected in the low energy range (see Figure 3.5 in dashed-red) and the corrected electron density and temperature were obtained using equations (3.2) and (3.3) (see the values given in the legend). We can quantify the correction on n_e and T_e by introducing relative errors on both quantities:

$$\Delta_{n_e} = \frac{n_e^{\text{corrected}} - n_e^{\text{measured}}}{n_e^{\text{measured}}}, \tag{3.4}$$

$$\Delta_{T_e} = \frac{T_e^{\text{corrected}} - T_e^{\text{measured}}}{T_e^{\text{measured}}}. \tag{3.5}$$

The correction will always lead to positive Δ_{n_e} and negative Δ_{T_e}. In the example shown in Figure 3.5a, the electron density and temperature are only slighty modified by the correction with $\Delta_{n_e} \approx 0.03$ and $\Delta_{T_e} \approx -0.02$. The correction in Figure 3.5b is more significant but still acceptable, with $\Delta_{n_e} \approx 0.14$ and $\Delta_{T_e} \approx -0.12$.

For the entire data set presented in this manuscript, Δ_{n_e} varied between $\Delta_{n_e}^{\min}$ = 2% and $\Delta_{n_e}^{\max}$ = 20% and $\left|\Delta_{T_e}\right|$ between $\left|\Delta_{T_e}^{\min}\right|$ = 1% and $\left|\Delta_{T_e}^{\min}\right|$ = 15% for iodine.

With noble gases, where contamination of the walls and the probe was not an issue, the correction never exceeded 10% ($\Delta_{n_e}^{\max} = \left|\Delta_{T_e}^{\max}\right| = 10\%$ and $\Delta_{n_e}^{\min} = \left|\Delta_{T_e}^{\min}\right| = 1\%$).

3.2.2.3 Repeatability of the measurements

In order to properly estimate the systematic error of the Langmuir probe measurements, we reproduced the same plasma conditions with several probes on different experimental campaigns, over several months (see Figure 3.6). Note that this error is due to the plasma behavior itself (walls contamination, discharge fluctuations) and is completely independent of the previously described correction. The effect of the different probe sizes has also been removed by correcting the measured electron density values as follows:

$$n_{e,\text{plotted}} = n_{e,\text{measured}} \times \left\langle S_{probe} \right\rangle / S_{probe}, \tag{3.6}$$

with $\left\langle S_{probe} \right\rangle$ the mean probe section value taken over the full dataset. The procedure has also been conducted with iodine to give the same results: a systematic error of ±15% on the electron density and of ±10% on the electron temperature.

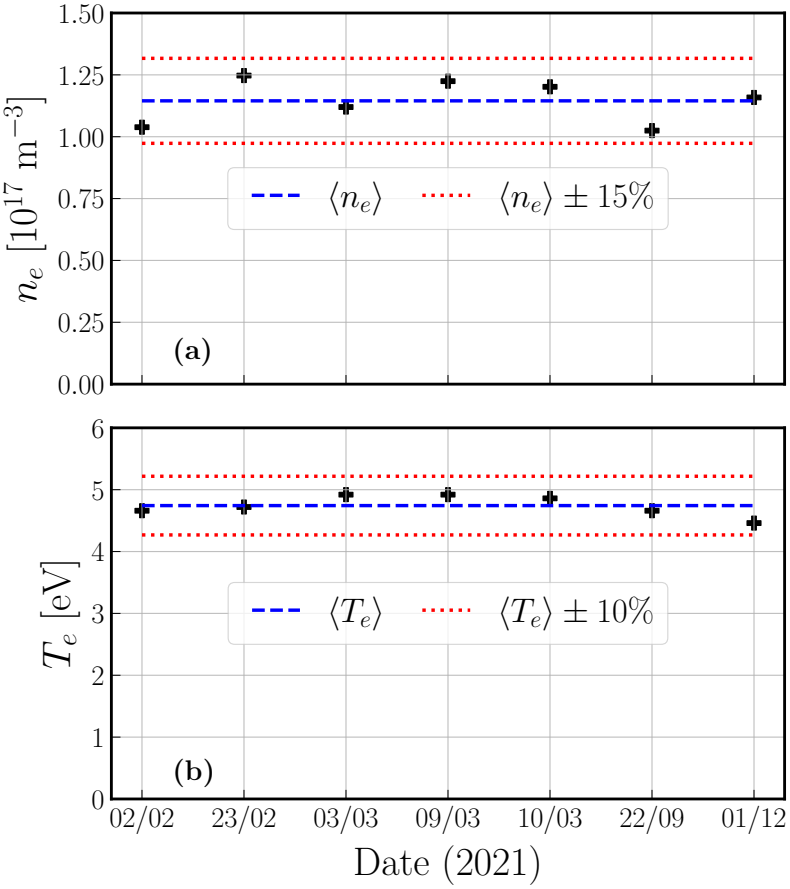

Figure 3.6: Langmuir probe systematic error caracterization. Measurements were taken in argon, over several months, in the center of the discharge (z = 6.5 cm) for a pressure of 5 mTorr and a discharge power of 100 W. (a) The electron density exhibits a systematic error of ± 15%. (b) The electron temperature exhibits a systematic error of ± 10%.

To summarize the discussion on accuracy and repeatability of the Langmuir probe measurements conducted in this work, we gathered the systematic and correction error bars. Over all the measurements taken within PEGASES thruster using the MFPA software, if you do not apply the correction procedure, the final values for n_e and T_e are given by:

- With noble gases:

$$n_e = n_e(\mathrm{MFPA})^{+\left|(1+\Delta_{n_e}^{max})\times(1.15)-1\right|}_{-\left|(1+\Delta_{n_e}^{min})\times(0.85)-1\right|} = \mathrm{n_e(MFPA)}^{+26.5\%}_{-13.3\%} \tag{3.7}$$

$$T_e = T_e(\mathrm{MFPA})^{+\left|(1+\Delta_{T_e}^{min})\times(1.10)-1\right|}_{-\left|(1+\Delta_{T_e}^{max})\times(0.9)-1\right|} = \mathrm{T_e(MFPA)}^{+8.9\%}_{-19\%} \tag{3.8}$$

- With iodine:

$$n_e = n_e(\mathrm{MFPA})^{+\left|(1+\Delta_{n_e}^{max})\times(1.15)-1\right|}_{-\left|(1+\Delta_{n_e}^{min})\times(0.85)-1\right|} = \mathrm{n_e(MFPA)}^{+38\%}_{-13.3\%} \tag{3.9}$$

$$T_e = T_e(\mathrm{MFPA})^{+\left|(1+\Delta_{T_e}^{min})\times(1.10)-1\right|}_{-\left|(1+\Delta_{T_e}^{max})\times(0.9)-1\right|} = \mathrm{T_e(MFPA)}^{+8.9\%}_{-23.5\%} \tag{3.10}$$

3.2.3 LP benchmark on noble gases

The Langmuir probe diagnostics has been first used on noble gases to validate the procedure on plasmas much more studied than iodine ones. These first experimental results are critical to further validate plasma numerical models.

3.2.3.1 Influence of discharge power on the electrons

The goal of this subsection is to retrieve the classical results about the influence of the discharge power on the electrons in an ICP discharge running with a noble gas (xenon, krypton or argon).

In Figure 3.7, the effect of the discharge power on the electron density n_e and the electron temperature T_e is studied along the thruster axis. Measurements were taken in xenon plasmas for three different discharge powers (50, 100 and 200 W) and a constant pressure of 3.5 mTorr. Doubling the discharge power roughly doubles the electron density everywhere in the discharge but has almost no effect on the electron temperature as already shown by Godyak [133] in the center of argon ICP discharge. At this pressure, in xenon, the density profiles are not fully symmetric within the discharge but tend to localize near the antenna. Spatial gradients are clearly observed with a decrease of T_e along the axis.

An increase of the discharge power "Maxwellianize" the EEPF as shown in Figure 3.8a and explained by Godyak in [133]. Measurements were taken in xenon plasmas for a fixed pressure of 2.5 mTorr and two extreme discharge powers: 23 W and 300 W. Physically, a high electron density (produced by a high discharge power) favours electron-electron collisions that will equalize the distribution temperature of low and middle energy electron groups. Increasing the discharge also limits the fall in the inelastic energy range by favouring two-step ionization processes.

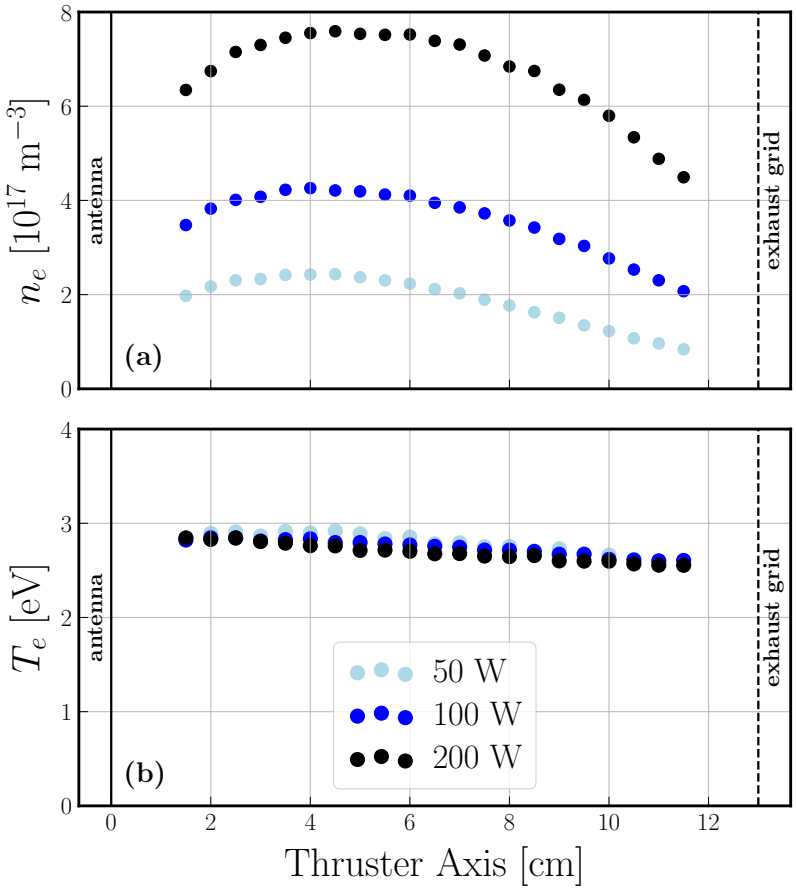

Figure 3.7: Langmuir probe measurements in xenon plasmas for a pressure of 3.5 mTorr and a discharge power of 50, 100 and 200 W. (a) Spatial profiles of the electron density n_e [m^{-3}] along the thrust axis. (b) Spatial profiles of the electron temperature T_e [eV] along the thrust axis.

Finally, the electrons spatial uniformity is addressed in Figure 3.8b. The measurements were taken in an argon discharge for a fixed pressure of 2.5 mTorr and a fixed discharge power of 100 W on three different locations along the thrust axis: $z = 2$ cm near the antenna, $z = 6.5$ cm in the middle of the discharge and $z = 11$ cm near the exhaust grid. The analysis is analog to what Bredin did with the same setup during his Ph.D. thesis [123]. The EEPF are less Maxwellian when the distance from the antenna increases, with a significant depletion observed above the first excitation energies. Whatever the position along the thrust axis, low energy electrons are trapped in the bulk and isothermal (parallel slopes below 10 eV). However, far away from the antenna, high energy electrons escape more easily to the walls inducing a decrease of the effective electron temperature (see Figure 3.7(b)). The fall in the inelastic range seems to be well limited for $z = 2$ cm contrary to what is observed for $z = 11$ cm: the power deposition is clearly non uniform in the discharge.

3.2.3.2 Influence of pressure on the electrons

The goal of this subsection is to retrieve the classical results about the influence of pressure on the electrons in an ICP discharge running with a noble gas (xenon, krypton or argon).

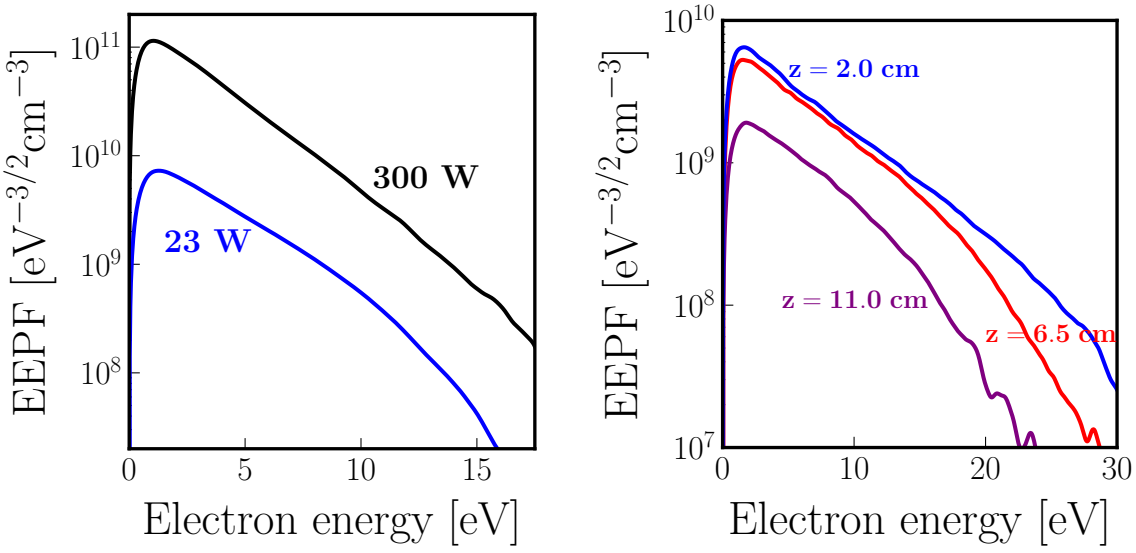

Figure 3.8: (a) Electron Energy Probability Functions (EEPF) taken in xenon plasmas for two discharge powers: 23 and 300W. Measurements were taken at $z = 6.5$ cm for a pressure of 2.5 mTorr. (b) Electron energy probability functions (EEPF) taken in an argon plasma for a pressure of 2.5 mTorr and a discharge power of 100W at three different location along the thruster axis: $z = 2.0$ cm, $z = 6.5$ cm and $z = 11.0$ cm.

In Figure 3.9, spatial profiles of n_e and T_e are plotted for pressures from 0.3 to 3.5 mTorr in xenon plasmas where the discharge power has been fixed to 100 W. At very low-pressure (0.3-0.5 mTorr), electrons are perfectly isothermal and the density profile exhibits a typical and symmetrical dome-like shape. However, when pressure increases, the energy relaxation length [119], that was introduced and discussed in Chapter 1, becomes shorter and the electrons localize near the antenna. Spatial gradients also appear in the electron temperature profiles. Overall, the maximum plasma density increases with increasing pressure but the values near the exhaust grid are close to $5{\times}10^{16}$ m^{-3} whatever the pressure. Classically, the electron temperature falls with an increase of pressure because of an increasing number of collisions that will limit the ion losses at the wall for a given density.

The effect of pressure on the EEPF is studied in Figure 3.10. Argon EEPFs were taken in the middle of the discharge ($z = 6.5$ cm) for pressures from 0.7 to 13 mTorr and a discharge power of 100 W. At the lowest pressure (0.7 mTorr), the EEPF exhibits a peak at low energy (below 5 eV), already observed by Godyak, and typical of ICP discharges at low gas pressure [131, 133]: the EEPF has a three temperatures profile. When pressure is increased, the peak disappears and the high energy tail is more and more depleted: profiles tend to Maxwellianize as already observed [131, 133]. The Druveystein profile often observed when pressure or power is increased is not always physical but may rather be due to a too large probe circuit resistance whose effect increases with plasma density [133].

Finally, a comparison between noble gases electron properties is presented in Figure 3.11. The electron densities and the electron temperatures measured in xenon, krypton and argon plasmas for a discharge power of 100 W are plotted

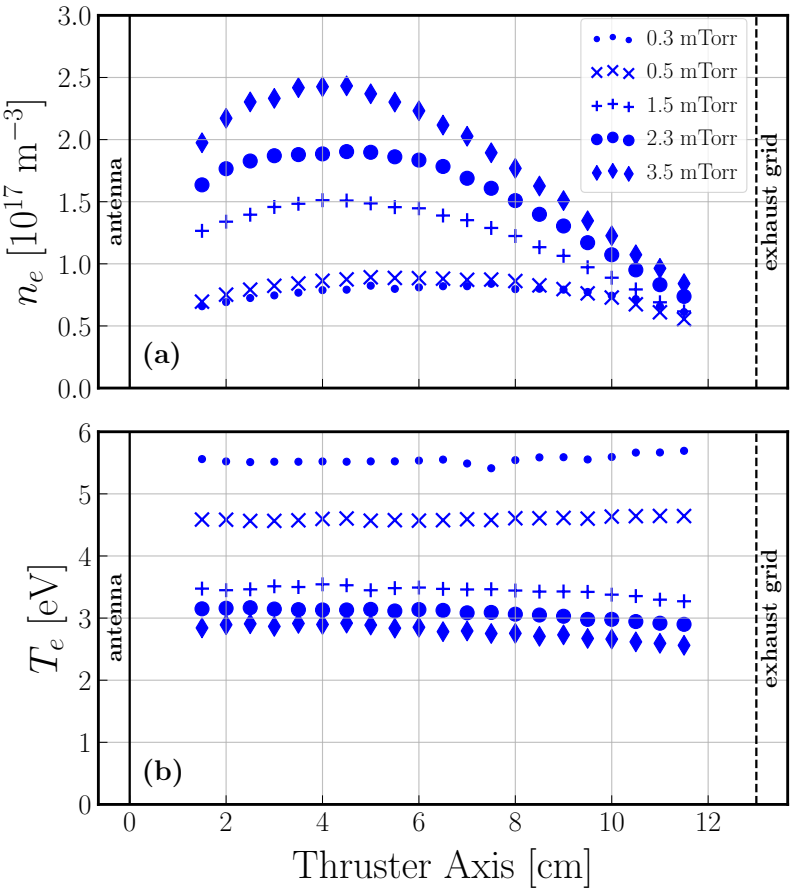

Figure 3.9: Langmuir probe measurements in xenon plasmas for a discharge power of 50 W and pressures from 0.3 to 3.5 mTorr. (a) Spatial profiles of the electron density n_e [m^{-3}] along the thrust axis. (b) Spatial profiles of the electron temperature T_e [eV] along the thrust axis.

against the neutral pressure. Measurements were taken in the center of the discharge ($z = 6.5$ cm). No correction has been applied to the plotted values but non-symmetric error bars have been included using equations (3.7) and (3.8) to take all errors into account (see subsection 3.2.2 for more details).

Previous results are retrieved: the electron density tends to increase with the pressure while the electron temperature decreases. Moreover, the bigger the atom the lower is the electron temperature which is expected since the ionization energies of noble gases satisfy :

$$\mathcal{E}_{\text{iz, Xe}} = 12.1 \text{ eV} < \mathcal{E}_{\text{iz, Kr}} = 14.0 \text{ eV} < \mathcal{E}_{\text{iz, Ar}} = 15.76 \text{ eV},$$

where the numerical values are taken from the NIST website [34]. The former ranking on the ionization energies also explains why xenon allows to achieve higher plasma densities than the two other noble gases for the same pressure.

3.2.3.3 Derivation of classical plasma physics parameters

Some classical plasma physics parameters can be inferred from the previous electron density and temperature measurements. Let's introduce some of them

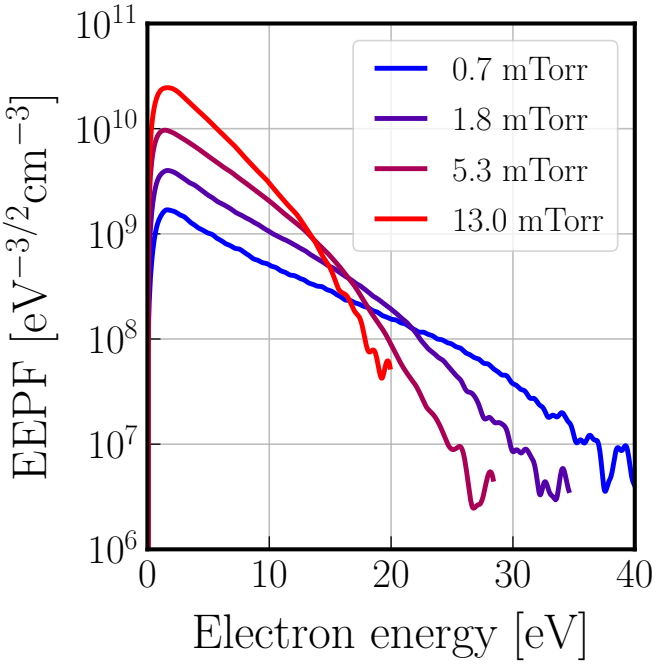

Figure 3.10: Electron energy probability functions (EEPF) taken in argon plasmas for a discharge power of 100W and a pressure from 0.7 mTorr to 13 mTorr. Measurements were taken at $z = 6.5$ cm.

before studying their values and variations in the discharge.

The **electron thermal speed** $\overline{v}_e$ is the typical velocity of the thermal motion of electrons in a plasma. It reads:

$$\overline{v}_e = \sqrt{\frac{k_B T_e}{m_e}}. \tag{3.11}$$

If the electrons in a plasma are displaced from a uniform background of ions, electric fields will be built up in such a direction as to restore the neutrality of the plasma by pulling the electrons back to their original positions. Because of their inertia, the electrons will overshoot and oscillate around their equilibrium positions with a characteristic frequency known as the **plasma frequency** (or **electron plasma frequency**) ω_{pe} [129]. This oscillation is so fast that the massive ions do not have time to respond to the oscillating field and may be considered as fixed. The plasma frequency reads:

$$\omega_{pe} = \sqrt{\frac{n_e e^2}{\varepsilon_0 m_e}}. \tag{3.12}$$

The **Debye length** λ_{De} is a characteristic distance over which ions and electrons can be separated in a plasma [129] or over which the electrostatic fields are shown to be screened [119]. It is a measure of how far into the plasma the potential of an electrode or probe is observed and is equal to the ratio of the electron thermal

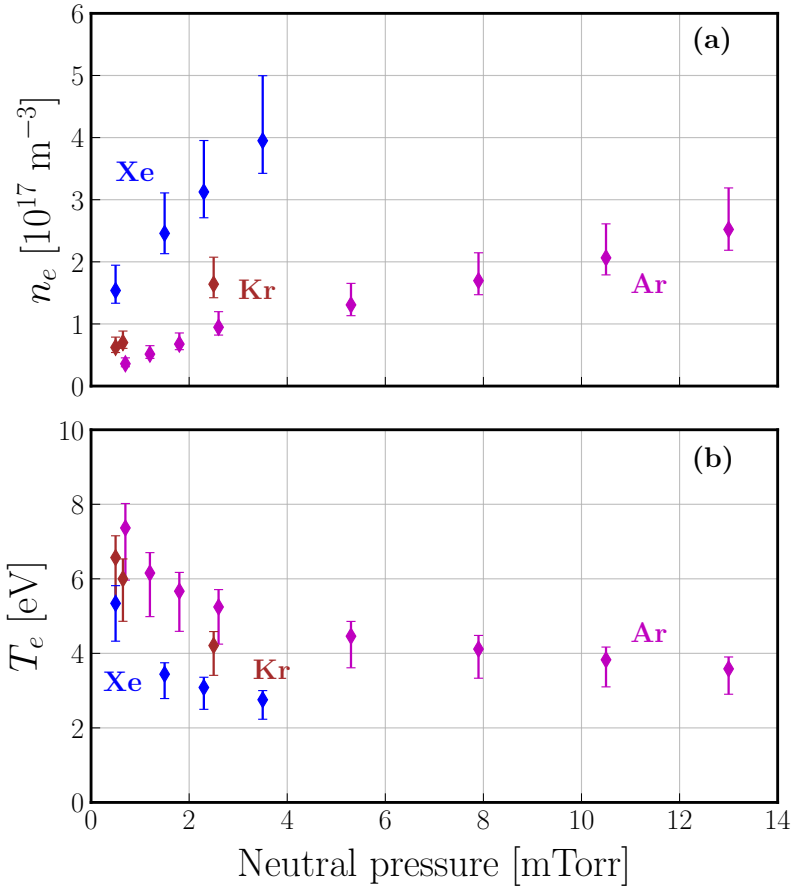

Figure 3.11: Langmuir probe measurements in xenon (Xe), krypton (Kr) and argon (Ar) plasmas for a fixed discharge power of 100 W. Measurements were taken in the center of the discharge for $z = 6.5$ cm. The effect of pressure is studied on the available range for each gas. The plotted values (diamonds) are directly taken from the MFPA software and the asymmetric error bars are given by equation (3.7) for n_e and equation (3.8) for T_e. (a) The electron density n_e [m^{-3}] is plotted against the neutral pressure [mTorr]. (b) The electron temperature T_e [eV] is plotted against the neutral pressure [mTorr].

velocity divided by the plasma frequency:

$$\lambda_{\mathrm{De}} = \frac{\overline{v}_e}{\omega_{\mathrm{pe}}} = \sqrt{\frac{\varepsilon_0 k_{\mathrm{B}} T_e}{n_e e^2}}, \tag{3.13}$$

where ε_0 is the permittivity of free space.

The **electron inertial length** (or **skin depth**) δ_e is a characteristic distance over which evanescent electromagnetic waves in a non magnetized plasma diminish [119]. It is equal to the ratio of the speed of light divided by the plasma frequency:

$$\delta_e = \frac{c}{\omega_{\mathrm{pe}}} = \sqrt{\frac{m_e}{\mu_0 n_e e^2}}, \tag{3.14}$$

where μ_0 is the vacuum permeability.

From the previous definitions, one infers:

$$\frac{\delta_e}{\lambda_{\mathrm{De}}} = \frac{c}{\overline{v}_e} \gg 1, \tag{3.15}$$

meaning that electromagnetic waves have a much larger range of effect that electrostatic fields in plasmas.

Then, with noble gases plasmas, only one positive ion species is dominant and quasineutrality ensures $n_e = n_{\mathrm{X}^+}$, with X in {Xe, Kr, Ar}. Thus, previous Langmuir probe measurements give access to two additional plasma parameters.

The **ion plasma frequency** $\omega_{\mathrm{pi,X}}$ (depending on the atomic species X) is the typical frequency other which ions respond to an oscillating electric field:

$$\omega_{\mathrm{pi,X}} = \sqrt{\frac{n_{\mathrm{X}^+} e^2}{\varepsilon_0 m_X}}. \tag{3.16}$$

Note that the X^+ ion plasma frequency is $(m_X/m_e)^{1/2}$ times lower than the electron plasma frequency.

The **Bohm speed** $u_{\mathrm{B,X}}$ (depending on the atomic species X) is derived from the Bohm sheath criterion [129]. It says that for the sheath to form, ions must acquire a velocity greater than the acoustic velocity or sound speed:

$$u_{\mathrm{B,X}} = \sqrt{\frac{k_{\mathrm{B}} T_e}{m_{\mathrm{X}}}}. \tag{3.17}$$

Note that the Bohm speed for X^+ ions is $(m_X/m_e)^{1/2}$ times lower than the electron thermal speed.

The former defined plasma parameters are plotted against neutral pressure in Figure 3.12 for xenon, krypton and argon plasmas. The parameters are derived from n_e and T_e measurements presented in Figure 3.11. In Figure 3.13, spatial profiles of λ_{De}, ω_{pe}, u_{B} and $\overline{v}_e$ are plotted along the thruster axis. Results are derived from xenon measurements presented in Figure 3.9.

Within our experimental device, the Debye length λ_{De} is always between 20 μm and 100 μm, decreasing with pressure, the mass of the atom and is minimum where the electron density is maximum. Such short values explain why it is mandatory to build Langmuir probe as small as possible (with wire radius below 100 μm and probe holder radius as small as possible) in order to perform accurate measurements.

The skin depth δ_e is always between 0.5 cm and 3 cm, decreasing with pressure and the atom mass. It has been computed using the density value in the middle of the discharge (z = 6.5 cm), although the skin depth is probably governed by the electron density value near the antenna.

Bohm and thermal speed values are typical of ICP discharge with respectively magnitude around 3000 m.s^{-1} and 10^6 m.s^{-1}. These values decrease with pressure

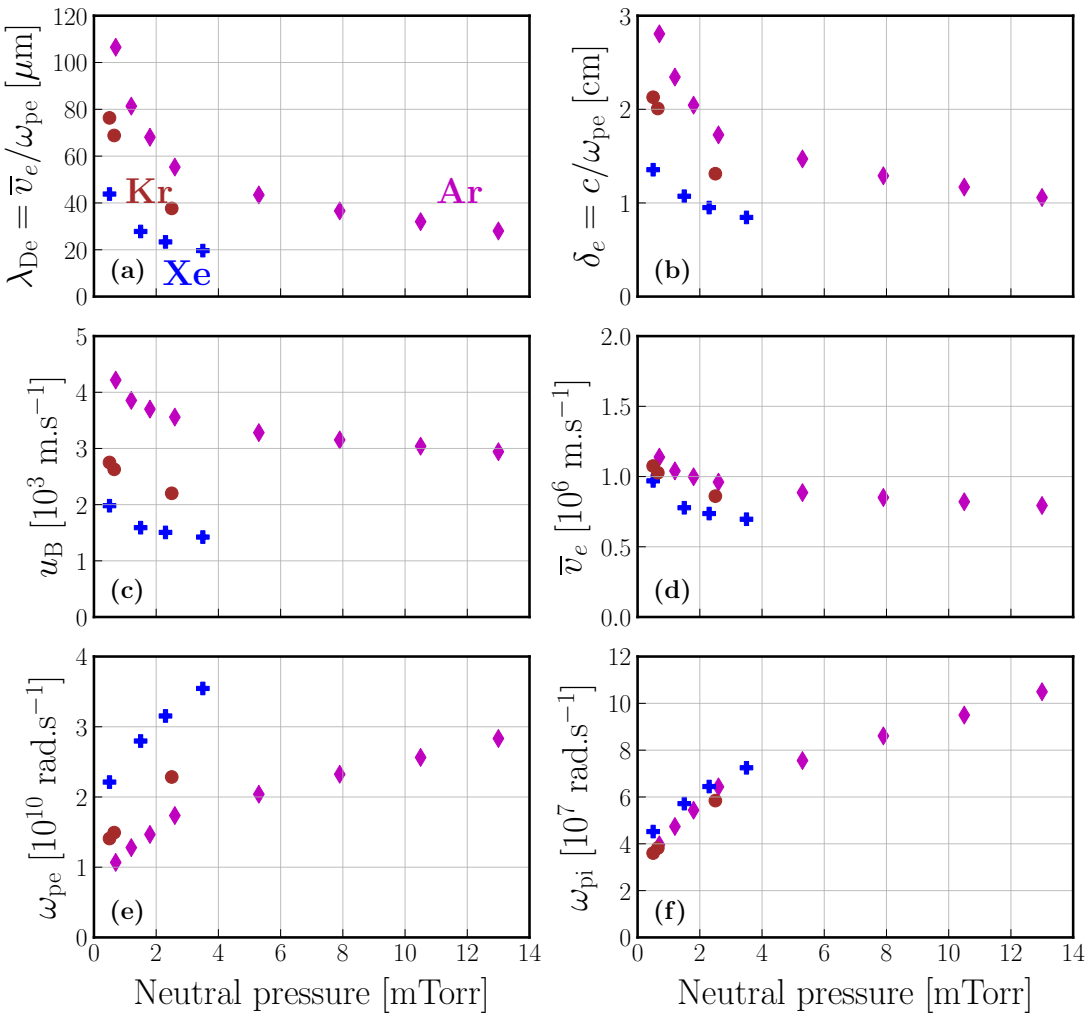

Figure 3.12: Influence of pressure on some plasma physics parameters deduced from Langmuir probe measurements in argon, krypton and xenon plasmas for a fixed discharge power of 100 W. Measurements were taken in the center of the discharge (z = 6.5 cm). (a) Debye length λ_{De} [μm]. (b) Electron inertial length δ_e [cm]. (c) Bohm speed u_B [m.s^{-1}]. (d) Electron thermal speed $\overline{v}_e$ [m.s^{-1}]. (e) Electron plasma frequency ω_{pe} [rad.s^{-1}]. (f) Ion plasma frequency ω_{pi} [rad.s^{-1}].

(decreasing electron temperature), spatially constant (because T_e is fairly constant) and higher for a small atom.

Finally, the values for the ion and electron plasma frequency show that we are operating in the intermediate-frequency domain [119]:

$$\omega_{RF} \lesssim \omega_{pi} \ll \omega_{pe}, \tag{3.18}$$

with $\omega_{RF} \approx 2.5 \times 10^7$ rad.s^{-1}.

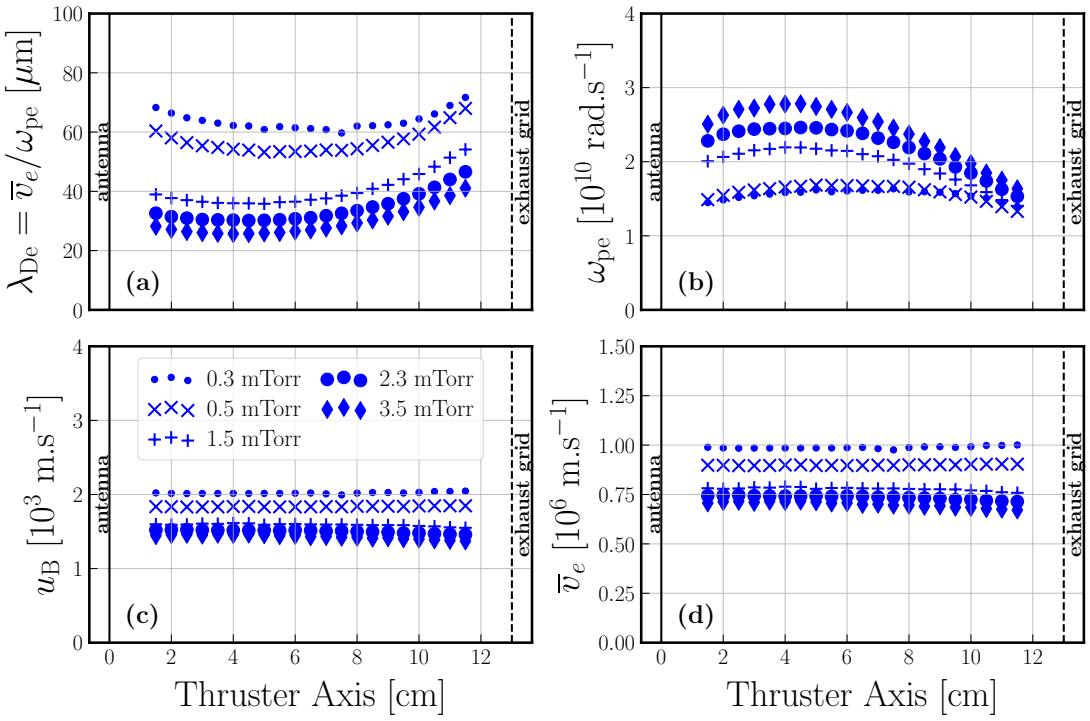

Figure 3.13: Spatial profiles of some plasma physics parameters deduced from Langmuir probe measurements in xenon plasmas for a fixed discharge power of 50 W. Measurements were taken along the thrust axis for pressures from 0.3 to 3.5 mTorr. (a) Debye length λ_{De} [μm]. (b) Electron plasma frequency ω_{pe} [rad.s^{-1}]. (c) Bohm speed u_B [m.s^{-1}]. (d) Electron thermal speed $\overline{v}_e$ [m.s^{-1}].

3.3 Laser-induced detachment

In this section, the laser-induced detachment technique, first proposed by Bacal [134], is presented in details. It allows to measure the electronegativity which is the ratio of the negative ion density over the electron density. Some limitations of the procedure in our experimental setup are also discussed.

3.3.1 Principle and experimental setup

In our experimental conditions, I^- is likely to be the dominant negative ion. It is produced by dissociative attachement (DEA) on molecules:

$$I_2 + e^- \longrightarrow I^- + I\,. \tag{3.19}$$

Note that previous works in much higher pressure iodine discharges [26, 121, 135] also detected I_3^- and I_2^- negative ions. The measurement of the electronegativity α, defined as the ratio of the negative ion density n_{I^-} over the electron density n_e, is carried out using the laser-induced detachment technique, developed in hydrogen plasmas by Bacal in the late 1970's [134]. The technique is adapted here for iodine plasmas. The experimental setup and typical signals are shown in Figures 3.14-3.15.

A Nd-YAG ns-laser from Quanta-Ray is tripled to obtain a laser beam at 355 nm able to photo-detach the electrons from I^- (photon energy: $h\nu = 3.49$ eV $> \varepsilon_A = 3.0590463$ eV, the electron affinity [78]), according to the following process:

$$I^- + h\nu \longrightarrow I + e^-. \tag{3.20}$$

The optical setup used is presented in Figure 3.14b. Four mirrors from Opto4U with a R_{max} at 45° for wavelengths between 351 and 355 nm were used, and eliminated residual light at 532 and 1064 nm. The laser energy was modified using a 25.4 mm diameter half-wave plate at 355 nm from Optoprim and a polarizer cube from Lambda Research Optics (HPB-25-4U-355): in this way, the beam shape was not modified when the energy was changed, which could occur if the pump prisms had been handled to modify the laser energy. The laser energy was measured after passing through the plasma chamber.

The newly created electrons are captured by using a 200 μm diameter and 3 mm-long tungsten probe (see Figure 3.14a) which is biased above the plasma potential and located at the center of the laser beam. The probe is inserted inside the plasma and can move from $z = 1$ cm to $z = 11$ cm, along with the laser beam (by using a movable mirror; see Figure 3.14b). However, due to limited optical access through the lateral windows, the spatial scan was only done from $z = 1$ cm to $z = 9.7$ cm.

By using the electrical circuit shown in Figure 3.15a, the time-varying current collected by the probe (triggered on the laser pulse) was separated from the DC current to the probe. The typical time-varying signal is shown in Figure 3.15b. After the laser pulse, a current pulse (due to photo-detached electrons) is collected on the probe and lasts a few micro-seconds before the relaxation to equilibrium. Bacal [134, 136] showed that the electronegativity is equal to the ratio of this current pulse over the DC current. Given our electrical circuit, we have:

$$\alpha = \frac{\Delta j_{e_{AC}}}{j_{e_{DC}}} = \frac{47}{(47\times 50)/(47+50)}\frac{\Delta V_{e_{AC}}}{V_{e_{DC}}} = 1.94\,\frac{\Delta V_{e_{AC}}}{V_{e_{DC}}}, \tag{3.21}$$

where the voltages are measured on an oscilloscope.

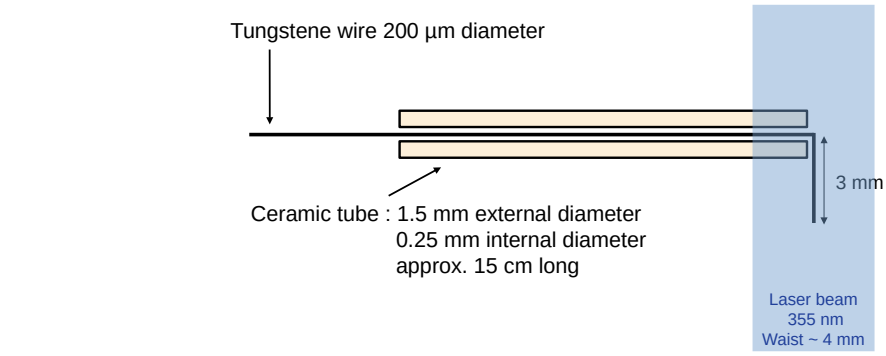

(a)

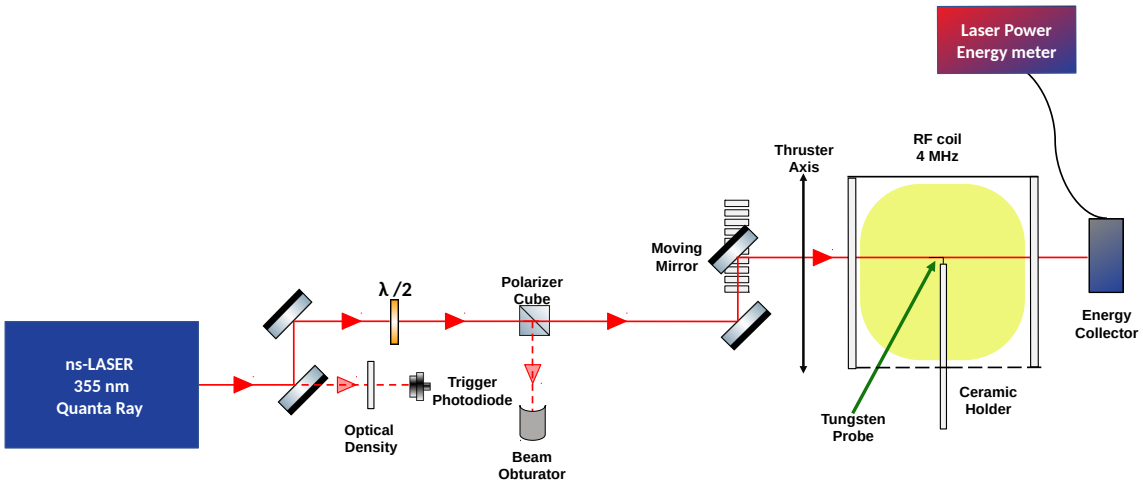

(b)

Figure 3.14: (a) Photodetachment probe design and characteristics. The laser beam is represented in blue. (b) Optical setup for the laser photodetachment with the laser beam in red.

3.3.2 Saturation analyses

The photodetachment signal must saturate with both the laser beam energy and the potential applied to the probe. The theoretical photodetachment fraction is a function of the photodetachment cross section σ and the laser energy E_{Laser}, according to

$$\alpha = \alpha_0 \left(1 - \exp\left(-\frac{\sigma}{S}\frac{E_{\text{Laser}}}{h\nu}\right)\right), \tag{3.22}$$

where α_0 is the electronegativity of the probed area (reached at saturation), and S the laser beam surface [134, 136]. In our experiments, $S \approx 0.25$ cm^2 (circular laser beam with a diameter of about 5.6 mm). Saturation with respect to the laser energy is shown in Figure 3.16a for a fixed position ($z = 9$ cm) at 0.75 mTorr and 100 W, and the probe biased at +40 V. The experimental data are fitted using equation 3.22, α_0 and σ being the fitting parameters. A photodetachment cross section of 2×10^{-17} cm^2 is retrieved, in agreement with the measured value for I^- at 3.49 eV [137], which confirms our assumption on the dominant negative ion. However, note that although the laser wavelength used here was larger than the threshold for I_3^- (4.226

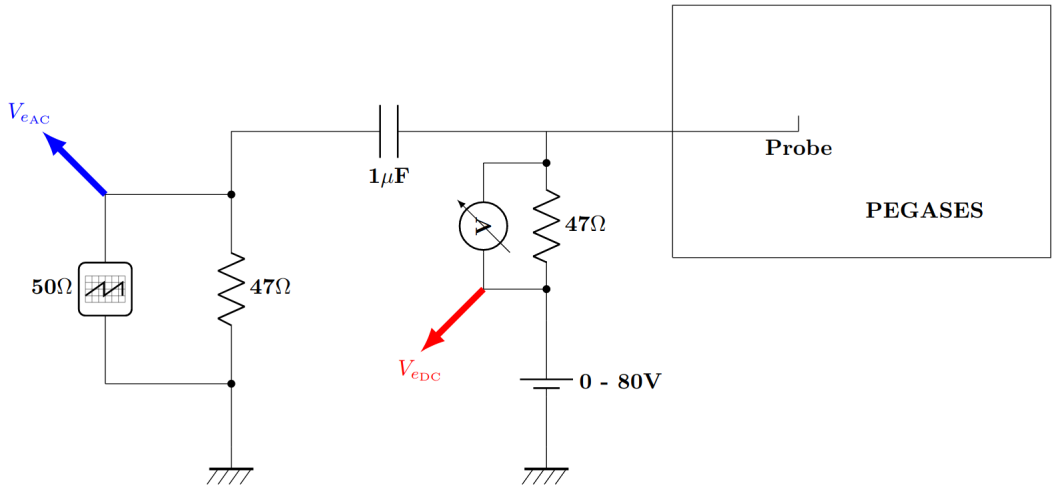

(a)

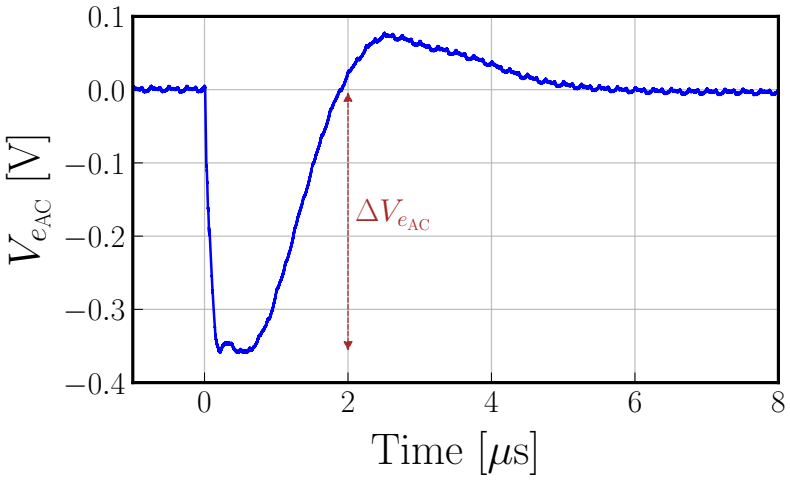

(b)

Figure 3.15: (a) Electrical circuit used to separately collect the alternative and the direct current from the photodetachement probe. (b) Typical alternative photodetachment signal obtained for a pressure of 1.5 mTorr and a discharge power of 100 W at $z = 3$ cm from the antenna. In this situation, $\Delta V_{e_{AC}} = 0.36$ V and $V_{e_{DC}} = 5.22$ V: the resulting electronegativity is close to 0.134.

eV threshold [138]), it was short enough to photodetach electrons from I_2^- (2.524 eV threshold [79]). Consequently, even if we are confident that I^- is the dominant negative ion, we could not formally exclude the presence of I_3^- which would not be detected by our diagnostic.

The voltage applied to the probe has to be high enough to collect all the photodetached electrons. A saturation analysis with respect to the probe bias is presented in Figure 3.16b. Data were acquired at $z = 5$ cm for a pressure of 0.65 mTorr and a discharge power of 50 W. In this case, 35 V was enough to collect more than 95% of the detached electrons. This voltage is significantly above the plasma potential and the probe could therefore perturb the plasma. It was checked, by using a floating probe located only a few millimeters away from the measuring probe, that the floating potential was never significantly affected by this large bias.

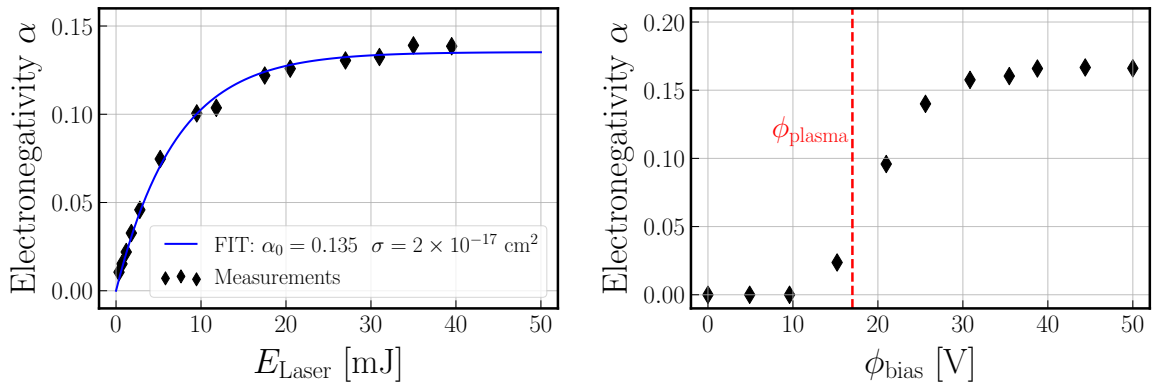

(a) (b)

Figure 3.16: (a) Saturation analysis with the laser energy for a fixed bias voltage of 40 V. Experimental data were taken at $z = 9$ cm for a pressure of 0.75 mTorr and a discharge power of 100 W. The saturated electronegativity α_0 and the photodetachement cross section σ are inferred by fitting with equation (3.22). (b) Saturation analysis with the bias voltage of the probe for a fixed laser energy of 40 mJ. Experimental data were taken at $z = 5$ cm for a pressure of 0.65 mTorr and a discharge power of 50 W. The plasma potential ϕ_{plasma} is indicated in red and measured using the Langmuir probe.

The saturation analyses were done at each operating conditions that are reported here. While a laser energy of 40 mJ was enough in all conditions, the bias voltage had to be adjusted when pressure was increased because of the change in plasma potential and the strong spatial gradients. For instance at $p_{\text{neutrals}} \geq 10$ mTorr, where strong spatial gradients of the electron density were evidenced (see Figure 3.26) and the electron density was greater than 10^{18} m^{-3} near the antenna, the bias voltage had to be increased up to 55 V in order to reach saturation (see Figure 3.17 where the influence of the probe location and the pressure on the bias voltage is studied).

Finally, photodetachment measurements were repeated several times over several days and the observed variations in the electronegativity never exceeded ±10%.

3.3.3 Accuracy and limitations of the technique

In order to verify: (i) the absence of perturbation induced by the biased PD probe and (ii) the correctness of the PD measurements, we performed some electrical checks.

Fisrt, it is possible to retrieve classical current-voltage characteristics using the electrical circuit described in Figure 3.15a. Indeed, one can plot the direct current extracted from the PD probe $j_{e_{\text{DC}}}$ as a function of the bias voltage ϕ_{bias}. Such a curve, taken from a 0.75 mTorr - 100 W iodine plasma at the location $z = 9$ cm, is plotted in Figure 3.18. The classical Langmuir theory (see [129] for more details) is applicable to estimate n_e and T_e. We found: $n_e = 3\,(\pm 1.5) \times 10^{17}$ m^{-3} and $T_e = 2.7\,(\pm 0.5)$ eV. The measured MFPA values, for the same conditions, were: $n_e = 1.63\,(\pm 0.25) \times 10^{17}$ m^{-3} and $T_e = 3.38\,(\pm 0.34)$ eV which validates the method.

Then, instead of using the PD probe described in Figure 3.14a, we inserted the Langmuir probe described in Figure 3.1a, biased the reference probe (RP) using the

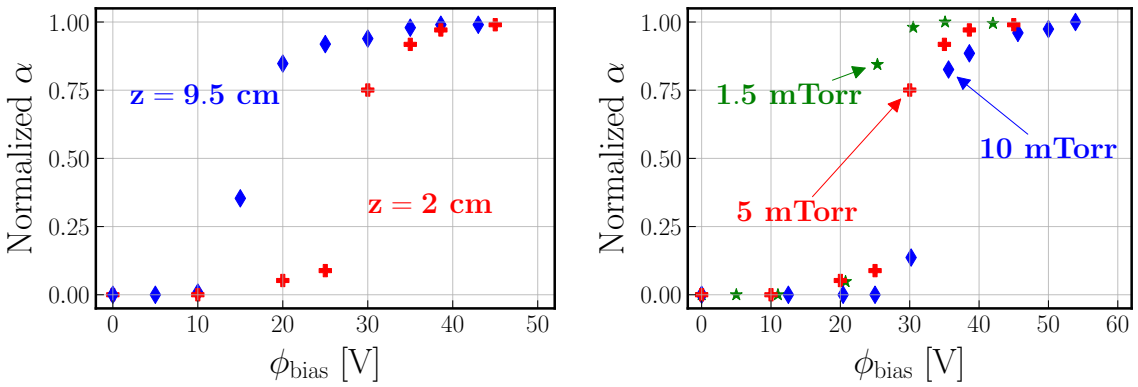

Figure 3.17: Normalized electronegativity as a function of the bias voltage ϕ_{bias} [V]. (a) Measurements were taken in an iodine plasma for a pressure of 5 mTorr and a discharge power of 200 W at two different locations: $z = 2$ cm near the antenna where the electron density is maximum and $z = 9.5$ cm near the exhaust grid. (b) Measurements were taken in an iodine plasma at a fixed location $z = 2$ cm and fixed discharge power of 200 W for three different pressures: 1.5, 5 and 10 mTorr.

PD electrical circuit (see Figure 3.15a) and used the very close measuring probe (RP) to measure the floating potential ϕ_f using a voltmeter. If the floating potential measurements was influenced by the bias voltage, it would prove the PD technique incorrect.The former procedure was performed in argon and iodine plasmas both within the dielectric prototype and the fully conductor one. Results obtained in an iodine plasma for a pressure of 15 mTorr and a discharge power of 160 W are presented in Figure 3.19. In each case, the bias voltage has taken the following values: 0 V, 10 V, 20 V, 30 V and 40 V. With the conductor walls, the floating potential was very little influenced by the bias voltage. The discrepancies in the ϕ_f measurements between a non-biased probe and a probe biased to +40 V never exceeded 3 V. However, with the dielectric walls, the conclusions are different. The floating potential was strongly modified by the bias voltage and it is the reason why we performed the photodetachment measurements only inside the thruster with conductor walls. Physically, once again, the return current hardly flows and the plasma potential increases everywhere and mostly where the plasma resistance is the largest. The saturation occurs exactly at the same location as already observed while measuring the electron density in Figure 3.3. It is also worth noticing that the floating potential measurements are the same when $\phi_{bias} = 0$ V, whatever the walls nature (identical blue markers in subfigures (a) and (b)).

Independently from the previous measurements, it is possible to use the MFPA software (see subsection 3.2.1) to measure the difference between the plasma potential and the floating potential: $\phi_{plasma} - \phi_f$. Finally, spatial profiles of the plasma potential can be reconstructed by summing the two independent voltage measurements: $\phi_{plasma} = \phi_f + (\phi_{plasma} - \phi_f)$. Such plasma potential profiles are shown in Figure 3.20. They were obtained in a 15 mTorr - 160 W iodine plasma both with dielectric and conductor walls. The bias voltage was set to 40 V. With the dielectric walls, the plasma potential is strictly equal to the bias voltage for $z \leq 6$ cm meaning that it is impossible to collect the newly created electrons after the laser

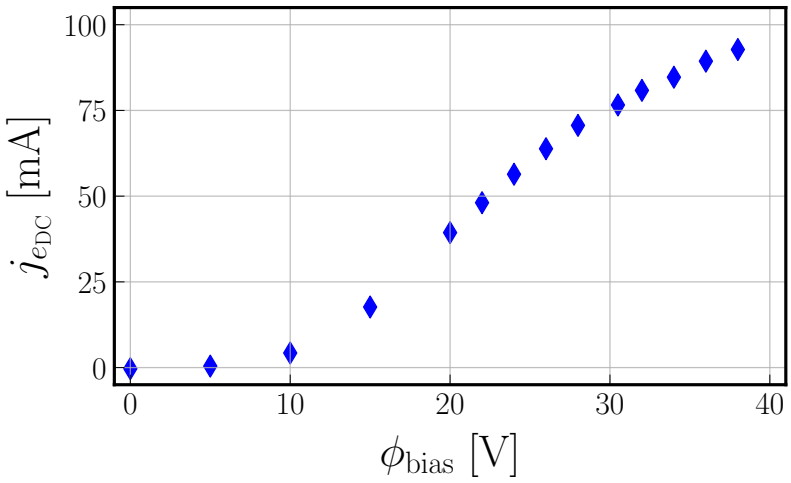

Figure 3.18: Current - voltage characteristics (I-V curve) obtained, using the photodetachment electrical circuit (see Figure 3.15a), by collecting the DC current while increasing the bias voltage of the probe. Measurements were performed in an iodine plasma, at the location $z = 9$ cm, for a pressure of 0.75 mTorr and a discharge power of 100 W.

shoot. In this case, because the ionic return current is limited, the plasma potential has to follow the bias voltage and the photodetachment technique cannot be applied: it is impossible to bias the probe above the plasma potential. Nevertheless, with the conductor walls, the plasma potential stays well below the bias voltage and the photodetachment diagnostics is applicable. Note, however, that when one experiments for a long time in iodine, the walls are polluted and their conductive properties deteriorate. In such conditions, the electrostatic diagnostics might give erroneous results even if the walls were perfectly conductor at the beginning of the experiments.

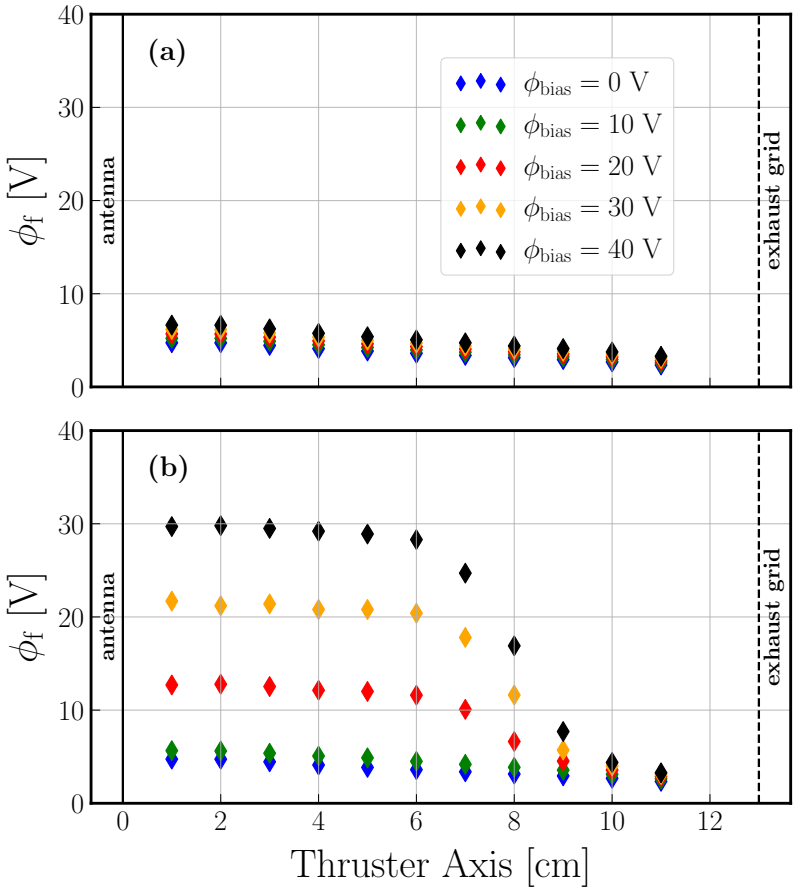

Figure 3.19: Spatial profiles of the floating potential ϕ_f for various bias voltage in an iodine plasma. The pressure is fixed at 15 mTorr and the discharge power at 160 W. (a) Conductor walls. (b) Dielectric walls.

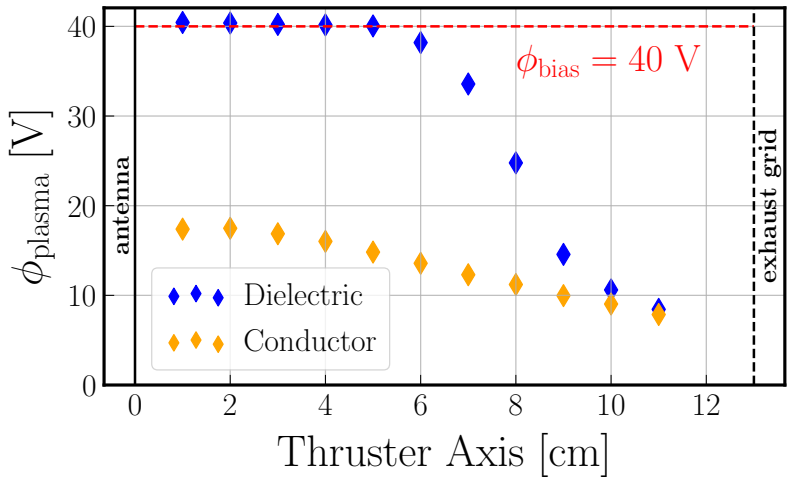

Figure 3.20: Reconstructed plasma potential spatial profiles along the thrust axis in a 15 mTorr - 160 W iodine plasma both for conductor and dielectric walls. The bias voltage is set to 40 V.

3.4 Iodine versus noble gases for electric propulsion applications

In this section, iodine and noble gases plasma properties are compared in typical operating conditions of electric propulsion (pressure below 3 mTorr and discharge power of 100 W). Figure 3.21 shows the spatial variations of electron density and electron temperature in iodine, xenon and krypton plasmas at 0.5 mTorr and a discharge power of 100 W. For the three gases, the well-known features of very low-pressure ICP discharges are retrieved: electrons are isothermal because of highly non-local electron kinetics and the electron density profiles have a quite flat dome-like shape [58]. It has also been found that doubling the discharge power roughly doubles the electron density, and only weakly affects the electron temperature.

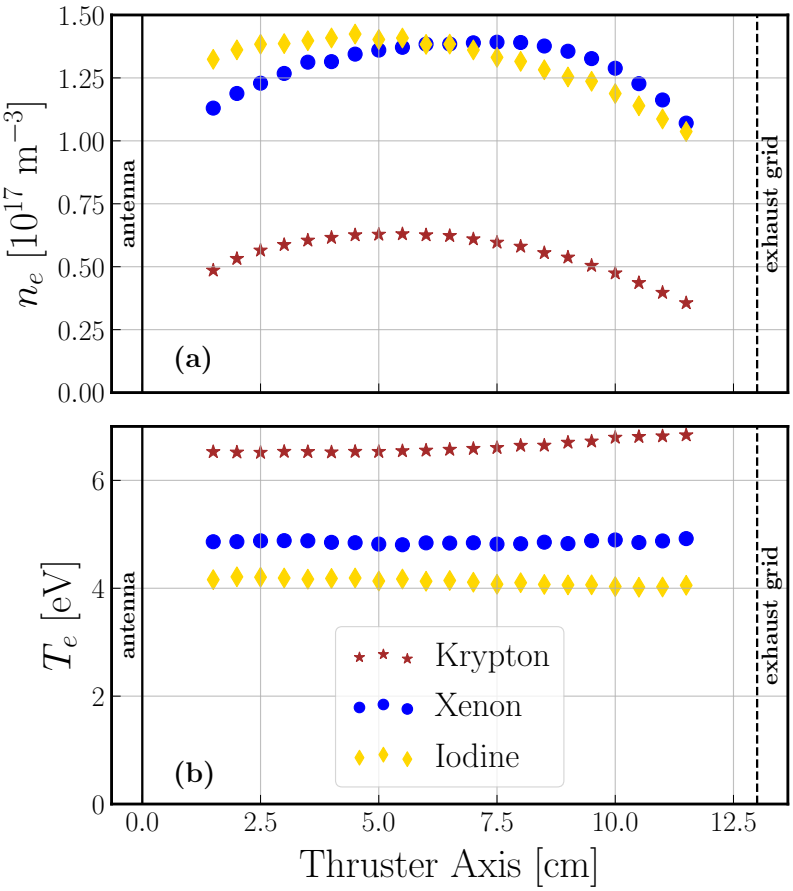

Figure 3.21: Langmuir probe measurements in iodine, xenon and krypton plasmas for a pressure of 0.5 mTorr and a discharge power of 100 W. (a) Spatial profiles of the electron density n_e [m^{-3}] along the thrust axis. (b) Spatial profiles of the electron temperature T_e [eV] along the thrust axis.

As it can be seen, the electron density in iodine and xenon are very close with a maximum around 1.5×10^{17} m^{-3}. We note, however, that the density maxima are not located at the same position, with a slight localisation near the antenna in iodine (that will be observed more clearly at higher pressures). This observation suggests that the energy relaxation length [119], is shorter in iodine, which could be explained by the additional energy loss channels in a molecular plasma. The

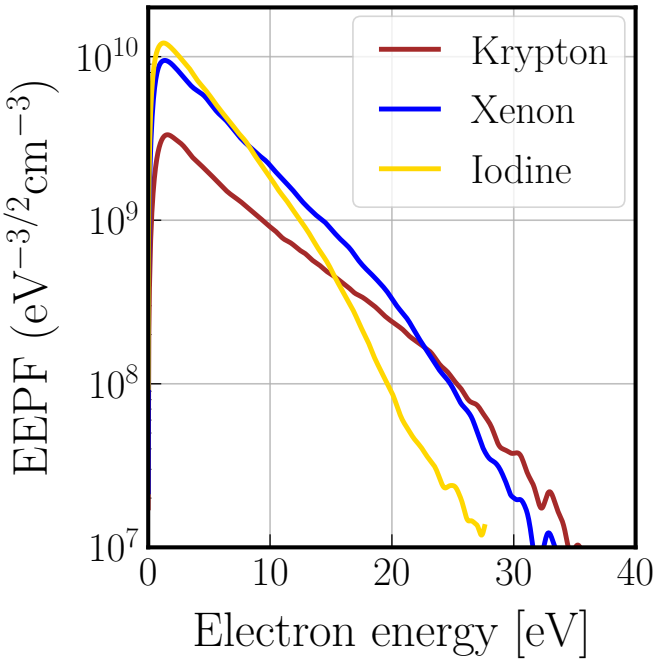

Figure 3.22: Measured EEPF at z = 6.5 cm during Langmuir probe measurements in iodine, xenon and krypton plasmas for a pressure of 0.5 mTorr and a discharge power of 100 W.

electron temperature is lower in iodine than in xenon which is expected since the ionization energy of atomic and diatomic iodine ($\varepsilon_{iz,I}$ = 10.45 eV, ε_{iz,I_2} = 9.31 eV) are lower than that for xenon ($\varepsilon_{iz,Xe}$ = 12.1 eV). Krypton electron density values are at least twice lower than in xenon and iodine. This confirms that krypton is not as efficient as xenon and/or iodine to achieve large plasma densities. The higher ionization energy of krypton ($\varepsilon_{iz,Kr}$ = 14.0 eV) explains this lower efficiency, as well as the higher electron temperature of 6.5 eV. The ionization energies are taken from the NIST website [34].

The EEPF recorded at z = 6.5 cm are shown in Figure 3.22. They are mostly Maxwellian at low energies and a significant depletion is seen well above the first excitation energies. As already reported in argon discharges [133], this is because the major electron energy loss mechanism in the low-pressure (free fall) regime comes from fast electrons escaping to the wall. The depletion in iodine arises at lower energy than with noble gases, both because the sheath potential is lower (because T_e is lower), and because the excitation energies are lower. Note that the EEPF in krypton also exhibits a peak at low energy, already observed in argon, and typical in ICP at low gas pressure [131, 133].

To summarize, at low pressure (0.5 mTorr) and sufficiently high discharge power, iodine plasmas appear as efficient as xenon to achieve high density plasmas. In these conditions, the iodine plasma is turquoise (see Figure 2.9b) and is probably highly dissociated ($n_{I_2} \ll n_I$). A significant fraction of molecules would lead to a strong emission in the range 500-600 nm (yellow color, see Figure 1.1a). The dominant species are expected to be I^+, e^- and I. Since negative ions are produced by dissociative attachment, the negative ion density is expected to be low.

We now examine the results shown in Figure 3.23, obtained for the same dis-

charge power of 100 W, but at the higher pressure of 2.5 mTorr. As before, the electron density and the electron temperature are plotted versus the distance from the antenna. The EEPF measured at $z = 6.5$ cm are shown in Figure 3.24. For these plasma conditions, we add argon measurements to extend the comparison to additional alternative propellants.

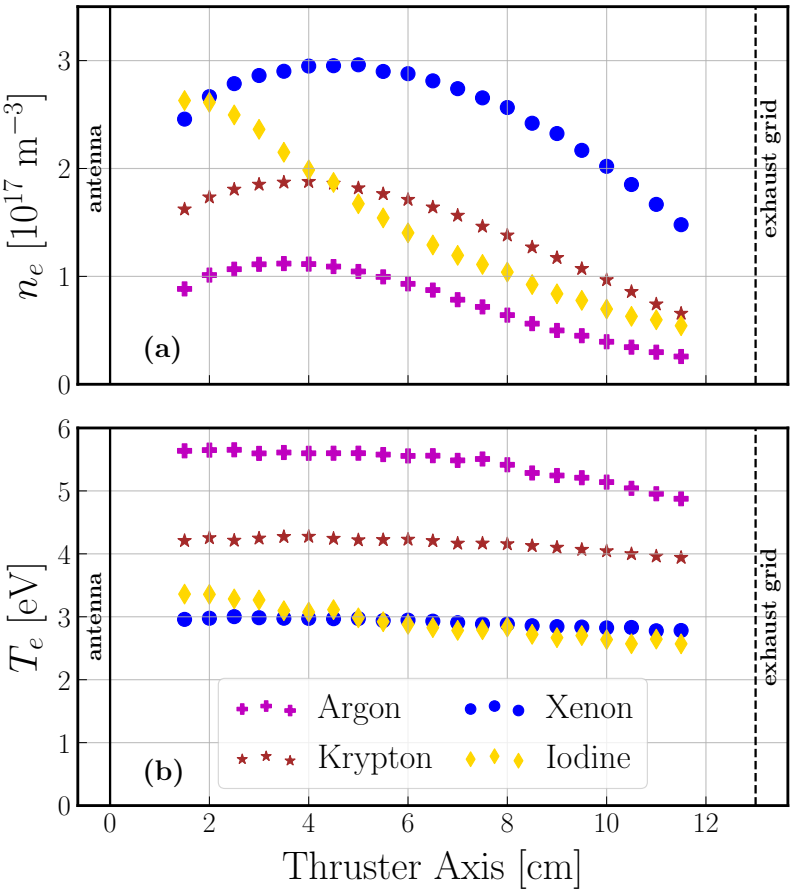

Figure 3.23: Langmuir probe measurements in iodine, xenon, krypton and argon plasmas for a pressure of 2.5 mTorr and a discharge power of 100 W. (a) Spatial profiles of the electron density n_e [m^{-3}] along the thrust axis. (b) Spatial profiles of the electron temperature T_e [eV] along the thrust axis.

Iodine and xenon electron density profiles are now significantly different. Near the antenna, the electron density is about 2.5×10^{17} m^{-3} and the temperature about 3 eV in both gases. However, in the case of iodine, the density is maximal near the antenna and falls off quickly, down to 0.5×10^{17} m^{-3} at $z = 11.5$ cm. On the contrary, the electron density profile in xenon still exhibits a dome-like shape, but with a maximum closer to the antenna at $z = 5$ cm (where $n_e \approx 3 \times 10^{17}$ m^{-3}). The density near the exhaust grid is three times higher than in iodine. The electron temperature is almost constant in xenon, around 3 eV, while in iodine it decays as the distance from the antenna increases. Overall, these results are consistent with the conclusion drawn before; the energy relaxation length must be shorter in iodine, leading to stronger localisation of the discharge where the RF power is deposited, i.e. in the skin depth close to the antenna. The results in krypton and argon are quite similar to that in xenon but with lower electron densities and higher electron

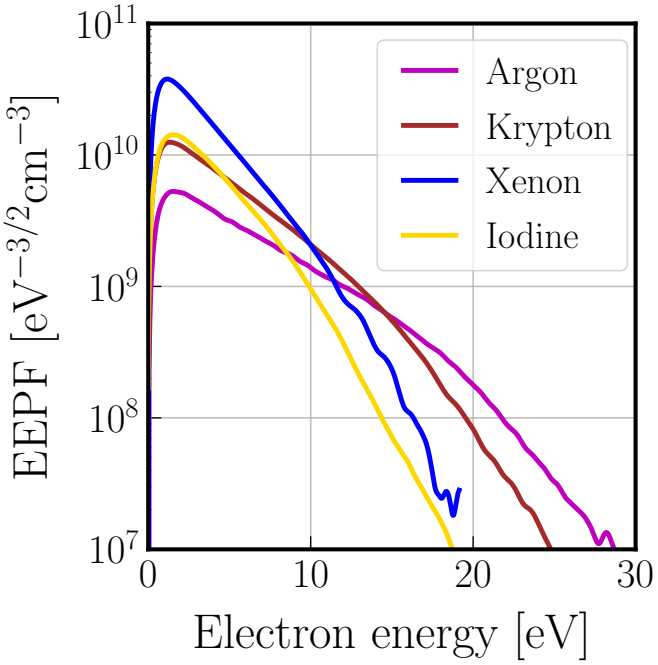

Figure 3.24: Measured EEPF at $z = 6.5$ cm during Langmuir probe measurements in iodine, xenon, krypton and argon plasmas for a pressure of 2.5 mTorr and a discharge power of 100 W.

temperature, in agreement with the higher ionization potential of these noble gases ($\mathcal{E}_{\text{iz, Ar}} = 15.76$ eV [34]). The EEPFs are shown in Figure 3.24. The conclusions drawn at 0.5 mTorr stay true but the low energy peak is less pronounced in krypton.

To summarize this comparison between iodine and noble gases and draw conclusions on the relative efficiency for electric propulsion applications, the electron density measured in the center of the discharge ($z = 6.5$ cm) is plotted as a function of the discharge power in Figure 3.25 for two pressures: 0.6 mTorr and 2.5 mTorr. Efficiency of a plasma thruster may be defined in different ways. A way to evaluate this is to calculate the thrust-to-power ratio, usually defined in the rocket engineer community has the thrust in mN, divided by the power in kW. In a Gridded-Ion-Thruster, the thrust is proportional to the ion flux, and therefore to the plasma density. The power is the sum of the thrust power and the power absorbed to generate the plasma. It becomes then clear that to maximize the thrust-to-power ratio, ones needs to reach the highest plasma density for the smallest power required to generate the plasma. Langmuir probe measurements indeed evaluate the plasma density for a given absorbed power.

In light of the above, one could state the following: (i) at low pressure (and therefore mass flow rates) and for a sufficient input power, iodine appears to be the most efficient propellant, (ii) as soon as the pressure (and/or the mass flow rate) increases, xenon appears more suitable. This could be expected and comes from the electronegative and molecular nature of iodine. (iii) Because of a high ionization energy and a lower mass, argon is not competitive. Krypton is less efficient than xenon, but it could be a good compromise at large mass flow rates since it is less expensive than xenon.

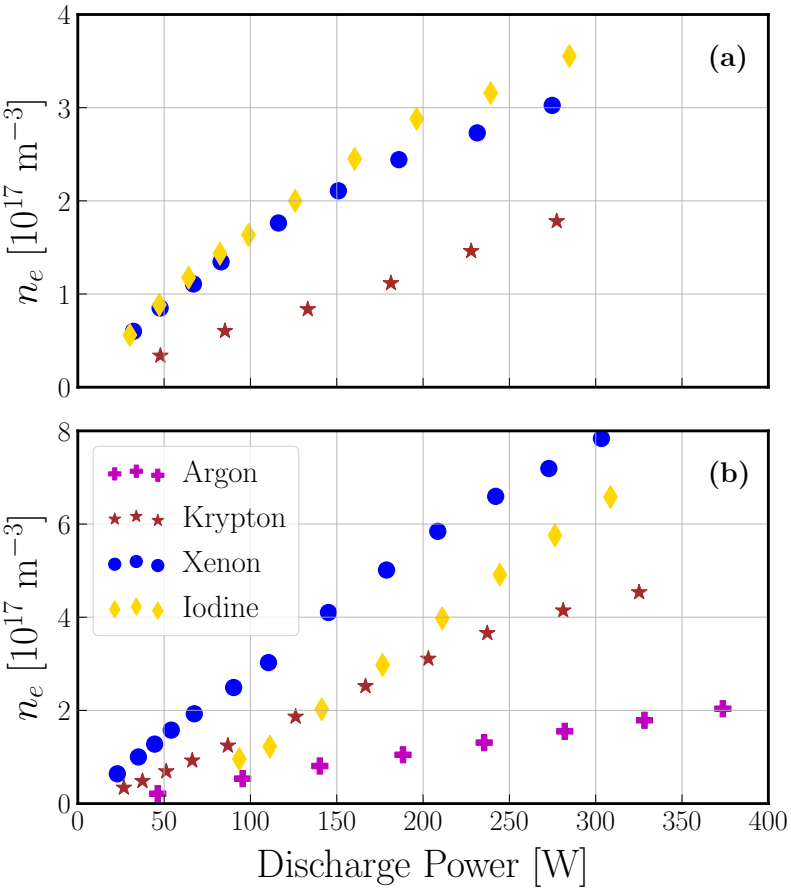

Figure 3.25: Electron density n_e [m^{-3}] versus discharge power [W] in PEGASES thruster operating with iodine, xenon, krypton or argon. Measurements were taken at $z = 6.5$ cm using a Langmuir probe. (a) 0.6 mTorr. (b) 2.5 mTorr.

3.5 Charged particles measurements in iodine plasmas

3.5.1 Electrons characterization

3.5.1.1 Density and temperature measurements

Iodine plasmas have been investigated in a larger parameter space, than what has been presented so far, in order to better capture the transition to higher pressure regimes, and construct a large data base for future comparisons with numerical simulations. Langmuir probe measurements have been performed at fixed discharge power (200 W) and the pressure was varied from 0.5 mTorr to 15 mTorr. Results are shown in Figure 3.26.

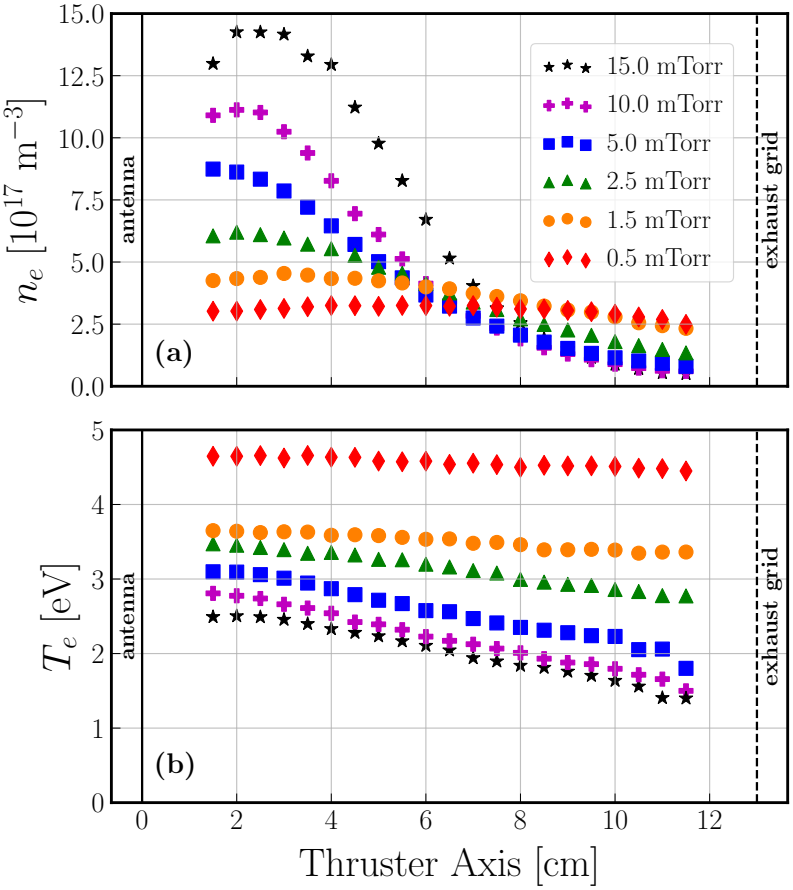

Figure 3.26: Langmuir probe measurements in a purely iodine plasma for a discharge power of 200 W and pressures from 0.5 mTorr to 15 mTorr. (a) Spatial profiles of the electron density n_e [m^{-3}] along the thrust axis. (b) Spatial profiles of the electron temperature T_e [eV] along the thrust axis.

The density peaks near the antenna as the pressure increases. At 15 mTorr, the electron density reaches up to 1.5×10^{18} m^{-3} at $z = 1.5$ cm, and then strongly decreases down to 4×10^{16} m^{-3} at $z = 11.5$ cm. The plasma is almost stratified. In the antenna region, the electron density increases with pressure, while in the extraction region, typically for $z > 6$ cm, the electron density decreases with pressure.

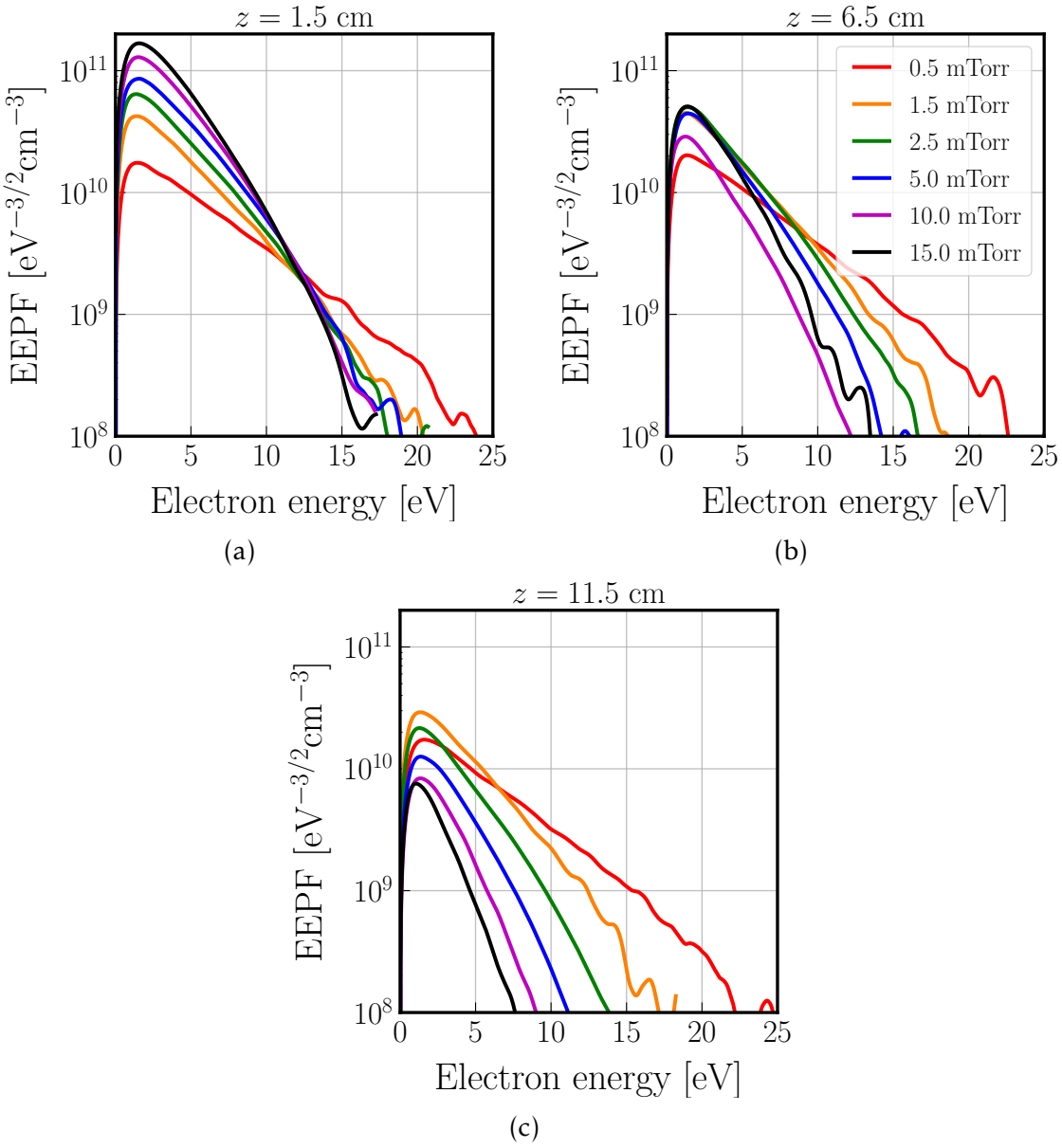

Figure 3.27: Langmuir probe measurements in a purely iodine plasma for a discharge power of 200 W and pressures from 0.5 mTorr to 15 mTorr. Measured EEPFs at: (a) $z = 1.5$ cm, (b) $z = 6.5$ cm, (c) $z = 11.5$ cm.

Increasing the pressure also introduces significant gradients in the electron temperature. At 0.5 mTorr, the temperature drops by only 0.2 eV, with a mean of 4.5 eV. At 15 mTorr, the temperature drop is nearly 1.2 eV for a mean temperature of 2 eV. For completeness, the EEPFs are plotted in Figures 3.27a, 3.27b and 3.27c for three different locations ($z = 1.5$ cm, $z = 6.5$ cm and $z = 11.5$ cm). The electron cooling and density gradients are clearly seen, without drastic change in the distribution shapes.

Finally, it is interesting to underline some key characteristics of the experimental results in iodine for the comparison with models in Chapters 5 and 6. At very low pressure (≤ 1 mTorr), the electron temperature is uniform and the electron density gradients are modest. This regime is particularly adapted for global modeling. For low-intermediate pressures (1 mTorr $\leq p_{\text{plasma}} \leq 3$ mTorr), gradients become non

negligible and global modeling is expected to partially fail. For higher pressures (> 3 mTorr), gradients are too stiff and global modeling will not be appropriate but fluid modeling or PIC simulations will. Results for $p_{\text{plasma}} \geq 3$ mTorr show that the localized power deposition (in the skin depth) produces a stratified plasma. The very high electron density near the antenna suggests that iodine is fully dissociated near the antenna and only partially dissociated in the extraction region.

3.5.1.2 Plasma physics parameters with iodine

The study of plasma physics parameters, defined and presented for noble gases in section 3.2.3.3, is extended to iodine. The Debye length λ_{De}, the plasma frequency ω_{pe} and the electron thermal speed $\overline{v}_e$ are plotted along the thruster axis using the electron density and temperature values presented in Figure 3.26 and obtained in iodine plasmas for a discharge power of 200 W. Because performed for a higher discharge power, the Debye length appears shorter for iodine than what was presented for noble gases. However, the order of magnitude is the same: a few tens of microns. At 15 mTorr, near the antenna, the value is only of 10 μm.

Then, the calculated skin depth is around 1 cm for any pressure between 0.5 and 15 mTorr. Thus, since the power is deposited in a comparable way whatever the pressure, the strong localisation near the antenna with pressure only results from the fact that the relaxation length of the energy becomes shorter as the pressure increases (the length is inversely proportional to the gas density, see equation (1.42) or [119]).

Next, the plasma frequency and electron thermal speed follow respectively the electron density and electron temperature profiles because of their definition (see subsection 3.2.3.3). The values are typical of ICP discharge and appear bigger than with noble gases (higher electron density and electron temperature).

Finally, note that the Bohm speed and the ion plasma frequency have not been plotted because the positive ions composition of our iodine plasmas (both I^+ and I_2^+ are present) is not known at this point.

3.5.2 Negative ions characterization

3.5.2.1 Electronegativity measurements

Electronegativity spatial profiles are shown in Figure 3.29. Measurements were taken for five different pressures from 0.5 to 15 mTorr and a discharge power of 200 W. At 0.5 mTorr, the electronegativity is very low with a maximum of 0.02 at $z = 5.5$ cm. The profile presents a dome-like shape, although it is hardly seen in the log-scale used in Figure 3.29. In these conditions (large power, very low pressure) the plasma is fully dissociated and the negative ion production by dissociative attachement is very weak (almost no molecules). The plasma is composed mainly of iodine atoms, and is electropositive, which explains that in this case iodine behaves pretty much like xenon (as observed in the previous subsection).

When the pressure is increased, strong gradients appear and the electronegativity profiles always present a minimum in the antenna region. The localization increases as the pressure increases. The electronegativity close to the antenna is only a few percents but reaches almost $\alpha = 3$ at 15 mTorr for $z = 9.5$ cm. The spatial variation of the electronegativity does not follow that of electrons, and of the plasma

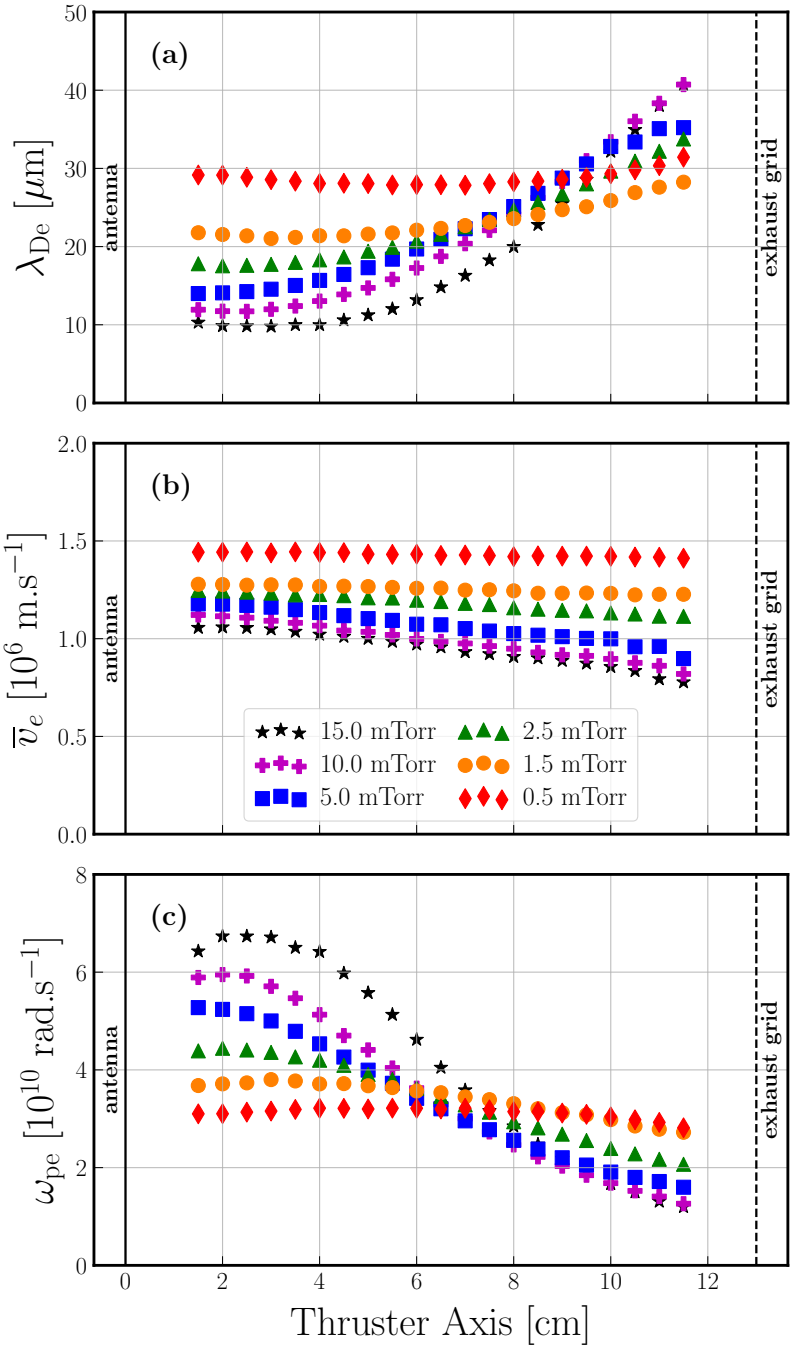

Figure 3.28: Spatial profiles of some plasma physics parameters deduced from Langmuir probe measurements in iodine plasmas for a fixed discharge power of 200 W. Measurements were taken along the thrust axis for pressures from 0.5 to 15 mTorr. (a) Debye length λ_{De} [μm]. (b) Electron thermal speed $\overline{v}_e$ [m.s^{-1}]. (c) Electron plasma frequency ω_{pe} [rad.s^{-1}].

potential (see previous subsection). The negative ions therefore seem far from Boltzmann equilibrium; i.e. they remain where they are created (by dissociative attachment of I_2) and do not follow the plasma potential profile (see subsection 3.5.2.2). This feature can be explained by a local balance between loss and creation processes of negative ions. Near the antenna, I^- are expected to be lost by ion recombination

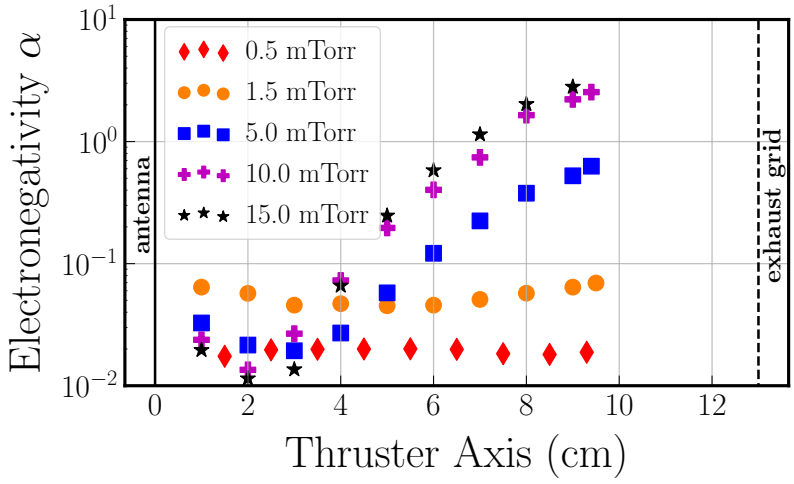

Figure 3.29: Spatial profiles of the electronegativity α for five different pressures from 0.5 to 15 mTorr and a fixed discharge power of 200 W.

with positive ions I^+ or by electron impact detachment. If we consider a recombination rate coefficient of about 5×10^{-14} m^3.s^{-1}, with $n_e \approx n_{I^+} \approx 10^{18}$ m^{-3} near the antenna, we get a loss frequency of 50 kHz. Assuming that negative ions drift at an average velocity of 1000 m.s^{-1}, one gets a mean travelling distance of 2 cm, that is much shorter than the plasma size, which confirms the local balance assumption.

The influence of discharge power on the electronegativity is studied in Figure 3.30. The measurements are conducted at a constant pressure of 5 mTorr but for two different discharge powers: 120 W and 200 W. The spatial profiles are presented in subfigure (a). As expected, when the discharge power increases, the electronegativity decreases (the electrons density increases and the I_2 molecules are more dissociated). This is observed at every position. However, subfigure (b) shows that the electronegativity ratio (red diamonds) is strongly non-uniform while the electron density ratio (green stars) is almost independent of space. The negative ion density profile is obtained by multiplying the measured electronegativity and electron density profiles. It turns out that increasing the discharge power by a factor of 5/3 decreases the negative ion density by a factor of 4 at $z = 3$ cm, near the antenna, but it barely affects the negative ion density near the exhaust grid. (see (c) in Figure 3.30). This result strengthens the hypothesis of non-local power deposition, leading to highly non-uniform dissociation processes.

To summarize the general idea: at higher pressure the dissociation is higher near the antenna, where the power deposition is localized, leading to very small electronegativity because negative ions are not efficiently produced via dissociative attachment and efficiently destroyed by recombination or electron detachment (because the plasma density is high). Inversely, away from the antenna, the power deposition is negligible, the electron density and temperature are low, and consequently the dissociation is small. This leads to high electronegativity because dissociative attachment becomes very efficient and negative ions destruction inefficient due to lower plasma density.

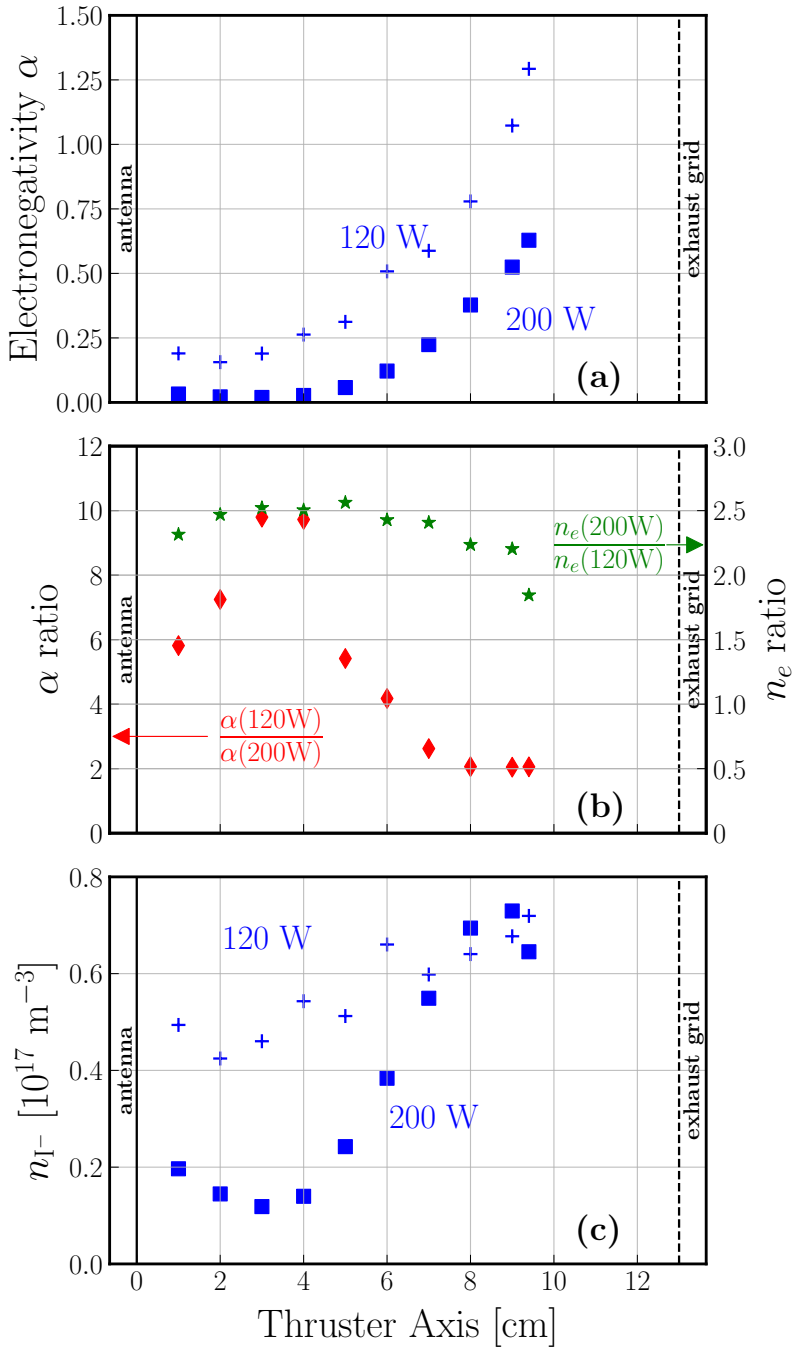

Figure 3.30: (a) Electronegativity spatial profiles along the thruster axis for a pressure of 5 mTorr and two different discharge powers: 120 W and 200 W. (b) Ratios of the electronegativity and electron density profiles at 5 mTorr and for two different discharge powers: 120 W and 200 W. Note that the discharge power values have been exchanged between α ratio and n_e ratio. (c) I^- density spatial profiles for two different discharge powers: 120 W and 200 W.

3.5.2.2 Boltzmann Violation

Negative ions are often considered to be in Boltzmann equilibrium in low-pressure electronegative discharges. When collisions and inertial terms are neglected, the

momentum equations for electrons and negative ions read:

$$\nabla(n_e e T_e) = -e n_e \mathbf{E}, \tag{3.23}$$
$$\nabla(n_{I^-} e T_{I^-}) = -e n_{I^-} \mathbf{E}, \tag{3.24}$$

where temperatures are expressed in volts. In 1D and with the isothermal approximation, the system of equations becomes:

$$\frac{\mathrm{d}\phi}{T_e} = \frac{\mathrm{d}n_e}{n_e}, \tag{3.25}$$
$$\frac{\mathrm{d}\phi}{T_{I^-}} = \frac{\mathrm{d}n_{I^-}}{n_{I^-}}. \tag{3.26}$$

when the electric field is derived from a potential ϕ. Introducing the temperature ratio $\gamma = T_e/T_{I^-}$, the previous equations become:

$$\gamma \frac{\mathrm{d}n_e}{n_e} = \frac{\mathrm{d}n_{I^-}}{n_{I^-}}. \tag{3.27}$$

Finally, spatial integration gives the electronegativity as a function of the electron density:

$$\alpha(z) = \alpha^0 \left(\frac{n_e(z)}{n_e^0} \right)^{\gamma - 1}, \tag{3.28}$$

where n_e^0 and α^0 are integration constants at $z = z_0$.
The previous formula, computed using the electron density measurements, is compared to electronegativity measurements at 0.5 mTorr and 15 mTorr for different values of γ (see Figure 3.31). We chose $z_0 = 1.5$ cm at 0.5 mTorr and $z_0 = 2$ cm at 15 mTorr.

At very low pressure (subfigure (a)), there is a good agreement between the Boltzmann equilibrium approximation and the actual measurements when $\gamma = 3$. This low value of γ requires that atoms and ions produced from molecular dissociation are very energetic, resulting in temperatures around or above the electron-volt. This seems quite extreme but confirmed by negative ions thermal speed measurements presented in subsection 3.5.2.3. It is possible that the probe used to collected the electron photo-detached current slightly perturbs the potential. However, negative ions are probably near Boltzmann equilibrium and confined in high plasma potential regions.

However, at 15 mTorr (subfigure (b)), negative ions are clearly not in Boltzmann equilibrium. Whatever the value of γ, the discrepancy between the measured electronegativity and the Boltzmann equilibrium theory exceeds two orders of magnitude near the exhaust grid even if $T_e = T_{I^-}$. This indicates that negative ions are destroyed by volume processes faster than they can drift in the electric field.

3.5.2.3 Ions thermal speed characterization

As first proposed by Devynck *et al.* [139], the laser-induced detachment technique gives access to an estimation of the negative ion velocity. Indeed, the PD signal, shown in Figure 3.32, exhibits a plateau region where the absolute collected electron current is constant and maximum before starting decreasing. The time for which

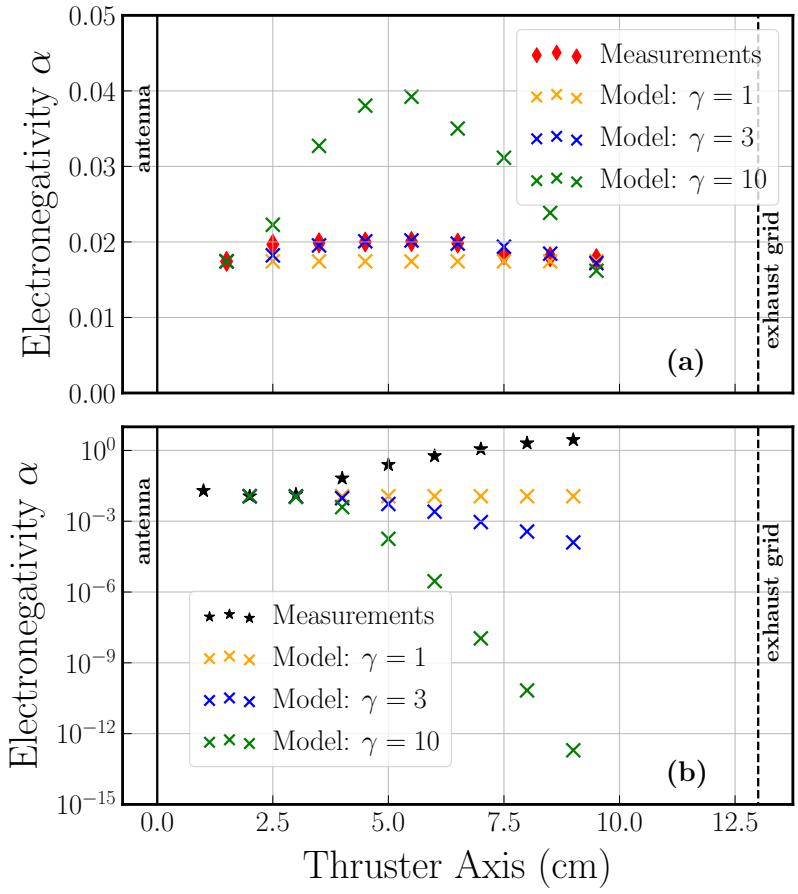

Figure 3.31: Electronegativity α measured and calculated using Boltzmann equilibrium theory for a discharge power of 200W. In the model, γ is the temperature ratio T_e/T_{I^-}. (a) 0.5 mTorr. (b) 15 mTorr.

the signal starts decreasing coincide with the arrival of the fastest negative ions in the probe collection zone where they will progressively replace the photodetached electrons ($\tau_{I^-,\text{fast}}$ on Figure 3.32). Then, more and more negative ions are coming back to the collection zone and the signal becomes null before its sign changes for $t = \overline{\tau}_{I^-}$, considered as the mean travel time. Finally, the signal reaches steady state when the slowest negative ions are back at time $\tau_{I^-,\text{slow}}$.

The previously defined characteristic times give an estimation of three characteristic velocities for I^- ions because the travel distance is known, fixed at $R_{\text{PD,beam}} - r_{\text{PD,probe}} \approx 2.7$ mm :

$$v_{I^-,\text{fast}} = \frac{R_{\text{PD,beam}} - r_{\text{PD,probe}}}{\tau_{I^-,\text{fast}}}, \tag{3.29}$$

$$\overline{v}_{I^-} = \frac{R_{\text{PD,beam}} - r_{\text{PD,probe}}}{\overline{\tau}_{I^-}}, \tag{3.30}$$

$$v_{I^-,\text{slow}} = \frac{R_{\text{PD,beam}} - r_{\text{PD,probe}}}{\tau_{I^-,\text{slow}}}. \tag{3.31}$$

$v_{I^-,\text{fast}}$ is the fastest velocity reached by I^- ions while $v_{I^-,\text{slow}}$ is the slowest. $\overline{v}_{I^-}$ can be considered as the drift velocity [140]. Finally, three estimated temperatures are

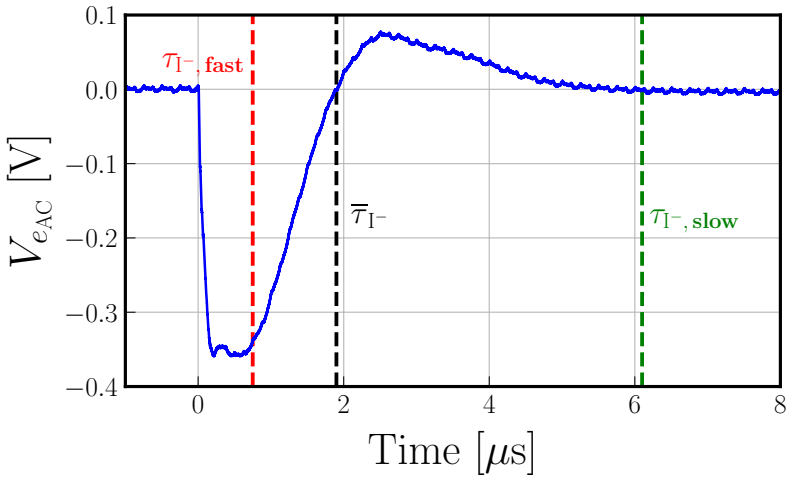

Figure 3.32: Photodetachment signal obtained for a pressure of 1.5 mTorr and a discharge power of 100 W at $z = 3$ cm from the antenna. The negative ions characteristic times ($\tau_{I^-,fast}$, $\overline{\tau}_{I^-}$ and $\tau_{I^-,slow}$) are indicated by vertical dashed lines.

derived:

$$T_{I^-,fast} = \frac{\pi}{8}\frac{m_I}{e}v^2_{I^-,fast}, \tag{3.32}$$

$$\overline{T}_{I^-} = \frac{\pi}{8}\frac{m_I}{e}\overline{v}^2_{I^-}, \tag{3.33}$$

$$T_{I^-,slow} = \frac{\pi}{8}\frac{m_I}{e}v^2_{I^-,slow}. \tag{3.34}$$

The previously defined times, velocities and temperatures are calculated for the PD signal shown in Figure 3.32 and gathered in Table 3.1.

Table 3.1: Characteristic times, velocities and temperatures of I^- ions evaluated in a 1.5 mTorr - 100 W iodine plasma at $z = 3$ cm away from the antenna.

	Fast	**Intermediate**	**Slow**
Time [μs]	0.8	1.9	6.1
Velocity [m.s^{-1}]	3.4 $\times 10^3$	1.5 $\times 10^3$	4.6 $\times 10^2$
Temperature [eV]	6.0	1.1	0.1

In the plasma conditions studied, the electron temperature was about 3.6 eV which indicates that negative ions are three times less hot than the electrons but much hotter than the surrounding neutral species. This may be due to the energy gain during the dissociative attachment process, which produces hot fragments because of the high electron affinity of iodine.

The effect of pressure on the I^- motion is studied in Figure 3.33. The drift velocity $\overline{v}_{I^-}$ is plotted against the neutral pressure in subfigure (a). The velocity decreases with pressure meaning that collisions play a role on the I^- velocity (as evidenced for H^- ions by Devynck in [139]). The Bohm speeds (or ion accoustic velocities) for I^+ and I_2^+ ions are also plotted and it turns out that $\overline{v}_{I^-}$ is of the same order of magnitude and always situated between both values. With an increasing pressure, it

seems that the negative ion mean speed gets closer to the I_2^+ Bohm speed which is thought to be the dominant positive species at high pressure far away from the antenna (z = 9.5 cm). Such a behavior was also observed in [136, 140], where the H^- mean speed was very close to the H_3^+ Bohm speed, with H_3^+ being the dominant positive species. The negative ion temperature is plotted in subfigure (b), it is always between 3 or 5 times smaller than the electron temperature and exhibits the same behavior against pressure. This value of the temperatures ratio is very close to the one giving the best agreement between Boltzmann equilibrium theory and experiments at low pressure in Figure 3.31.

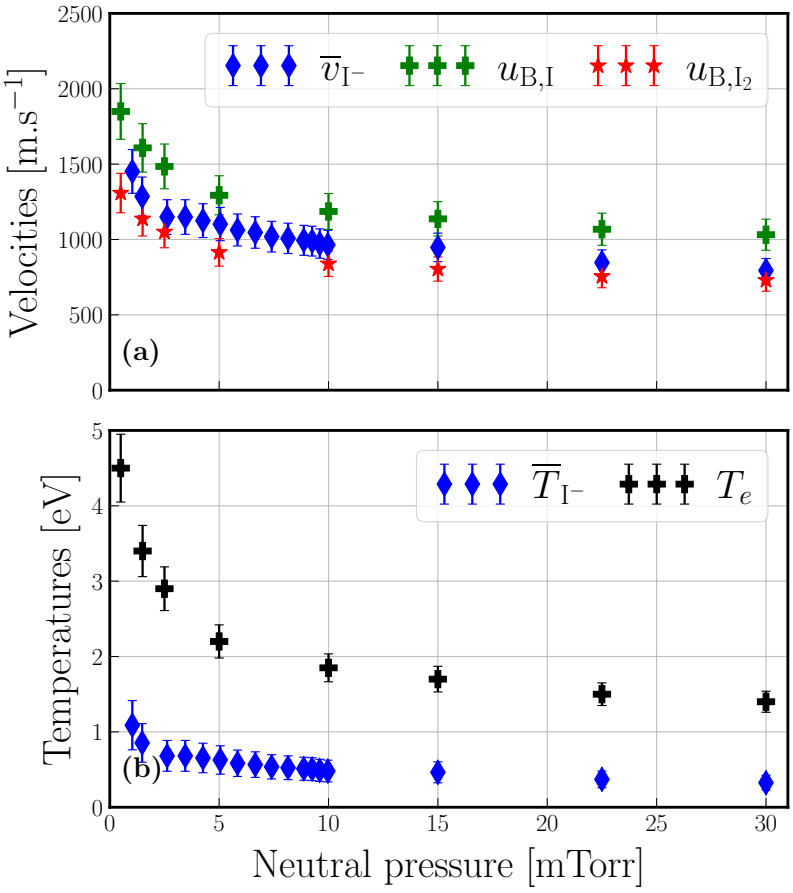

Figure 3.33: Influence of neutral pressure on negative ions motion properties. Measurements where taken in iodine plasmas for a fixed discharge power of 200 W at z = 9.5 cm. The error bars are ± 10%. (a) The mean velocity $\overline{v}_{I^-}$ is plotted as a function of the neutral pressure. Bohm speed are also plotted for I^+ and I_2^+ ions using measured electron temperatures. (b) The mean temperature $\overline{T}_{I^-}$ is plotted as a function of the neutral pressure. Electron temperatures are also plotted in the same graph.

The effect of discharge power has also been investigated but no net influence on the negative ion velocity was found. Concerning the effect of the probe location, the negative ion mean temperature follows approximatively the electron temperature spatial variations (see Figure 3.26), staying always in the range $[\frac{1}{5}T_e;\frac{1}{3}T_e]$.

3.5.3 Synthesis on charged particle densities

The negative ion density n_{I^-} is derived from the measured electronegativity α and electron density n_e. Then, assuming quasineutrality, one gets the positive density n_+ by adding the electron density and the negative ion density. Here n_+ accounts for all the possible positive ions present in the iodine plasma. Figure 3.34 shows the charged species density profiles on the same graph at 0.5 mTorr and 15 mTorr for a discharge power of 200 W while Figure 3.35 shows the charged species density profiles (n_e, n_{I^-}, n_+) on separate graphs with the same vertical axis for pressure between 0.5 mTorr and 15 mTorr.

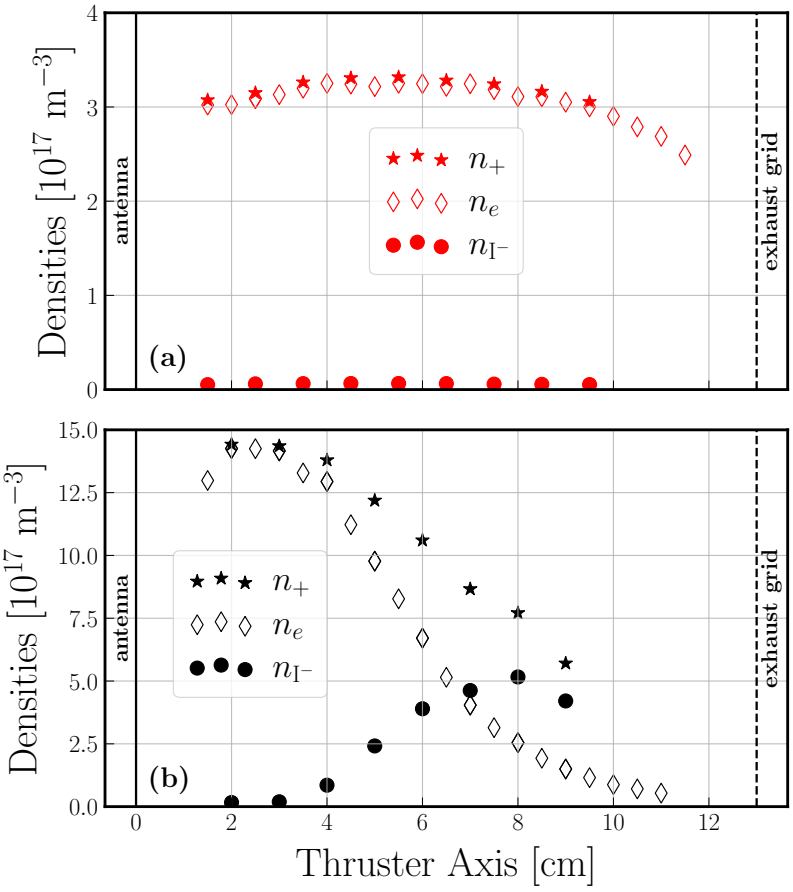

Figure 3.34: Electron density n_e, negative ion I^- density n_{I^-} and positive density n_+ spatial profiles for a discharge power of 200 W. (a) 0.5 mTorr. (b) 15 mTorr.

At the lowest pressure of 0.5 mTorr, it is almost impossible to distinguish between n_e and n_+, i.e. the negative ion density is negligible. The dominant positive ion species is likely to be I^+, which would explain the similarity between iodine and xenon plasmas for these operating conditions (high power, low pressure). Given the rather low electron temperatures measured in this discharge, no doubly-charged ions are expected to be found. The situation is different at 15 mTorr. Near the antenna (and up to $z = 3$ cm), the negative ion density is negligible and $n_e \approx n_+$. However, while the electron density strongly decays away from the antenna, I^- ions gradually become the dominant negative species, with a density maximum around $z = 8$ cm, where $\alpha > 2$. The resulting positive ion density profile decays less abruptly than the electron density profile, which partially explains the observed difference

with the xenon plasma case. In this higher pressure case, it is difficult to infer what would be the dominant positive ion. Both I^+ and I_2^+ are likely to be present, with different spatial density profiles. However, the very low electronegativity measured close to the antenna suggests a strongly dissociated plasma and thus that I^+ prevails over I_2^+ in this region. In between these two extreme pressures, the transition is smooth and negative ions start to play a significant role for pressures above 5 mTorr only.

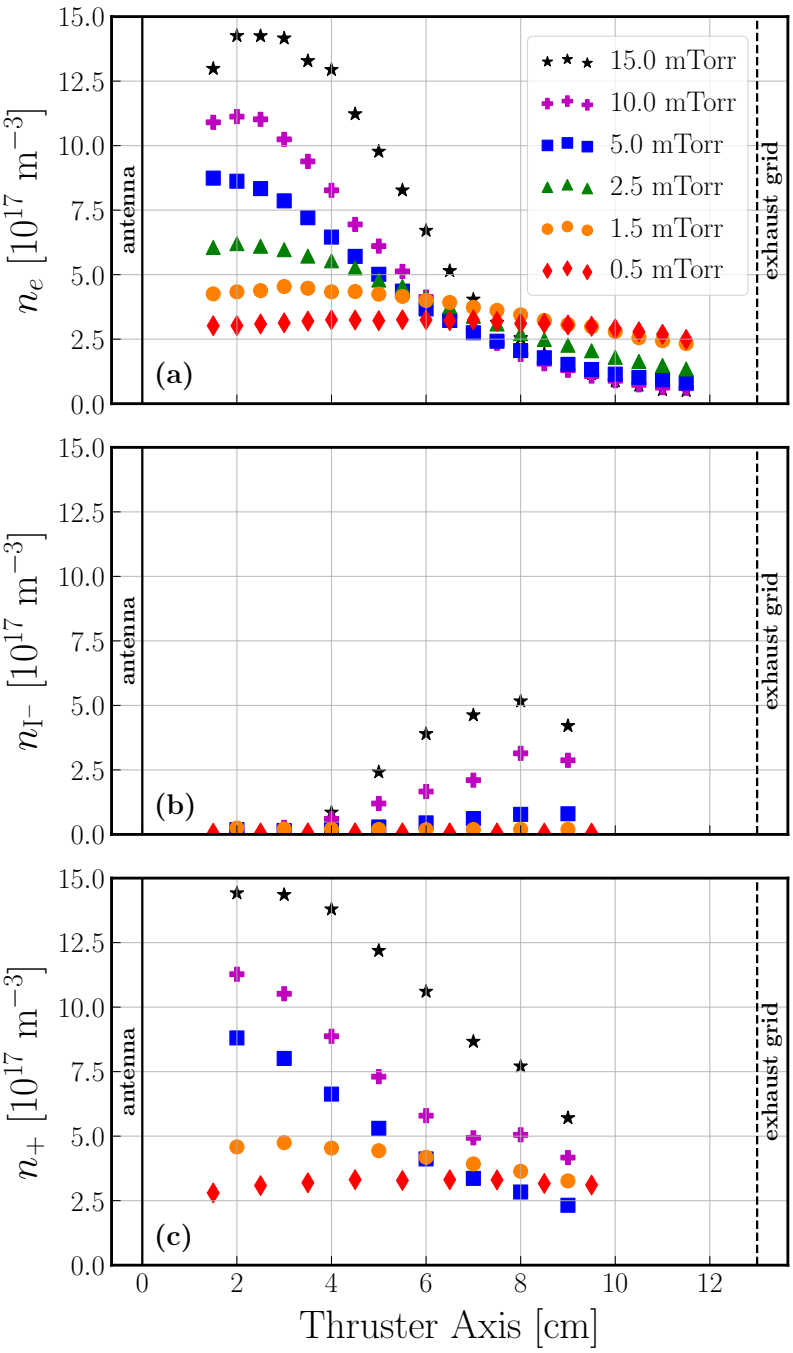

Figure 3.35: Charged species density spatial profiles in iodine plasmas generated for pressures from 0.5 to 15 mTorr with a discharge power of 200 W. (a) Electron density n_e. (b) I^- negative ion density n_{I^-}. (c) Positive ions density $n_+ = n_e + n_{I^-}$.

3.6 Chapter digest

In this chapter, charged-particles densities have been measured in low-pressure iodine plasmas used for electric propulsion in the space industry. Measurements were performed by using Langmuir probe and laser-induced detachment techniques. Measurements were also carried out in xenon, krypton and argon, three noble gases either routinely used (xenon and krypton) or considered as an alternative (argon) in electric propulsion. The main conclusions of this first investigation is that iodine is as good, if not better than, xenon at low gas flow rates, i.e. at low gas pressures. This is because although iodine is a molecular gas, molecules are easily dissociated and at the lowest pressure the plasma is probably fully dissociated. The ionization potential of iodine atoms is lower than that of xenon atoms, consequently the energy cost for an electron–ion pair creation is lower in iodine than in xenon despite the dissociation energy cost.
However, as pressure increases, the situation quickly reverses and iodine loses its advantage. In our experiments, where the distance between the antenna generating the plasma and the extracting grids is large, we found that the high density plasma localizes near the antenna when the pressure increases, and this effect is much more pronounced in iodine. This demonstrates that the electron energy relaxation length becomes shorter in iodine, due to its molecular nature. The ionization (or mass) efficiency becomes lower than that of xenon at higher pressures. The phenomenon is further enhanced by the electronegative nature of iodine. As the plasma transports away from the antenna, electrons cool down, the dissociation degree decreases, and consequently the dissociative electron attachment rate responsible for negative ion generation drastically increases. As a consequence, it was found that the negative ion density is larger than the electron density in the extraction region for pressures above 5 mTorr (note that these experiments are performed without magnetic filter).
These results have been published in reference [1] and presented in several international conferences (see Related publications in page xiii).

CHAPTER 4

NEUTRAL SPECIES MEASUREMENTS

Contents

4.1 Introduction

This chapter presents the optical diagnostics developed to probe neutral species (atoms and molecules) in low-pressure iodine plasmas.

Section 4.2 describes the absorption and laser-induced fluorescence (LIF) techniques and their application within the PEGASES thruster, on excited atomic species only, to obtain temperature profiles along the thrust axis, with argon and iodine.

Although measurements on excited states are useful for temperature measurements, the population of these states is negligible compared to that of the ground state (typically their density is three orders of magnitude lower) and no information about the density of the ground state can be obtained by probing them. Besides, the temperature of those excited states is often different from the ground state temperature (depending on their lifetime and their creation process). More sophisticated techniques are required to probe the ground state of a species. In Section 4.3, three laser diagnostics are developed, refined and applied to the iodine cell where the operating pressures provide strong optical signals and good confidence in the results. Firstly, the rate of molecular dissociation is obtained using a laser absorption diagnostic at 488 nm. Secondly, the TALIF technique (Two-photon Absorption Laser Induced Fluorescence) was developed during this thesis and is applied to obtain local absolute temperature and relative density measurements for the atoms. Finally, laser absorption at 1315 nm (developed by Marmuse [22]) is used to measure the population difference between the first two atomic states (the ground state $I(^2P^o_{3/2})$ and the first excited state $I(^2P^o_{1/2})$). These latter measurements, coupled with dissociation rate measurements, provide an absolute value of the density of the two probed atomic levels.

Finally, Section 4.4 is an application to the PEGASES thruster of the three laser diagnostics developed on the iodine cell. Difficulties related to low pressures had to be overcome but essential information regarding the spatial distribution of neutral species is obtained.

The main findings of the chapter are gathered in a summary at the end.

4.2 Diagnostics of excited species

One of the difficulties encountered when developing optical diagnostics for the study of plasmas is that the first excited levels (excluding peculiarities and exotic levels) are generally of very high energy (above 6.77 eV in the case of iodine and 11.54 eV for argon) and difficult to access or even inaccessible from the ground state by basic techniques such as absorption or Laser Induced Fluorescence (LIF). Absolute measurement of the ground state density is sometimes impossible using only these two diagnostics. The only solution is to develop more sophisticated techniques such as Two-Photon Absorption Laser Induced Fluorescence (TALIF), which gives access to transitions in the UV. Another solution, if one is only interested in the absolute measurement of the ground state temperature, is to probe directly the transitions between excited states (shorter in energy and therefore in the visible or near-IR), preferably metastable, and to deduce properties of the ground level by making more or less strong assumptions.

In this first section, the focus is on diagnostics, developed for both argon and iodine, to measure excited state temperatures and population differences using absorption and LIF techniques.

4.2.1 Absorption spectroscopy and LIF diagnostics

The absorption and LIF techniques are described in this first subsection using argon as an example. Argon has its isotope 40 much more abundant than the others (>99 %), so it will be considered that argon has no other isotopes. In addition, the nuclear spin number of argon is 0, so no hyperfine structure needs to be taken into account.

4.2.1.1 Absorption spectroscopy

Absorption spectroscopy is a powerful tool for measuring the temperature of the species, as well as their population difference, involved in the transition being probed. Although it only gives access to spatially integrated measurements, a lot of information about neutral species can be obtained if the transition is correctly chosen. A good transition has a high absorption (a few tens of per cent) and occurs between metastable states whose lifetime is long enough to consider that their temperature is in equilibrium with that of the ground state.

Optical setup

The optical setup used to perform absorption spectroscopy on argon inside the PEGASES thruster is shown in Figure 4.3, while the energy diagram of the probed levels is given in Figure 4.2.

The absorption transition occurs between the metastable lower $4s[3/2]_2^\circ$ and the upper $4p[3/2]_1$ states around 12943.50 cm^{-1} (772.376 nm), where we used Racah notation for excited levels. The lower state is metastable with a lifetime of 38 s [141], so we will assume that its temperature is in equilibrium with the temperature of the atomic ground state. A grating-stabilised external cavity laser diode (Toptica DFB#1200) is used to produce the beam between 772 and 773.87 nm. The wavelength of the diode is varied by simultaneously sweeping the diode current and

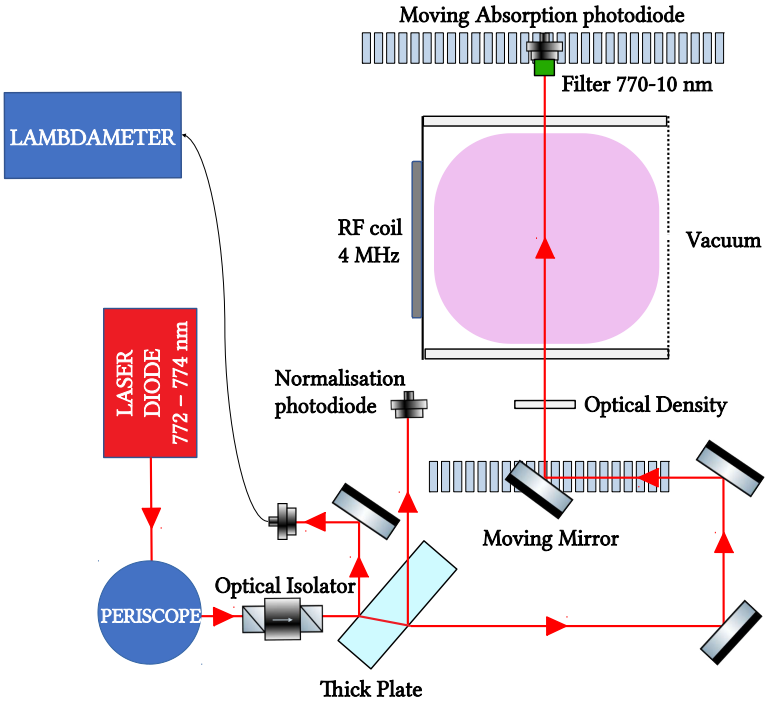

Figure 4.1: Schematics of the optical setup used for the argon absorption spectroscopy at 12943.50 cm^{-1} (772.376 nm). Mirrors and the absorption photodiode are mounted on rails to perform measurements along the thruster axis.

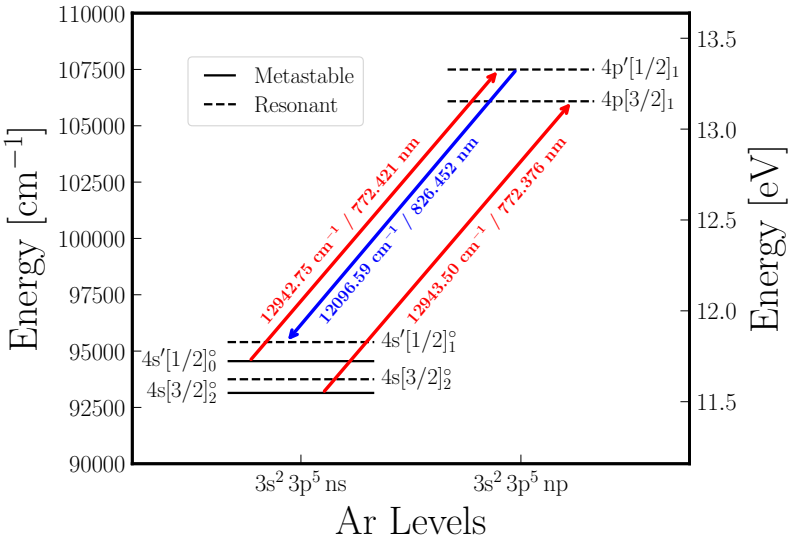

Figure 4.2: Energy diagram of the argon levels probed by using absorption spectroscopy at 12943.50 cm^{-1} (772.376 nm) and laser induced fluorescence (LIF) at 12096.59 cm^{-1} (826.452 nm) after an absorption at 12942.75 cm^{-1} (772.421 nm).

grating angle using a piezoelectric actuator. A wavemeter (High Finesse WSU, with a measurement resolution of 5 MHz (FWHM) and an accuracy of 30 MHz) is used for relative wavenumber measurement. The beam passes through the thruster once (at $z = Cst$) and its intensity is monitored by an amplified Si photodiode placed be-

hind a bandpass filter centered at 770 nm. The electrical signal is recorded by a NI-DAQ USB system controlled by a LabVIEW program. A semi-reflective prism is used to deflect the beam and record the reference signal I_0. Before entering the plasma, and to avoid any saturation phenomenon, the beam intensity is attenuated with an optical density. The last mirror and the absorption photodiode are mounted on rails in order to make measurements along the axis of the thruster, from $z = 1$ cm to $z = 9.9$ cm.

Beer-Lambert law and spectral line profile

The absorption of the radiation can be described by the Beer-Lambert law:

$$I(\tilde{\nu}) = I_0(\tilde{\nu}) e^{-\sigma(\tilde{\nu})\Delta n^* L}. \tag{4.1}$$

I_0 and I are the beam intensities entering and leaving the plasma, L is the length of the absorbing plasma, Δn^* is the average population difference of excited species along the light of sight involving the degeneracies and $\sigma(\tilde{\nu})$ is the cross section of the transition. The product $\sigma(\tilde{\nu})\Delta n^*$ is often referred as the absorption coefficient $\kappa(\tilde{\nu})$ while the product $\sigma(\tilde{\nu})\Delta n^* L$ is the optical depth $d(\tilde{\nu})$. Here, $\tilde{\nu}$ [cm^{-1}] is the wavenumber and, to avoid any confusion, it is proportional to the frequency ν [MHz] by using:

$$\nu[\mathrm{MHz}] = \frac{\mathrm{c[m.s^{-1}]}}{10^4} \times \tilde{\nu}[\mathrm{cm^{-1}}]. \tag{4.2}$$

In equation (4.1), the cross section $\sigma(\tilde{\nu})[\mathrm{m}^2]$ is proportional to the spectral line profile $g(\tilde{\nu})$[cm] (whose intergral over $\tilde{\nu}$ is 1), through the relation:

$$\sigma(\tilde{\nu}) = \sigma_0 \times g(\tilde{\nu}), \tag{4.3}$$

with σ_0 the wavenumber-integrated cross section in cm.

The spectral line profile $g(\tilde{\nu})$ may have various shapes but, in a plasma, the spectral broadening has mainly two origins: collisional broadening or Doppler broadening.

• The collisional broadening is homogeneous, the resulting profile, including radiative emission, has a **Lorentzian** shape:

$$\mathcal{L}(\tilde{\nu}) = \frac{2}{\pi\Delta_{\mathcal{L}}} \times \frac{1}{1 + \left(\frac{2\tilde{\nu}}{\Delta_{\mathcal{L}}}\right)^2}. \tag{4.4}$$

The Lorentzian Full Width at Half Maximum (FWHM) is here denoted $\Delta_{\mathcal{L}}$ and can be expressed as $\Delta_{\mathcal{L}} = A' + \gamma_{\mathrm{col}}$, where $A' = (A + Q)/2$ accounts for the radiative (A) and non-radiative de-excitation (quenching, Q) of the upper level and γ_{col} for the dephasing collisions.

• Doppler broadening, which is inhomogeneous, causes a **Gaussian** profile $\mathcal{G}(\tilde{\nu})$. When atoms or molecules are moving, their velocity relative to the observer follows a Maxwell distribution, which is temperature dependent. Through Doppler

effect, the velocity distribution induces a frequency distribution also depending on temperature:

$$\mathcal{G}(\tilde{\nu}) = \frac{2}{\Delta_{\mathcal{G}}}\sqrt{\frac{\ln(2)}{\pi}}\exp\left(-\ln(2)\left(\frac{2\tilde{\nu}}{\Delta_{\mathcal{G}}}\right)^2\right), \tag{4.5}$$

with $\Delta_{\mathcal{G}}$ the Gaussian FWHM which can be expressed as

$$\Delta_{\mathcal{G}} = \frac{\tilde{\nu}_0}{c}\sqrt{\frac{8k_{\mathrm{B}}T}{m}\ln(2)}, \tag{4.6}$$

where $\tilde{\nu}_0$ is the resonance wavenumber. In practice,

$$\frac{\Delta_{\mathcal{G}}}{\tilde{\nu}_0} = 7.16\times10^{-7}\sqrt{\frac{T[\mathrm{K}]}{M[\mathrm{kg.mol^{-1}}]}}. \tag{4.7}$$

• Each of the broadening phenomenon described previously occurs simultaneously in a plasma. Hence, spectral profiles cannot be considered perfectly Lorentzian or Gaussian but a mix of both. Mathematically, the resulting **Voigt** profile $\mathcal{V}(\nu)$ is the convolution of a Gaussian and a Lorentzian:

$$\mathcal{V}(\tilde{\nu}) = \int_{-\infty}^{+\infty}\mathcal{G}(\tilde{\nu}')\mathcal{L}(\tilde{\nu}-\tilde{\nu}')\,\mathrm{d}\tilde{\nu}'. \tag{4.8}$$

Doppler-free saturated absorption measurement

By performing a Doppler-free saturated absorption measurement using the experimental set-up shown schematically in Figure 4.3, we are able to determine $\Delta_{\mathcal{G}}$ and $\Delta_{\mathcal{L}}$. The setup used for the absorption spectroscopy has been modified. The laser beam passes through a first $\lambda/2$ polarisation plate which is used to bring the beam to a horizontal polarisation. In this polarised state, the beam passes unperturbed through the cubic beam splitter and into the plasma. It is then directed to a quarter-wave plate that transforms the light into circular polarisation, and then to an optical density to attenuate the intensity before leaving again. The two passes through the quarter-wave plate are equivalent to a half-wave plate and the objective is to generate a vertically polarised beam. Polarised vertically, the beam passes back through the plasma and is then fully reflected by the beam splitter back to the photodiode.

The first laser is called the pump laser, and is used to saturate the transition, while the second laser is called the probe laser. For atoms with a non-zero velocity, a different Doppler shift for each laser is induced, preventing any coupling between the pump and probe lasers except at certain crossing frequencies: the medium is therefore not transparent and the probe laser is absorbed. If the two lasers are placed so that the beam goes in opposite directions, the atoms with exactly zero velocity are saturated by the pump, the medium is then transparent for the probe laser. As a result, the absorption line of the pump laser is modified with a region of transparency (whose profile is Lorentzian) caused by the zero-velocity atoms in the middle of the Doppler-enhanced absorption line. Further information on Doppler-free saturated absorption can be found for example in the work of Preston [142].

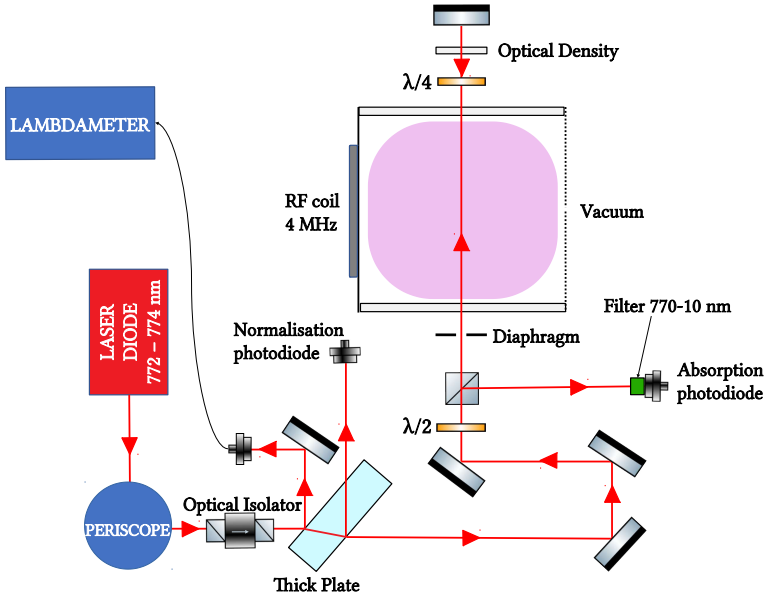

Figure 4.3: Schematics of the optical setup used for the argon saturated absorption spectroscopy at 12943.50 cm^{-1} (772.376 nm).

A measured Doppler-free saturated absorption signal is shown in Figure 4.4. The Gaussian FWHM $\Delta_\mathcal{G}$ is about 0.04 $cm^{-1} \approx 1200$ MHz, while the Lorentzian FWHM $\Delta_\mathcal{L}$ is about 0.003 $cm^{-1} \approx 90$ MHz. For completeness, $A' = 5.18$ MHz for the studied transition according to Wiese *et al.* [143]. This means that the dephasing collisions, $\gamma_{\text{col}} = \Delta_\mathcal{L} - A'$, are responsible for the majority of the homogeneous broadening, as already observed in oxygen discharges [144]. Most of all, there is more than one order of magnitude of difference between the two FWHMs, meaning that the absorption signal can be fitted by a Gaussian without considering the Lorentzian contribution; by simply using:

$$d(\tilde{\nu}) = -\ln\left(\frac{I(\tilde{\nu})}{I_0(\tilde{\nu})}\right) = d_0 \exp\left(-\frac{m_{\text{Ar}}c^2}{2k_{\text{B}}T}\left(\frac{\tilde{\nu}-\tilde{\nu}_0}{\tilde{\nu}_0}\right)^2\right), \tag{4.9}$$

where the temperature T, the resonance wavenumber $\tilde{\nu}_0$ and the optical depth magnitude

$$d_0 = \frac{\sigma_0 \Delta n^* L}{\tilde{\nu}_0}\sqrt{\frac{m_{\text{Ar}}c^2}{2\pi k_{\text{B}}T}}, \tag{4.10}$$

are the unknown fitting parameters.

Saturation analysis

The Beer-Lambert relation (equation (4.1)) is valid only if the transitions are not optically saturated. A saturation analysis has thus to be performed. The results are shown in Figure 4.5. In subfigure (a), the Gaussian fitted optical depth is plotted as a function of the wavenumber for different laser powers. The optical depth decreases with laser power when the power increases too much, showing a saturation effect

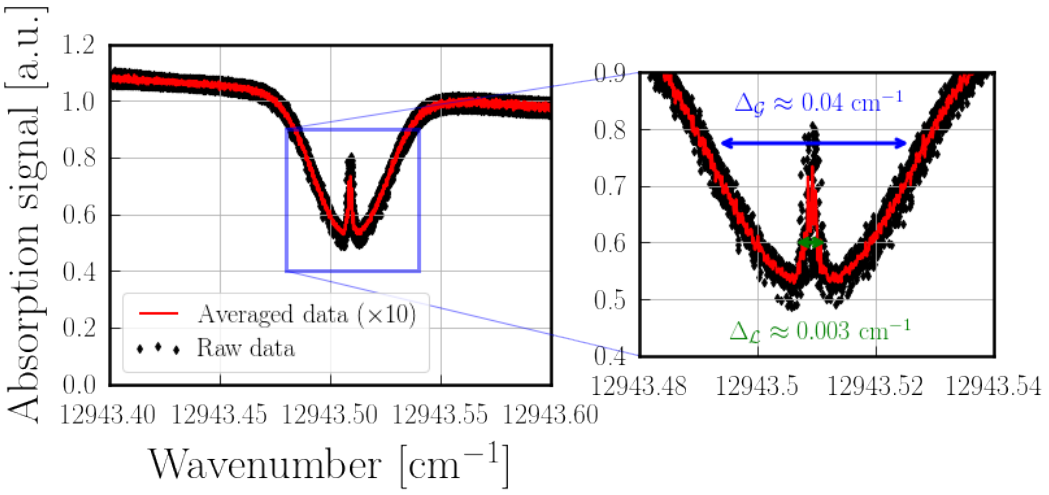

Figure 4.4: Doppler-free saturated absorption signal taken in a 5 mTorr-100 W argon plasma @ 772.376 nm.

because of the equalization of the populations between the upper and lower level. Reporting the maximum values as a function of laser power, in subfigure (b), a good agreement with the saturation formula[1]:

$$d(P) = \frac{d_0}{\sqrt{1 + P/P_{\text{sat}}}}, \tag{4.11}$$

is retrieved, with $d_0 = 0.602$ and $P_{\text{sat}} = 2$ mW. In the following, the experiments were all conducted with a laser power around 180 μW. For lower laser power, the signal-to-noise ratio was not good enough to perform reliable measurements.

In subfigure (c), gas temperatures extracted from the Gaussian fit (using equation (4.9)) are plotted as a function of the laser power. Despite the saturation of the optical depth, the measured temperature is very stable: the five measurements lies within the value of 497.4 ± 49 K. In the case of a purely inhomogeneous profile, Delsart [145] showed that the temperature is independent of the saturation.

Excited species density measurement

Finally, one can deduce the population difference Δn^* by taking into account the saturation and by reversing equation (4.10):

$$\Delta n^* = \frac{d_0 \tilde{\nu}_0}{\sigma_0 L} \sqrt{\frac{2\pi k T}{m_{\text{Ar}} c^2}}, \tag{4.12}$$

where σ_0 can be linked to the absorption oscillator strength of the transition $f_{12} = 0.0306$, by using:

$$f_{12} = \frac{2\varepsilon_0 m_e c}{\pi e^2} \sigma_0, \tag{4.13}$$

[1] To be exact, saturation depends on the intensity of the laser beam. In practice, the study has been performed with laser power.

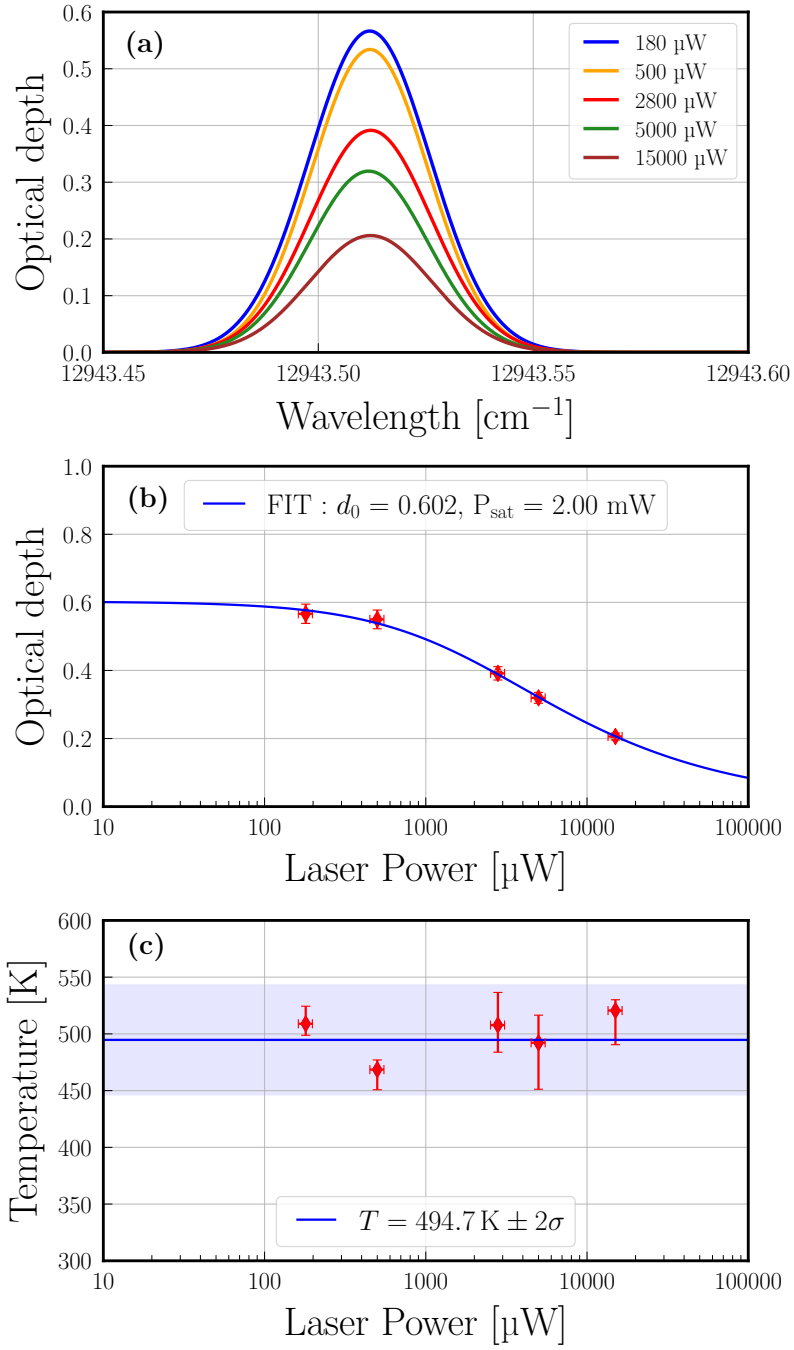

Figure 4.5: Saturation analysis of the 772.376 nm transition in a 10 mTorr-140 W argon plasma. (a) The Gaussian fitted optical depth is plotted for five different laser powers. (b) The optical depth maxima are plotted as a function of the laser power [μW]. Equation (4.11) allows for the determination of d_0 and P_{sat}. (c) Gas temperature [K] as a function of the laser power [μW].

from [146]. Note that this last relation is only valid when the normalization integral of the spectral line profile g is taken over ω [rad/s] (in this case, σ_0 is expressed in m^2 rad.s^{-1}).

The population of the upper level is often neglected as the energy difference between the two states is around 12943.5 $cm^{-1} \approx 1.605$ eV, and $\Delta n^* = n_1^* - \frac{g_1}{g_2} n_2^* =$

$n_1^* - \frac{5}{3}n_2^*$ simply becomes $\Delta n^* = n_1^*$, with n_1^* the density of the lower metastable level. As an example, taken from Figure 4.5 for a laser power of 180 μW, we find n_1^* of the order of 6×10^{16} m^{-3}, about 0.3 % of the ground state density.

4.2.1.2 Laser Induced fluorescence

In the previous chapter (see Chapter 3), all measurements on the charged particles were obtained along the thruster axis, in the middle of the discharge ($x = 0, y = 0, z$). Diagnosis by absorption spectroscopy allows us to measure the temperature along the thruster axis but with integrated values along the $\hat{\mathbf{x}}$-axis ($< x >, y = 0, z$). To obtain local temperature information, it is possible to collect the fluorescence induced by the absorption of 1 or 2 photons, respectively called LIF or TALIF. This type of diagnostic offers locality but the fluorescent signal is often weak and the signal-to-noise ratio is not as good as with absorption spectroscopy, mostly deteriorated by the strong plasma emission. The collected fluorescence signal depends on the branching ratios of de-excitation and quenching, it is proportional to $A/(\sum_i A_i + Q)$. The temperature determination is most of the times an easy task but an absolute measurement of density is much more difficult as the photon detection must be properly calibrated (accurate measurement of the solid angle of collection and exact translation of the amount of photons collected into electrical voltage).

With argon, the LIF diagnostic has been applied by collecting the fluorescence light from the 4p'$[1/2]_1$ level to the 4s'$[1/2]_1^\circ$ level at 12096.59 cm^{-1} (826.452 nm) following the absorption from the 4s'$[1/2]_0^\circ$ level at 12942.75 cm^{-1} (772.421 nm), as shown in Figure 4.2. Induced fluorescence by the absorption at 772.376 nm was also investigated but no fluorescent signal was detected at 810.3693 nm, mostly because of the strong plasma emission of light around 810 nm.

The chosen transition has been shown to saturate even for very weak laser power but it has no impact on the measured temperature in the case of a purely inhomogeneous broadening as shown by Delsart [145]. It would be mandatory to choose an other transition if we wanted to precisely measure the population difference between the two excited states but it is not the case, as the temperature is the only relevant information we want to get from this diagnostic.

The LIF optical setup used with argon is shown in Figure 4.6. The absorption wavelength being very close to the one used to perform absorption spectroscopy (772.421 nm versus 772.376 nm), we used the same laser diode. Instead of going directly to the plasma at a fixed z, the beam has been deviated to go through the main vacuum chamber and through the centered hole of the exhaust grid, to finally propagate inside the plasma along the thrust axis in the middle of the discharge. Thus, the fluorescence can be perpendicularly collected, through the lateral windows, by using a lens of focal length $f = 5.2$ cm and a photodiode located in the $2f - 2f$ configuration, behind a band-pass filter centered around 830 nm. The lens and photodiode can move along the $\hat{\mathbf{z}}$-axis. We used a 1500 Hz chopper and a lock-in amplifier (SR830-DSP from Standford Research systems) to increase the sensibility of the detection. To obtain a square temporal gate, we reduced the beam size (and thus the transit time) by using a telescope and inserting the chopper at the waist.

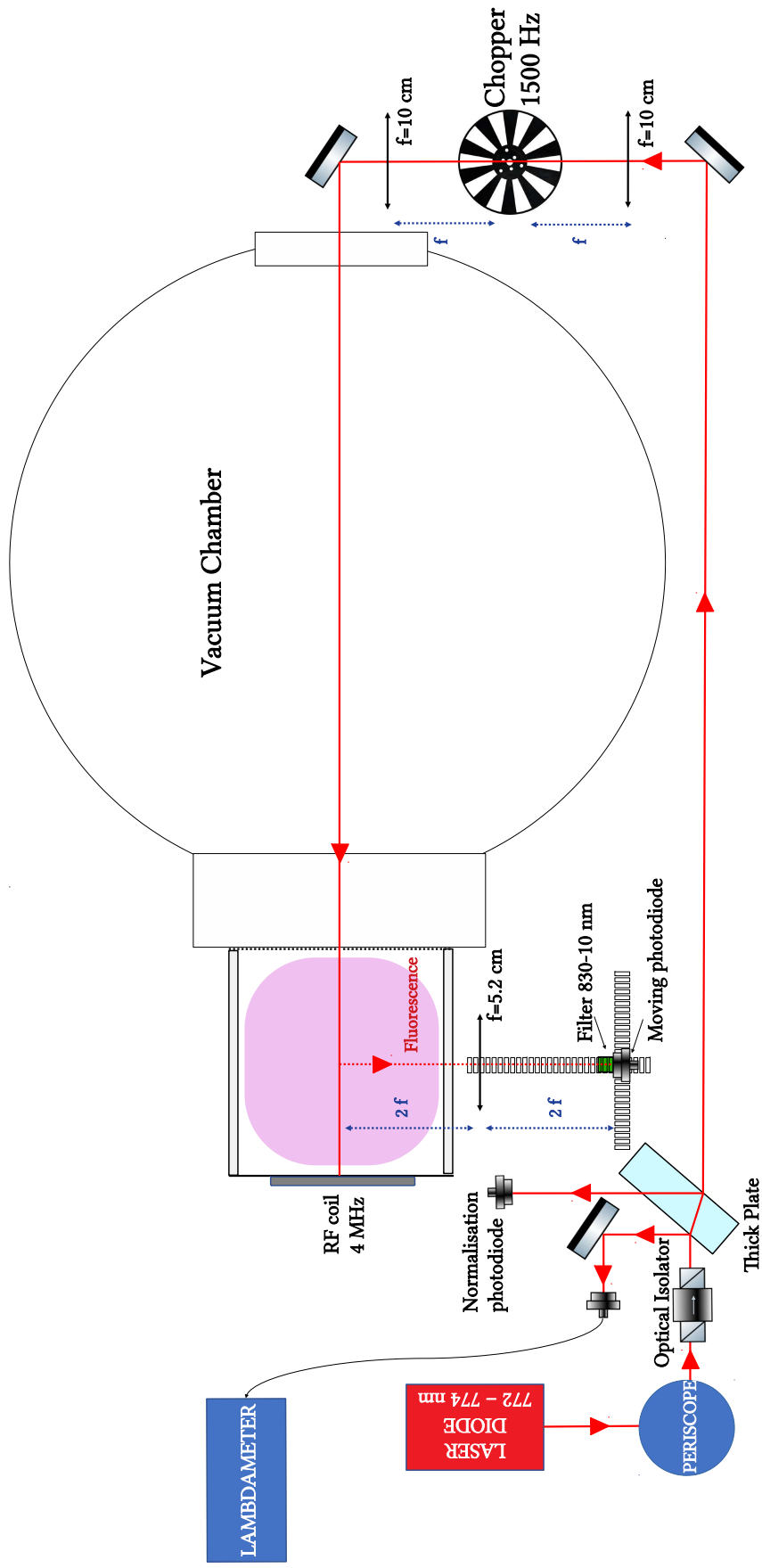

Figure 4.6: Schematics of the optical setup used for the argon Laser induced fluorescence diagnostic. The fluorescence at 826.452 nm is induced by absorption at 772.421 nm. A 1500 Hz-chopper is used to increase the signal-to-noise ratio.

4.2.2 Absorption and LIF measurements in PEGASES running with argon

4.2.2.1 Temperature

An example of typical signals obtained by performing absorption spectroscopy and LIF diagnostics inside PEGASES thruster at the same location along the thrust axis ($z \approx 6.5$ cm) is given in Figure 4.7. In each case, the signal has been fitted by the Gaussian profile of equation (4.9). As expected, the temperature in the discharge center, measured by LIF, is much higher than the temperature, averaged along the line of sight, measured by absorption. Roughly, the difference has always been measured between 100 K and 250 K (see Figure 4.10 for more details). The signal-to-noise ratio is also better with absorption than with LIF inducing smaller 2-σ error bars. Note that for $z \geq 8$ cm, the LIF signal-to-noise ratio was close to 1 (very weak signal because of the very low electron density in this region) and, most of the times, no temperature could be properly fitted.

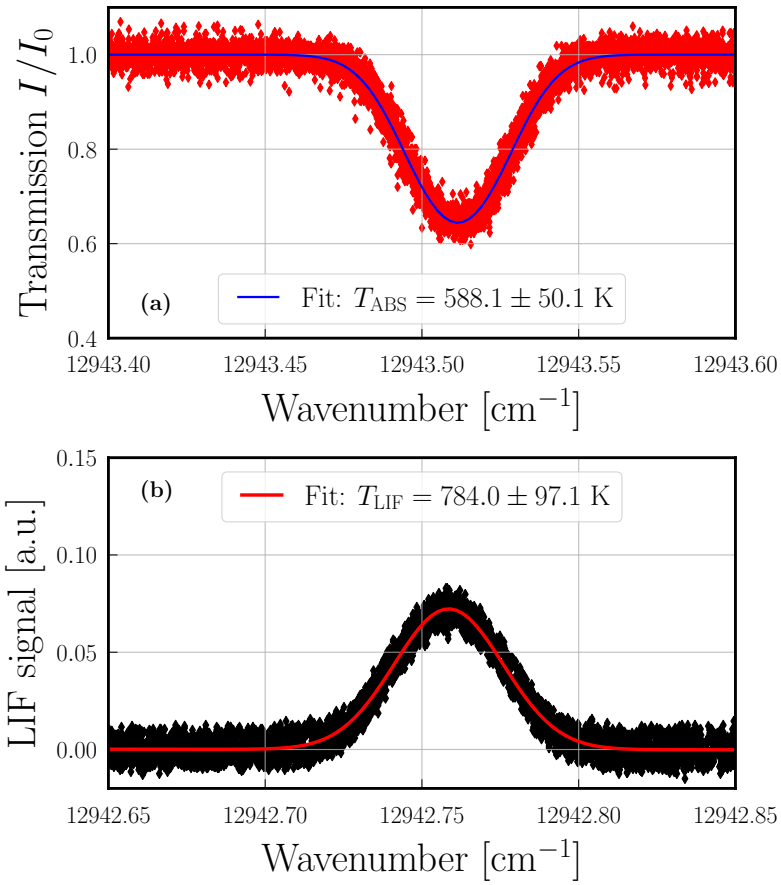

Figure 4.7: Optical signals in a 15 mTorr-200 W argon plasma running in PEGASES thruster at the location $z \approx 6.5$ cm measured by using (a) absorption spectroscopy and (b) LIF. The Gaussian fitted temperatures are given in legend.

The temperature spatial profiles are first investigated by using both absorption and LIF. The effect of discharge power is studied for a fixed pressure of 15, 5 and 2.5 mTorr in Figure 4.8 while the effect of pressure is investigated for a fixed discharge power of 200, 100 and 50 W in Figure 4.9. In each figure, on the left are

plotted the temperatures measured by using absorption spectroscopy and on the right are plotted the temperatures measured by using LIF.

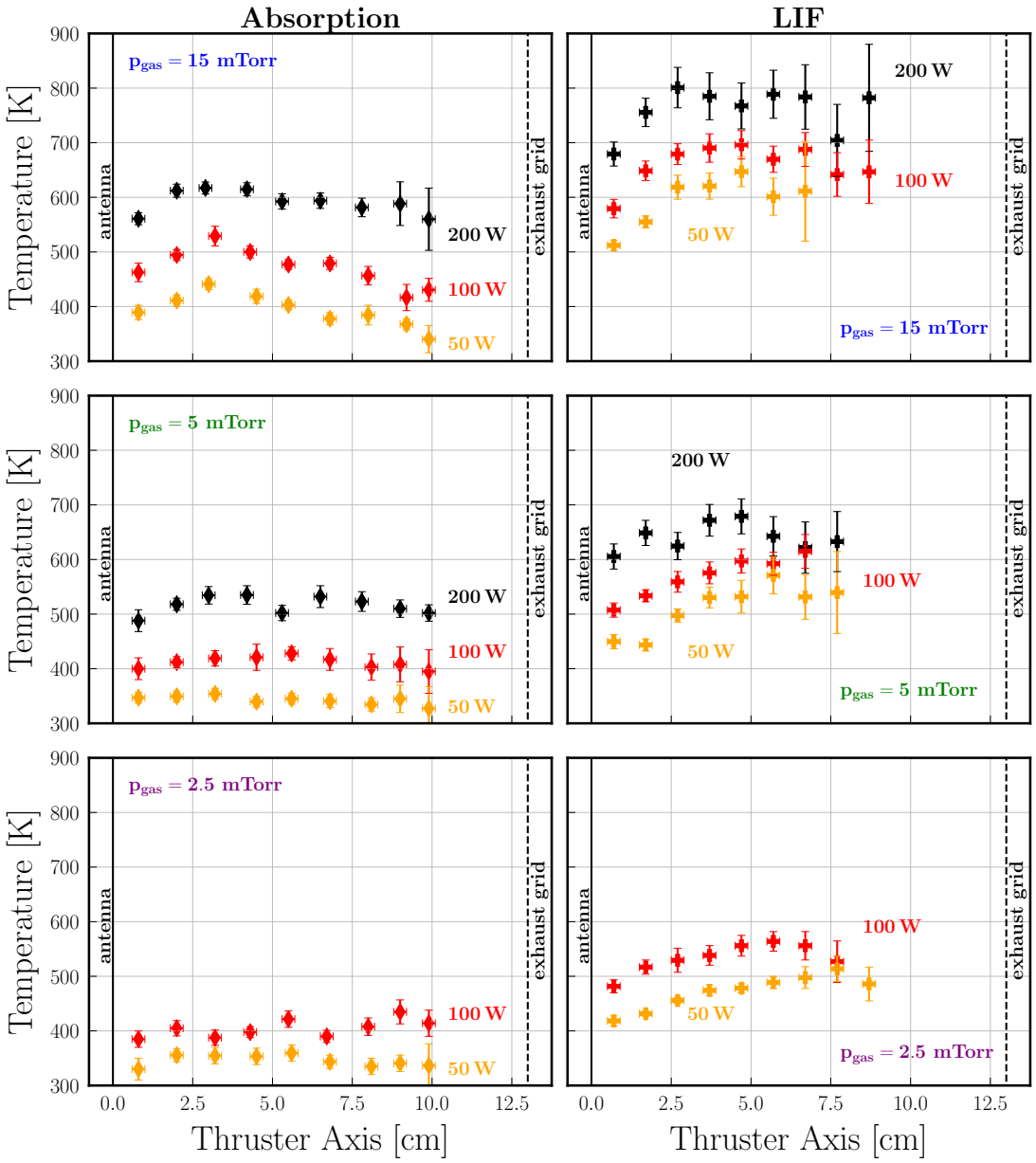

Figure 4.8: Spatial profiles of the gas temperature along the thruster axis measured by using absorption (left) and LIF (right) diagnostics. In each plot, the influence of power is studied for a fixed pressure (15 mTorr, 5 mTorr or 2.5 mTorr).

Both discharge power and pressure increase the temperature. By increasing the discharge power, the electron density increases and more numerous elastic collisions between neutrals and electrons heat the gas. Also, the ion flux bombarding the walls increases and the newly created neutrals (by neutralization of the ions at the walls) are hotter than the ones in the bulk, inducing an increase of the global temperature. By doubling the discharge power, the temperature is roughly increased by 100 K everywhere. The measured temperatures are in the range [300 K-600 K] for absorption and [400 K-800 K] for LIF diagnostics. The spatial scans measured by absorption appear much flatter than those measured by LIF, the latter showing a

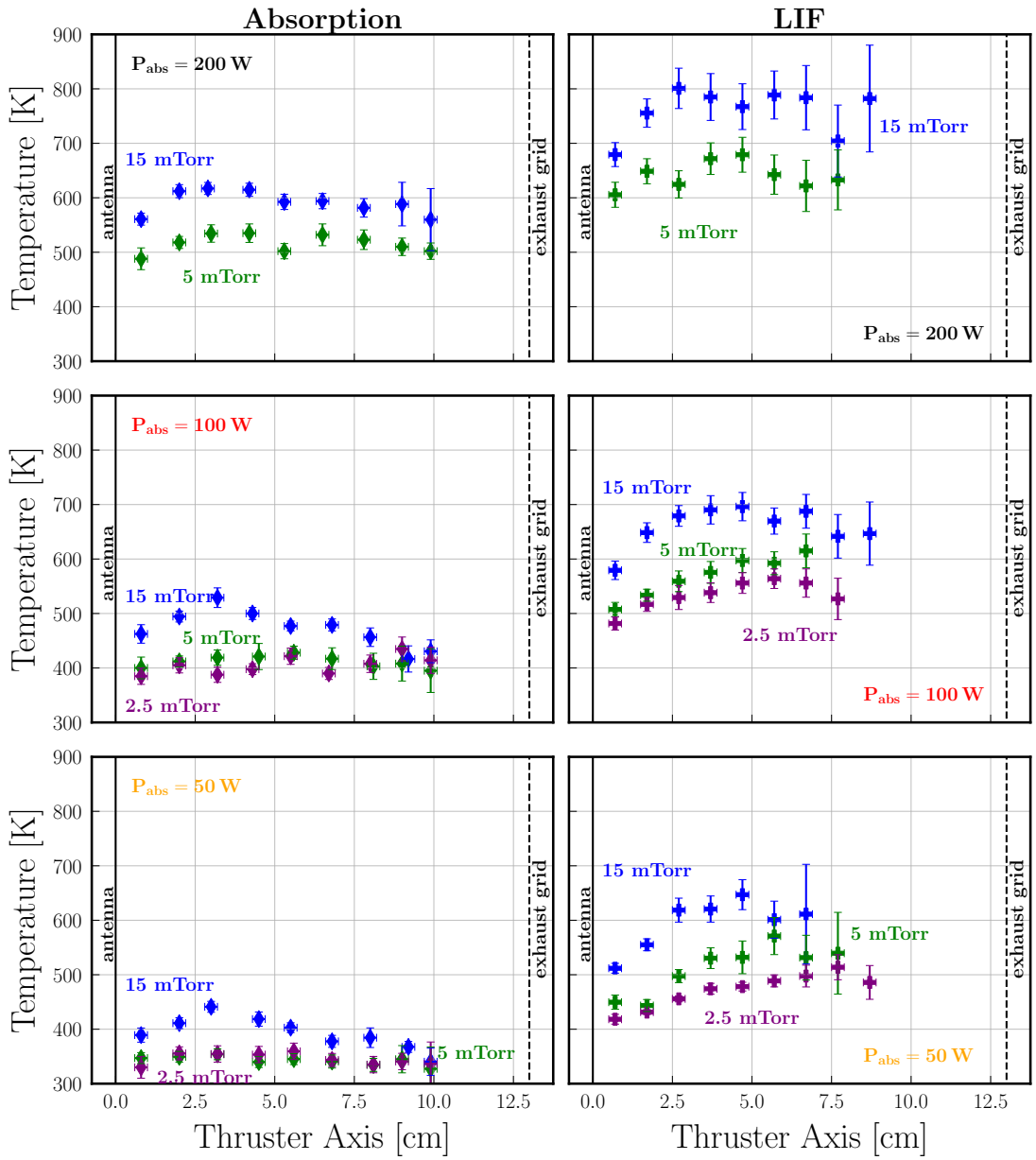

Figure 4.9: Spatial profiles of the gas temperature along the thruster axis measured by using absorption (left) and LIF (right) diagnostics. In each plot, the influence of pressure is studied for a fixed discharge power (200 W, 100 W or 50 W).

dome shape for any pressure. At 2.5 mTorr and 100 W, for example, the absorption profile can be considered constant at 400 K which is not the case for the LIF profile. With increasing pressure, the profiles (both with absorption and LIF) tend to localise near the antenna, as already observed with the electron density profiles in Chapter 3.

Furthermore, the temperature profiles clearly show a temperature jump at the walls. Indeed, if we continuously extend the spatial profiles of absorption and LIF until $z = 0$, the value reached T_{edge} is well above the temperature values at the walls T_{wall} plotted in Chapter 2 (see Figure 2.20). This phenomenon is classical in plasma physics and has already been observed with other gases (with CF_4 for instance in [147]). The temperature jump at the antenna ($\Delta T_{wall} = T_{edge} - T_{wall}$)

depends on both pressure and power and its value seems to exceed 100 K for the majority of the experimental conditions studied.

In the following, we are interested in global behavior with pressure and power. First, for each plasma operating conditions plotted in Figures 4.9 and 4.8, we calculated the spatial average temperature, both for LIF ($< T_{\mathrm{LIF}} >_z$) and absorption ($< T_{\mathrm{ABS}} >_z$) diagnostics. In Figure 4.10, are plotted the resulting temperature ratio $< T_{\mathrm{LIF}} >_z / < T_{\mathrm{ABS}} >_z$ (top subfigure) and the temperature difference $< T_{\mathrm{LIF}} >_z - < T_{\mathrm{ABS}} >_z$ (bottom subfigure) as a function of the discharge power.

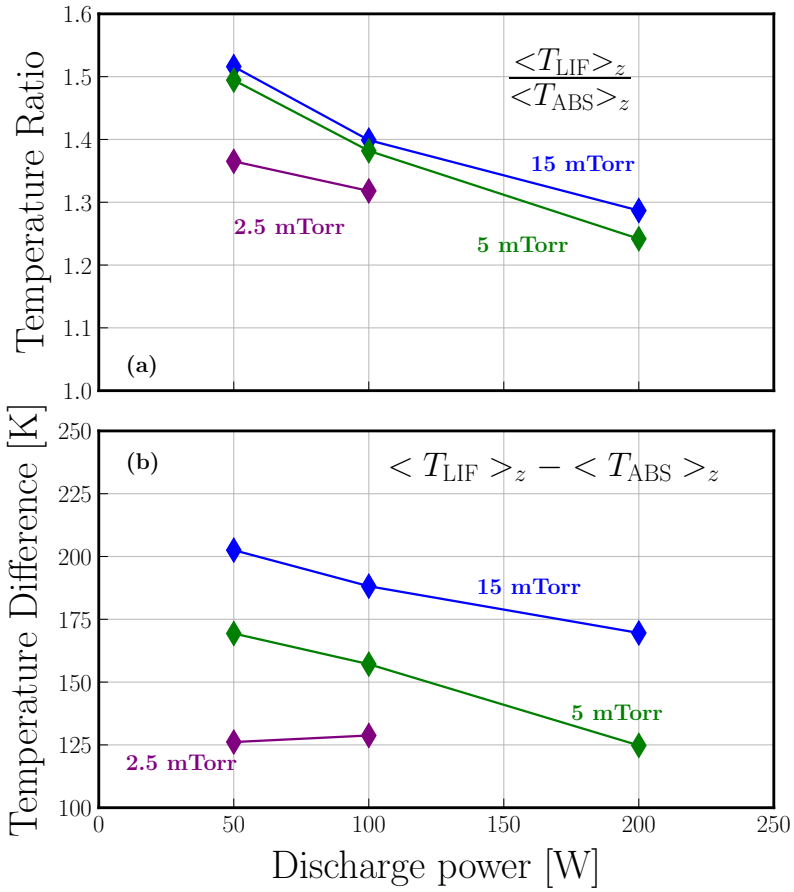

Figure 4.10: (a) Ratio of the spatial-averaged temperature measured by LIF over the spatial-averaged temperature measured by absorption as a function of the discharge power for three pressures (2.5, 5 and 15 mTorr). (b) Difference between the spatial-averaged temperature measured by LIF and the spatial-averaged temperature measured by absorption as a function of the discharge power for three pressures (2.5, 5 and 15 mTorr).

Increasing the discharge power decreases both the temperature ratio and the temperature difference while for a fixed power, increasing the pressure increases the temperature ratio and temperature difference. To summarize, at low power and high pressure the temperature inside the thruster is inhomogeneous with strong spatial gradients while at low pressure and high discharge power the profiles must be flatter.

In addition, in the top subfigure of Figure 4.11, all the temperatures measured by absorption spectroscopy, in the center of the discharge (z = 6.5 cm), at 50, 100

and 200 W are gathered and plotted as a function of pressure. In subfigure (b), the effect of discharge power is studied for five different pressures (2.5, 5, 12, 15 and 23 mTorr). A 2D-fitting analysis has been performed on the data plotted in

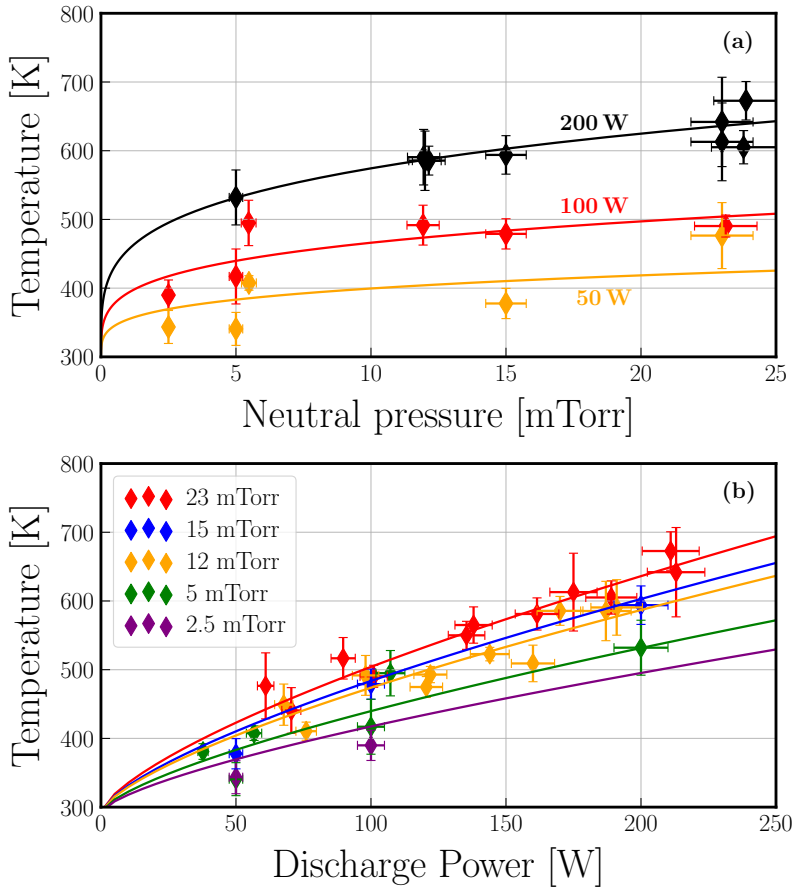

Figure 4.11: Influence of (a) the gas pressure and (b) the discharge power, on the gas temperature measured in the middle of the discharge (z = 6.5 cm) by using absorption spectroscopy. The solid lines are plotted by using the fitting formula of equation (4.14).

Figure 4.11 to retrieve a simple power law for the temperature depending on both the gas pressure p_{gas} [mTorr] and the discharge power P_{abs} [W]:

$$T(p_{\text{gas}}, P_{\text{abs}}) \;=\; 293 + 3.97 \times p_{\text{gas}}^{0.238} \times P_{\text{abs}}^{0.701}. \tag{4.14}$$

This formula has been plotted in Figure 4.11 for every operating condition.

4.2.2.2 Reconstruction of the transverse temperature profile

The following reasoning has been introduced by Marmuse [22].

So far, the Beer-Lambert formula (see equation (4.1)) has been written assuming homogeneous spatial profiles of the temperature T and the density Δn^* along the line of sight. In reality, both of these quantities are depending on the spatial coordinates $x \in [-L/2\,;\,L/2]$. We propose to modify the law of absorption by introducing the spatial dependence on x.

Let's set $I(x,\tilde{\nu})$ the spectral radiance at a position x along the line of sight and for the wavenumber $\tilde{\nu}$. $I(\tilde{\nu}) = I(x = L/2, \tilde{\nu})$ is the radiance exiting the plasma and $I_0(\tilde{\nu}) = I(x = -L/2, \tilde{\nu})$ the entering radiance or the reference radiance. By considering a small portion of light of length dx, the law of absorption reads:

$$\mathrm{d}I(x,\tilde{\nu}) \;=\; -\kappa(x,\tilde{\nu})I(x,\tilde{\nu})\mathrm{d}x, \tag{4.15}$$

where, by assuming the broadening to be locally Gaussian, the absorption coefficient $\kappa(x,\tilde{\nu})$ can be written as:

$$\kappa(x,\tilde{\nu}) \;=\; \sigma_0 \Delta n^*(x)\mathcal{G}(\tilde{\nu}-\tilde{\nu}_0, T(x)). \tag{4.16}$$

Then, by integrating the local law of absorption along the line of sight, one gets:

$$\int_{-L/2}^{L/2} \frac{-\mathrm{d}I(x,\tilde{\nu})}{I(x,\tilde{\nu})} \;=\; \sigma_0 \int_{-L/2}^{L/2} \Delta n^*(x)\mathcal{G}(\tilde{\nu}-\tilde{\nu}_0, T(x))\,\mathrm{d}x, \tag{4.17}$$

and finally,

$$-\ln\left(\frac{I(\tilde{\nu})}{I_0(\tilde{\nu})}\right) \;=\; \frac{\sigma_0}{\tilde{\nu}_0}\sqrt{\frac{m_{\mathrm{Ar}}c^2}{2\pi k}} \int_{-L/2}^{L/2} \frac{\Delta n^*(x)}{\sqrt{T(x)}} \exp\left(-\frac{m_{\mathrm{Ar}}c^2}{2k_{\mathrm{B}}T(x)}\left(\frac{\tilde{\nu}-\tilde{\nu}_0}{\tilde{\nu}_0}\right)^2\right)\mathrm{d}x. \tag{4.18}$$

The density and temperature profiles, $\Delta n^*(x)$ and $T(x)$, are unknown and to proceed further in the reasoning, they must be assumed.

The thruster can be considered as symmetrical with respect to the $x = 0$ plane (or yz plane). This means that both $T(x)$ and $\Delta n^*(x)$ are even functions of x. Besides, the temperature is maximum in the center of the discharge (as observed with LIF measurements) and because the simplest solution of the heat diffusion equation (assuming a constant source term) is quadratic, we assume that it is the case:

$$T(x) \;=\; T_{\max} + (T_{\mathrm{edge}} - T_{\max})\left(\frac{2x}{L}\right)^2, \tag{4.19}$$

where $T_{\max}$ is the maximum temperature and $T_{\mathrm{edge}} = T_{\mathrm{wall}} + \Delta T_{\mathrm{wall}}$ is the wall temperature once the temperature jump has been taken into account. Concerning the density difference profile, $\Delta n^*(x) = n_1^*(x) - \frac{5}{3}n_2^*(x)$, it is more difficult to make an assumption. If we neglect n_2^*, the profile of n_1^* is mainly influenced by two opposite profiles [2]: (i) the electron profile which reaches its maximum at $x = 0$ and tends to 0 in $x = \pm L/2$, that could be assumed as a cosine profile, (ii) the neutrals ground state profile which is proportional to 1/T(x), assuming an isobar plasma, and therefore depleted at the center with a minimum in $x = 0$. Without further experimental information, it is difficult to say more and we assume that the $\Delta n^*(x)$ profile is constant:

$$\Delta n^*(x) \;=\; \Delta n^*. \tag{4.20}$$

All things considered, the left hand-side of equation (4.18), obtained by absorption spectroscopy, is fitted by the right-hand side where $T(x)$ is given by equation (4.19) and $T_{\max}$, $\tilde{\nu}_0$ and $A = \frac{\sigma_0}{\tilde{\nu}_0}\sqrt{\frac{m_{\mathrm{Ar}}c^2}{2\pi k_{\mathrm{B}}}}\Delta n^*$ are the three fitting parameters. T_{edge} is fixed.

[2] The production term of n_1^* is proportional to $n_{\mathrm{Ar}} \times n_e$.

In Figure 4.12, the reconstruction procedure is applied to two different plasma conditions at the same location ($z \approx 4$ cm). In subfigure (a), for an argon plasma running at 15 mTorr and 200 W, the fitting procedure is able to reconcile the absorption and LIF measurements for $T_{edge} \approx 390$ K. If T_{edge} is lower than 390 K, T_{max} is constrained to be bigger than T_{LIF}. On the contrary, if T_{edge} is bigger than 390 K, T_{max} is constrained to be smaller than T_{LIF}. The value of 390 K appears much bigger than $T_{wall} = 325$ K measured on the outter surface of the thruster, as shown in Figure 2.20, meaning that a temperature jump of about 65 K can be deduced.

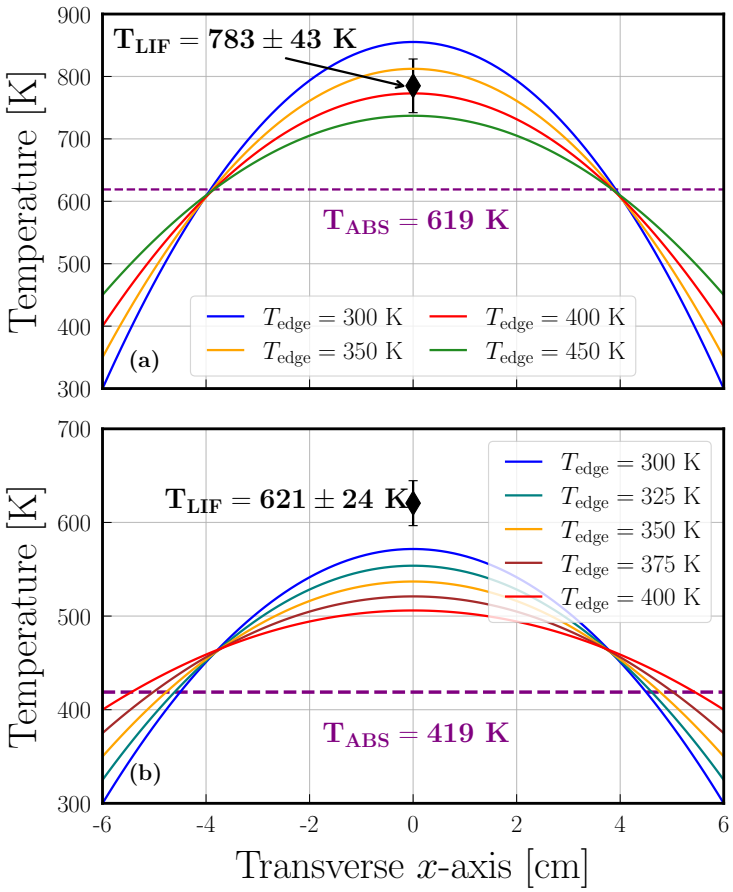

Figure 4.12: Reconstructed parabolic transverse temperature profiles (at $z = 3.7$ cm), for different values of T_{edge}, assuming a constant density profile. (a) 15 mTorr - 200 W. (b) 15 mTorr - 50 W.

In subfigure (b), for an argon plasma running at 15 mTorr and 50 W, no matching is found between T_{max} and T_{LIF} for a reasonable value of T_{edge}. Indeed, the assumption of a parabola shape for the temperature does not allow to reconcile absorption and LIF measurements. A temperature profile with stiffer gradients must be considered at low discharge power, which is in agreement with conclusions drawn from the study of Figure 4.10. Even if there are no physical reason for it, one could think of a temperature profile close to a Gaussian:

$$T(x) = T_\infty + (T_{max} - T_\infty) \exp\left[-\alpha \left(\frac{2x}{L}\right)^2\right]. \tag{4.21}$$

In that case, T_{max} and α will be the fitting parameters and T_∞ an input. T_{edge} is

finally equal to $T(\pm L/2) = T_\infty + (T_{max} - T_\infty)e^{-\alpha}$. In Figure 4.13, the reconstruction procedure is applied, once again to the case 15 mTorr-50 W at $z = 3.7$ cm, but with a transverse temperature gaussian profile, for different values of T_∞. A very good agreement is found for $T_\infty = 275$ K. It results in $T_{edge} = 327$ K and a temperature jump of about 25 K (by using the fitted formula of Figure 2.20).

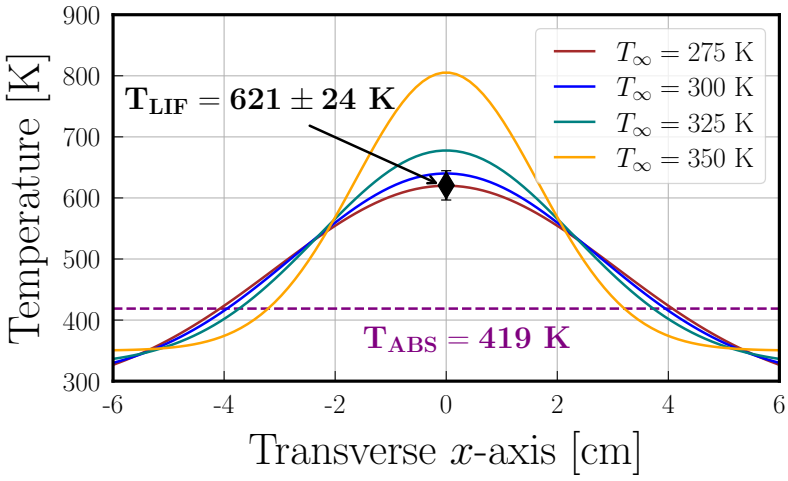

Figure 4.13: Reconstructed Gaussian transverse temperature profiles (at $z = 3.7$ cm, 15 mTorr and 50 W), for different values of T_∞, assuming a constant density profile.

4.2.2.3 What about ground state density measurements?

Once again, the absorption diagnostic being non local, no direct information about the argon atomic ground state density can be obtained without assuming spatial profiles. However, by using the LIF measurements, and by assuming that the plasma is everywhere isobar the absolute density measurements is derived from the equation of state of an ideal gas:

$$n_{Ar}(z) = \frac{p_{plasma}}{k_B T_{LIF}(z)}. \tag{4.22}$$

The same reasoning can also be applied to the transverse temperature profiles obtained in the previous subsection:

$$n_{Ar}(x) = \frac{p_{plasma}}{k_B T(x)}. \tag{4.23}$$

In Figure 4.14, the argon density profiles are plotted for a pressure of 15 mTorr and two discharge powers: 50 and 200 W. In the top subfigure, the density values along the thrust axis (z-axis) are directly calculated from LIF temperature measurements, presented in Figure 4.8. In the bottom subfigure, the reconstructed temperature profiles obtained in the last subsection at $z = 3.7$ cm are used to derive density profiles along the transverse x-axis. When the plasma is on, the atomic density appears much smaller than without plasma. This is explained by the increase of the exhaust velocity when the temperature increases.

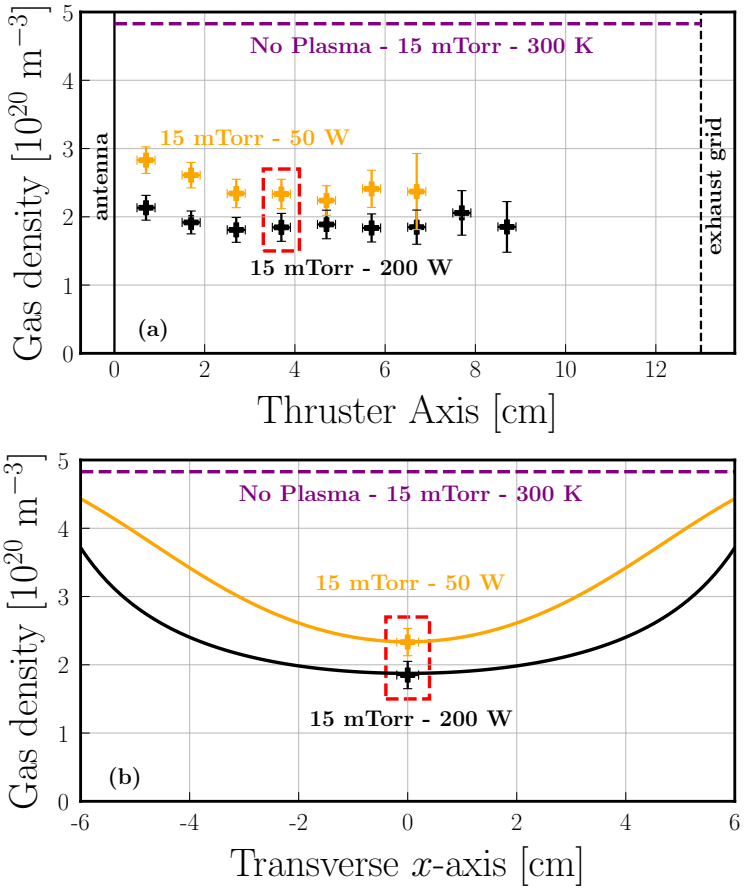

Figure 4.14: Ground state argon density spatial profiles at 15 mTorr and for two discharge powers: 50 and 200 W, obtained by assuming an isobar plasma. The red rectangle indicates the exact same position inside the discharge. (a) Spatial profile along the thrust axis. Values are calculated by using temperatures measured by LIF. (b) Spatial profiles along the transverse x-axis calculated by using the reconstructed temperature transverse profiles.

4.2.3 Iodine absorption spectroscopy at 11036.528 cm^{-1}

In this subsection, the implementation and results of an iodine plasma spectroscopic absorption diagnostic are presented. The temperature of an excited state of iodine is measured and the effect of the experimental conditions (position, pressure and discharge power) are studied. General conclusions on temperature measurements of neutral species in iodine plasma will be given at the end of the section when other optical diagnostics and their results will have been presented.

4.2.3.1 Optical setup and fitting procedure

The optical set-up used to perform absorption spectroscopy on iodine excited species inside the PEGASES thruster is shown in Figure 4.15, while the energy diagram of the probed levels was given in Figure 1.10.

The absorption transition occurs between the lower $(^3P_2)6s\ ^2[2]_{5/2}$ level and the upper $(^3P_2)6p\ ^2[2]^\circ_{7/2}$ around 11036.528 cm^{-1} (~905.8 nm). The setup is very similar as that used for argon in the previous subsection. Only the laser diode (DL 100 from

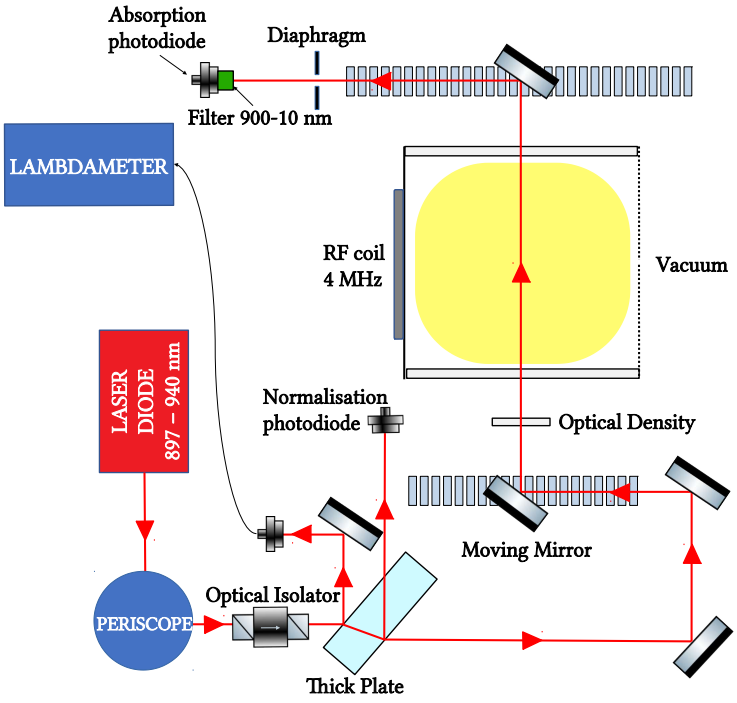

Figure 4.15: Schematics of the optical setup used for the iodine absorption spectroscopy at 11036.528 cm^{-1} (~905.8 nm). Mirrors are mounted on rails to perform measurements along the thruster axis. The photodiode has been displaced not to be disturbed by the strong plasma emission.

Toptica for wavelengths between 896.7 and 940 nm) and the bandpass filter (900-10 nm) have been changed to probe the chosen transition. Also, the photodiode has been displaced not to be disturbed by the strong plasma emission.

With iodine, the hyperfine structure must be taken into account and the absorption profile can no longer be considered as a simple Gaussian. Indeed, the transition probed occurs between the lower level of quantum number $J = 5/2$ and thus composed of six hyperfine levels (F in $\{0,1,2,3,4,5\}$) and the upper level of quantum number $J = 7/2$ also composed of six hyperfine levels (F in $\{1,2,3,4,5,6\}$) Thus, 16 transitions are allowed ($\Delta F = 0, \pm 1$) between 11036.2085 cm^{-1} and 11036.7266 cm^{-1}, where the energies of the levels are taken from [81] using the equation (1.7) (with $A = 47.27 \times 10^{-3}$ cm^{-1} and $B = -35.54 \times 10^{-3}$ cm^{-1} for the lower even level, and $A = 19.57 \times 10^{-3}$ cm^{-1} and $B = -36.84 \times 10^{-3}$ cm^{-1} for the upper odd level). The complete structure is provided in Marmuse's thesis [22] but since the laser diode used could only scan a maximum of 0.13 cm^{-1} in a row, we decided to work between 11036.36 and 11036.49 cm^{-1}. In this interval, 3 transitions occur. They are represented schematically in Figure 4.16a. The transition from $F = 5$ to $F' = 6$ (in red) occurs for a wavenumber $\tilde{\nu}_0$ which will be determined by the fitting procedure. The two other transitions occur at $\tilde{\nu}_1 = \tilde{\nu}_0 + \delta\tilde{\nu}_1$ ($F = 4 \rightarrow F' = 4$, in green) and $\tilde{\nu}_2 = \tilde{\nu}_0 + \delta\tilde{\nu}_2$ ($F = 3 \rightarrow F' = 2$, in brown) with $\delta\tilde{\nu}_1 = 0.020$ cm^{-1} and $\delta\tilde{\nu}_2 = 0.054$ cm^{-1}.

The absorption signal is fitted by assuming that each contribution is Gaussian at

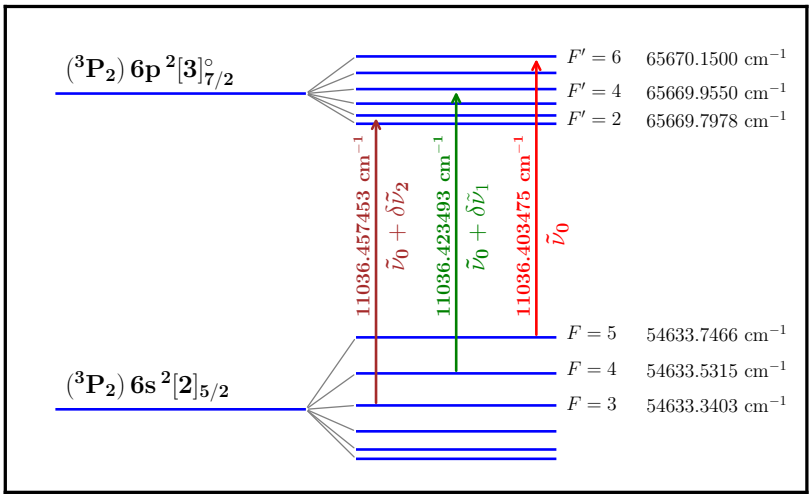

(a)

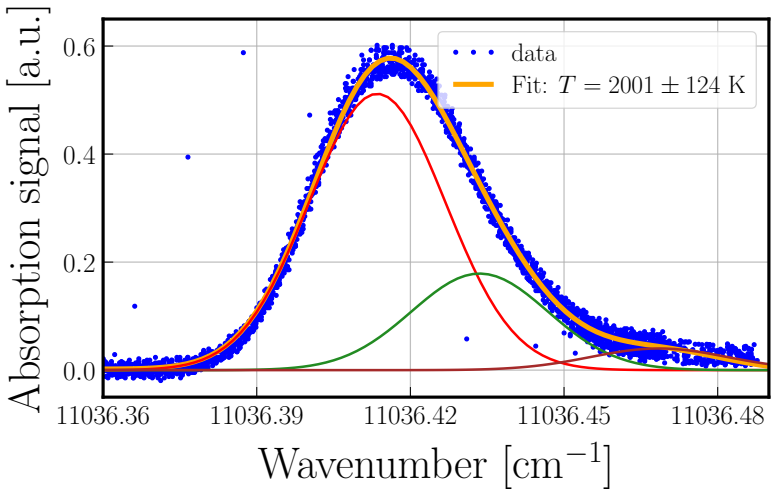

(b)

Figure 4.16: (a) Hyperfine structure of the 11036.46 cm^{-1} iodine transition. In this work, only the $F = 5 \rightarrow F' = 6$, $F = 4 \rightarrow F' = 4$ and $F = 3 \rightarrow F' = 2$ transitions are used. The energies and transitions values are taken from [81]. (b) Absorption signal measured in an iodine plasma running in PEGASES thruster at 22.5 mTorr-200 W (blue dots). The orange fitting curve, with a temperature 2001 ± 124 K (2-σ error bars), has been obtained using equation (4.24), the three Gaussian components are also plotted. The possible homogeneous broadening, not measured on this transition, is neglected.

the same temperature T. The fitting formula is:

$$d(\tilde{\nu}) = -\ln\left(\frac{I(\tilde{\nu})}{I_0(\tilde{\nu})}\right) = \sum_{k=0}^{2} D_k \exp\left(-\frac{m_I c^2}{2k_B T}\left(\frac{\tilde{\nu} - \tilde{\nu}_k}{\tilde{\nu}_k}\right)^2\right), \tag{4.24}$$

with D_0, D_1, D_2, $\tilde{\nu}_0$ and T the fitting parameters. Using Raccah algebra[3], D_0, D_1, D_2 are reduced to only one free parameter D, such that $D_0 = 0.796\,D$, $D_1 = 0.176\,D$ and $D_2 = 0.028\,D$. This relation is strictly valid if we neglect the homogeneous broadening, not measured on this transition. A typical signal, obtained at 22.5 mTorr-200 W, is given in Figure 4.16b. The three Gaussian components, maximum at $\tilde{\nu}_0$, $\tilde{\nu}_1$ and $\tilde{\nu}_2$, are represented as well as their sum (orange curve). As compared to [81] resonances values, a shift of about +0.01 cm^{-1} was noticed and could very well come from a wrong calibration of the wavemeter. The fitted temperature is 2001 ± 124 K. It is about three times what has been measured in argon for comparable plasma conditions. Such a difference can be explained by the molecular nature of iodine where atoms are essentially produced by dissociation processes that induce energetic fragments. Note, however, that the lower level used for the transition is not metastable but has a lifetime of 63 ns (de-excitation towards the ground state at 183.03 nm, $A = 1.6\times10^7$ s^{-1} [34]). Therefore, asserting that the measured temperature is that of the iodine atom in its ground state would be a very strong assumption.

Finally, a saturation analysis has been conducted (similar to the one presented with argon in Figure 4.5). Results are shown in Figure 4.17. In subfigure (a), the fitted optical depths are plotted as a function of the wavenumber for several laser powers. In subfigure (b), the optical depth maxima are plotted as a function of the laser power. The fitted formula of equation (4.11) has been applied to find $d_0 = 0.864$ and $P_{sat} = 451$ μW. The independence of the temperature measurement with the laser power variation was again observed but not represented. In practice, the experiments were conducted with a laser power of 15 μW.

4.2.3.2 Results

Let's start the discussion by looking at the spatial profiles obtained for different pressures (from 1.5 mTorr to 22.5 mTorr) and a discharge power fixed at 200 W, shown in Figure 4.18. The temperature profiles are plotted in subfigure (a) while the maximum of the absorption signals are presented in subfigure (b). Once again, pressure increases temperature and gives rise to gradients. At 1.5 mTorr, the temperature profile is rather flat (the maximum is around $z = 7$ cm) with values between 700 and 1000 K. At 5 and 15 mTorr, the temperature increases and the maximum of the profile gets closer to the antenna: the maximum values reached are respectively 1300 K at $z \approx 5$ cm and 1700 K at $z \approx 2.5$ cm. Finally, at 22.5 mTorr, the temperature keeps increasing but the localization close to the antenna fades, transport phenomena have appeared and induce a more symmetrical profile with a maximum, of more than 2000 K, at $z \approx 4$ cm and a temperature of 1300 K at $z \approx 10$ cm. The temperature jumps, already observed in argon, are again present and much more pronounced here. By extrapolation of the temperature profiles to $z = 0$ cm, the temperature jumps seem to reach several hundred Kelvin for the highest pressures. The value $T_{edge} \approx 600$ K seems a good approximation whatever the pressure. Note that in this study, the temperatures must be slightly overestimated due to the neglect of

[3]The relative weight of hyperfine transitions is given by the $6j$-coefficients [148]:

$$(2F'+1)\begin{Bmatrix} J & J' & 1 \\ F' & F & I \end{Bmatrix}^2.$$

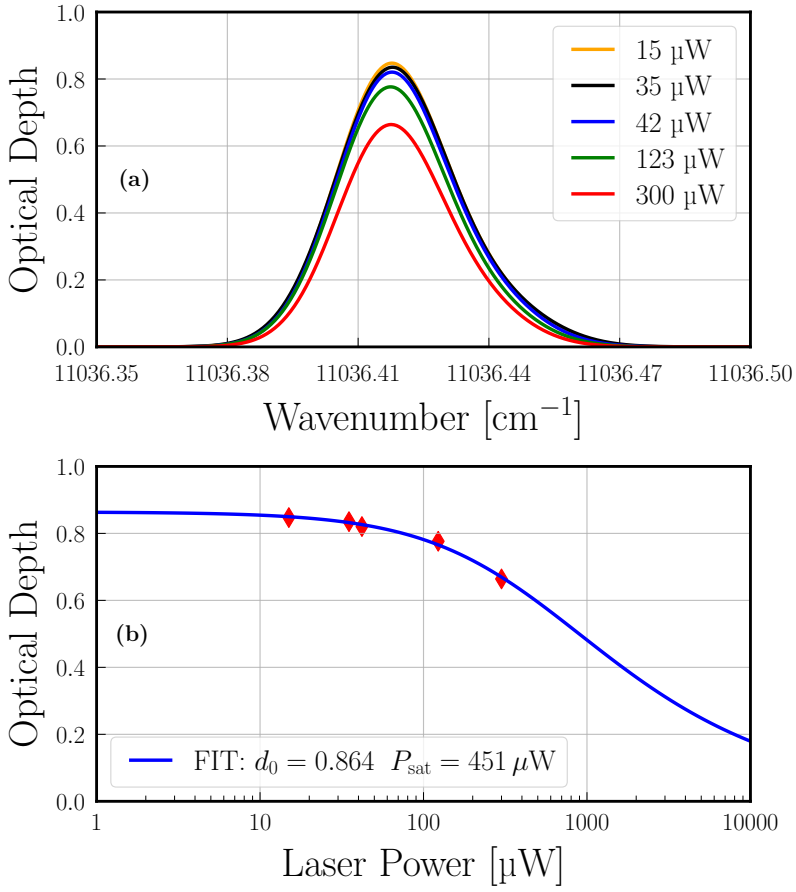

Figure 4.17: Saturation analysis of the 11036.46 cm^{-1} transition in a 15 mTorr-200 W iodine plasma. (a) The Gaussian fitted optical depth is plotted for five different laser powers. (b) The optical depth maxima are plotted as a function of the laser power [μW]. Equation (4.11) allows for the determination of d_0 and P_{sat}.

homogeneous broadening.

The signal amplitude (subfigure (b)) increases with pressure everywhere in the plasma. Except at 1.5 mTorr, where the profile has a dome-like shape centered around $z = 6$ cm, the profiles are localized near the antenna with a maximum at around $z = 1.5$ cm.

Finally, the effect of pressure and discharge power on temperature is studied in Figure 4.19. In subfigure (a), the influence of pressure was performed for a fixed discharge power of 200 W. As previously observed with the spatial profiles, increasing the pressure strongly increases the temperature. The effect of the discharge power, studied in subfigure (b), is less obvious. As we have already highlighted with Figure 2.12, the range of discharge power available to operate an iodine plasma in PEGASES is quite limited, especially for pressures above 2 mTorr. For instance, we are not able to operate an iodine plasma below 120 W or above 220 W at 15 mTorr. At 5 and 15 mTorr, a very slight increase with discharge power is observed. At 1 mTorr, the available range of discharge powers is wider but no clear effect is observed and the signals are too noisy to draw any conclusion. Such an almost constant behavior of the temperature with discharge power had already been observed by Marmuse in

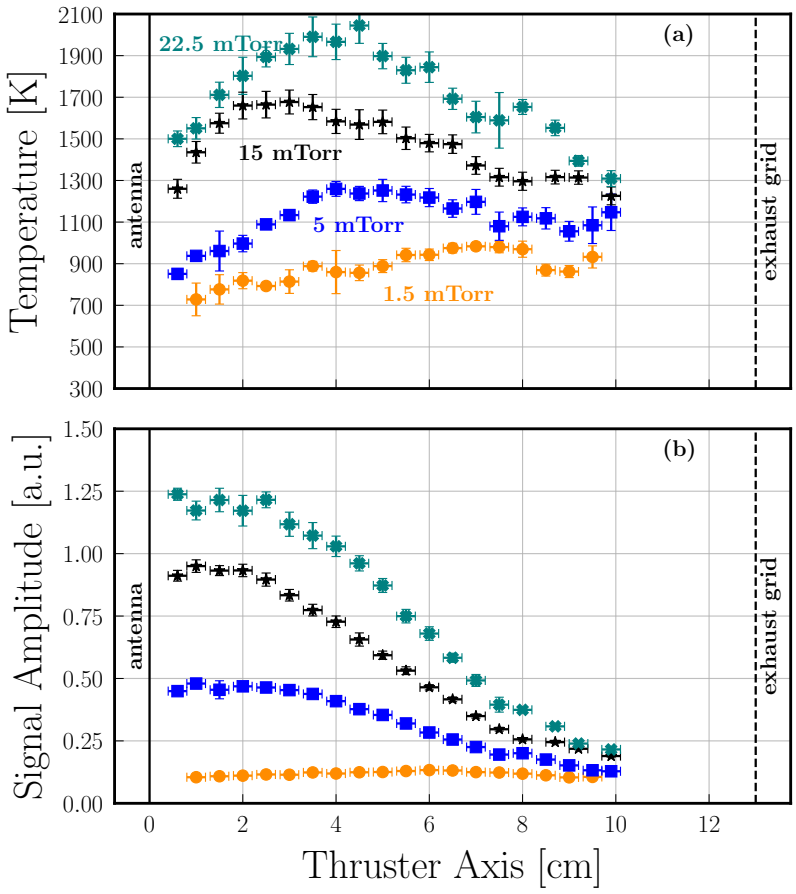

Figure 4.18: Spatial profiles obtained by using absorption spectroscopy around 11036.4 cm^{-1} in iodine plasmas generated in PEGASES thruster for pressures from 1.5 to 22.5 mTorr with a discharge power of 200 W. (a) Temperature of the excited iodine atoms [K]. (b) Absorption signal amplitude [a.u.].

his thesis [22]. This is most likely one of the limitations of the line of sight integrated absorption techniques: averaging strongly attenuates local gradients.

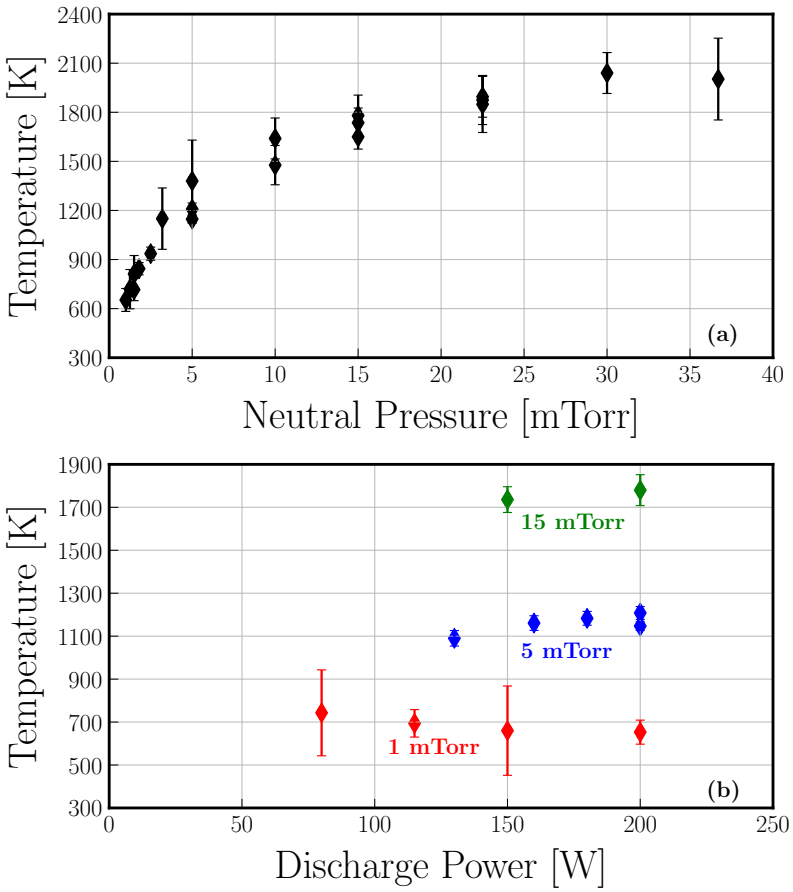

Figure 4.19: Influence of (a) the neutral pressure and (b) the discharge power, on the temperature of excited atoms measured, at z = 3.5 cm, by using absorption spectroscopy on iodine plasmas at 11036.4 cm^{-1}. The study with pressure was conducted at a fixed discharge power of 200 W.

4.3 Development of diagnostics for studying iodine ground state species

In the previous section, atomic temperature measurements in iodine plasmas were presented. However, they concerned a non-metastable excited atomic state with a short lifetime, most likely not thermalized, and with a population that is negligible compared to that of the atomic ground state $I_{3/2}$. In order to measure the temperature and absolute density of the atomic ground state, we had to develop more sophisticated diagnostics such as TALIF (to measure the atomic temperature and relative density) or to take advantage of the degeneracy of the ground state by studying, by laser absorption at 1315 nm, an optically forbidden transition (to access the density difference between the two degenerate ground state levels). The effective absorption cross section of this transition was measured by Ha *et al.* [49] with relative accuracy and the optical diagnostic already developed by Marmuse during his thesis [22]. Concerning the molecules, the dissociation rate is obtained by taking advantage of the photo-dissociation of the iodine molecule beyond 20000 cm^{-1}, using a laser diode at 488 nm. A similar method had been developed by Marinov *et al.* for chlorine plasmas [108] and used by Marmuse on iodine plasmas [22], but with a broadband light source leading to a more difficult interpretation of the results, despite the very precise knowledge of the effective absorption cross section (see [68] for iodine). The last two diagnostics lead to the absolute density of the atomic ground state.

While the ultimate goal is obviously to measure these quantities within the PEGASES thruster, the low working pressures (0.04 - 4 Pa) are hardly compatible with the development of efficient diagnostics and the obtaining of strong measurement signals. This is why, in the first instance, we used the iodine cell (whose pressure, before ignition of the plasma, is between 2 and 30 Pa), presented in Section 2.4 to perfect the diagnostics and learn crucial information about iodine plasmas.

4.3.1 Molecular absorption and dissociation efficiency in iodine plasma

In this first subsection, we take advantage of the purely dissociative part of the molecular absorption cross section, beyond 20000 cm^{-1}, to directly measure the dissociation rate in iodine plasmas. The relevant information for a good understanding of what follows has been given in the subsection 1.2.3.2.

4.3.1.1 Laser for molecular absorption

The I_2 molecule has a strong optical absorption cross section in the visible part of the electromagnetic spectrum, with a purely dissociative part, beyond 20000 cm^{-1} (i.e. below 500 nm) (see Figure 1.5). To study the absorption and deduce the molecular dissociation rate, we use the LBX-488 HPE diode-pumped blue laser from Oxxius. This very compact continuous wave laser ($40 \times 40 \times 100\,mm^3$) can emit up to 1 watt at a wavelength centered around 488.9 nm at its maximum power. The central wavelength of emission was measured using a miniature low-resolution fibre spectrometer (Flame from Ocean Optics) and was shown to shift towards the

blue as the power is decreased by the electronic controller (see Figure 4.20). The spectral profile is slightly asymmetric, with a FWHM of about 0.5 nm.

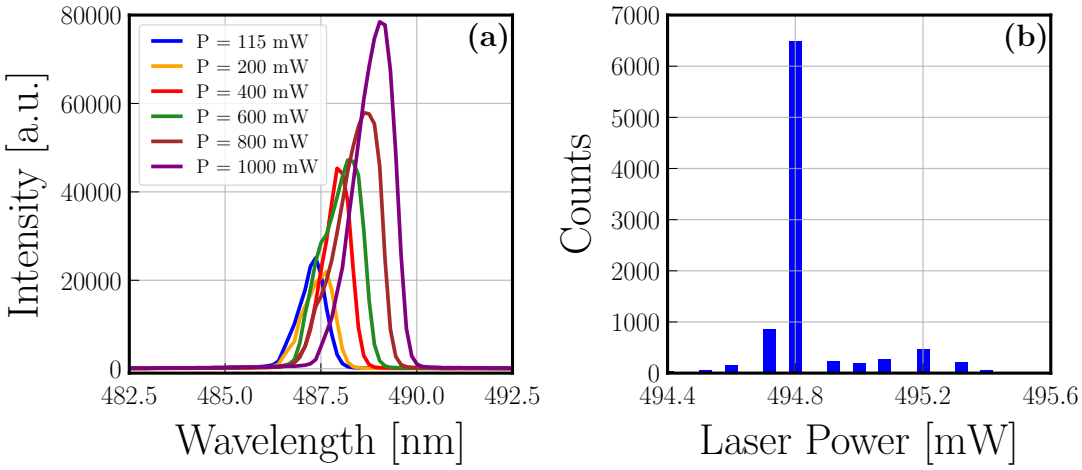

Figure 4.20: (a) Spectrum of the Oxxius laser as a function of power, recorded with a Flame spectrometer (Ocean Optics). (b) Power histogram (for a set point of 494.8 mW) recorded over 10 minutes with a 10 A powermeter (Ophir).

The laser beam is asymmetrical with a "top-hat" shape, and its dimensions are $6 \times 1\,\mathrm{mm}^2$ at the center of the cell. The laser power is stabilised by an internal photodiode. This stabilisation is important so that transmission measurements can be compared without having to measure variations in input power. A power measurement, recorded with an Ophir 10 A powermeter over a period of 10 minutes, is shown in Figure 4.20.

4.3.1.2 Measurement procedure

With the precise knowledge of the absorption cross section (shown in Figure 1.5), the measurement is straightforward. We record the power transmitted by the @ 488.9 nm CW laser through the cell for different values of applied RF power (see the experimental setup in Figure 4.21).

The plasma operating conditions can also be varied by changing the initial molecular density. Two examples of measurements are shown in Figure 4.22. When the plasma is switched off, the absorption is due to the density of the molecules present and the transmission increases when they are dissociated by the plasma. Two questions arise:

- A sharp increase in atomic temperature has been measured (and will be presented in subsection 4.3.2) as power and pressure increase. Does the effective cross section, well known at room temperature and for an equilibrium gas, remain the same in the plasma?

- The transmitted optical power seems to saturate as a function of plasma power, especially at low pressure. Can we conclude that a molecular dissociation rate of 100% is reached?

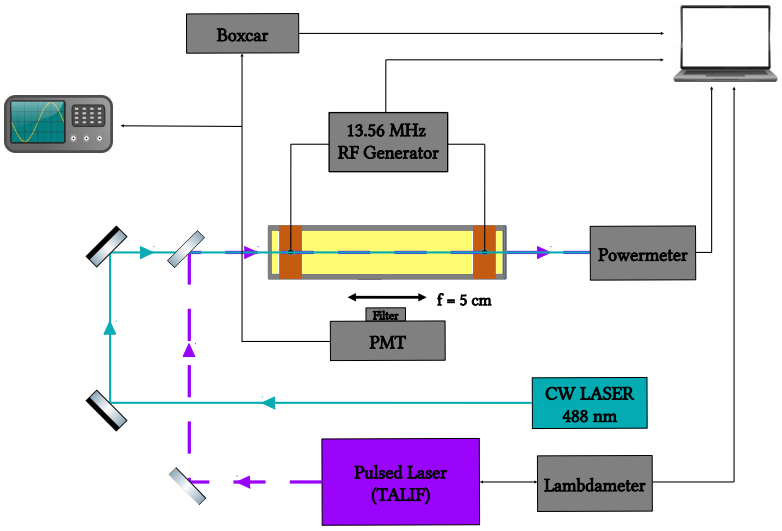

Figure 4.21: Experimental setup schematics. The continuous laser beam used for molecular photodissociation can be superimposed to the pulsed laser used for TALIF.

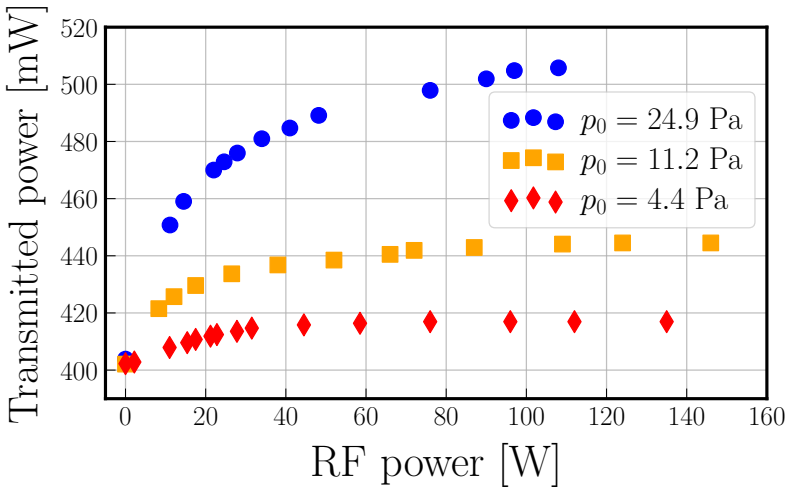

Figure 4.22: Optical transmission through the plasma cell as a function of the excitation power of the plasma, for two initial pressures. The input laser power was adjusted to get a transmitted power of about 400 mW when the plasma was OFF.

4.3.1.3 Variation of the absorption cross section with temperature

When the plasma is in operation, the temperature of the atoms can reach more than 1200 K (see subsection 4.3.2). In order to know the consequences of this heating on the molecular absorption spectrum, we first assume that the translation temperature of the molecules and the vibration temperature are equal to those of the atoms. In plasmas, other vibrational excitation mechanisms can occur through electron-molecule collisions. However, recent calculations [28] have shown that the reaction rates are negligible for the usual temperatures and electron densities (see discussion in subsection 1.4.2.4).

The values of the absorption cross sections are well known at room temperature [63], but change with temperature due to the change of the vibrational population (cf. [108] as an example of calculation for Cl_2). We propose to evaluate this dependence in the case of iodine by an approximate calculation of the absorption in the diffusive part of the spectrum, beyond 20000 cm^{-1}.

According to the Franck-Condon principle [59, 60], the probability of a transition between the ground level and a repulsive potential $V(r)$, is proportional to:

$$f_{v''}|\langle\epsilon'|\mu(r)|v''\rangle|^2, \tag{4.25}$$

where $|v''\rangle$ is the bound initial wave function of the vibrational level v'', $|\epsilon'\rangle$ is the free final function at continuum energy ϵ', $\mu(R)$ the dipole moment function and $f_{v''}$ the relative population. The energy ϵ' depends on the excitation wavelength according to :

$$\epsilon' = E_{v''} + h\nu, \tag{4.26}$$

where $E_{v''}$ is the energy of the v'' level.

In a first approximation, the wave function of the excited repulsive state can be replaced by a delta function, which is zero except at the classical turning point r_e [149]. The effect of a changing potential slope appears in the normalisation of the delta function, leading to a $[V'(r_e)]^{-1}$ factor [150, 151]. The electronic transition probability becomes proportional to :

$$[V'(r_e)]^{-1} f_{v''}\mu(r_e)|\phi_{v''}(r_e)|^2, \tag{4.27}$$

with r_e verifying the condition:

$$V(r_e) = E_{v''} + h\nu.$$

This assumption makes it possible to evaluate the transition probability without the knowledge of the wave functions of the continuum. The dependence of the partial absorption cross sections for each v'' on the wavelength is given by equation (4.27) and the sum of these partial cross sections is weighted, as a function of temperature, by $f_{v''}$ given by the relation :

$$f_{v''} = \frac{\exp(-E_{v''}/k_B T)}{\sum_{v''} \exp(-E_{v''}/k_B T)}. \tag{4.28}$$

As an example, we represent on Figure 4.23 the contributions for the first 8 vibrational levels (from 0 to 7), for four temperatures (300, 600, 900 and 1200 K), for the repulsive state $^1\Pi(1_u)$. As the temperature increases, the effective partial cross section for $v = 0$ decreases sharply but is compensated by the increase of the partial cross sections corresponding to the other vibrational levels. The absorption efficiency also increases towards the blue, due to the more populated v-levels, which have a radial wave function of larger spatial extension at short distances. The effect of the partial cross section compensation will be enhanced with two excited potentials.

To calculate the variation of the effective cross section as a function of temperature and taking into account the two excited potentials $^1\Pi(1_u)$ and $B^3\Pi(0_u^+)$, we used the following assumptions:

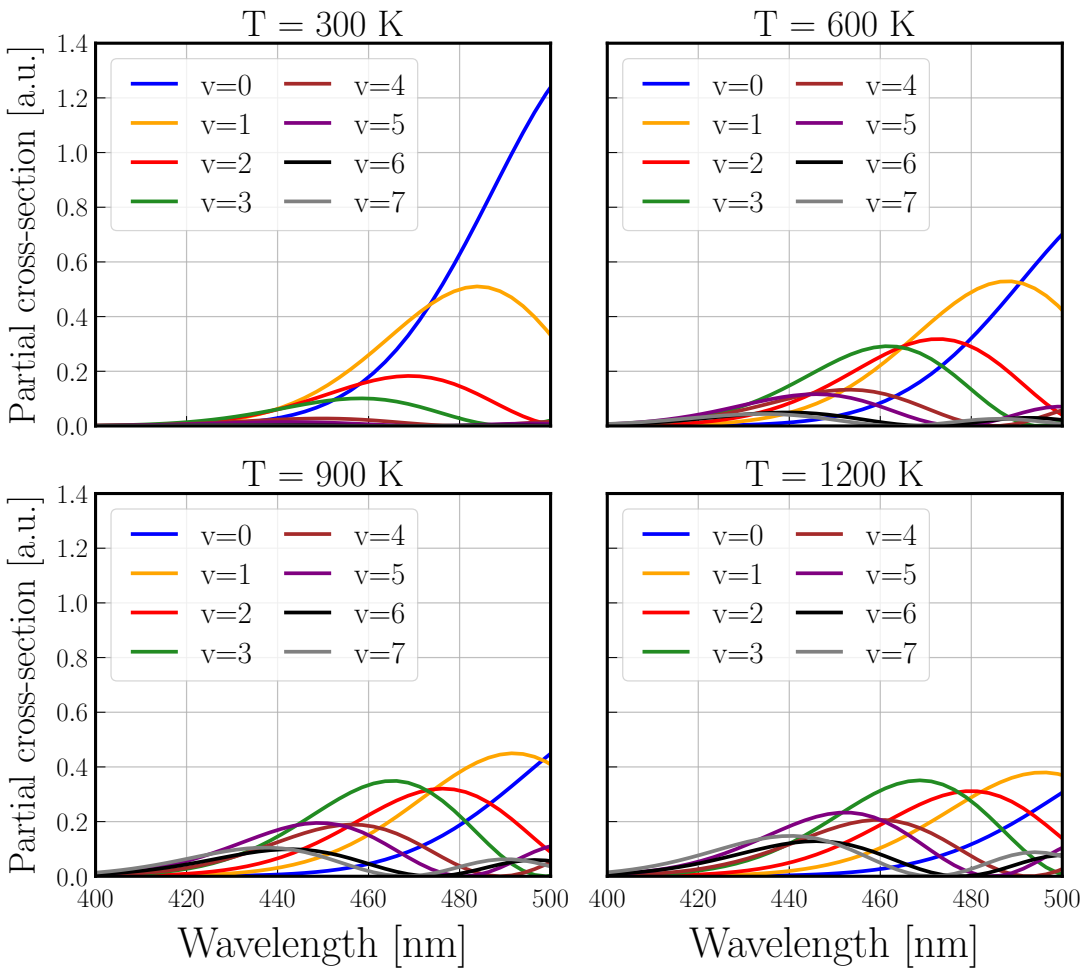

Figure 4.23: Partial absorption cross sections to the repulsive state $^1\Pi(1_u)$ for the first 8 vibrational levels (from 0 to 7) of the molecular ground state and for four temperatures (300, 600, 900 and 1200 K).

1. The vibrational levels of the ground state are described by a Morse potential [52] whose wave functions are known analytically.

2. At short inter-nuclear distances, the excited potentials are represented as exponential polynomials with the parameters of the reference [42]. This representation is usual for the $^1\Pi(1_u)$ state but less common for the $B^3\Pi(0_u^+)$ state, which has an attractive part at short distance. Nevertheless, since the intensity of the transition is determined by the shape of the repulsive branch of the potential in the Franck-Condon region, this potential can be described by a repulsive branch if the shape of the deduced wave function is the same at short range as that described by an attractive potential, such as a Morse potential. It is even possible to "continuumize" the spectrum even in the dissociation limit [152].

3. The dipole moments $\mu(r)$ of the $^1\Pi(1_u)$ and $B^3\Pi(0_u^+)$ states vary linearly with the internuclear distance [153].

4. Finally, to take into account the rotation, we calculate the spectrum for the

single rotational transition $J'' = J_{av}(T)$, where $J_{av}(T)$ is the average J value for the temperature [152].

We first compare our calculation with the experimental cross sections measured at room temperature by multiplying our result by a scaling factor. The results are presented in Figure 4.24. Despite the approximate model used, we reproduce the experimental cross section appropriately as a function of wavelength. We also present in the same figure the effective cross sections for 4 different temperatures. They vary very little at the wavelength used in the experiment (488.9 nm), with a variation of less than 5% for the different temperatures studied, around $1.72{\times}10^{-18}$ cm^2. In the rest of our analysis, we will neglect this variation.

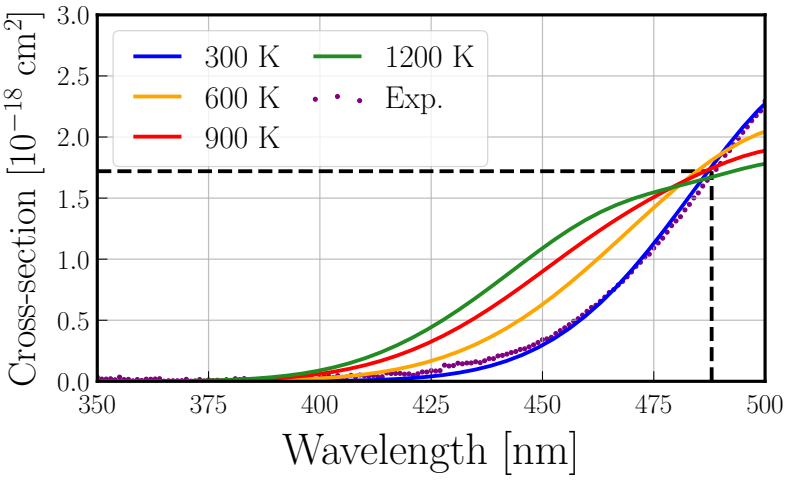

Figure 4.24: Calculated absorption cross sections from the molecular ground state X $^1\Sigma_g^+$ to the $^1\Pi(1_u)$ and $B^3\Pi(0_u^+)$ states for four different temperatures. A scaling factor has been applied to match our calculation and the experimental data from [68]. The vertical dashed line indicates the wavelength of our CW laser (488.9 nm). For this particular wavelength, the temperature has almost no effect on the absorption cross section and the value retained is $1.72{\times}10^{-18}$ cm^2.

4.3.1.4 Saturation: Are all molecules dissociated?

As the iodine cell is sealed, the transmission of the inner faces cannot be measured. However, we can get rid of this data by varying, without plasma, the pressure in the cell, by modifying the temperature of the "cold finger", and by verifying by the Beer-Lambert law (see equation (4.1)) the evolution of the transmission as a function of the pressure. In Figure 4.25 we plot the laser power either as a function of the cold finger temperature or as a function of the density calculated by assuming an ideal gas law and by using the empirical laws [50, 51] presented in Figure 1.2. At 488.9 nm, using the experimental value of $\sigma = 1.72 \times 10^{-18}$ cm^2, determined previously, a very good agreement is found. We deduce a transmitted power of $P_{\text{ref}} = 505.8$ mW when the molecular density goes to zero. It can be seen as the reference power laser value.

We now measure the dissociation rate for a given operating temperature of 1.8 °C. For this temperature, without plasma, the transmitted power is $P_{\text{off}} =$

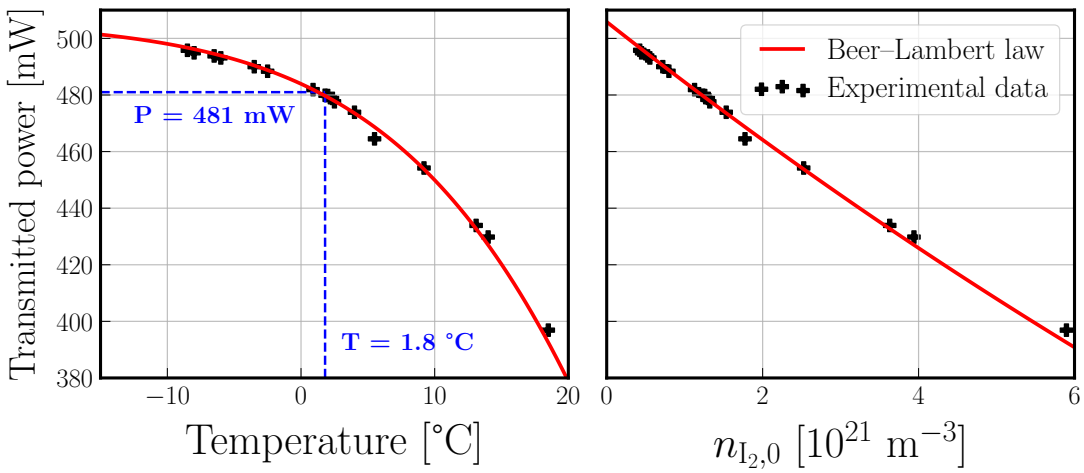

Figure 4.25: Transmitted laser power as a function of the "cold finger" temperature (left) and the initial molecular density (right) when the plasma is off. A very good agreement with the Beer-Lambert law is retrieved by using the previously determined absorption cross section of 1.72×10^{-18} cm^2. If the cell was empty ($n_{I_2,0} = 0$), a maximal transmitted power $P_{ref} = 505.8$ mW should be measured.

481 mW. We turn on the plasma for power values of 108 and 120 W, and record transmitted powers P_{on} of (501 ± 1) mW and (502.1 ± 1.5) mW respectively. The dissociation rate is defined as:

$$\eta = 1 - \frac{n_{I_2}}{n_{I_2,0}}, \tag{4.29}$$

with $n_{I_2,0}$ the initial molecular density (when the plasma is off) and n_{I_2} the molecular density when the plasma is on. By using Beer-Lambert law (equation (4.1)), one gets:

$$\frac{P_{on}}{P_{ref}} = \exp(-\sigma n_{I_2} L), \tag{4.30}$$

$$\frac{P_{off}}{P_{ref}} = \exp(-\sigma n_{I_2,0} L), \tag{4.31}$$

and finally,

$$\eta = 1 - \frac{\log(P_{on}/P_{ref})}{\log(P_{off}/P_{ref})}, \tag{4.32}$$

of 81 and 85%. This measurement shows that the dissociation rate, even when the transmitted power saturates with the plasma power, is less than 100%. The absorption measurement is an integrated measurement along the tube and there are still undissociated molecules on both sides of the two copper electrodes. As we can see in Figure 2.22, the plasma is often less bright in these regions.

Finally, the value of the density fixed by the "cold finger" temperature is quite compatible with the empirical data. We can deduce from the transmission without plasma a value of the initial laser power, by reversing the Beer-Lambert law. The dissociation rate or the value of the molecular density can be determined for different plasma conditions.

4.3.1.5 Dissociation rate for different plasma conditions

In Figure 4.26, two sets of measurements of the relative density $n_{I_2}/n_{I_2,0}$, are shown as a function of the plasma RF power for different initial pressures. Unfortunately, we could not compare all these pressures on the same graph because, due to the pollution of the cell at high plasma power, we had to change the electrical connectors and heat it strongly. Between these two series of recordings, the electrical coupling is different as well as the properties of the internal surface, which can play an important role in the recombination processes and in fine, in the plasma efficiency.

Nevertheless, we observe that at lower pressure, a lower electrical power is necessary to dissociate the molecules (even if the effect is not very strong). For example, on the left of Figure 4.26, 50 % of dissociation is obtained at 12 W for an initial pressure of 2.8 Pa whereas 26 W are necessary at 12.1 Pa of initial pressure. Note that, whatever the initial pressure and whatever the set of measurements, for enough RF power, the dissociation rate saturates and never exceeds 85 %.

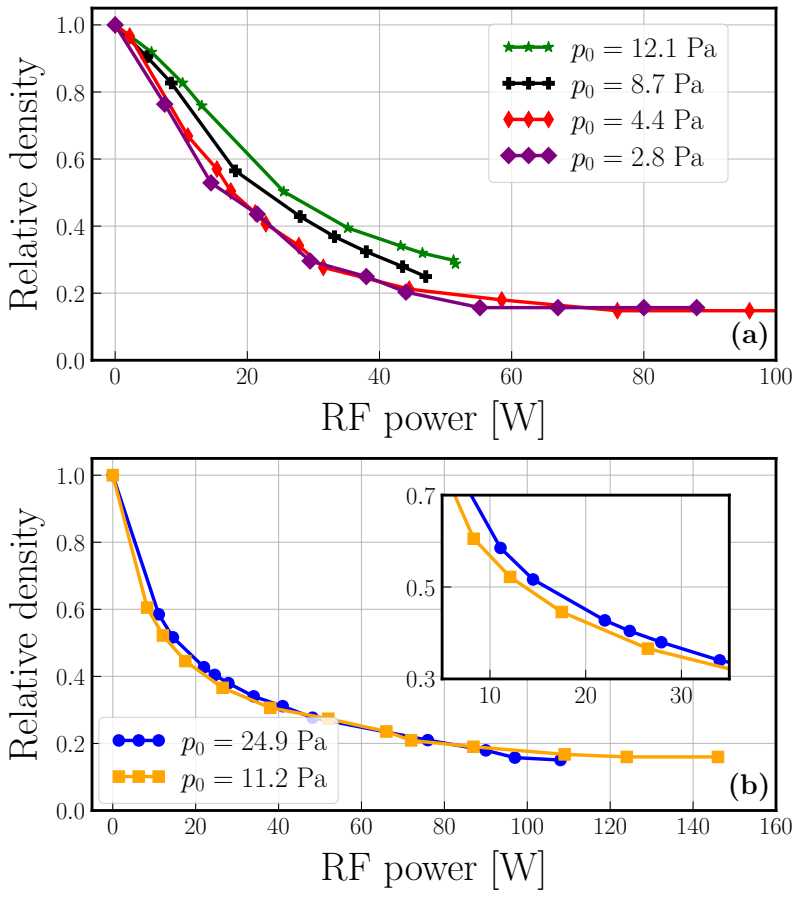

Figure 4.26: Measurements of the relative molecular density $n_{I_2}/n_{I_2,0} = 1 - \eta$ as a function of the plasma RF power for different initial pressures. Figures (a) and (b) represent two distinct sets of measurements that cannot be compared because the electrical configuration in each case was different.

4.3.2 TALIF from the atomic ground state

The TALIF method was introduced in Chapter 1. We simply recall that the first levels accessible by a two-photon odd-parity preserving transition, starting from the $5s^2 5p^5\,{}^2P^o_{3/2}$ ground level of I, are those of the $5s^2 5p^4 ({}^3P_2) 6p^o$ electron configuration, located around $65000\,cm^{-1}$. Among these, we mainly applied excitation towards the $({}^3P_2)6p\,{}^2[1]^o_{3/2}$ level, with detection of the fluorescence at 804 nm. Occasionally, we also excited the $({}^3P_2)6p\,{}^2[3]^o_{7/2}$ level, which fluoresces only at 905 nm. The reader can refer to Figure 1.11, where the energy diagram of the levels of atomic iodine, with the two-photon absorption and infrared fluorescence transitions used in the experiment are indicated.

4.3.2.1 Optical setup

The experimental scheme is shown in Figure 4.21. To produce the radiation around 300 nm, a commercial singlemode continuous titanium:sapphire (Ti:Sa) laser (Coherent MBR 110 pumped by a 10 W Verdi Nd:YAG laser) is used as the master laser to injection-seed a home-built nanosecond pulsed Ti:Sa (slave) laser [144]. The frequency of the seed laser (operating around 900 nm) was monitored by a wave-meter (Ångstrom WSU from High Finesse, with a measurement resolution of 5 MHz FWHM and a precision of 30 MHz) calibrated daily with a ^{133}Cs saturated-absorption stabilized diode laser. Reliability of the calibration process could be checked measuring the wavenumber of the other Cs D line, as explained in more details in Appendix D. The slave laser comprised a Ti:Sa crystal pumped at 532 nm by a 20 Hz frequency-doubled Nd:YAG laser (Quantel CFR200). The laser line-width, in the Fourier-transform limited regime, i.e. only limited by the finite duration of the pulse (about 6 ns), was about 25 MHz FWHM. The pulsed laser delivered 10 mJ pulses in the near infrared, which, after a stage of frequency doubling in a $5 \times 5 \times 10$ mm^3 AR-coated BBO crystal ($\theta = 25.6°$, $\phi = 0°$), produced radiation around 450 nm with an energy of about 2 mJ. Summation of the primary and secondary radiations in a $4 \times 4 \times 10$ mm^3 AR-coated BBO crystal ($\theta = 38.3°$, $\phi = 90°$) produced 300 nm pulses with an energy of about 1 mJ.

The generated beams were spatially separated using a fused-silica Pellin-Broca prism and the UV light was reflected by dielectric mirrors coated for the UV. In the cell, the size of the ultraviolet beam, as imaged by a UV camera beam profiler (Thorlab - BC106N-UV/M), was $1.28 \times 1.15\,mm^2$ (figures are for radii at $1/e^2$ times the peak intensity). At the output, the energy was recorded for each laser shot with a PC-interfaced laser energy meter (Pulsar from Ophir).

Fluorescence at 804 nm emitted perpendicularly to the laser beam was collected by a lens with a 50 mm focal length (2f/2f configuration), imaged onto a horizontal slit, passed through an interference filter (with a central wavelength of 800 nm and a 40 nm FWHM) to attenuate the background due to plasma emission, and detected with a red-enhanced photomultiplier (PM) (Hamamatsu R3896), with a gated voltage-divider circuit (Hamamatsu C1392-56) to avoid saturation by plasma emission. To compare the fluorescence between 804 and 905 nm, another PM was used (Hamamatsu R5108) with another interference filter (with a central wavelength of 905 nm, 10 nm FWHM). The fluorescence signal was observed with an oscilloscope (Lecroy 6100A) and recorded through a boxcar integrator (Stanford SR 280), with integration over a 200 ns temporal gate for each laser shot. A Labview™ program

was used to record the fluorescence intensity, the ultraviolet pulse energy and the seed laser wavelength.

4.3.2.2 Atoms produced by photodissociation

In subsection 4.3.1, we used a 488 nm laser to measure the rate of molecular dissociation. This laser has the advantage to also produce pairs of atoms by photodissociation. We will use these atoms to measure the lifetime of the $(^3P_2)6p\,^2[1]^o_{3/2}$ level (see below), in addition to the measurement in a plasma. Indeed, beyond 20000 cm^{-1}, light absorption in the diffusive part of the molecular spectrum leads to formation of atom pairs in states $I(^2P^o_{3/2}) + I(^2P^o_{3/2})$ or $I(^2P^o_{3/2}) + I(^2P^o_{1/2})$ [43], with a proportion of atoms in each level that depends on the wavelength [44, 45]. At the pressures used however (and because the plasma is off), the population in the $I(^2P^o_{1/2})$ level remains negligible, due to quenching by collisions with molecules (at rate $Q = K_{\text{quench},I_2-I_{1/2}} \times n_{I_2}$ with $K_{\text{quench},I_2-I_{1/2}}$ the quenching coefficient and n_{I_2} the molecular density), which leads to fast de-excitation of the $I(^2P^o_{1/2})$ level towards the equilibrium population with the ground state, at T_{gas}. For I_2, the value of coefficient $K_{\text{quench},I_2-I_{1/2}}$, $3.23\times10^{-17}\,m^3\,s^{-1}$ (see subsection 1.4.4.2), leads to de-excitation rates ranging from 1.5×10^4 to $3\times10^5\,s^{-1}$.

For atoms in the ground state, losses are dominated by wall recombination processes, the rate of which $K_{\text{wall,I}}$ makes wall removal of I atoms more important, for the pressures used, than three-body recombination, the rate of which is about $4\times10^{-42}\,m^6\,s^{-1}$ at 23°C [154]. The steady-state density n_I of iodine atoms produced is thus given by: $n_I = 2\sigma\phi n_{I_2}/K_{\text{wall,I}}$, where σ is the I_2 absorption cross section and ϕ the photon flux [118].

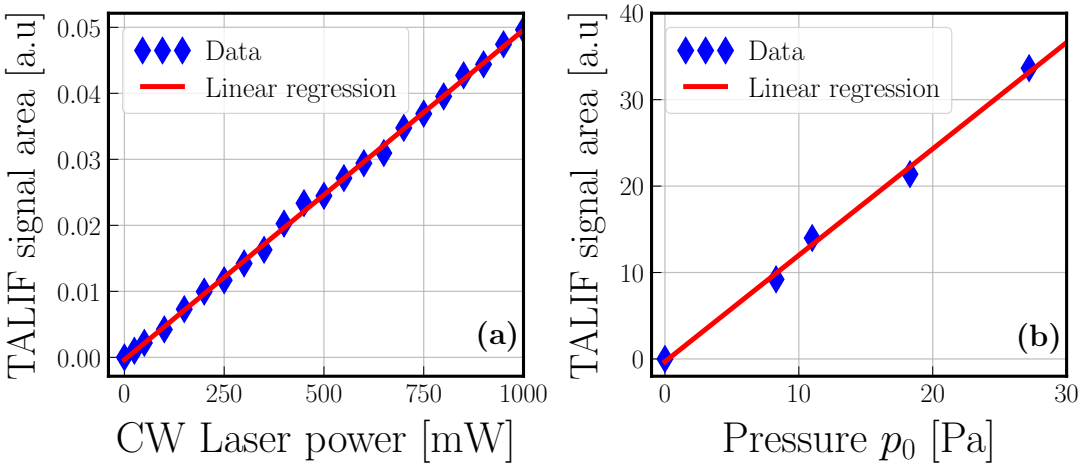

Figure 4.27: Frequency-integrated area of the TALIF signal at resonance towards the $(^3P_2)6p\,^2[1]^o_{3/2}$ level ($\sigma = 3\times11176.9940\,cm^{-1}$) recorded following molecular photodissociation. (a) As a function of CW laser power, for a pressure of 28.4 Pa, an energy of the pulsed laser of 320 μJ and a detection voltage V_{PM} = 0.65 kV. (b) As a function of pressure, for a CW power of 1 W, an energy of the pulsed laser of 160 μJ and a detection voltage V_{PM}=0.7 kV. The signals were averaged over 10 shots.

The photodissociation laser (which is the same than the one used to determine the dissociation rate in the previous subsection) is superimposed on the TALIF laser

(see Figure 4.21), with the last dichroic miroir, R_{max} around 300 nm, allowing the wavelength 488 nm to pass (cf. Figure 4.21). We detected the photodissociation-produced ground state atoms by TALIF following $^2P^o_{3/2} \rightarrow (^3P_2)6p\,^2[1]^o_{3/2}$ excitation. Figure 4.27 shows the evolution of the TALIF signal area as a function of the power of the photodissociation laser or of pressure, i.e. the molecular density. In both cases, the linear variation of the signal confirms that the dominant term for atom loss is the $K_{wall,I}$ term.

4.3.2.3 Atomic spectroscopy and temperature measurements

The temperature of the ground state atoms can be measured by TALIF spectroscopy using the Doppler broadening of the observed absorption profile. For this application iodine has two disadvantages: it is a heavy atom, the spectroscopic lines of which thus undergo relatively little Doppler broadening, and it has multiple transitions due to its hyperfine structure (linked to the nuclear spin $I = 5/2$ of the only naturally occurring isotope ^{127}I). One must thus disentangle the hyperfine structure from the Doppler-broadened profiles, in order to get unbiased temperature measurements. As a preliminary matter, the use of a high-resolution pulsed laser makes it possible to check the hyperfine structure quantitatively, both as concerns the positions and the relative intensities of the hyperfine components, by Doppler-free two-photon spectroscopy.

Doppler-free two-photon spectroscopy

When a gaseous sample is illuminated by two counter-propagating beams produced by the same laser, absorption of one photon from each beam leads to excitation with fully balanced 1st-order Doppler broadening, with all velocity classes contributing simultaneously, thus giving rise to a narrow resonance, the width of which reduces to the natural width [155]. In a plasma, this Doppler-free homogeneous bandwidth can be increased, however, by collisional dephasing, as observed, for example, in an oxygen glow discharge [144] or demonstrated with argon in the previous section.

The Doppler-free resonance signal appears superimposed on the ordinary Doppler-broadened profile that corresponds to absorption of two photons from the same beam. Figure 4.28 shows two Doppler-free spectra centered around the resonances from $5s^25p^5\,^2P^o_{3/2}$ to $(^3P_2)6p\,^2[1]^o_{3/2}$ and $(^3P_2)6p\,^2[3]^o_{7/2}$ levels, respectively. To record these Doppler-free spectra, a mirror was placed at the exit of the tube in order to reflect the beam along its original path.

The Doppler-free spectrum that we observe for the $(^3P_2)6p\,^2[1]^o_{3/2}$ and $(^3P_2)6p\,^2[3]^o_{7/2}$ levels are found to agree with the literature as concerns the hyperfine structure (within $0.002\,cm^{-1}$). A systematic shift of the barycenters by $-0.169\,cm^{-1}$ (i.e. towards lower energies) with respect to the figures of the NIST atomic spectra database [34] appears, however, the precision of which must be evaluated carefully. We therefore recommend a correction $-0.169(11)\,cm^{-1}$. For the interested reader, the explanation is given in Appendix D or in [2] and comes from an absolute mispositioning in energy of the excited levels with respect to the $5s^25p^5\,^2P^o_{1/2}$ level which had itself been inaccurately positioned. Such a shift could have been estimated from the literature.

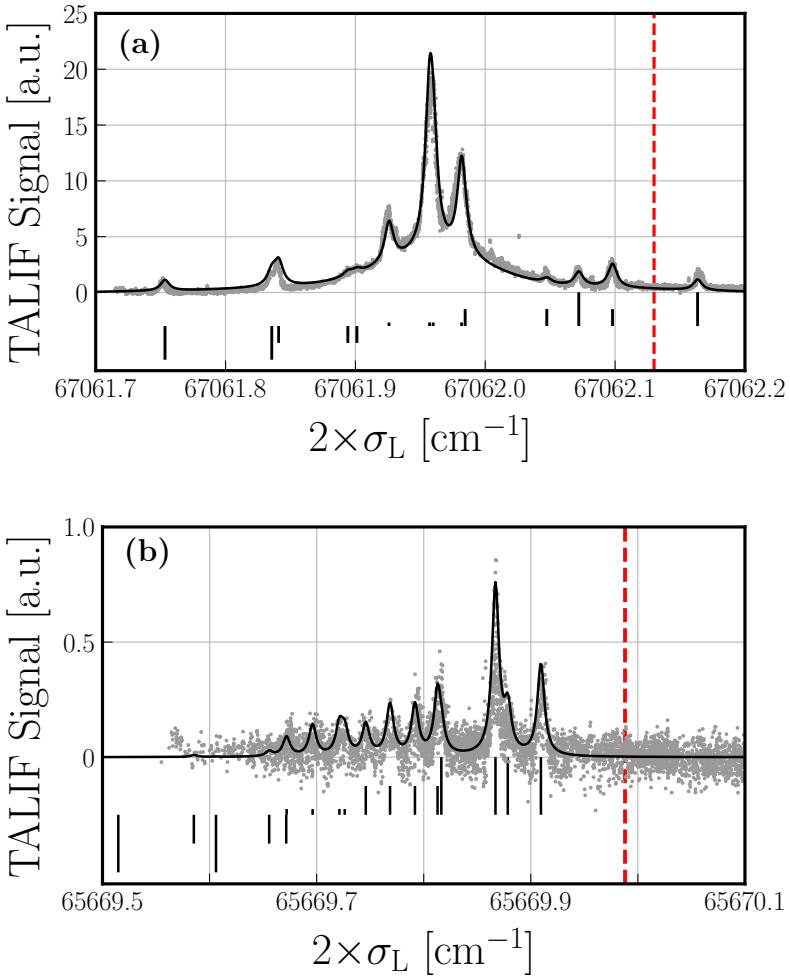

Figure 4.28: Fluorescence spectra in Doppler-free configuration. (a) $(^3P_2)6p\,^2[1]^o_{3/2}$ level of I around 67062.130 cm^{-1}. The atoms are produced in a plasma excited by a power of 20 W with an initial pressure of 5 Pa and detected with an R3896 PMT. The data points are fitted by the sum (continuous line) of a Doppler-free and a Doppler-broadened hyperfine multiplet, the former with a homogeneous linewidth of 0.0082 cm^{-1} and the latter assuming a translational temperature of 530 K. Relative weights of the hyperfine transitions are given in [2]. (b) Fluorescence following two-photon excitation of the $(^3P_2)6p\,^2[3]^o_{7/2}$ level of I around 65669.988 cm^{-1}. The atoms are produced in a plasma excited by a power of 40 W with an initial pressure of 25 Pa and detected with an RR5108 PMT. The black vertical segments show the positions of the hyperfine transitions, with a height proportional to the change ΔF of total angular momentum, in the [-2, +2] interval. In both cases, the hyperfine multiplet experimentally appears globally red-shifted by -0.169 cm^{-1} , with respect to the position given by the NIST atomic spectra database [34, 81].

Temperature measurement and relative density

For temperature measurements, we have probed the most favorable transition for two-photon excitation reachable with our laser system, to the level $(^3P_2)6p\,^2[1]^o_{3/2}$. We also checked the quadratic dependence of the TALIF signal on the laser intensity in the perturbative regime, with an energy not exceeding 400 μJ and using a colli-

mated beam. Focusing the laser beam with a 200 mm lens makes higher-order non-linear phenomena appear, like amplified spontaneous emission or photo-ionization, as well as a TALIF signal even in the absence of plasma excitation, due to molecular photo-dissociation. In the latter condition, the dependence of the TALIF signal on energy saturates.

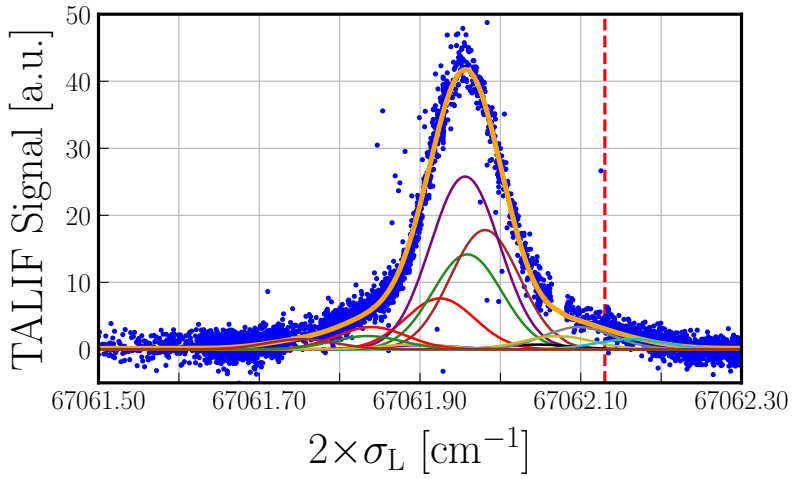

Figure 4.29: TALIF profile of the I $5p^5\,{}^2P^o_{3/2} \rightarrow ({}^3P_2)6p\,{}^2[1]^o_{3/2}$ line at an initial pressure $p_0 = 6.2\,\text{Pa}$ and with an RF power discharge of 40 W. The raw spectrum is shown together with a multi-peak Gaussian fit. The determined temperature is $T = 567 \pm 15\,\text{K}$. The contributions of the different hyperfine-structure components is also represented, with their respective weight. The red dashed line is the position of the barycenter of the transition, as given by [81].

An example of TALIF profile is given on Figure 4.29. The temperature is determined by a multi-peak Gaussian fit taking the different hyperfine components into account. Evolution of the temperature and of the relative density of I atoms in the ground ${}^2P^o_{3/2}$ level are shown in Figure 4.30, as functions of the excitation power and for different pressures. The temperature increases with the RF power, and this increase is all the more important as the pressure is high. It can go up to 1250 K due to the kinetic energy that atoms acquire during molecular dissociation, as already observed in Cl_2 [156] and confirmed by infrared laser absorption (see subsection 4.3.3). A measure of the relative ground state atomic density is given by the area of the TALIF signal. To compare the evolution of the density for different operating conditions, a scaling factor is applied to have the same slope at the origin, because the collection efficiency of the optical detection or the electronic gains can change from day to day. Moreover, we have not corrected the measurements by quenching, which can depend on temperature, and thus on power.

For different pressures, the ground state atom densities saturate with the RF power what must undoubtedly account for the saturation of molecular dissociation in the plasma. In any case, the decrease of the signal area explains why temperature measurements at high power are less accurate. The signal area saturates and the width of the Gaussian becomes wider and wider. Thus, the signal maximum decreases even more. In addition, the background noise, caused by plasma emission, also increases with the applied RF power.

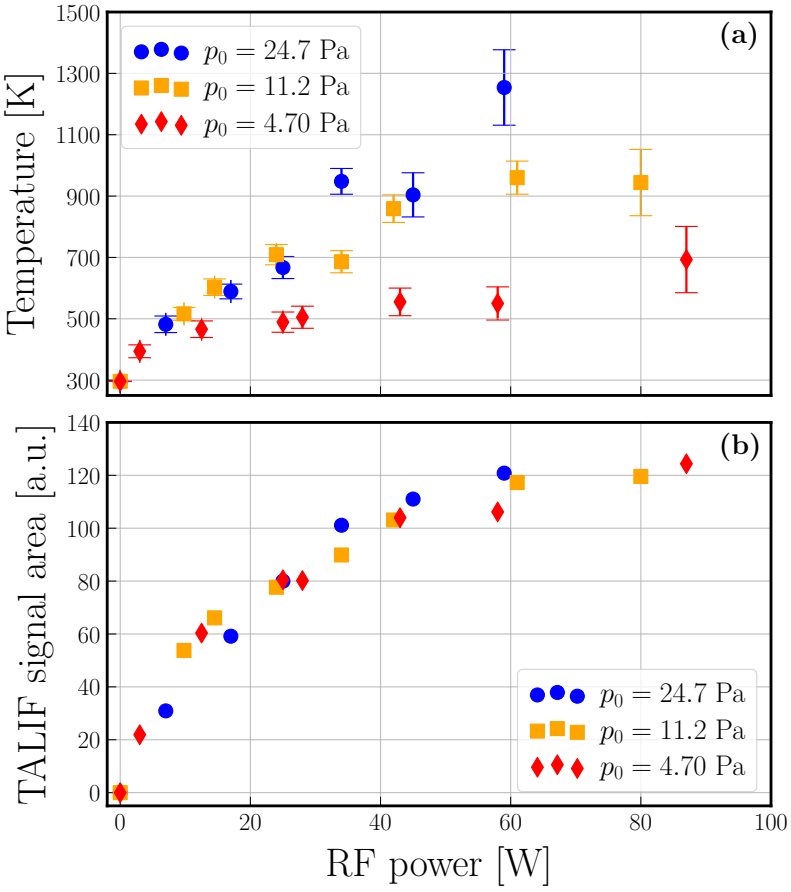

Figure 4.30: (a) Atomic gas temperature as a function of RF power for different pressures. (b) Relative area from TALIF signal as a function of RF power for different initial pressures.

I ($^2P^o_{1/2}$) detection

The population of atoms in the ground state saturates with RF power (cf. Figure 4.30), but in addition to the saturation of molecular dissociation (observed in subsection 4.3.1), it could be that the atoms are excited in the fine-structure excited $^2P^o_{1/2}$ level by electron collisions.

We have therefore tried to probe this level, taking the reduction of the excitation energy by the fine structure, numerically $7602.970(5)\,cm^{-1}$, into account. Within the limits of the wavelengths accessible to our laser system, we tried different excitation schemes (towards the $(^3P_1)6p\,^2[1]^o_{1/2}$, $(^3P_2)7p\,^2[2]^o_{3/2}$ and $(^3P_1)6p\,^2[2]^o_{3/2}$ levels), taking care to adapt the detection settings to each possible fluorescence scheme (which concerns both the filter and detector). We did not observe any signal, although we will show (in subsection 4.3.3) that this population is not negligible, which certainly means that the probed transition probabilities are very weak.

4.3.2.4 Measurement of the radiative lifetime of the $(^3P_2)6p\,^2[1]^o_{3/2}$ level

In order to measure the lifetime of the $(^3P_2)6p\,^2[1]^o_{3/2}$ states, we could produce atoms excited to that level either in a plasma or by photodissociation, and actually took ad-

vantage of the availability of these two methods. In a plasma, the number of atoms can be larger, so the TALIF response is bigger, but the signal is noisier (due to radio frequency excitation), with a larger background due to the electronic excitation of atoms followed by fluorescence. Moreover, as the RF power applied to the plasma increases, the gas heats up, the dissociation rate changes and the quenching coefficient gets modified because it depends on the molecular density. We have therefore limited plasma excitation to very low RF powers (between 2 and 8 watts). When atoms are produced by photodissociation, the signal is not noisy but weaker, because the density of neutral atoms produced is smaller, which limits the pressure range that can be used to above 8 Pa.

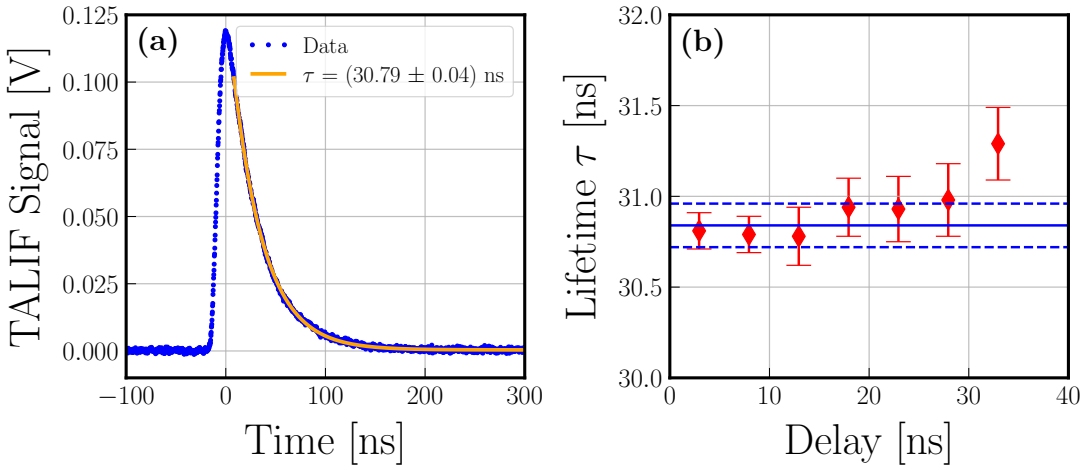

Figure 4.31: (a) TALIF signal recorded for a pressure of 19.1 Pa, with a photodissociation laser power of 1 W and a detection voltage V_{PM} = 0.7 kV. Numerical fitting gives a decay time of 30.95 ± 0.04 ns. (b) Dependence of the decay time on the initial delay of the interpolation. Eliminating the last point (at about 33 ns), the interpolation result gives a value for τ of 30.84 ns with an uncertainty of $2\sigma_{stat}$ = 0.1 ns.

Figure 4.31 shows an example of a TALIF signal record and the way it can be fitted with an exponential decay curve, taking into account both the detector fall time (2.2 × 1.5 ns) and the transit time spread (1.2 ns). A first term, in the uncertainty budget of the lifetime measurement, comes from the dependence of the output on the domain over which fitting is performed. The corresponding uncertainty is such that $2\sigma_{stat}$ = 0.1 ns in the example shown on Figure 4.31. A second term in the uncertainty budget appears, due to long term fluctuations that produce a systematic shift of each short term measurement, when the lifetime measurement gets repeated under identical conditions. The statistics of these more systematic fluctuations contribute another $2\sigma_{syst}$ = 0.4 ns.

Figure 4.32 shows a Stern-Volmer plot, i.e. the de-excitation rate of the TALIF signals as a function of pressure p_0, when atoms are produced either in a plasma or by photodissociation. The intercept at $p_0 = 0$ determines the radiative lifetime ($\tau = 1/A$) of the $(^3P_2)6p\,^2[1]^o_{3/2}$ states, as being 35.5 ± 0.9 ns. The linear variation of the de-excitation rate as a function of pressure gives the value of the quenching coefficient: $k_Q = (9.0 \pm 1.3) \times 10^{-10}\,cm^3\,s^{-1}$.

The lifetime of the $(^3P_2)6p\,^2[1]^o_{3/2}$ state has already been measured and calculated. Kono *et al.* [50] measured a value of 39^{+4}_{-8} ns, with large possible systematic

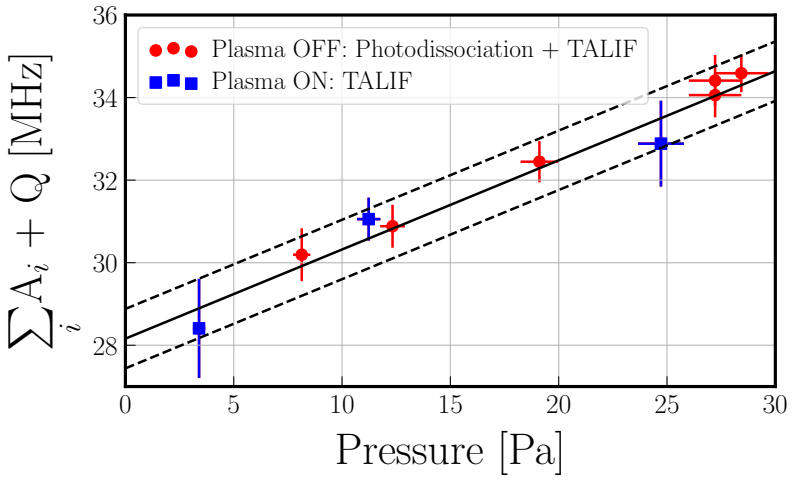

Figure 4.32: Stern–Volmer plot: de-excitation rate of the $(^3P_2)6p\,^2[1]^o_{3/2}$ TALIF signal against the pressure. The measurement points are obtained with a plasma (blue square) or by photodissociation (red point). The error on the pressure is determined by the error on the temperature of the "cold finger", estimated at 0.5°C. The error on the lifetime, represented at 2σ, is the sum of the statistic and systematic error. We have not represented the error on the slope, which is ± 7 %.

errors. Recently, new calculations of probabilities for some atomic iodine transitions yielded a τ value of 32.5 ± 1.2 ns [30]. While coming closer to calculation than the former measurement, our result shows a slight discrepancy of theory with respect to experiment, which can open the way to more precise investigations.

4.3.3 Atomic absorption at 7602.970 cm^{-1} (1315 nm)

The transition $5s^25p^5\ ^2P^\circ_{3/2} \rightarrow 5s^25p^5\ ^2P^\circ_{1/2}$ in atomic iodine at 7602.970 cm^{-1} is used to measure the line of sight averaged density and temperature of the iodine I atom by absorption spectroscopy. This transition and its six hyperfine components have been presented in subsection 1.3.2.1. The total integrated absorption cross section, $G = \int_{\tilde{\nu}} \tilde{\nu}^{-1}\ \sigma(\tilde{\nu})\ \mathrm{d}\tilde{\nu} = (1050 \pm 250)$ fm^2, was measured by diode laser absorption spectroscopy [49], as well as the relative strength $Q(F, F')$, for the transition $F' \leftarrow F$, of the different hyperfine components. This experiment was proposed and implemented by Marmuse [22] on the PEGASES thruster but the neglect of the upper level population has led to a misinterpretation of the results that we wish to rectify.

4.3.3.1 Optical setup

The absorption spectroscopy optical setup is represented Figure 4.33. An grating-stabilized external cavity diode laser (Toptica DL100) is used to produce the near-IR beam around 1.315 μm. The diode wavelength is varied by simultaneously scanning the diode current and the grating angle through a piezo-actuator. An infrared wavemeter (High Finesse WS-U IR) allows the relative measurement of the wavenumber. The beam passes through the cell once and its intensity is monitored by an amplified InGaAs photodiode placed behind an IR band-pass filter. The electrical signal is recorded through a NI-DAQ USB system controlled though a Lab-

VIEW™ program. To avoid any saturation (which was checked), only a reflection of the incident beam passes through the cell.

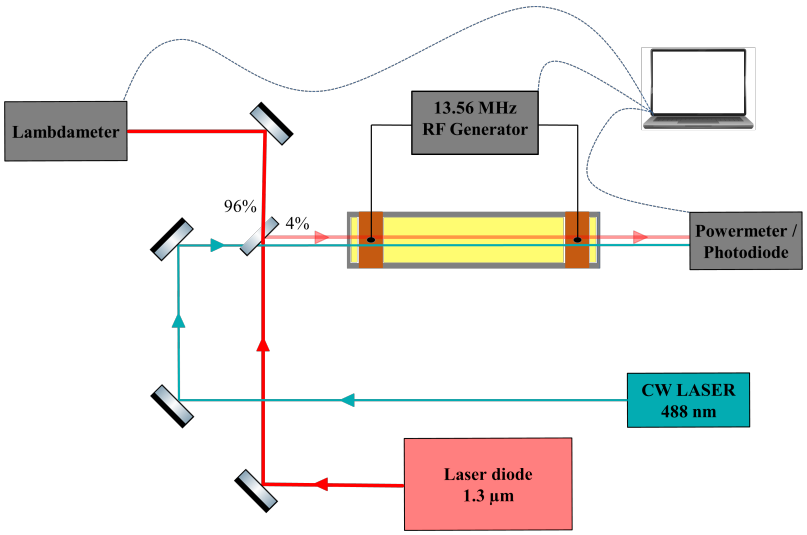

Figure 4.33: 1315 nm absorption spectroscopy setup used with the iodine cell.

4.3.3.2 Absorption spectra

Due to the limited scan range of the laser, the peaks had to be acquired in different records. With the interval of the position of the peaks and the relative strength of the transitions, the identification is easy. Then, to increase the sampling of the recorded points, we can limit the scan to one transition. Generally, we used the $3 \leftarrow 4$ transition which presents the most intense absorption ($Q(4,3) = 0.375$ from [49]). An example of recording and fitting is shown in Figure 4.34.

The absolute position of the resonance is shifted towards the blue by about 0.1 cm^{-1} because we do not have a reference wavelength source in the IR for absolute calibration. The transmitted intensity, apart from absorption, varies linearly due to the change in diode current for scanning, which results in a power variation of about 5%. The signal is normalized by turning off the laser to measure any background noise caused by the plasma emission, and by setting a transmission of 1 to the wavenumber corresponding to the resonance position. Here, to avoid saturation, only 4 % of the laser beam is directed to the iodine cell, while 96 % of the beam is sent to the lambdameter to minimise acquisition time. We have not carried out a systematic study of I_{sat} (as shown in Figures 4.5 and 4.17), in particular because the signal is rather weak, only of a few %. Nevertheless, for a plasma with an RF power of 23 W and an initial pressure $p_0 = 27.25$ Pa, decreasing the laser intensity (20 mW/cm^2) by a factor of 3 did not change the absorption signal.

4.3.3.3 Temperature and population difference density

During the operation of the plasma, the population of the $^2P^\circ_{1/2}$ is expected not to be negligible because the energy gap between both levels is only of 0.9426 eV, with an estimated electron temperature between 1 and 5 eV. Under these conditions, the

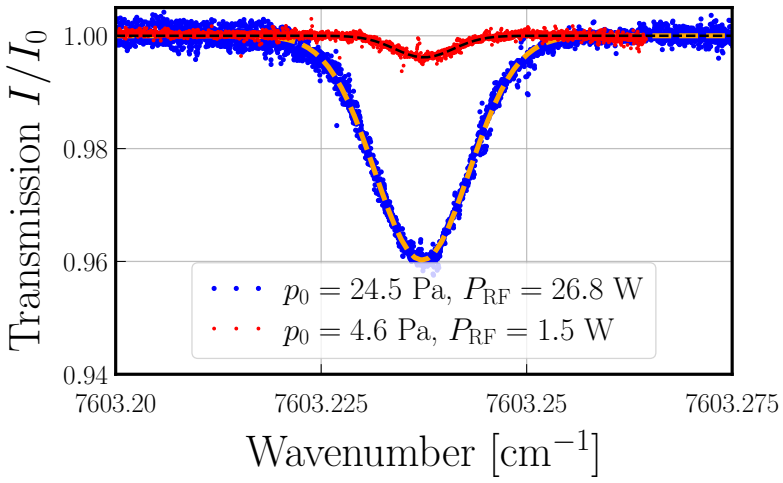

Figure 4.34: Measured absorption profile for the $^2P^\circ_{3/2}$ ($F = 4$) to $^2P^\circ_{1/2}$ ($F' = 3$) hyperfine transition as a function of the laser wavenumber, for a typical signal and for the signal with the minimum recorded absorption. The dashed-lines represent a fit of the experimental data. For the initial pressure of 24.5 Pa and a RF power of 26.8 W, the temperature is 774 ± 18 K and the population difference density Δn =7.6×10^{14} at/cm^3. For the minimal recorded absorption, with an initial pressure of 4.6 Pa and a RF power of 1.5 W, the temperature is 306 ± 24 K and the population difference density is 4.6×10^{13} at/cm^3.

averaged population difference along the line of sight is defined as:

$$\Delta n \;=\; n_{I_{3/2}} - \frac{g_{I_{3/2}}}{g_{I_{1/2}}} n_{I_{1/2}} \;=\; n_{I_{3/2}} - 2n_{I_{1/2}}, \tag{4.33}$$

with notations introduced in Chapter 1. Then, we recall that

$$d(\tilde{\nu}) = \sigma(\tilde{\nu})\,\Delta n\, L, \tag{4.34}$$

and the reference [49] gives the integrated absorption cross section:

$$G \;=\; \int_{\tilde{\nu}} \tilde{\nu}^{-1}\, \sigma(\tilde{\nu})\, \mathrm{d}\tilde{\nu}. \tag{4.35}$$

Therefore, after dividing the relation (4.34) by $\tilde{\nu}$, and neglecting the variation of wavenumber across the transition ($\tilde{\nu}_0 \approx \tilde{\nu}$, with $\tilde{\nu}_0$ the central wavenumber of the transition), one gets:

$$\tilde{\nu_0}^{-1} \int_{\tilde{\nu}} d(\tilde{\nu})\, \mathrm{d}\tilde{\nu} = G\,\Delta n\, L. \tag{4.36}$$

In our case, only one transition is considered ($3 \leftarrow 4$) and the absorption peak is modeled as a Doppler-broadened peak, similar to what we did for argon with equation (4.9):

$$d(\tilde{\nu}) \;=\; -\ln\left(\frac{I(\tilde{\nu})}{I_0(\tilde{\nu})}\right) \;=\; d_0 \exp\left(-\frac{m_I c^2}{2k_B T_I}\left(\frac{\tilde{\nu}-\tilde{\nu}_0}{\tilde{\nu}_0}\right)^2\right). \tag{4.37}$$

The peak width is determined only by Doppler broadening if we can neglect the one due to the collision. This spectral broadening is inverse to the relaxation time of the coherences, τ_2, which depends on τ_1, the excited-state decay, and the collisional dephasing rate γ_{col} as: $1/\tau_2 = 1/(2\tau_1) + \gamma_{\text{col}}$. $1/\tau_1$ depends on the quenching rate $Q = n_{\text{I}_2} \times k_Q$ (with k_Q the quenching coefficient) and spontaneous emission by the Einstein coefficient A: $\frac{1}{\tau_1} = A + Q$. At the pressures used (from 1.5 to 30 Pa), $1/\tau_1$ can reach a maximum of 0.2 MHz [113]. The determination of γ_{col} is more difficult, but can be done by Doppler-free spectroscopy with a spectraly narrow laser. To fix an order of magnitude, it has been shown that in an oxygen plasma (and with pressure of 67 Pa) that the decay time of the coherence is about 16 times shorter than the decay time of the population because of electronic, atomic and molecular collisions in the plasma [144]. Taking this order of magnitude (similar to what we found with argon in Section 4.2), we obtain for $1/\tau_2$ a width of about 3.2 MHz, well below what can be expected as Doppler broadening (FWHM $\simeq$ 250 MHz at 300 K).

In practice, the optical depth maximum d_0 and the temperature T_{I}, deduced from the Gaussian fitted signal, gives the population difference density Δn by combining equations (4.37) and (4.36):

$$\Delta n = \frac{d_0}{Q(4,3)\,G\,L}\sqrt{\frac{2\pi k_{\text{B}} T_{\text{I}}}{m_{\text{I}} c^2}}, \tag{4.38}$$

where $Q(4,3)$ is introduced because we only fitted the $3 \leftarrow 4$ trasition peak of the full spectrum.

4.3.3.4 Relative ground state population

In the example of Figure 4.34, the plasma power was $P_{\text{RF}} = 26.8$ W and the initial molecular density was $n_{\text{I}_2,0} = 6.05 \times 10^{21}$ m^{-3} ($p_0 = 24.5$ Pa). Interpolation by the Beer-Lambert law yields a temperature of 774 K and a population difference density of 7.6×10^{20} m^{-3}. While the temperature is close to what was measured with TALIF (see next subsection for a more detailed comparison between both methods) the density value is relatively small as compared to $n_{\text{I}_2,0}$ and indicates that the population in the $^2\text{P}^\circ_{1/2}$ upper level could be significant. Indeed, under very similar plasma conditions, we recorded a dissociation rate η of 61% (cf. Figure 4.25). If all the atomic density was in the $^2\text{P}^\circ_{3/2}$ state, the value of Δn would be: $n_{\text{I}_{3/2}} = 2\eta n_{\text{I}_2,0} = 7.38 \times 10^{21}$ m^{-3}. There is a factor 10 of difference between the two results and the discrepancy probably comes from the population of the $^2\text{P}^\circ_{1/2}$ level.

However, we can combine the 2 distinct measurements to have access to the relative density populations, noted $n_{\text{I}_{3/2}}$ for $^2\text{P}^\circ_{3/2}$ and $n_{\text{I}_{1/2}}$ for $^2\text{P}^\circ_{1/2}$. The measurements are linked such that:

$$2\,\eta\, n_{\text{I}_2,0} = n_{\text{I}_{3/2}} + n_{\text{I}_{1/2}}, \tag{4.39}$$

$$\Delta n = n_{\text{I}_{3/2}} - 2n_{\text{I}_{1/2}}, \tag{4.40}$$

which leads to the populations:

$$n_{\text{I}_{3/2}} = \frac{4}{3}\eta\, n_{\text{I}_2,0} + \frac{1}{3}\Delta n, \tag{4.41}$$

$$n_{\text{I}_{1/2}} = \frac{2}{3}\eta\, n_{\text{I}_2,0} - \frac{1}{3}\Delta n. \tag{4.42}$$

Continuing with the same example, we find $n_{I_{3/2}} = 5.17 \times 10^{21}$ m^{-3} and $n_{I_{1/2}} = 2.21 \times 10^{21}$ m^{-3}, so there are 29.9 % of atoms in the $^2P^\circ_{1/2}$ level in these plasma conditions.

To conclude, the influence of the error bar on the experimental determination of G (1050 ± 250 fm^2 [49]), must be evaluated. In Table 4.1, we detail what would be the results on the same example but for different values of G.

Table 4.1: Influence of the integrated absorption cross section G on the measured densities.

G [fm^2]	Δn [10^{21} m^{-3}]	$n_{I_{3/2}}$ [10^{21} m^{-3}]	$n_{I_{1/2}}$ [10^{21} m^{-3}]	$n_{I_{1/2}}/(n_{I_{1/2}} + n_{I_{3/2}})$
800	1.00	5.26	2.13	28.8 %
1050	0.76	5.17	2.21	29.9 %
1300	0.62	5.13	2.25	30.5 %

While the effect on Δn is direct and substantial through equation (4.38), the effect on the densities is minor (only a few percent for $n_{I_{3/2}}$ and no more than 5% for $n_{I_{1/2}}$ and its relative atomic population) because in the example studied, $\eta = 0.61$ so that $\eta \times n_{I_2,0} \gg \Delta n$. In this case, the densities values are mostly determined by the term $\eta \times n_{I_2,0}$ in equations (4.41) and (4.42). However, for very low dissociation rates, $\eta \times n_{I_2,0}$ might be comparable to Δn. In that case, an error on G directly induces an error on the densities.

4.3.3.5 Measurements in the plasma

The results of the combined atomic absorption at 1315 nm (to measure the atomic temperature T_I and the average population difference along the line of sight Δn) and the molecular absorption at 488 nm (to measure the dissociation rate η) are gathered in Figure 4.35. The effect of the RF power is studied for three different pressures: 24.5 Pa, 11.9 Pa and 4.6 Pa. The dissociation rate values are extracted from measurements presented in Figure 4.26. The initial operating pressure are not exactly the same between both measurements but still very close so considered equal.

In subfigure (a), the temperature increases with both pressure and power. The behaviors are very similar to what was measured by using TALIF and presented in Figure 4.30. However, TALIF temperatures are always hotter than the temperatures measured by absorption. At 11.9 Pa, for instance, the absorption temperature reaches around 725 K while more than 900 K was measured by using TALIF for a similar initial pressure. The discrepancy is explained by the non-local and integrated measurement of the absorption while the TALIF signal emanates from the center of the discharge, where the temperature is higher. A saturation is reached for a sufficient high RF power, probably coming from the increase of the iodine thermal conductivity when the temperature increases (see Chapter 5 for the expression of the thermal conductivity).

The measured average population differences along the line of sight Δn are plotted in subfigure (b). Both pressure and RF power make Δn increase. The densities $n_{I_{3/2}}$ (full markers) and $n_{I_{1/2}}$ (open markers) are plotted in subfigure (c) and exhibit the same behavior with power and pressure. As expected, the population in the upper level is smaller than in the lower level population but not negligible at all.

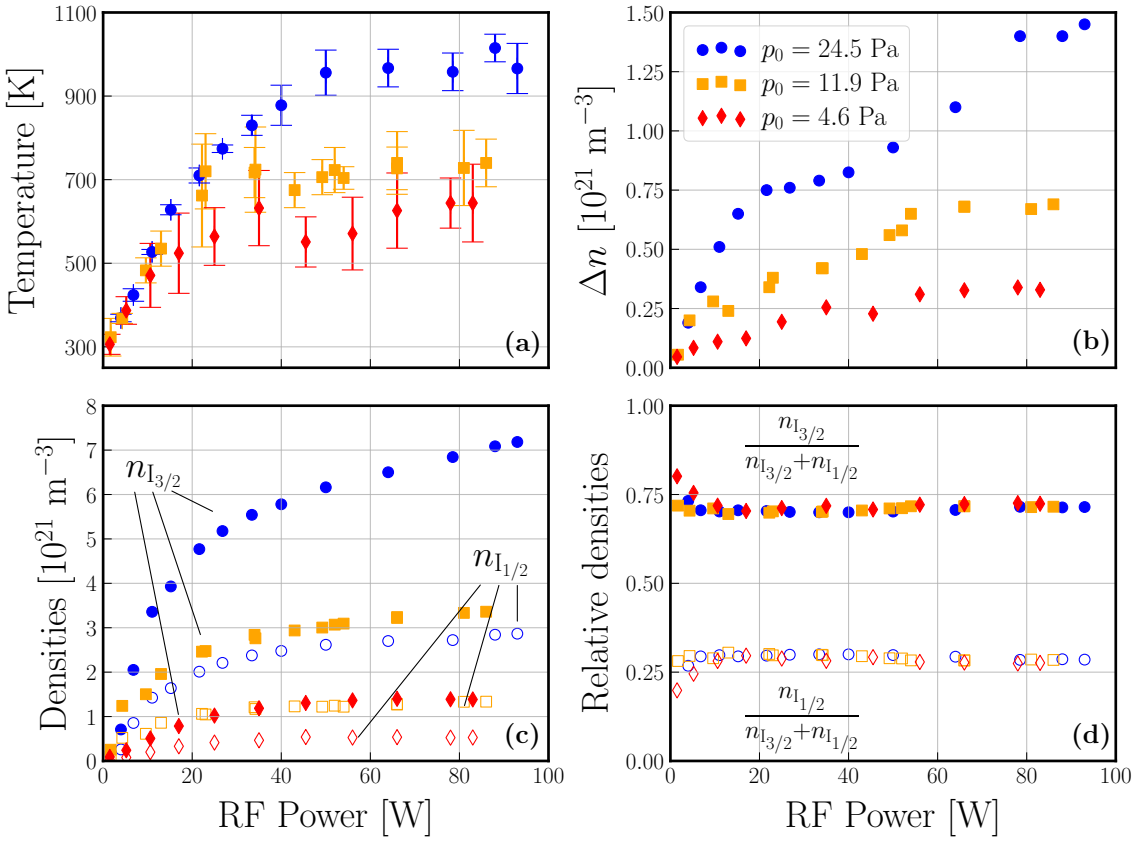

Figure 4.35: Combined results of the absorption at 1315 nm and the molecular absorption at 488.9 nm. The effect of the RF power is studied for three different pressures: 24.5 Pa, 11.9 Pa and 4.6 Pa. (a) Atomic temperature [K]. (b) Average population difference along the line of sight Δn [m^{-3}]. (c) Densities $n_{I_{3/2}}$ (full markers) and $n_{I_{1/2}}$ (open markers) [m^{-3}]. (d) Relative atomic population of $n_{I_{3/2}}$ (full markers) and $n_{I_{1/2}}$ (open markers).

In subfigure (d), the relative atomic densities are plotted and shown to be independent of pressure and RF power. Except at very low power, there is always more than 25 % in the upper level and less than 75% in the lower level (which means that the ratio $n_{I_{1/2}}/n_{I_{3/2}}$ is close to 33 %). This observation suggests that the loss and creation processes of the $I_{1/2}$ are almost independent of pressure, probably meaning that the quenching of excited states by molecules is negligible. As the electronic temperature in the cell was not measured, it is impossible to calculate what the population ratio would be if the Boltzmann equilibrium at T_e was satisfied. Nevertheless, it is common to find T_e between 2 and 5 eV in this type of discharge. This gives a population ratio $n_{I_{1/2}}/n_{I_{3/2}}$ between 19.5 % and 31.2 %.

4.3.4 Summary of optical measurements on the iodine cell

Table 4.2 provides a summary of the optical measurements made on the iodine cell.

Table 4.2: Summary of optical measurements on the iodine cell

	TALIF	ABS 488 nm	ABS 1315 nm	ABS 488 nm + ABS 1315 nm
T_{I}	✓(local)	—	✓(integrated)	✓(integrated)
η	—	✓(integrated)	—	✓(integrated)
Δn	—	—	✓(integrated)	✓(integrated)
$n_{\mathrm{I}_{3/2}}$	✓(local, relative)	—	—	✓(integrated)
$n_{\mathrm{I}_{1/2}}$	—	—	—	✓(integrated)
n_{I_2}	—	✓(integrated)	—	✓(integrated)

4.4 Diagnostics of iodine ground state species within PEGASES thruster

4.4.1 TALIF

In order to make local measurements along the thruster axis of the atomic ground state, we used TALIF on the most efficient transition (from $5s^2 5p^5\,{}^2P^o_{3/2}$ to $(^3P_2)6p\,{}^2[1]^o_{3/2}$). Due to logistical problems, the laser used on the test cell was not available and we used a dye laser whose spectral width prevents the determination of the atomic temperature but relative density measurements were obtained and are presented in the following.

4.4.1.1 Optical setup and basic verifications

The schematic of the optical setup is shown in Figure 4.36 in top and side views. To probe the desired transition (around 298.2 nm), a nanosecond dye laser from Sirah pumped by a doubled Nd: YAG laser (532 nm) was used. A frequency doubling crystal at the output of the laser and the use of Rhodamine 110 as a dye allowed to obtain an output wavelength between 294 and 307 nm with an laser energy up to 4 mJ. Total reflection prisms (not shown) were used to hold the achromatic flux. The laser enters the thruster through a side window and the signal is collected perpendicularly through the window on the top. TALIF signal detection is enabled by a lens (in 2f/2f configuration), an adjustable slit, an interference filter (800±20 nm) and a red-enhanced photomultiplier (Hamamatsu R3896), with a gated voltage-divider circuit (Hamamatsu C1392-56) to avoid saturation by plasma emission. The laser energy was recorded at the output for each laser shot with a PC-interfaced laser energy meter (Pulsar from Ophir). The final mirror and detection elements were independently movable to allow measurements along the thrust axis, from $z \approx 1.5$ cm to $z \approx 7.5$ cm.

By changing the dye to pyridine 1, we were able to generate laser shots for wavelengths between 334 and 360 nm, allowing us to probe the transition from the $5s^2 5p^5\,{}^2P^o_{1/2}$ to the $(^3P_2)6p\,{}^2[1]^o_{3/2}$ levels, with the advantage of reaching the same upper level and therefore not having to modify the detection. However, once again, no signal was detected, even at the highest pressure.

In Figure 4.37, a signal recorded in a 5 mTorr - 200 W plasma while varying the laser wavenumber is shown. The signal-to-noise ratio is typical of TALIF measurements made on the thruster. Contrary to absorption measurements presented next, signals have been detected for working pressures characteristic of space propulsion (around 1 mTorr), which makes TALIF the diagnostic of choice for characterising the operation of electric thrusters.

In Figure 4.38, the TALIF signal has been recorded as a function of the laser energy. As expected with the two-photon absorption, an E^2-law is retrieved, this comes from the fact that the density signal is proportional to the square of the photon flux which is proportional to the laser energy ($n_I \propto \phi^2 \propto E^2$).

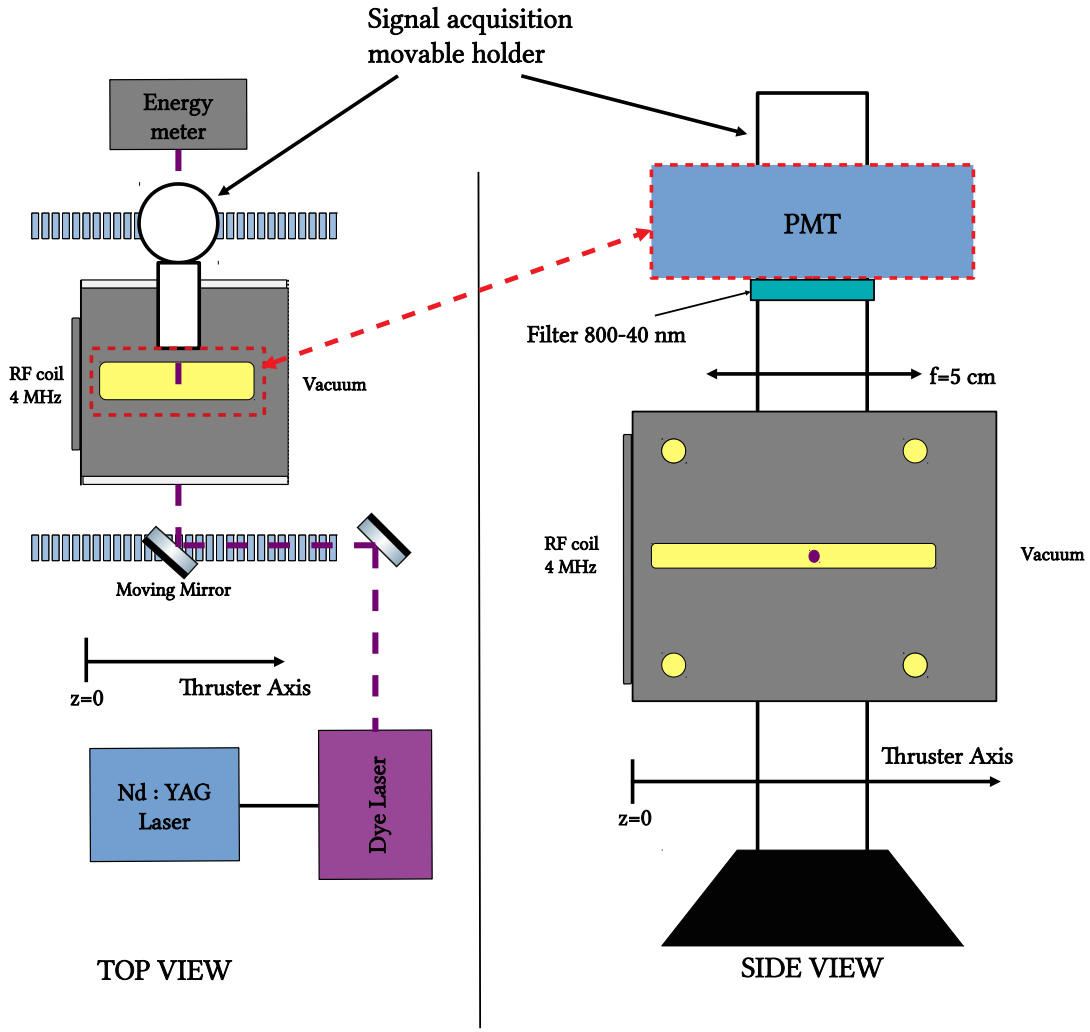

Figure 4.36: Optical setup used to perform TALIF on the PEGASES thruster (left: view from above, right: view from the side). The pulsed laser beam coming out of the dye laser is represented by a dashed purple line, it enters the thruster through a lateral windows (purple point on the side view). The fluorescence is collected perpendicularly through the window situated on the top of the thruster.

4.4.1.2 Measurements within PEGASES

Spatial profiles

As we have done with each diagnostic within the thruster, we begin our investigation by studying the spatial variations. In Figure 4.39, the relative atomic density profiles obtained for pressures of 5, 10 and 15 mTorr and a discharge power of 200 W are plotted. To obtain the signal amplitude, we positioned the laser at resonance and recorded the maximum [4]. In the bottom subfigure, the background signal is plotted and can be interpreted as the signal emitted by the plasma around 800 nm. The TALIF signal was always smaller than the background signal and increases with pressure (more than 25 times smaller at $z = 2$ cm for a pressure of 5 mTorr but only twice smaller at $z = 7.5$ cm for a pressure of 15 mTorr).

[4]The large spectral width of the laser allows to use the maximum rather than the integral.

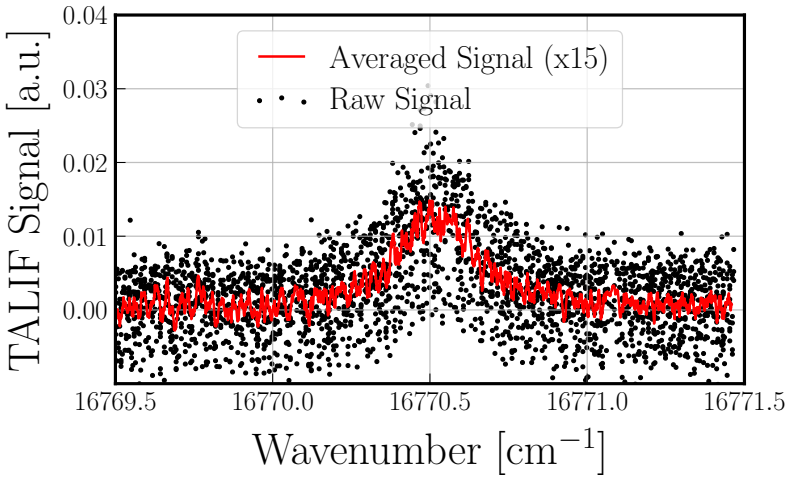

Figure 4.37: TALIF signal intensity [arb. units] as a function of laser wavenumber [cm^{-1}]. Measurements are taken at $z = 5$ cm in a 5 mTorr-150 W iodine plasma.

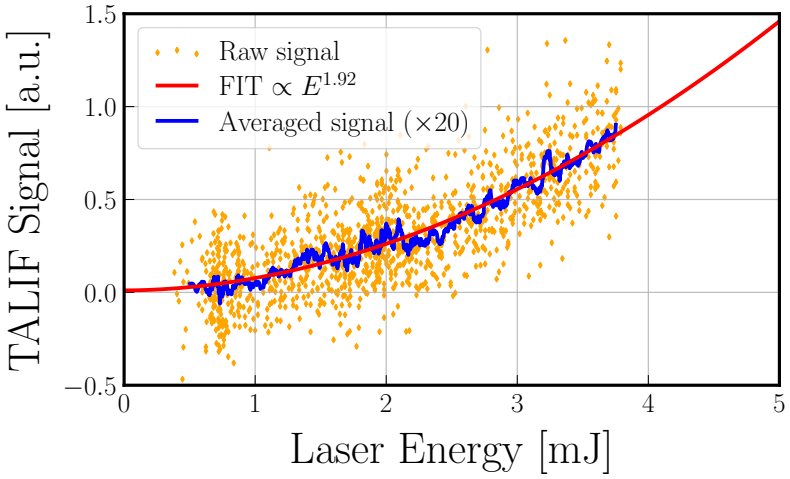

Figure 4.38: TALIF signal intensity [arb. units] as a function of laser pulse energy. Measurements are taken at $z = 5$ cm in a 5 mTorr-200 W iodine plasma, at resonance (16770.5 cm^{-1}).

The atomic density spatial profiles are minimum around $z = 2$ cm and increase with z. Gradients are more pronounced at higher pressure. In the last chapter we understood that as the pressure increases, the relaxation length of the energy becomes shorter and shorter and the electron profiles localise closer and closer to the antenna. This means that the power is most efficiently deposited close to the antenna and dissociation is maximum there. One would have expected to find a maximum atomic density profile close to the antenna but the opposite is observed. This can be explained by a very strong increase in the atomic temperature near the antenna, expected due to the exothermic nature of dissociation, which leads to a depletion of neutral species to maintain an isobaric pressure within the plasma. This is confirmed by the spatial profiles of temperatures of excited species presented in Figure 4.18, even if the measurements were line of sight integrated.

This result demonstrates the importance of neutrals transport in iodine plasmas

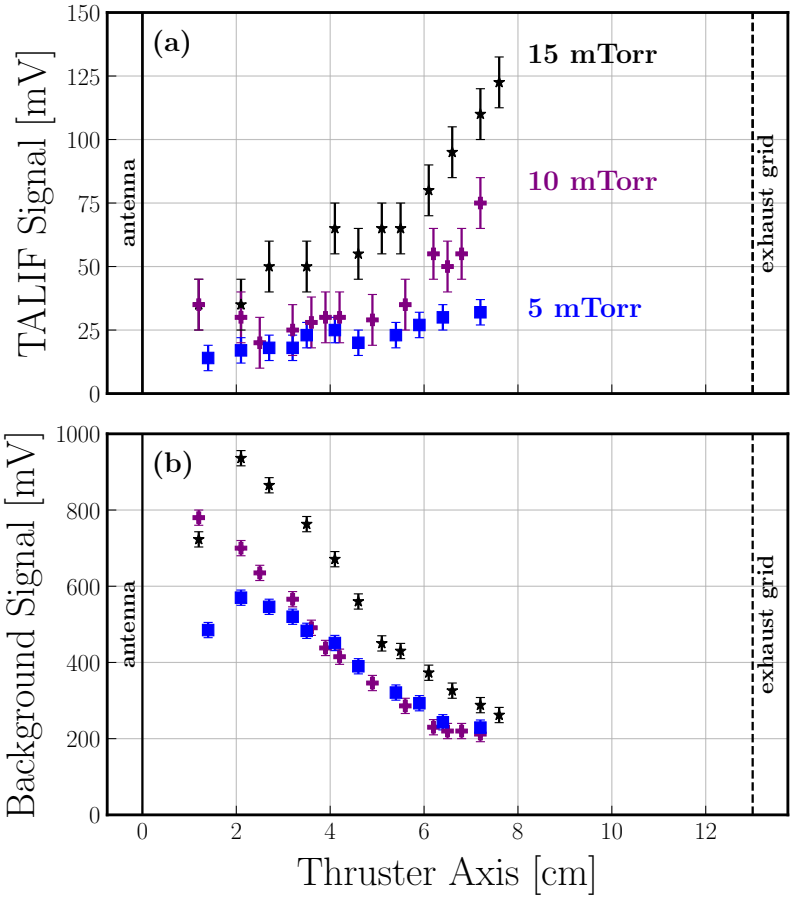

Figure 4.39: (a) Spatial profiles of the TALIF signal at resonance [mV] along the thrust axis for three pressures (5, 10 and 15 mTorr) and a discharge power of 200 W. (b) Spatial profiles of the background signal in the same operating conditions.

and is one of the main findings of the thesis, as it exhibits the multidimensional nature of the discharge and the impossibility of considering it as homogeneous when pressure rises.

Discharge power and pressure influence

In a second step, we studied the influence of discharge power and pressure at a fixed position (z=5 cm).

In Figure 4.40, for 3 different pressures (1, 5 and 15 mTorr), the area of the TALIF signals, recorded when varying the laser wavenumber, is plotted as a function of the discharge power. A decay is observed as the power increases, regardless of the pressure. Taking into account the previously observed spatial patterns, this was expected. Indeed, as the power increases, the gas temperature increases and the center of the plasma becomes devoid of atoms. Although the atoms are massively produced in the core of the plasma, close to the exciter antenna, they are transported towards the walls in all three directions. Along the transverse x and y axes, the ground state atomic spatial profiles probably exhibit the same minimum in the center of the discharge.

In Figure 4.41, the influence of pressure is studied for a fixed discharge power of 200 W. The TALIF area signal increases with pressure as already observed pre-

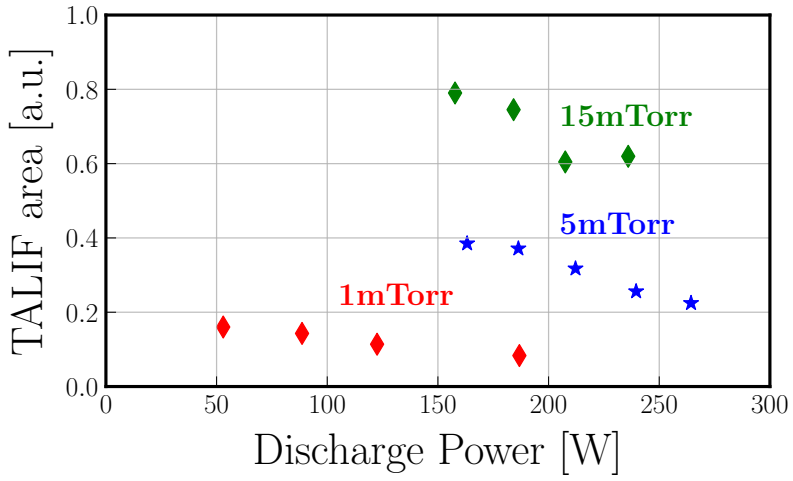

Figure 4.40: TALIF signal area [arb. units] as a function of the discharge power [W] for three different pressures (1, 5 and 15 mTorr). Measurements are taken at $z = 5$ cm.

viously. At this plasma location, the data are well fitted by a power law with an exponent of 0.71.

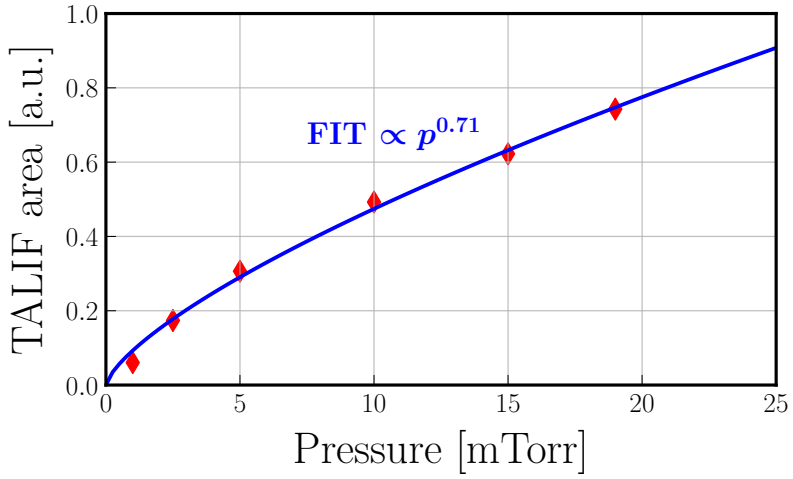

Figure 4.41: TALIF signal area [arb. units] as a function of the pressure [mTorr]. Measurements are taken at $z = 5$ cm for a discharge power of 200 W.

4.4.2 Molecular absorption

The molecular absorption @ 488 nm, performed on the iodine cell and presented in subsection 4.3.1, has been conducted on the thruster. Nevertheless, the smallness of the absorption signals forced us to study the transmitted power signals temporally. For pressure above 10 mTorr, we were able to measure the line of sight averaged molecular density and the dissociation rate.

4.4.2.1 Optical setup and measurement procedure

Setup and validation of the method without plasma

By using photodissociation within the iodine cell makes it possible to obtain a difference in transmitted power with and without plasma ($P_{on} - P_{off}$) of several tens of mW for the highest pressures, which allows simple interpretation of the signals. On the other hand, the cell has the great disadvantage of not being able to be emptied and therefore does not give direct access to the reference transmitted power P_{ref}. Only an extrapolation with Beer Lambert's law gives access to this data (see Figure 4.25).

With the thruster, P_{ref} is simply obtained by measuring the transmitted power as the laser passes through the empty discharge. P_{on} is obtained when the plasma is running and P_{off}, when the gas is injected but the RF excitation is off. The only difficulty comes from the weak signals, due to the low working pressures, and from the accuracy of the measuring device.

The optical setup is presented in Figure 4.42. The CW laser from Oxxius simply passes through the cell once at a fixed z position along the thrust axis. The transmitted power is recorded over time by using a Labview™ program.

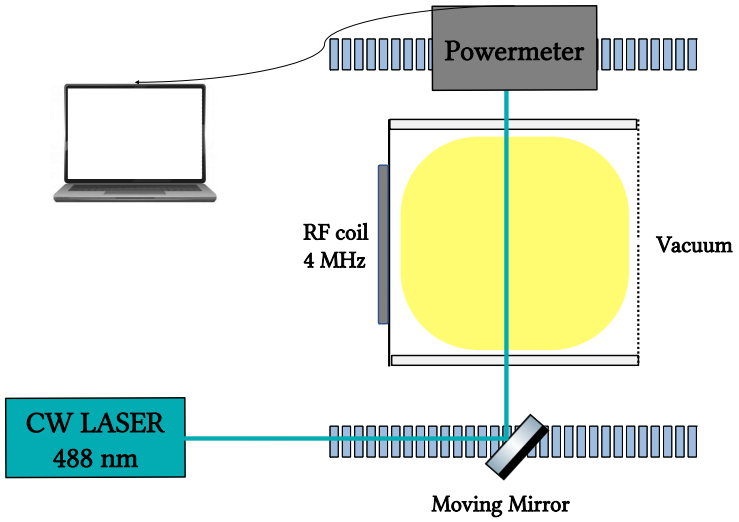

Figure 4.42: Optical setup used to perform molecular absorption within PEGASES thruster.

To check that the measurements will be interpretable despite the low working pressures, we first operate without plasma. Using equation (4.31), we can optically measure the pressure inside the discharge and compare it to the value measured by the pressure gauge. Without plasma, the optical pressure reads:

$$p_{I_2,0} = -\frac{k_B T_{I_2,0}}{\sigma L} \log\left(\frac{P_{off}}{P_{ref}}\right), \tag{4.43}$$

with $T_{I_2,0}$ the temperature of the injected iodine, $L = 13$ cm and $\sigma = 1.72\times10^{-18}$ cm^2. In Figure 4.43, the optical signal converted to pressure is compared to the pressure measured by the gauge with $T_{I_2,0} = 315$ K. Several interesting conclusions can be drawn from this comparison. The overall agreement between both pressures is

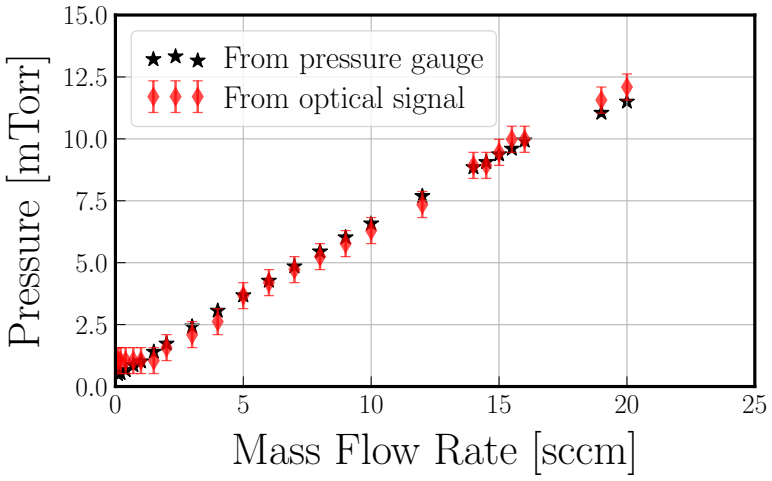

Figure 4.43: Comparison between the pressure measured by the gauge and the optical signal converted to pressure, deduced from equation (4.43) as a function of the iodine injection mass flow rate.

rather good and we can be confident that the photodissociation measurements will be correct within the thruster. Nevertheless, nothing really meaningful can be measured below 2 mTorr where the precision of the measuring device ±0.1 mW is bigger than the expected signals. Finally, at low mass flow rates (between 3 and 12 sccm), the pressure from optical absorption seems to be slightly smaller than the pressure measured by the gauge and at high mass flow rates (above 15 sccm) it is the opposite. This comes from the assumption that the temperature of injection is constant whatever the mass flow rate. Indeed, if we take $T_{I_2,0}$ = 300 K, the agreement is excellent at high mass flow rates (around 20 sccm) and for low mass flow rates (below 12 sccm) $T_{I_2,0}$ = 330 K gives the better agreement. In conclusion, the temperature of injection slightly seems to decrease with mass flow rate, which was not expected.

Measurement procedure with plasma

The measurement procedure, within an iodine plasma, follows three steps identified in Figure 4.44, where the transmitted power signal was recorded over time when the laser passed trough an iodine plasma running at 10 mTorr and 200 W:

- Step 1: the plasma is on and stable, P_{on} is measured (green zone).
- Step 2: the RF excitation is switched off but the iodine gas is still injected, after a few seconds the transmitted power reaches a minimum and P_{off} is obtained (orange zone).
- Step 3: the gas injection is stopped by closing the valve, after a few seconds P_{ref} is measured (blue zone).

In order to limit the disturbance caused by the cooling of the discharge, once the RF is switched off, step 2 must not last more than a few seconds. Also, because the

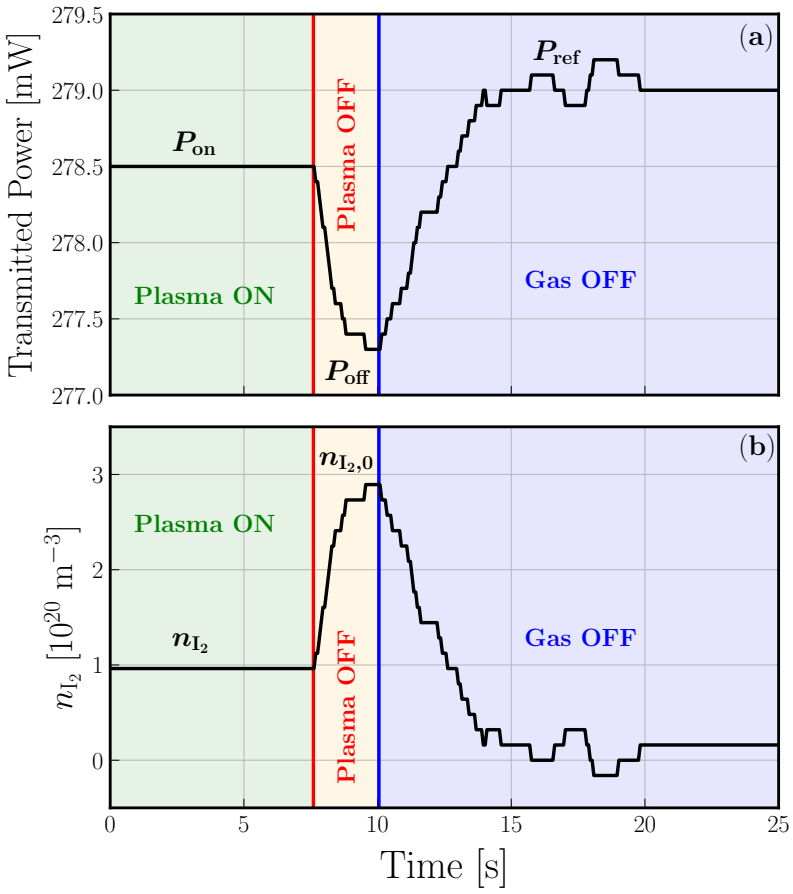

Figure 4.44: (a) Temporal evolution of the transmitted CW laser power during a molecular absorption experiment at 488 nm. (b) Temporal evolution of the line of sight integrated molecular density obtained by applying equation (4.30) with the transmitted power temporal signal, $L = 13$ cm, $\sigma = 1.72 \times 10^{-18}$ cm^2 and the value $P_{ref} = 279.1$ mW. The red vertical line indicates the time when the RF excitation is switched off and the blue vertical line, the time when the gas valve is closed.

plasma cannot be switched on instantaneously, we measured the reference transmitted power at the end.

In subfigure (a), the transmitted power is plotted as a function of time. The red vertical line indicates when the RF is switched off and the blue line when the injection valve is closed. P_{off} and P_{ref} are generally obtained with an error bar of ± 0.1 mW coming from the measurement accuracy of the powermeter.

In subfigure (b), the transmitted power signal is converted into the line of sight integrated molecular density n_{I_2} by using Beer-Lambert law (equation (4.30)), with $L = 13$ cm, $\sigma = 1.72 \times 10^{-18}$ cm^2 and the value $P_{ref} = 279.1$ mW. Depending on the value chosen for P_{ref} (between 279.0 mW and 279.2 mW) , we find n_{I_2} between 8.02×10^{19} m^{-3} and 1.12×10^{20} m^{-3}.

Because of the low working pressures, the jumps in transmitted powers between each step (of a few mWs) are very small compared to the transmitted powers of around 280 mW. This allows to simplify the dissociation rate expression (equa-

tion (4.32)), by using the approximation $\log(1+x) \underset{x\ll 1}{\approx} x$:

$$\eta = 1 - \frac{\log\left(1+\frac{P_{on}-P_{ref}}{P_{ref}}\right)}{\log\left(1+\frac{P_{off}-P_{ref}}{P_{ref}}\right)} \approx 1 - \frac{P_{on}-P_{ref}}{P_{off}-P_{ref}} \approx \frac{P_{on}-P_{off}}{P_{ref}-P_{off}} \tag{4.44}$$

With the example of Figure 4.44, a dissociation rate between 61.1 % and 70.6 % is measured.

Correction of the disturbances

Most of the time, the transmitted power signal did not look like the one presented in Figure 4.44 but was similar to the one presented in Figure 4.45. When the plasma is off after reaching a minimum value, the transmitted power starts to increase because the discharge cools down and the optical transmission of the windows evolve rapidly. This effect was very pronounced for low pressures (≤ 5 mTorr). Thus, when the gas is turned off, the reference transmitted power is recorded within a discharge that is no longer in the same state as when the plasma was on. This clearly affects the measured density and dissociation rate.

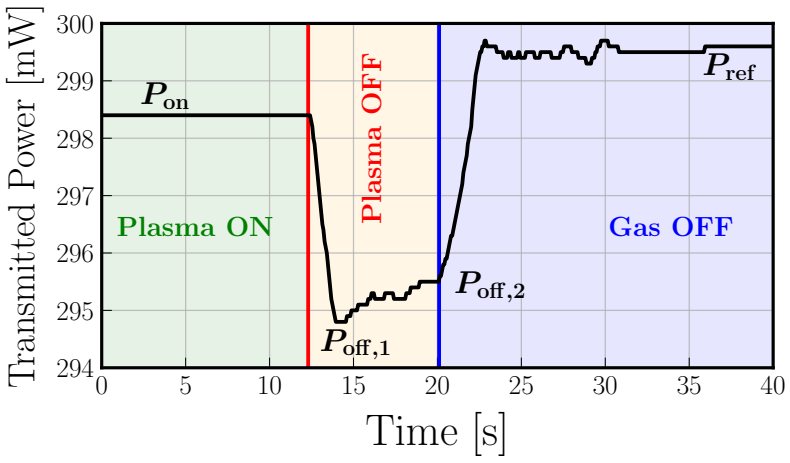

Figure 4.45: Typical signal of the temporal evolution of the transmitted CW laser power during a molecular absorption experiment at 488 nm. The red vertical line indicates the time when the RF excitation is switched off and the blue vertical line, the time when the gas valve is closed. $P_{off,1}$ and $P_{off,2}$ are introduced because within just a few seconds after switching off the RF excitation, the transmitted power has been significantly modified by the cooling of the discharge and the optical transmission of the windows has changed.

We propose to correct the measurement procedure by introducing $P_{off,1}$ and $P_{off,2}$. $P_{off,1}$ is the transmitted power minimum value obtained just after the stopping of the RF excitation and $P_{off,2}$ is the transmitted power value obtained just before the injection valve is closed. Then, we introduce the corrected reference transmitted power

$$P'_{ref} = P_{ref} - (P_{off,2} - P_{off,1}). \tag{4.45}$$

P'_{ref} can be seen as the reference transmitted power that we would get if we immediately went from "plasma ON" to "Gas OFF". The molecular densities expressions (equations (4.30) and (4.31)) are thus modified into:

$$n_{\text{I}_2} = -\frac{1}{\sigma L}\log\left(\frac{P_{\text{on}}}{P'_{\text{ref}}}\right), \tag{4.46}$$

$$n_{\text{I}_2,0} = -\frac{1}{\sigma L}\log\left(\frac{P_{\text{off},2}}{P_{\text{ref}}}\right). \tag{4.47}$$

The expression retained for $n_{\text{I}_2,0}$ could have been $-\log\left(P_{\text{off},1}/P'_{\text{ref}}\right)\Big/(\sigma L)$ but the error between both formulas does not exceed 0.5 % given the amplitude of the absorption signals. Finally, the dissociation rate is modified into:

$$\eta = \frac{P_{\text{ref}}P_{\text{on}} - P'_{\text{ref}}P_{\text{off},2}}{P'_{\text{ref}}P_{\text{ref}} - P'_{\text{ref}}P_{\text{off},2}}. \tag{4.48}$$

4.4.2.2 Measurements within PEGASES

The smallness and perturbations of the absorption signals prevented us from conducting a conclusive study for pressures less than or equal to 5 mTorr. Spatial scans along the thrust axis were obtained at 10 and 15 mTorr for a discharge power of 200 W. Results are presented in Figure 4.46.

In the top subfigure, the line of sight averaged molecular density is plotted. The molecular density profiles are minimum around $z = 2$ cm and tend to increase with increasing z. Spatial gradients are also increased with pressure. At 15 mTorr, the ratio of the density measured at $z = 9$ cm over the density measured at $z = 2$ cm is around 2. These profiles tend to indicate a hotter plasma near the antenna, as shown by absorption measurement of iodine excited atomic species (see Figure 4.18). It also confirms the idea, detailed in Chapter 3, that the negative ions, produced by dissociative attachment of the molecule, are mostly created near the grid. They are fully consistent with the TALIF measurements (presented in Figure 4.39) and confirm the neutrals transport. At $z = 8$ cm, measurements were also conducted for pressures of 5 mTorr and 22.5 mTorr. At 5 mTorr, signals are hard to interpret and error bars significant, the dissociation rate could only be estimated between 60% and 97.5%.

In the bottom subfigure, the dissociation rate is plotted. For 10 mTorr and 15 mTorr, the spatial profiles are very similar with dissociation rate values slightly bigger at the lower pressure. The rates are maximum near the antenna (with a value around 80 %) and slightly decrease with z. The error bars are significant but the line of sight integrated dissociation rate inside the discharge can be situated between 60 % and 80 %, with an expected fully dissociated plasma in the center of the discharge.

The effect of the discharge power on the dissociation rate has also been studied. For a fixed pressure (10, 15 and 22.5 mTorr) and at two different positions ($z = 2$ and $z = 8$ cm), the discharge power was varied between 125 W and 250 W. Surprisingly, no net influence of the discharge power was observed as if the maximum line of sight integrated dissociation rate was already obtained at 125 W. While we believe that the plasma is 100 % dissociated at the center of the discharge and that the spatial profiles are modified by a net increase in power, this result shows the limitations

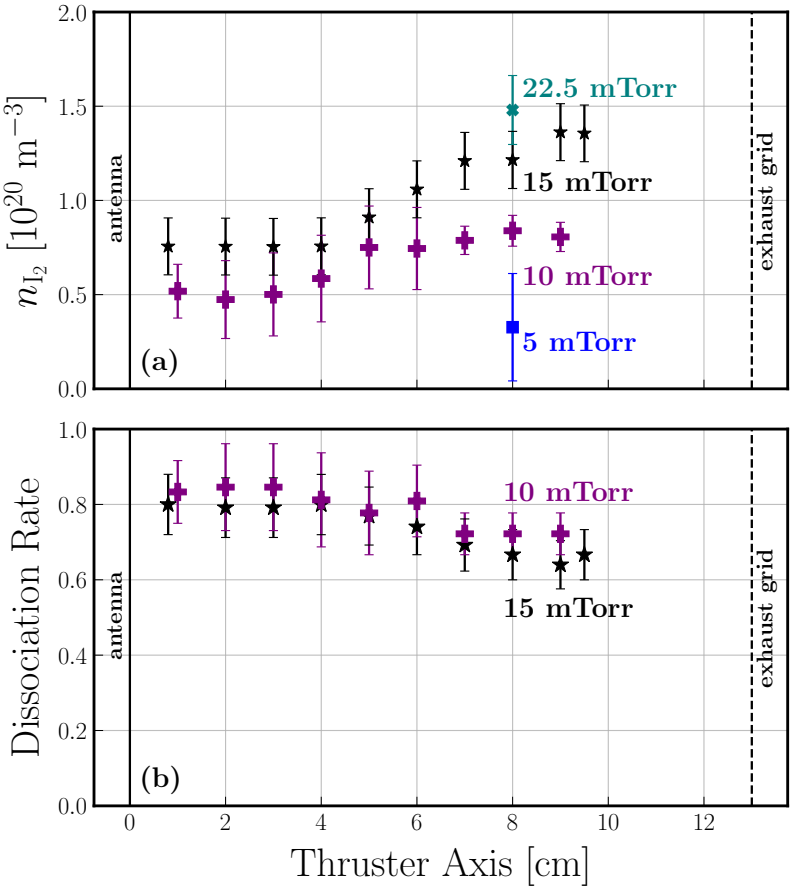

Figure 4.46: Spatial profiles of (a) the line of sight averaged molecular density and (b) the dissociation rate, along the thrust axis obtained by performing molecular absorption at 488 nm at 10 mTorr and 15 mTorr. At $z = 8$ cm, measurements were also performed for pressures of 5 mTorr and 22.5 mTorr. The vertical error bars take into account all the uncertainties on the determination of the different transmitted powers: P_{ref}, P_{on}, $P_{off,1}$ and $P_{off,2}$.

of non-local absorption measurements. Still, we gathered the mean values of this study in Table 4.3. As already observed with the spatial profiles, there is no clear effect of the pressure at a fixed position but the dissociation rate at $z = 8$ cm appears around 5% smaller than at $z = 2$ cm.

Table 4.3: Dissociation rate (%) measured within PEGASES thruster for several pressures at two positions along the thrust axis. The measurements were performed for discharge power values between 125 W and 250 W. The error bars take into account the standard deviation and the uncertainty of each measurement.

η (%)	10 mTorr	15 mTorr	22.5 mTorr
$z = 2$ cm	80.5 ± 14.1	77.2 ± 10.8	80.6 ± 6.8
$z = 8$ cm	73.6 ± 6.4	72.9 ± 7.2	76.3 ± 7.6

4.4.3 Absorption at 1315 nm

The atomic absorption at 1315 nm, conducted on the iodine cell and presented in subsection 4.3.3, is now applied to the thruster. This experiment had already been conducted by Marmuse during his thesis [22] but in what follows, a spatial study has been added and the $I_{1/2}$ level population is taken into account.

4.4.3.1 Optical setup and measurement procedure

The optical setup used to perform atomic absorption at 7602.970 cm^{-1} (1315 nm) within the thruster is presented in Figure 4.47. The optical material used is the same as the one described in subsection 4.3.3.1. The beam is passed seven times through the plasma to increase the absorption path length. Brewster angles windows were added on each side of the thruster to avoid internal reflections of the beam when the beam goes through a window. Because of the Brewster windows, the absorption length per path is now 19.5 cm (it was 12 cm with the classical windows). In order to study the behavior along the thrust axis, the beam was moved back and forth over the shortest possible distance of about 2.3 cm. Four positions were thus probed: between 0.8 cm and 3.1 cm centered around $z_1 = 1.95$ cm, between 3.1 and 5.4 cm centered around $z_2 = 4.25$ cm, between 4.8 and 7.2 cm centered around $z_3 = 6$ cm and between 6.5 and 8.8 cm centered around $z_4 = 7.65$ cm.

The measurement procedure is the same as the one presented in subsection 4.3.3.1 where the $^2P^\circ_{3/2}$ ($F = 4$) to $^2P^\circ_{1/2}$ ($F' = 3$) hyperfine transition is probed (a shift of 0.23 cm^{-1} has been observed between the measurements inside the thruster and inside the cell which is expected to come from the non-calibrated wavemeter used). The best transmission signal is presented in Figure 4.48 (less than 2 % of absorption despite 7 passes, evidencing the difficulty of this experiment for very low pressures) as a function of the laser wavenumber, it was recorded around the location $z = z_4 = 7.65$ cm in a 30 mTorr-200 W iodine plasma. The profile has been fitted by a Gaussian profile (see equation (4.37)) and gives a temperature of 1393 ± 19 K and a line of sight averaged difference of population $\Delta n = 7.99^{+2.50}_{-1.54} \times 10^{19}$ m^{-3} (the error bars on the density come from the uncertainty on the measurement of the total integrated cross section of absorption, $G = 1050 \pm 250$ fm^2 from Ha *et al.* [49]). This value of Δn is one order of magnitude smaller than the molecular density injected to run a 30 mTorr iodine plasma which indicates that the population of the $^2P^\circ_{1/2}$ level is, once again, not negligible. In the best case, the signal-to-noise ratio was around 2 but for most of the measurements, it was much smaller than 1 and no temperature could be fitted properly. One could only obtain the difference of population by direct integration of the absorption signal using equation (4.36).

4.4.3.2 Measurements within PEGASES

Spatial profiles of the line of sight averaged difference of population Δn measured for five different pressures (from 5 mTorr to 30 mTorr) are plotted in Figure 4.49. As previsouly mentioned, the values were obtained by direct integration of the absorption signals which could not be properly fitted by a Gaussian profile. No temperature spatial profiles could be properly obtained, even at 30 mTorr.

Whatever the pressure, Δn spatial profiles increase with z and the values are one order of magnitude smaller than the injected molecular density values: the pop-

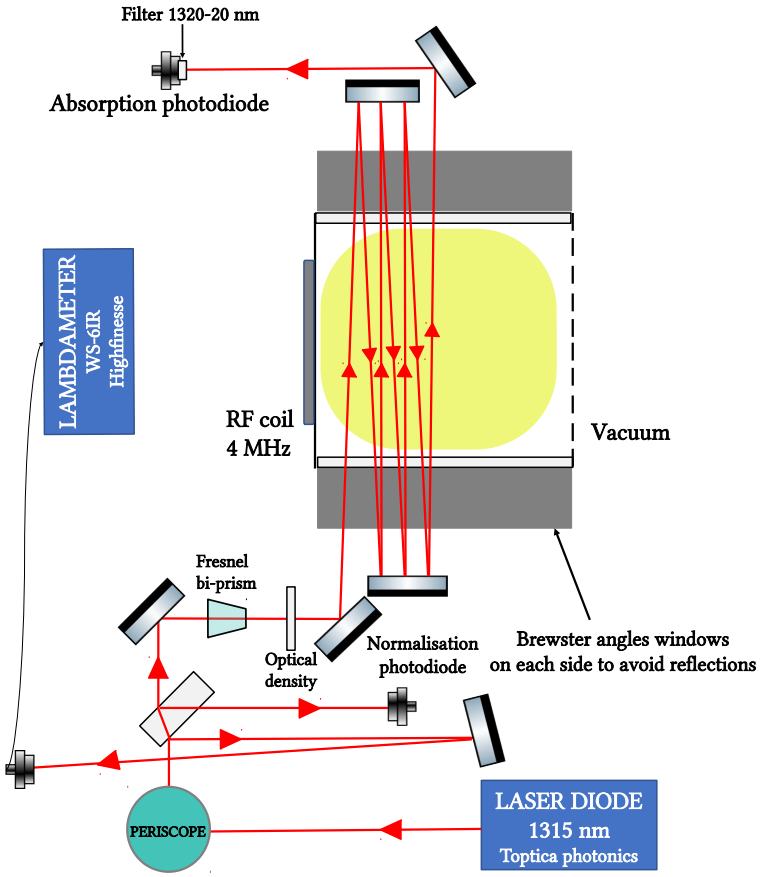

Figure 4.47: Optical setup for the atomic absorption experiment at 7602.970 cm^{-1} (1315 nm) within the PEGASES thruster. The laser is passed seven times through the plasma, to increase the absorption path length.

ulation in the $^2P^\circ_{1/2}$ level is not negligible. The profiles are consistent with TALIF measurements as gradients increase with pressure and the atomic density is minimum near the antenna because of gas heating.

The biggest and best signals were recorded around the location $z_4 = 7.65$ cm and a study with pressure has been conducted at that location. Temperatures could be fitted for pressures between 3 mTorr and 30 mTorr with error bars strongly decreasing with pressure. Measurements are presented in Figure 4.50. In the top subfigure, the Gaussian fitted temperatures are plotted against pressure (black diamonds). The temperature increases with pressure to go from 811.9 ± 212 K at 3 mTorr to 1393 ± 29 K at 30 mTorr. To extend the discussion, we add on this graph the temperature values obtained by performing absorption measurements at 905.8 nm on iodine atomic excited species at the same location (red crosses). The values are extracted from measurements performed between 6.5 cm and 9 cm, at 1.5, 5, 15 and 22.5 mTorr of pressure and presented in Figure 4.18. The error bars indicate the minimum and maximum values measured on this spatial interval (including error bars). The trends with pressure are very similar but temperatures of the excited states are between 100 and 300 K hotter than the temperatures of the atomic ground state species. It should not be forgotten that the homogeneous broadening has been neglected when measuring the temperature of the excited state and that it is quite

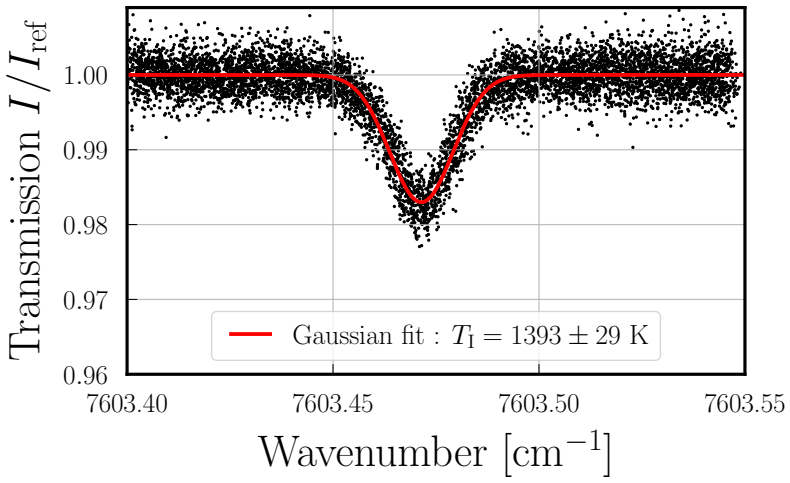

Figure 4.48: Best transmission profile for the $^2\mathrm{P}^\circ_{3/2}$ ($F = 4$) to $^2\mathrm{P}^\circ_{1/2}$ ($F' = 3$) hyperfine transition as a function of the laser wavenumber, measured for a pressure of 30 mTorr and a discharge power of 200 W around the location $z_4 = 7.65$ cm. The red line represents a Gaussian fit of the experimental data which gives a temperature of 1393 ± 29 K and a line of sight averaged difference of population $\Delta n = 7.99^{+2.50}_{-1.54} \times 10^{19}$ m^{-3}.

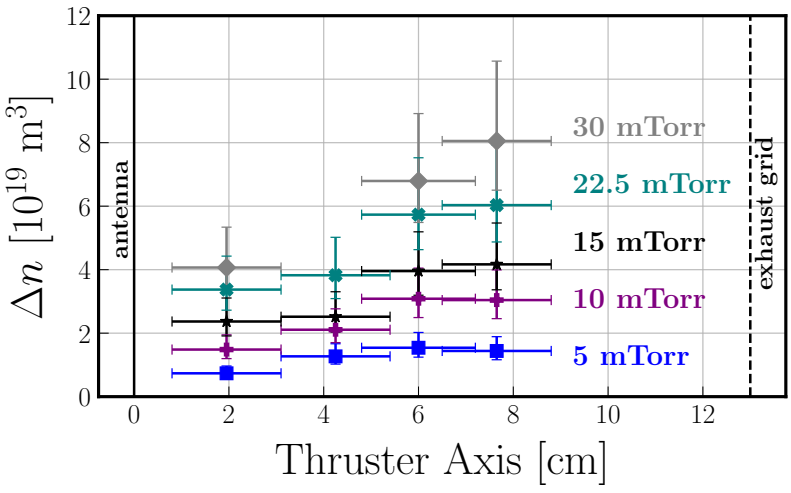

Figure 4.49: Spatial scans of the line of sight averaged difference of population Δn along the thrust axis for five different pressures (5, 10, 15, 22.5 and 30 mTorr) and a discharge power of 200 W. The horizontal error bars indicate the spatial interval over which the laser was moving back and forth to cross the plasma seven times, centered on z_1, z_2, z_3 and z_4 (see text). The asymmetric vertical error bars take into account the uncertainty on the measurement of the total integrated cross section of absorption, $G = 1050 \pm 250$ fm^2 from Ha *et al.* [49].

possible that taking it into account will lead to a decrease in the measured temperature of about 10%, which would make it possible to reconcile the two absorption measurements.

In the bottom subfigure, the line of sight averaged difference of population Δn shows a linear behavior with pressure, indicating that the quenching of the upper

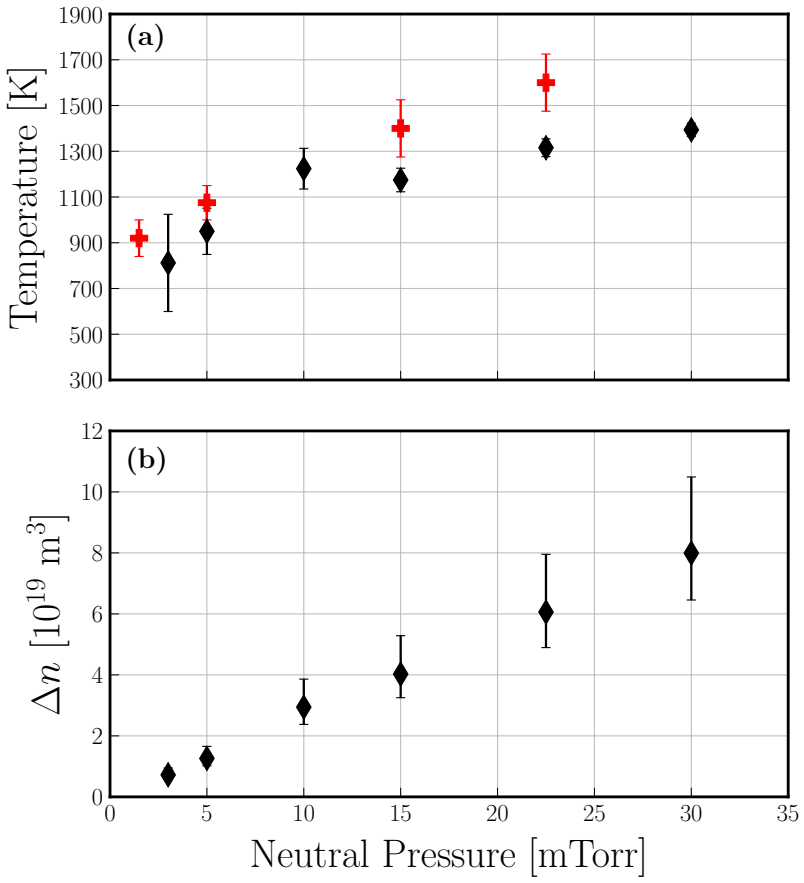

Figure 4.50: Influence of the pressure on the 1315 nm absorption measurements (black diamonds). The back and forth laser beam was centered around $z_4 = 7.65$ cm and the discharge power fixed to 200 W. (a) Temperature deduced from a Gaussian fitted profile, the error bars represent 2-σ. The red crosses are the values obtained by performing absorption measurements at 905.8 nm on iodine atomic excited species at the same location (where the homogeneous broadening has been neglected). The values are extracted from measurements performed between 6.5 cm and 9 cm, at 1.5, 5, 15 and 22.5 mTorr of pressure, presented in Figure 4.18. The error bars indicate the mimimum and maximum values measured on this spatial interval (including error bars). (b) line of sight averaged difference of population Δn. The asymmetric vertical error bars take into account the uncertainty on the measurement of the total integrated cross section of absorption, $G = 1050 \pm 250$ fm^2 from Ha *et al.* [49].

level by the molecule might be negligible in the operating conditions of the thruster.

4.4.3.3 Determination of $n_{I_{3/2}}$ and $n_{I_{1/2}}$

Similar to what was done with the iodine cell, we combine the results of the atomic absorption measurements at 1315 nm with the results of the molecular absorption measurements at 488 nm to derive absolute line of sight integrated density measurements of the $^2P^\circ_{3/2}$ and $^2P^\circ_{1/2}$ levels, respectively $< n_{I_{3/2}} >_{x,L}$ and $< n_{I_{1/2}} >_{x,L}$. However, because of the Brewster windows used to perform atomic absorption at 1315 nm, the absorption length is not the same in both absorption experiments.

The definitions of the measured line of sight integrated dissociation rate and difference of population are:

$$< \eta >_{x,L} = \frac{1}{L} \int_{-L/2}^{L/2} \eta(x)\,\mathrm{d}x = \frac{1}{L} \int_{-L/2}^{L/2} \left((1 - \frac{n_{\mathrm{I}_2}(x)}{n_{\mathrm{I}_2,0}} \right) \mathrm{d}x = 1 - \frac{< n_{\mathrm{I}_2} >_{x,L}}{n_{\mathrm{I}_2,0}}, \tag{4.49}$$

$$< \Delta n >_{x,L'} = \frac{1}{L'} \int_{-L'/2}^{L'/2} \Delta n(x)\,\mathrm{d}x, \tag{4.50}$$

with $L = 13$ cm and $L' = 19.5$ cm. By taking $L = L'$ and using the abusive notation $f = < f >_{x,L}$, one gets back the equations (4.41) and (4.42) used with the iodine cell.

In equation (4.50), the integral takes into account the atoms present within the Brewster windows and need to be evaluated. The simplest solution is to assume that no plasma (no atoms) is present inside the windows but only molecules ($\Delta n(x) = 0$ for $x \in [\pm L/2; \pm L'/2]$). This is the assumption made in the following:

$$< \Delta n >_{x,L'} = \frac{1}{L'} \int_{-L/2}^{L/2} \Delta n(x)\,\mathrm{d}x = \frac{L}{L'} < \Delta n >_{x,L}. \tag{4.51}$$

The system of equations to solve is:

$$\frac{L'}{L} < \Delta n >_{x,L'} = < n_{\mathrm{I}_{3/2}} >_{x,L} - 2 < n_{\mathrm{I}_{1/2}} >_{x,L}, \tag{4.52}$$

$$2 n_{\mathrm{I}_2,0} < \eta >_{x,L} = < n_{\mathrm{I}_{3/2}} >_{x,L} + < n_{\mathrm{I}_{1/2}} >_{x,L'}, \tag{4.53}$$

which gives:

$$< n_{\mathrm{I}_{3/2}} >_{x,L} = \frac{4}{3} n_{\mathrm{I}_2,0} < \eta >_{x,L} + \frac{1}{3} \frac{L'}{L} < \Delta n >_{x,L'}, \tag{4.54}$$

$$< n_{\mathrm{I}_{1/2}} >_{x,L} = \frac{2}{3} n_{\mathrm{I}_2,0} < \eta >_{x,L} - \frac{1}{3} \frac{L'}{L} < \Delta n >_{x,L'}. \tag{4.55}$$

We take the case 15 mTorr-200 W at the location $z \approx 8$ cm, as an example and use results presented in Figure 4.49 and Figure 4.46. For that plasma operating condition, the pressure when the plasma is off is $p_{\mathrm{I}_2,0} \approx 12.5$ mTorr which conveys:

$$n_{\mathrm{I}_2,0} = \frac{p_{\mathrm{I}_2,0}}{k_{\mathrm{B}} T_{\mathrm{I}_2,0}} \approx 3.83 \times 10^{20}\ \mathrm{m}^{-3}, \tag{4.56}$$

the dissociation rate is $< \eta >_{x,L} = 67 \pm 7$ % and the line of sight integrated difference of population $< \Delta n >_{x,L'} = 4.15^{+1.26}_{-0.77} \times 10^{19}\ \mathrm{m}^{-3}$. The resulting line of sight integrated atomic densities are:

$$< n_{\mathrm{I}_{3/2}} >_{x,L} = 3.63^{+0.42}_{-0.38} \times 10^{20}\ \mathrm{m}^{-3}, \tag{4.57}$$

$$< n_{\mathrm{I}_{1/2}} >_{x,L} = 1.50^{+0.12}_{-0.15} \times 10^{20}\ \mathrm{m}^{-3}. \tag{4.58}$$

Spatial measurements of $< \eta >_{x,L}$ and $< \Delta n >_{x,L'}$, at 10 and 15 mTorr, presented in Figure 4.49 and Figure 4.46, are used to obtain the spatial profiles of $< n_{\mathrm{I}_{3/2}} >_{x,L}$ and $< n_{\mathrm{I}_{1/2}} >_{x,L}$. The results are presented in Figure 4.51.

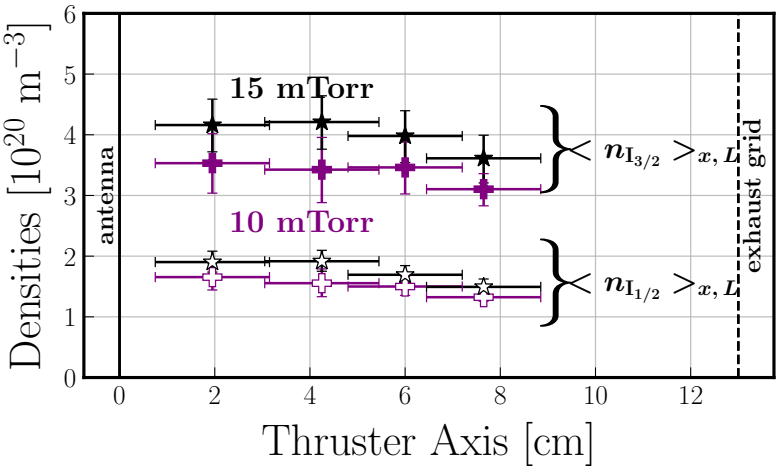

Figure 4.51: line of sight integrated density measurements of the $^2P^\circ_{3/2}$ and $^2P^\circ_{1/2}$ iodine levels ($< n_{I_{3/2}} >_{x,L}$ and $< n_{I_{1/2}} >_{x,L}$ respectively) along the thrust axis at 10 and 15 mTorr for a discharge power of 200 W.

The spatial profiles are almost flat for $< n_{I_{3/2}} >_{x,L}$ and slightly decreasing for $< n_{I_{1/2}} >_{x,L}$. Once again, the absorption technique masks the gradients and gives flat spatial profiles while at the center of the discharge, the profiles are clearly minimum near the antenna and increasing with z (cf TALIF results in Figure 4.39).

Finally, the relative population between the excited and the ground state can be questioned. Without considering any other process than excitation and de-excitation (see Chapter 5 for the full equation), the balance between both levels is given by:

$$K_{\mathrm{ex}_1,\mathrm{I}_{3/2}} n_e n_{\mathrm{I}_{3/2}} = K_{\mathrm{de-ex},\mathrm{I}_{1/2}} n_e n_{\mathrm{I}_{1/2}} \Longleftrightarrow \frac{n_{\mathrm{I}_{1/2}}}{n_{\mathrm{I}_{3/2}}} = \frac{K_{\mathrm{ex}_1,\mathrm{I}_{3/2}}}{K_{\mathrm{de-ex},\mathrm{I}_{1/2}}}. \tag{4.59}$$

In the case of Maxwellian electrons, the ratio of the reaction rates can be expressed as a function of the electron temperature to give:

$$\frac{n_{\mathrm{I}_{1/2}}}{n_{\mathrm{I}_{3/2}}} = \frac{1}{2}\exp\left(\frac{-\mathcal{E}_{\mathrm{ex}_1,\mathrm{I}_{3/2}}}{T_e}\right), \tag{4.60}$$

known as the Boltzmann equilibrium, with $\mathcal{E}_{\mathrm{ex}_1,\mathrm{I}_{3/2}} = 0.9426$ eV.

In Figure 4.52, are plotted the ratios of the excited population over the ground state population at 10 mTorr along the thrust axis, measured via absorption and calculated at Boltzmann equilibrium by using the measured electron temperature presented in Figure 3.26.

The trend is well reproduced but the agreement is not satisfactory. The discrepancy observed may potentially come from terms neglected when approximating a Boltzmann equilibrium, i.e. recombination at the walls of the ground state atoms or creation of the excited state via dissociation processes (knowing that the dissociation is maximal in this region). The main difference certainly comes from the fact that we are comparing local measurements with line of sight averaged measurements. In any case, the population of the excited state I($^2P^\circ_{1/2}$) is never negligible in our experimental conditions.

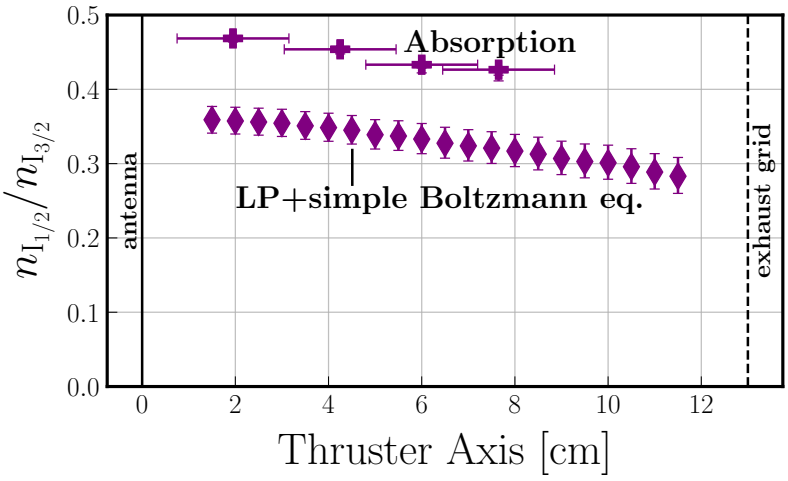

Figure 4.52: Ratio of the excited population over the ground state population at 10 mTorr along the thrust axis determined by absorption measurements and calculated at Boltzmann equilibrium using the measured electron temperature.

4.4.4 Summary of iodine optical measurements on PEGASES

Table 4.4 provides a summary of the optical measurements made on the PEGASES thruster running with iodine.

Table 4.4: Summary of optical measurements on the thruster running with iodine.

	TALIF	ABS 488 nm	ABS 1315 nm	ABS 488 nm + ABS 1315 nm	ABS 905 nm
T_I	—	—	✓ (integrated)	✓ (integrated)	✓ (integrated, excited state)
η	—	✓ (integrated)	—	✓ (integrated)	—
Δn	—	—	✓ (integrated)	✓ (integrated)	—
$n_{I_{3/2}}$	✓ (local, relative)	—	—	✓ (integrated)	—
$n_{I_{1/2}}$	—	—	—	✓ (integrated)	—
n_{I_2}	—	✓ (integrated)	—	✓ (integrated)	—

4.5 Chapter digest

In this chapter, several optical diagnostics were presented and applied to iodine plasmas to probe neutral species (atoms and molecules). Despite our ultimate interest in measuring the temperature and density of the fundamental levels, we first presented absorption techniques for probing excited states which revealed, above 5 mTorr, very clear heating near the antenna and strong spatial temperature gradients, but also the presence of strong temperature jumps near the walls whatever the pressure.
Prior to a thruster application, the techniques for probing the fundamental levels were perfected using a second device: an iodine cell where the working pressures are more favourable for optical diagnostics. By exploiting the structure of the iodine molecule, absorption at 488 nm allowed direct measurement of the molecular dissociation rate and absorption at 1315 nm allowed measurement of the population difference between the first two atomic levels of iodine ($^2P^\circ_{3/2}$ and $^2P^\circ_{1/2}$), as well as the atomic temperature. The combination of these two techniques allowed us to obtain an absolute measurement of the density of the two atomic species, with the major conclusions being the non-negligible population of the first excited state and most likely the total dissociation at the center of the two discharges.
Nevertheless, the absorption techniques, whose results are integrated along the line of sight, showed their limits in the thruster and the quest for a local diagnostic naturally led to the development of the TALIF method. Absolute temperature measurements were obtained within the iodine cell and relative measurements of the atomic ground state density were performed in the cell and in the thruster along the thrust axis. Down to 1 mTorr, the TALIF method has proven to work well, making it the diagnostic of choice for electric propulsion. Above 5 mTorr, the strong heating near the antenna leads to a depletion of the atoms in this region (where they are massively produced) and a multidimensional transport of neutrals.
Some of the previous results have been submitted (see [2]) or presented in several international conferences (see Related publications in page xiii).

CHAPTER 5

GLOBAL MODELING OF IODINE PLASMAS

Contents

5.1 Introduction

In the low-temperature plasma community, 0D volume-averaged models (also called global models) have rapidly become indispensable tools. These fast-solving and easy-to-use models are based on the temporal resolution of continuity equations coupled with a power balance equation in order to determine the different densities and the electronic temperature. They can be very accurate with the inclusion of metastable species and a very detailed chemistry. These models are relevant as long as spatial gradients are negligible and the isothermal assumption holds for the electrons. We will not make an exhaustive bibliography here, but we can cite the works at low-pressure on argon [157, 158], chlorine [95, 159–161], oxygen [92] and mixtures of those gases (same references).

In 2012, building on Goebel's early work [162, 163], Chabert *et al.* proposed a self-consistent global model of a gridded-ion thruster [114]. The power transfer from the RF generator to the plasma was included as well as the heating of the gas. The model allowed for the calculation of the densities and temperatures of the gas (xenon) and electrons. Grondein *et al.* adapted this model to iodine by introducing the first detailed chemistry of an iodine plasma [13, 85]. The species considered were:

$$I, I_2, I^+, I_2^+, I^-, e^-,$$

no electronic or vibrational excitation of the iodine molecule was taken into account. Plasma properties and thruster performances were determined for a wide range of typical operating conditions, and the iodine results had been compared to those for xenon under the same conditions and thruster configuration. The model demonstrated that iodine gives similar behavior and performances, and could lead to higher efficiencies than xenon for propellant mass flow rates below a certain value.

More recently, the particle balance equations of the iodine 0D model were slightly modified by Lucken [21, 86] and Marmuse [22] by adding some new calculated cross-sections (see Chapter 1). These models were still devoid of any consideration of excited states for the iodine molecule. Besides, Marmuse and Lucken did not use the self-consistent calculation of the absorbed power nor the equation for the gas temperature which was thus considered constant.

The first preliminary comparisons between experimental measurements, and 0D models were done by Marmuse [22], during his thesis. The comparisons between model and the experiments, performed within the PEGASES thruster and mostly for pressures between 1 and 5 Pa, revealed that most of the trends were captured, except for the evolution of central I_2 density with pressure. The agreement in absolute values was acceptable but largely perfectible. The discrepancies were assumed to come from an incomplete description of the electron power losses.

Very recently, Grondein's model was acceptably validated by measurements of electron density, electron temperature and electronegativity at very low pressure only (below 3 mTorr) presented in Chapter 3 of this manuscript, where the isothermal assumption still holds for the electrons (see also Esteves *et al.* [1]). The comparison also revealed weaknesses of the model that needed to be improved. The most obvious improvement was an update of the neutral gas heating model because the calculated gas temperature was underestimated. A direct consequence was that the

model underestimated the electron temperature, which in turns impacts all the particle balance equations. The gas heating only resulted from elastic collisions with charged-particles in the plasma volume. However, we believe that atoms gain energy in the dissociation reaction and that this term should be included. This also pleads for a model that solves independently for the atomic and molecular temperatures. Second, at the lowest pressure investigated, there could also be a strong contribution of fast neutrals generated at the wall by the neutralization of the ion flux. The neutralization of the ion flux term was included in the neutral particle balance equation but not in the neutral energy balance equation. However, even if neutrals are reflected back into the plasma with a small fraction of the ion energy gained in the sheath, the energy flux transferred to the neutral gas might be significant.

In this chapter, we propose to update Grondein's global model[1] by taking into account the newly available cross-sections presented in Chapter 1, as well as the remarks detailed above concerning the heating of neutral species. In order to compare our experimental results (presented in Chapter 3 and Chapter 4) with the model, the latter will be adaptable to both the thruster and the iodine cell geometries and will take into account the following species:

$$I_{3/2}, I_{1/2}, I_2, I^+, I_2^+, I^-, e^-,$$

where $I_{3/2}$ and $I_{1/2}$ respectively refers to the $I(^2P^\circ_{3/2})$ and $I(^2P^\circ_{1/2})$ atomic levels.

In a first subsection, the iodine reaction set, the geometrical and physical characteristics and the equations of the model will be detailed. Then, the model will be adapted to both thruster and iodine cell geometries and compared to the experimental measurements. The main findings of the chapter are gathered in a summary at the end.

[1] Just before the submission of this thesis, Lafleur *et al.* [17] updated Grondein's global model by taking into account the iodine cross-sections from Ambalampitiya *et al.* [28], including I^{2+} ions but treating neutrals as isothermal. Their model was validated using ion beam and propellant utilisation efficiency measurements. The majority of this chapter was written before the article was published and therefore no reference will be made to it.

5.2 General description

5.2.1 Reaction set

Unless otherwise stated, the reaction set is shown in Table 5.1. The various reactions and notations were all introduced in Section 1.4 of Chapter 1. Seven species are followed: $I_{3/2}$, $I_{1/2}$, I_2, I^+, I_2^+, I^- and e^-, where $I_{3/2}$ and $I_{1/2}$ respectively refer to the $I(^2P^\circ_{3/2})$ and $I(^2P^\circ_{1/2})$ atomic levels.

Reaction	Rate [$m^3.s^{-1}$]	Threshold energy	More details
Electron impact on $I_{3/2}$			Subsection 1.4.1
$I_{3/2} + e^- \longrightarrow I_{3/2} + e^-$	$K_{el,I_{3/2}}$	0. eV	
$I_{3/2} + e^- \longrightarrow I^+ + 2\,e^-$	$K_{iz,I_{3/2}}$	$\mathcal{E}_{iz,I_{3/2}} = 10.45$ eV	
$I_{3/2} + e^- \longrightarrow I_{1/2} + e^-$	$K_{ex_1,I_{3/2}}$	$\mathcal{E}_{ex_1,I_{3/2}} = 0.9426$ eV	
$I_{3/2} + e^- \longrightarrow I^*_{b_2} + e^-$	$K_{ex_2,I_{3/2}}$	$\mathcal{E}_{ex_2,I_{3/2}} = 6.7736$ eV	
$I_{3/2} + e^- \longrightarrow I^*_{b_3} + e^-$	$K_{ex_3,I_{3/2}}$	$\mathcal{E}_{ex_3,I_{3/2}} = 8.0473$ eV	
$I_{3/2} + e^- \longrightarrow I^*_{b_4} + e^-$	$K_{ex_4,I_{3/2}}$	$\mathcal{E}_{ex_4,I_{3/2}} = 8.1848$ eV	
Electron impact on $I_{1/2}$			Subsection 1.4.1
$I_{1/2} + e^- \longrightarrow I_{1/2} + e^-$	$K_{el,I_{1/2}}$	0. eV	
$I_{1/2} + e^- \longrightarrow I^*_{b_2} + e^-$	$K_{ex_2,I_{1/2}}$	$\mathcal{E}_{ex_2,I_{1/2}} = 5.8310$ eV	
$I_{1/2} + e^- \longrightarrow I^*_{b_3} + e^-$	$K_{ex_3,I_{1/2}}$	$\mathcal{E}_{ex_3,I_{1/2}} = 7.1047$ eV	
$I_{1/2} + e^- \longrightarrow I^*_{b_4} + e^-$	$K_{ex_4,I_{1/2}}$	$\mathcal{E}_{ex_4,I_{1/2}} = 7.2422$ eV	
$I_{1/2} + e^- \longrightarrow I_{3/2} + e^-$	$K_{de-ex,I_{1/2}}$	0. eV	
Electron impact on I_2			Subsection 1.4.2
$I_2 + e^- \longrightarrow I_2 + e^-$	K_{el,I_2}, K_{elm,I_2}	0. eV	
$I_2 + e^- \longrightarrow I_2^+ + 2\,e^-$	K_{iz,I_2}	$\mathcal{E}_{iz,I_{3/2}} = 9.31$ eV	
$I_2 + e^- \longrightarrow 2\,I_{3/2} + e^-$	K_{diss,I_2}	$\mathcal{E}_{diss,I_2} = 1.542$ eV	
$I_2 + e^- \longrightarrow I^+ + I_{3/2} + 2\,e^-$	$K_{diss.iz,I_2}$	$\mathcal{E}_{diss.iz,I_2} = 11.94$ eV	
$I_2 + e^- \longrightarrow I^- + I_{1/2}$	$K_{diss.att,I_2}$	0. eV	
$I_2 + e^- \longrightarrow I_2^* + e^-$	K_{ex,I_2}	$\mathcal{E}_{ex,I_2} = 2.18$ eV	
$I_2(v=0) + e^- \longrightarrow I_2(v=1,...,10) + e^-$	K_{vibr,I_2}	$\mathcal{E}_{vibr,I_2} = 0.02575$ eV	
Electron impact on ions			Subsection 1.4.3
$I_2^+ + e^- \longrightarrow I^+ + I_{3/2} + e^-$	K_{diss,I_2^+}	$\mathcal{E}_{diss,I_2^+} = 2.18$ eV	
$I^- + e^- \longrightarrow I_{3/2} + 2\,e^-$	K_{det,I^-}	$\mathcal{E}_{det,I^-} = 3.059$ eV	
Ions Recombination			Subsection 1.4.3
$I^- + I_2^+ \longrightarrow 3\,I_{3/2}$	$K_{rec,I_2^+-I^-}$	0. eV	
$I^- + I^+ \longrightarrow 2\,I_{3/2}$	K_{rec,I^+-I^-}	0. eV	
Quenching			Subsection 1.4.4
$I_2 + I_{1/2} \longrightarrow I_2 + I_{3/2}$	$K_{quench,I_2-I_{1/2}}$	0. eV	
Charge Transfer			Subsection 1.4.5
$I_2 + I^+ \longrightarrow I_2^+ + I_{3/2}$	$K_{ch.ex,I_2-I^+}$	0. eV	
Surface recombination			Subsection 1.4.6
$I_{3/2} \longrightarrow \frac{1}{2}\,I_2$	$K_{wall,I_{3/2}}$ [s^{-1}]	0. eV	
$I_{1/2} \longrightarrow \frac{1}{2}\,I_2$	$K_{wall,I_{1/2}}$ [s^{-1}]	0. eV	

Table 5.1: List of the reactions and notations used in the iodine global model. The 7 followed species are: $I_{3/2}$, $I_{1/2}$, I_2, I^+, I_2^+, I^- and e^-, where $I_{3/2}$ and $I_{1/2}$ respectively refers to the $I(^2P^\circ_{3/2})$ and $I(^2P^\circ_{1/2})$ atomic levels.

5.2.2 Geometry

The model consists of a cylindrical chamber with an inner radius R and a length L. We let $S_1 = \pi R^2$ and $S_2 = 2\pi RL$ be the surface areas of a closed cylinder. The plasma volume is $V = \pi R^2 L$ and the total surface is $S = 2\pi R^2 + 2\pi RL$. The neutral molecular gas is injected at a fixed particle flow rate Q_N. The exhaust grid has an

adjustable but constant transparency β_{neutrals} for neutral species and β_{ions} for ions. Generally, because of optical focusing effects, $\beta_{\text{neutrals}} \leq \beta_{\text{ions}}$.

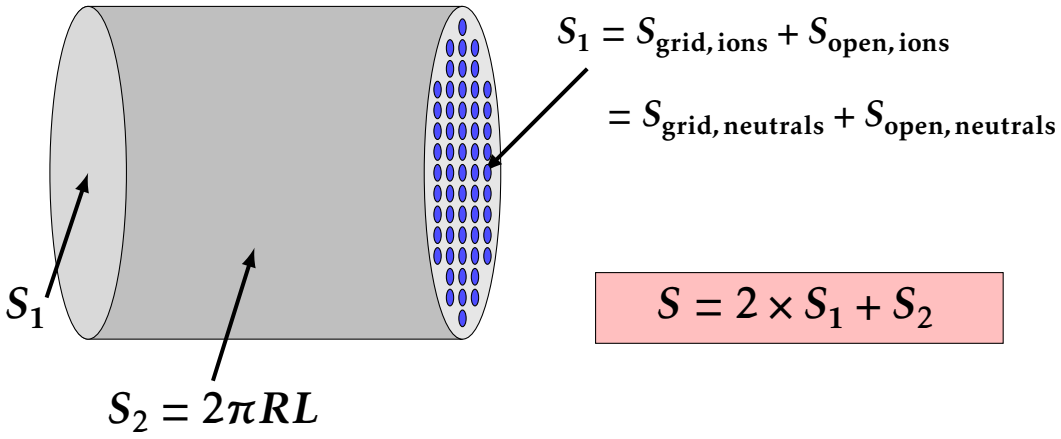

Figure 5.1: Schematics of the cylindrical chamber

Let's define the relevant particle loss areas of the chamber:

- $S_{\text{open,ions}} = S_1 \beta_{\text{ions}} = \pi R^2 \beta_{\text{ions}}$ and $S_{\text{open,neutrals}} = S_1 \beta_{\text{neutrals}} = \pi R^2 \beta_{\text{neutrals}}$ are the effective open areas across which ions and neutrals escape the chamber.
- $S_{\text{grid,ions}} = S_1 - S_{\text{open,ions}} = \pi R^2 (1 - \beta_{\text{ions}})$ and $S_{\text{grid,neutrals}} = S_1 - S_{\text{open,neutrals}} = \pi R^2 (1 - \beta_{\text{neutrals}})$ are the effective loss areas of the grids for ions and neutral species.
- $S_{\text{rec}} = S_1 + S_2 + S_{\text{grid,neutrals}} = \pi R^2 (2 - \beta_{\text{neutrals}}) + 2\pi RL$ is the area for atomic wall losses and production of molecules by wall recombination.

In order to consider the loss and neutralization of charged particles at the walls, one needs to introduce the edge-to-center plasma density ratios h_L and h_R, which accounts for the plasma density profile inside the thruster. Taking into account the influence of the negative ions, according to [164], they read:

$$h_L = 0.86 \left(3 + \frac{L}{2\lambda_{\text{in}}} + 0.2\ (1+\alpha)^{1/2}\ \frac{T_{\text{ions}}}{T_e} \left(\frac{L}{\lambda_{\text{in}}} \right)^2 \right)^{-1/2} \left(\frac{1}{\gamma} + \frac{\gamma - 1}{\gamma (1+\alpha)^2} \right)^{1/2}, \tag{5.1}$$

$$h_R = 0.80 \left(4 + \frac{R}{\lambda_{\text{in}}} + 0.41\ (1+\alpha)^{1/2}\ \frac{T_{\text{ions}}}{T_e} \left(\frac{R}{\lambda_{\text{in}}} \right)^2 \right)^{-1/2} \left(\frac{1}{\gamma} + \frac{\gamma - 1}{\gamma (1+\alpha)^2} \right)^{1/2}. \tag{5.2}$$

In the former expressions, $\lambda_{\text{in}} = \left[(n_{\text{I}_{3/2}} + n_{\text{I}_{1/2}} + n_{\text{I}_2}) \sigma_{\text{in}} \right]^{-1}$ is the mean-free-path for ion-neutral scattering and charge exchange collisions with $\sigma_{\text{in}} = 10^{-18}$ m^2, the ion-neutral elastic collision cross-section. T_{ions} is the temperature of the positive ions (assumed equal for all positive species $T_{\text{I}^+} = T_{\text{I}_2^+}$), $\alpha = n_{\text{I}^-}/n_e$ the electronegativity and $\gamma = T_e/T_{\text{I}^-}$ the ratio of negative species temperatures. We set $T_{\text{ions}} = 0.1$ eV and based on the observation made in Chapter 3, we choose $\gamma = 4$.

We also introduce a global density ratio h which reads:

$$h = \frac{2S_1 h_L + S_2 h_R}{S} = \frac{2\pi R (R h_L + L h_R)}{S}. \tag{5.3}$$

Positive ions and electrons are thus lost at the walls on the effective area hS while positive ions are neutralized on the effective area $hS_{\text{neutr,ions}}$ defined as:

$$hS_{\text{neutr,ions}} = hS - h_L S_{\text{open,ions}} = hS\left(1 - \frac{h_L}{h}\frac{S_{\text{open,ions}}}{S}\right). \tag{5.4}$$

5.2.3 Set of equations

In this subsection, the set of temporal equations is presented. In consists in particle balance equations for each species, an electron power balance equation and two neutral power balance equations: one for the atoms and one for the molecules. In the following, the temperatures are expressed in eV, the conversion formula to SI units is:

$$eT_e\ [\text{eV}] \ = \ k_{\text{B}} T_e\ [\text{K}]. \tag{5.5}$$

5.2.3.1 Particle balance

A particle balance equation is written for each species of the model. Time variations of the densities in these balance equations are described as the net result of the production and destruction of electrons, positive, and negative ions, and neutrals. Each source term has been written on a single line for ease of reading and its physical meaning is indicated alongside.

I_2 molecules

$$\begin{aligned}
\frac{\mathrm{d}n_{\text{I}_2}}{\mathrm{d}t} \ = \ & + \frac{Q_N}{V} && \text{I}_2 \text{ injection} \\
& - K_{\text{diss,I}_2} n_e n_{\text{I}_2} && \text{Dissociation} \\
& - K_{\text{diss.att,I}_2} n_e n_{\text{I}_2} && \text{Dissociative attachment} \\
& - K_{\text{diss.iz,I}_2} n_e n_{\text{I}_2} && \text{Dissociative ionization} \\
& - K_{\text{iz,I}_2} n_e n_{\text{I}_2} && \text{Molecular ionization} \\
& - K_{\text{ch.ex,I}_2\text{–I}^+} n_{\text{I}^+} n_{\text{I}_2} && \text{I}_2\text{-I}^+ \text{ charge exchange} \\
& + \frac{1}{2} K_{\text{wall,I}_{3/2}} n_{\text{I}_{3/2}} && \text{I}_{3/2} \text{ surface recombination} \\
& + \frac{1}{2} K_{\text{wall,I}_{1/2}} n_{\text{I}_{1/2}} && \text{I}_{1/2} \text{ surface recombination} \\
& + \Gamma_{\text{I}_2^+} \frac{S_{\text{neutr,ions}}}{V} && \text{I}_2^+ \text{ wall neutralization} \\
& - \Gamma_{\text{I}_2} \frac{S_{\text{open,neutrals}}}{V}. && \text{I}_2 \text{ exhaust}
\end{aligned} \tag{5.6}$$

$I_{3/2}$ atoms

$$\begin{aligned}
\frac{dn_{I_{3/2}}}{dt} = &+ 2K_{\text{diss},I_2} n_e n_{I_2} && \text{Dissociation}\\
&+ 3K_{\text{rec},I_2^+-I^-} n_{I_2^+} n_{I^-} && I_2^+\text{-}I^- \text{ recombination}\\
&+ 2K_{\text{rec},I^+-I^-} n_{I^+} n_{I^-} && I^+\text{-}I^- \text{ recombination}\\
&+ K_{\text{diss.iz},I_2} n_e n_{I_2} && \text{Dissociative ionization}\\
&+ K_{\text{det},I^-} n_e n_{I^-} && \text{Detachment}\\
&+ K_{\text{ch.ex},I_2-I^+} n_{I^+} n_{I_2} && I_2\text{-}I^+ \text{ charge exchange}\\
&+ K_{\text{quench},I_2-I_{1/2}} n_{I_{1/2}} n_{I_2} && I_{1/2} \text{ quenching by } I_2\\
&+ K_{\text{de-ex},I_{1/2}} n_e n_{I_{1/2}} && \text{Electronic de-excitation}\\
&- K_{\text{iz},I_{3/2}} n_e n_{I_{3/2}} && \text{Atomic ionization}\\
&- K_{\text{ex}_1,I_{3/2}} n_e n_{I_{3/2}} && \text{Electronic excitation from } I_{3/2}\\
&- K_{\text{wall},I_{3/2}} n_{I_{3/2}} && I_{3/2} \text{ surface recombination}\\
&+ \Gamma_{I^+} \frac{S_{\text{neutr,ions}}}{V} && I^+ \text{ wall neutralization}\\
&- \Gamma_{I_{3/2}} \frac{S_{\text{open,neutrals}}}{V}. && I_{3/2} \text{ exhaust}
\end{aligned} \tag{5.7}$$

$I_{1/2}$ atoms

$$\begin{aligned}
\frac{dn_{I_{1/2}}}{dt} = &+ K_{\text{ex}_1,I_{3/2}} n_e n_{I_{3/2}} && \text{Electronic excitation from } I_{3/2}\\
&+ K_{\text{diss.att},I_2} n_e n_{I_2} && \text{Dissociative attachment}\\
&- K_{\text{quench},I_2-I_{1/2}} n_{I_{1/2}} n_{I_2} && I_{1/2} \text{ quenching by } I_2\\
&- K_{\text{de-ex},I_{1/2}} n_e n_{I_{1/2}} && \text{Electronic de-excitation}\\
&- K_{\text{wall},I_{1/2}} n_{I_{1/2}} && I_{1/2} \text{ surface recombination}\\
&- \Gamma_{I_{1/2}} \frac{S_{\text{open,neutrals}}}{V}. && I_{1/2} \text{ exhaust}
\end{aligned} \tag{5.8}$$

Electrons

$$\begin{aligned}
\frac{dn_e}{dt} = &+ K_{\text{iz},I_{3/2}} n_e n_{I_{3/2}} && \text{Atomic ionization}\\
&+ K_{\text{iz},I_2} n_e n_{I_2} && \text{Molecular ionization}\\
&+ K_{\text{diss.iz},I_2} n_e n_{I_2} && \text{Dissociative ionization}\\
&+ K_{\text{det},I^-} n_e n_{I^-} && \text{Detachment}\\
&- K_{\text{diss.att},I_2} n_e n_{I_2} && \text{Dissociative attachment}\\
&- \Gamma_e \frac{S}{V}. && e^- \text{ flux to the walls}
\end{aligned} \tag{5.9}$$

I^- ions

$$\begin{aligned}\frac{dn_{I^-}}{dt} &= +K_{\text{diss.att},I_2} n_e n_{I_2} && \text{Dissociative attachment}\\ &\quad -K_{\text{rec},I_2^+-I^-} n_{I_2^+} n_{I^-} && I_2^+\text{-}I^- \text{ recombination}\\ &\quad -K_{\text{rec},I^+-I^-} n_{I^+} n_{I^-} && I^+\text{-}I^- \text{ recombination}\\ &\quad -K_{\text{det},I^-} n_e n_{I^-}. && \text{Detachment}\end{aligned} \tag{5.10}$$

I^+ ions

$$\begin{aligned}\frac{dn_{I^+}}{dt} &= +K_{\text{iz},I_{3/2}} n_e n_{I_{3/2}} && \text{Atomic ionization}\\ &\quad +K_{\text{diss.iz},I_2} n_e n_{I_2} && \text{Dissociative ionization}\\ &\quad -K_{\text{ch.ex},I_2-I^+} n_{I^+} n_{I_2} && I_2\text{-}I^+ \text{ charge exchange}\\ &\quad -K_{\text{rec},I^+-I^-} n_{I^+} n_{I^-} && I^+\text{-}I^- \text{ recombination}\\ &\quad -\Gamma_{I^+} \frac{S}{V}. && I^+ \text{ flux to the walls}\end{aligned} \tag{5.11}$$

I_2^+ ions

$$\begin{aligned}\frac{dn_{I_2^+}}{dt} &= +K_{\text{iz},I_2} n_e n_{I_2} && \text{Molecular ionization}\\ &\quad +K_{\text{ch.ex},I_2-I^+} n_{I^+} n_{I_2} && I_2\text{-}I^+ \text{ charge exchange}\\ &\quad -K_{\text{rec},I_2^+-I^-} n_{I_2^+} n_{I^-} && I_2^+\text{-}I^- \text{ recombination}\\ &\quad -\Gamma_{I_2^+} \frac{S}{V}. && I_2^+ \text{ flux to the walls}\end{aligned} \tag{5.12}$$

The expressions for the fluxes to the walls are:

$$\Gamma_{I_{3/2}} = \frac{1}{4} n_{I_{3/2}} \overline{v}_{I_{3/2}}, \tag{5.13}$$

$$\Gamma_{I_{1/2}} = \frac{1}{4} n_{I_{1/2}} \overline{v}_{I_{1/2}}, \tag{5.14}$$

$$\Gamma_{I_2} = \frac{1}{4} n_{I_2} \overline{v}_{I_2}, \tag{5.15}$$

$$\Gamma_{I^+} = h n_{I^+} u_{B,I^+}, \tag{5.16}$$

$$\Gamma_{I_2^+} = h n_{I_2^+} u_{B,I_2^+}, \tag{5.17}$$

$$\Gamma_{I^-} = 0, \tag{5.18}$$

$$\Gamma_e = \Gamma_{I_2^+} + \Gamma_{I^+}, \tag{5.19}$$

with $\overline{v}_P = \left(\frac{8eT_P}{\pi m_P}\right)^{1/2}$ and $u_{B,P^+} = \left(\frac{eT_e}{m_P}\right)^{1/2}$ the mean speed and the Bohm speed [2] of the particle $P \in \{I, I_2\}$ respectively. There are no losses of negative ions on the chamber walls, they are assumed to be confined by the sheaths.

[2] Despite the presence of negative ions, we use the classical Bohm speed formula [164].

5.2.3.2 Electron power balance

The plasma power balance, detailed in several works [13, 58, 114, 119, 157, 165], expresses that the power injected in the plasma - the absorbed power P_{abs} - is either used to heat up electrons, or lost during collision processes in the plasma and at the plasma boundaries:

$$\frac{\mathrm{d}}{\mathrm{d}t}\left(\frac{3}{2}n_e e T_e\right) = p_{\text{abs}} - p_{\text{loss}}, \tag{5.20}$$

where p_{abs} [W.m^{-3}] is the power absorbed by the electrons and p_{loss} [W.m^{-3}] is the total electron power loss per unit volume:

$$\begin{aligned}
p_{\text{loss}} = {} & + \mathcal{E}_{\text{diss},\text{I}_2} K_{\text{diss},\text{I}_2} n_e n_{\text{I}_2} && \text{Dissociation} \\
& + \mathcal{E}_{\text{diss.iz},\text{I}_2} K_{\text{diss.iz},\text{I}_2} n_e n_{\text{I}_2} && \text{Dissociative ionization} \\
& + \mathcal{E}_{\text{iz},\text{I}_2} K_{\text{iz},\text{I}_2} n_e n_{\text{I}_2} && \text{Molecular ionization} \\
& + \mathcal{E}_{\text{ex},\text{I}_2} K_{\text{ex},\text{I}_2} n_e n_{\text{I}_2} && \text{Electronic excitation} \\
& + \mathcal{E}_{\text{vibr},\text{I}_2} K_{\text{vibr},\text{I}_2} n_e n_{\text{I}_2} && \text{Vibrational excitation} \\
& + \mathcal{E}_{\text{det},\text{I}^-} K_{\text{det},\text{I}^-} n_e n_{\text{I}^-} && \text{Detachment} \\
& - \mathcal{E}_{\text{ex}_1,\text{I}_{3/2}} K_{\text{de-ex},\text{I}_{1/2}} n_e n_{\text{I}_{1/2}} && \text{Electronic de-excitation (gain)} \\
& + \mathcal{E}_{\text{iz},\text{I}_{3/2}} K_{\text{iz},\text{I}_{3/2}} n_e n_{\text{I}_{3/2}} && \text{Atomic ionization} \\
& + \sum_{j=1}^{4} \mathcal{E}_{\text{ex}_j,\text{I}_{3/2}} K_{\text{ex}_j,\text{I}_{3/2}} n_e n_{\text{I}_{3/2}} && \text{Electronic excitation from } \text{I}_{3/2} \\
& + \sum_{j=2}^{4} \mathcal{E}_{\text{ex}_j,\text{I}_{1/2}} K_{\text{ex}_j,\text{I}_{1/2}} n_e n_{\text{I}_{1/2}} && \text{Electronic excitation from } \text{I}_{1/2} \\
& + 3\frac{m_e}{m_{\text{I}}} e (T_e - T_{\text{I}_{3/2}}) n_e n_{\text{I}_{3/2}} K_{\text{el},\text{I}_{3/2}} && \text{I}_{3/2}\text{-e}^- \text{ elastic collision} \\
& + 3\frac{m_e}{m_{\text{I}}} e (T_e - T_{\text{I}_{1/2}}) n_e n_{\text{I}_{1/2}} K_{\text{el},\text{I}_{1/2}} && \text{I}_{1/2}\text{-e}^- \text{ elastic collision} \\
& + 3\frac{m_e}{m_{\text{I}_2}} e (T_e - T_{\text{I}_2}) n_e n_{\text{I}_2} K_{\text{el},\text{I}_2} && \text{I}_2\text{-e}^- \text{ elastic collision} \\
& + < \mathcal{E}_{\text{kin}} >_0^{\text{I}_2} \Gamma_e \frac{S_1 h_L + S_2 h_R}{V} && \text{Energy losses to the walls} \\
& + < \mathcal{E}_{\text{kin}} >_{\beta_{\text{ions}}}^{\text{I}_2} \Gamma_e \frac{S_{\text{grid,ions}} h_L}{V}. && \text{Energy losses to the grid}
\end{aligned} \tag{5.21}$$

The function $< \mathcal{E}_{\text{kin}} >$ represents the mean kinetic energy lost per electron leaving the discharge. The subscript $_{\beta_{\text{ions}}}$ indicates that the mean kinetic energy depends on the transparency of the walls for ions, and the superscript $^{\text{I}_2}$ indicates the working gas. From [13],

$$< \mathcal{E}_{\text{kin}} > = \frac{5}{2} e T_e + e\phi_{\text{sheath}}, \tag{5.22}$$

where ϕ_{sheath} [eV] is the sheath potential. The sheath potential can be calculated using the current balance between the positive ions that are accelerated through the

sheath and the thermal flux of electrons. Since the flux of negative ions that leave the plasma is negligible (virtually zero),

$$< \mathcal{E}_{\text{kin}} >^{\text{I}_2}_{\beta_{\text{ions}}} = eT_e \left[\frac{5}{2} - \ln \left(\frac{1}{1-\beta_{\text{ions}}} \sqrt{\frac{\pi m_e}{m_{\text{I}}}} \frac{\sqrt{2} n_{\text{I}^+} + n_{\text{I}_2^+}}{n_{\text{I}^+} + n_{\text{I}_2^+}} \right) \right]. \tag{5.23}$$

The formula depends on the ion grid transparency β_{ions}, and that we take $\beta_{\text{ions}} = 0$ when the surface considered does not contain a grid (i.e chamber walls). The function also depends on the ion densities which is not the case for an electropositive gas. For instance, $< \mathcal{E}_{\text{kin}} >^{\text{I}_2}_0$ varies between 7.76 eT_e when only I^+ is present and 8.1 eT_e when only I_2^+ is present.

The absorbed power depends on the arrangement used to excite the plasma. One possibility is to fix p_{abs} without dealing with the details of the power delivery. However, we prefer to adopt a self-consistent method of calculating the absorbed power for both the iodine cell and the thruster. Concerning the thruster, the physics of the plasma generation will be treated, following the work of Chabert *et al.* [114].

In practice, the equation (5.20) is written so as to isolate the temporal derivative of T_e:

$$\frac{\text{d}T_e}{\text{d}t} = \frac{2}{3} \frac{p_{\text{abs}} - p_{\text{loss}}}{e n_e} - \frac{T_e}{n_e} \frac{\text{d}n_e}{\text{d}t}. \tag{5.24}$$

5.2.3.3 Gas Heating

As already mentioned, we treat separately the atomic and molecular temperatures ($T_{\mathrm{I}} \neq T_{\mathrm{I}_2}$) but all the atomic species temperatures are considered equal ($T_{\mathrm{I}_{3/2}} = T_{\mathrm{I}_{1/2}} = T_{\mathrm{I}}$). The energy gained by the atoms in the dissociation processes is accounted for. Molecular dissociation by electron impact is assumed to create atoms with an energy excess of $\Delta\mathcal{E}_{\mathrm{diss}} = 0.5$ eV for each atom, while dissociative attachment produces an atom with an energy excess of $\Delta\mathcal{E}_{\mathrm{diss.att}} = 5$ eV. These mean energy values comes from ab initio calculations and private discussions with the team of N. Sisourat at LCPMR. Moreover, ions are reflected back into the plasma as neutrals with a small fraction of the ion energy gained in the sheath estimated at $s_{\mathrm{keep,ions}} \times 5eT_e$ where we take $s_{\mathrm{keep,ions}} = s_{\mathrm{keep,I^+}} = s_{\mathrm{keep,I_2^+}} = 0.045$. This value was obtained by performing a statistical study with Molecular Dynamic simulations of an energetic ions impacting perpendicularly a Si surface. The code was developped in thesis works of C.F. Abrams [166] and the code was made available to us by E. Despiau-Pujo [167].

Atoms Temperature

The atomic power balance equation is:

$$\frac{\mathrm{d}}{\mathrm{d}t}\left(\frac{3}{2}(n_{\mathrm{I}_{3/2}} + n_{\mathrm{I}_{1/2}})eT_{\mathrm{I}}\right) = \tag{5.25}$$

$$\begin{aligned}
&+ 3\frac{m_e}{m_{\mathrm{I}}}e(T_e - T_{\mathrm{I}})n_e\left(n_{\mathrm{I}_{3/2}}K_{\mathrm{el},\mathrm{I}_{3/2}} + n_{\mathrm{I}_{1/2}}K_{\mathrm{el},\mathrm{I}_{1/2}}\right) && \mathrm{e^-}\text{ - atoms elastic collisions}\\
&+ \sigma_{\mathrm{in}}\left(\Gamma_{\mathrm{I}_{3/2}} + \Gamma_{\mathrm{I}_{1/2}}\right)\left(n_{\mathrm{I}_2^+}m_{\mathrm{I}_2}u_{\mathrm{B},\mathrm{I}_2^+}^2 + n_{\mathrm{I}^+}m_{\mathrm{I}}u_{\mathrm{B},\mathrm{I}^+}^2\right) && \mathrm{I^+}, \mathrm{I_2^+}\text{ - atoms elastic collisions}\\
&- \kappa_{\mathrm{I}}\frac{e}{k_{\mathrm{B}}}\left(\frac{T_{\mathrm{I}} - T_{\mathrm{edge}}}{\Lambda_0}\right)\frac{S}{V} && \text{Atomic heat flux}\\
&- \frac{16}{3}\frac{m_{\mathrm{II}_2}}{m_{\mathrm{I}} + m_{\mathrm{I}_2}}e(T_{\mathrm{I}} - T_{\mathrm{I}_2})n_{\mathrm{I}_{3/2}}n_{\mathrm{I}_2}\Omega_{\mathrm{I}_{3/2}\mathrm{I}_2}^{(1,1)} && \mathrm{I_{3/2}}\text{ - }\mathrm{I_2}\text{ elastic collisions}\\
&- \frac{16}{3}\frac{m_{\mathrm{II}_2}}{m_{\mathrm{I}} + m_{\mathrm{I}_2}}e(T_{\mathrm{I}} - T_{\mathrm{I}_2})n_{\mathrm{I}_{1/2}}n_{\mathrm{I}_2}\Omega_{\mathrm{I}_{1/2}\mathrm{I}_2}^{(1,1)} && \mathrm{I_{1/2}}\text{ - }\mathrm{I_2}\text{ elastic collisions}\\
&+ \Delta\mathcal{E}_{\mathrm{diss.att},\mathrm{I}_2}K_{\mathrm{diss.att},\mathrm{I}_2}n_e n_{\mathrm{I}_2} && \text{Energy gain via Diss. attachment}\\
&+ 2\Delta\mathcal{E}_{\mathrm{diss},\mathrm{I}_2}K_{\mathrm{diss},\mathrm{I}_2}n_e n_{\mathrm{I}_2} && \text{Energy gain via Dissociation}\\
&+ s_{\mathrm{keep,I^+}} \times (5eT_e) \times \Gamma_{\mathrm{I^+}}\frac{S_{\mathrm{neutr,ions}}}{V}, && \text{Wall neutralization of the } \mathrm{I^+}\text{ flux}
\end{aligned} \tag{5.26}$$

with κ_{I} the atomic iodine thermal conductivity, fitted as a function of the atomic temperature, from [168]:

$$\kappa_{\mathrm{I}} = 6.32 \times 10^{-5}\left(\frac{e}{k_{\mathrm{B}}}T_{\mathrm{I}}\right)^{0.768}, \tag{5.27}$$

Λ_0 the heat diffusion length given by equation (1.36), T_{edge} the edge temperature (the wall temperature taking into account the temperature jump at the walls due to thermal accommodation). m_{II_2} and $\Omega_{\mathrm{I}_{3/2}\mathrm{I}_2}^{(1,1)}$ are respectively the reduced mass of the system I-$\mathrm{I_2}$ and the Chapman-Cowling integral of the elastic collision between $\mathrm{I_{1/2}}$ and $\mathrm{I_2}$, whose expressions are given in Chapter 1 or in Appendix C.

Molecules Temperature

The power balance equation for molecules reads:

$$
\begin{aligned}
&\frac{\mathrm{d}}{\mathrm{d}t}\left(\frac{3}{2}n_{\mathrm{I}_2}eT_{\mathrm{I}_2}\right) = \\
&\quad + 3\frac{m_e}{m_{\mathrm{I}_2}}e(T_e - T_{\mathrm{I}_2})n_e n_{\mathrm{I}_2}K_{\mathrm{el},\mathrm{I}_2} && \mathrm{e^-}\text{ - }\mathrm{I_2}\text{ elastic collisions} \\
&\quad + \sigma_{\mathrm{in}}\Gamma_{\mathrm{I}_2}\left(n_{\mathrm{I}_2^+}m_{\mathrm{I}_2}u^2_{\mathrm{B},\mathrm{I}_2^+} + n_{\mathrm{I}^+}m_{\mathrm{I}}u^2_{\mathrm{B},\mathrm{I}^+}\right) && \mathrm{I^+},\ \mathrm{I_2^+}\text{ - }\mathrm{I_2}\text{ elastic collisions} \\
&\quad - \kappa_{\mathrm{I}_2}\frac{e}{k_{\mathrm{B}}}\left(\frac{T_{\mathrm{I}_2} - T_{\mathrm{edge}}}{\Lambda_0}\right)\frac{S}{V} && \text{Molecular heat flux} \\
&\quad - \frac{16}{3}\frac{m_{\mathrm{II}_2}}{m_{\mathrm{I}} + m_{\mathrm{I}_2}}e(T_{\mathrm{I}_2} - T_{\mathrm{I}})n_{\mathrm{I}_{3/2}}n_{\mathrm{I}_2}\Omega^{(1,1)}_{\mathrm{I}_{3/2}\mathrm{I}_2} && \mathrm{I_{3/2}}\text{ - }\mathrm{I_2}\text{ elastic collisions} \\
&\quad - \frac{16}{3}\frac{m_{\mathrm{II}_2}}{m_{\mathrm{I}} + m_{\mathrm{I}_2}}e(T_{\mathrm{I}_2} - T_{\mathrm{I}})n_{\mathrm{I}_{1/2}}n_{\mathrm{I}_2}\Omega^{(1,1)}_{\mathrm{I}_{1/2}\mathrm{I}_2} && \mathrm{I_{1/2}}\text{ - }\mathrm{I_2}\text{ elastic collisions} \\
&\quad + s_{\mathrm{keep},\mathrm{I}_2^+} \times (5eT_e) \times \Gamma_{\mathrm{I}_2^+}\frac{S_{\mathrm{neutr,ions}}}{V}, && \text{Wall neutralization of the } \mathrm{I_2^+}\text{ flux}
\end{aligned}
\tag{5.28}
$$

with κ_{I_2} the molecular iodine thermal conductivity, fitted as a function of the atomic temperature, from [168]:

$$
\kappa_{\mathrm{I}_2} = 2.42 \times 10^{-5}\left(\frac{e}{k_{\mathrm{B}}}T_{\mathrm{I}_2}\right)^{0.849}. \tag{5.29}
$$

5.2.3.4 Numerical resolution

The code has been fully written in *Python* language by Marmuse [22] but greatly expanded and automated during this thesis. The differential equations are solved using the "integrate.solve_ivp" function from the *Scipy* library. The 5th order "BDF" method has been applied with an adaptive time step. The equations are solved until steady-state conditions are obtained which typically occurs after a simulation time of a few milliseconds.

5.3 Global modeling of the iodine cell

In this section, the 0D model is adapted and applied to the iodine cell. A comparison with the experimental results presented in Chapter 4 will allow to validate or invalidate various hypotheses of the model. We will also look at the predictions of the model for physical quantities that could not be measured in the cell (temperature and electron density, electronegativity, etc.)

5.3.1 Adaptation of the model to the iodine cell

5.3.1.1 Geometrical considerations and initialization

The calculated length of the cell is reduced to the zone located between the electrodes: $L = 15$ cm (while the cell length is 25 cm). The radius is kept identical to the experiments: $R = 1.5$ cm. No flow is needed ($Q_N = 0$ s^{-1}) nor any grid ($\beta_{\text{neutrals}} = \beta_{\text{ions}} = 0$). The initial density of molecules is $n_{I_{2,0}}$. All other species densities are set to 0 at $t = 0$. The edge temperature is set to 300 K.

5.3.1.2 Self-consistent calculation of the absorbed power

The absorbed power is calculated from the equation introduced in Chapter 2:

$$P_{\text{abs}} = \frac{1}{2} R_{\text{ind,cell}} I_0^2, \tag{5.30}$$

with I_0 the RF signal amplitude and

$$R_{\text{ind,cell}} = \frac{V}{\sigma_{\text{cell}} S^2} = \frac{m_e \nu_{\text{m}}}{n_e e^2} \frac{V}{S^2}, \tag{5.31}$$

the inductive resistance of the plasma [119]. The electron-neutral momentum transfer collision frequency has been given in equation (1.39). The RF power is plotted as a function of the RF signal amplitude I_0 in Figure 5.2. The experimental measurements (taken for an initial pressure of 11.9 Pa) are compared to the simulation results with ν_{m} calculated using the atomic iodine elastic cross-section. As discussed in Chapter 1, the accuracy of this cross section is under investigation, so we also present, in Figure 5.2, results using the elastic cross section of xenon (atom with almost the same mass, see Table 1.10 for the mean value of the iodine and xenon elastic cross-sections on the interval [1 eV ; 10 eV]). The trend is well reproduced but the model systematically overestimates the power (a factor 3 with the xenon cross-section and almost 6 with the iodine cross-section). Equation (5.31), has been derived considering a constant electron density profile, which is certainly a too simple approximation.

The overestimation of the power for a given current has no impact on the results presented in the following since the electron-neutral elastic collisions do not come into play in the continuity equations and are negligible in the energy equations.

5.3.2 Results

Experimentally, the absorbed power has not been calculated and the only available quantity is the RF power delivered by the generator. Thorsteinsson [95] assumed

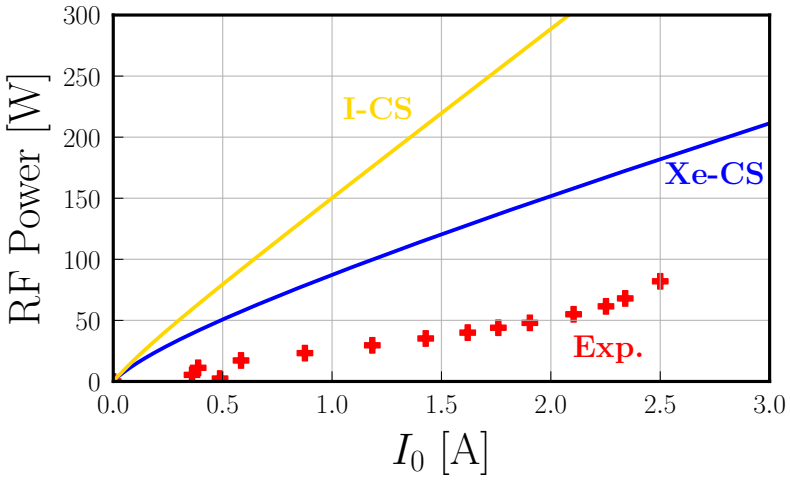

Figure 5.2: Evolution of the RF power (with $P_{abs} = 0.75\ P_{RF}$ in the simulations) as a function of the current amplitude. The experimental data are compared to the simulations obtained with ν_m calculated by considering either the elastic cross-section of atomic iodine or xenon.

the absorbed power to be a fraction of the RF power and we do the same here and we choose:

$$P_{abs} = 0.75\ P_{RF}. \tag{5.32}$$

This assumption has been used to generate Figure 5.2. To be exact, the ratio of P_{abs} over P_{RF} is the power transfer efficiency (PTE) that depends on the pressure and the input power but without further experimental data we assumed a constant value for all the operating conditions.

5.3.2.1 Procedure to compare measurements and simulations ($p_0 = 11.9$ Pa)

In Chapter 4, we measured for three different initial pressures p_0 (4.5 Pa, 11.9 Pa and 24.5 Pa) the molecular dissociation fraction η, the atomic temperature T_I and the population difference $\Delta n = n_{I_{3/2}} - 2n_{I_{1/2}}$, as a function of the RF power. We will use these experimental measurements to fix the last unknown of the problem, namely the wall sticking probability γ_{wall} and to evaluate the relevance of some assumptions (for instance concerning the value of the quenching rate).

Experimentally, the dissociation fraction was shown to saturate at a value between 85% and 90% (see Figure 4.26). However, we only model the positive column (volume between the electrodes) where the dissociation fraction is expected to be almost 100 % for sufficient input power. At high power, the remaining molecules (detected by absorption) are assumed to be located outside the volume between the electrodes. This volume represents 3/25 = 12 % of the cell volume. Thus, the measured dissociation fractions are artificially multiplied by 100/88 to suppress the contribution of the molecules located outside of the inter-electrode region.

In what follows, we take the experimental results obtained for an initial pressure of 11.9 Pa as an example to describe the procedure. The results are presented in Figure 5.3.

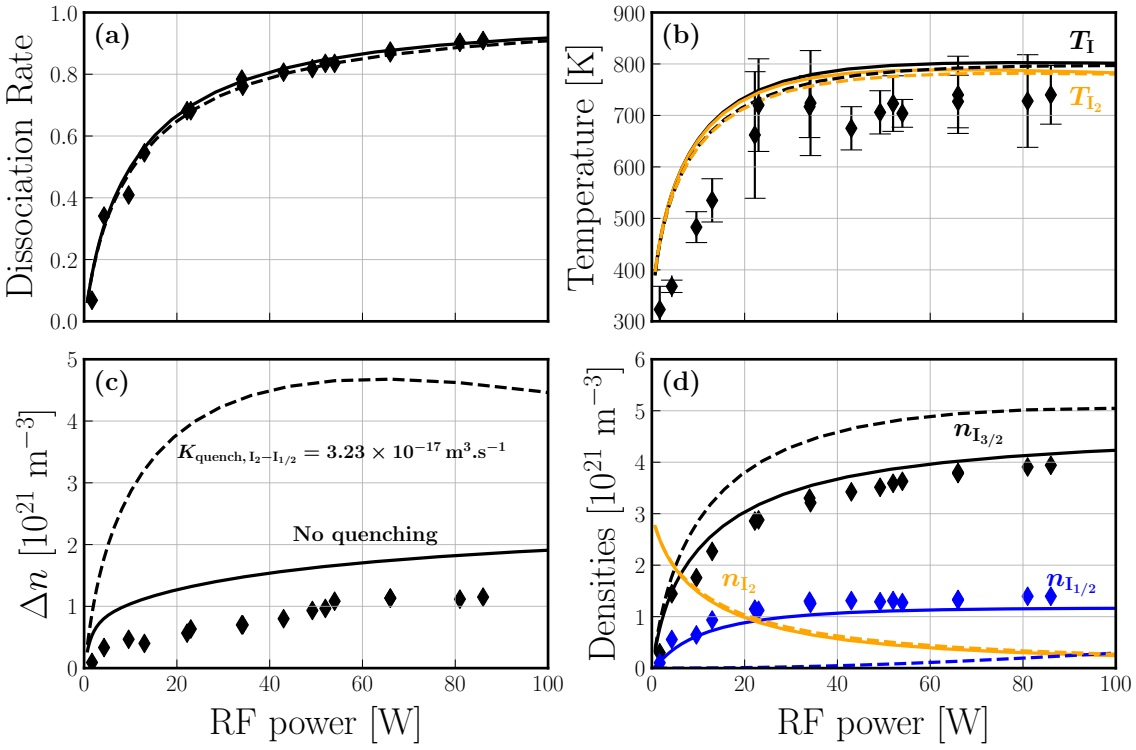

Figure 5.3: Comparison between experimental measurements and simulation results of the iodine cell for an initial pressure of 11.9 Pa. The simulations were performed taking into account the quenching of the atomic species excited by the molecules (dotted line) or not (solid line) and $\gamma_{wall} = 0.003$. Four physical quantities are plotted as a function of the RF power (with $P_{abs} = 0.75\ P_{RF}$ in the simulations). (a) dissociation fraction $\eta = 1 - n_{I_2}/n_{I_{2,0}}$. (b) Atomic ($T_I$) and molecular ($T_{I_2}$) temperatures. (c) Degeneracy weighted population difference $\Delta n = n_{I_{3/2}} - 2n_{I_{1/2}}$. (d) Atomic ($n_{I_{3/2}}$ and $n_{I_{1/2}}$) and molecular (n_{I_2}) densities.

The first step is to choose the γ_{wall} value. To do this, we use the evolution of the dissociation fraction with RF power and look for the γ_{wall} value that minimises the difference between the measurements and the simulation. In sub-figure (a), we see that the agreement is excellent for $\gamma_{wall} = 0.003$. This value may seem low but similar values (and even lower) have already been measured in oxygen plasmas generated in quartz cells [169]. In a second step, we can compare the other measured quantities starting with the atomic temperature in sub-figure (b). The evolution of the atomic temperature with power is well reproduced with notably a saturation at high power, resulting partly from the dependence of the thermal conductivity to the temperature (see equation (5.27)). The higher discrepancies at low power may be due to an overestimation of the power transfer efficiency (in Figure 2.11, the PTE is increasing with the current). Note that, the molecular temperature is almost equal to the atomic temperature. Then, the behavior of the Δn population difference is studied in sub-figure (c). The experimental values, presented in Figure 4.35, have been multiplied by 25/15 to fit the simulated optical length. We see that the effect of quenching (dashed lines) is predominant and that the agreement is better (though not perfect) when we neglect it (solid lines), which will be the case in the following of this section. Indeed, the selected reaction rate for quenching, presented in

Chapter 1, seems to be largely overestimated for an iodine plasma. Finally, in sub-figure (d), the densities of the neutral species are plotted and compared with those obtained by combining the absorption measurements at 488 nm and 1315 nm (presented in Chapter 4). Neglecting quenching, the agreement is very satisfactory. The absence or not of quenching has no effect on the molecular density, as was the case for the dissociation fraction.

Although not studied in iodine plasmas, the quenching of the excited state by the molecule has been intensively studied by using photodissociation and although there may be doubts about the value of the reaction rate taken in this thesis, it seems surprising that it has to be cancelled out to reconcile experiments and simulations. It is possible that the addition of a term for the direct production of the excited atomic state via molecular dissociation would help, but we do not have cross sections for such a process (see Chapter 1).

5.3.2.2 Further experimental comparisons (p_0 = 4.6 Pa to p_0 = 24.5 Pa)

To further compare the model and the experiments, we apply the procedure detailed in the previous subsection for additional initial pressures of 4.6 and 24.5 Pa. The results, as well as those already presented for an initial pressure of 11.9 Pa, are shown in Figure 5.4.

The value of γ_{wall} was adjusted to best approximate the dissociation fraction curve (sub-figure (a)). The values retained are $\gamma_{\text{wall}} = 0.007$ at 4.6 Pa, $\gamma_{\text{wall}} = 0.003$ at 11.9 Pa and $\gamma_{\text{wall}} = 0.0015$ at 24.5 Pa. Note that the agreement is not optimal and that there is no reason for γ_{wall} to be independent of RF power (since the wall temperature increases with power, which was not considered neither), but it is common to see a growth of gamma with the dissociation fraction [95], and so a higher γ_{wall} at lower pressure for the same power.

Then, the trend for the Δn density difference between the atomic levels is well reproduced by the model but the simulated values are systematically overestimated which may reveal missing terms in the continuity equation for $I_{1/2}$. Note that the agreement is less good at high pressure where the model also overestimates the temperature.

Indeed and finally, while the trend in atomic temperature is captured regardless of pressure (especially the saturation at high power), the values only rarely agree with experiments. If we evaluate the importance of the heating terms in the energy equation for the atoms, we find that the main contribution (>75 %) comes from the collisions between the I_2^+ ions and the atoms:

$$\sigma_{\text{in}} \left(\Gamma_{I_{3/2}} + \Gamma_{I_{1/2}} \right) n_{I_2^+} m_{I_2} u_{B,I_2^+}^2. \tag{5.33}$$

However, this term is only an average estimate which in reality should depend on the pressure. At high pressure, the use of the Bohm speed in the expression seems exaggerated and it would probably be more correct to replace it by the thermal velocity, which would lead to a decrease in the overall term (since $u_{B,I_2^+} \gg \overline{v}_I$). Conversely, at low pressure, the use of the thermal velocity in the atomic flux expression could be replaced by the Bohm speed, which would increase this term.

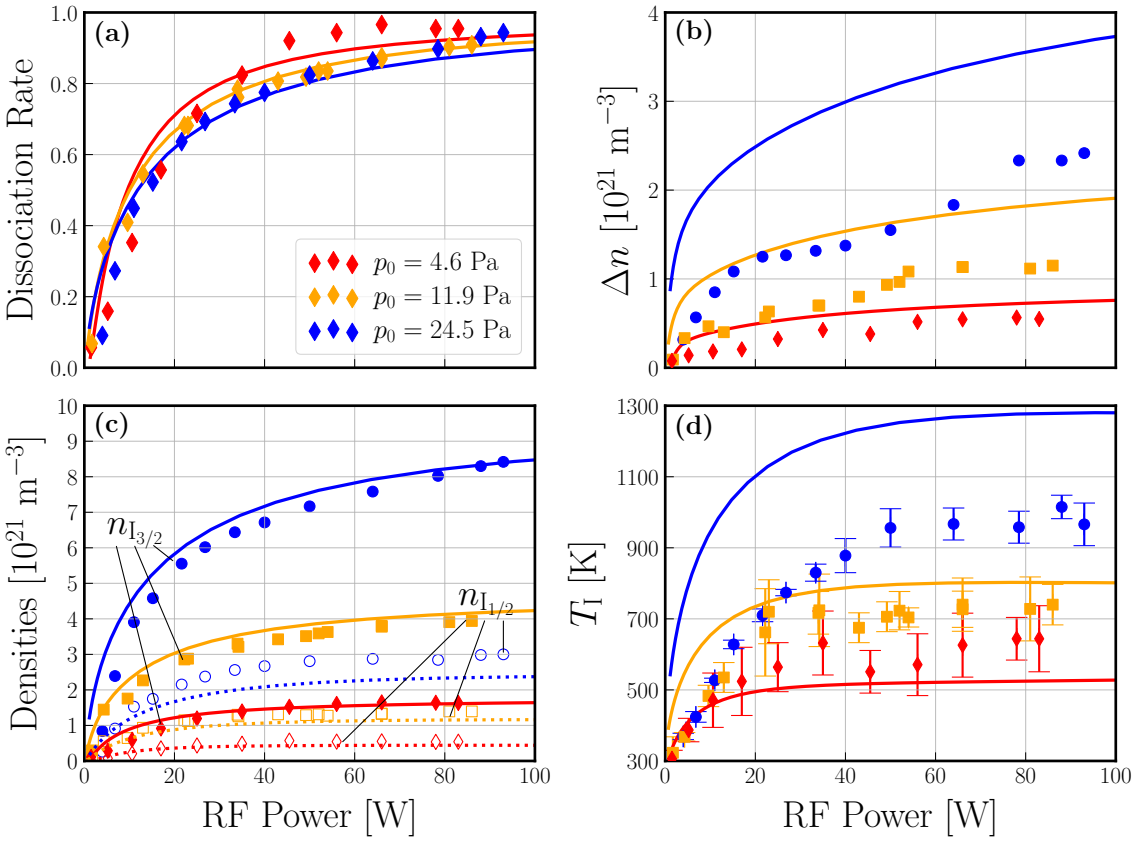

Figure 5.4: Comparison between experimental measurements and simulation results of the iodine cell for an initial pressure of 4.5, 11.9 and 24.5 Pa. The wall sticking probability is set to 0.007 (4.5 Pa), 0.003 (11.9 Pa) and 0.0015 (24.5 Pa). Four physical quantities are plotted as a function of the RF power (with $P_{abs} = 0.75\ P_{RF}$ in the simulations). (a) dissociation fraction $\eta = 1 - n_{I_2}/n_{I_{2,0}}$. (b) Degeneracy weighted population difference $\Delta n = n_{I_{3/2}} - 2n_{I_{1/2}}$. (c) Atomic densities ($n_{I_{3/2}}$ and $n_{I_{1/2}}$). (d) Atomic temperature T_I.

5.3.2.3 Model predictions

To conclude this section, we can now use the model to estimate plasma quantities that we were unable to measure. We take as an example the case of an initial pressure of 11.9 Pa where the model reproduced the experimental results relatively well.

In Figure 5.5, the densities of the charged species are plotted as a function of RF power. We see that I^- and I_2+ ions are largely dominant with a density above 10^{18} m^{-3}. The electron and I^+ densities are more than one order of magnitude lower. One can wonder if under these conditions, the negative ions I_3^- are not to be included in the model as they were shown to be the dominant negative species at higher pressures [26].

In Figure 5.6, the electronic temperature, the atomic and molecular temperatures, the electronegativity ($\alpha = n_{I^-}/n_e$) and the ionization rate ($(n_{I^+} + n_{I_2^+})/n_{neutrals}$) are plotted as a function of the RF power.

The electron temperature is quite high at very low power and it decreases with the RF power and is between 1.5 and 2 eV above 20 W, where all three curves are very close. Interestingly, the model predicts a lower electron temperature for the

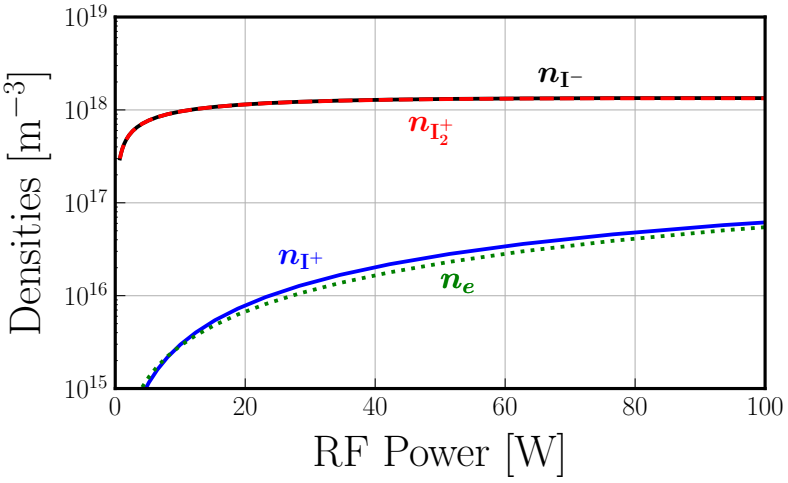

Figure 5.5: Charged-particles densities predicted by the model for an initial pressure of 11.9 Pa.

lower initial pressure, this may also be caused by the wrong estimation of the power transfer efficiency.

The atomic and molecular temperatures are almost equal, especially at the highest pressure. However, for low pressure, high power, the curves start to differ. This will be discussed in the next section and in Chapter 6.

Classically, the electronegativity decreases with power and increases with pressure. Values higher than 1000 are obtained at very low power for the highest pressure. This result coroborates the works published in the early years of electronegative plasmas [26, 76, 77], in which the electronegativity in iodine plasmas was measured to be as big.

Finally, the ionization rate is very low and saturates with power, not exceeding 5×10^{-4} at the lowest pressure.

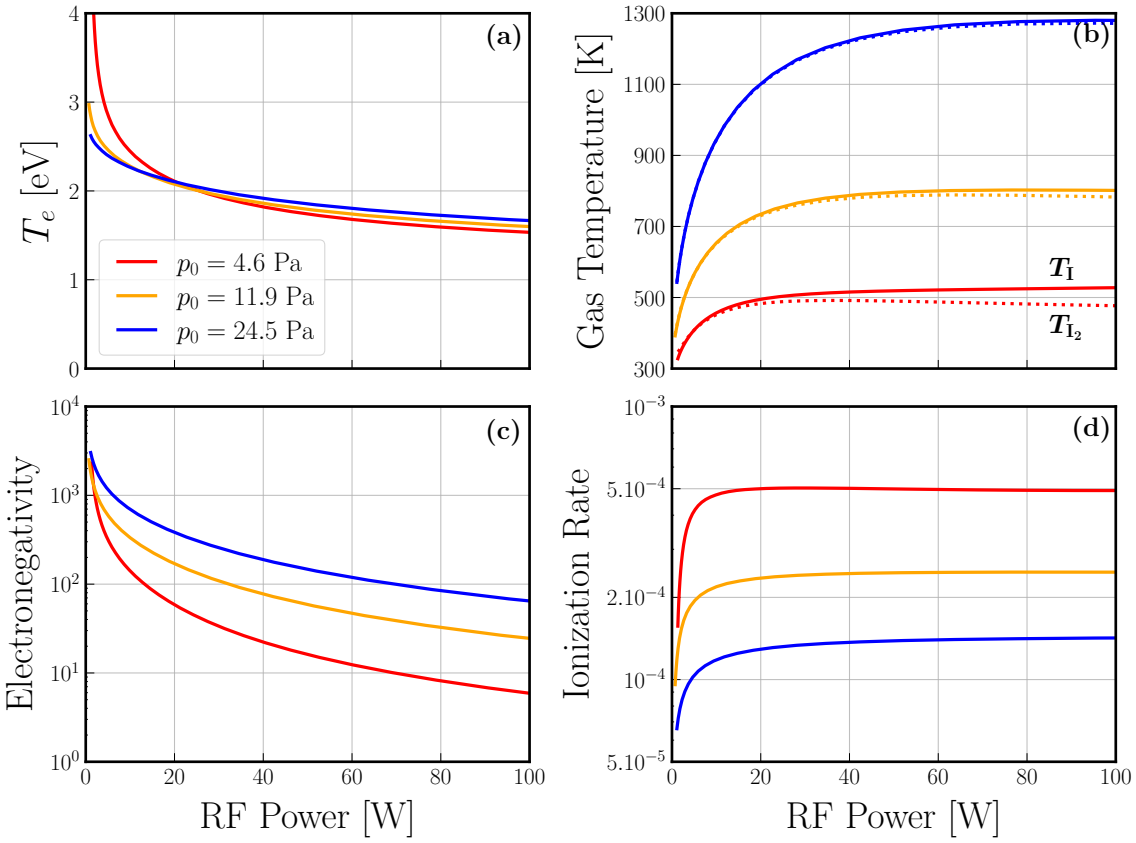

Figure 5.6: Iodine cell global modelling results as a function of the RF power for three different initial pressures (4.6, 11.9 and 24.5 Pa). (a) Electron temperature T_e [eV]. (b) Neutral species temperature [K]. (c) Electronegativity $\alpha = n_{I^-}/n_e$. (d) Ionization rate $(n_{I^+} + n_{I_2^+})/n_{\text{neutrals}}$.

5.4 Global modeling of the PEGASES thruster

In this section, the model is first adapted to the thruster characteristics. Then, the simulation results are compared to experimental measurements presented in Chapter 3 and Chapter 4. In the following, the quenching reaction is not taken into account and we have checked afterwards that it has a negligible influence at low pressure and only a minor one at higher pressure.

5.4.1 Adaptation of the model to the PEGASES thruster

5.4.1.1 Self-consistent calculation of the absorbed power

Theoretical background

Taking up the work of Chabert *et al.* [114] (which was re-used without any modification by Grondein *et al.* [13]) we consider that the plasma is generated by circulating an RF current, of amplitude I_{coil}. In the original model, the formulas were derived for a coil surrounding the cylindrical chamber. However, experimentally we use a flat coil and we slightly modified the formulas to take it into account. The induced electromagnetic field is responsible for the plasma generation. The coil has N_{coil} turns and its total length is l_{coil}. The absorbed power is calculated from the equation introduced in Chapter 2:

$$P_{abs} = \frac{1}{2} R_{ind} I_{coil}^2, \tag{5.34}$$

with

$$R_{ind} = \frac{2\pi N_{coil}^2}{l_{coil}\omega_{RF}\varepsilon_0} \mathrm{Re}\left[\frac{ikR'}{J_1(kR')}\varepsilon_p J_0(kR')\right]. \tag{5.35}$$

where $R' = a \times R$ ($a > 0$ is a free parameter, $a = 1$ gives back the expression from [114]), ε_0 is the vacuum permittivity, J_0 and J_1 the 0^{th} and 1^{st} modified Bessel functions, $k = \frac{\omega_{RF}}{c}\varepsilon_p^{1/2}$ and

$$\varepsilon_p = 1 - \frac{\omega_{pe}^2}{\omega_{RF}(\omega_{RF} - j\nu_m)} \tag{5.36}$$

is the plasma complex permittivity with ν_m the electron momentum transfer collision frequency, given by equation (1.39).

Determination of the coil properties

The unknowns of equation 5.35 are the coil parameters (N_{coil} and l_{coil}) and $a = R'/R$. In order to determine these parameters, we use the global model working with xenon (a model working with argon, krypton and xenon is described in Appendix A) and seek for the best fitting parameters to match the experimental results of the power transfer efficiency, shown in Figure 2.11, and measured for a fixed pressure of 2.5 mTorr. Let's simply recall that the power transfer efficiency (PTE) reads:

$$PTE = \frac{P_{abs}}{P_{RF}} = \frac{R_{ind}}{R_{ind} + R_{coil}}, \tag{5.37}$$

with $R_{coil}(I_{coil})$ given by equation (2.6).

The total resistance $R_{ind} + R_{coil}$ and the power transfer efficiency are plotted as a function of the coil current in Figure 5.7. Model results (line) have been obtained by using $a = 0.2$ and $N_{coil}^2/l_{coil} = 1.64 \times 10^4$ m^{-1}, choosing xenon measurements as a reference. In the following, the values of a and N_{coil}^2/l_{coil} are fixed and assumed to be the same for all gases and all working pressures. The agreement between experiments and model for krypton and argon is also remarkable especially concerning the minimum current for which the discharge can be operated.

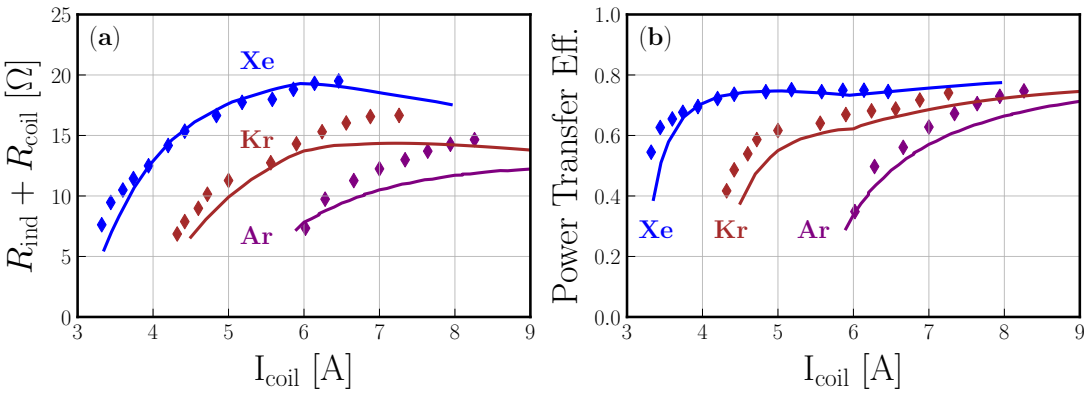

Figure 5.7: Comparison between the global model simulations (line) and the experimental measurements (markers) for argon, krypton and xenon obtained in the PEGASES thruster for a fixed pressure of 2.5 mTorr. (a) The sum of the inductive resistance and the coil resistance is plotted as a function of the coil current. (b) The power transfer efficiency (PTE) is plotted as a function of the coil current.

The same procedure has been applied to iodine and the results are plotted in Figure 5.8. The agreement is much less satisfactory than with the noble gases. The uncertainty on the iodine elastic collision reaction rates $K_{el,I_{3/2}}$ and $K_{el,I_{1/2}}$, discussed in Chapter 1, could be a cause of error. We added the result of a simulation where the atomic iodine elastic reaction rates were set equal to the xenon rate: $K_{el,I_{3/2}} = K_{el,I_{1/2}} = K_{el,Xe}$, the other reactions rates being unchanged (dashed line).

The same study was carried out at 0.6 mTorr (with the four gases), keeping the same coil properties and the agreement was not good, R_{ind} being largely underestimated by the model. Such a discrepancy could be due to stochastic heating which is not taken into account in the model and which could be non-negligible at very low pressure.

To conclude, the self-consistent calculation of the discharge power being independent of the simulation results, we keep the above mentioned values for the coil. Similarly, the elastic collisions between electrons and neutrals play no role in the continuity equations and are largely negligible in the energy equations (for our operating conditions) so the use of the elastic cross-section of iodine or xenon has almost no effect on the simulated quantities (much less than 1 % of difference on the calculated densities). In the following, we will use the elastic cross-section of xenon. The explanation is given by Figure 5.9. The experimental plasma breakdown operating conditions (flow rate and coil current) are compared to the simulated breakdown operating conditions obtained with either the xenon or iodine elastic cross-section. The overall agreement is better with xenon (mostly at high flow rates, although not

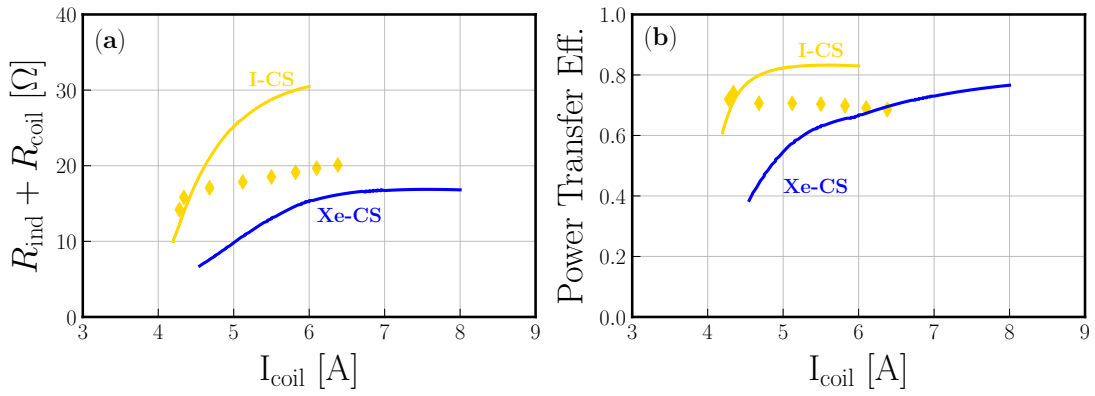

Figure 5.8: Comparison between the global model simulations and the experimental measurements (markers) for iodine obtained in the PEGASES thruster for a fixed pressure of 2.5 mTorr. The model was run with either the iodine elastic cross-section (gold) or the xenon elastic momentum transfer cross-section (blue). (a) The sum of the inductive resistance and the coil resistance is plotted as a function of the coil current. (b) The power transfer efficiency (PTE) is plotted as a function of the coil current.

perfect) and justifies our choice.

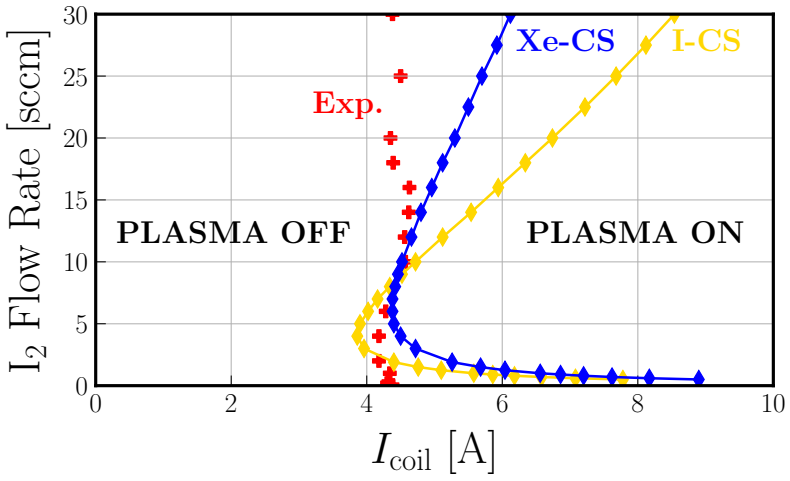

Figure 5.9: Iodine plasma breakdown operating conditions (flow rate versus the coil current). The experimental values are compared to the values simulated by the model using either the xenon elastic cross-section or the iodine cross-section.

5.4.1.2 Input parameters and initial conditions

A cylindrical geometry has been kept in the model while our experiments were conducted in a nearly cubical thruster: it has been decided to keep the same thruster axis length and to adjust the inner radius in order to reach the same internal volume ($V \approx 1.25 \times 10^{-3}$ m^3). To adapt the model to the experimental setup, the RF excitation frequency has been set to 4 MHz and the grid transparency $\beta_{neutrals}$ to 10 %.

Since the exhaust grid is not polarized, we have used $\beta_{ions} = \beta_{neutrals}$. All model input parameters are summarized in Table 5.2.

Table 5.2: Parameters used in the model.

Thruster	Grid settings	Coil properties	Iodine constants
$R = 5.5$ cm	$\beta_{neutrals} = 0.1$	$\omega_{RF} = 2\pi \times 4$ MHz	$m_I = \frac{1}{2} m_{I_2} = 126.9$ uma
$L = 13$ cm	$\beta_{ions} = 0.1$	$N_{coil}^2 / l_{coil} = 1.64 \times 10^4$ m^{-1}	$\sigma_{in} = 10^{-18}$ m^2
$T_{edge} = 600$ K		$a = 0.2$	

Based on the observation of Figure 4.18, a large temperature jump exists whatever the pressure. We decide to set: $T_{edge} = 600$ K.

The remaining unknown is the wall sticking probability γ_{wall} (see Chapter 1 for more details), the value of which depends on the surface material, the wall temperature, the dissociation fraction, etc... In iodine, no precise experimental study has yet been carried out and we do not have an explicit formula as a function of the dissociation fraction, as is the case for chlorine [95]. We will therefore use experimental measurements to determine this value.

The model is run until a steady state is reached, when the study is performed as a function of the discharge power or the pressure, the initial conditions are taken equal to the final values of the previous converged simulation.

5.4.2 Comparisons to experiments

The model inputs are the coil current and the I_2 mass flow rate, while the experimental control parameters are the pressure and the power. In order to compare similar plasma conditions, the model has been run over a very large range of mass flow rates and coil currents to insure that we could find cases with output neutral pressure and absorbed power similar to the experimental ones.

5.4.2.1 Influence of neutral pressure

In the first part of this subsection, the global model is compared to the measured electron density, electron temperature and electronegativity as a function of the neutral pressure (see Figure 5.10). The discharge power is fixed at 200 W and $\gamma_{wall} = 0.05$. The experimental values are taken from Figure 3.26 for the electron density and the electron temperature and from Figure 3.29 for the electronegativity. The bars in the figure indicate the minimal and maximal measured values (where repeatability errors have been included, see Chapter 3 for more details) recorded along the spatial profile, while the marker is the value averaged over the spatial profile. At very low pressure, where the spatial profiles are quite flat, there are only little differences between the minimum, the maximum and the average. Inversely, at higher pressure, there are major discrepancies between these values, leading to very large bars.

Such a study has already been carried out in the framework of this thesis using Grondein's model [13] (see Esteves *et al.* [1] for the details). These results are reported on the figures with a dashed blue line. The results obtained with the updated model are plotted in red. As in the studied conditions, the electronegativity

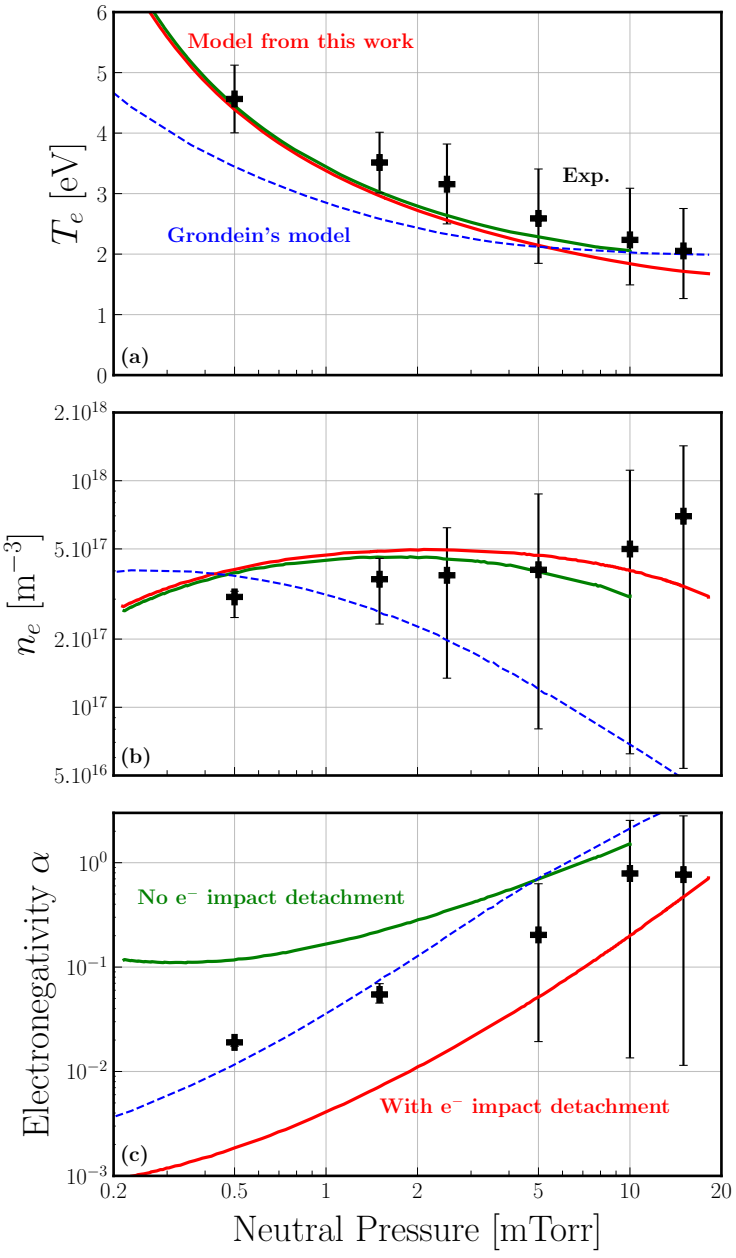

Figure 5.10: The iodine global model is compared to experimental measurements in PEGASES thruster for a fixed discharge power of 200 W and $\gamma_{\text{wall}} = 0.05$. The effect of neutral pressure is studied. The markers represent the mean value measured all along the thrust axis while the errorbars evidence the minimal and maximal values. The dashed blue line represent the results from Esteves *et al.* [1] by using Grondein's model [13]. (a) The simulated and measured by Langmuir probe electron temperature T_e is plotted versus the neutral pressure. (b) The simulated and measured by Langmuir probe electron density n_e is plotted versus the neutral pressure. (c) The simulated and measured by photodetachment electronegativity α is plotted versus the neutral pressure. The influence of the electron impact detachment reaction is added.

varies significantly, we have also used these results to evaluate the consistency of the current cross-section for detachment, which as discussed in Chapter 1, is based on

only one calculation so far and is considered to be rather high, the simulations were performed with (green) and without (red) the electron impact detachment process.

For pressures below 3 mTorr, where spatial profiles are fairly flat, the comparison between Grondein's model and experiments was acceptable for the electron density and the electronegativity. However, the electron temperature was systematically underestimated by the model. With the updated model, the electron temperature is well captured whatever the pressure. This comes from the additional neutral gas heating terms, described above, that were not included in Grondein's model. For the same pressure, as the temperature of the neutrals increases, their density decreases as well. This leads to fewer collisions and therefore more transport. In order to maintain the same ionisation rate, T_e must increase. Also, the electron density, is slightly overestimated but closer to the mean experimental values, even at 10 mTorr. Concerning the electronegativity, the trend is well reproduced but the difference between both simulations (with or without the electron impact detachment process) is striking and the experimental values lie between both curves, meaning that, as pointed out in Chapter 1, the cross-section for this reaction might have been overestimated (or the wall sticking probability γ_{wall} has been underestimated, see next subsection). The absence or not of this cross-section in the reaction set has only a minor impact on T_e and n_e.

In a second part, the global model is compared to the measured atomic temperature, dissociation fraction, difference of population between the two first atomic states, molecular densities and reconstructed atomic densities as a function of the neutral gas pressure (see Figure 5.11). Once again, the discharge power is fixed at 200 W. The experimental values are taken from Figure 4.50 and Figure 4.19 for the atomic temperature, from Figure 4.46 for the dissociation fraction, from Figure 4.49 and Figure 4.50 for Δn and from Figure 4.46 and Figure 4.51 for the densities. The bars in the figure indicate the minimal and maximal measured values recorded along the spatial profile, while the marker is the value averaged over the spatial profile, except for the atomic temperature where measurements were performed at a single location ($z = 7.65$ cm).

In what follows, the comparison with experiments should be taken with caution since the measurements were mostly obtained for pressures above 3 mTorr, where the optical signals were sufficient but where the spatial gradients are non-negligible and the uniform electron temperature, and the validity of the model that goes with it, are questionable. It should also be remembered that measurements obtained by absorption are integrated on the line of sight and not local as were the measurements of the charged species.

In subfigure (a), we see that the model largely underestimates the atomic temperature, which is mostly flat only 100 K above T_{edge}. It starts increasing for pressures above 3 mTorr. A slight rise in temperature is also observed at very low pressure, it comes from the energetic ions that release some of their energy, acquired in the sheath, to the neutral gas after neutralisation at the wall. Interestingly, the atomic and molecular temperatures differ. In this global model, this is explained by the very high dissociation fraction and the fact that almost all the heating terms of the molecules are proportional to the molecular density: without molecules, no heating. However, this model does not account for density gradients and we will see in the next chapter that atoms and molecules do exchange energy and that their

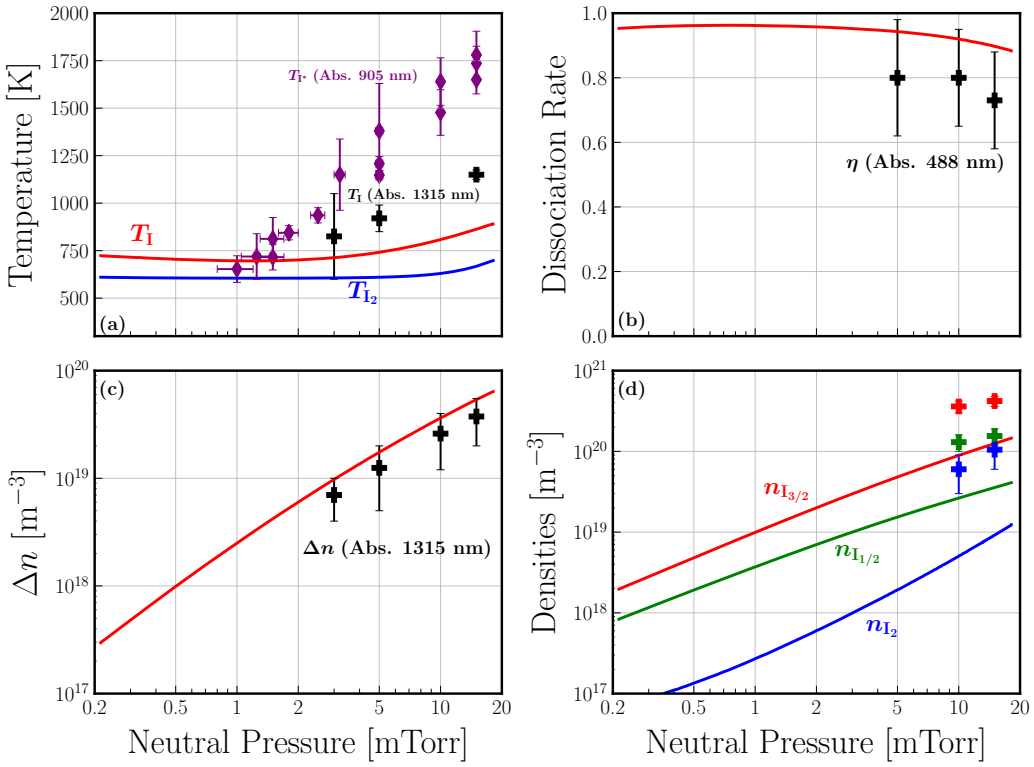

Figure 5.11: The iodine global model is compared to experimental measurements in PEGASES thruster for a fixed discharge power of 200 W and $\gamma_{wall} = 0.05$. The effect of neutral pressure is studied. The markers represent the mean value measured all along the thrust axis while the errorbars evidence the minimal and maximal values. (a) Atomic and molecular temperatures, the experimental data are taken from Figure 4.50 and Figure 4.19. (b) Dissociation fraction, the experimental data are taken from 4.46. (c) $\Delta n = n_{I_{3/2}} - 2n_{I_{1/2}}$, experimental data are taken from Figure 4.49 and Figure 4.50. (d) Neutral species densities, experimental data are taken from Figure 4.46 and Figure 4.51.

temperature should not differ significantly.

Then, in subfigure (b), the dissociation fraction is very high, more than 90 % below 10 mTorr. The only remaining molecules are produced via recombination at the walls (with $\gamma_{wall} = 0.05$ in this case). The experimental errorbars are very large but the simulated dissociation fraction may be overestimated, meaning that the value of γ_{wall} might have been underestimated.

Finally, the agreement between the simulated and the measured Δn is satisfying and the trend with pressure is well captured. However, the model clearly underestimates the neutral species densities as compared to the values found in Chapter 4.Because the agreement is not good on the dissociation rate, the agreement cannot be good on the molecular density. The calculation of the experimental atomic densities directly depends on the value of the dissociation rate which explains the discrepancies observed. The discrepancy could even be bigger if the temperature was correctly captured by the model. As the spatial profiles show gradients, the global model shows its limits here.

In the following subsection, we shall restrict our comparison to pressures below

3 mTorr, where the assumption of isothermal electrons still holds, and the global model approach is more appropriate.

5.4.2.2 Influence of the discharge power for pressure < 3 mTorr

The experimental results presented in this section were all obtained at a fixed position $z = 6.5$ cm, in the middle of the discharge. The discharge power was varied over the largest range available in order to get the largest range of electron density values and the mass flow rate was adapted to keep a constant pressure. Experiments were conducted at 0.6, 1.0 and 2.5 mTorr. Unless otherwise stated, the electron impact detachment reaction is incorporated into the model and $\gamma_{\text{wall}} = 0.15$. This value of γ_{wall} comes from the chlorine global model of Thorsteinsson *et al.* (see Figure 3 in [95]) where, in the case of an anodised aluminum surface, the experimental values of γ_{wall} measured by Guha *et al.* [170] tend to 0.15 when the plasma is fully dissociated.

In Figure 5.12, we choose to plot the electronegativity (±10%) versus the electron density ($^{+38}_{-13}$%, see Chapter 3 for details) rather than the discharge power. In this way, we directly check the particle balance equations and we partially short-circuit the power balance equation. The measured values are in good agreement with the model with $\gamma_{\text{wall}} = 0.15$. The electronegativity increases greatly when the electron density (or the discharge power) decreases. For very low discharge power, where the discharge could not be maintained, very high electronegativity values are expected which was observed in early works on iodine plasmas [76, 77].

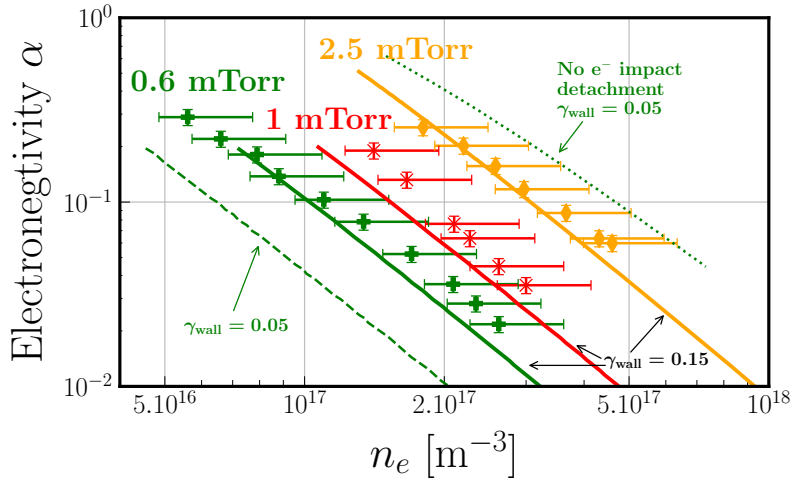

Figure 5.12: The electronegativity $\alpha = n_{I^-}/n_e$ is plotted againt the electron density n_e. The global model is compared to experimental measurements in PEGASES thruster for three different pressures (0.6, 1.0 and 2.5 mTorr). The solid lines are simulations with $\gamma_{\text{wall}} = 0.15$. At 0.6 mTorr, two more curves are plotted with $\gamma_{\text{wall}} = 0.05$: one taking into account the electron detachment process (dashed) and an other without the electron detachement process (dotted).

At 0.6 mTorr, we added two simulation results obtained for $\gamma_{\text{wall}} = 0.05$ with and without considering the electron detachment reaction. Not including the detachment process at all seems wrong (assuming that the reaction rates for I^-/I^+ and I^-/I_2^+ recombination are accurate). Unfortunately, it is not possible to

determine the precise value of γ_{wall} because of the remaining doubts about the magnitude of the detachment cross section. If the cross-section used is accurate, $\gamma_{wall} \approx 0.15 - 0.2$ seems to be consistent (though, there is no reason to take the same value for different pressures [95]). However, if the cross-section is overestimated, the value of gamma must automatically be adjusted downwards to match the experimental results. Within our experimental setup, it seems reasonable to set γ_{wall} between 0.05 and 0.2.

The electron density is plotted as a function of the discharge power in Figure 5.13, with $^{+38}_{-13}$% errorbars. The agreement between experimental measurements and the global model is quite good. The trends are well captured by the model and the discrepancies never exceed a factor 2. It is worth noticing, however, that the model slightly overestimates the density. The experimental values are all very close, as seen in Figure 3.26, even if the density profiles evolve drastically as pressure increases.

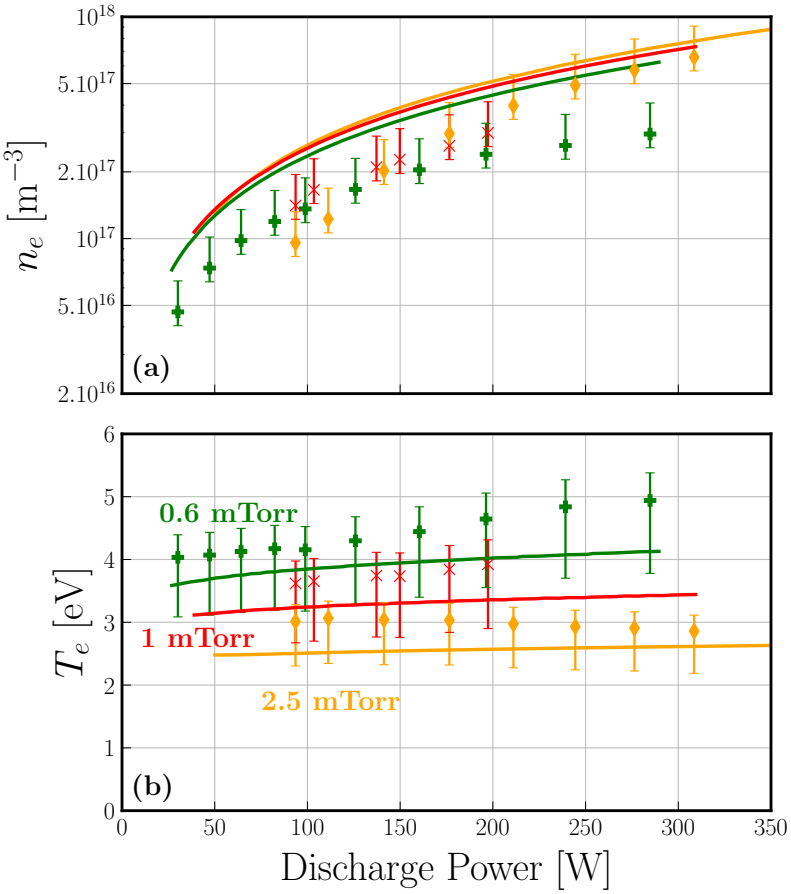

Figure 5.13: The iodine global model, with $\gamma_{wall} = 0.15$, is compared to experimental Langmuir Probe measurements in PEGASES thruster for three different pressures (0.6, 1.0 and 2.5 mTorr). (a) The electron density T_e is plotted versus the discharge power. (b) The electron Temperature T_e is plotted versus the discharge power.

To complete our detailed comparison between experiments and global modelling, the electron temperature ($^{+9}_{-19}$%, see Chapter 3 for details) is plotted as a function of the discharge power in sub-figure (b). The model systematically lies

within the experimental errorbars and the simulated electron temperature slightly increases with discharge power, as observed experimentally. This was not the case in Esteves *et al.* [1], which indicates that the added gas heating terms better capture the physics of the discharge.

To conclude this section, we show in Figure 5.14 the densities of the seven simulated species as a function of discharge power for a neutral pressure at 0.6 mTorr. It can be seen that the plasma is highly dissociated (>90%) at high discharge power and that the ionization degree can be up to a few percents, this regime is very favourable for electric propulsion. Even if I^+ is the dominant ion, note that I_2^+ and I^- can become significant and even dominant at lower discharge powers. Finally, the first two atomic states are very close to a Boltzmann equilibrium at T_e.

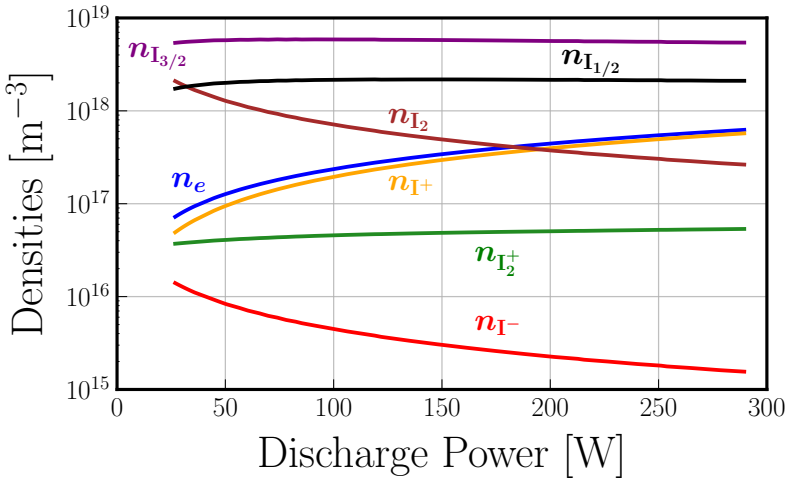

Figure 5.14: Densities predicted by the model as a function of the discharge power for a neutral pressure of 0.6 mTorr.

5.5 Chapter digest

In this chapter, an updated iodine global model has been presented and compared to experimental results on two different geometries. Compared to the previous models, the reaction set has been completed (using the work presented in Chapter 1), the first atomic excited species $I(^2P^\circ_{1/2})$ has been included, the neutral gas heating model has been improved (by including the contribution of fast neutrals generated at the wall by the neutralization of the ion flux and energy gains via dissociation processes) and the temperatures of the atoms and molecules are no longer considered equal. The physics of the plasma generation are also considered in both geometries to self-consistently calculate the absorbed power.

Comparisons on the iodine cell validated the behaviour of neutral species. The neutrals temperatures and densities trends are well captured as a function of the RF power when the wall sticking probability value is adjusted. The dissociation is very high and the equilibrium of charged species is dominated by I^- negative ions and I_2^+ positive ions, although the inclusion of the I_3^- species should be considered. The quenching of the atomic excited state by the molecules seems to be negligible and processes of production of the same excited state by molecular dissociation must be added to complete the comparisons. Finally, although updated, the energy equation for neutral species has shown limitations and more sophisticated heating terms should be considered.

Concerning the comparisons with the thruster, the model well captures the general features. The calculated electron densities and electron temperatures are comparable to the measured ones, and the trends with the neutral gas pressure and absorbed RF power are well reproduced. The model predicts a very strong dissociation in the conditions explored, i.e. very low pressure and high RF power. While the trends for the electronegativity are also well reproduced, the doubts on the magnitude of the electron impact detachment cross-section make it impossible to conclude on the value of the wall sticking probability γ_{wall}, which has only be estimated to be between 0.05 and 0.2.

The atomic and molecular densities have been measured for pressures above 3 mTorr only, where the global model assumptions break down; electrons are no longer isothermal and consequently the profiles start to strongly deviate from the standard case well described by global modelling. So that it is difficult to further discuss comparisons on neutrals measurements. Still, the dissociation fraction is very high as confirmed by direct measurements of the rate fraction itself and of the low electronegativity. In order to correctly describe the strong localization of the plasma near the antenna observed at higher pressures, it will be necessary to use at least one-dimensional models.

Similar results have been published in reference [1] and presented in several international conferences (see Related publications in page xiii). The content of this chapter is intended to be submitted to a journal.

CHAPTER 6

1D MULTI-FLUID MODELING OF IODINE NEUTRAL SPECIES

Contents

6.1 Introduction

Most of the experimental diagnostics implemented on the PEGASES thruster yielded one-dimensional spatial profiles along the thrust axis, at the center of the discharge, where very strong gradients were revealed as the pressure increased. Indeed, measurements of electron density and, electron temperature, electronegativity and relative atomic density evidenced large gradients.

Nevertheless, the absorption measurements of the neutral species presented in Chapter 4, since they were integrated along the transverse line of sight, did not give a clear picture of the behavior of the neutral species (especially for the molecules) in the center of the discharge. Also, at best, due to the location of the windows on the thruster, only 9 cm out of 13 cm were optically accessible (about one third of the discharge was not optically accessible) .

The global model presented in the previous chapter captured most of the experimentally observed trends, but is not intended to model gradients. In particular, global models fail when there are strong gradients of electron temperature. The thruster model was, therefore, only validated for pressure below 3 mTorr and by using charged-particles measurements.

For all these reasons, we decided to implement a one-dimensional multi-fluid code, simulating the center of the discharge, from the antenna, to the exhaust grid. Ideally, a self-consistent code coupling charged and neutral species would have been implemented (it will be done in the future), but this was not feasible within the given time frame of the thesis. The crucial missing information concerned the neutral species, since the measurements of the charged species provided us with absolute measurements over almost the entire length of the thruster axis (10 cm out of the total 13 cm). Thus, we decided to use the multi-fluid approach to simulate the behavior of the three dominant neutral species in our iodine plasmas: I_2 molecules, $I_{3/2}$ atoms and excited $I_{1/2}$ atoms. The electron density and temperature were treated as input parameters and we used values obtained Langmuir probe measurements.

The aim of the work of this chapter is to obtain one-dimensional profiles of the densities, fluid velocities and temperatures of the three simulated species. To this end, it will be necessary to take into account the inertia terms and to consider the energy equations with conductive heat fluxes to close the moment hierarchy.

The model is described in Section 6.2 and the simulation results are compared to experiments in Section 6.3. The main findings of the chapter are gathered in a summary at the end.

6.2 Model description

6.2.1 Multi-fluid formalism

For ease of reading, only the main ideas will be developed in the following. For more details, concerning the derivation of the fluid equations and of the collision source terms, the reader can refer to Appendix B and Appendix C.

6.2.1.1 General equations

Following the works of Benilov [111, 112], let us consider the general binary collision between α and β

$$\alpha + \beta \longrightarrow \text{products.} \tag{6.1}$$

The 3D conservative fluid equations (mass density, momentum and total energy) for the α neutral species are:

$$\partial_t(m_\alpha n_\alpha) + \nabla\cdot(m_\alpha n_\alpha \mathbf{u}_\alpha) = m_\alpha w_\alpha, \tag{6.2}$$

$$\partial_t(m_\alpha n_\alpha \mathbf{u}_\alpha) + \nabla\cdot(m_\alpha n_\alpha \mathbf{u}_\alpha\mathbf{u}_\alpha) + \nabla p_\alpha = -\sum_\beta \mathbf{r}^{(m)}_{\alpha\beta} + \mathbf{w}^{(m)}_\alpha, \tag{6.3}$$

$$\partial_t\left[n_\alpha\left(\frac{3k_\mathrm{B}T_\alpha}{2} + \frac{m_\alpha \mathbf{u}_\alpha^2}{2}\right)\right] + \nabla\cdot\left[\left(n_\alpha\left(\frac{3k_\mathrm{B}T_\alpha}{2} + \frac{m_\alpha \mathbf{u}_\alpha^2}{2}\right) + p_\alpha\right)\mathbf{u}_\alpha + \mathbf{q}_\alpha\right] = -\sum_\beta r^{(e)}_{\alpha\beta} + w^{(e)}_\alpha. \tag{6.4}$$

Here, m_α, n_α, $\mathbf{u}_\alpha$, $p_\alpha = n_\alpha k_\mathrm{B} T_\alpha$, and $\mathbf{q}_\alpha$ are the mass, the density, the mean velocity, the hydrostatic pressure, and the heat flux density of the species α. $\mathbf{r}^{(m)}_{\alpha\beta}$ and and $r^{(e)}_{\alpha\beta}$ are rates of loss per unit volume of, respectively, momentum and energy of the species α due to elastic collisions with the species β. w_α , $\mathbf{w}^{(m)}_\alpha$ and $w^{(e)}_\alpha$ are rates of change of the number density, momentum, and energy of the species a due to inelastic collisions. The former notations implicitly take into account the sum of all the inelastic processes that affect the α particule:

$$w_\alpha = \sum_{\text{process}} w_{\alpha,\text{process}}, \tag{6.5}$$

$$\mathbf{w}^{(m)}_\alpha = \sum_{\text{process}} \mathbf{w}^{(m)}_{\alpha,\text{process}}, \tag{6.6}$$

$$w^{(e)}_\alpha = \sum_{\text{process}} w^{(e)}_{\alpha,\text{process}}. \tag{6.7}$$

$$\tag{6.8}$$

The reader is referred to [111, 112], or Appendix C, in order to find the general expression for the rates. Here, we will particularise the equations to the appropriate reaction set and derive the consequent rates.

6.2.1.2 Reduction to the 1D geometry

Since the electron density and temperature measurements are used as input to the model and these measurements were made one-dimensionally along the thruster axis, the general equations, with $\alpha \in \{I_{3/2}, I_{1/2}, I_2\}$, are reduced to one dimension:

$$\partial_t(m_\alpha n_\alpha) + \partial_z(m_\alpha n_\alpha u_\alpha) = m_\alpha w_\alpha, \tag{6.9}$$

$$\partial_t(m_\alpha n_\alpha u_\alpha) + \partial_z\left(m_\alpha n_\alpha u_\alpha^2 + p_\alpha\right) = -\sum_\beta r_{\alpha\beta}^{(m)} + w_\alpha^{(m)}, \tag{6.10}$$

$$\partial_t\left[n_\alpha\left(\frac{3k_B T_\alpha}{2} + \frac{m_\alpha u_\alpha^2}{2}\right)\right] + \partial_z\left[\left(n_\alpha\left(\frac{3k_B T_\alpha}{2} + \frac{m_\alpha u_\alpha^2}{2}\right) + p_\alpha\right)u_\alpha + q_\alpha\right] = -\sum_\beta r_{\alpha\beta}^{(e)} + w_\alpha^{(e)}. \tag{6.11}$$

Note that when reducing from 3D to 1D geometry, no surface-averaged effects have been included in the model, especially no atomic wall recombination (the atomic wall recombination is only taken into account in $z = 0$ and $z = 13$ cm). The neutralisation of the ion flux at the walls has not been included either. We expect the transport of gas particles in the perpendicular plane to be less important than in the axial direction as the plasma density gradients are stronger along the thrust axis. Additionally, to the best of our knowledge there is no existing reduced model that integrates the transport effects in the transverse direction for a multi-component gas. For this reason, we choose a purely 1D geometry.

6.2.2 Set of reactions

The reaction set used in the multi-fluid code is shown in Table 6.1. Collisions are classified into four different categories:

1. **Elastic** collisions between **neutrals**;
2. **Elastic** collisions between **electrons** and **neutrals**;
3. **Inelastic** collisions between **electrons** and **neutrals**;
4. **Inelastic** collisions between **neutrals**.

The collision rate notations for continuity, momentum and energy equations are also given in the table. Details of the calculations of these rates are provided in Appendix C.

Table 6.1: List of volumic reactions and source terms considered in the multi-fluid model. See Appendix C for the calculation of the elastic and inelastic rates.

Reaction	Density rates	Momentum rates	Energy rates
Elastic collisions between neutrals			
$I_{3/2} + I_{1/2} \rightarrow I_{3/2} + I_{1/2}$	—	$r^{(m)}_{I_{3/2}I_{1/2}} = r^{(m)}_{I_{1/2}I_{3/2}}$	$r^{(e)}_{I_{3/2}I_{1/2}} = r^{(e)}_{I_{1/2}I_{3/2}}$
$I_2 + I_{3/2} \rightarrow I_2 + I_{3/2}$	—	$r^{(m)}_{I_2I_{3/2}} = r^{(m)}_{I_{3/2}I_2}$	$r^{(e)}_{I_2I_{3/2}} = r^{(e)}_{I_{3/2}I_2}$
$I_2 + I_{1/2} \rightarrow I_2 + I_{1/2}$	—	$r^{(m)}_{I_2I_{1/2}} = r^{(m)}_{I_{1/2}I_2}$	$r^{(e)}_{I_2I_{1/2}} = r^{(e)}_{I_{1/2}I_2}$
Elastic collisions between electrons and neutrals			
$I_2 + e^- \rightarrow I_2 + e^-$	—	$r^{(m)}_{I_2e} = 0$	$r^{(e)}_{I_2e}$
$I_{3/2} + e^- \rightarrow I_{3/2} + e^-$	—	$r^{(m)}_{I_{3/2}e} = 0$	$r^{(e)}_{I_{3/2}e}$
$I_{1/2} + e^- \rightarrow I_{1/2} + e^-$	—	$r^{(m)}_{I_{1/2}e} = 0$	$r^{(e)}_{I_{1/2}e}$
Inelastic collisions between electrons and neutrals			
$I_2 + e^- \rightarrow 2\,I_{3/2} + e^-$	$w_{I_2,\mathrm{diss}} = -\frac{1}{2} w_{I_{3/2},\mathrm{diss}}$	$w^{(m)}_{I_2,\mathrm{diss}} = -w^{(m)}_{I_{3/2},\mathrm{diss}}$	$w^{(e)}_{I_2,\mathrm{diss}} = -w^{(e)}_{I_{3/2},\mathrm{diss}}$
$I_{3/2} + e^- \rightarrow I_{1/2} + e^-$	$w_{I_{3/2},\mathrm{ex}} = -w_{I_{1/2},\mathrm{ex}}$	$w^{(m)}_{I_{3/2},\mathrm{ex}} = -w^{(m)}_{I_{1/2},\mathrm{ex}}$	$w^{(e)}_{I_{3/2},\mathrm{ex}} = -w^{(e)}_{I_{1/2},\mathrm{ex}}$
$I_{1/2} + e^- \rightarrow I_{3/2} + e^-$	$w_{I_{1/2},\text{de-ex}} = -w_{I_{3/2},\text{de-ex}}$	$w^{(m)}_{I_{1/2},\text{de-ex}} = -w^{(m)}_{I_{3/2},\text{de-ex}}$	$w^{(e)}_{I_{1/2},\text{de-ex}} = -w^{(e)}_{I_{3/2},\text{de-ex}}$
Inelastic collisions between neutrals			
$I_{1/2} + I_2 \rightarrow I_{3/2} + I_2$	$w_{I_{1/2},\mathrm{quench}} = -w_{I_{3/2},\mathrm{quench}}$	$w^{(m)}_{I_{1/2},\mathrm{quench}} = -w^{(m)}_{I_{3/2},\mathrm{quench}}$	$w^{(e)}_{I_{1/2},\mathrm{quench}} = -w^{(e)}_{I_{3/2},\mathrm{quench}}$

The spontaneous de-excitation of the excited atom whose lifetime of $\tau_{\text{rad}} = 140$ ms [49] is included in the model but not indicated in the table. Also, as already mentioned in Chapter 1 and Chapter 5, no production of $I_{1/2}$ via dissociation is taken into account because of a lack of cross section. Then, during the quenching collision, the restitution of energy from the excited atom to the molecule is not taken into account. Finally, it is worth noticing that we do not consider any term as a result from the collisions between ions and neutrals, as we do not have measurements of the ion profiles (density for each ion, velocity or temperature). The discussion of the results will be done in awareness of this simplification.

The balance between atoms and molecules is ensured at the boundaries of the domain ($z = 0$ and $z = l_z$) via atomic recombination. The details of this process are given in subsection 6.2.3.3.

6.2.3 Closure terms

6.2.3.1 Heat Flux

For the heat-flux vector of each of the different species, we assume a Fourier's law with empirical values of the thermal conductivity. As a result, the heat flux reads

$$q_\alpha = -\kappa_\alpha \partial_z T_\alpha, \tag{6.12}$$

with the atomic and molecular iodine thermal conductivities experimentally obtained [168] and fitted with the following formula as a function of their temperatures,

$$\kappa_{\text{I}} = 6.32\times10^{-5} T_{\text{I}}^{0.768} \text{ and } \kappa_{\text{I}_2} = 2.42\times10^{-5} T_{\text{I}_2}^{0.849}. \tag{6.13}$$

6.2.3.2 Boundary conditions

We model the atom surface recombination at the boundaries of the computational domain. We assume the distribution function at the wall to be a Maxwellian and the wall sticking probability γ_{wall} (the ratio of the atoms recombining at the surface over the number of atom/wall collisions) of excited iodine and the ground state to be equal. As a result, the fluxes of particles read

$$n_{\text{I}}\mathbf{u}_{\text{I}}|_{\text{wall}} = \frac{1}{4} n_{\text{I}} \overline{v}_{\text{I}} \left(\frac{2\gamma_{\text{wall}}}{2-\gamma_{\text{wall}}} \right) \mathbf{n}, \tag{6.14}$$

$$n_{\text{I}_2}\mathbf{u}_{\text{I}_2}\big|_{\text{wall}} = -\frac{1}{2} \left(n_{\text{I}_{1/2}}\mathbf{u}_{\text{I}_{1/2}}\big|_{\text{wall}} + n_{\text{I}_{3/2}}\mathbf{u}_{\text{I}_{3/2}}\big|_{\text{wall}} \right), \tag{6.15}$$

where $\overline{v}_{\text{I}} = \sqrt{8k_{\text{B}}T_{\text{edge}}/(\pi m_{\text{I}})}$ and $\mathbf{n}$ is the outward pointing normal to the boundary. We assume all the species to thermalize by collisions with the wall. This yields

$$T_{\text{I}_{1/2}}\big|_{\text{wall}} = T_{\text{I}_{3/2}}\big|_{\text{wall}} = T_{\text{I}_2}\big|_{\text{wall}} = T_{\text{edge}}. \tag{6.16}$$

Note that T_{edge} is not directly the wall temperature, but the temperature of the gas near the wall. This temperature is not necessarily equal to the wall temperature because of the well known thermal accommodation factor (not included here).

6.2.3.3 Volumetric injection of neutral particles

The one-dimensional geometry of our model does not allow for the injection of neutral gas as done in the experiments, which is performed in the lateral wall that is parallel to the simulation axis. For this reason, we model a volumetric source of particles in order to ensure the pressure to be equal to the experimental one. Note that the pressure depends on the local composition of the gas and hence is not prescribed by the initial condition. We choose a source of particles that relaxes the total pressure to the experimental pressure at time scales that are much longer than the transport processes and hence this injection does not have an effect on the local transport at steady state. This volumetric source is taken from [16], where an additional term is added into the right-hand-side of the continuity equation (6.9) of the molecular iodine. The term reads

$$\dot{\rho}_{I_2} = \frac{m_{I_2}}{\tau_{\text{flow}}}\left(n_{I_2}^{\text{inj}} - n_{I_2}\right), \tag{6.17}$$

where $n_{I_2}^{\text{inj}}$ is defined by the specified pressure and τ_{flow} is a characteristic flow residence time. Unlike the work by Levko et al. [16], where the gas is assumed to be isothermal, in this work we solve the energy equation and consequently, the injection of the gas at a certain temperature needs to be taken into account. For this reason, we add the following term in the right-hand-side of the energy equation (6.11):

$$\dot{E}_{I_2} = \frac{3}{2}\frac{\dot{\rho}_{I_2}}{m_{I_2}} k_B T_{\text{inj}}, \tag{6.18}$$

where the injection temperature $T_{\text{inj}} = 300$ K.

6.2.3.4 Input: electron density and temperature from LP measurements

As written above, the code does not self-consistently calculate the densities of charged species and in the selected reaction set, the only charged particles to be considered are electrons. Therefore, the spatial profiles of the electron temperature and the electron density are obtained from a fit of the experimental measurements obtained by Langmuir probe. Since the experimental measurements only go from $z = 1.5$ cm to $z = 11.5$ cm, it was necessary to postulate the values of electron densities and temperatures at the boundaries of the domain ($z = 0$ cm and $z = 13$ cm). We have chosen to impose:

$$n_e(z = 0\text{ cm}) = \frac{1}{2} n_e(z = 1.5\text{ cm}), \qquad n_e(z = 13\text{ cm}) = \frac{1}{2} n_e(z = 11.5\text{ cm}), \tag{6.19}$$

$$T_e(z = 0\text{ cm}) = 0.8 \times T_e(z = 1.5\text{ cm}), \quad T_e(z = 13\text{ cm}) = 0.8 \times T_e(z = 11.5\text{ cm}). \tag{6.20}$$

The space fitting formula has been chosen to be a 5^{th} order polynomial. In Figure 6.1, the fitting procedure has been applied to the electron experimental measurements obtained in an iodine plasma at a pressure of 15 mTorr and a discharge power of 200 W.

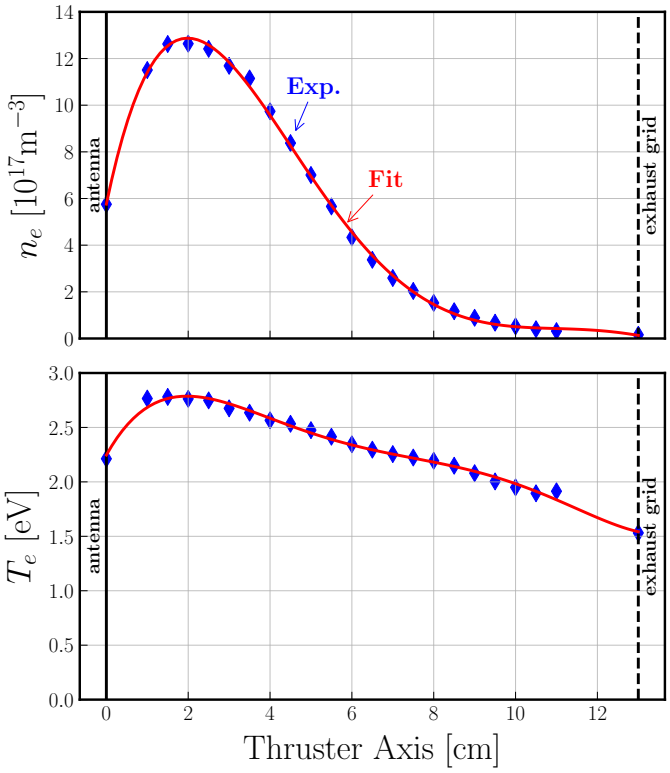

Figure 6.1: Electron density and temperature spatial profiles measured by using Langmuir probe in an iodine plasma at 15 mTorr and 200 W (blue markers). Artificial values at $z = 0$ cm and $z = 13$ cm have been added to constrain the 5$^{\text{th}}$ order polynomial (red curve).

6.2.4 Numerical resolution

6.2.4.1 Initial conditions

To reduce the computational time, the initial conditions for the fluid model have been computed by using the solutions of a simplified isothermal (temperature T_{gas}) volume-averaged model whose equations are:

$$\begin{aligned}\frac{\mathrm{d}n_{\mathrm{I}_2}}{\mathrm{d}t} &= -K_{\text{diss},\mathrm{I}_2} n_e n_{\mathrm{I}_2} + \frac{1}{2} K_{\text{wall},\mathrm{I}_{3/2}} n_{\mathrm{I}_{3/2}} + \frac{1}{2} K_{\text{wall},\mathrm{I}_{1/2}} n_{\mathrm{I}_{1/2}} \\ &\quad + \frac{p_{\text{gas}} - (n_{\mathrm{I}_{3/2}} + n_{\mathrm{I}_{1/2}} n_{\mathrm{I}_2}) k_{\mathrm{B}} T_{\text{gas}}}{k_{\mathrm{B}} T_{\text{gas}} \tau_{\text{flow}}}, \end{aligned} \tag{6.21}$$

$$\begin{aligned}\frac{\mathrm{d}n_{\mathrm{I}_{3/2}}}{\mathrm{d}t} &= 2K_{\text{diss},\mathrm{I}_2} n_e n_{\mathrm{I}_2} + K_{\text{quench},\mathrm{I}_2-\mathrm{I}_{1/2}} n_{\mathrm{I}_{1/2}} n_{\mathrm{I}_2} + K_{\text{de-ex},\mathrm{I}_{1/2}} n_e n_{\mathrm{I}_{1/2}} \\ &\quad - K_{\text{ex}_1,\mathrm{I}_{3/2}} n_e n_{\mathrm{I}_{3/2}} - K_{\text{wall},\mathrm{I}_{3/2}} n_{\mathrm{I}_{3/2}} + \frac{n_{\mathrm{I}_{1/2}}}{\tau_{\text{rad}}}, \end{aligned} \tag{6.22}$$

$$\begin{aligned}\frac{\mathrm{d}n_{\mathrm{I}_{1/2}}}{\mathrm{d}t} &= K_{\text{ex}_1,\mathrm{I}_{3/2}} n_e n_{\mathrm{I}_{3/2}} - K_{\text{quench},\mathrm{I}_2-\mathrm{I}_{1/2}} n_{\mathrm{I}_{1/2}} n_{\mathrm{I}_2} - K_{\text{de-ex},\mathrm{I}_{1/2}} n_e n_{\mathrm{I}_{1/2}} \\ &\quad - K_{\text{wall},\mathrm{I}_{1/2}} n_{\mathrm{I}_{1/2}} - \frac{n_{\mathrm{I}_{1/2}}}{\tau_{\text{rad}}}. \end{aligned} \tag{6.23}$$

No flows are modelled here, the last term in the equation (6.21) guarantees a constant neutral pressure equal to p_{gas}.

6.2.4.2 Numerical scheme

Let us consider the conservative variables, convective fluxes and diffusive fluxes of the species α, respectively:

$$U = \begin{pmatrix} \rho_\alpha = m_\alpha n_\alpha \\ \Gamma_\alpha = m_\alpha n_\alpha u_\alpha \\ E_\alpha = n_\alpha \left(\frac{3k_B T_\alpha}{2} + \frac{m_\alpha u_\alpha^2}{2} \right) \end{pmatrix}, \quad \mathcal{F}(U) = \begin{pmatrix} \Gamma_\alpha \\ \frac{2}{3}\left(\frac{\Gamma_\alpha^2}{\rho_\alpha} + E_\alpha \right) \\ \frac{5}{3}\frac{E_\alpha \Gamma_\alpha}{\rho_\alpha} - \frac{1}{3}\frac{\Gamma_\alpha^3}{\rho_\alpha^2} \end{pmatrix}, \quad \mathcal{H}(U) = \begin{pmatrix} 0 \\ 0 \\ q_\alpha . \end{pmatrix} \tag{6.24}$$

The system to solve is :

$$\partial_t U + \partial_z \mathcal{F}(U) + \partial_z \mathcal{H}(U) = \mathcal{S} \tag{6.25}$$

where $\mathcal{S}$ contains all the collisional source terms, as explained above.

Discretisation

We use a finite volume discretization, as explained below. The domain is divided into N elements of equal length Δz. We write the integral form of equation (6.25) for each element $i \in N$ as:

$$\frac{\mathrm{d}}{\mathrm{d}t} \int_{\Omega_i} U \, \mathrm{d}\Omega + \oint_{S_i} \mathbf{F} \cdot \mathbf{n} \, \mathrm{d}\sigma + \oint_{S_i} \mathbf{H} \cdot \mathbf{n} \, \mathrm{d}\sigma = \int_{\Omega_i} \mathcal{S} \, \mathrm{d}\Omega \tag{6.26}$$

where Ω_i is the i-th cell volume, S_i is the surface of Ω_i and $\mathbf{n}$ is the outward normal to S_i. We then set :

$$\overline{U}_i = \frac{1}{\Delta z} \int_{\Omega_i} U \, \mathrm{d}\Omega, \tag{6.27}$$

in order to write :

$$\frac{\mathrm{d}}{\mathrm{d}t} \overline{U}_i + \frac{1}{\Delta z} \left(F_{i+1/2} - F_{i-1/2} \right) + \frac{1}{\Delta z} \left(H_{i+1/2} - H_{i-1/2} \right) = \overline{S}_i \tag{6.28}$$

For the convective fluxes, we use a *Lax-Friedrich* scheme in order to compute the numerical flux at the interface between the i-th and $(i+1)$-th cells:

$$F_{i+1/2}(\overline{U}_L, \overline{U}_R) = \frac{1}{2}\left[\mathcal{F}\left(\overline{U}_L\right) + \mathcal{F}\left(\overline{U}_R\right) \right] - \frac{|\lambda_{i+1/2}^{max}|}{2} \left(\overline{U}_R - \overline{U}_L \right), \tag{6.29}$$

and we use $\lambda_{i+1/2}^{max} = \max\left(\lambda_i^{max}, \lambda_{i+1}^{max} \right)$, defined as the maximum eigenvalues of the Jacobian matrix of the homogeneous Euler equations of both neighboring cells to the interface. $\overline{U}_{L/R}$ are the reconstructed values at the left/right of the interface. The reconstruction is performed in order to achieve second order accuracy with a TVD (total variation diminishing) MUSCL (Monotonic Upwind Scheme for Conservation Laws) scheme [171].

For discretization of the heat flux at the cell interface, we use a second-order central scheme, as follows

$$q_{\alpha_{i+1/2}}(\overline{U}_i, \overline{U}_{i+1}) = -\frac{\kappa_{\alpha_{i+1/2}}}{\Delta z} \left(T_{\alpha_{i+1}} - T_{\alpha_i} \right). \tag{6.30}$$

Here, the thermal conductivity at the interface is approximated as $\kappa_{\alpha_{i+1/2}} = (\kappa_{\alpha_i} + \kappa_{\alpha_{i+1}})/2$.

We use the method of lines that separates the space and time integrations, as used in [172]. Consequently, after the computation of the fluxes, as explained above, we obtain an ODE in time, as follows:

$$\frac{d}{dt}\overline{U}_i = \overline{R}_i, \quad \text{with} \quad \overline{R}_i = -\frac{1}{\Delta z}(F_{i+1/2} - F_{i-1/2}) - \frac{1}{\Delta z}(H_{i+1/2} - H_{i-1/2}) + \overline{S}_i. \tag{6.31}$$

This ODE is resolved with a third-order TVD Runge Kutta scheme, which, as proposed by [173], reads,

$$\overline{U}_i^{(1)} = \overline{U}_i^n + \Delta t \overline{R}_i^n, \tag{6.32}$$

$$\overline{U}_i^{(2)} = \frac{3}{4}\overline{U}_i^n + \frac{1}{4}\overline{U}_i^{(1)} + \frac{1}{4}\Delta t \overline{R}_i^{(1)}, \tag{6.33}$$

$$\overline{U}_i^{n+1} = \frac{1}{3}\overline{U}_i^n + \frac{2}{3}\overline{U}_i^{(2)} + \frac{2}{3}\Delta t \overline{R}_i^{(2)}. \tag{6.34}$$

Here, the superindex denotes the quantities computed at a given time, e.g., $\overline{U}_i^n = \overline{U}_i(t^n)$. The numerical scheme has a Courant-Friedrichs-Lewy (CFL) condition for numerical stability [174], where the time step is chosen at every time step from the following condition,

$$\Delta t < \min_{\substack{i \in N, \\ \alpha, \beta \in s}} \left(\frac{\Delta z}{\lambda_i^{max}}, \frac{(\Delta z)^2}{2\kappa_{\alpha_i}}, \nu_{\alpha\beta}^{-1} \right).$$

Jacobian and eigen values

The Jacobian matrix associated to $\mathcal{F}(U)$ reads :

$$J = \begin{pmatrix} 0 & 1 & 0 \\ -\frac{2}{3}\left(\frac{\Gamma_\alpha}{\rho_\alpha}\right)^2 & \frac{4}{3}\frac{\Gamma_\alpha}{\rho_\alpha} & \frac{2}{3} \\ \frac{2}{3}\left(\frac{\Gamma_\alpha}{\rho_\alpha}\right)^3 - \frac{5}{3}\frac{E_\alpha \Gamma_\alpha}{\rho_\alpha^2} & \frac{5}{3}\frac{E_\alpha}{\rho_\alpha} - \left(\frac{\Gamma_\alpha}{\rho_\alpha}\right)^2 & \frac{5}{3}\frac{\Gamma_\alpha}{\rho_\alpha} \end{pmatrix}. \tag{6.35}$$

and its eigen values are:

$$\lambda \in \left\{ u_\alpha, u_\alpha - \sqrt{\frac{5}{3}\frac{k_B T_\alpha}{m_\alpha}}, u_\alpha + \sqrt{\frac{5}{3}\frac{k_B T_\alpha}{m_\alpha}} \right\}. \tag{6.36}$$

6.3 Results and comparison to experiments

In this section, the multi-fluid simulation results are compared to the experimental measurements presented in Chapter 4. The influence of several simulation parameters is studied.

6.3.1 General picture at 15 mTorr-200 W

In this first subsection, the case of an iodine plasma for a pressure of 15 mTorr and a discharge power of 200 W is used as reference. The simulations have been carried out by fixing $T_{edge} = 600$ K as in Chapter 5 and by taking $\gamma_{wall} = 0.15$. In Figure 6.2, we look at several outputs of the multi-fluid code (along the thrust axis) and compare with the experimental results when possible. It should be kept in mind that the simulations are performed at the center of the discharge where the majority of the measurements were obtained by absorption and therefore averaged along the direction perpendicular to the simulated direction.

In subfigure (a), the densities of the three simulated species $n_{I_{3/2}}$, $n_{I_{1/2}}$ and n_{I_2} are plotted. The spatial profile of the atomic ground state density is minimum for $z \approx 3$ cm and rises sharply at the walls. As observed experimentally, the strong heating near the antenna (see subfigure (b)) leads to a depletion of neutrals. Comparison with TALIF measurements (from Figure 4.39) of the ground state relative density suggests that, while the trend is consistent, the gradients are more pronounced experimentally (more on this later). The profile of the excited state is fairly flat, with a rise at the walls caused by the non-zero value chosen for $n_{I_{1/2}}$ at the walls. The molecular density is largely negligible (at least one order of magnitude smaller than the atomic density), with almost 100% dissociation close to $z \approx 3$ cm, where the atomic density is minimal (see subfigure (f)). The spatial density also rises towards the walls.

In subfigure (b), the temperatures of the three species are plotted. The profiles of $T_{I_{3/2}}$, $T_{I_{1/2}}$ are almost identical with very strong gradients and strong heating with a maximum of 1350 K around $z = 3$ cm. The molecular temperature is slightly lower (about 150 K less at the maximum) but exhibits the same spatial variations. The spatial profile of atomic temperature, obtained by absorption at 905 nm (on a non-metastable excited atomic state, see Figure 4.18), is very similar to the simulated profiles with, however, higher measured temperatures (about 300 K higher). The absorption at 1315 nm (see Figure 4.50) provided very few temperature measurements but for $z = z_4 = 7.65$ cm, the order of magnitude is consistent with the simulations.

In subfigure (c), the fluid velocities of the three species are plotted. The atoms have a very small drift (fluid) velocity with a motion directed towards the walls (negative values near the antenna and positive near the grid). For the molecules, however, the analysis is completely different. The fluid flows are directed towards the center of the domain (positive velocity near the antenna and negative near the grid) and the fluid velocities reached are non-negligible (Mach number greater than 0.4 at the maximum). The very strong dissociation leads to a collapse of the molecular population around $z = 3$ cm and almost zero molecular partial pressure (see subfigure (d)) at this location. Molecular pressure gradients cause this inward movement of the molecules according to Fick's law. Atomic partial pressures are mostly

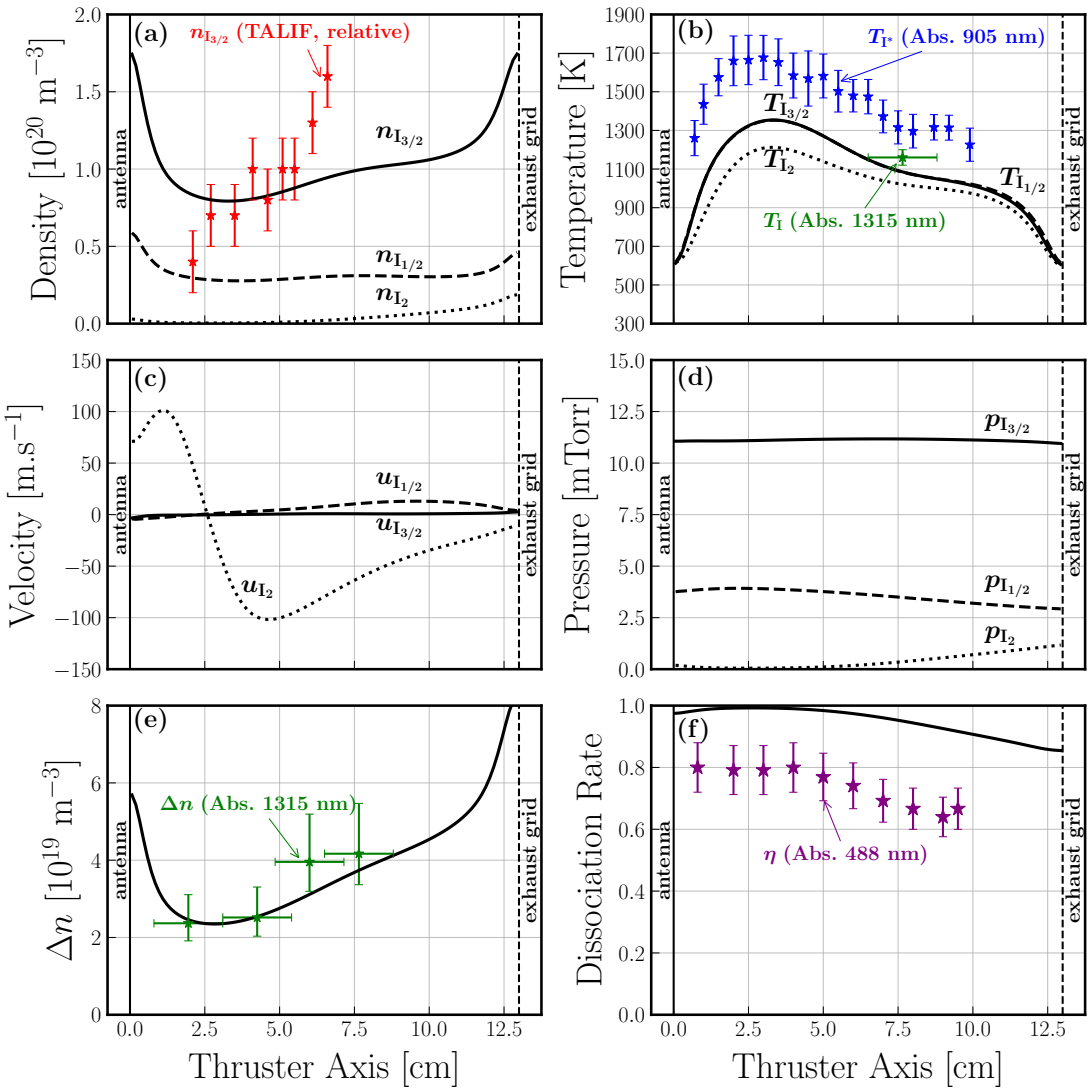

Figure 6.2: Multi-fluid simulations along the thrust axis for a neutral pressure of 15 mTorr and a discharge power of 200 W, with T_{edge} = 600 K and γ_{wall} = 0.15. (a) Densities of $I_{3/2}$, $I_{1/2}$ and I_2. TALIF relative measurements of $n_{I_{3/2}}$, first presented in Figure 4.39, are also plotted. (b) Temperatures of $I_{3/2}$, $I_{1/2}$ and I_2 with measurements from absorption at 1315 nm (from Figure 4.50) and at 905 nm (atomic excited state, see Figure 4.18). (c) Fluid velocities of $I_{3/2}$, $I_{1/2}$ and I_2. (d) Partial pressures of $I_{3/2}$, $I_{1/2}$ and I_2. (e) $\Delta n = n_{I_{3/2}} - 2n_{I_{1/2}}$, measurements from absorption at 1315 nm are also plotted (from Figure 4.49). (f) Dissociation rate with absorption measurements at 488 nm, taken from Figure 4.46.

flat and do not exhibit a minimum.

In subfigure (e), the degeneracy-weighted atomic population difference $\Delta n = n_{I_{3/2}} - 2n_{I_{1/2}}$ is compared to the absorption measurements made at 1315 nm (see Figure 4.49). The measurements and the model agree almost perfectly on trend and values.

Finally, the dissociation fraction, defined here as

$$\eta = \frac{1}{2}\frac{n_{\text{atom}}}{\frac{1}{2}n_{\text{atom}} + n_{\text{I}_2}}, \tag{6.37}$$

is presented in subfigure (f). It is always above 85 % and is above 99 % for $z = 3$ cm: even at 15 mTorr, a very high dissociation fraction is observed along the thrust axis. The absorption measurements at 488 nm are also obtained by integration along the line of sight and the molecular profile is also minimal at the center, such that experimental dissociation fractions are lower than those simulated. Note however that the trend is well reproduced.

6.3.2 Influence of the edge temperature

One of the free parameters of the fluid model is the edge temperature. Ideally, a boundary condition should be implemented that takes into account the wall temperature jump in a self-consistent way (see [167] for instance). Indeed, experimentally, it seems that this value is well above 300 K and depends on both the pressure and the discharge power (see discussions of Figure 4.18). However, we have chosen to study the variation of T_{edge} in a simpler way, by varying it between 300 and 600 K and observing the influence of such a change on the code outputs. In Figure 6.3, the variation of T_{edge} is materialized by a colored area, delimited by a continuous line ($T_{\text{edge}} = 600$ K) and a dashed line ($T_{\text{edge}} = 300$ K). In this subsection, the simulated case is for a pressure of 15 mTorr and a discharge power of 200 W, γ_{wall} is fixed at 0.15. Experimental results, with their determination technique, are plotted in each graph.

The atomic temperature $T_{\text{I}_{3/2}}$ is studied in subfigure (a). The spatial profiles have the same shape whatever the temperature at the walls. Although the temperature difference between the two extreme cases is 300 K at the edges of the domain, the temperature difference is very small (less than 100 K) in the zone of strong dissociation (between $z = 1$ and $z = 5$ cm). In the case where $T_{\text{edge}} = 300\ K$, the larger temperature rise is provided by stronger density gradients near the walls (see subfigure (b)). Indeed, in subfigure (b), for z ranging from 1 cm to 12 cm there is very little difference in the simulated ground state densities $n_{\text{I}_{3/2}}$. The real differences appear only in the last centimetre near the walls.

In subfigures (c), (d) and (e) the influence of the temperature at the walls is studied on, respectively, Δn, the dissociation fraction and n_{I_2}. In subfigure (e), direct measurements of molecular density, obtained by absorption at 488 nm are also plotted (taken from Figure 4.46). Although the trends agree, there is more than one order of magnitude of difference between the simulations and the experiments, highlighting the limitations of the comparison between local simulations and spatially integrated absorption experiments. The discrepancy could be partly explained by the large number of cold molecules located near the windows and detected by absorption but not modelled. As for the atoms, the real differences between the extreme cases ($T_{\text{edge}} = 300\ K$ and $T_{\text{edge}} = 600\ K$) occur in the last centimetre near the walls, but the behavior in the discharge bulk is only slightly modified, as shown by the very similar dissociation rates. However, for instance, the value reached by n_{I_2} for $T_{\text{edge}} = 300$ K is 3 times greater than in the case of $T_{\text{edge}} = 600$ K (6×10^{19} m^{-3} against 2×10^{19} m^{-3}). This leads to more quenching for cold walls and thus to a

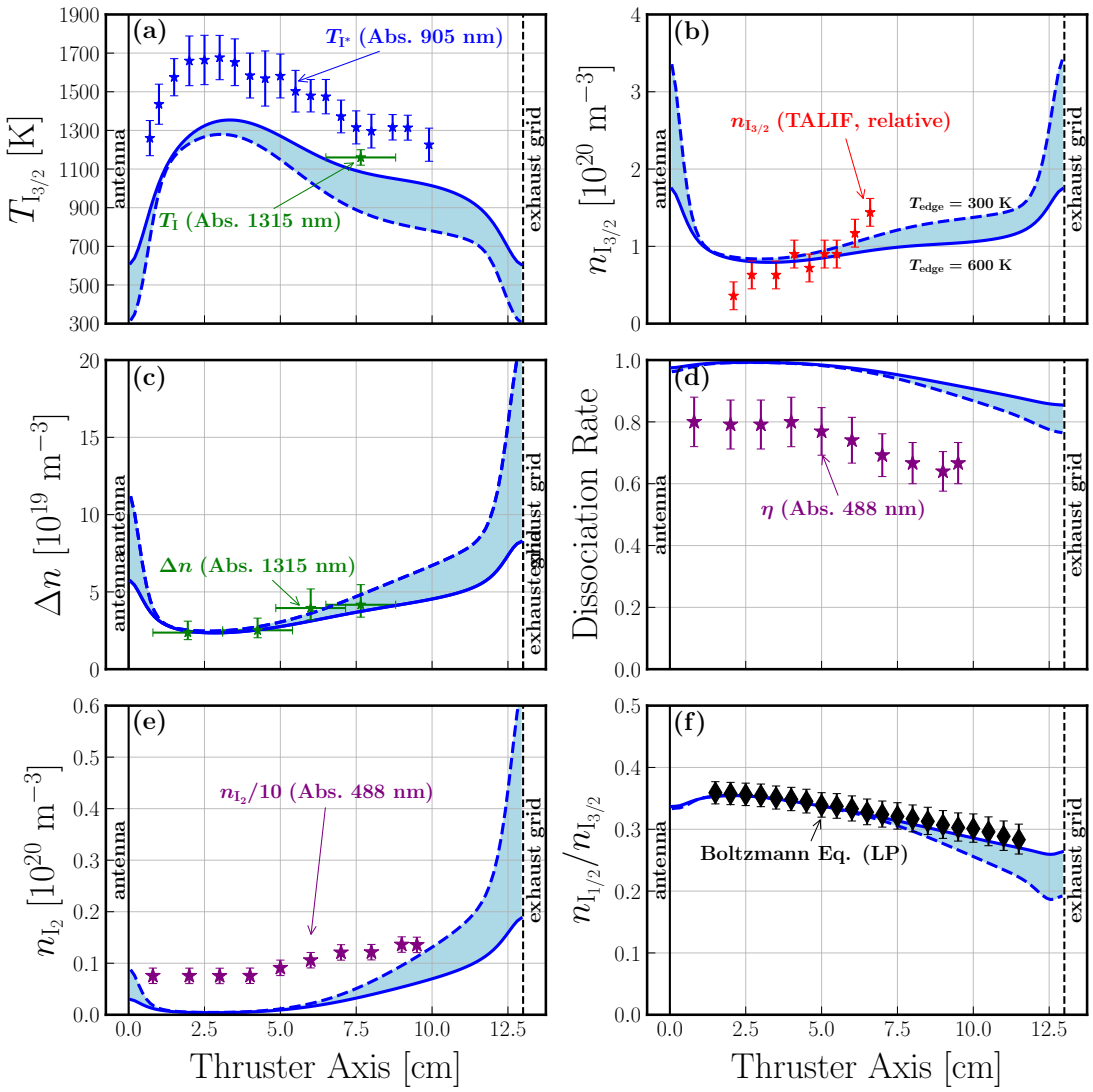

Figure 6.3: Influence of the edge temperature T_{edge} on multi-fluid simulations along the thrust axis for a neutral pressure of 15 mTorr and a discharge power of 200 W, with $\gamma_{wall} = 0.15$. The colored zone indicates an edge temperature, T_{edge}, between 300 K (dashed line) and 600 K (solid line). (a) Temperature of $I_{3/2}$ with measurements from absorption at 1315 nm (from Figure 4.50) and at 905 nm (atomic excited state, see Figure 4.18). (b) Density of $I_{3/2}$ and TALIF relative measurements of $n_{I_{3/2}}$, first presented in Figure 4.39. (c) $\Delta n = n_{I_{3/2}} - 2n_{I_{1/2}}$, measurements from absorption at 1315 nm are also plotted (from Figure 4.49). (d) Dissociation rate with absorption measurements at 488 nm, taken from Figure 4.46. (e) Density of I_2 with absorption measurements at 488 nm, taken from Figure 4.46, the experimental data are divided by a factor of 10. (f) Ratio $n_{I_{3/2}}/n_{I_{1/2}}$ and comparison with Boltzmann equilibrium computed with electron temperature from Figure 3.26.

lower relative population of $n_{I_{1/2}}$ compared to $n_{I_{3/2}}$, as observed in subfigure (f). In this later case, the Boltzmann equilibrium at T_e (computed by using Langmuir probe measurements, see Figure 3.26) between the two atomic levels starts to fail for $z > 8$ cm.

6.3.3 Influence of the wall sticking probability

The second undetermined parameter is the wall sticking probability γ_{wall}. In the previous chapter (see Chapter 5), we estimated it between 0.05 and 0.2 and therefore choose to study its influence on this interval. The results are presented in Figure 6.4 with a colored area indicating a γ_{wall} value between 0.05 (solid line) and 0.2 (dashed line). In this subsection, the simulated case is for a pressure of 15 mTorr and a discharge power of 200 W, T_{edge} is fixed at 600 K. The order of the subfigures is the same as in the previous subsection: (a) atomic temperature $T_{\text{I}_{3/2}}$, (b) ground state atomic density $n_{\text{I}_{3/2}}$, (c) Δn, (d) dissociation rate, (e) molecular density n_{I_2} and (f) atomic density ratio $n_{\text{I}_{1/2}}/n_{\text{I}_{3/2}}$.

The immediate effect of an increase in the wall sticking probability is to increase the molecular density (see subfigure (e)) and thus decrease the dissociation rate (see subfigure (d)). The increase in n_{I_2}, induces more quenching, thus a decrease in the $n_{\text{I}_{1/2}}$ population and ultimately a decrease in the atomic population ratio (see subfigure (f)).

What is less direct, however, is a decrease in the atomic temperature as γ_{wall} increases and the consequences this has on the atomic density values. In order to understand what is happening, we plot the temperature difference $T_{\text{I}_{3/2}} - T_{\text{I}_2}$ for different values of γ_{wall} in Figure 6.5. The lower γ_{wall}, the greater the temperature difference between atoms and molecules. This phenomenon is similar to the one observed in Chapter 5 when the temperature equilibrium of the two species was never reached in the global model. Because of the very strong dissociation: (i) T_{I_2} is reduced because the majority of the heating terms for the molecule are proportional to n_{I_2}; (ii) the collisions between atoms and molecules are no longer efficient and the atomic temperature increases. Then, because we are modeling for a fixed neutral pressure, the increase of the atomic temperature induces a decrease of the atomic density despite the higher dissociation efficiency.

For a value of $\gamma_{\text{wall}} = 0.05$, the agreement between temperature measurements of atomic excited species by absorption at 905 nm and the simulated temperatures is quite good.

6.3.4 Influence of the quenching of $\text{I}_{1/2}$ by I_2

As discussed in Chapter 1 and Chapter 5, the value of the quenching reaction rate of $\text{I}_{1/2}$ excited atoms by I_2 molecules has not been measured in an iodine plasma and some doubts exist on its magnitude. Here, we study the influence of this mechanism on the simulation outputs. The results are presented in Figure 6.6 considering the quenching process ($K_{\text{quench.},\text{I}_{1/2}-\text{I}_2} = 3.23 \times 10^{-17}$ m^3.s^{-1}, solid line) or no quenching ($K_{\text{quench.},\text{I}_{1/2}-\text{I}_2} = 0$ m^3.s^{-1}, dashed line). In this subsection, the simulated case is for a pressure of 15 mTorr and a discharge power of 200 W, γ_{wall} is fixed at 0.15 and $T_{\text{edge}} = 600$ K.

It turns out that whether or not quenching is taken into account has very little influence on the results. For example, temperatures or dissociation rates are not affected by the presence or absence of quenching (not represented). Only the density of atomic states is slightly modified. In subfigure (a), Δn is only affected for $z \geq 7$ cm and in small proportions. The same is true for the ratio $n_{\text{I}_{3/2}}/n_{\text{I}_{1/2}}$ in subfigure (b). The case at 15 mTorr being the one generated at higher pressure, one can consider

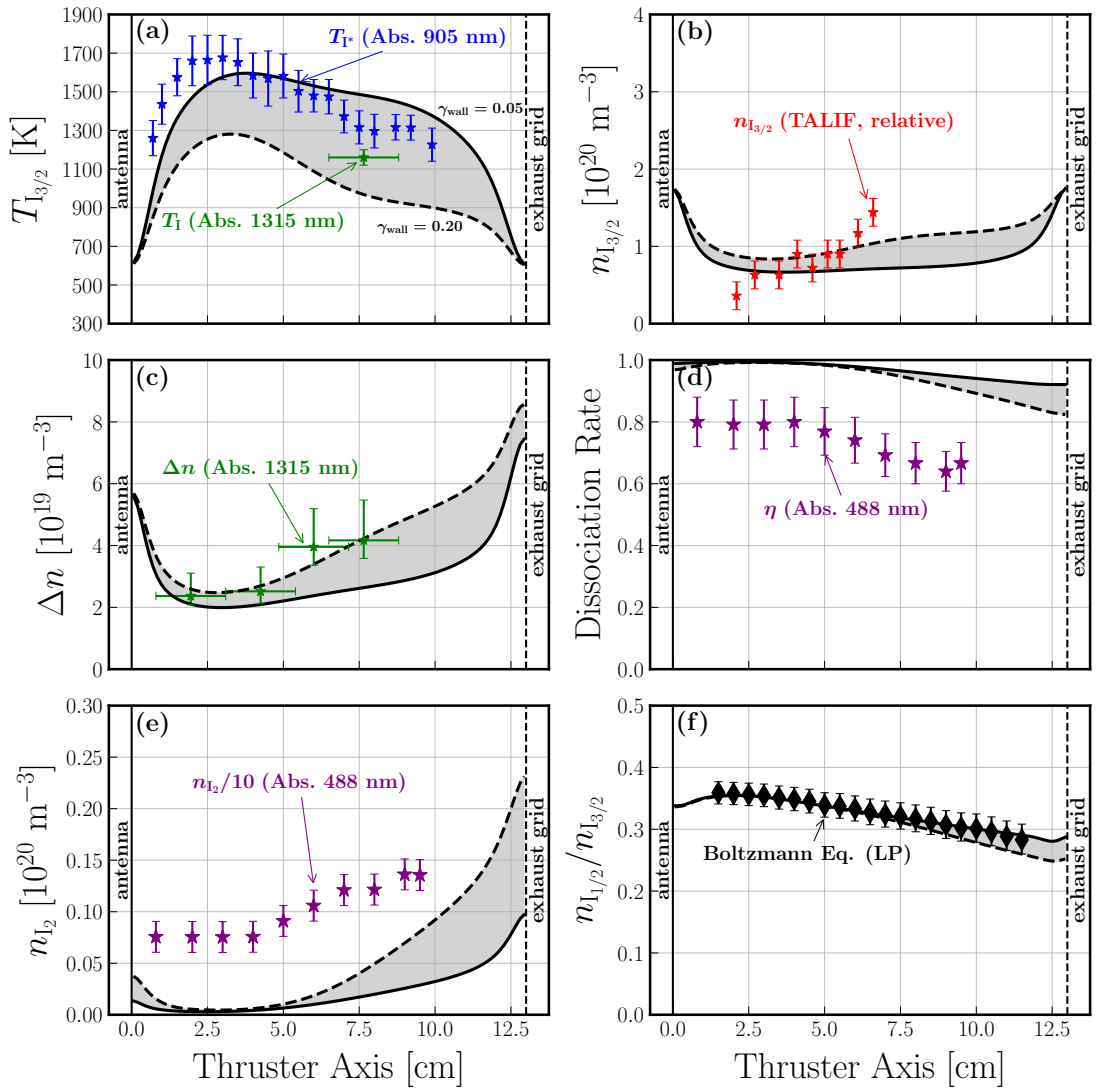

Figure 6.4: Influence of the wall sticking probability γ_{wall} on multi-fluid simulations along the thrust axis for a neutral pressure of 15 mTorr and a discharge power of 200 W, with T_{edge} = 600 K. The colored zone indicates a wall sticking probability, γ_{wall}, between 0.05 (solid line) and 0.20 (dashed line). (a) Temperature of $I_{3/2}$ with measurements from absorption at 1315 nm (from Figure 4.50) and at 905 nm (atomic excited state, see Figure 4.18). (b) Density of $I_{3/2}$ and TALIF relative measurements of $n_{I_{3/2}}$, first presented in Figure 4.39. (c) $\Delta n = n_{I_{3/2}} - 2n_{I_{1/2}}$, measurements from absorption at 1315 nm are also plotted (from Figure 4.49). (d) Dissociation rate with absorption measurements at 488 nm, taken from Figure 4.46. (e) Density of I_2 with absorption measurements at 488 nm, taken from Figure 4.46, the experimental data are divided by a factor of 10. (f) Ratio $n_{I_{3/2}}/n_{I_{1/2}}$ and comparison with Boltzmann equilibrium computed with electron temperature from Figure 3.26.

that the addition or not of quenching for simulations at lower pressure will have a negligible effect.

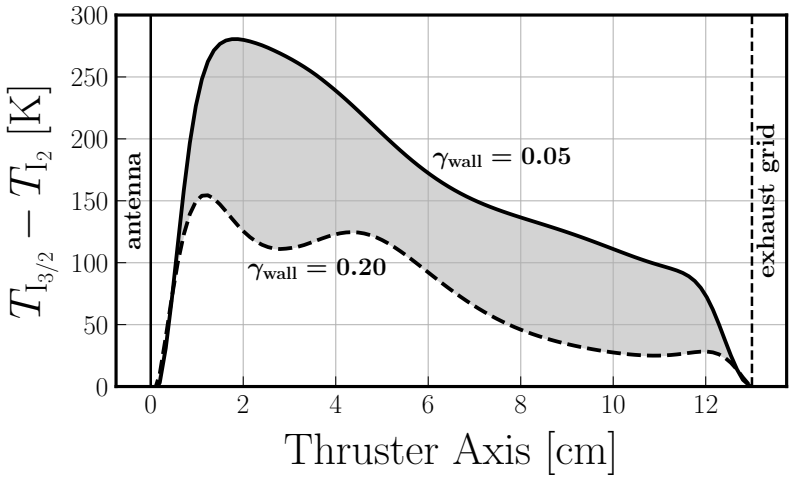

Figure 6.5: Influence of the wall sticking probability γ_{wall} on the temperature difference between ground state atoms and molecules ($T_{I_{3/2}} - T_{I_2}$) along the thrust axis for a neutral pressure of 15 mTorr and a discharge power of 200 W, with T_{edge} = 600 K. The colored zone indicates a wall sticking probability, γ_{wall}, between 0.05 (solid line) and 0.20 (dashed line).

6.3.5 Pressure influence

6.3.5.1 Study for different pressures

In Figure 6.7 the effect of pressure on different physical quantities measured during this thesis is studied, the discharge power is 200 W. The simulations were all obtained with T_{edge} = 600 K. As in the previous subsection, the colored area indicates a variation of γ_{wall} between 0.05 (solid line) and 0.2 (dashed line).

In subfigure (a), the relative $n_{I_{3/2}}$ measurements obtained by TALIF are compared to the simulated profiles at 5, 10 and 15 mTorr. The agreement is good, although the experimental gradients, which are clearly observed with pressure, are less pronounced in the simulations. It should be remembered that γ_{wall} is considered the same at z = 0 and z = 13 cm but could very well be different, which the model does not take into account. To explain a steeper rise in $n_{I_{3/2}}$ with z, several options are possible. It may be that T_{edge} is weaker at the grid than at the antenna and that γ_{wall} is larger at the grid. These two independent phenomena decrease both the ratio $n_{I_{3/2}}/n_{I_{1/2}}$ value (see subfigures (f) in Figure 6.6 and Figure 6.3)). Besides, the density of the excited atomic state $n_{I_{1/2}}$ could very well fall to zero at the walls and induce stiffer gradients in both $n_{I_{3/2}}$ and Δn profiles.

In subfigure (b), Δn is investigated and simulations are compared to 1315 nm absorption measurements at 5, 10 and 15 mTorr. The trends are very well reproduced and the measured values appear twice as high as those simulated. As explained above, this discrepancy is due to the non-local nature of the absorption experiment.

Finally, in subfigure (c) the simulated ground state temperatures are compared to the 905 nm absorption measurements performed on a metastable atomic state at 1.5, 5 and 15 mTorr. The measured values seem slightly higher than the simulations but the spatial variations are very well reproduced and γ_{wall} = 0.05 gives acceptable results. In particular, the location of the profiles towards the antenna as the pressure increases is well captured. The choice of T_{edge} = 600 K also seems appropriate.

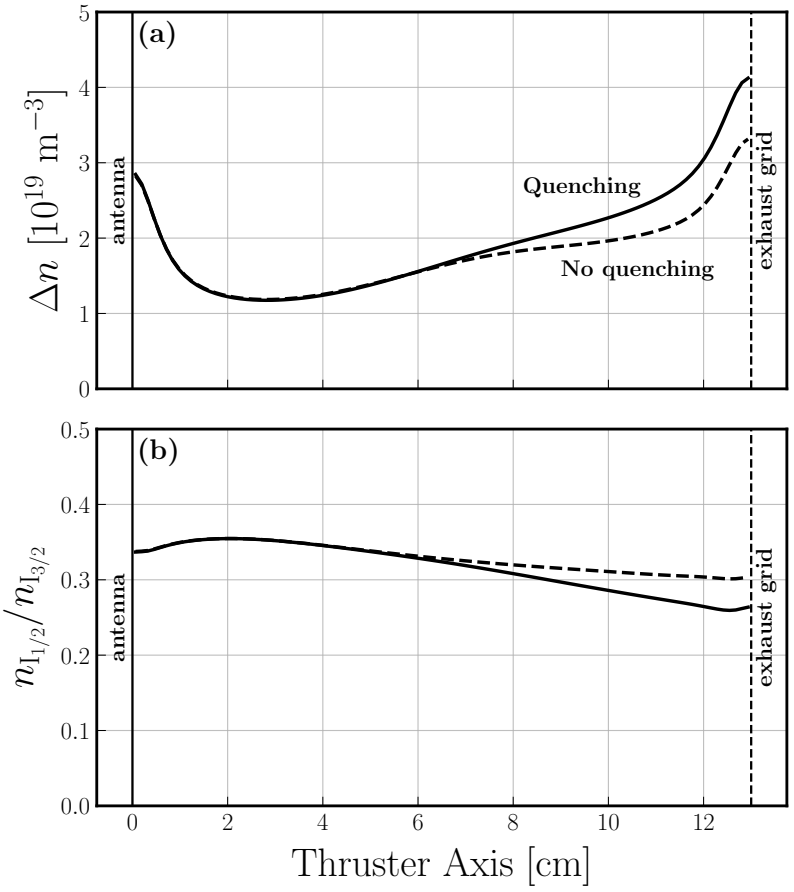

Figure 6.6: Influence of the quenching reaction on multi-fluid simulations along the thrust axis for a neutral pressure of 15 mTorr and a discharge power of 200 W, with T_{edge} = 600 K and γ_{wall} = 0.15. The solid line has been generated by using $K_{quench.,I_{1/2}-I_2} = 3.23 \times 10^{-17}$ m^3.s^{-1} and the dashed line with $K_{quench.,I_{1/2}-I_2}$ = 0 m^3.s^{-1}. (a) Difference of atomic populations, $\Delta n = n_{I_{3/2}} - 2n_{I_{1/2}}$. (b) Ratio of atomic populations, $n_{I_{3/2}}/n_{I_{1/2}}$.

6.3.5.2 Behavior at very low pressure (0.5 mTorr)

We are now interested in the lowest pressure available, namely 0.5 mTorr, for a discharge power of 200 W. No optical experiments have been conducted at such a low pressure, so the simulation results cannot be compared with measurements. In Figure 6.8, the densities, velocities and temperatures of the three species simulated with γ_{wall} = 0.15 and T_{edge} = 300 K are plotted.

All profiles are almost perfectly symmetrical. The dissociation is here almost constant and reaches a mean value around 96 %. It is interesting to note that the electron density is almost everywhere higher than the molecular density. The Boltzmann equilibrium is also perfectly satisfied between both atomic states. It is easy to see why these operating conditions are favourable for iodine electric propulsion. The composition of the plasma must be almost identical to that of a xenon plasma: only atoms, positive ions I^+ and electrons. The molecules and their electron collision products (negative I^- ions and positive I_2^+ ions) must be completely negligible. This is in agreement the very low electronegativity values measured in Chapter 3.

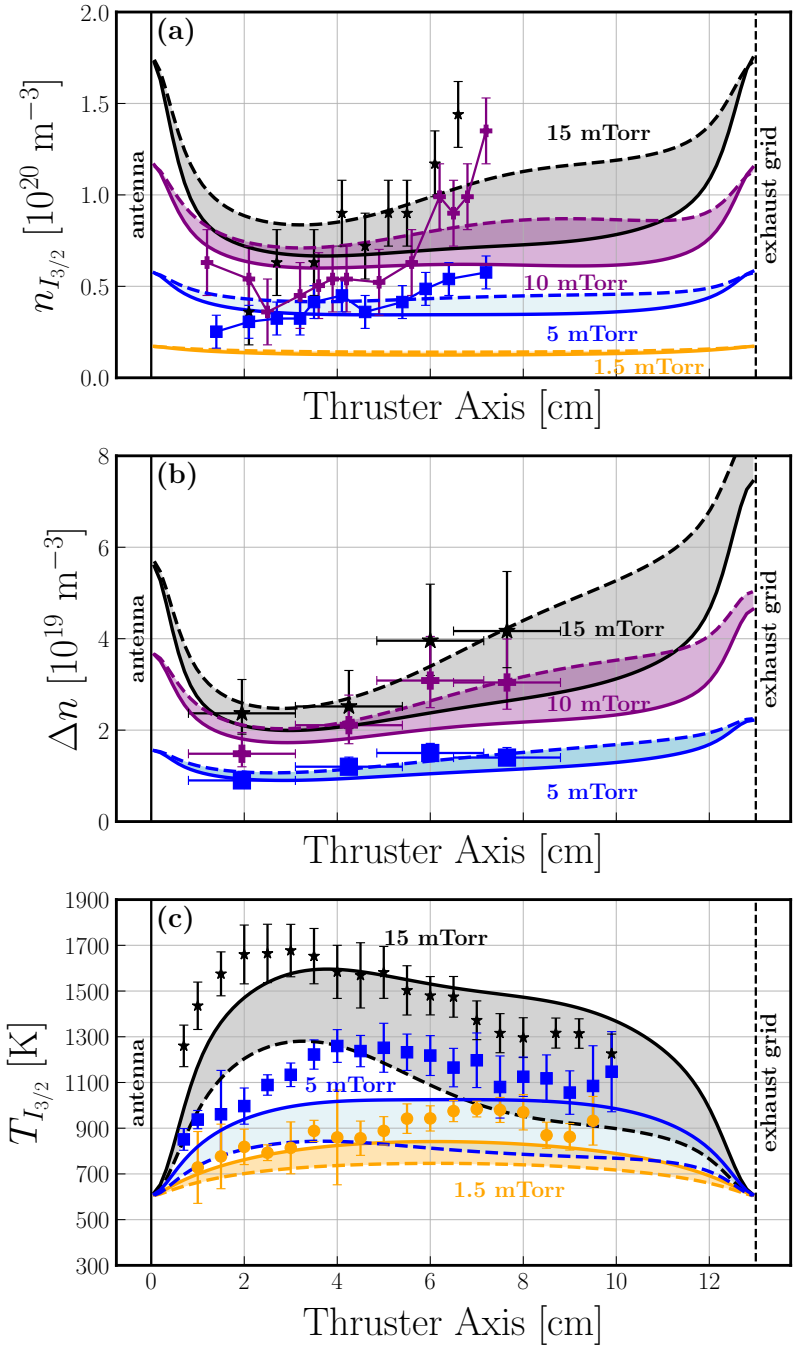

Figure 6.7: Influence of the neutral pressure on multi-fluid simulations along the thrust axis for a discharge power of 200 W, with T_{edge} = 600 K. The colored zone indicates a wall sticking probability, γ_{wall}, between 0.05 (solid line) and 0.20 (dashed line). (a) Simulated density of $I_{3/2}$ at 1.5, 5, 10 and 15 mTorr and TALIF relative measurements of $n_{I_{3/2}}$ at 5, 10 and 15 mTorr, first presented in Figure 4.39. (b) Simulated $\Delta n = n_{I_{3/2}} - 2n_{I_{1/2}}$ and measurements from absorption at 1315 nm at 5, 10 and 15 mTorr (from Figure 4.49). (c) Simulated temperature of $I_{3/2}$ and measurements of the temperature of an excited atomic state at 1.5, 5 and 15 mTorr (measurements were obtained by absorption at 905 nm, see Figure 4.18).

A model (fluid or PIC) including all charged and neutral species would allow to

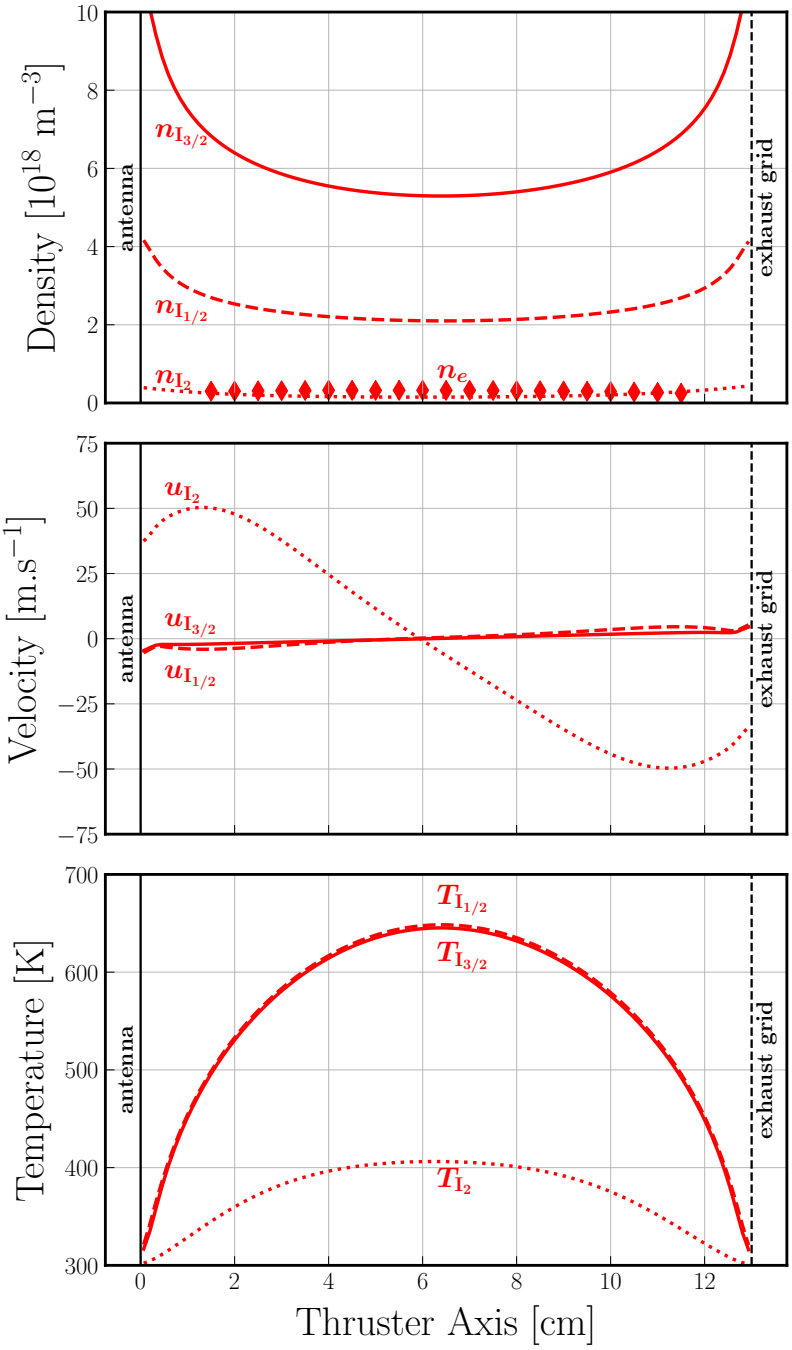

Figure 6.8: Multi-fluid simulations along the thrust axis for a neutral pressure of 0.5 mTorr and a discharge power of 200 W, with T_{edge} = 300 K and γ_{wall} = 0.15. (a) Densities of $I_{3/2}$, $I_{1/2}$ and I_2. The electron density n_e obtained via Langmuir probe measurements, which served as an input of the simulation, is also plotted. (b) Fluid velocities of $I_{3/2}$, $I_{1/2}$ and I_2. (b) Temperatures of $I_{3/2}$, $I_{1/2}$ and I_2.

definitively close this discussion.

The temperatures of the atoms, slightly different from each other but very close reaching around 650 K at the maximum, are not at all in equilibrium with the molecular temperature whose profile only reaches 405 K at the center. Once again, the extreme dissociation prevents both the heating of the molecules and their ther-

malization with the atoms. Note that if we had set T_{edge} to 600 K and let the molecules injection temperature to 300 K, the molecular temperature profile would have had a minimum in the center which is not physical.

6.3.6 Influence of the discharge power

Here we are interested in the influence of the discharge power on, mainly, the temperature. Indeed, different absorption experiments used during this thesis have shown a very weak dependence of the temperature on the discharge power. In the following, we try to provide some explanations for these observations.

In Figure 6.9, the atomic and molecular temperatures are plotted for discharge powers of 120 W and 200 W. For both powers, T_{edge} is fixed at 300 K and γ_{wall} at 0.15. Because of the higher electron density at higher power, the temperatures at 200 W are higher than at 120 W everywhere. Also, dissociation is higher, close to the antenna, at higher power and therefore the difference between atomic and molecular temperature is higher at 200 W. We can therefore assume that as the power increases, the temperatures increase. This induces a decrease of the neutral species densities and particularly of the atomic ground state density when the power increases as observed experimentally in Figure 4.40.

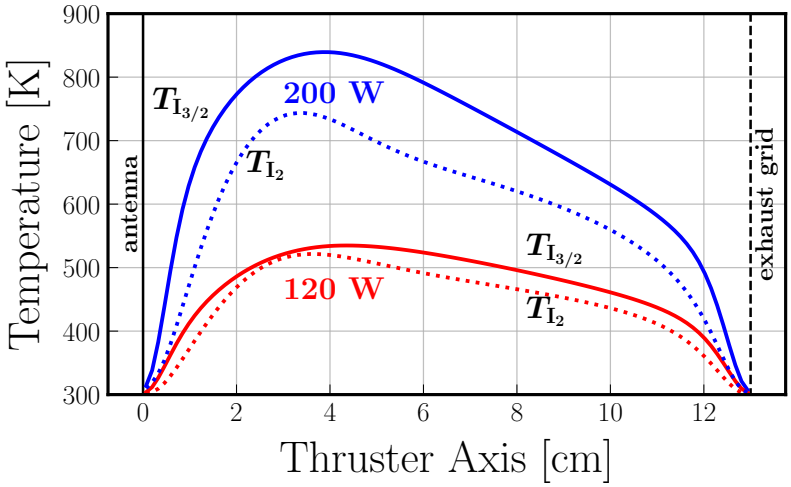

Figure 6.9: Influence of the discharge power on the atomic (solid line) and molecular temperature (dotted line). Simulations are generated by using Langmuir probe measurements at 5 mTorr and for two different discharge powers: 200 W and 120 W, with T_{edge} = 300 K and γ_{wall} = 0.15.

Nevertheless, in Figure 6.10, we plot the ground state temperature for two different powers but using different γ_{wall} = 0.05 at 120 W and γ_{wall} = 0.15 at 200 W. We immediately see that the gap between the two profiles is reduced compared to Figure 6.9. This may be an explanation for the low sensitivity of temperature to discharge power in the absorption measurements.

Finally, the last explanation may come from the minimum density profiles in the centerwith very strong gradients near the walls. Indeed, if we focus on the absorption experiment at 1315 nm, according to equation (4.18), the optical signal to integrate along the line of sight is proportional to $\Delta n(x)/\sqrt{T(x)}$, where x is the transverse direction. This means that the signal maximum comes from the edges,

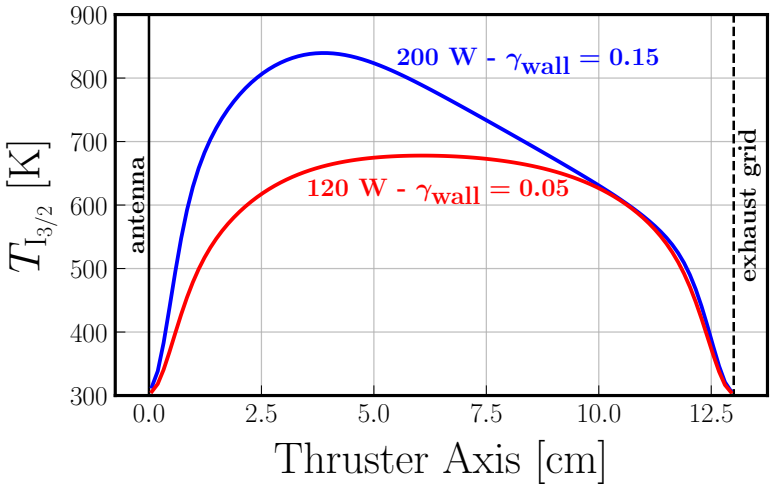

Figure 6.10: Simulated temperature of the atomic ground state at 5 Torr for two different discharge powers (120 W and 200 W) and different wall sticking probability values (0.05 or 0.20). T_{edge} is set to 300 K.

rather than the center, and at this point the temperature differences for two different powers are reduced.

6.3.7 How to reconcile absorption measurements and fluid simulations?

On several occasions in the above sections, comparisons between density measurements obtained by absorption and fluid simulations performed in the center of the discharge have failed. One is entitled to ask if there is no way to do better with the tools at our disposal.

Ideally, Langmuir probe measurements should be made along the transverse axis where the absorption laser beam propagates. Thus, we could use our code, without modifying it, to simulate this direction perpendicular to the thruster axis. Nevertheless, these probe measurements have not been performed during this thesis and an alternative must be found.

The only option left is to postulate a transverse profile (from $x = -l_x/2$ to $x = l_x/2$) of n_e and T_e and to use the electronic measurements at a given $z, x = 0$ to obtain the absolute values of the transverse profiles. Once in our possession, these profiles can be used to perform multi-fluid simulations. We would then have the transverse profiles of the different neutral species and we could reconstruct the optical signals from the simulations (using equation (4.18)). In this way the comparison with the absorption measurements would make more sense.

This work was not done in this thesis, but the primary idea for transverse electronic profiles would be to consider:

$$T_e(x, z = z_0) = T_e(x = 0, z = z_0) = T_{e0}, \tag{6.38}$$

$$n_e(x, z = z_0) = n_e(x = 0, z = z_0)\left[1 - \left(\frac{2x}{l_x}\right)\right]^{1/2} = n_{e0}\left[1 - \left(\frac{2x}{l_x}\right)\right]^{1/2}, \tag{6.39}$$

where the density profile is taken from [119].

6.4 Chapter digest

In this chapter, a one-dimensional multi-fluid code has been proposed to study the neutral dynamics along the axis of the thruster, at the center of the discharge. This code has been used to simulate the density, velocity and temperature profiles of three neutral iodine species: I_2, $I_{3/2}$ and $I_{1/2}$. The code takes into account the inertia terms and heat fluxes of each species, and uses the electron density and temperature measurements presented in Chapter 3 as input.
The model equations have been presented in summary form and the reader can use Appendix C to obtain the full equations. The closure terms, numerical schemes and boundary conditions used have been specified. The initialization is done by means of a global model. The simulations are carried out for a fixed neutral pressure so that the flow is not simulated.
All the spatial evolutions observed experimentally and presented in Chapter 4 were retrieved in the simulations. Due to very strong heating (which localises near the antenna as the pressure increases), the density profiles of the neutral species are minimal in the center and maximal near the walls. For pressures ranging from 0.5 to 15 mTorr, dissociation is very high, easily reaching more than 95% at the location of the electron density maximum. This extreme molecular dissociation leads to a lower heating of the molecules than that of the atoms: the thermal equilibrium between the three species is never observed. Indeed, the very low molecular density, which may become lower than the electronic density, prevents to reach an equilibrium between the different temperatures of the heavy species.
The influence of the edge temperature T_{edge}, the wall sticking probability γ_{wall}, the neutral pressure and the discharge power was investigated. Increasing T_{edge}, automatically increases the temperature of the whole profiles but attenuates the gradients near the walls. Indirectly, decreasing γ_{wall}, increases the atomic temperature by accentuating the temperature difference between atoms and molecules and thus decreasing the thermal homogenization of the different species. As an example, at 15 mTorr and for a discharge power of 200 W, T_{edge} = 600 K and γ_{wall} = 0.05 allow the model to reproduce quite accurately the temperature measurements obtained on an atomic excited state by absorption at 905 nm (see Section 4.2). It should be noted, however, that γ_{wall} and T_{edge} are certainly different at each end of the domain, which has not been considered here. It should also be noted that T_{edge} in our modeling is not directly the wall temperature, but the temperature of the gas near the wall. This temperature is not necessarily equal to the wall temperature because of the well known thermal accommodation factor (not included here).

Finally, the absolute measurements of atomic and molecular densities obtained by absorption and presented in chapter 4 could not be reconciled with the model. The measured densities are always largely higher than the simulated densities and the measured dissociation fraction is lower than the simulated one. The explanation comes from the fact that we compare local simulations with integrated measurements along the axis transverse to the axis of the thruster where the density profiles are, most likely, minimum in the center. Ways to reconcile the model with the absorption measurements are indicated.
These results have not been published yet but were presented during the 75th Gaseous Electronics Conference, where I was selected as a Student Award for Excellence finalist (see Related publications in page xiii).

CONCLUSION

In conclusion, we answer the various questions raised in the introduction by outlining what has been achieved in this thesis and indicating what work might be undertaken to further the understanding of low pressure iodine plasmas in order to support the use of iodine as an alternative propellant to xenon.

Diagnostics of low-pressure iodine plasmas

- Which experimental diagnostics are best suited to study low-pressure iodine plasmas?

On the one hand, charged-particles (electrons and I^- negative ions) densities have been measured in low pressure iodine plasmas used for electric propulsion in the space industry and the results have been presented in Chapter 3. Measurements were performed along the thrust axis of an ICP discharge used as the ionization stage of a gridded-ion-thruster by using Langmuir probe and laser-induced detachment techniques. The electron energy distribution function and the electron temperature were also measured. These techniques have been shown to be well suited to low-pressure iodine plasmas, provided that the discharge surfaces are conductive and allow good return current path. Quasi-neutrality made it possible to obtain density profiles of the positive ions without distinguishing the respective contribution of I^+ and I_2^+. The use of a Faraday probe, mass spectrometry or any other diagnostics able to distinguish between the positive ion species would be an interesting addition to this work. Furthermore, it was assumed that the I_3^- were negligible under the operating conditions of electric propulsion, but the use of laser-induced detachment with a laser energy superior to 4.23 eV (wavelength shorter than 293 nm) would allow to confirm or not this assumption.

On the other hand, several optical diagnostics were presented and applied to iodine plasmas to probe neutral species (atoms and molecules), in Chapter 4. First, an atomic excited species was probed by absorption at 905 nm. This technique provided accurate temperature measurements along the thrust axis, even though the probed atomic excited, non-metastable, is probably not in exact thermal equilibrium with the ground state atoms. Then, techniques for probing the fundamental levels were developped using a second device: an iodine cell where the working pressures are more favourable for optical diagnostics. By exploiting the structure

of the iodine molecule, absorption at 488 nm allowed direct measurement of the molecular dissociation rate and absorption at 1315 nm allowed measurement of the population difference between the first two atomic levels of iodine ($^2P^\circ_{3/2}$ and $^2P^\circ_{1/2}$), as well as the atomic temperature. The combination of these two techniques allowed us to obtain an absolute measurement of the density of the two atomic species, with the major conclusions being the non-negligible population of the first excited state and most likely the total dissociation at the centre of the two discharges. Nevertheless, the absorption techniques, whose results are integrated along the line of sight, showed their limits in the thruster and the quest for a local diagnosis naturally led to the development of the TALIF method. Absolute temperature measurements were obtained within the iodine cell and relative measurements of the atomic ground state density were performed in the cell and in the thruster along the thrust axis. Down to 1 mTorr, the TALIF method has proven to work well, making it the diagnostic of choice for electric propulsion.

The next step is obviously to use the TALIF technique with a single-mode laser within the thruster to determine temperature profiles for the atomic ground state. The second is to continue investigating two-photon absorption patterns to probe the $I(^2P^\circ_{1/2})$ level population, which have never been detected directly so far, in our experiments. Another missing piece of information is the translational temperature of the molecules. Two important difficulties make this measurement quite challenging. On the one hand, the plasma is often very largely dissociated in our experimental conditions, which makes it difficult to detect the few remaining molecules. Secondly, a temperature measurement can be based on the interpretation of the Doppler profile of a resonant transition probed with a single-frequency laser. The signal obtained will depend on the population of the initial level, which in the case of a molecule is distributed between many vibrational levels and rotations. Another solution, assuming equal translational and rotational temperatures, would be to probe the different rotational levels, which are very numerous in an iodine plasma due to the smallness of the rotation constant (inversely proportional to the mass). Finally, an important development of our experimental setups would be to pulse the discharges in order to study the temporal behavior in post-discharge. Two important pieces of information could be determined: (i) the wall sticking probability coefficient γ_{wall}, by measuring, for example, the decrease of the atomic signal as a function of time; (ii) the thermalization coefficient of the atoms by measuring the temporal evolution of their temperature.

Simulations of low-pressure iodine plasmas

- Are there sufficient theoretical data to model low-pressure iodine plasmas?
- How to accurately model low-pressure iodine plasmas?

Chapter 1 presented an updated set of iodine cross-sections which was used in two different models of low-pressure iodine plasmas. Compared to other molecules much more studied by the low-temperature plasma community, such as O_2, N_2 or Cl_2, the reaction set is limited and largely perfectible, especially with regard to vibrational and rotational excitations. Nevertheless, we have shown that it is sufficient to capture the essential behaviour of iodine plasmas.

In Chapter 5, an updated iodine global model has been presented and compared to experimental results on two different geometries. Compared to the previous models, the reaction set has been completed, the first atomic excited species $I(^2P^\circ_{1/2})$ has been included, the neutral gas heating model has been improved and the temperatures of the atoms and molecules are no longer considered equal. The physics of the plasma generation are also considered in both geometries to self-consistently calculate the absorbed power. Comparisons on the iodine cell validated the behaviour of neutral species. The neutrals temperatures and densities trends were well captured as a function of the RF power when the wall sticking probability value was adjusted. Although updated, the energy equation for neutral species has shown limitations and more sophisticated heating terms should be considered. Concerning the comparisons with the thruster, the global model well captured the general features. The calculated electron densities and electron temperatures are comparable to the measured ones, and the trends with the neutral gas pressure and absorbed RF power are well reproduced. The model predicts a very strong dissociation in the conditions explored, i.e. very low pressure and high RF power. While the trends for the electronegativity are also well reproduced, the doubts on the magnitude of the electron impact detachment cross-section made it impossible to conclude on the value of the wall sticking probability γ_{wall}, which has only been estimated to be between 0.05 and 0.2. However, the model validation for pressures above 3 mTorr, using neutral species measurements was not completed because in those operating conditions, the global model assumptions break down; electrons are no longer isothermal and consequently the profiles start to strongly deviate from the standard case well described by global modelling. An alternative model, able to capture spatial gradients, was needed.

Therefore, in Chapter 6, a one-dimensional multi-fluid code has been proposed to study the neutral dynamics along the axis of the thruster, at the centre of the discharge. This code has been used to simulate the density, velocity and temperature profiles of three neutral iodine species: I_2, $I_{3/2}$ and $I_{1/2}$, taking into account the inertia terms and heat fluxes of each species, and using the electron density and temperature measurements presented in Chapter 3 as input. All the spatial evolutions observed experimentally and presented in Chapter 4 were retrieved in the simulations. The influence of the edge temperature T_{edge}, the wall sticking probability γ_{wall}, the neutral pressure and the discharge power was investigated. As an example, at 15 mTorr and for a discharge power of 200 W, $T_{\text{edge}} = 600$ K and $\gamma_{\text{wall}} = 0.05$

allow the model to reproduce quite accurately the temperature measurements obtained on an atomic excited state by absorption at 905 nm (see Section 4.2). It should be noted, however, that γ_{wall} and T_{edge} are certainly different at each end of the domain, which has not been considered here. It should also be noted that T_{edge} in our modeling is not directly the wall temperature, but the temperature of the gas near the wall. This temperature is not necessarily equal to the wall temperature because of the well known thermal accommodation factor (not included here). Finally, the absolute measurements of atomic and molecular densities obtained by absorption and presented in chapter 4 could not be reconciled with the model. The measured densities are always largely higher than the simulated densities and the measured dissociation fraction is lower than the simulated one. The explanation comes from the fact that we compare local simulations with integrated measurements along the axis transverse to the axis of the thruster where the density profiles are, most likely, minimum in the center. Ways to reconcile the model with the absorption measurements were indicated.

The logical continuation of this work is the development of a self-consistent model allowing the simulation of neutral and charged species simultaneously, in at least one dimension. There are several possible paths. The first is to use a multi-fluid code to simulate all species. The second, which is the one that is favoured in the thesis of N. Lequette, at LPP, is to treat the neutral species with the fluid code developed in the framework of this thesis and to treat the charged species using a Particle-In-Cell code. Although expensive in terms of computation, the extension to 2D would be an undeniable asset to simulate, for example, optical absorption signals and compare them to those measured but also to deepen our understanding of transport phenomena. Additionally, the treatment of wall temperature jumps due to thermal accommodation should be integrated into the models.

Physics of low-pressure iodine plasmas

- To what extent are low-pressure iodine plasmas spatially homogeneous?
- What is the behavior of neutral species (atoms and molecules) in an iodine plasma?
- What are the main transport and heating mechanisms in iodine plasmas?

The two experimental devices used (presented in Chapter 2), allowed the study of iodine plasmas in two different pressure ranges. Between 0.5 and 30 mTorr for the ICP discharge and between 30 and 225 mTorr of initial molecular pressure for the iodine cell. The common point between the two experiments is the almost complete dissociation reached at the center of the discharges for a sufficient incident power and the non-negligible population of the first atomic excited state, never far from Boltzmann equilibrium at T_e, with the atomic ground state.

Within the cell, the charged species have not been probed but the global model predicts a very large domination of negative I^- ions and positive I_2^+ ions, estimating the electronegativity at more than 1000 for the lowest powers, which seems to be in agreement with the experimental observations of the XXth century. The inclusion of the I_3^- species should be considered for these operating conditions. The quenching of the atomic excited state by the molecules seems to be negligible and processes of production of the same excited state by molecular dissociation must be added to complete the comparisons. Atomic temperatures were measured and reached more than 1000 K at the highest pressures.

Within the thruster, spatial gradients appeared as soon as the pressure was increased. The high density plasma localized near the antenna when the pressure increases. At 15 mTorr, for instance, the electron density decreases by a factor of 50 within less than 10 cm. This demonstrates that the electron energy relaxation length is short in iodine, due to its molecular nature. As the plasma transports away from the antenna, electrons cool down, the dissociation degree decreases, and consequently the dissociative electron attachment rate responsible for negative ion generation drastically increases. As a consequence, it was found that the negative ion density is larger than the electron density in the extraction region for pressures above 5 mTorr (note that these experiments are performed without magnetic filter). The negative ions were found to be very hot (only 3 to 5 times less hot than the electron temperature) and did not follow Boltzmann equilibrium, being destroyed near the antenna before exploring the potential. Also above 5 mTorr, very clear heating near the antenna (with temperatures above 1500 K) and strong spatial temperature gradients were evidenced, and the presence of strong temperature jumps near the walls whatever the pressure. Due to very strong heating (which localises near the antenna as the pressure increases), the density profiles of the neutral species are minimal in the centre and maximal near the walls. For pressures ranging from 0.5 to 15 mTorr, dissociation is very high, easily reaching more than 95% at the location of the electron density maximum. This extreme molecular dissociation leads to a lower heating of the molecules than that of the atoms: the thermal equilibrium between the three neutral species is never observed in the simulations, which remain

to be proved experimentally.

Although strong heating has been demonstrated and dissociation processes are mainly responsible, it is not clear what energy to attribute to the fragments of a dissociation process since it is not known, a priori, through which excited intermediate state the molecule transited before dissociating. Precise ab initio calculations are required to further our understanding of such collisional processes.

Iodine for Electric Propulsion

- How do iodine plasmas behave compared to noble gases plasmas ?
- Are negative ions an obstacle to the use of iodine as an alternative propellant?

Iodine versus noble gases

Langmuir probe measurements were also carried out in xenon, krypton and argon, three noble gases either routinely used (xenon and krypton) or considered as an alternative (argon) in electric propulsion. The main conclusions of this investigation is that iodine is as good, if not better than, xenon at low gas flow rates, i.e. at low gas pressures. This is because although iodine is a molecular gas, molecules are easily dissociated and at the lowest pressure the plasma is probably fully dissociated. The ionization potential of iodine atoms is lower than that of xenon atoms, consequently the energy cost for an electron–ion pair creation is lower in iodine than in xenon despite the dissociation energy cost.

However, as pressure increases, the situation quickly reverses and iodine loses its advantage. In our experiments, where the distance between the antenna generating the plasma and the extracting grids is large, we found that the high density plasma localizes near the antenna when the pressure increases, and this effect is much more pronounced in iodine. This demonstrates that the electron energy relaxation length becomes shorter in iodine, due to its molecular nature. The ionization (or mass) efficiency becomes lower than that of xenon at higher pressures. The phenomenon is further enhanced by the electronegative nature of iodine.

The global model has been adapted to the four alternative propellants and it is possible to use it as a predictive tool. In Figure CCL.1, we simulate what would be the thruster efficiency (defined as the Thrust-to-Power ratio times the ratio of the ion flux extracted to the neutral flux injected) of our experimental prototype if the grids were biased. The simulation parameters are fixed to : $\beta_{\text{neutrals}} = 0.2$, $\beta_{\text{ions}} = 0.5$ and $V_{\text{grid}} = 1000$ V. The gap between the two grids is $d_{\text{grid}} = 1.5$ mm. The thruster efficiency is plotted against the input mass flow rate for a fixed ion current density extracted by the grids equal to the Child-Langmuir limit current:

$$J_{\text{CL,X}} = \frac{4}{9}\varepsilon_0 \left(\frac{2e}{m_{\text{X}}}\right)^{1/2} \frac{V_{\text{grid}}^{3/2}}{d_{\text{grid}}^2},$$

with ε_0 the vacuum permittivity, as proposed by Chabert [114]. The Child-Langmuir formula retained for iodine is weighted by the ions density:

$$J_{\text{CL,iodine}} = \frac{n_{\text{I}^+}}{n_{\text{I}^+} + n_{\text{I}_2^+}} J_{\text{CL,I}} + \frac{n_{\text{I}_2^+}}{n_{\text{I}^+} + n_{\text{I}_2^+}} J_{\text{CL,I}_2}$$

The following conclusions are retrieved: (i) at low pressure (and therefore mass flow rates) and for a sufficient input power, iodine appears to be the most efficient propellant, (ii) as soon as the pressure (and/or the mass flow rate) increases, xenon appears more suitable. This could be expected and comes from the electronegative and molecular nature of iodine. (iii) Because of a high ionization energy and a lower

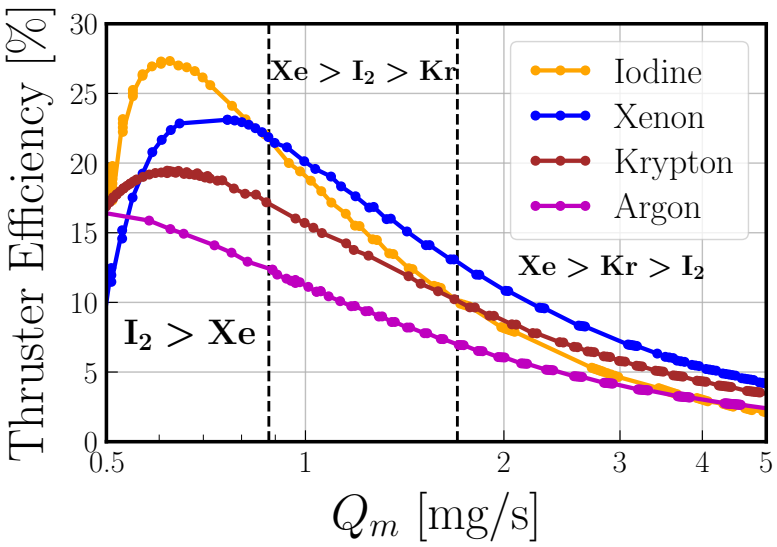

Figure CCL.1: Global modeling simulated thruster efficiency [%] as a function of the mass flow rate [mg/s] obtained at Child-Langmuir limit current for four different propellants: iodine, xenon, krypton and argon.

mass, argon is not competitive. Krypton is less efficient than xenon, but it could be a good compromise at large mass flow rates since it is less expensive than xenon.

It should be noted that the work presented in this thesis concerns gridded-ion-thrusters, devoid of a magnetic field. However, in the Electric Propulsion community, Hall effect thrusters or Electron Cyclotron Resonance (ECR) thrusters are massively used. The behavior of iodine within these thrusters must be much more studied and iodine performances compared to those of noble gases. In particular, the physics of these prototypes is complex and the electronic temperature exceeds 10 or even 20 eV, an area unexplored by our experiments and simulations where I^{2+} ions should no longer be neglected. Also, for the Hall effect thruster, the use of a neutralising cathode operating with iodine remains an unresolved challenge at present.

Towards PEGASES 2.0

In the previous comparison between alternative propellants, iodine has shown its suppremacy in a regime where it is used as an atomic propellant, devoid of any molecular properties. Indeed, at very low flux, dissociation is almost complete and the negative ions, produced by dissociative attachment, are completely negligible compared to the electrons. However, in the initial concept of PEGASES, iodine was introduced for its ability to massively produce negative ions. In conclusion of this thesis we would like to look back at this founding idea by performing Langmuir probe and photodetachment measurements within the thruster where a magnetic field has been applied.

The electron and negative ion density profiles measured along the thruster axis are plotted in Figure CCL.2. Measurements were performed in an iodine plasma for a pressure of 2 mTorr and a discharge power of 120 W. The magnetic field spatial profile is highlighted in blue, it has a gaussian shape with a maximum of 235 Gauss at $z = 6$ cm and was generated by adding magnets above and below the thruster.

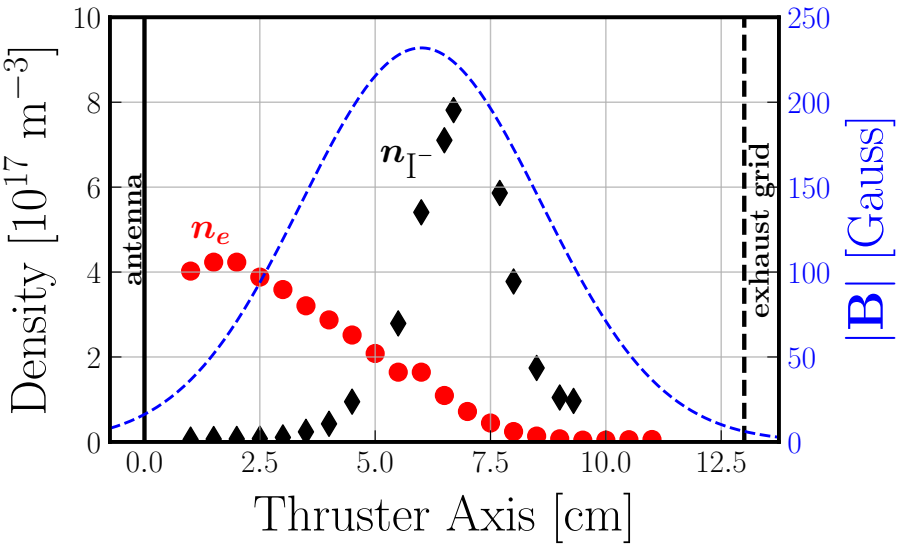

Figure CCL.2: Electron and I^- negative ion density profiles along the thrust axis for a pressure of 2 mTorr and a discharge power of 120 W in the presence of a magnetic field.

The magnetic field acts as a filter in the sense that it considerably reduces the electron density (and the electron temperature not represented) and downstream is a very electronegative plasma that in some conditions may be an ion-ion plasma. In the case presented, a maximum electronegativity of 50 was measured. For such a device to be used in electric propulsion, the position of the grid would have to coincide with the maximum negative ion density. Suitable extraction grids should then be used to generate a flow of fast neutrals.

In the original concept of PEGASES thruster, an alternative polarisation of the extraction grids was envisaged to alternately extract negative and positive ions, the whole of which would be quasi-neutral on average. However, in reference [175], from the field of microelectronics etching, it has been demonstrated that the passage of a jet of ions (positive or negative) through grids with a large aspect ratio (generally around 10) leads to very effective neutralisation (more than 90 % for negative ions). Placing such unpolarised grids at the location of maximum ion density would allow the production of fast neutrals without the need for a neutralising cathode: this would be close to the ideal thruster.

APPENDIX A

PHYSICO-CHEMISTRY OF NOBLE GASES USED FOR ELECTRIC PROPULSION

A.1 Chemical physics properties and brief presentation

The three noble gases studied in this thesis are argon, krypton and xenon, whose atomic notations are given in figure A.1.

Figure A.1: Argon, Krypton and Xenon atomic notations. The atomic mass is given in atomic unit.

Argon is the third noble gas after Helium and Neon, it is the third most abundant component of the Earth's atmosphere. The main argon isotopes present on Earth are argon 40 for 99.6%, argon 36 for 0.34% and argon 38 for 0.06%. Argon is an inert gas widely used in plasma physics laboratories for its low cost and low hazard. Its low mass and high ionization energy prevent it from being massively used by the Electric Propulsion community.

Krypton is the fourth noble gas in the periodic table with 5 known stable isotopes: ^{80}Kr, ^{82}Kr, ^{83}Kr, ^{84}Kr and ^{86}Kr. It is also inert but much more expensive than argon. It has recently become an alternative to xenon for Electric Propulsion due to the scarcity of the latter, despite its inferior performance. For instance, Starlink, a satellite internet constellation operated by *SpaceX* is composed of thousands of satellites in low Earth orbit, thrusted by Hall thrusters fueled with krypton.

Xenon is the 5th noble gas, odourless, colourless and non-flammable like argon and krypton. It is the rarest and most expensive of the non-radioactive noble gases and is extracted by fractional distillation of air that has become liquid. It is

very rare in the earth's atmosphere, representing only a tiny fraction: 0.0000087%. Among the 7 stable isotopes, the most abundant are ^{129}Xe, ^{131}Xe and ^{132}Xe. Xenon and its derivatives are used in a wide range of applications aerospace (by far the most widely used propellant for satellites), medicine, astrophysical research and the semiconductor industry, although annual production is limited to 6×10^4 kg. As krypton and xenon are co-produced together, the xenon market (price and demand) also affects the krypton market.

In the cold plasma community, and more particularly for optical diagnostics, xenon is used to calibrate the atomic density of oxygen atoms, using the TALIF method (see subsection 4.3.2). It is therefore necessary to know the precise two-photon absorption cross section of Xe [176].

A.2 Cross-section dataset

The reaction sets selected come from the Biagi database on LXCAT [35, 177]. For each of the three gases simulated, the datasets account for elastic scattering, electron impact ionization and three or four level-averaged excitation reactions as presented in Table A.1. No metastable states are accounted for. The reaction rates are calculated by integrating collision cross-sections over maxwellian distributions.

Reaction	Process	Rate [$m^3.s^{-1}$]	Threshold [eV]	Reference
Xenon				
$Xe + e^- \longrightarrow Xe + e^-$	Elastic	$K_{el,Xe}$	0	[177]
$Xe + e^- \longrightarrow Xe^+ + 2e^-$	Ionization	$K_{iz,Xe}$	12.13	[177]
$Xe + e^- \longrightarrow Xe^* + e^-$	Excitation 1	$K_{ex1,Xe}$	8.315	[177]
$Xe + e^- \longrightarrow Xe^* + e^-$	Excitation 2	$K_{ex2,Xe}$	9.447	[177]
$Xe + e^- \longrightarrow Xe^* + e^-$	Excitation 3	$K_{ex3,Xe}$	9.917	[177]
$Xe + e^- \longrightarrow Xe^* + e^-$	Excitation 4	$K_{ex4,Xe}$	11.70	[177]
Krypton				
$Kr + e^- \longrightarrow Kr + e^-$	Elastic	$K_{el,Kr}$	0	[177]
$Kr + e^- \longrightarrow Kr^+ + 2e^-$	Ionization	$K_{iz,Kr}$	14.00	[177]
$Kr + e^- \longrightarrow Kr^* + e^-$	Excitation 1	$K_{ex1,Kr}$	9.915	[177]
$Kr + e^- \longrightarrow Kr^* + e^-$	Excitation 2	$K_{ex2,Kr}$	11.30	[177]
$Kr + e^- \longrightarrow Kr^* + e^-$	Excitation 3	$K_{ex3,Kr}$	12.00	[177]
$Kr + e^- \longrightarrow Kr^* + e^-$	Excitation 4	$K_{ex4,Kr}$	12.75	[177]
Argon				
$Ar + e^- \longrightarrow Ar + e^-$	Elastic	$K_{el,Ar}$	0	[177]
$Ar + e^- \longrightarrow Ar^+ + 2e^-$	Ionization	$K_{iz,Ar}$	15.76	[177]
$Ar + e^- \longrightarrow Ar^* + e^-$	Excitation 1	$K_{ex1,Ar}$	11.60	[177]
$Ar + e^- \longrightarrow Ar^* + e^-$	Excitation 2	$K_{ex2,Ar}$	13.00	[177]
$Ar + e^- \longrightarrow Ar^* + e^-$	Excitation 3	$K_{ex3,Ar}$	14.00	[177]

Table A.1: List of the reactions used in the global model for noble gases. The dataset used is called "Biagi-v7.1" [177], on the LXCAT website (database described in [35]), and has been extracted from Magboltz v7.1 (extensive data compilations by S.F. Biagi, coded into his FORTRAN Monte Carlo code Magboltz [178]).

A.3 Global modeling

In this section, the global model for noble gases is described: the equations will be written for a noble species X where X ∈ {Ar, Kr, Xe}.

The species included in the model are neutrals X, positive ions X^+ and electrons e^-. Nevertheless, the discharge can be considered perfectly inductive (without any capacitive coupling) which ensures very thin sheaths (a few Debye lengths only) and thus quasineutrality to be assumed everywhere in the plasma:

$$n_{X^+} = n_e. \tag{A.1}$$

The system of particle balance equations to solve is:

$$\frac{\mathrm{d}n_{X^+}}{\mathrm{d}t} = n_X n_{X^+} K_{\mathrm{iz,X}} - \Gamma_{X^+}\frac{S}{V}, \tag{A.2}$$

$$\frac{\mathrm{d}n_X}{\mathrm{d}t} = \frac{Q_N}{V} + \Gamma_{X^+}\frac{S_{\mathrm{neutr,ions}}}{V} - n_X n_{X^+} K_{\mathrm{iz,X}} - \Gamma_X\frac{S_{\mathrm{open,neutrals}}}{V}. \tag{A.3}$$

The expressions for the fluxes to the walls are:

$$\Gamma_{X^+} = h n_{X^+} u_{\mathrm{B,X^+}},\ \ \Gamma_X = \frac{1}{4} n_X \overline{v}_X, \tag{A.4}$$

with $\overline{v}_X = \left(\frac{8eT_X}{\pi m_X}\right)^{1/2}$ and $u_{\mathrm{B,X}} = \left(\frac{eT_e}{m_X}\right)^{1/2}$, respectively the mean speed and the Bohm speed of the particle X. The h_L and h_R factors are given by [58] :

$$h_L = 0.86\left(3 + \frac{L}{2\lambda_{\mathrm{in}}} + 0.2\frac{T_{X^+}}{T_e}\left(\frac{L}{\lambda_{\mathrm{in}}}\right)^2\right)^{-1/2}, \tag{A.5}$$

$$h_R = 0.8\left(4 + \frac{R}{\lambda_{\mathrm{in}}} + 0.41\frac{T_{X^+}}{T_e}\left(\frac{R}{\lambda_{\mathrm{in}}}\right)^2\right)^{-1/2}, \tag{A.6}$$

where σ_{in} the cross-section for ions-neutrals elastic collisions is set to 10^{-18} m^2 for all gases, and T_{X^+} is fixed to 0.1 eV. Those formulas are the electropositive counterparts of the ones used for iodine.
The neutral power balance equation reads:

$$\begin{aligned}\frac{\mathrm{d}}{\mathrm{d}t}\left(\frac{3}{2}n_X e T_X\right) = &+ 3\frac{m_e}{m_X}e(T_e - T_X)n_e n_X K_{\mathrm{el,X}} \\ &+ \sigma_{\mathrm{in}}\Gamma_X n_{X^+} m_X u_{\mathrm{B,X}}^2 \\ &+ s_{\mathrm{keep,X^+}} \times (5eT_e)\Gamma_{X^+}\frac{S_{\mathrm{neutr,ions}}}{V} \\ &- \kappa_X \frac{e}{k_B}\left(\frac{T_X - T_{\mathrm{wall}}}{\Lambda_0}\right)\frac{S}{V},\end{aligned} \tag{A.7}$$

with temperatures in eV. κ_X is the thermal conductivity depending on T_X taken from [168]. We assumed that the energy gained by ions in the sheath is $5eT_e$.
Finally, the electron power balance is:

$$\frac{\mathrm{d}}{\mathrm{d}t}\left(\frac{3}{2}n_e e T_e\right) = p_{\mathrm{abs}} - p_{\mathrm{loss}}, \tag{A.8}$$

where p_{abs} [W.m^{-3}] is the absorbed power by the electrons and p_{loss} [W.m^{-3}] is the total electron power loss per unit volume:

$$\begin{aligned} p_{\text{loss}} = & \left(\varepsilon_{\text{iz,X}} K_{\text{iz,X}} + \sum_{j=1}^{N_{\text{ex,X}}} \varepsilon_{\text{exj,X}} K_{\text{exj,X}} + 3\frac{m_e}{m_{\text{X}}} e(T_e - T_{\text{X}}) K_{\text{el,X}}\right) n_e n_{\text{X}} \\ & + \frac{1}{V}\left[< \varepsilon_{\text{kin}} >_0^{\text{X}} (S_1 h_L + S_2 h_R) + < \varepsilon_{\text{kin}} >_{\beta_{\text{ions}}}^{\text{X}} S_{\text{grid,ions}} h_L \right] \Gamma_{\text{X}^+}. \end{aligned} \tag{A.9}$$

The sheath potential can be calculated using the current balance between the positive ions that are accelerated through the sheath and the thermal flux of electrons:

$$< \varepsilon_{\text{kin}} >_{\beta_{\text{ions}}}^{\text{X}} = eT_e \left[\frac{5}{2} - \ln\left(\frac{1}{1-\beta_{\text{ions}}} \sqrt{\frac{2\pi m_e}{m_{\text{X}}}} \right) \right]. \tag{A.10}$$

$< \varepsilon_{\text{kin}} >_{\beta_{\text{ions}}}^{\text{X}}$ values are given in Table A.2.

Physical Quantity	Argon (Ar)	Krypton (Kr)	Xenon (Xe)
Mass			
m_{X} [a.m.u.]	39.95	83.80	131.3
Energy lost at the surface prefactor			
$< \varepsilon_{\text{kin}} >_0^{\text{X}}$ [no unit]	7.179	7.549	7.774
Number of excitation levels			
$N_{\text{ex,X}}$ [no unit]	3	4	4

Table A.2: Physical quantities used for the global model with noble gases. X refers to the atomic species (Ar, Kr or Xe).

APPENDIX B

DISTRIBUTION FUNCTIONS, CROSS-SECTIONS AND REACTION RATES

B.1 Distribution function, Boltzmann equation and macroscopic variables

The following is extracted from [58, 119].

B.1.1 Kinetic theory

For a given species, we introduce a distribution function $f(\mathbf{r},\mathbf{v},t)$ in the six-dimensional phase space $(\mathbf{r},\mathbf{v})$ of particle positions and velocities, with the interpretation that $f(\mathbf{r},\mathbf{v},t)\,\mathrm{d}^3r\,\mathrm{d}^3v$ is the number of particles inside a six-dimensional phase space volume $\mathrm{d}^3r\,\mathrm{d}^3v$ at $(\mathbf{r},\mathbf{v})$ at time t.

By taking the velocity moments of the distribution function, one can then calculate macroscopic quantities. They are the basic variables of the fluid theory. The first of these is the particle density defined as

$$n(\mathbf{r},t) \;=\; \int f(\mathbf{r},\mathbf{v},t)\,\mathrm{d}^3v. \tag{B.1}$$

The drift velocity is obtained by taking the following velocity moment

$$\mathbf{u}(\mathbf{r},t) \;=\; \frac{1}{n(\mathbf{r},t)}\int \mathbf{v} f(\mathbf{r},\mathbf{v},t)\,\mathrm{d}^3v. \tag{B.2}$$

Finally, the total kinetic energy density is given by:

$$w(\mathbf{r},t) \;=\; \int \frac{1}{2}m\mathbf{v}^2 f(\mathbf{r},\mathbf{v},t)\,\mathrm{d}^3v, \tag{B.3}$$

where m is the particle mass. The temperature T can be deduced from the total kinetic energy:

$$\begin{aligned} w(\mathbf{r},t) \;&=\; \frac{3}{2}p(\mathbf{r},t) + \frac{1}{2}mn(\mathbf{r},t)\mathbf{u}(\mathbf{r},t)^2 \\ &=\; \frac{3}{2}n(\mathbf{r},t)k_{\mathrm{B}}T(\mathbf{r},t) + \frac{1}{2}mn(\mathbf{r},t)\mathbf{u}(\mathbf{r},t)^2, \end{aligned} \tag{B.4}$$

where $p(\mathbf{r},t) = n(\mathbf{r},t)k_\mathrm{B}T(\mathbf{r},t)$ is the isotropic pressure. No viscosity will be accounted for in this thesis.

In a plasma, the evolution of the distribution function is governed by Boltzmann equation:

$$\frac{\partial f}{\partial t} + \mathbf{v}\cdot\nabla_\mathbf{r} f + \frac{\mathbf{F}}{m}\cdot\nabla_\mathbf{v} f = \left.\frac{\partial f}{\partial t}\right|_\mathrm{col}, \tag{B.5}$$

where $\left.\frac{\partial f}{\partial t}\right|_\mathrm{col}$ accounts for the collisions. The fluid equations (presented in Chapter 6) are obtained from the velocity moments of the Boltzmann equation.

Unless otherwise stated, the velocity distribution function used in this thesis will be a Maxwellian (Maxwell-Boltzmann) distribution function

$$f(\mathbf{v}) = n\left(\frac{m}{2\pi k_\mathrm{B}T}\right)^{3/2}\exp\left(-\frac{m\mathbf{v}^2}{2k_\mathrm{B}T}\right). \tag{B.6}$$

B.1.2 Simplification and convenient notations

Since the Maxwellian velocity distribution is isotropic, the distribution can also be expressed entirely in terms of the scalar speed $v = |\mathbf{v}|$ rather than the velocity vector, $\mathbf{v}$. The speed distribution

$$f_\mathrm{s}(v) = n\left(\frac{m}{2\pi k_\mathrm{B}T}\right)^{3/2} 4\pi v^2\exp\left(-\frac{mv^2}{2k_\mathrm{B}T}\right), \tag{B.7}$$

gives the proportion of particles with speeds between v and $v + \mathrm{d}v$ and the density reads:

$$n = \int_0^\infty f_\mathrm{s}(v)\,\mathrm{d}v = \int_0^\infty f_\mathrm{e}(\mathcal{E})\,\mathrm{d}\mathcal{E}. \tag{B.8}$$

In this thesis, however, the convenient variable are the energy $\mathcal{E} = \frac{1}{2}\frac{m}{e}v^2$, expressed in eV and the corresponding energy distribution function $f_\mathrm{e}(\mathcal{E})$:

$$f_\mathrm{e}(\mathcal{E}) = 2n\left(\frac{1}{T}\right)^{3/2}\left(\frac{\mathcal{E}}{\pi}\right)^{1/2}\exp\left(-\frac{\mathcal{E}}{T}\right), \tag{B.9}$$

where the temperature is expressed in eV:

$$k_\mathrm{B}T[\mathrm{K}] = eT[\mathrm{eV}]. \tag{B.10}$$

B.2 Cross-section of a binary collision

Every collision process considered in this thesis can be written as

$$\alpha + \beta \longrightarrow \text{products}. \tag{B.11}$$

The scattering angle of a particle α colliding with a target particle β depends on the impact parameter b (defined as the hypothetical distance of what would be the closest approach of the centers of the two particles if there were no interaction between them), and every angle does not have the same probability. This effect is taken into account by introducing a differential cross-section

$$I_{\alpha\beta}(v,\theta) \;=\; \frac{b}{\sin\theta}\left|\frac{\mathrm{d}b}{\mathrm{d}\theta}\right|. \tag{B.12}$$

The quantity

$$I_{\alpha\beta}(v,\theta)\,\mathrm{d}\theta\, n_\beta v \mathrm{d}t, \tag{B.13}$$

is the probability for the particle α to be scattered with an angle between θ and $\theta+\mathrm{d}\theta$ in the time lapse dt against the particles β of density n_β. Only one angular parameter θ is chosen because a binary collision system features a cylindrical symmetry. The cross-section $\varsigma_{\alpha\beta}$ is the integral over all the scattering angles of the differential cross section

$$\varsigma_{\alpha\beta}(v) \;=\; 2\pi\int_0^\pi I_{\alpha\beta}(v,\theta)\sin\theta\;\mathrm{d}\theta. \tag{B.14}$$

For an elastic process, the kinetic energy of the fictitious particle in the center of mass frame is conserved, and the momentum transfer in the direction of the initial velocity vector $\mathbf{v}$ is $(1-\cos\theta)\mathbf{v}$. The momentum transfer cross-section is therefore

$$\sigma_{\alpha\beta}(v) \;=\; Q^{(1)}_{\alpha\beta}(v) \;=\; 2\pi\int_0^\pi (1-\cos\theta) I_{\alpha\beta}(v,\theta)\sin\theta\;\mathrm{d}\theta. \tag{B.15}$$

In Chapter 1, unless otherwise specified, the term cross-section with the notation σ will refer to the momentum transfer cross-section.

B.3 Reaction rate

In the case of a negligible relative motion between the colliding species, the particles creation and loss, after the reaction (B.11), read:

$$\pm n_\alpha n_\beta K_{\alpha\beta}, \tag{B.16}$$

where $K_{\alpha\beta}$ is called the reaction rate in $\mathrm{m}^3.\mathrm{s}^{-1}$.

Electron-heavy species collisions

Given a set of momentum transfer cross-sections for a given reaction, the reaction rate (or rate constant in $\mathrm{m}^3.\mathrm{s}^{-1}$) for an electron-neutral or electron-ion collision is computed by integrating the product of cross section and speed over the particle distribution function:

$$K_{\alpha\beta} \;=\; \frac{1}{n}\left\langle v Q^{(1)}_{\alpha\beta}(v)\right\rangle_v \;=\; \frac{1}{n}\left\langle \sqrt{\frac{2e\mathcal{E}}{m_e}}\,Q^{(1)}_{\alpha\beta}(\mathcal{E})\right\rangle_{\mathcal{E}}. \tag{B.17}$$

In this thesis, the reaction rate of a collision occurring between an electron (labelled e) and an heavy particle (ion, atom or molecule, labelled h) will be mostly taken as a function of the electron temperature:

$$K_{\mathrm{he}}(T_e) = \left(\frac{m_e}{2\pi k_{\mathrm{B}} T_e}\right)^{\frac{3}{2}} \int_0^{+\infty} 4\pi v^2 \exp\left(-\frac{m_e v^2}{2k_{\mathrm{B}} T_e}\right) \times v\, Q_{\mathrm{he}}^{(1)}(v)\, \mathrm{d}v. \tag{B.18}$$

Collisions between heavy species

In the case of a collision between two heavy species (α and β), the relative motion of the species must be taken into account.

In Chapter 1 and Chapter 5, this relative motion is neglected and the reaction rates are computed by assuming the same temperature for both heavy species. Equation (B.18) is used with the gas temperature and the reduced mass $m_{\alpha\beta} = m_\alpha m_\beta/(m_\alpha + m_\beta)$ instead of the electron temperature and the electron mass respectively.

In Chapter 6, in the case of a multi-fluid description of neutral species, the relative motion of different heavy species cannot be neglected anymore. The question is addressed in Section C.4 of Appendix C.

APPENDIX C

MULTI-FLUID FORMALISM AND DERIVATION OF SOURCE TERMS

In this appendix, the temperatures are expressed in Kelvin [K]. Unless otherwise stated, the collision reads:

$$\alpha + \beta \overset{k_{\alpha\beta}}{\rightarrow} \text{products}, \tag{C.1}$$

where $k_{\alpha\beta}$, the generalized rate constant [$\mathrm{m}^3.\mathrm{s}^{-1}$], is key because when a particle is created or lost after the reaction (C.1), the net change of particle density reads:

$$\pm n_\alpha n_\beta k_{\alpha\beta}. \tag{C.2}$$

C.1 Generalized rate constant

The friction force for each pair of species (α, β) is usually assumed to be proportional to their relative mean velocity. This implies that the frequency of inter-species collisions is not affected by the relative motion of the species, which is true if the velocity of this motion is much smaller than the thermal velocity or, in other words, if the Mach number of this motion is small (which is true in most cases, see Section C.2). It also assumes the distribution function to be a drifting Maxwellian. Otherwise, the thermal friction can appear. However, in conditions in which the multi-fluid approach is essential, the Mach numbers of the relative motion of the species are finite and the temperatures of the species are unequal. Hence, the friction force should be calculated by taking into account the finite values of the Mach numbers of the relative motion of the species and of the non-equality of their temperatures. There are several ways of solving this problem. During this thesis, we used Benilov's formalism [111, 112]. Let's introduce the generalized rate constant $k_{\alpha\beta}$ [111], that depends on the Mach number $M_{\alpha\beta}$ of the relative motion:

$$k_{\alpha\beta} = 4e^{-M_{\alpha\beta}^2}\sqrt{\frac{2k_\mathrm{B}T_{\alpha\beta}}{\pi m_{\alpha\beta}}}\int_0^{+\infty}\xi^3 e^{-\xi^2}\times Q_{\alpha\beta}^{(1)}\left(\sqrt{\frac{2k_\mathrm{B}T_{\alpha\beta}}{m_{\alpha\beta}}}\xi\right)\times F^{(n)}\left(2M_{\alpha\beta}\xi\right)\mathrm{d}\xi, \tag{C.3}$$

where,

$$m_{\alpha\beta} = \frac{m_\alpha m_\beta}{m_\alpha + m_\beta}, \text{ is the reduced mass.} \tag{C.4}$$

$$T_{\alpha\beta} = \frac{m_\alpha T_\beta + m_\beta T_\alpha}{m_\alpha + m_\beta}, \text{ is the reduced temperature.} \tag{C.5}$$

$$M_{\alpha\beta} = \sqrt{\frac{m_{\alpha\beta}}{2k_\mathrm{B}T_{\alpha\beta}}}\left|\mathbf{u}_\beta - \mathbf{u}_\alpha\right|, \text{ is the Mach number.} \tag{C.6}$$

$$v_{\alpha\beta} = \left|\mathbf{v}_\beta - \mathbf{v}_\alpha\right|, \text{ is the relative speed.} \tag{C.7}$$

$$Q^{(1)}_{\alpha\beta}(v_{\alpha\beta}) = 2\pi\int_0^\pi (1-\cos\theta) I_{\alpha\beta}(v_{\alpha\beta},\theta)\sin\theta\,\mathrm{d}\theta, \tag{C.8}$$

is the momentum transfer cross-section.

$$I_{\alpha\beta}(v_{\alpha\beta},\theta) = \frac{b}{\sin\theta}\left|\frac{\mathrm{d}b}{\mathrm{d}\theta}\right|, \tag{C.9}$$

is the differential cross-section, with b the impact parameter and θ the scattering angle.

$$F^{(n)}(x) = \frac{\sinh(x)}{x}. \tag{C.10}$$

C.2 Simplified reaction rate (small drift between species or small Mach number of the relative motion)

In most cases, the collision will occur between an electron e^- and an heavy species h :

$$\mathrm{h} + \mathrm{e}^- \longrightarrow \text{products}, \tag{C.11}$$

Naturally, $m_e \ll m_\mathrm{h}$ and $T_\mathrm{h} \ll T_e$, which results :

$$m_\mathrm{he} \approx m_e, \qquad T_\mathrm{he} \approx T_e, \qquad M_\mathrm{he} \approx \left|\frac{\mathbf{u}_e}{\overline{v}_e}\right| \ll 1, \qquad F^{(n)}(2M_\mathrm{he}\xi) \approx 1,$$

with $\overline{v}_e = \left(\frac{k_\mathrm{B}T_e}{m_e}\right)^{1/2}$ the electron thermal speed. Thus, the generalized reaction rate constant (equation (C.3)) becomes:

$$\begin{aligned} k_\mathrm{he} &= 4\sqrt{\frac{2k_\mathrm{B}T_e}{\pi m_e}}\int_0^{+\infty}\xi^3 e^{-\xi^2} Q^{(1)}_\mathrm{he}\left(\sqrt{\frac{2kT_e}{m_e}}\xi\right)\mathrm{d}\xi \\ &= \left(\frac{m_e}{2\pi k_\mathrm{B}T_e}\right)^{\frac{3}{2}}\int_0^{+\infty} 4\pi v^2 e^{-\frac{m_e v^2}{2k_\mathrm{B}T_e}} \times v\, Q^{(1)}_\mathrm{he}(v)\,\mathrm{d}v \quad \text{, with } \xi = \sqrt{\frac{m_e}{2k_\mathrm{B}T_e}}v. \\ &= \frac{1}{n}\left\langle v\, Q^{(1)}_\mathrm{he}(v)\right\rangle_\mathbf{v} = K_\mathrm{he}, \end{aligned} \tag{C.12}$$

where K_he is the commonly used rate constant (see equation (B.18)).

For any other binary collision between α and β in which the Mach number can be neglected, one can write:

$$k_{\alpha\beta} = K_{\alpha\beta}, \tag{C.13}$$

using $T_{\alpha\beta}$ the reduced temperature and $m_{\alpha\beta}$ the reduced mass. The reaction rate $K_{\alpha\beta}$ has been used in Chapter 1 and Chapter 5.

C.3 Modified Chapman-Cowling Integrals

We define collision rates averaged over the distribution function of the colliding species. Depending on the moment considered, the weight of the average is different. In this work, we use the definition proposed by Chapman-Cowling [179] and generalized by Benilov [111, 112] for drifting Maxwellian for arbitrary Mach numbers:

$$\Omega_{\alpha\beta}^{(l,r,n)} = e^{-M_{\alpha\beta}^2}\sqrt{\frac{kT_{\alpha\beta}}{2\pi m_{\alpha\beta}}}\int_0^{+\infty}\xi^{2r+3}e^{-\xi^2}Q_{\alpha\beta}^{(l)}\left(\sqrt{\frac{2kT_{\alpha\beta}}{m_{\alpha\beta}}}\xi\right)F^{(n)}\left(2M_{\alpha\beta}\xi\right)\mathrm{d}\xi \tag{C.14}$$

$$\Omega_{\alpha\beta}^{(l,r,m)} = e^{-M_{\alpha\beta}^2}\sqrt{\frac{kT_{\alpha\beta}}{2\pi m_{\alpha\beta}}}\int_0^{+\infty}\xi^{2r+3}e^{-\xi^2}Q_{\alpha\beta}^{(l)}\left(\sqrt{\frac{2kT_{\alpha\beta}}{m_{\alpha\beta}}}\xi\right)F^{(m)}\left(2M_{\alpha\beta}\xi\right)\mathrm{d}\xi \tag{C.15}$$

where,

$$F^{(m)}(x) = 3\,\frac{x\cosh(x)-\sinh(x)}{x^3} \tag{C.16}$$

Note that $k_{\alpha\beta}$ and $\Omega_{\alpha\beta}^{(1,0,n)}$ are proportional to each other: $k_{\alpha\beta} = 8\times\Omega_{\alpha\beta}^{(1,0,n)}$.

The limit case $M_{\alpha\beta}\longrightarrow 0$ is interesting because the previous integrals tend toward the classical Chapman-Cowling integrals [179]:

$$\Omega_{\alpha\beta}^{(l,r,n)} \underset{M_{\alpha\beta}\longrightarrow 0}{\longrightarrow} \Omega_{\alpha\beta}^{(l,r)} = \sqrt{\frac{kT_{\alpha\beta}}{2\pi m_{\alpha\beta}}}\int_0^{+\infty}\xi^{2r+3}e^{-\xi^2}Q_{\alpha\beta}^{(l)}\left(\sqrt{\frac{2kT_{\alpha\beta}}{m_{\alpha\beta}}}\xi\right)\mathrm{d}\xi \tag{C.17}$$

$$\Omega_{\alpha\beta}^{(l,r,m)} \underset{M_{\alpha\beta}\longrightarrow 0}{\longrightarrow} \Omega_{\alpha\beta}^{(l,r)} = \sqrt{\frac{kT_{\alpha\beta}}{2\pi m_{\alpha\beta}}}\int_0^{+\infty}\xi^{2r+3}e^{-\xi^2}Q_{\alpha\beta}^{(l)}\left(\sqrt{\frac{2kT_{\alpha\beta}}{m_{\alpha\beta}}}\xi\right)\mathrm{d}\xi \tag{C.18}$$

In this work, only $\Omega_{\alpha\beta}^{(1,0,n)}$, $\Omega_{\alpha\beta}^{(1,1,m)}$ and $\Omega_{\alpha\beta}^{(1,1,n)}$ are used.

C.4 Derivation of multi-fluid source terms

In this section, the source terms of the fluid equations used in Chapter 6 are derived. The general expressions, given by Benilov [111, 112], for inelastic and elastic source terms are:

Inelastic collisions

$$w_\alpha = -k_{\alpha\beta} n_\alpha n_\beta \tag{C.19}$$

$$\mathbf{w}_\alpha^{(m)} = -m_\alpha k_{\alpha\beta} n_\alpha n_\beta \left[\mathbf{u}_\alpha - \frac{m_{\alpha\beta} T_\alpha}{m_\alpha T_{\alpha\beta}} \left(\frac{2}{3} \frac{\Omega_{\alpha\beta}^{(1,1,m)}}{\Omega_{\alpha\beta}^{(1,0,n)}} - 1 \right) (\mathbf{u}_\beta - \mathbf{u}_\alpha) \right] \tag{C.20}$$

$$\begin{aligned} w_\alpha^{(e)} = & -k_{\alpha\beta} n_\alpha n_\beta \left[\frac{3k_B T_\alpha}{2} + \frac{m_\alpha \mathbf{u}_\alpha^2}{2} - \frac{m_{\alpha\beta} T_\alpha}{m_\alpha T_{\alpha\beta}} \left(\frac{2}{3} \frac{\Omega_{\alpha\beta}^{(1,1,m)}}{\Omega_{\alpha\beta}^{(1,0,n)}} - 1 \right) m_\alpha \mathbf{u}_\alpha \cdot (\mathbf{u}_\beta - \mathbf{u}_\alpha) \right] \\ & - k_{\alpha\beta} n_\alpha n_\beta \frac{m_{\alpha\beta} T_\alpha}{m_\alpha T_{\alpha\beta}} \left(\frac{2}{3} \frac{\Omega_{\alpha\beta}^{(1,1,n)}}{\Omega_{\alpha\beta}^{(1,0,n)}} + \frac{2}{3} \mathcal{M}_{\alpha\beta}^2 \left(1 - 2 \frac{\Omega_{\alpha\beta}^{(1,1,m)}}{\Omega_{\alpha\beta}^{(1,0,n)}} \right) - 1 \right) \frac{3k_B T_\alpha}{2} \end{aligned} \tag{C.21}$$

Elastic collisions

$$\mathbf{r}_{\alpha\beta}^{(m)} = \frac{16}{3} m_{\alpha\beta} \Omega_{\alpha\beta}^{(1,1,m)} n_\alpha n_\beta (\mathbf{v}_\alpha - \mathbf{u}_\beta) \tag{C.22}$$

$$r_{\alpha\beta}^{(e)} = \frac{16}{3} \frac{m_{\alpha\beta}}{m_\alpha + m_\beta} \Omega_{\alpha\beta}^{(1,1,m)} n_\alpha n_\beta \left(3 \frac{\Omega_{\alpha\beta}^{(1,1,n)}}{\Omega_{\alpha\beta}^{(1,1,m)}} k_B (T_\alpha - T_\beta) + \frac{m_\alpha T_\beta \mathbf{u}_\alpha + m_\beta T_\alpha \mathbf{u}_\beta}{T_{\alpha\beta}} (\mathbf{v}_\alpha - \mathbf{u}_\beta) \right) \tag{C.23}$$

Recall that the species included in the model are: I_2 molecules, $I_{1/2}$ and $I_{3/2}$ atoms and electrons. Four types of collision are considered:

1. **Elastic** collisions between an **electron** and a **neutral** species
2. **Inelastic** collisions between an **electron** and a **neutral** species
3. **Elastic** collisions between **neutrals**
4. **Inelastic** collisions between **neutrals**

Note that ions are not included in the model and, consequently, no collisions between ions and neutrals are accounted for, even if the formalism allows for it.

C.4.1 Elastic collisions between an electron and a neutral species

The following applies to elastic reactions between an electron and a heavy species $\mathrm{h} \in \{\mathrm{I}_2, \mathrm{I}_{1/2}, \mathrm{I}_{3/2}\}$. The simplified rates are:

$$\mathbf{r}_{\mathrm{he}}^{(m)} = \mathbf{0}, \tag{C.24}$$

$$r_{\mathrm{he}}^{(e)} = \frac{16}{3} n_e n_{\mathrm{h}} \Omega_{\mathrm{he}}^{(1,1)} \times 3 \frac{m_e}{m_{\mathrm{h}}} k_{\mathrm{B}} (T_{\mathrm{h}} - T_e). \tag{C.25}$$

C.4.2 Inelastic collisions between an electron and a neutral species

The following applies to **dissociation**, atomic **excitation** and atomic **de-excitation**. The rates for the reactant heavy species are:

$$w_{\mathrm{h}} = -K_{\mathrm{h}e} n_{\mathrm{h}} n_e, \tag{C.26}$$

$$\mathbf{w}_{\mathrm{h}}^{(m)} = -m_{\mathrm{h}} K_{\mathrm{h}e} n_{\mathrm{h}} n_e \mathbf{u}_{\mathrm{h}}, \tag{C.27}$$

$$w_{\mathrm{h}}^{(e)} = -K_{\mathrm{h}e} n_{\mathrm{h}} n_e \left[\frac{3 k_B T_{\mathrm{h}}}{2} + \frac{m_{\mathrm{h}} \mathbf{u}_{\mathrm{h}}^2}{2} \right]. \tag{C.28}$$

The rates for the produced heavy species are the same with an opposite sign. However, the energy term for **dissociation** has to be slightly modified since the produced atoms are energetic. Considering that only $\mathrm{I}_{3/2}$ atoms are produced during the dissociation of I_2, the creation term reads:

$$w_{\mathrm{I}_{3/2}}^{(e)} = K_{\mathrm{diss},\mathrm{I}_2} n_{\mathrm{I}_2} n_e \left[\frac{3 k_B T_{\mathrm{I}_2}}{2} + \frac{m_{\mathrm{I}_2} \mathbf{u}_{\mathrm{I}_2}^2}{2} + 2\Delta\mathcal{E}_{\mathrm{diss},\mathrm{I}_2} \right]. \tag{C.29}$$

This is similar to what was done in the global model presented in Chapter 5 with $\Delta\mathcal{E}_{\mathrm{diss},\mathrm{I}_2} = 0.5$ eV. The factor 2 comes from the production of 2 atoms for 1 process.

C.4.3 Elastic collisions between neutrals

The following applies to elastic collisions between two different heavy species h_1 and h_2. In this case, we treat the collision as a hard spheres collision, whose momentum transfer cross-section reads:

$$Q_{\mathrm{h}_1\mathrm{h}_2}^{(1)} = \pi \left(\frac{d_{\mathrm{h}_1} + d_{\mathrm{h}_2}}{2} \right)^2, \tag{C.30}$$

where d_{h_1} and d_{h_2} are h_1 and h_2 diameters.

Then to derive $\mathbf{r}_{\mathrm{h}_1\mathrm{h}_2}^{(m)}$ and $r_{\mathrm{h}_1\mathrm{h}_2}^{(e)}$, in the case of hard sphere collisions, one needs to to evaluate $\Omega_{\mathrm{h}_1\mathrm{h}_2}^{(1,1,m)}$ and $\Omega_{\mathrm{h}_1\mathrm{h}_2}^{(1,1,n)}$, with $Q_{\mathrm{h}_1\mathrm{h}_2}^{(1)}$ given by equation (C.30):

$$\Omega_{\mathrm{h}_1\mathrm{h}_2}^{(1,1,m)} = \Omega_{\mathrm{h}_1\mathrm{h}_2}^{(1,1)} \times \frac{3}{8} \left(\frac{\sqrt{\pi}\,\mathrm{erf}(\mathcal{M}_{\mathrm{h}_1\mathrm{h}_2})}{\mathcal{M}_{\mathrm{h}_1\mathrm{h}_2}} \left(1 + \mathcal{M}_{\mathrm{h}_1\mathrm{h}_2}^2 - \frac{1}{4\mathcal{M}_{\mathrm{h}_1\mathrm{h}_2}^2} \right) + e^{-\mathcal{M}_{\mathrm{h}_1\mathrm{h}_2}^2} \left(1 + \frac{1}{2\mathcal{M}_{\mathrm{h}_1\mathrm{h}_2}^2} \right) \right) \tag{C.31}$$

$$\Omega_{\mathrm{h}_1\mathrm{h}_2}^{(1,1,n)} = \Omega_{\mathrm{h}_1\mathrm{h}_2}^{(1,1)} \times \frac{1}{16} \left(\frac{\sqrt{\pi}\,\mathrm{erf}(\mathcal{M}_{\mathrm{h}_1\mathrm{h}_2})}{\mathcal{M}_{\mathrm{h}_1\mathrm{h}_2}} \left(3 + 12\mathcal{M}_{\mathrm{h}_1\mathrm{h}_2}^2 + 4\mathcal{M}_{\mathrm{h}_1\mathrm{h}_2}^4 \right) + e^{-\mathcal{M}_{\mathrm{h}_1\mathrm{h}_2}^2} \left(10 + 4\mathcal{M}_{\mathrm{h}_1\mathrm{h}_2}^2 \right) \right) \tag{C.32}$$

with $\mathrm{erf} : \mathcal{M} \longmapsto \mathrm{erf}(\mathcal{M})$ the Gauss error function and

$$\Omega_{\mathrm{h}_1\mathrm{h}_2}^{(1,1)} = Q_{\mathrm{h}_1\mathrm{h}_2}^{(1)} \times \sqrt{\frac{k T_{\mathrm{h}_1\mathrm{h}_2}}{2\pi m_{\mathrm{h}_1\mathrm{h}_2}}}. \tag{C.33}$$

This formula was used in Chapter 1.
Only low Mach numbers (<0.4) are required in this thesis and the following approximations are used:

$$\frac{\Omega^{(1,1,m)}_{\mathrm{h_1h_2}}}{\Omega^{(1,1)}_{\mathrm{h_1h_2}}} \underset{\mathcal{M}_{\mathrm{h_1h_2}}\longrightarrow 0}{=} 1+\frac{\mathcal{M}^2_{\mathrm{h_1h_2}}}{5}+\mathrm{o}(\mathcal{M}^3_{\mathrm{h_1h_2}}), \tag{C.34}$$

$$\frac{\Omega^{(1,1,n)}_{\mathrm{h_1h_2}}}{\Omega^{(1,1)}_{\mathrm{h_1h_2}}} \underset{\mathcal{M}_{\mathrm{h_1h_2}}\longrightarrow 0}{=} 1+\mathcal{M}^2_{\mathrm{h_1h_2}}+\mathrm{o}(\mathcal{M}^3_{\mathrm{h_1h_2}}), \tag{C.35}$$

$$\frac{\Omega^{(1,1,n)}_{\mathrm{h_1h_2}}}{\Omega^{(1,1,m)}_{\mathrm{h_1h_2}}} \underset{\mathcal{M}_{\mathrm{h_1h_2}}\longrightarrow 0}{=} 1+\frac{4\mathcal{M}^2_{\mathrm{h_1h_2}}}{5}+\mathrm{o}(\mathcal{M}^3_{\mathrm{h_1h_2}}.) \tag{C.36}$$

The low-Mach approximations are justified in Figure C.1 where the formulae show a very good agreement with the exact formulae, for Mach numbers inferior to 1.

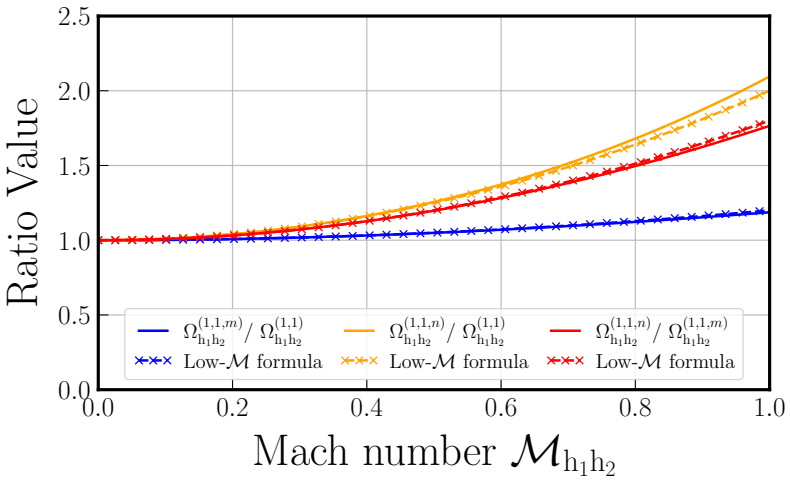

Figure C.1: Cross-sections for momentum transfer ratios when considering hard sphere collisions between h_1 and h_2 as a function of the Mach number. Simplest equivalent formulae at low Mach are also plotted to evidence the good matching for $\mathcal{M}_{\alpha\beta}<1$.

Finally, the expressions used for $\mathbf{r}^{(m)}_{\mathrm{h_1h_2}}$ and $r^{(e)}_{\mathrm{h_1h_2}}$ are:

$$\mathbf{r}^{(m)}_{\mathrm{h_1h_2}}=\frac{16}{3}\left(1+\frac{\mathcal{M}^2_{\mathrm{h_1h_2}}}{5}\right)m_{\mathrm{h_1h_2}}\Omega^{(1,1)}_{\mathrm{h_1h_2}}n_{\mathrm{h_1}}n_{\mathrm{h_2}}(\mathbf{u}_{\mathrm{h_1}}-\mathbf{u}_{\mathrm{h_2}}) \tag{C.37}$$

$$r^{(e)}_{\mathrm{h_1h_2}}=\frac{16}{3}\left(1+\frac{\mathcal{M}^2_{\mathrm{h_1h_2}}}{5}\right)\frac{m_{\mathrm{h_1h_2}}}{m_{\mathrm{h_1}}+m_{\mathrm{h_2}}}\Omega^{(1,1)}_{\mathrm{h_1h_2}}n_{\mathrm{h_1}}n_{\mathrm{h_2}}\times \left[3\left(1+\frac{4\mathcal{M}^2_{\mathrm{h_1h_2}}}{5}\right)k_B(T_{\mathrm{h_1}}-T_{\mathrm{h_2}})+\frac{m_{\mathrm{h_1}}T_{\mathrm{h_2}}\mathbf{u}_{\mathrm{h_1}}+m_{\mathrm{h_2}}T_{\mathrm{h_1}}\mathbf{u}_{\mathrm{h_2}}}{T_{\mathrm{h_1h_2}}}(\mathbf{u}_{\mathrm{h_1}}-\mathbf{u}_{\mathrm{h_2}})\right] \tag{C.38}$$

In Chapter 5, equation (C.38) was used by setting the velocities to 0.

C.4.4 Inelastic collisions between neutrals

The following applies to inelastic collisions between two different heavy species h_1 and h_2. It is used to derive the source terms for the **quenching** process in the multi-fluid model.

We assume the inelastic collision to be a Maxwell molecule collision, i.e. the momentum transfer cross-section is proportional to the inverse of the energy:

$$Q^{(1)}_{\mathrm{h}_1\mathrm{h}_2} \propto 1/\xi. \tag{C.39}$$

Under this assumption, the modified Chapman-Cowling integrals compute exactly and one can find:

$$\frac{\Omega^{(1,1,n)}_{\mathrm{h}_1\mathrm{h}_2}}{\Omega^{(1,0,n)}_{\mathrm{h}_1\mathrm{h}_2}} = \frac{1}{2}\left(3+\mathcal{M}^2_{\mathrm{h}_1\mathrm{h}_2}\right), \qquad \frac{\Omega^{(1,1,m)}_{\mathrm{h}_1\mathrm{h}_2}}{\Omega^{(1,0,n)}_{\mathrm{h}_1\mathrm{h}_2}} = \frac{3}{2}. \tag{C.40}$$

Finally, the expression for the rates are:

$$\begin{aligned} w_{\mathrm{h}_1} &= -k_{\mathrm{h}_1\mathrm{h}_2} n_{\mathrm{h}_1} n_\beta \\ \mathbf{w}^{(m)}_{\mathrm{h}_1} &= -m_{\mathrm{h}_1} k_{\mathrm{h}_1\mathrm{h}_2} n_{\mathrm{h}_1} n_{\mathrm{h}_2} \mathbf{u}_{\mathrm{h}_1} \qquad \text{(C.41)} \\ w^{(e)}_{\mathrm{h}_1} &= -k_{\mathrm{h}_1\mathrm{h}_2} n_{\mathrm{h}_1} n_{\mathrm{h}_2} \left[\frac{3k_B T_{\mathrm{h}_1}}{2}\left(1-\frac{m_{\mathrm{h}_1\mathrm{h}_2} T_{\mathrm{h}_1}}{m_{\mathrm{h}_1} T_{\mathrm{h}_1\mathrm{h}_2}}\mathcal{M}^2_{\mathrm{h}_1\mathrm{h}_2}\right)+\frac{m_{\mathrm{h}_1}\mathbf{u}^2_{\mathrm{h}_1}}{2}\right] \qquad \text{(C.42)} \end{aligned}$$

The rates for the produced heavy species are the same with an opposite sign.

APPENDIX D

ABSOLUTE ENERGY SHIFT OF THE IODINE ATOMIC EXCITED STATES

The following is extracted from [2].

Wavelength calibration

The lambdameter used for wavelength measurements was calibrated daily with a saturated-absorption stabilized diode laser, using the the $6s\,^2S_{1/2}\,F = 4 \rightarrow 6p\,^2P^o_{3/2}\,F' = 5$ component of the D2 line of cesium at 852.1 nm. Reliability of that calibration at remote wavelengths was checked by measuring the position of two hyperfine components of the D1 transition, the wavelength of which, ca 894.3 nm, offers the advantage of being very close, in the infrared, to the wavelength of 894.6 nm generated, before frequency tripling, for $5s^2 5p^5\,^2P^o_{3/2} \rightarrow (^3P_2)6p\,^2[1]^o_{3/2}$ excitation of iodine. The offset between the reference and measured frequencies was no more than 15 MHz. Another effect to consider is a possible frequency shift of the injected pulsed laser relative to the measured frequency of the CW seeder. Heterodyne measurements made it possible to check that the pulsed laser mean output frequency is equal to that of the seed laser to within 20 MHz and may drift by 20 MHz during the pulse [180]. The sum of these three contributions gives a possible systematic error of $15 + 20 + 20 = 55$ MHz. The tripled frequency thus appears determined with an uncertainty of 165 MHz and the precision of the measured frequency of the two-photon transition around $65000\,cm^{-1}$ is 330 MHz, i.e. $0.011\,cm^{-1}$.

Energy levels of atomic iodine

As for the existing data on the excited levels of atomic iodine, the relative energies of the levels between 50000 and 80000 cm^{-1} have reached a precision of 0.005 cm^{-1}, thanks to infrared Fourier-transform (IR-FT) spectroscopy [81]. IR spectroscopy, however, cannot determine absolute energies with respect to the atomic ground level. As a consequence, the re-optimization carried out after IR-FT spectroscopy has only improved the positions of these upper states with respect to the lowest

level from an excited configuration, namely $(^3P_2)6s\,^2[2]_{5/2}$, the assumed energy of which, 54633.46 cm^{-1}, remained the one provided by the previous review of the energy levels [80]. This combination remains today the one given in the NIST atomic data table for I I [34], the energy levels of which are thus identical to those of [81] for excited configurations below 80000 cm^{-1}. The same study also provided the magnetic dipole and electric quadrupole hyperfine structure constants of 37 even levels and 42 odd levels, which makes it possible to calculate the corresponding hyperfine structures [81]. Atomic energy levels, as listed in the table, are to be considered as the barycenters of the hyperfine multiplets.

The 54633.46 cm^{-1} energy of the $(^3P_2)6s\,^2[2]_{5/2}$ level [34, 80, 81], which serves as the basis for the upper part of the spectrum, comes from vacuum ultra-violet (VUV) spectroscopy of the corresponding resonance line, which yielded a wavelength of 183.0380 nm [181].

Knowing the fine-structure interval of the $(^3P_2)6s\,^2[2]$ doublet from spectroscopy of the upper transitions related to both its $J = 5/2$ and $J = 3/2$ states, one can deduce the $(^3P_2)6s\,^2[2]_{5/2} - 5p^5\,^2P^o_{1/2}$ interval from the measurement of the 206.1633 nm wavelength of the $(^3P_2)6s\,^2[2]_{3/2} - 5p^5\,^2P^o_{1/2}$ transition, which has been attributed a 48489.73 cm^{-1} wavenumber. The difference provides a measure of the fine structure interval of the ground term, 7603.15 cm^{-1} [181], which was the value retained in the 1962 review of the I I spectrum [80].

However, this 7603.15 cm^{-1} value of the ground term $^2P^o_{1/2} - {}^2P^o_{3/2}$ fine-structure interval appeared but marginally compatible with the 7602.7 cm^{-1} value that had been repeatedly published by Murakawa [182–184], as with the independent measurement of a wavenumber of 7605.03 ± 0.1 cm^{-1} in air, i.e. 7602.95 ± 0.1 cm^{-1} in vacuum [185]. Another value of the same interval could be deduced from the wavenumbers of the $(^3P_2)7s\,^2[2]_{3/2} - 5p^5\,^2P^o_{3/2}$ and $(^3P_2)7s\,^2[2]_{3/2} - 5p^5\,^2P^o_{1/2}$ transitions, as measured by Martin [80], and even though the uncertainty of the corresponding $72294.1 - 64692.1 = 7602.0\,cm^{-1}$ difference must be of the order of $1\,cm^{-1}$, it also suggested that the 7603.15(6) cm^{-1} value could be slightly overestimated. That was confirmed by IR-FT spectroscopy, which finally found a mean fine-structure interval of 7602.977 ± 0.003 cm^{-1} [83], i.e. a value lower by 0.180 cm^{-1} (sic) than the one deduced from VUV spectroscopy [181].

A precise measurement of the fine-structure interval of the ground term does not give immediate information on the energy of higher-excited levels. It tells a lot, however, on what the uncertainty of VUV spectroscopy must have been, to make a VUV-wavenumber difference miss the much more accurate value later obtained by IR-FT spectroscopy by 0.18 cm^{-1}. As the 206 nm line was measured with a greater care and "relative to international secondary standards in the iron arc spectrum" [181], while the 178 and 183 nm wavelengths were measured in a less direct way "making use of the combination principle", uncertainties of 0.09 and 0.18 cm^{-1}, for the 206 nm and VUV lines respectively, appear reasonable. Smaller uncertainties, taking into account all data described above but ours, would make some corrections of the energies of the first three excited levels of I I go beyond a standard deviation. On this basis, explicit optimization of the energy levels already leads to recommend a revision of the energy of the $(^3P_2)6s\,^2[2]_{5/2}$ level, hence of the energies of all upper levels, by -0.120 ± 0.075 cm^{-1}. Despite the fact this does not look very precise, the recommendation already implies, however, that the upper energy levels of I I actually lie well below the ± 0.005 cm^{-1} uncertainty intervals that have been attached to

them in the commonly used data table [34].

Much more information is brought forward by our observation of a −0.169(12) cm^{-1} shift of the two studied levels of the $(^3P_2)6p$ configuration. Injection of their updated positions into the energy level-optimization algebra makes the shift of the whole upper spectrum much more precise, with a recommended correction of −0.169(11) cm^{-1} (one can make the a posteriori remark that since the wavenumber associated to the 178 nm line directly determines the energy of one of these levels, its uncertainty could not have been smaller in absolute value). Concurrently, the wavenumber of the 206 nm line, which had appeared changed from the original 48489.73 cm^{-1} [181] to a strikingly different 48489.911 cm^{-1} in the NIST table [34], gets restored to a 48489.744 cm^{-1} value much closer to the original one. The fact the associated correction drops back to 0.014 cm^{-1}, i.e. much less than the 0.09 cm^{-1} uncertainty that we have attached to it, may be regarded as a demonstration of the consistency of the spectrometry of the 206 nm line [181], the accurate measurement of the ground-term fine structure [83] and the present laser-spectroscopy measurements of the $(^3P_2)6p[1]^o_{3/2}$ and $(^3P_2)6p[3]^o_{7/2}$ wavenumbers (see subsection 4.3.2).

BIBLIOGRAPHY

[1] B. Esteves, F. Marmuse, C. Drag, A. Bourdon, A. Alvarez Laguna, and P. Chabert, "Charged-particles measurements in low-pressure iodine plasmas used for electric propulsion", Plasma Sources Science and Technology **31**, 085007 (2022) (cit. on pp. xiii, 1, 2, 21, 39, 117, 188, 209, 210, 215, 216).

[2] B. Esteves, C. Blondel, P. Chabert, and C. Drag, "Two-photon absorption laser induced fluorescence (TALIF) detection of atomic iodine in low-temperature plasmas and a revision of the energy levels of I I", Journal of Physics B: Atomic, Molecular and Optical Physics, 10 . 1088 / 1361 - 6455 / acb7b6 (2023) (cit. on pp. xiii, 155, 156, 186, 267).

[3] A. Alvarez Laguna, B. Esteves, A. Bourdon, and P. Chabert, "A regularized high-order moment model to capture non-Maxwellian electron energy distribution function effects in partially ionized plasmas", Physics of Plasmas **29**, 083507 (2022) (cit. on p. xiii).

[4] A. Alvarez Laguna, B. Esteves, J.-L. Raimbault, A. Bourdon, and P. Chabert, "Discussion on the transport processes in electrons with non-Maxwellian energy distribution function in partially-ionized plasmas", *Submitted to* Plasma Physics and Controlled Fusion (2022) (cit. on p. xiii).

[5] B. Esteves, C. Drag, A. Bourdon, A. Alvarez Laguna, and P. Chabert, "Experimental and numerical investigation of a gridded ion thruster running with different propellants (I_2, Xe, Kr, Ar)", in 37th International Electric Propulsion Conference (2022), https://tinyurl.com/25vfr8v8 (cit. on p. xiii).

[6] G. R. Brewer, M. R. Currie, and R. C. Knechtli, "Ionic and Plasma Propulsion for Space Vehicles", Proceedings of the IRE **49**, 1789–1821 (1961) (cit. on p. 1).

[7] S. Mazouffre, "Electric propulsion for satellites and spacecraft: established technologies and novel approaches", Plasma Sources Science and Technology **25**, 033002 (2016) (cit. on p. 1).

[8] P. Dietz, W. Gärtner, Q. Koch, P. E. Köhler, Y. Teng, P. R. Schreiner, K. Holste, and P. J. Klar, "Molecular propellants for ion thrusters", Plasma Sources Science and Technology **28**, 084001 (2019) (cit. on pp. 1, 3).

[9] J. Szabo and M. Robin, "Plasma Species Measurements in the Plume of an Iodine Fueled Hall Thruster", Journal of Propulsion and Power **30**, 1357–1367 (2014) (cit. on pp. 1, 2).

[10]K. Holste, P. Dietz, S. Scharmann, K. Keil, T. Henning, D. Zschätzsch, M. Reitemeyer, B. Nauschütt, F. Kiefer, F. Kunze, J. Zorn, C. Heiliger, N. Joshi, U. Probst, R. Thüringer, C. Volkmar, D. Packan, S. Peterschmitt, K.-T. Brinkmann, H.-G. Zaunick, M. H. Thoma, M. Kretschmer, H. J. Leiter, S. Schippers, K. Hannemann, and P. J. Klar, "Ion thrusters for electric propulsion: Scientific issues developing a niche technology into a game changer", Review of Scientific Instruments **91**, 061101 (2020) (cit. on p. 1).

[11]K. Holste, W. Gärtner, D. Zschätzsch, S. Scharmann, P. Köhler, P. Dietz, and P. J. Klar, "Performance of an iodine-fueled radio-frequency ion-thruster", The European Physical Journal D **72**, 9 (2018) (cit. on pp. 1, 2).

[12]D. Rafalskyi, J. M. Martínez, L. Habl, E. Zorzoli Rossi, P. Proynov, A. Boré, T. Baret, A. Poyet, T. Lafleur, S. Dudin, and A. Aanesland, "In-orbit demonstration of an iodine electric propulsion system", Nature **599**, 411–415 (2021) (cit. on pp. 1, 2).

[13]P. Grondein, T. Lafleur, P. Chabert, and A. Aanesland, "Global model of an iodine gridded plasma thruster", Physics of Plasmas **23**, 033514 (2016) (cit. on pp. 1, 2, 14, 21, 22, 24, 27, 29, 32, 38, 39, 188, 195, 206, 209, 210).

[14]J. Yang, S. Jia, Z. Zhang, X. Zhang, T. Jin, L. Li, Y. Cai, and J. Cai, "Performance of a 4 cm iodine-fueled radio frequency ion thruster", Plasma Science and Technology **22**, 094006 (2020) (cit. on p. 1).

[15]X. Niu, X. Li, H. Liu, and D. Yu, "Fluid simulation of ionization process in iodine cusped field thruster", The European Physical Journal D **73**, 169 (2019) (cit. on p. 1).

[16]D. Levko and L. L. Raja, "Fluid modeling of inductively coupled iodine plasma for electric propulsion conditions", Journal of Applied Physics **130**, 173302 (2021) (cit. on pp. 1, 2, 14, 21, 223).

[17]T. Lafleur, L. Habl, E. Zorzoli Rossi, and D. Rafalskyi, "Development and validation of an iodine plasma model for gridded ion thrusters", Plasma Sources Science and Technology **31**, 114001 (2022) (cit. on pp. 1, 2, 21, 39, 41, 189).

[18]T. Kaiho, in *Iodine Chemistry and Applications* (Wiley, 2014) (cit. on p. 2).

[19]K. Hora, "Iodine production and industrial applications", IDD Newsletter **44** (2016), https://www.ign.org/newsletter/idd_aug16_iodine_production.pdf (cit. on p. 2).

[20]P. Chabert, *Propulseur a plasma electronegatif*, European Patent, EP1957792B1, 2005, https://patents.google.com/patent/EP1957792B1/fr (cit. on p. 2).

[21]R. Lucken, "Theory and simulation of low-pressure plasma transport phenomena : Application to the PEGASES Thruster", PhD thesis (Université Paris-Saclay, 2019), http://www.theses.fr/2019SACLX046 (cit. on pp. 2, 3, 21, 28, 30, 32, 33, 37, 39, 45, 188).

[22]F. Marmuse, "Iodine plasmas : experimental and numerical studies. Application to electric propulsion", PhD thesis (Sorbonne Université, 2020), http://www.theses.fr/2020SORUS110 (cit. on pp. 2, 3, 14, 18, 21, 22, 24, 27, 28, 32, 33, 37, 49, 52, 53, 56, 57, 120, 134, 139, 143, 145, 160, 178, 188, 198).

[23]J. Szabo, M. Robin, S. Paintal, B. Pote, V. Hruby, and C. Freeman, "Iodine Plasma Propulsion Test Results at 1–10 kW", IEEE Transactions on Plasma Science **43**, 141–148 (2015) (cit. on p. 2).

[24]M. J. Martínez, D. Rafalskyi, and A. Aanesland, "Development and Testing of the NPT30-I2 Iodine Ion Thruster", 36th International Electric Propulsion Conference, 1–11 (2019) (cit. on p. 2).

[25]R. S. Stewart, G. A. Woolsey, J. M. Brown, J. R. M. Coulter, and K. G. Emeléus, "Correlation of Spectroscopic and Electrical Properties of Glow Discharges through Iodine", Proceedings of the Royal Irish Academy. Section A: Mathematical and Physical Sciences **64**, 85–91 (1964), http://www.jstor.org/stable/20488636 (cit. on p. 2).

[26]G. A. Woolsey, I. C. Plumb, and D. B. Lewis, "Langmuir probe characteristics in a positive-ion/negative-ion plasma", Journal of Physics D: Applied Physics **6**, 1883 (1973) (cit. on pp. 2, 13, 44, 93, 203, 204).

[27]H. Liebl and W. W. Harrison, "Study of an iodine discharge in a duoplasmatron", International Journal of Mass Spectrometry and Ion Physics **22**, 237–246 (1976) (cit. on p. 2).

[28]H. B. Ambalampitiya, K. R. Hamilton, O. Zatsarinny, K. Bartschat, M. A. P. Turner, A. Dzarasova, and J. Tennyson, "Electron Scattering Cross-Section Calculations for Atomic and Molecular Iodine", Atoms **9**, 103 (2021) (cit. on pp. 2, 13, 21, 22, 24–31, 147, 189).

[29]H. Yadav, M. Vinodkumar, C. Limbachiya, P. C. Vinodkumar, and N. J. Mason, "Low energy electron interactions with Iodine molecule (I_2)", Journal of Quantitative Spectroscopy and Radiative Transfer **250**, 107035 (2020) (cit. on pp. 2, 13, 21, 26, 27, 29, 30).

[30]D. Filin, I. M. Savukov, and J. Colgan, "CI-MBPT line strengths and atomic probabilities for some transitions of neutral iodine", Journal of Physics B: Atomic, Molecular and Optical Physics **53**, 145003 (2020) (cit. on pp. 2, 6, 16, 160).

[31]T. E. Steinberger and E. E. Scime, "Laser-induced fluorescence of singly ionized iodine", Journal of Propulsion and Power **34**, 1235–1239 (2018) (cit. on p. 2).

[32]P. Grondein, "Investigation de l'iode comme propergol pour la propulsion ionique à grilles", PhD thesis (Paris 6, 2016), http://theses.fr/2016PA066350 (cit. on pp. 3, 52, 56).

[33]L. T. Calvoso Habl, "Investigation of DC and RF biased gridded ion thruster plume phenomena", PhD thesis (Institut Polytechnique de Paris, 2022), https://theses.hal.science/tel-03689405 (cit. on p. 3).

[34]A. Kramida, Y. Ralchenko, J. Reader, and N. A. Team, *NIST Atomic Spectra Database* (ver. 5.9), [Online, 2022, March 22]. National Institute of Standards and Technology, Gaithersburg, MD, 2021, https://physics.nist.gov/asd (cit. on pp. 6, 13, 19, 23–25, 87, 101, 103, 141, 155, 156, 268, 269).

[35]S. Pancheshnyi, S. Biagi, M. Bordage, G. J. M. Hagelaar, L. Morgan, A. Phelps, and L. Pitchford, "The LXCat project: Electron scattering cross sections and swarm parameters for low temperature plasma modeling", Chemical Physics **398**, 10.1016/j.chemphys.2011.04.020 (2012) (cit. on pp. 6, 252).

[36]B. D. Van Sijde, J. J. A. M. Van der Mullen, and D. C. Schram, "Collisional radiative models in plasmas", Beiträge aus der Plasmaphysik **24**, 447–473 (1984) (cit. on p. 6).

[37]H. C. Kim, F. Iza, S. S. Yang, M. Radmilović-Radjenović, and J. K. Lee, "Particle and fluid simulations of low-temperature plasma discharges: benchmarks and kinetic effects", Journal of Physics D: Applied Physics **38**, R283 (2005) (cit. on p. 6).

[38]L. L. Alves, A. Bogaerts, V. Guerra, and M. M. Turner, "Foundations of modelling of nonequilibrium low-temperature plasmas", Plasma Sources Science and Technology **27**, 023002 (2018) (cit. on p. 6).

[39]J. Van Dijk, G. M. W. Kroesen, and A. Bogaerts, "Plasma modelling and numerical simulation", Journal of Physics D: Applied Physics **42**, 190301 (2009) (cit. on p. 6).

[40]S. Gerstenkorn and P. Luc, *Atlas du spectre d'absorption de la molecule d'iode 14800-20000 cm^{-1}* (1978), https://ui.adsabs.harvard.edu/abs/1978adsa.book....G (cit. on pp. 6, 10).

[41]R. D. Verma, "Ultraviolet resonance spectrum of the iodine molecule", Journal of Chemical Physics **32**, 738–749 (1960) (cit. on pp. 6, 9, 10).

[42]J. Tellinghuisen, "Least-squares analysis of overlapped bound-free absorption spectra and predissociation data in diatomics: The C($^1\Pi_u$) state of I_2", Journal of Chemical Physics **135**, 054301 (2011) (cit. on pp. 6, 11, 149).

[43]J. J. Larsen, I. Wendt-Larsen, and H. Stapelfeldt, "Controlling the branching ratio of photodissociation using aligned molecules", Physical review letters **83**, 1123–1126 (1999) (cit. on pp. 6, 154).

[44]J. R. Wiesenfeld and R. H. Young, "Branching ratio for the production of I($^2P_{1/2}$) in the photodissociation of I_2", Chemical Physics **58**, 51–56 (1981) (cit. on pp. 6, 154).

[45]T. F. Hunter and C. M. Leong, "Absolute yields of I($^2P_{1/2}$) in I_2 photodissociation using a laser optoacoustic technique", Chemical Physics **111**, 145–153 (1987) (cit. on pp. 6, 28, 154).

[46]G. M. Lawrence, "Resonance Transition Probabilities in Intermediate Coupling for Some Neutral Non-Metals", Astrophysical Journal **148**, 261 (1967) (cit. on pp. 6, 16).

[47]R. H. Garstang, "Transition probabilities of forbidden lines", Journal of Research of the National Bureau of Standards. Section A, Physics and Chemistry **68**, 61 (1964) (cit. on pp. 6, 16, 17).

[48]R. Engleman, B. A. Palmer, and S. J. Davis, "Transition probability and collision broadening of the 1.3-μm transition of atomic iodine", Journal of the Optical Society of America **73**, 1585–1589 (1983) (cit. on pp. 6, 16, 17).

[49]T.-K. Ha, Y. He, J. Pochert, M. Quack, R. Ranz, G. Seyfang, and I. Thanopoulos, "Absolute integrated band strength and magnetic dipole transition moments in the $^2P_{3/2} \rightarrow ^2P_{1/2}$ fine structure (with hyperfine structure) transition of the iodine atom: Experiment and theory", Berichte der Bunsengesellschaft für physikalische Chemie **99**, 384–392 (1995) (cit. on pp. 6, 16, 17, 145, 160–162, 164, 178, 180, 181, 222).

[50]A. Kono and S. Hattori, "Radiative-lifetime measurements for I I and I II", Journal of the Optical Society of America **69**, 253–255 (1979) (cit. on pp. 6, 8, 16, 150, 159).

[51]J. Tellinghuisen, "Transition strengths in the visible–infrared absorption spectrum of I_2", Journal of Chemical Physics **76**, 4736–4744 (1982) (cit. on pp. 8, 11, 150).

[52]S. Lukashov, A. Petrov, and A. Pravilov, in *The Iodine Molecule* (Cham: Springer International Publishing, 2018) (cit. on pp. 9, 10, 13, 27, 30, 149).

[53]I. J. McNaught, "The electronic spectrum of iodine revisited", Journal of Chemical Education **57**, 101 (1980) (cit. on p. 9).

[54]G. Herzberg, in *Molecular Spectra and molecular structure*, Vol. 1 (Read Books Limited, 2013) (cit. on p. 9).

[55]J. T. Gudmundsson, E. Kawamura, and M. A. Lieberman, "A benchmark study of a capacitively coupled oxygen discharge of the oopd1 particle-in-cell Monte Carlo code", Plasma Sources Science and Technology **22**, 035011 (2013) (cit. on pp. 10, 37, 45).

[56]R. D'alterio, R. Mattson, and R. Harris, "Potential curves for the I_2 Molecule: An undergraduate physical chemistry experiment", Journal of Chemical Education **51**, 282 (1974) (cit. on p. 10).

[57]J. Tellinghuisen, "The D' → A' transition in I_2", Journal of Molecular Spectroscopy **94**, 231–252 (1982) (cit. on p. 10).

[58]M. A. Lieberman and A. J. Lichtenberg, in *Principles of plasma discharges and materials processing*, Second edition (Wiley-Interscience, 2005) (cit. on pp. 11, 13, 40, 100, 195, 253, 255).

[59]J. Franck and E. G. Dymond, "Elementary processes of photochemical reactions", Transactions of the Faraday Society **21**, 536–542 (1926) (cit. on pp. 11, 148).

[60]E. Condon, "A Theory of Intensity Distribution in Band Systems", Physical Review **28**, 1182–1201 (1926) (cit. on pp. 11, 148).

[61]E. U. Condon, "The Franck-Condon principle and related topics", American journal of physics **15**, 365–374 (1947) (cit. on p. 11).

[62]W. E. Curtis and S. F. Evans, "The spectra of the halogen molecules. Part I. Iodine", Proceedings of the Royal Society of London. Series A, Containing Papers of a Mathematical and Physical Character **141**, 603–625 (1933) (cit. on p. 11).

[63]J. Tellinghuisen, "Resolution of the visible-infrared absorption spectrum of I_2 into three contributing transitions", Journal of Chemical Physics **58**, 2821–2834 (1973) (cit. on pp. 11, 148).

[64]J. Tellinghuisen, "The Franck-Condon Principle in Bound-Free Transitions", in *Advances in Chemical Physics* (John Wiley & Sons, Ltd, 1985), pp. 299–369 (cit. on p. 11).

[65]C. Teichteil and M. Pelissier, "Relativistic calculations of excited states of molecular iodine", Chemical Physics **180**, 1–18 (1994) (cit. on p. 11).

[66]J. Williamson, "Teaching the Rovibronic Spectroscopy of Molecular Iodine", Journal of Chemical Education **84**, 1355 (2007) (cit. on p. 11).

[67]D. Schwarzer, J. Schroeder, and C. Schröder, "Quantum Yields for the Photodissociation of Iodine in Compressed Liquids and Supercritical Fluids", Zeitschrift für Physikalische Chemie **215**, 183 (2001) (cit. on p. 11).

[68]A. Saiz-Lopez and J. M. C. Plane, "Novel iodine chemistry in the marine boundary layer", Geophysical research letters **31**, L04112 (2004) (cit. on pp. 12, 145, 150).

[69]J. Ye, L. S. Ma, and J. L. Hall, "Molecular iodine clock", Physical Review Letters **87**, 270801 (2001) (cit. on p. 11).

[70]J. B. Burkholder, S. P. Sander, J. P. D. Abbatt, J. R. Barker, C. Cappa, J. D. Crounse, T. S. Dibble, R. E. Huie, C. E. Kolb, M. J. Kurylo, et al., *Chemical kinetics and photochemical data for use in atmospheric studies; evaluation number 19*, tech. rep. (Jet Propulsion Laboratory, NASA, 2020), http://hdl.handle.net/2014/49199 (cit. on p. 12).

[71]M. C. R. Cockett, R. J. Donovan, and K. P. Lawley, "Zero kinetic energy pulsed field ionization (ZEKE-PFI) spectroscopy of electronically and vibrationally excited states of I_2^+: The $A\ ^2\Pi_{3/2,u}$ state and a new electronic state, the $a\ ^4\Sigma_u^-$ state", Journal of Chemical Physics **105**, 3347–3360 (1996) (cit. on pp. 12, 27).

[72]J. Spencer-Smith, "LXXXIII. Negative ions of iodine. Part II. Ion beams", The London, Edinburgh, and Dublin Philosophical Magazine and Journal of Science **19**, 1016–1027 (1935) (cit. on pp. 12, 32).

[73]R. Healey, "LXXX. The behaviour of electrons in iodine vapour", The London, Edinburgh, and Dublin Philosophical Magazine and Journal of Science **26**, 940–953 (1938) (cit. on pp. 12, 21, 29).

[74]R. Buchdahl, "Negative ion formation in iodine vapor by electron impacts", Journal of Chemical Physics **9**, 146–152 (1941) (cit. on pp. 12, 21, 29).

[75]M. A. Biondi and R. E. Fox, "Dissociative attachment of electrons in iodine. III. Discussion", Physical Review **109**, 2012 (1958) (cit. on pp. 12, 29).

[76]W.-C. Tam and S. F. Wong, "Dissociative attachment of halogen molecules by 0–8 eV electrons", Journal of Chemical Physics **68**, 5626–5630 (1978) (cit. on pp. 12, 204, 213).

[77]K. G. Emeleus and J. R. M. Coulter, "Notes on discharges in low-pressure iodine vapour", International Journal of Electronics **54**, 777–786 (1983) (cit. on pp. 12, 204, 213).

[78]R. J. Peláez, C. Blondel, C. Delsart, and C. Drag, "Pulsed photodetachment microscopy and the electron affinity of iodine", Journal of Physics B: Atomic, Molecular and Optical Physics **42**, 125001 (2009) (cit. on pp. 13, 29, 33, 93).

[79]M. T. Zanni, T. R. Taylor, B. J. Greenblatt, B. Soep, and D. M. Neumark, "Characterization of the I_2^- anion ground state using conventional and femtosecond photoelectron spectroscopy", Journal of Chemical Physics **107**, 7613–7619 (1997) (cit. on pp. 13, 95).

[80]L. Minnhagen, "The energy levels of neutral atomic iodine", Arkiv Fysik **21**, 415–478 (1962), https://www.osti.gov/biblio/4803016 (cit. on pp. 15, 16, 19, 22, 268).

[81]E. Luc-Koenig, C. Morillon, and J. Verges, "Etude Expérimentale et Théorique de l'Iode Atomique. Observation du Spectre d'Arc Infrarouge, Classification et Structure Hyperfine", Physica Scripta **12**, 199 (1975) (cit. on pp. 15–17, 19, 139–141, 156, 157, 267, 268).

[82]D. Cerny, R. Bacis, B. Bussery, M. Nota, and J. Verges, "Experimental determination and calculation of the collision relaxation rates in the 5 $^2P_{1/2}$ and 5 $^2P_{3/2}$ levels of atomic iodine", Journal of Chemical Physics **95**, 5790–5798 (1991) (cit. on p. 17).

[83]E. Luc-Koenig, C. Morillon, and C. Vergès, "Etude de la transition "interdite" $^2P_{1/2} \rightarrow ^2P_{1/2}$ de la configuration np5 dans le brome et l'iode par spectrometrie de fourier", Physica **70**, 175–189 (1973) (cit. on pp. 17, 18, 268, 269).

[84]V. Jaccarino, J. G. King, R. A. Satten, and H. H. Stroke, "Hyperfine structure of I 127. Nuclear magnetic octupole moment", Physical Review **94**, 1798 (1954) (cit. on p. 18).

[85]J. R. Hamilton and J. Tennyson, *Consultancy project for LPP. I_2 and I^- data.* Tech. rep., (Private communication) (Quantemol Ltd, 2015) (cit. on pp. 21, 22, 24, 27, 29, 188).

[86]R. Lucken, F. Marmuse, A. Bourdon, P. Chabert, and A. Tavant, "Global model of a magnetized ion thruster with xenon and iodine", in 36th International Electric Propulsion Conference (2019), http://electricrocket.org/2019/678.pdf (cit. on pp. 21, 188).

[87]J. R. Hamilton and J. Tennyson, *Iodine: I_2 molecule and I atom*, tech. rep., (Private communication) (Quantemol Ltd, 2017) (cit. on pp. 21, 33).

[88]M. Poline, X. Yuan, S. Badin, M. C. Ji, S. Rosén, S. Indrajith, R. D. Thomas, H. T. Schmidt, H. Zettergren, A. S. P. Gomes, and N. Sisourat, "Final-state-resolved mutual neutralization in I^+ - I^- collisions", Physical Review A **106**, 012812 (2022) (cit. on pp. 21, 30, 33).

[89]C. Greaves, "Ion-Ion Recombination in Iodine Afterglows", Journal of Electronics and Control **17**, 171–180 (1964) (cit. on pp. 21, 32).

[90]M. L. Hause, B. D. Prince, and R. J. Bemish, "A guided-ion beam study of the collisions and reactions of I^+ and I_2^+ with I_2", Journal of Chemical Physics **142**, 074301 (2015) (cit. on pp. 21, 37, 38).

[91]O. Zatsarinny, K. Bartschat, G. Garcia, F. Blanco, L. R. Hargreaves, D. B. Jones, R. Murrie, J. R. Brunton, M. J. Brunger, M. Hoshino, et al., "Electron-collision cross sections for iodine", Physical Review A **83**, 042702 (2011) (cit. on p. 21).

[92]J. T. Gudmundsson and E. G. Thorsteinsson, "Oxygen discharges diluted with argon: dissociation processes", Plasma Sources Science and Technology **16**, 399 (2007) (cit. on pp. 21, 188).

[93]E. Kemaneci, J.-P. Booth, P. Chabert, J. van Dijk, T. Mussenbrock, and R. P. Brinkmann, "A computational analysis of the vibrational levels of molecular oxygen in low-pressure stationary and transient radio-frequency oxygen plasma", Plasma Sources Science and Technology **25**, 025025 (2016) (cit. on p. 21).

[94]S. Huang and J. T. Gudmundsson, "A particle-in-cell/Monte Carlo simulation of a capacitively coupled chlorine discharge", Plasma Sources Science and Technology **22**, 055020 (2013) (cit. on pp. 21, 30, 37, 45).

[95]E. G. Thorsteinsson and J. T. Gudmundsson, "A global (volume averaged) model of a chlorine discharge", Plasma Sources Science and Technology **19**, 015001 (2009) (cit. on pp. 21, 32, 33, 38, 40, 44, 188, 199, 202, 209, 213, 214).

[96]T. E. Magin, M. Panesi, A. Bourdon, R. L. Jaffe, and D. L. Schwenke, "Coarse-grain model for internal energy excitation and dissociation of molecular nitrogen", Chemical Physics **398**, 90–95 (2012) (cit. on p. 25).

[97]E. Torres, R. L. Jaffe, D. Schwenke, and T. E. Magin, "Coarse-grain cross sections for rovibrational excitation and dissociation of the N_2-N system", Chemical Physics **533**, 110701 (2020) (cit. on p. 25).

[98]B. M. Smirnov and H. Reiss, in *Physics of Ionized Gases* (John Wiley & Sons, 2001) (cit. on pp. 26, 32).

[99]G. J. Tallents, in *An introduction to the atomic and radiation physics of plasmas* (Cambridge University Press, 2018) (cit. on pp. 27, 28).

[100]H. M. Rosenstock, K. Draxl, B. W. Steiner, and J.-T. Herron, *Energetics of gaseous ions*, tech. rep. (National Standard Reference Data System, 1977), https://apps.dtic.mil/sti/citations/ADD095037 (cit. on p. 29).

[101]D. Mathur and C. Badrinathan, "A new channel for observing giant resonances: Dissociative ionization of molecular iodine by electrons", Physics Letters A **123**, 345–348 (1987) (cit. on p. 29).

[102]R. S. Mulliken, "Iodine revisited", Journal of Chemical Physics **55**, 288–309 (1971) (cit. on p. 30).

[103]K.-P. Huber, in *Molecular spectra and molecular structure: IV. Constants of diatomic molecules* (Springer US, 2013) (cit. on p. 30).

[104]B. D. Prince, D. J. Levandier, and R. J. Bemish, "Application of a first generation collisional radiative model for iodine to optical emissions from the plume of an iodine Hall effect thruster", in 53rd AIAA/SAE/ASEE Joint Propulsion Conference (2017), p. 4634 (cit. on p. 30).

[105]D. E. Shemansky, J. M. Ajello, and I. Kanik, "Electron Excitation Function of the N_2 Second Positive System", American Physical Journal **452**, 472 (1995) (cit. on p. 30).

[106]G. L. Rogoff, J. M. Kramer, and R. B. Piejak, "A model for the bulk plasma in an RF chlorine discharge", IEEE transactions on plasma science **14**, 103–111 (1986) (cit. on p. 30).

[107]D. L. Thompson, "Monte Carlo classical dynamical study of the Cl + Cl_2 and I + I_2 systems: Vibrational relaxation and atom-exchange reactions", Journal of Chemical Physics **60**, 4557–4567 (1974) (cit. on p. 31).

[108]D. Marinov, M. Foucher, E. Campbell, M. Brouard, P. Chabert, and J.-P. Booth, "High sensitivity ultra-broad-band absorption spectroscopy of inductively coupled chlorine plasma", Plasma Sources Science and Technology **25**, 035019 (2016) (cit. on pp. 31, 145, 148).

[109]T. H. Y. Yeung and J. Sayers, "An RF probe technique for the measurement of plasma electron concentrations in the presence of negative ions", Proceedings of the Physical Society. Section B **70**, 663 (1957) (cit. on p. 32).

[110]K. Fritioff, J. Sandström, D. Hanstorp, A. Ehlerding, M. Larsson, G. F. Collins, D. J. Pegg, H. Danared, A. Källberg, and A. Le Padellec, "Electron-impact detachment from Cl^-", Physical Review A **68**, 012712 (2003) (cit. on p. 33).

[111]M. S. Benilov, "Multifluid equations of a plasma with various species of positive ions and the Bohm criterion", Journal of Physics D: Applied Physics **29**, 364–368 (1996) (cit. on pp. 34, 219, 259, 261).

[112]M. S. Benilov, "A kinetic derivation of multifluid equations for multispecies nonequilibrium mixtures of reacting gases", Physics of Plasmas **4**, 521–528 (1997) (cit. on pp. 34, 219, 259, 261).

[113]A. I. Chichinin, "Chemical properties of electronically excited halogen atoms X ($^2P_{1/2}$)(X = F, Cl, Br, I)", Journal of Physical and Chemical Reference Data **35**, 869–928 (2006) (cit. on pp. 36, 37, 163).

[114]P. Chabert, J. Arancibia-Monreal, J. Bredin, L. Popelier, and A. Aanesland, "Global model of a gridded-ion thruster powered by a radiofrequency inductive coil", Physics of Plasmas **19**, 073512 (2012) (cit. on pp. 38, 188, 195, 196, 206, 247).

[115]L. Brewer and J. B. Tellinghuisen, "Detection of iodine atoms by an atomic fluorescence technique: application to study of diffusion and wall recombination", Journal of Chemical Physics **54**, 5133–5138 (1971) (cit. on p. 39).

[116]G. P. Kota, J. W. Coburn, and D. B. Graves, "The recombination of chlorine atoms at surfaces", Journal of Vacuum Science & Technology A: Vacuum, Surfaces, and Films **16**, 270–277 (1998) (cit. on p. 39).

[117]E. Wassermann, W. E. Falconer, and W. A. Yager, "Photodissociation of Molecular Iodine", Berichte der Bunsengesellschaft für physikalische Chemie **72**, 248–252 (1968) (cit. on p. 39).

[118]G. E. Katsoprinakis, G. Chatzidrosos, J. A. Kypriotakis, E. Stratakis, and T. P. Rakitzis, "High steady-state column density of $I(^2P_{3/2})$ atoms from I_2 photodissociation at 532 nm: Towards parity non-conservation measurements", Scientific Reports **6**, 1–8 (2016) (cit. on pp. 39, 154).

[119]P. Chabert and N. Braithwaite, in *Physics of Radio-Frequency Plasmas* (Cambridge University Press, 2011) (cit. on pp. 40, 42, 79, 86, 88, 89, 91, 100, 107, 195, 199, 238, 255).

[120]V. A. Godyak, "Nonequilibrium EEDF in gas discharge plasmas", IEEE Transactions on Plasma Science **34**, 755–766 (2006) (cit. on p. 42).

[121]J. R. Henry, "Étude d'un plasma de gaz électronégatif: spectrométrie de masse et propagation des ondes ioniques longitudinales", (printed version only), PhD thesis (Université Paris VII, 1972) (cit. on pp. 44, 93).

[122]L. Popelier, "Développement du propulseur PEGASES : source inductive à haute performance et accélération successive de faisceaux d'ions positifs et d'ions négatifs", PhD thesis (Ecole Polytechnique, 2012), http://www.theses.fr/2012EPXX0063 (cit. on p. 50).

[123]J. Bredin, "Développement de diagnostics électrostatiques pour le filtrage magnétique et la formation du plasma ion-ion dans le propulseur PEGASES", PhD thesis (Ecole Polytechnique, 2013), https://pastel.archives-ouvertes.fr/pastel-00993207 (cit. on pp. 50, 52, 81, 85).

[124]C. Bowick, in *RF circuit design*, RF Bundle, RF Circuit Design Series (Elsevier, 2011) (cit. on p. 52).

[125]V. A. Godyak, R. B. Piejak, and B. M. Alexandrovich, "Experimental setup and electrical characteristics of an inductively coupled plasma", Journal of Applied Physics **85**, 703–712 (1999) (cit. on p. 59).

[126]W. Jitschin, "Gas Flow", in *Handbook of Vacuum Technology* (John Wiley & Sons, Ltd, 2016) Chap. 4, pp. 83–166 (cit. on pp. 62, 65).

[127]M. J. Druyvesteyn, "Der Niedervoltbogen", Zeitschrift für Physik **64**, 781–798 (1930) (cit. on p. 77).

[128]H. M. Mott-Smith and I. Langmuir, "The Theory of Collectors in Gaseous Discharges", Physical Review **28**, 727–763 (1926) (cit. on p. 77).

[129]F. F. Chen, in *Introduction to plasma physics and controlled fusion*, Vol. 1 (Springer, 1984) (cit. on pp. 77, 88, 90, 96).

[130]V. A. Godyak and B. M. Alexandrovich, "Comparative analyses of plasma probe diagnostics techniques", Journal of Applied Physics **118**, 233302 (2015) (cit. on pp. 77, 80–82).

[131]V. A. Godyak, "RF discharge diagnostics: Some problems and their resolution", Journal of Applied Physics **129**, 041101 (2021) (cit. on pp. 77, 80–82, 86, 101).

[132]V. A. Godyak and V. I. Demidov, "Probe measurements of electron-energy distributions in plasmas: what can we measure and how can we achieve reliable results?", Journal of Physics D: Applied Physics **44**, 269501 (2011) (cit. on pp. 77, 81, 82).

[133]V. A. Godyak, R. B. Piejak, and B. M. Alexandrovich, "Electron energy distribution function measurements and plasma parameters in inductively coupled argon plasma", Plasma Sources Science and Technology **11**, 525–543 (2002) (cit. on pp. 81, 84, 86, 101).

[134]M. Bacal, G. W. Hamilton, A. M. Bruneteau, H. J. Doucet, and J. Taillet, "Measurement of H^- density in plasma by photodetachment", Review of Scientific Instruments **50**, 719–721 (1979) (cit. on pp. 93, 94).

[135]C. M. Philip, J. R. M. Coulter, and K. G. Emeleus, "Ion content of cold cathode glow discharges in iodine", International Journal of Electronics **29**, 565–573 (1970) (cit. on p. 93).

[136]M. Bacal, "Photodetachment diagnostic techniques for measuring negative ion densities and temperatures in plasmas", Review of Scientific Instruments **71**, 3981 (2000) (cit. on pp. 93, 94, 114).

[137]M. Neiger, "Quantitative Investigation of the Radiation of the Negative Iodine Ion", Zeitschrift für Naturforschung A **30**, 474–484 (1975) (cit. on p. 94).

[138]T. R. Taylor, K. R. Asmis, M. T. Zanni, and D. M. Neumark, "Characterization of the I_3 radical by anion photoelectron spectroscopy", Journal of Chemical Physics **110**, 7607–7609 (1999) (cit. on p. 95).

[139]P. Devynck, "Mesure de la densité et de la vitesse des ions H^- par photodétachement laser", Revue de physique appliquée **24**, 207–214 (1989) (cit. on pp. 111, 113).

[140]M. Nishiura, M. Sasao, and M. Bacal, "H^- laser photodetachment at 1064, 532, and 355 nm in plasma", Journal of applied physics **83**, 2944–2949 (1998) (cit. on pp. 112, 114).

[141]H. Katori and F. Shimizu, "Lifetime measurement of the $1s_5$ metastable state of argon and krypton with a magneto-optical trap", Physical review letters **70**, 3545 (1993) (cit. on p. 121).

[142]D. W. Preston, "Doppler-free saturated absorption: Laser spectroscopy", American Journal of Physics **64**, 1432–1436 (1996) (cit. on p. 124).

[143]W. L. Wiese, J. W. Brault, K. Danzmann, V. Helbig, and M. Kock, "Unified set of atomic transition probabilities for neutral argon", Physical Review A **39**, 2461–2471 (1989) (cit. on p. 125).

[144]P. Lottigier, A. Jucha, L. Cabaret, C. Blondel, and C. Drag, "Single-mode scannable nanosecond Ti: sapphire laser for high-resolution two-photon absorption laser-induced fluorescence (TALIF)", Applied Physics B **125**, 1–10 (2019) (cit. on pp. 125, 153, 155, 163).

[145]C. Delsart, *Lasers et optique non linéaire: cours, exercices et problèmes corrigés*, Physique-LMD, universités-écoles d'ingénieurs (Ellipses, 2008), https://books.google.fr/books?id=UzYOPQAACAAJ (cit. on pp. 126, 128).

[146]R. C. Hilborn, "Einstein coefficients, cross sections, f values, dipole moments, and all that", American Journal of Physics **50**, 982–986 (1982) (cit. on p. 127).

[147]H. Abada, P. Chabert, J.-P. Booth, J. Robiche, and G. Cartry, "Gas temperature gradients in a CF_4 inductive discharge", Journal of applied physics **92**, 4223–4230 (2002) (cit. on p. 132).

[148]D. A. Steck, *Cesium D line data*, (revision 2.2.1, 21 November 2019) (2019), https://steck.us/alkalidata/cesiumnumbers.pdf (cit. on p. 141).

[149]R. N. Zare and D. R. Herschbach, "Doppler line shape of atomic fluorescence excited by molecular photodissociation", Proceedings of the IEEE **51**, 173–182 (1963) (cit. on p. 148).

[150]E. J. Heller, "Quantum corrections to classical photodissociation models", Journal of Chemical Physics **68**, 2066–2075 (1978) (cit. on p. 148).

[151]V. V. Eryomin and N. E. Kuz'menko, "A new reflection method for solving direct and inverse problems for diatomic bound-free transitions", Chemical physics **136**, 127–139 (1989) (cit. on p. 148).

[152]J. Tellinghuisen, A. R. Whyte, and L. F. Phillips, "Kinetics of molecular iodine following argon fluoride (ArF) laser excitation: thermal dissociation of the A'(2u) state", Journal of Physical Chemistry **88**, 6084–6087 (1984) (cit. on pp. 149, 150).

[153]J. Tellinghuisen, "Intensity analysis of overlapped discrete and continuous absorption by spectral simulation: The electronic transition moment for the $B - X$ system in I_2", Journal of Chemical Physics **134**, 084301 (2011) (cit. on p. 149).

[154]J. K. K. Ip and G. Burns, "Recombination of iodine atoms by flash photolysis over a wide temperature range. II I_2 in He, Ar, Xe, N_2, CO", Journal of Chemical Physics **56**, 3155–3161 (1972) (cit. on p. 154).

[155]F. Biraben, B. Cagnac, and G. Grynberg, "Experimental evidence of two-photon transition without Doppler broadening", Physical Review Letters **32**, 643 (1974) (cit. on p. 155).

[156]G. Cunge, R. Ramos, D. Vempaire, M. Touzeau, M. Neijbauer, and N. Sadeghi, "Gas temperature measurement in CF_4, SF_6, O_2, Cl_2, and HBr inductively coupled plasmas", Journal of Vacuum Science & Technology A: Vacuum, Surfaces, and Films **27**, 471–478 (2009) (cit. on p. 157).

[157]C. Lee and M. A. Lieberman, "Global model of Ar, O_2, Cl_2, and Ar/O_2 high-density plasma discharges", Journal of Vacuum Science & Technology A: Vacuum, Surfaces, and Films **13**, 368–380 (1995) (cit. on pp. 188, 195).

[158]J. T. Gudmundsson, "On the effect of the electron energy distribution on the plasma parameters of an argon discharge: a global (volume-averaged) model study", Plasma Sources Science and Technology **10**, 76 (2001) (cit. on p. 188).

[159]E. Despiau-Pujo and P. Chabert, "Global model of instabilities in low-pressure inductive chlorine discharges", Plasma Sources Science and Technology **18**, 045028 (2009) (cit. on p. 188).

[160]E. G. Thorsteinsson and J. T. Gudmundsson, "A global (volume averaged) model of a Cl_2/Ar discharge: I. Continuous power", Journal of Physics D: Applied Physics **43**, 115201 (2010) (cit. on p. 188).

[161]E. G. Thorsteinsson and J. T. Gudmundsson, "A global (volume averaged) model of a Cl_2/Ar discharge: II. Pulsed power modulation", Journal of Physics D: Applied Physics **43**, 115202 (2010) (cit. on p. 188).

[162]D. M. Goebel, "Ion source discharge performance and stability", The Physics of Fluids **25**, 1093–1102 (1982) (cit. on p. 188).

[163]D. M. Goebel, "Analytical Discharge Model for RF Ion Thrusters", IEEE Transactions on Plasma Science **36**, 2111–2121 (2008) (cit. on p. 188).

[164]P. Chabert, "An expression for the h_l factor in low-pressure electronegative plasma discharges", Plasma Sources Science and Technology **25**, 025010 (2016) (cit. on pp. 191, 194).

[165]S. Ashida, C. Lee, and M. A. Lieberman, "Spatially averaged (global) model of time modulated high density argon plasmas", Journal of Vacuum Science & Technology A: Vacuum, Surfaces, and Films **13**, 2498–2507 (1995) (cit. on p. 195).

[166]C. Abrams, "Molecular Dynamics Simulations of Plasma-surface Chemistry", PhD thesis (University of California, Berkeley, 2000), https://books.google.fr/books?id=PqVNAQAAMAAJ (cit. on p. 197).

[167]E. Despiau-Pujo, "Etching of III-V semiconductors in inductively coupled chlorine plasmas", PhD thesis (Ecole Polytechnique, 2009), https://pastel.archives-ouvertes.fr/pastel-00005582 (cit. on pp. 197, 229).

[168]R. A. Svehla, *Estimated Viscosities and Thermal Conductivities of Gases at High Temperatures*, tech. rep. (1963), https://books.google.fr/books?id=jVHuwgpr9JoC (cit. on pp. 197, 198, 222, 253).

[169]A. S. Morillo-Candas, C. Drag, J.-P. Booth, T. C. Dias, V. Guerra, and O. Guaitella, "Oxygen atom kinetics in CO_2 plasmas ignited in a DC glow discharge", Plasma Sources Science and Technology **28**, 075010 (2019) (cit. on p. 201).

[170]J. Guha, V. M. Donnelly, and Y.-K. Pu, "Mass and Auger electron spectroscopy studies of the interactions of atomic and molecular chlorine on a plasma reactor wall", Journal of Applied Physics **103**, 013306 (2008) (cit. on p. 213).

[171]B. Van Leer, "Towards the ultimate conservative difference scheme. V. A second-order sequel to Godunov's method", Journal of Computational Physics **32**, 101–136 (1979) (cit. on p. 225).

[172]A. Alvarez Laguna, T. Magin, M. Massot, A. Bourdon, and P. Chabert, "Plasma-sheath transition in multi-fluid models with inertial terms under low pressure conditions: comparison with the classical and kinetic theory", Plasma Sources Science and Technology **29**, 025003 (2020) (cit. on p. 226).

[173]S. Gottlieb and C.-W. Shu, "Total variation diminishing Runge-Kutta schemes", Mathematics of computation **67**, 73–85 (1998) (cit. on p. 226).

[174]J. H. Ferziger, M. Perić, and R. L. Street, in *Computational methods for fluid dynamics*, Vol. 3 (Springer, 2002) (cit. on p. 226).

[175]S. Samukawa, K. Sakamoto, and K. Ichiki, "Generating high-efficiency neutral beams by using negative ions in an inductively coupled plasma source", Journal of Vacuum Science & Technology A: Vacuum, Surfaces, and Films **20**, 1566–1573 (2002) (cit. on p. 249).

[176]C. Drag, F. Marmuse, and C. Blondel, "Measurement of the two-photon excitation cross-section of the $6p'[3/2]_2$ and $6p'[1/2]_0$ levels of Xe I at the wavelengths 224.3 and 222.6 nm", Plasma Sources Science and Technology **30**, 075026 (2021) (cit. on p. 252).

[177]S. F. Biagi, *Biagi-v7.1 database*. retrieved on January 10, 2020., 2004, www.lxcat.net (cit. on p. 252).

[178]S. F. Biagi, "A multiterm Boltzmann analysis of drift velocity, diffusion, gain and magnetic-field effects in argon-methane-water-vapour mixtures", Nuclear Instruments and Methods in Physics Research Section A: Accelerators, Spectrometers, Detectors and Associated Equipment **283**, 716–722 (1989) (cit. on p. 252).

[179]S. Chapman, T. G. Cowling, D. Burnett, and C. Cercignani, in *The Mathematical Theory of Non-uniform Gases: An Account of the Kinetic Theory of Viscosity, Thermal Conduction and Diffusion in Gases*, Cambridge Mathematical Library (Cambridge University Press, 1990) (cit. on p. 261).

[180]L. Cabaret and C. Drag, "Highly scannable injection seeded nanosecond Ti: sapphire ring laser", The European Physical Journal-Applied Physics **51**, 20702 (2010) (cit. on p. 267).

[181]C. Kiess and C. Corliss, "Description and analysis of the first spectrum of iodine", Journal of Research of the National Bureau of Standards. Section A, Physics and Chemistry **63**, 1 (1959) (cit. on pp. 268, 269).

[182]K. Murakawa, "über die Spektren I II, I I und Cl II", Zeitschrift für Physik **109**, 162–174 (1938) (cit. on p. 268).

[183]K. Murakawa and S. Suwa, "Das Bogenspektrum des Jods und das Quadrupolmoment von I^{127}", Zeitschrift für Physik **137**, 575–582 (1954) (cit. on p. 268).

[184]K. Murakawa, "The Arc Spectrum of Iodine and the Quadrupole Moment of I^{127}", Journal of the Physical Society of Japan **13**, 484–492 (1958) (cit. on p. 268).

[185]F. E. Eshbach and R. A. Fisher, "The first spectrum of Iodine in the region between 0.8 and 2.2 μm", Journal of the Optical Society of America **44**, 868–869 (1954) (cit. on p. 268).

DOCTORAL SCHOOL

Titre : Étude des plasmas d'iode pour les applications de propulsion spatiale

Mots clés : plasmas d'iode, propulsion électrique, diagnostics optiques, diagnostics électriques, simulations fluides, modèle global

Résumé : Depuis les années 1960, le gaz privilégié dans le domaine de la propulsion spatiale électrique est le xénon, un atome lourd et facile à ioniser. Néanmoins, sa production annuelle limitée et une demande grandissante obligent à trouver une alternative pérenne, aux performances comparables. L'iode est un candidat viable pour lui succéder. Dans ce travail, nous tâchons de comprendre comment et pourquoi l'iode, à l'état plasma, peut envisager sereinement la bataille avec ses concurrents dans la course à l'espace.

D'une part, ont été mis en place et développés, deux montages expérimentaux de plasmas d'iode (un propulseur à grille et une cellule en quartz) au sein desquels différents diagnostiques électriques et optiques (sonde de Langmuir, photodétachement, absorption, TALIF) ont été développés et appliqués avec succès, dont certains pour la première fois. Ces travaux expérimentaux ont permis de mesurer les valeurs absolues de densité et de température de différentes espèces du plasmas, mettant en lumière des mécanismes de chauffage important.

D'autre part, un travail rigoureux de bibliographie sur les données collisionnelles de l'iode atomique et moléculaire, a permis de développer des outils de simulation numérique visant à reproduire le fonctionnement des plasmas d'iode. Premièrement, un modèle 0D, a été mis à jour et enrichi pour prendre en compte le chauffage des espèces neutres. Deuxièmement, un modèle multi-fluide 1D des trois espèces neutres majoritaires ($I(^2P^\circ_{3/2})$, $I(^2P^\circ_{1/2})$, I_2) a été développé afin de simuler leurs densités, vitesses et températures le long de l'axe de poussée.

Les comparaisons expériences-modèles ont montré que: (i) à faible débit d'injection, le plasma est complètement dissocié et composé d'atomes I, d'ions I^+ et d'électrons. Dans ce régime de fonctionnement, où la dissociation est peu coûteuse énergétiquement, l'iode peut révolutionner le domaine de la propulsion électrique en étant plus performant que ses concurrents nobles (argon, krypton et xénon) ; (ii) à plus haut débit, les molécules ne sont plus négligeables et produisent facilement des ions négatifs I^- et moléculaires I_2^+. Dans ces conditions là, l'iode n'est plus compétitif pour la propulsion, le krypton offrant même de meilleures performances.

Title : Investigation of iodine plasmas for space propulsion applications

Keywords : iodine plasmas, electric propulsion, optical diagnostics, electrical diagnostics, fluid simulations, global modeling

Abstract : Since the 1960s, the most used gas for electric space propulsion has been xenon, a heavy atom that is easy to ionise. However, its limited annual production and growing demand require to find a sustainable alternative with comparable performance. Iodine is a viable candidate to succeed it. In this work, we try to understand how and why iodine, in its plasma state, can serenely face the battle with its competitors in the space race.

On the one hand, two experimental iodine plasma setups (a gridded-ion thruster and a quartz cell) were used, in which various electrical and optical diagnostics (Langmuir probe, photodetachment, absorption, TALIF) were developed and successfully applied, some of them for the first time. This experimental work allowed the measurement of the absolute values of density and temperature of different species in the plasma, highlighting important heating mechanisms.

On the other hand, a rigorous bibliography on the collision data of atomic and molecular iodine allowed the development of numerical simulation tools aiming at reproducing the functioning of iodine plasmas. Firstly, a 0D model was updated and enriched to take into account the heating of neutral species. Secondly, a 1D multi-fluid model of the three major neutral species ($I(^2P^\circ_{3/2})$, $I(^2P^\circ_{1/2})$, I_2) has been developed to simulate their densities, velocities and temperatures along the thrust axis.

Experimental-modeling comparisons have shown that: (i) at low injection rates, the plasma is completely dissociated and composed of I atoms, I^+ ions and electrons. In this operating regime, where dissociation is energetically inexpensive, iodine can revolutionize the field of electric propulsion by outperforming its noble competitors (argon, krypton and xenon); (ii) at higher flow rates, the molecules are no longer negligible and easily produce negative I^- and molecular I_2^+ ions. Under these conditions, iodine is no longer competitive for propulsion, with krypton offering even better performance.

Institut Polytechnique de Paris
91120 Palaiseau, France